

REPORT DOCUMENTATION PAGE			Form Approved OMB NO. 0704-0188		
<p>The public reporting burden for this collection of information is estimated to average 1 hour per response, including the time for reviewing instructions, searching existing data sources, gathering and maintaining the data needed, and completing and reviewing the collection of information. Send comments regarding this burden estimate or any other aspect of this collection of information, including suggestions for reducing this burden, to Washington Headquarters Services, Directorate for Information Operations and Reports, 1215 Jefferson Davis Highway, Suite 1204, Arlington VA, 22202-4302. Respondents should be aware that notwithstanding any other provision of law, no person shall be subject to any penalty for failing to comply with a collection of information if it does not display a currently valid OMB control number.</p> <p>PLEASE DO NOT RETURN YOUR FORM TO THE ABOVE ADDRESS.</p>					
1. REPORT DATE (DD-MM-YYYY) 19-06-2017		2. REPORT TYPE Final Report		3. DATES COVERED (From - To) 1-Oct-2010 - 31-Dec-2016	
4. TITLE AND SUBTITLE Final Report: Blast Induced Thresholds for Neuronal Networks (BITNeT)			5a. CONTRACT NUMBER W911NF-10-1-0526		
			5b. GRANT NUMBER		
			5c. PROGRAM ELEMENT NUMBER 611103		
6. AUTHORS Dale Bass, Barclay Morrison, David F. Meaney, Ted Abel			5d. PROJECT NUMBER		
			5e. TASK NUMBER		
			5f. WORK UNIT NUMBER		
7. PERFORMING ORGANIZATION NAMES AND ADDRESSES University of Pennsylvania Office of Research Services 3451 Walnut Street, Suite P-221 Philadelphia, PA 19104 -6205			8. PERFORMING ORGANIZATION REPORT NUMBER		
9. SPONSORING/MONITORING AGENCY NAME(S) AND ADDRESS (ES) U.S. Army Research Office P.O. Box 12211 Research Triangle Park, NC 27709-2211			10. SPONSOR/MONITOR'S ACRONYM(S) ARO		
			11. SPONSOR/MONITOR'S REPORT NUMBER(S) 58155-LS-MUR.117		
12. DISTRIBUTION AVAILABILITY STATEMENT Approved for Public Release; Distribution Unlimited					
13. SUPPLEMENTARY NOTES The views, opinions and/or findings contained in this report are those of the author(s) and should not be construed as an official Department of the Army position, policy or decision, unless so designated by other documentation.					
14. ABSTRACT Connecting the human brain response to blast loading across multiple length scales – from synapses through to circuit pathways and neurobehavior – remains a key challenge for developing countermeasures to limit the effects of blast in the military. Our MURI intends to help fill this gap by conducting a series of experiments connecting cell, tissue, and animal responses, developing scaling rules to predict the human experience. We examine circuits constructed in vitro and in vivo, and assess the effect of blast-induced circuit changes on the subsequent neurological impairment. We recruited and collaborate with experts in each of the necessary knowledge					
15. SUBJECT TERMS Blast induced threshold, neuronal networks, BITNet					
16. SECURITY CLASSIFICATION OF:			17. LIMITATION OF ABSTRACT UU	15. NUMBER OF PAGES	19a. NAME OF RESPONSIBLE PERSON David Meaney
a. REPORT UU	b. ABSTRACT UU	c. THIS PAGE UU			19b. TELEPHONE NUMBER 215-573-3155

RPPR
as of 18-Dec-2017

Agency Code:

Proposal Number:

Agreement Number:

Organization:

Address: , ,

Country:

DUNS Number:

EIN:

Date Received:

Report Date:

for Period Beginning and Ending

Title:

Begin Performance Period:

End Performance Period:

Report Term: -

Submitted By:

Email:

Phone:

Distribution Statement: -

STEM Degrees:

STEM Participants:

Major Goals:

Accomplishments:

Training Opportunities:

Results Dissemination:

Plans Next Period:

Honors and Awards:

Protocol Activity Status:

Technology Transfer:

Blast Induced Threshold of Neuronal Networks (BITNet)

A Multidisciplinary University Research Initiative

FINAL REPORT

Sponsored by: Army Research Office

Program Manager: Elmar Schmiesser, Ph.D. (Years 1+2)

Frederick Gregory, Ph.D. (Years 3-6)

David Stepp, Ph.D. (Years 1-6)

Participants:

Duke University (Dale Bass, Ph.D.)

Columbia University (Barclay Morrison, Ph.D.)

University of Pennsylvania (Ted Abel, Ph.D., David Meaney, Ph.D.)

EXECUTIVE SUMMARY

Connecting the human brain response to blast loading across multiple length scales – from synapses through to circuit pathways and neurobehavior – remains a key challenge for developing countermeasures to limit the effects of blast in the military. Our MURI intends to help fill this gap by conducting a series of experiments connecting cell, tissue, and animal responses, developing scaling rules to predict the human experience. We examine circuits constructed *in vitro* and *in vivo*, and assess the effect of blast-induced circuit changes on the subsequent neurological impairment. We recruited and collaborate with experts in each of the necessary knowledge domains to solve the complex problem of neuronal activation, injury, and tolerance to primary blast injury.

Our broad tasking areas include:

- examining the multiscale physics of blast wave transmission to the brain
- defining the thresholds for alterations in synaptic function, neural connectivity, and neuronal loss after blast
- identifying the transition point between synaptic/cellular changes and larger scale circuit dysfunction, leading to blast thresholds for altering circuit function.

In the initial year of the project, we achieved the following milestones:

- Assembled the equipment infrastructure and established standard operating protocols for blast testing at each of the three partner sites, allowing direct comparison of data collected across the programs
- Developed a novel coupled blast tube receiver for exposing *in vitro* preparations to a blast input pulse
- Started developing tolerance criteria for neuronal loss and dysfunction after blast
- Designed new imaging methods for measuring activity and network topology in *in vitro* neural preparations, applying these methods to models of physical and chemical injury
- Initiated studies of blast exposure to mice, beginning the process of developing scaling relationships across species
- To consider the impact of blast on the microvasculature, we built a new *in vitro* model of the blood brain barrier that would complement other *in vitro* preparations (dissociated cortical neurons, organotypic slice cultures).

In the second year of the project, we:

- Studied the process of blast wave transfer in the mouse, human, and *in vitro* preparations. Developed scaling criteria for apnea impairments
- Modeled the physics of blast wave transmission in the human, mouse and ferret
- Established a cellular tolerance threshold for blood brain barrier compromise *in vitro* following blast exposure, and for cellular death in organotypic slice cultures *in vitro*, and synaptic morphology changes *in vitro*
- Examined the alterations in synaptic signaling with changes in presynaptic release, postsynaptic changes in receptor content, and glial ensheathment
- Developed automated behavioral testing platform for measuring behavioral changes in rodents after blast exposure

- Developed and tested novel neurobehavior tasks for gyrencephalic animals; applying these tasks to identify new behavioral changes following blast.

In the third year of the project, we:

- Developed several animate finite element models of the brain and skull across length scales to examine scaling relationships
- Developed new tolerance data for bleeding within the brain (mild and moderate) following blast exposure
- Developed new scaling relationships for pressure and time across species
- Formulated new thresholds for BBB disruption following single or repeated blast exposure
- Measured the relative time window of recovery BBB compromise after blast
- Developed measures of impairment in organotypic hippocampal circuit function following blast
- Developed methodology to create a pure blast TBI model in the rodent, measuring the complex behavioral changes
- Developed and tested a new in vitro model for examining the response to blast exposure in vitro

In the fourth year of the project, we:

- Discovered a potentially new mechanism of tissue injury (shear shock)
- Used shear wave elasticity imaging (SWEI) to measure material properties in the living brain, and assess the influence of temperature on these properties
- Extended our neurotrauma scaling to include effects from blast induced barotrauma
- Continued our work to scale blast loading to gyrencephalic species (ferret)
- Extended our thresholds for in vitro compromise of the BBB to the living brain, working across labs to develop the corresponding in vivo BBB threshold
- Examined the effects of primary blast on the synchrony of activity throughout the hippocampus in vitro
- Measured thresholds for deficits in long term potentiation in vitro after blast
- Completely characterized the histopathological changes in the brain following primary blast, demonstrating that glial reactivity is the most prominent and persisting change after injury
- Characterized changes in hippocampal circuitry following primary blast injury, establishing thresholds for changes in synaptic remodeling 5 days following primary blast
- Evaluated the primary and secondary effects of serum extravasation on mixed neuronal/glial networks, showing that even very low serum exposure can affect the structure of networks within 24h

In the fifth year of the project, we:

- Used simulations of the mechanical response of the brain to blast exposure and estimated scaling relationships for severe brain injury following blast

- Developed and tested simulations of different shocktube designs (circular, square cross section) to study how the planarity of the shockwave is developed and maintained over the entire length of the tube
- Systematically studied the relative importance of placing the animal inside or just outside the shocktube exit, clarifying a great deal of confusion in the current literature
- Developed empirical data supporting a new phenomenon in tissue – the development of a transverse shock wave in the brain
- Defined the threshold for blood-brain barrier disruption in vivo following blast exposure
- Determined the critical threshold for blast exposure to cause neuronal cell death in organotypic hippocampal slice cultures
- Studied the relative threshold for loss of long-term potentiation (LTP) in OHSC after blast exposure
- Extended the studies of LTP deficits and neuronal loss to multiple blast exposures
- Identified thresholds for alterations in neural circuit alterations and viability following blast exposure in vitro
- Confirmed the role that primary blast alone can play in hippocampal deficits following blast exposure
- Extended a new imaging technology (miniaturized endoscope imaging) into use for studying the effect of blast injury on CA1 hippocampal networks in awake, behaving mice

In the extension year of funding, we:

- developed tolerance criteria for the loss in long term potentiation within the hippocampus in vitro after blast exposure
- discovered that we could reverse the deficits caused by blast in vitro by using a PDE-4 inhibitor
- extended the in vitro studies of hippocampal dysfunction after blast exposure to demonstrate changes occur following blast overpressure in vivo, are not associated with neuronal degeneration, but are associated with hippocampal-based deficits
- produced the first evidence of neuronal network dysfunction in vivo after blast in vivo using a new endoscopic imaging system in awake behaving animals; this dysfunction included a transient loss in activity and an alteration in hippocampal encoding after exposure
- created a new diagnostic for concussion after blast exposure, developing a technique for isolating neuronal exosomes after blast exposure. Recent work indicates we have a highly sensitive and specific method for detecting concussion using serum blood samples
- developed an analytical model of shear shock in brain tissue, supporting this model with ultrasound –based measurements of shear shock in brain tissue in situ
- expanded to the focus of the studies to examine the brain microbiome, as a subset of the murine microbiome, as a possible modulator of the response to blast overpressure

PERSONNEL SUPPORTED

The following are the personnel supported, wholly or in part, by the MURI:

University of Pennsylvania

Dave Meaney, Ph.D., (Penn PI) has supervised all aspects of the activities at Penn and is the overall project PI

Ted Abel, Ph.D., (Penn co-I) has provided expertise on the neurobehavioral testing and supervises one of the postdoctoral fellows (Hernandez) on the project

YungChia Chen, M.S., (graduate student; Johns Hopkins Univ/UMBC) has background in blast physics and provides design and testing expertise for the in vivo aspects of the project

Pepe Hernandez, Ph.D., has background in electrophysiology and neural behavior and provides experimental design input to the neurobehavior testing

Tanya Merdiushev, B.S., (Project Manager) is the project manager and supervises staff associated with the project in the Penn group

David Gullotti, B.S., (Research technician, Loyola University) provides support on both simulations of synaptic signaling and conduct of the neurobehavior testing

Tapan Patel, B.S. (Graduate Student, University of Delaware), provides support on the optical imaging methods for assessing neural activity (now completing his MD degree at the University of Pennsylvania)

Scott Ventre, (Undergraduate student, University of Pennsylvania), develops in silico models of neural network activity

Laura Baehr, B.S., (research technician), provides support for the cell culturing activities on the project.

Pedro Goncalves, B.S. (undergraduate intern, Georgia Tech) provides technical expertise for device fabrication and design

Tom Wolfemate, B.S., (undergraduate summer intern, University of Pennsylvania) provides cell culture experience and calcium imaging

Phoung Dong, B.S., (undergraduate workstudy; summer intern; University of Pennsylvania) provides support for cell culture and slice studies

Shanti Tummala, Ph.D., (postdoctoral fellow; Illinois Institute of Technology) provides experience in slice physiology and acute slice calcium imaging

Katie Kopil, Ph.D. (postdoctoral fellow; University of Pennsylvania) provides expertise for slice electrophysiology

Emily Sewell, B.S., (research technician), provides support for the cell culturing activities on the project.

Cheng Su, B.S., (undergraduate summer intern, University of Pennsylvania) provides cell culture experience and calcium imaging

Miguel de la Torre, (undergraduate workstudy student; University of Pennsylvania) provided support for the immunohistochemistry activities of the project

Shanti Tummala, Ph.D., (postdoctoral fellow; Illinois Institute of Technology) provides experience in slice physiology and acute slice calcium imaging

Matthew Hemphill, Ph.D., (postdoctoral fellow, Harvard University) is responsible for the in vitro cell culture network model and also works on the in vivo imaging aspect of the proposal

Brandon Parveese, (undergraduate summer intern; University of Pennsylvania) provided network simulation support and algorithm develop for the in vivo imaging aspects of the projects

David Gullotti, B.S., (Research technician, Loyola University) provides support on both simulations of synaptic signaling and conduct of the neurobehavior testing

Pedro Goncalves, B.S. (undergraduate intern, Georgia Tech) provides technical expertise for device fabrication and design

Tom Wolfemate, B.S., (undergraduate summer intern, University of Pennsylvania) provides cell culture experience and calcium imaging

Phoung Dong, B.S., (undergraduate workstudy; summer intern; University of Pennsylvania) provides support for cell culture and slice studies

Anthony Choo, Ph.D. (Postdoctoral fellow, University of Pennsylvania) provides technical expertise for the simulation of synaptic signaling

Duke University:

Cameron R 'Dale' Bass, Ph.D. (Duke University PI) has overseen all aspects of the research at Duke University.

Bruce Capehart, MD (Duke University Investigator) has overseen all medical aspects of the research at Duke University and has consulted on human blast behavior as Director of the OEF/OIF Veterans Program at the Durham VA Medical Center.

Roger Nightingale, Ph.D. (Duke University) consults on biomechanics issues for head trauma as needed.

Postdoctoral Associates

Jason Luck, (Ph.D. from Duke University) has consulted with graduate student investigators on the subjects of blunt trauma and impact injury.

Alayna Panzer, B.A., M.A., PhD (PhD from University of Guelph) has a background in blast physiology and psychology was a postdoctoral research associate whose main focus is psychological and physiological aspects of blast traumatic brain injury.

PhD Candidates

Matthew Panzer, B.S, M.Sc. (90% effort, Ph.D. graduate student, University of Waterloo, Duke University) has a background in blast computational biomechanics and is currently a graduate research assistant whose main focus is blast traumatic brain injury.

Garrett Wood, B.S. (h.D. graduate student, Duke University) has a background in biomedical engineering and is currently a graduate research assistant whose main focus was blast traumatic brain injury.

Jay Shridharani, B.S., M.S. (Ph.D. graduate student, Virginia Tech, Duke University) has a background in biomedical engineering and was currently a graduate research assistant whose main focus was blast traumatic brain injury.

NDSEG Fellowship - Allison Schmidt, M.S. (Ph.D. graduate student, Olin College) has a background in biomedical engineering and biomechanics and is a graduate research assistant whose main focus is statistics and characterization of materials.

Allen Yu, B.S. (Ph.D. graduate student, Duke University) has a background in biomedical engineering with an emphasis in impact biomechanics and is a graduate research assistant whose main focus is traumatic brain injury.

Caryn Urbanczyk, M.S. (Ph.D. graduate student, UCSD) has a background in biomedical engineering and biomechanics and whose main focus is ultrasound characterization of materials.

Duke Fellowship- Courtney Cox, BS (Ph.D. graduate student, Mercer) has a background in biomechanics. She has been tasked to this project as needed, provide scientific support.

Hattie Cutcliffe, BS (departmental fellowship, Ph.D. graduate student, Duke) has a background in biomechanics. She was tasked to this project as needed to provide scientific support.

Duke Fellowship - Maria Ortiz, M.S. (Ph.D. graduate student, Duke University) has a background in biomedical engineering and biomechanics. Her focus was blunt impact neurotrauma.

Duke Fellowship - Brian Bigler, M.S. (Ph.D. graduate student, Purdue U) has a background in biomedical engineering and biomechanics and is a graduate research assistant whose main focus is shear shock characterization.

Duke Fellowship, Anna Knight, BS (Ph.D. graduate student, Duke University) has a background in biomedical engineering and biomechanics and is a graduate research assistant whose main focus is injury biomechanics.

Undergraduate Students, Graduated

Duke Fellowship, Chris Eckersley (Duke University) graduated in 2016 from Columbia University Engineering in the biomedical engineering department. He assisted part-time on experimental setup and data collection.

Duke Fellowship, Virginia Chen (Undergraduate, Duke University) has a background in biomedical engineering and assisted in biological testing on an ongoing basis and as a summer project.

Elizabeth Palm (Undergraduate, Duke University) has a background in biomedical engineering and previously assisted in project testing/analysis.

Duke Fellowship - Calvin Lee, B.S. (Technician, Duke University) has a background in biomedical engineering and was tasked to this project to provide test/design support for biological testing.

Duke fellowship - Christopher Rich, has a background in biomedical engineering and has assisted in project testing/analysis and is a Pratt fellow candidate assigned to this project.

Duke fellowship - Christopher Rzeznick, has a background in biomedical engineering and has assisted in project testing/analysis and is a Pratt fellow candidate assigned to this project.

Duke fellowship - Rasheed Alhadi, has a background in biomedical engineering and has assisted in project testing/analysis and is a Pratt fellow candidate assigned to this project.

Duke fellowship - George Tsertsev has a background in biomedical engineering and has assisted in project testing/analysis and is a Pratt fellow candidate assigned to this project.

Duke fellowship, Anna Knight, has a background in biomedical engineering and has assisted in project testing/analysis and is a Pratt fellow candidate assigned to this project.

Duke fellowship – Kaustav Shah has a background in biomedical engineering and has assisted in project testing/analysis and is a Pratt fellow candidate assigned to this project.

Duke fellowship - Jingwei Deng has a background in biomedical engineering and has assisted in project testing/analysis and is a Pratt fellow candidate assigned to this project.

Brendan Smith (Undergraduate, Duke University) has a background in biomedical engineering and has assisted in project testing/analysis for this project.

Ivonna Dumamyan (Undergraduate, Duke University) has a background in biomedical engineering and has assisted in project testing/analysis for this project.

Matthew Mallick (Undergraduate, Duke University) has a background in biomedical engineering and has assisted in project testing/analysis for this project.

Jackson Moore (Undergraduate, Duke University) has a background in biomedical engineering and has assisted in project testing/analysis for this project.

Research Associates

Tina Naik, M.S. (Cornell University) has a background in biomedical engineering with an emphasis in impact biomechanics and is a research associate in animal research for neurotrauma. She and was tasked to this project to provide test/design support/animal handling and animal test support.

Calvin Lee, B.S. (30% effort, Technician, Duke University) has a background in biomedical engineering and was tasked to this project to provide test/design support for biological testing.

Bryan Kinda, B.S. (Technician, Duke University) has a background in biomedical engineering and was previously tasked to this project to provide test/design support for biological testing.

Kyle Matthews, B.S. (Duke University) has a background in biomedical engineering with an emphasis research instrumentation. He was tasked to this project to provide test/design support.

Jason Kait, M.S. (Duke University) has a background in biomedical engineering. Mr Kait assisted with numerous animal experiments.

Allen Yu, B.S. (Technician, Duke University) has a background in biomedical engineering and was tasked to this project to provide test/design support.

Columbia University:

20% Barclay Morrison, Ph.D. (Columbia University PI) has overseen all aspects of the research at Columbia University.

Post-doc

John Finan, Ph.D. (Ph.D. from Duke University) has a background in cellular biomechanics and was temporarily tasked to the project to help move it forward.

Graduate Students, Graduated

Edward Vogel, M.S. (Ph.D. graduate student, University of Maryland) has a background in biomedical engineering and biomechanics and is currently a graduate research assistant whose main focus is blast traumatic brain injury. He is committed to this project full-time. Thesis title: 'Pathobiological Mechanisms and Treatment of Electrophysiological Dysfunction Following Primary Blast-Induced Traumatic Brain Injury'

Gwen Effgen, Ph.D. graduated and has a background in physics and was a graduate research assistant whose main focus was blast traumatic brain injury. She was committed to this project full-time. Thesis title: 'Improving outcomes after repetitive mild traumatic brain injury from shock wave exposure or stretch injury'.

Christopher Hue, Ph.D. graduated has a background in biomedical engineering and was a graduate research assistant whose main focus was blast traumatic brain injury. He was committed to this project full-time. Thesis title: 'Blood-Brain Barrier Dysfunction and Repair after Blast-Induced Traumatic Brain Injury'

Woo Hyeun Kang, Ph.D. graduated has a background in biochemistry whose main focus is changes in electrophysiological function after mechanical injury. He was tasked to this project to help move it forward. Thesis title: 'Reducing the Societal Costs of Traumatic Brain Injury: Astrocyte-Based Therapeutics and Functional Injury Tolerance of the Living Brain'

Graduate Students, Enrolled

Sowmya Sundaresh, B.S. (Ph.D. graduate student, SUNY Stony Brook) has a background in biomedical engineering with an emphasis in neuroscience is a graduate research assistant whose main focus is traumatic brain injury. She is committed to this project full-time.

Undergraduate Students, Graduated

Ayelet Lobel (Barnard College) graduated in 2015 in the Department of Physics at Barnard College. She assists part-time on this project for tissue sample preparation, data collection, and blast injury execution.

Steve Rwema (Columbia University) graduated in 2016 from Columbia University Engineering in the biomedical engineering department. He assisted part-time on experimental setup and data collection.

Andrea Ortuno (Columbia University) graduated in 2016 from Columbia University Engineering in the biomedical engineering department. She assisted part-time on this project for data collection.

Stephanie Yang (Columbia University) graduated in 2016 from Columbia University Engineering in the biomedical engineering department. She assisted part-time on this project for maintaining slice cultures.

John Brady, B.S. (Columbia University) graduated in 2015 from Columbia University Engineering from the biomedical engineering department with an interest in neuroscience. He assisted part-time on this project for data collection and analysis.

Siqi Cao, B.S. (Columbia University) graduated in 2015 from Columbia University Engineering from the biomedical engineering department. She assisted part-time on this project for data collection and analysis.

Frances Cho, B.A. (Columbia University) graduated in 2015 from the neuroscience department at Columbia University. She assisted part-time on this project for data collection and analysis.

Shruthi Nammalwar, B.S. (Columbia University) graduated in 2015 from Columbia University Engineering from the biomedical engineering department. She assisted part-time on this project for data collection and analysis.

Tiffany Ong, B.S. (Columbia University) graduated in 2015 from Columbia University from the neuroscience department. She assisted part-time on this project for data collection and analysis.

Cosmas Sibindi (Columbia University) graduated in 2017 from Columbia University Engineering in the biomedical engineering department. He assisted part-time on this project for experimental set-up and data collection.

Nathalie Morales (Columbia University) graduated in 2017 from Columbia University in the biology department. She assisted part-time on this project for experimental set-up and data collection.

Andrew Dobitsch (Columbia University) graduated in 2016 from Columbia University in the neuroscience department. He assisted part-time on this project for data collection.

John Tyson III, B.A. (undergraduate, Richmond University) graduated in 2016 from Richmond University in the Physics department. He assisted on this project with experimental setup and data collection.

Jessica Villacorta (St. Mary's University, TX) graduated in 2015 from St. Mary's University. She assists part-time on this project for data collection, analysis and electrophysiology.

Zoe Ross (Columbia University) graduated in 2016 from Columbia University with an interest in neuroscience. She assists part-time on this project for data collection and analysis.

Sam Weinreb (Columbia University) graduated in 2015 from Columbia University. He assists part-time on this project for data collection and analysis.

Kiet Vo, B.A., B.S. (Whitman College and Columbia University) has a background in natural and mathematical sciences and biomedical engineering. He graduated Columbia University in 2012. He temporarily assisted part-time on this project for data collection and analysis.

Syed Haider (City College of NY) graduated City College of NY in 2013 and has a background in biological sciences and is currently a senior. He temporarily assisted part-time on this project for data collection and analysis.

Zafirah Baksh (Columbia University) graduated Columbia University in 2013 has a background in electrical engineering. She assists part-time on this project for electrophysiology data collection and analysis.

Elena Ripp (Columbia University) graduated Columbia University in 2014 with a background in applied math. She assists part-time on this project for tissue sample preparation.

Akaljot Singh (Columbia University) graduated from Columbia University in 2015 in neuroscience. He assists part-time on this project for data collection and analysis.

High School Students

Aaron Huang (high school, Pleasantville High School) was a rising senior with an interest in medicine and biomedical engineering. He assists part-time on this project for experimental set-up and data collection.

Lamia Ateshian (high school, Horace Mann School) was a rising freshman in college at MIT with an interest in medicine and biomedical engineering. She assists part-time on this project for experimental set-up and data collection.

Charles Levin (Teaneck High School) was a rising senior with an extensive interest in medicine and specifically neurophysiology. He assists part-time on this project for setting up and analyzing blast trials.

University of Pennsylvania:

Dave Meaney, Ph.D., (Penn PI) has supervised all aspects of the activities at Penn and is the overall project PI

Ted Abel, Ph.D., (Penn co-I) has provided expertise on the neurobehavioral testing and supervises one of the postdoctoral fellows (Hernandez) on the project

Ph.D. Students

YungChia Chen, M.S., (graduate student; Johns Hopkins Univ/UMBC) has background in blast physics and provides design and testing expertise for the in vivo aspects of the project

Pepe Hernandez, Ph.D., has background in electrophysiology and neural behavior and provides experimental design input to the neurobehavior testing

Tapan Patel, B.S. (Graduate Student, University of Delaware), provides support on the optical imaging methods for assessing neural activity (now completing his MD degree at the University of Pennsylvania)

Pallab Singh, (graduate student; University of Rochester) performed the NMDA receptor mechanosensitivity work in the first phase of the project

Jina Ko, (graduate student; Rice University) performed the exosome analysis in the last year of the project.

Alex Modupgepke (graduate student, Smith College) developed new functional imaging algorithms for examining connectivity after blast exposure

Postdoctoral fellows

Shanti Tummala, Ph.D., (postdoctoral fellow; Illinois Institute of Technology) provides experience in slice physiology and acute slice calcium imaging
Anthony Choo, Ph.D. (Postdoctoral fellow, University of Pennsylvania) provides technical expertise for the simulation of synaptic signaling
Katie Kopil, Ph.D. (postdoctoral fellow; University of Pennsylvania) provides expertise for slice electrophysiology
Matthew Hemphill, Ph.D., (postdoctoral fellow, Harvard University) is responsible for the in vitro cell culture network model and also works on the in vivo imaging aspect of the proposal

Research Assistants

Matt Beamer, B.S., (research technician), provides support for the cell culturing activities on the project.
Julia Valenziano, B.S., (research technician), provides support for the cell culturing activities on the project.
David Gullotti, B.S., (Research technician, Loyola University) provides support on both simulations of synaptic signaling and conduct of the neurobehavior testing
Laura Baehr, B.S., (research technician), provides support for the cell culturing activities on the project.
Tanya Merdiushev, B.S., (Project Manager) is the project manager and supervises staff associated with the project in the Penn group
Matt Beamer, B.S., (research technician), provides support for the cell culturing activities on the project.
Emily Sewell, B.S., (research technician), provides support for the cell culturing activities on the project.

Undergraduate students

Scott Ventre, (Undergraduate student, University of Pennsylvania), develops in silico models of neural network activity
Pedro Goncalves, B.S. (undergraduate intern, Georgia Tech) provides technical expertise for device fabrication and design
Tom Wolfemate, B.S., (undergraduate summer intern, University of Pennsylvania) provides cell culture experience and calcium imaging
Phoung Dong, B.S., (undergraduate workstudy; summer intern; University of Pennsylvania) provides support for cell culture and slice studies
Cheng Su, B.S., (undergraduate summer intern, University of Pennsylvania) provides cell culture experience and calcium imaging
Miguel de la Torra, (undergraduate workstudy student; University of Pennsylvania) provided support for the immunohistochemistry activities of the project

Section I: Duke University Final report

As a MURI partner, Duke had three primary responsibilities over the proposed 5 years of this project:

1. In collaboration with Penn and Columbia, to provide consistent and reproducible blast devices for measuring:
 - a. Cell death and dysfunction in organotypic brain slices and dissociated cortical cultures.
 - b. Behavioral changes in small organisms after blast loading, including gyrencephalic organisms.
2. In collaboration with Penn and Columbia, to develop interspecies scaling methods for blast loading that allow scaling from the subcellular level through animal models to the human. This includes regional and cell-specific response.
3. Defining and validating blast wave transmission to the in vivo brain.

In addition to the initially targeted efforts, Duke had several late spinout efforts that may bring important insights into blast neurotrauma and general neurotrauma. This includes a novel preliminary investigation of a potential microbiome of the brain that may have important physiological interactions with the physical insults in blast and blunt trauma but extends to the relevance of shear shock physics likely relevant for blast and blunt trauma.

INVESTIGATION OF SHEAR SHOCK BEHAVIOR APPLICABLE TO NEUROTRAUMA

Existing Hypotheses on Traumatic Brain Injury

Moderate-to-severe TBI in humans is often associated with skull fracture, contusions across multiple gyri, intracranial hemorrhage, brain swelling and progressive grey matter damage. However, in milder cases where these pathophysiological hallmarks of TBI are not present, current diagnostic imaging often shows little or no pathology and is only weakly correlated with clinical outcome (Hammoud and Wasserman., 2002).

While the exact mechanism for focal injuries is a subject of debate, movement of the brain within the skull has been accepted as a major etiological factor. Abrupt deceleration of the head and its inertial effect, cause a momentum transfer and the brain to collide with the inside of the skull. However, there is still a large question mark regarding the causal mechanism of diffuse axonal injury because torn, sheared or generally damaged neural tracts often appear away from expected coup and contrecoup injury sites.

Diffuse axonal injury, a feature in blunt and blast TBI, consists of white matter damage characterized by disrupted axonal transport, axonal swelling, and axonal detachment. Common locations for diffuse axonal injuries are the cortical-medullary junction, internal capsule, and corpus callosum (Grujicic et al., 2012). Modeling studies suggested inertial cavitation as a possible TBI mechanism, with pressure wave interactions in the confined environment causing damage (Nusholtz, 1995; Nusholtz et al., 1995). This would be strongly dependent on local tissue geometry and mechanical properties (Estrada and Franck, 2014). However, other mechanisms potentially linked with the occurrence of diffuse axonal injuries are temporal evolution and spatial distribution of maximum normal and shear stresses within the brain.

Blunt Impact Trauma Mechanics

Traumatic brain injury is defined as damage to the brain resulting from an external mechanical force, such as during rapid acceleration or deceleration, crush, impact, blast, or penetration by a projectile. Brain injuries can occur by a variety of mechanisms and may result in lifelong physical,

cognitive, or psychological impairment. Closed-head injuries are a type of traumatic brain injury in which there may be significant relative displacement of the brain where the skull and dura mater remain intact (Feng et al., 2010).

Causes of impact related TBI include contusion of the brain from deformation or fracture of the skull, contusion from movement against interior an surface of the skull, or indirect contusion of the brain opposite the site of impact (Melvin et al., 1994). Upon impact, the skull can undergo large elastic or plastic deformation.

In contrast, impulsive loading will produce minimal deformation of the skull and the means through which TBI occurs is more subtle. Inertial mechanisms include cerebrovascular ischemia due to increased subdural pressure or occlusion, tissue stresses produced from motion of the brain relative to the skull, or hematoma from rupture of bridging vessels (Melvin et al., 1994).

Blast Induced Traumatic Brain Injury

It is important distinguish the physics of blast interaction with a body from that of blunt trauma. Blunt impact is characterized by a relatively long duration (>100 ms) generating large momentums and strains. In contrast, blast exposure typically has very short durations (<30 ms) resulting in low impulse and relatively small momentum transfer compared with blunt impact (Bass et al., 2012). Blast-induced brain injuries range from mild to serious or fatal trauma from primary blast impingement on the head in the absence of blunt trauma. Direct effects of the shock overpressure are known as primary blast (White et al., 1971)

An ideal blast wave is characterized by a sharp amplitude rise followed by an exponential decay below ambient pressure conditions and finally a return to the original unstressed state. From an initially undisturbed medium, a shock wave will evolve as a surface discontinuity across which velocity, temperature, and pressure gradients undergo nearly instantaneous change.

Unless substantially affected by interactions with its environment, an unconfined blast wave will generally expand spherically from its source and can be defined by its peak overpressure, positive overpressure duration, and impulse (Iremonger, 1997). These idealized waves are known as Friedlander-type, or free-field waves (Figure 1).

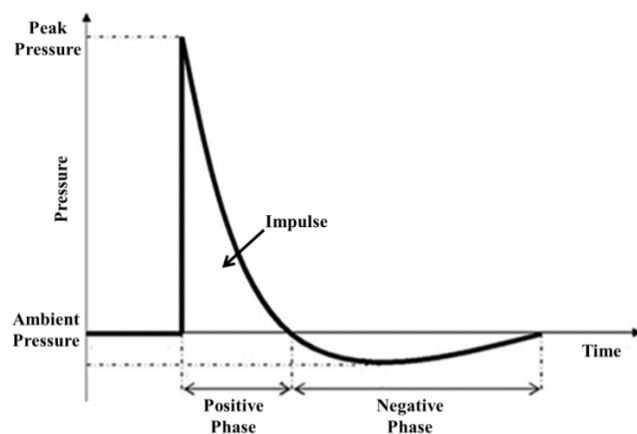


Figure 1: Ideal Friedlander type free-field blast waveform

However, when compressional shock waves interact with external objects, complex blast fields form including reflected pressure waves. As a blast wave enters a biological tissue, functionally a soft solid, high rate stress waves with longitudinal and shear components develop. Based on wave amplitude and speed, the impedance mismatches and extended duration can have devastating effects as the shock

passes through the tissue (Shridharani et al., 2012). It is likely that strain and strain rate both contribute significantly to injuries from blast exposure and that viscoelastic behavior plays an important role.

Cellular, behavioral, and neurocognitive dysfunctions have been empirically and experimentally linked as symptoms of blast TBI. Researchers have hypothesized that blast-brain injuries may be influenced by CSF cavitation, skull flexure, or rotational and translational head accelerations (Panzer, 2012; Panzer et al., 2011).

Viscoelastic Material Characterization of Brain Tissue

Multiple factors contribute to difficulty in consistently describing brain material mechanics. The neuroarchitecture of brain tissue is naturally inhomogeneous and anisotropic (Zhang et al., 2004). Neural tissue is notoriously difficult to test, especially in the human, as *in vivo* testing is challenging and the tissue deteriorates rapidly post mortem. Due to the low stiffness of brain tissue, large differences in measured material properties may occur when the tissue is no longer constrained by the cranium.

Computational simulations depend on accurate descriptions of the material properties of the brain, but to date, most of the data from published literature has been collected *in vitro*, at room temperature, leaving *in vivo* properties largely unexplored (e.g. Galford and McElhaney, 1970; Miller and Chinzei, 2002; Ommaya, 1968; Prange and Margulies, 2002; Shuck and Advani, 1972). Previously reported *in vitro* complex shear stiffness and relaxation values have been highly variable, spanning roughly three orders of magnitude (Chatelin et al., 2010; Cheng and Bilston, 2007).

This variation may partly be attributed to experimental technique and partly attributed to the brain's substantial geometric complexity, which encompasses the presence of structures including meningeal layers, fluid filled ventricles, white and gray matter tracts, sulci, and gyri, all of which present unique challenges to ascertaining accurate mechanical response.

Differences in material modeling also likely contribute to variation. Selection of material model, as well as model constraints imposed, can significantly alter reported mechanical properties. This makes it difficult to directly compare findings. Therefore, consistent definition of material model simplifies comparison of interspecies differences in brain tissue mechanics.

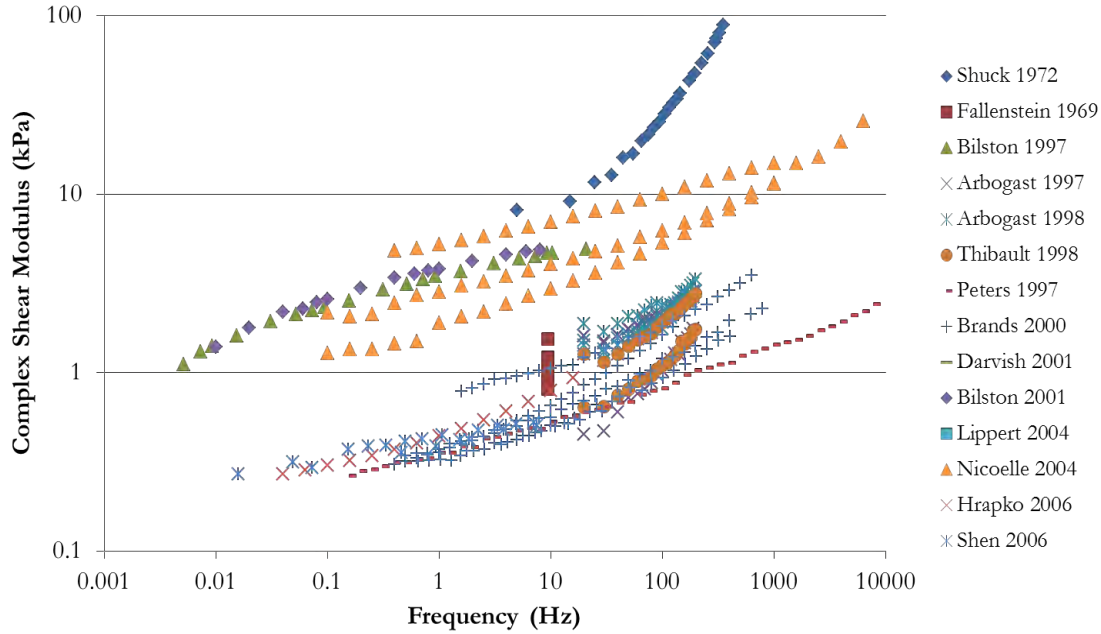


Figure 2: While published literature is extensive, it is mostly limited to animal studies *in vitro* and there is little consensus among authors on the accuracy of material properties. Shear modulus values span demonstrate frequency dependence, is associated with strong viscoelasticity (adapted from Panzer, 2012).

Material / Mechanical Modeling of Brain Tissue

Characterizing the mechanical properties of soft tissue, in particular brain tissue has long been a concern among biomechanists. With advances in computational simulation, and a desire among researchers to create a single brain material model that fits most experimental results, this has been given even greater attention. Numerous constitutive equations have been proposed and historically, linear viscoelastic, quasi-linear viscoelastic (QLV), and non-linear viscoelastic models have been commonly used to describe the material response of biological tissues (Lucas et al., 2008; van Dommelen et al., 2006).

- Linear Viscoelasticity assumes that a material has a strain proportional to stress at any given time. The hereditary integral formulation for stress in linear viscoelasticity is given in (Equation 1) where σ is stress, ε is strain, τ is a dummy integration variable, and the relaxation function G is time dependent but independent of strain. (Estes and McElhaney, 1970; Galford and McElhaney, 1970; Miller and Chinzei, 2002).

$$\sigma(t) = \sigma_0 + \int_0^t G(t - \tau) \frac{d\varepsilon(\tau)}{d\tau} d\tau \quad (\text{Equation 1})$$

- Quasi Linear Viscoelasticity incorporates time and strain dependence into a separable formulation between the instantaneous elastic function and the generalized relaxation function, ((Equation 2). The instantaneous elastic stress (σ^e) commonly appears as a Fung non-linear form (Equation 3), where A and β are model coefficients. The relaxation function is usually a Prony series of exponential decay terms (Equation 4). When applied to materials with memory, this methodology allows for fitting of arbitrary strain and requires no step-strain input assumptions. (Darvish and Crandall, 2000; Urbanczyk et al., 2012; Wood, 2015).

$$\sigma(\varepsilon, t) = \int_0^t G(t - \tau) \frac{d\sigma^e}{d\varepsilon} \frac{d\varepsilon(\tau)}{d\tau} d\tau \quad (\text{Equation 2})$$

$$\sigma^e(\varepsilon) = A(e^{\beta\varepsilon} - 1) \quad (\text{Equation 3})$$

$$G(t) = G_\infty + \sum_{i=1}^n G_n e^{-t/\tau_n} \quad (\text{Equation 4})$$

- Poroelasticity theories explain that because the brain is composed of hydrated tissue, a pure viscoelastic description would be limited given inherent coupling between deformation and hydrodynamic behavior. Poroelastic models are useful in examining long-time behavior and have tended to focus on neurosurgical applications (Cheng and Bilston, 2007).
- Nonlinear viscoelasticity theory requires no *a priori* assumptions and can be used for any shear strain magnitudes and histories. (Equation 5 represents a fully nonlinear Green-Rivlin viscoelastic constitutive model, developed by Takhounts (1998). Nonlinear viscoelastic effects in the brain constitutive relation are important because they tend to be more accurate for finite deformations. Injury patterns predicted by nonlinear models permit the development of discontinuities in the form of shock or acceleration waves (Takhounts et al., 2003).

$$\begin{aligned} \underline{\sigma}(t) = & \int_0^t \left[\mathbf{I} \underline{G}_1 \underline{\dot{\varepsilon}}(\tau_1) + \underline{G}_2 \underline{\dot{\varepsilon}}(\tau_1) \right] d\tau_1 \\ & + \int_0^t \int_0^t \left\{ \mathbf{I} \left[\underline{G}_3 \underline{\dot{\varepsilon}}(\tau_1) \underline{\dot{\varepsilon}}(\tau_2) + \underline{G}_4 \underline{\dot{\varepsilon}}(\tau_1) \underline{\dot{\varepsilon}}(\tau_2) \right] + \underline{G}_5 \underline{\dot{\varepsilon}}(\tau_1) \underline{\dot{\varepsilon}}(\tau_2) + \underline{G}_6 \underline{\dot{\varepsilon}}(\tau_1) \underline{\dot{\varepsilon}}(\tau_2) \right\} d\tau_1 d\tau_2 \\ & + \int_0^t \int_0^t \int_0^t \left\{ \mathbf{I} \left[\underline{G}_7 \underline{\dot{\varepsilon}}(\tau_1) \underline{\dot{\varepsilon}}(\tau_2) \underline{\dot{\varepsilon}}(\tau_3) + \underline{G}_8 \underline{\dot{\varepsilon}}(\tau_1) \underline{\dot{\varepsilon}}(\tau_2) \underline{\dot{\varepsilon}}(\tau_3) \right] + \underline{G}_9 \underline{\dot{\varepsilon}}(\tau_1) \underline{\dot{\varepsilon}}(\tau_2) \underline{\dot{\varepsilon}}(\tau_3) \right. \\ & \left. + \underline{G}_{10} \underline{\dot{\varepsilon}}(\tau_1) \underline{\dot{\varepsilon}}(\tau_2) \underline{\dot{\varepsilon}}(\tau_3) + \underline{G}_{11} \underline{\dot{\varepsilon}}(\tau_1) \underline{\dot{\varepsilon}}(\tau_2) \underline{\dot{\varepsilon}}(\tau_3) + \underline{G}_{12} \underline{\dot{\varepsilon}}(\tau_1) \underline{\dot{\varepsilon}}(\tau_2) \underline{\dot{\varepsilon}}(\tau_3) \right\} d\tau_1 d\tau_2 d\tau_3 \end{aligned} \quad (\text{Equation 5})$$

Regardless of the experimental outcome variable to be studied, the choice of material model and its inherent constraints influence variation and response curves in reported data. These models have varying degrees of complexity, each with its own advantages and challenges.

Classical Mechanics Testing and Experimental Design

Experimental models have used a variety of techniques and species to develop a reproducible model of trauma that exhibits anatomical, physiological and functional responses similar to those reported clinically. Standard experimental techniques including stress-relaxation, creep, and oscillation tests have been used extensively in the literature to determine necessary material properties in tension, compression, and shear.

In some of the first *in vitro* brain tissue investigations, Estes and McElhaney (1970) and Galford and McElhaney (1970) each conducted uniaxial compression stress-relaxation tests on human and monkey brain tissues at strain rates varying between 0.08 and 40 s⁻¹. Results showed substantial short-time relaxation and a log-linear relationship with compliance.

To characterize viscoelastic brain behavior under small strain, *in vitro* experiments used a dynamic frequency sweep, often in shear (Arbogast and Margulies, 1998; Garo et al., 2007). Nicolle et al., (2005) investigated variation within the corona radiata resulting in complex shear moduli of 2.1 – 18.7 kPa for a

range of 0.1 – 6310 Hz, but could not find conclusive evidence of anisotropy at small strain or strain rates.

Indentation with a spherical tip is another commonly used *in vitro* and *in vivo* testing method. Gefen and Margulies (2004) and Miller et al., (2000) performed experiments on porcine brain samples by performing oscillatory tests through a hole cut through the skull close to midline. *In vivo* results were comparable to trends in *in vitro* dynamic strain sweep.

Diagnostic Imaging Derived Material Properties

Motivated to find more accurate experimental approaches to measure physiological parameters and reduce the variability seen in *in vitro* characterization new imaging protocols were developed. Current diagnostic imaging modalities vividly demonstrate changes in brain anatomy with severe injuries (Munkeby and Lyng, 2004; Pickett et al., 2001), but in milder cases clinical imaging shows little or no evidence of pathology and is often uncorrelated with clinical outcome (Hammoud and Wasserman., 2002). Neuroimaging techniques such as MRI and CT can't be used to measure material property changes, only to visualize anatomic changes. They also have practical limits of expense and radiation exposure.

Recently, successful studies with magnetic resonance elastography (MRE) have been used *in vivo* to estimate brain elasticity. However, this technique has limitations related to low spatial resolution, long acquisition time, the need for external mechanical coupling, transmission through multiple tissue layers and establishment of standing wave patterns for imaging. (Green et al., 2008; Kruse et al., 2008; Sack et al., 2008). Shear wave elasticity imaging (SWEI) provides an alternate, method of establishing accurate and biofidelic material properties for brain.

SWEI is an acoustic radiation force impulse (ARFI)-based ultrasound imaging technique able to sensitively, non-invasively and non-destructively assess qualitative and quantitative stiffness *in vivo* (Doherty et al., 2013; Sarvazyan et al., 1998). SWEI is used clinically in liver and heart tissue (Hsu et al., 2007; Palmeri et al., 2008) and has been explored experimentally in brain (Macé et al., 2011; Urbanczyk et al., 2015). It shows substantial benefit over previous methods to sensitively and specifically evaluate pathophysiological changes in brain material properties *in vivo*, without disruption to living physiology.

Shear Wave Elasticity – High Rate Ultrasound Imaging

Ultrasound transient elastography by shear wave imaging uses a high rate ultrasound acquisition imaging system, which enables real-time visualization of transient shear waves propagating in the human body. Transient elastography techniques initially used external vibrators to generate motion, but evolved to use radiation force from focused ultrasonic beams. A burst of ultrasound is transmitted by a conventional probe and focused on a small zone of tissue causing a displacement. The generated shear wave propagates through the tissue and is detected via time-of-flight based reconstruction of ultrasonically tracked data (Palmeri et al., 2008; Pinton et al., 2006). After shear wave speed estimation, the relationship between shear wave speed and underlying tissue properties can be inferred. Under a linear, isotropic approximation the shear modulus (μ) is simply defined in terms of wave speed (c_T) and density (ρ).

$$c_T = \sqrt{\frac{\mu}{\rho}} \quad (\text{Equation 6})$$

The potential of this technique to estimate the anisotropy of brain mechanical properties is explored in Macé et al., 2011 and Urbanczyk et al., 2015. However, as the viscosity is non-negligible in the brain, one should keep in mind that the magnitude measured by SWEI is the group shear velocity.

Even though linearly propagating low amplitude shear waves are routinely visualized, the detection of large amplitude shock shear waves is challenging due to the difficulties associated with visualizing the sharp shock profile. High frame-rate acoustoelasticity techniques are capable of accurately measuring tissue properties across a broad range of frequencies (Gennisson et al., 2007). Shear wave propagation can be observed throughout the entire imaging plane and a high frame-rate movie of elastic displacement is generated with the same imaging versatility of a conventional diagnostic ultrasound scanner (Pinton et al., 2009). The technique can measure rapid and transient large amplitude motion at large depths in the brain and provide insight into the immediate biomechanical response to trauma.

Nonlinear Wave Propagation in Neurological Tissue

The nonlinear behavior of longitudinal waves in fluids or solids is well established from a theoretical and experimental point of view (Hamilton and Blackstock, 1998). By comparison, the detection of shear shock waves remains relatively unexplored. Most biological systems exhibit time-dependent or viscoelastic behavior, with some non-negligible dissipation and dispersion occurring naturally (Pohlhammer and O'Brien, 1980). The effects of dispersion, dissipation and the distance of propagation alter wave profiles, complicating analysis.

In nonlinear wave equations, the *superposition principle* does not generally apply. They are more difficult to analyze mathematically and no general analytical method for their solution exists. Nonlinearity is introduced by expansion of the stress-strain relation, taking into account large particle velocities and strains. The strain-energy density for a weakly nonlinear elastic regime and for incompressible isotropic solids can be written as:

$$W = \mu I_2 + \frac{1}{3} A I_3 + D I_2^2 \quad (\text{Equation 7})$$

where μ , A , and D are the second, third, and fourth order elastic constants and I_2 and I_3 are second and third order strain invariants (Hamilton et al., 2004). This formulation permits separation of effects of nonlinear shear deformation when compressibility is negligible. Adapting nonlinear acoustics techniques to nonlinear shear waves, Pinton et al., (2010) studied the reflection of shear shock waves and determined that they do not always follow the Snell-Descartes law of reflection. Instead, the shock will have an angle of reflection different from the angle of incidence, with an amplitude several times larger than the incident wave.

Third and fourth order elasticity has previously been modeled for several wave polarizations (Wochner et al., 2008), and for anisotropic conditions (Destrade et al., 2010). With simplifying assumptions, the equations of motion can express particle velocity as a scalar equation to model shear shock waves in polarized geometry (Pinton et al., 2010).

$$\frac{d^2 v}{dx dt} = \frac{c_T}{2} \frac{d^2 v}{dx^2} + \frac{\beta}{3c_T^3} \frac{d^2 v^3}{dt^2} \quad (\text{Equation 8})$$

For shear waves, the nonlinearity observed in high amplitude transverse waves at $f_0=100$ Hz results in the generation of odd harmonics $3f_0$, $5f_0$, meaning that nonlinearity is cubic, instead of quadratic (Jacob et al., 2007).

Analytical Shear Shock Wave Solutions

In elastic media - The normal stress components are continuous across a transverse shock while the shear stress component undergoes a discontinuous jump of finite amount. Chu, (1967, 1964) examined an incompressible perfectly elastic material occupying an infinite half-space. The author proposed that a material initially in the state of a homogeneous strain and in static equilibrium will

eventually transform into a transverse shock in the course of propagation and that the square of the wave speed is a monotone increasing function. Currie (1972, 1971) expanded this result for certain classes of elastic materials, in a state of arbitrary homogeneous strain, two purely transverse shock waves of arbitrary strength can propagate in every direction.

In non-linear viscoelastic media – Shocks of arbitrary intensity can be generalized to materials with memory. The presence of memory does not negate the jump across a shock wave of small intensity, but viscoelasticity is commonly expected to have a decaying effect on stress (Coleman and Gurtin, 1966), but may interact with shock formation. In nonlinear viscoelastic media, transverse wave solutions are possible where the fourth elastic modulus is positive (Jordan and Puri, 2005b).

Experimental Observation of Nonlinear Wave Distortion

About two decades after theoretical predictions of the existence of shear shock waves, Catheline et al., (2004, 2003) reported results of an experimental study in which a transverse shock wave was observed in agar/gelatin phantoms using a high-rate ultrasound scanner. The authors showed shock formation over a distance of a few wavelengths for a linear 100 Hz input. They compared their experimental data to predictions from a modified Burger's model. The stress-strain relationship was expressed as:

$$\sigma = E\varepsilon + \gamma\varepsilon^3 - \eta \frac{d\varepsilon}{dt} \quad (\text{Equation 9})$$

The slope of the displacement field steepens for both positive and negative values as a consequence of symmetry with the propagation direction (Figure 3A). As predicted by theory, for such a wave one can observe odd harmonics at 100, 300, 500 Hz in the velocity power spectral density (Figure 3B) (Jacob et al., 2007).

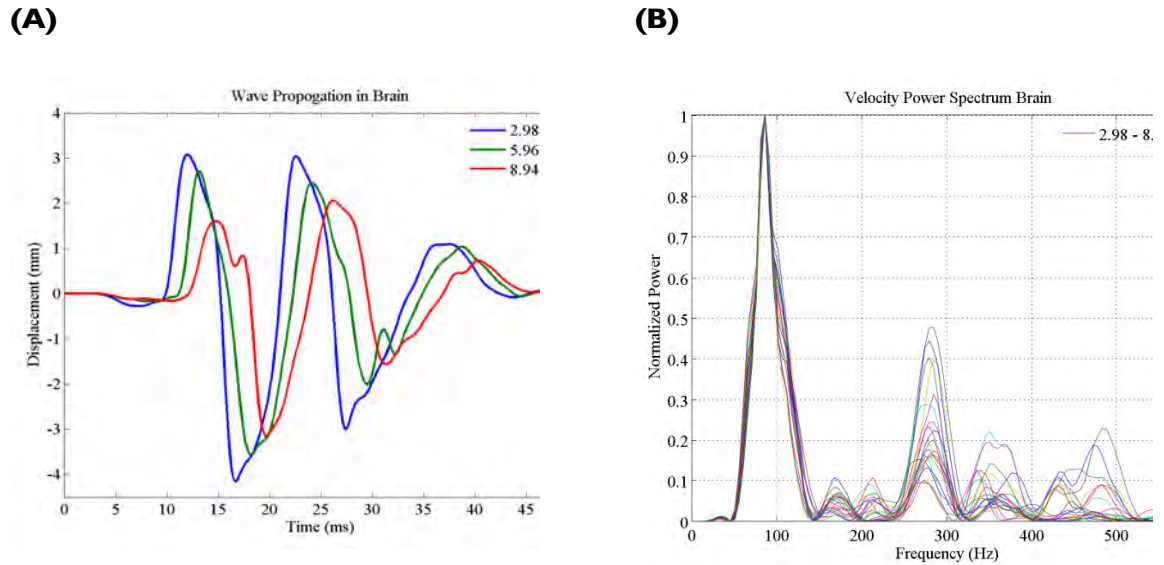


Figure 3: (A) Nonlinear displacement profile and (B) corresponding power spectrum for development of a shock front waveform in a porcine brain/gelatin phantom.

Material Characterization of Porcine Brain by Shear Wave Elasticity Imaging

Experimental validation provides the internal properties needed to modulate behavioral response in computational simulations. They depend on accurate descriptions of the brain, but previously reported *in vitro* complex shear stiffness and relaxation values have been highly variable, (Chatelin et al., 2010; Cheng and Bilston, 2007), and *in vivo* properties have been left largely unexplored. Variation may be attributed to experimental technique and to the brain's substantial geometric complexity, which encompasses the presence of structures including meningeal layers, fluid filled ventricles, white and gray matter tracts, sulci, and gyri, all of which present unique challenges to ascertaining accurate mechanical response. Selection of material model, as well as with the influence of constraints imposed by that model, can significantly alter reported mechanical properties. Significant structural and functional diversity has motivated finding more accurate experimental approaches to measure physiological parameters.

This study develops a novel application of shear wave elasticity imaging (SWEI) to assess porcine brain tissue shear modulus *in vivo*. SWEI is a quantitative ultrasound technique that has been used here to examine changes in brain tissue shear modulus as a function of several experimental and physiological parameters. Animal studies were performed using two different ultrasound transducers to explore the differences between physical response with closed skull and open skull arrangements. *In vivo* intracranial pressure (ICP) in four animal subjects was varied over a relevant physiological range (2-40 mmHg), and was correlated with shear wave speed and stiffness estimates in brain tissue. I found that stiffness does not vary with modulation of ICP (Figure 45). Additional *in vitro* porcine specimens (n=14) were used to investigate variation in brain tissue stiffness with temperature, confinement, spatial location, and transducer orientation. I found a statistically significant decrease in stiffness with increased temperature (23%) (Figure 4B) and an increase in stiffness with decreasing external confinement (22 - 37%) (Figure 4C).

This study demonstrated the feasibility of using SWEI to characterize porcine brain tissue both *in vitro* and *in vivo*. Our results underline the importance of temperature and skull derived boundary conditions on brain stiffness and suggests that physiological ranges of ICP do not significantly affect *in situ* brain tissue properties. SWEI allowed for brain material properties to be experimentally-characterized in a physiological setting and provides a stronger basis for assessing brain injury in computational models.

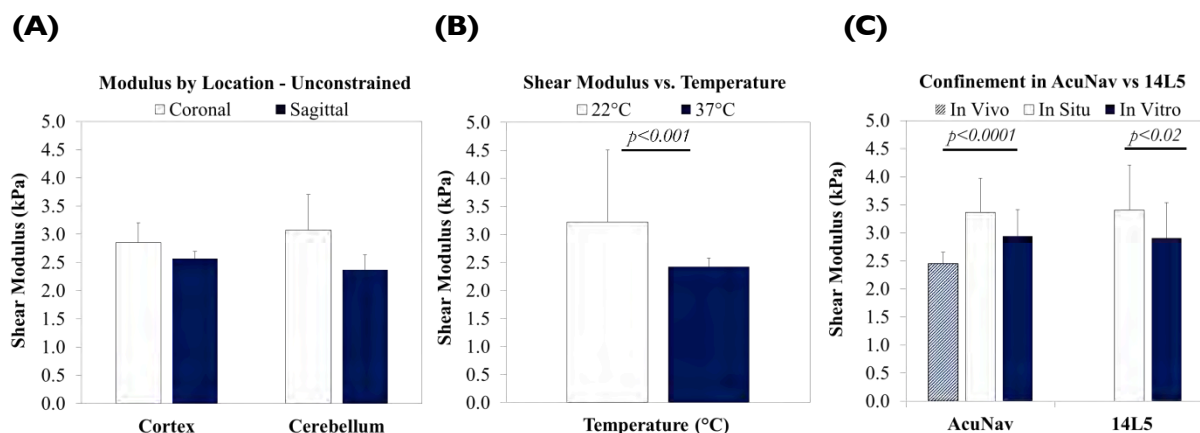


Figure 4: Shear modulus is significantly decreased at physiological temperature compared to ambient but varies neither between cerebral and cerebellar lobes, nor between sagittal and coronal planes within each region. Removing the brain from skull confinement increases tissue stiffness (Urbanczyk et al., 2015).

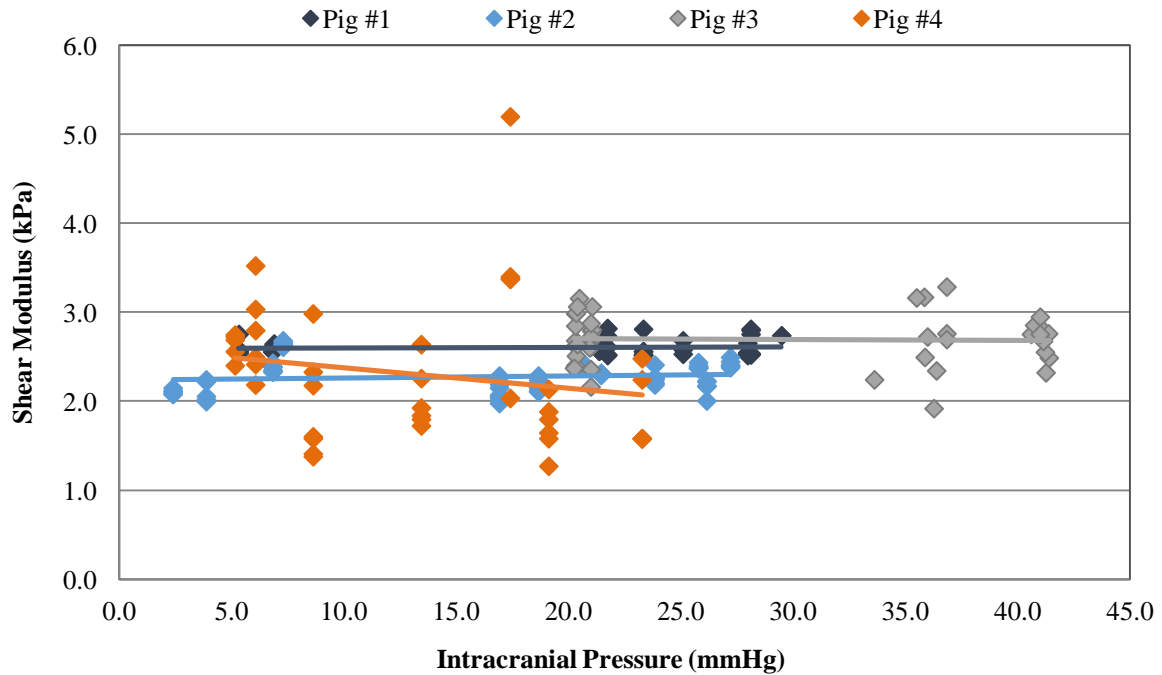


Figure 5: Intracranial pressure versus shear modulus for *in vivo* pig studies. ICP variation under external constraint (skull) does not affect the shear modulus of cerebral brain (Urbanczyk et al., 2015).

Optimization and Validation of Fractional QLV for Brain Shear Testing

Substantial physical and material complexity of the brain is often overlooked in favor of a homogenous, isotropic representation. While series and parallel combinations of springs and dashpots can provide a useful description of the viscoelastic properties, biological tissues exhibit more complex behavior that cannot not all be accounted for by these discrete models. Brain displays non-exponential time-dependent behavior in creep and stress relaxation that vary as a power-law.

The strain response of a fractional order element is seen to be intermediate between the step and ramp responses for the simple elastic and viscous fluid models. Fractional order differentiation provides an adjustable material memory parameter for describing the stress/strain behavior of viscoelastic materials (Podlubny, 2001). Fractional order derivative operators are non-local, meaning that all the past values of the function are required to compute the fractional derivative at any time step (Libertiaux and Pascon, 2009). These operators make good tools for modeling hereditary materials.

This study used a novel fractional derivative quasi-linear viscoelastic (QLV) model to provide an accurate, computable and efficient model for brain. The new material model for arbitrary strain / time histories combined a fractional order QLV model with an non-linear instantaneous elastic function (Equation 3) and a Mittag-Leffler (Equation 11) based relaxation function ((Equation 10) derived from a fractional three-parameter solid, as in Figure 6 (Urbanczyk et al., 2012).

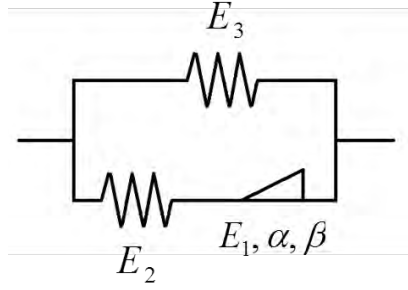


Figure 6: Three parameter solid fractional version.

The Mittag-Leffler QLV function is governed by five model parameters (β_1 , ρ_1 , E_3 , α , β). Numerically, this relation was solved as the additions of long term behavior to the summation of local behaviors, with each part its own integral relation (Urbanczyk and Bass, 2012). Experimentally, time, displacement, and force histories were recompiled from brain indentation and rheological testing. The fractional QLV model was used to fit compressional and torsional step stress relaxation data and optimize the five model parameters. An annealing algorithm was used to ensure that the global optimum was found.

The fractional QLV model significantly reduces the number of necessary parameters

$$G_\alpha(t) = E_3(\beta\rho)^\alpha \left[\left(\frac{1}{(\beta\rho)^\alpha} \right) + \left(\frac{(\beta\rho)^\alpha - 1}{(\beta\rho)^\alpha} \right) E_\alpha[-(\beta\rho)^\alpha] \right] \quad (\text{Equation 10})$$

$$E_\alpha(z) = \sum_{k=0}^{\infty} \frac{z^k}{\Gamma(\alpha k + \beta)} \quad (\text{Equation 11})$$

from the complex, coupled, Green-Rivlin model (Takhounts et al., 2003) and is more functionally robust than a Prony series QLV analysis (Darvish and Crandall, 2001) based on exponential relaxation behavior. It is better able to estimate both peak (short times) and long term behavior well, and requires far less experimental overhead or *a priori* material parameter estimation. This model improves accuracy and versatility over alternative models and will be able to incorporate non-isotropic, inhomogeneous behavior.

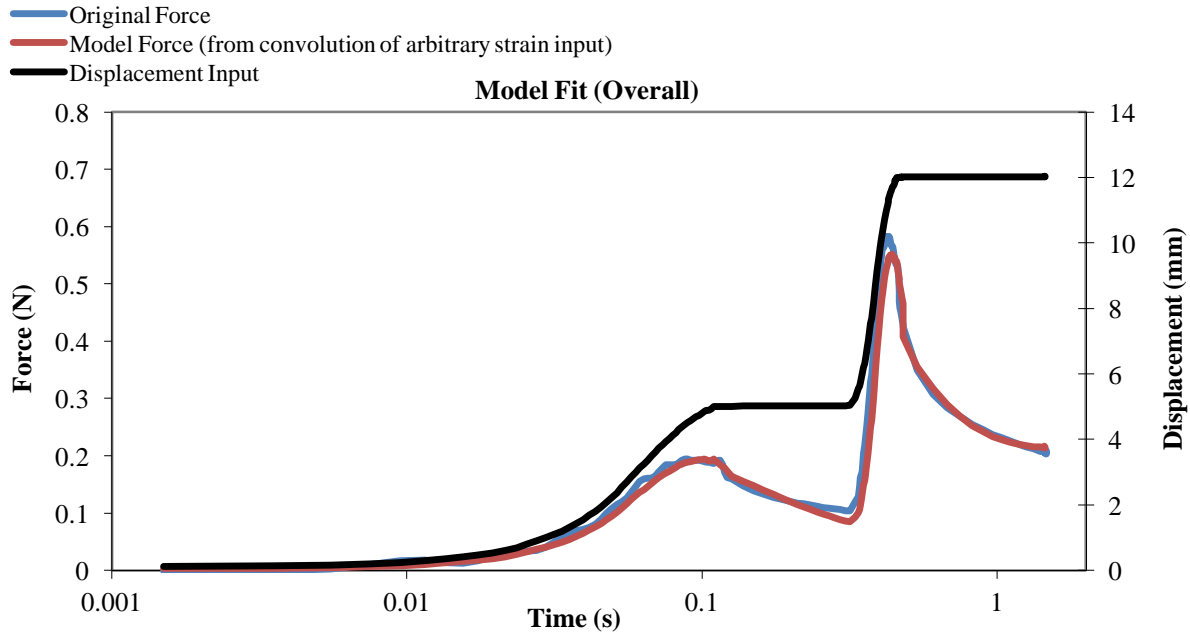


Figure 7: Recompiled displacement and force histories for a two-step shear stress relaxation test, used to optimize parameters for the fractional QLV model. The model estimates both peak (short times) and long term behavior well.

REFERENCES

- Arbogast, K.B., Margulies, S.S., 1998. Material characterization of the brainstem from oscillatory shear tests. *J. Biomech.* 31, 801–7.
- Bass, C.R., Panzer, M.B., Rafaels, K. a, Wood, G., Shridharani, J., Capehart, B., 2012. Brain injuries from blast. *Ann. Biomed. Eng.* 40, 185–202.
- Catheline, S., Gennisson, J.L., Delon, G., Fink, M., Sinkus, R., Abouelkaram, S., Culioli, J., 2004. Measuring of viscoelastic properties of homogeneous soft solid using transient elastography: an inverse problem approach. *J. Acoust. Soc. Am.* 116, 3734–3741.
- Catheline, S., Gennisson, J.-L., Tanter, M., Fink, M., 2003. Observation of Shock Transverse Waves in Elastic Media. *Phys. Rev. Lett.* 91, 164301.
- Chatelin, S., Constantinesco, A., Willinger, R., 2010. Fifty years of brain tissue mechanical testing: from in vitro to in vivo investigations. *Biorheology* 47, 255–276.
- Cheng, S., Bilston, L.E., 2007. Unconfined compression of white matter. *J. Biomech.* 40, 117–24.
- Chu, B.T., 1964. Finite amplitude waves in incompressible perfectly elastic materials. *J. Mech. Phys. Solids* 12, 45–57.
- Chu, B.T., 1967. Transverse shock waves in incompressible elastic solids. *J. Mech. Phys. Solids* 15, 1–14.
- Coleman, B.D., Gurtin, M.E., 1966. Thermodynamics and One Dimensional Shock Waves in Materials with Memory. *Proc. R. Soc. A Math. Phys. Eng. Sci.* 292, 562–574.
- Coulouvrat, F., 2009. A quasi-analytical shock solution for general nonlinear progressive waves. *Wave Motion* 46, 97–107.
- Currie, P., 1971. A note on shock waves in elastic Hadamard and Green materials. *Zeitschrift für Angew. Math. und Phys. ZAMP* 22, 355–359.
- Currie, P., 1972. Shock waves in homogeneously-strained incompressible elastic materials: The Mooney-Rivlin material. *Acta Mech.* 58, 53–58.

- Darvish, K., Crandall, J., 2000. Comparison Between a Quasilinear and a Nonlinear Viscoelastic Model for Brain Tissue. ASME-PUBLICATIONS-BED 4–5.
- Darvish, K.K., Crandall, J.R., 2001. Nonlinear viscoelastic effects in oscillatory shear deformation of brain tissue. *Med. Eng. Phys.* 23, 633–45.
- Destrade, M., Gilchrist, M.D., Ogden, R.W., 2010. Third- and fourth-order elasticities of biological soft tissues. *J. Acoust. Soc. Am.* 127, 2103–9.
- Doherty, J.R., Trahey, G.E., Nightingale, K.R., Palmeri, M.L., 2013. Acoustic Radiation Force Elasticity Imaging in Diagnostic Ultrasound. *IEEE Trans. Ultrason. Ferroelectr. Freq. Control* 60, 685–701.
- Estes, M., McElhaney, J.H., 1970. Response of brain tissue to compressive loading. *Mech.*
- Estrada, J., Franck, C., 2014. Microcavitation as a neuronal damage mechanism in blast traumatic brain injury, in: *Proceedings of the Society of Engineering Science*. p. 2014.
- Faul, M., Xu, L., Wald, M., Coronado, V., 2010. Traumatic brain injury in the United States: emergency department visits, hospitalizations and deaths 2002–2006. *Centers Dis. Control Prev. Natl. Cent. for Inj. Prev. Control*.
- Feng, Y., Abney, T.M., Okamoto, R.J., Pless, R.B., Genin, G.M., Bayly, P. V., 2010. Relative brain displacement and deformation during constrained mild frontal head impact. *J. R. Soc. Interface* 7, 1677–1688.
- Galford, J.E., McElhaney, J.H., 1970. A viscoelastic study of scalp, brain, and dura. *J. Biomech.* 3, 211–221.
- Gao, X., Chen, J., 2011. Mild traumatic brain injury results in extensive neuronal degeneration in the cerebral cortex. *J. Neuropathol. Exp. Neurol.* 70, 183–191.
- Garo, a, Hrapko, M., van Dommelen, J. a W., Peters, G.W.M., 2007. Towards a reliable characterisation of the mechanical behaviour of brain tissue: The effects of post-mortem time and sample preparation. *Biorheology* 44, 51–8.
- Gefen, A., Margulies, S.S., 2004. Are in vivo and in situ brain tissues mechanically similar? *J. Biomech.* 37, 1339–52.
- Gennarelli, T.A., 1992. Mechanisms of brain injury. *J. Emerg. Med.* 11, 5–11.
- Gennisson, J.-L., Rénier, M., Catheline, S., Barrière, C., Bercoff, J., Tanter, M., Fink, M., 2007. Acoustoelasticity in soft solids: assessment of the nonlinear shear modulus with the acoustic radiation force. *J. Acoust. Soc. Am.* 122, 3211–3219.
- Green, M.A., Bilston, L.E., Sinkus, R., 2008. In vivo brain viscoelastic properties measured by magnetic resonance elastography. *NMR Biomed* 21, 755–764.
- Grujicic, M., d'Entremont, B., Pandurangan, B., Grujicic, a, LaBerge, M., Runt, J., Tarter, J., Dillon, G., 2012. A study of the blast-induced brain white-matter damage and the associated diffuse axonal injury. *Multidiscip. Model. Mater. Struct.* 8, 213–245.
- Hamilton, M., Blackstock, D., 1998. *Nonlinear acoustics*. Academic Press, San Diego.
- Hamilton, M.F., Ilinskii, Y. a., Zabolotskaya, E. a., 2004. Separation of compressibility and shear deformation in the elastic energy density (L). *J. Acoust. Soc. Am.* 116, 41.
- Hammoud, D.A., Wasserman, B.A., 2002. Diffuse axonal injuries: pathophysiology and imaging. *Neuroimaging Clin. N. Am.* 12, 205–216.
- Hsu, S.J.S., Bouchard, R.R., Dumont, D.D.M., Wolf, P.D., Trahey, G.E., 2007. In vivo assessment of myocardial stiffness with acoustic radiation force impulse imaging. *Ultrasound Med. Biol.* 33, 1706–1719.
- Iremonger, M.J., 1997. Physics of detonations and blast waves, in: *Scientific Foundations of Trauma*. Butterworth-Heinemann, New York, pp. 189–199.
- Jacob, X., Catheline, S., Gennisson, J.-L., Barrière, C., Royer, D., Fink, M., 2007. Nonlinear shear wave interaction in soft solids. *J Acoust Soc Am* 122, 1917–1926.

- Jordan, P.M., Puri, A., 2005a. Growth/decay of transverse acceleration waves in nonlinear elastic media. *Phys. Lett. A* 341, 427–434.
- Jordan, P.M.M., Puri, A., 2005b. A note on traveling wave solutions for a class of nonlinear viscoelastic media. *Phys. Lett. A* 335, 150–156.
- Kruse, S. a, Rose, G.H., Glaser, K.J., Manduca, A., Felmlee, J.P., Jack, C.R., Ehman, R.L., 2008. Magnetic resonance elastography of the brain. *Neuroimage* 39, 231–7.
- Langlois, J.A., Rutland-brown, W., Wald, M.M., 2006. The Epidemiology and Impact of Traumatic Brain Injury A Brief Overview. *J Head Trauma Rehabil* 21, 11–14.
- Libertiaux, V., Pascon, F., 2009. Viscoelastic modeling of brain tissue: A fractional calculus-based approach. *Lect. Notes Appl. Comput. Mech.* 46 LNACM, 81–90.
- Lucas, S.R., Bass, C.R., Salzar, R.S., Oyen, M.L., Planchak, C., Ziemba, A., Shender, B.S., Paskoff, G., 2008. Viscoelastic properties of the cervical spinal ligaments under fast strain-rate deformations. *Acta Biomater.* 4, 117–25.
- Macé, E., Cohen, I., Montaldo, G., Miles, R., Fink, M., 2011. In Vivo Mapping of Brain Elasticity in Small Animals Using Shear Wave Imaging. *IEEE Trans. Med. Imaging* 30, 550–558.
- Melvin, J., Lighthall, J.W., Ueno, K., 1994. Brain Injury Biomechanics, in: Levine, R. (Ed.), *Head and Neck Injury*. SAE International, Warrendale, Pennsylvania, USA, Warrendale, pp. 53–94.
- Miller, K., Chinzei, K., 2002. Mechanical properties of brain tissue in tension. *J. Biomech.* 35, 483–90.
- Miller, K., Chinzei, K., Orsengo, G., Bednarz, P., 2000. Mechanical properties of brain tissue in-vivo: experiment and computer simulation. *J. Biomech.* 33, 1369–76.
- Munkeby, B., Lyng, K., 2004. Morphological and hemodynamic magnetic resonance assessment of early neonatal brain injury in a piglet model. *J. Magn. Reson. Imaging* 20, 8–15.
- Nicolle, S., Lounis, M., Willinger, R., Palierne, J.-F., 2005. Shear linear behavior of brain tissue over a large frequency range. *Biorheology* 42, 209–23.
- Nusholtz, G.S., 1995. Cavitation/boundary effects in a simple head impact model. *Aviat. Space. Environ. Med.* 66, 661–667.
- Nusholtz, G.S., Wylie, E.B., Glascoe, L.G., 1995. Internal cavitation in simple head impact model. *J. Neurotrauma* 12, 707–714.
- Ommaya, A.K., 1968. Mechanical properties of tissues of the nervous system. *J. Biomech.* 1, 127–138.
- Palmeri, M.L., Wang, M.H., Dahl, J.J., Frinkley, K.D., Nightingale, K.R., 2008. Quantifying hepatic shear modulus in vivo using acoustic radiation force. *Ultrasound Med. Biol.* 34, 546–58.
- Panzer, M.B., 2012. Numerical Simulation of Primary Blast Brain Injury. Duke University.
- Panzer, M.B., “Dale” Bass, C.R., Rafaels, K. a., Shridharani, J., Capehart, B.P., 2011. Primary Blast Survival and Injury Risk Assessment for Repeated Blast Exposures. *J. Trauma Inj. Infect. Crit. Care* XX, 1.
- Panzer, M.B., Matthews, K. a, Yu, A.W., Morrison, B., Meaney, D.F., Bass, C.R., 2012. A Multiscale Approach to Blast Neurotrauma Modeling: Part I - Development of Novel Test Devices for in vivo and in vitro Blast Injury Models. *Front. Neurol.* 3, 46.
- Pickett, W., Arden, C., Brison, R.J., 2001. A population-based study of potential brain injuries requiring emergency care. *C. Can. Med. Assoc. J.* 165, 288–92.
- Pinton, G., Coulouvrat, F., Gennisson, J.-L., Tanter, M., 2010. Nonlinear reflection of shock shear waves in soft elastic media. *J. Acoust. Soc. Am.* 127, 683–691.
- Pinton, G., Gennisson, J., Tanter, M., Coulouvrat, F., 2014. Adaptive motion estimation of shear shock waves in soft solids and tissue with ultrasound. *IEEE Trans. Ultrason. Ferroelectr. Freq. Control* 61, 1489–503.
- Pinton, G.F., 2013. Shear shock wave propagation in the brain : high frame-rate ultrasound imaging , characterization, and simulations.

- Pinton, G.F., Dahl, J.J., Rosenzweig, S.J., Trahey, G.E., 2009. A heterogeneous nonlinear attenuating full-wave model of ultrasound. *IEEE Trans Ultrason Ferroelectr Freq Control* 56, 474–488.
- Pinton, G.F., Dahl, J.J., Trahey, G.E., 2006. Rapid tracking of small displacements with ultrasound. *IEEE Trans. Ultrason. Contr.* 53, 1103–1117.
- Podlubny, I., 2001. Geometric and Physical Interpretation of Fractional Integration and Fractional Differentiation 18.
- Pohlhammer, J., O'Brien, W., 1980. The relationship between ultrasonic attenuation and speed in tissues and the constituents: water, collagen, protein, and fat, in: Fullerton, G., Zagzebski, J.A. (Eds.), *Medical Physics of CT and Ultrasound: Tissue Imaging and Characterization*. American Association of Physicists in Medicine, New York, pp. 409–435.
- Prange, M., Margulies, S., 2002. Regional, directional, and age-dependent properties of the brain undergoing large deformation. *J Biomech Eng* 124, 244–252.
- Pun, P.B.L., Kan, E.M., Salim, A., Li, Z., Ng, K.C., Moochhala, S.M., Ling, E.-A., Tan, M.H., Lu, J., 2011. Low level primary blast injury in rodent brain. *Front. Neurol.* 2, 19.
- Sack, I., Beierbach, B., Hamhaber, U., Klatt, D., Braun, J.J., 2008. Noninvasive measurement of brain viscoelasticity using magnetic resonance elastography. *NMR Biomed.* 21, 265–271.
- Sarvazyan, A., Rudenko, O., Swanson, S., Fowlkes, J., Emelianov, S., 1998. Shear Wave Elasticity Imaging: A New Ultrasonic Technology of Medical Diagnostics. *Ultrasound Med. Biol.* 24, 1419–1435.
- Shridharani, J.K., Wood, G.W., Panzer, M.B., Capehart, B.P., Nyein, M.K., Radovitzky, R. a, Bass, C.R. "Dale," 2012. Porcine head response to blast. *Front. Neurol.* 3, 70.
- Shuck, L., Advani, S., 1972. Rheological response of human brain tissue in shear. *J. Basic Eng.* 94, 905.
- Takhounts, E.G., 1998. Experimental determination of constitutive equations for human and bovine brain tissue. University of Virginia.
- Takhounts, E.G., Crandall, J.R., Darvish, K., 2003. On the importance of nonlinearity of brain tissue under large deformations. *Stapp Car Crash J.* 47, 79–92.
- Urbanczyk, C. a., Palmeri, M.L., Bass, C.R., 2015. Material Characterization of in Vivo and in Vitro Porcine Brain Using Shear Wave Elasticity. *Ultrasound Med. Biol.* 41, 713–723.
- Urbanczyk, C., Bass, C., 2012. Fractional Standard Linear Solid Derivation.
- Urbanczyk, C., Panzer, M., Bass, C., 2012. Optimization and Validation of Fractional QLV for Brain Material Property characterization. *Biomed. Eng. Soc. Annu. Conf.*
- Van Dommelen, J. a W., Jolandan, M.M., Ivarsson, B.J., Millington, S. a, Raut, M., Kerrigan, J.R., Crandall, J.R., Diduch, D.R., 2006. Nonlinear viscoelastic behavior of human knee ligaments subjected to complex loading histories. *Ann. Biomed. Eng.* 34, 1008–18.
- Vink, R., McIntosh, T.K., Demediuk, P., Weiner, M.W., Faden, a I., 1988. Decline in intracellular free Mg^{2+} is associated with irreversible tissue injury after brain trauma. *J. Biol. Chem.* 263, 757–761.
- White, C.S., Jones, R.K., Damon, E.G., Fletcher, E.R., Richmond, D.R., 1971. *The biodynamics of air blast*, Sciences-New York.
- Wochner, M.S., Hamilton, M.F., Ilinskii, Y. a, Zabolotskaya, E. a, 2008. Cubic nonlinearity in shear wave beams with different polarizations. *J. Acoust. Soc. Am.* 123, 2488–95.
- Wood, G., 2015. Interspecies Scaling in Blast Neurotrauma. Duke University.
- Xiong, Y., Mahmood, A., Chopp, M., 2013. Animal models of traumatic brain injury. *Nat. Rev. Neurosci.* 14, 128–42.
- Zabolotskaya, E. a., Hamilton, M.F., Ilinskii, Y. a., Meegan, G.D., 2004. Modeling of nonlinear shear waves in soft solids. *J. Acoust. Soc. Am.* 116, 2807.
- Zhang, L., Yang, K.H., King, A.I., 2004. A Proposed Injury Threshold for Mild Traumatic Brain Injury. *J. Biomech. Eng.* 126, 226.

Tasks Matched to Initial MURI Efforts

Task A. Examine the multiscale physics of blast wave transmission to the brain.

[A1] Define and validate a finite element model of blast wave transmission through the human brain.

The MURI collaboration has made substantial progress in exploring the relevant multiscale physics of blast transmission including published work by Panzer et al (2012) on the development and validation of a human finite element model, unpublished work by Panzer et al (2012c) on the development and validation of a ferret finite element model, and work by Bigler et al(2012) on a mouse finite element model for blast.

Brain tissue properties, including the properties in vivo have been published by Urbanczyk et al (2012). These properties include the effect of rate and in vivo confinement. Validation data including porcine, ferret, mouse and rabbit and human cadaver response have been studied in this project (Shridharani, 2012, Wood, 2012 unpublished, Yu, 2012 unpublished). The MURI collaboration has substantial (DTI) Diffusion Tensor Imaging (DTI) data from ferrets which may be used to compare hypotheses and support scaling to human results.

Principal results include:

- 1. Development of a novel high rate material model for brain properties. Using a new quasilinear viscoelastic formulation based on the fractional calculus (Urbanczyk 2013, Bass 2013 unpublished).*

Brain material models have been developed that more provide more biofidelic high rate relaxation. This formulation is based on a fractional order viscoelastic model of the form shown in **Figure 8**.

A.

$$\sigma = E_1 \tau^\alpha D^\alpha(\varepsilon); \quad \tau = \frac{1}{\beta}$$

B.

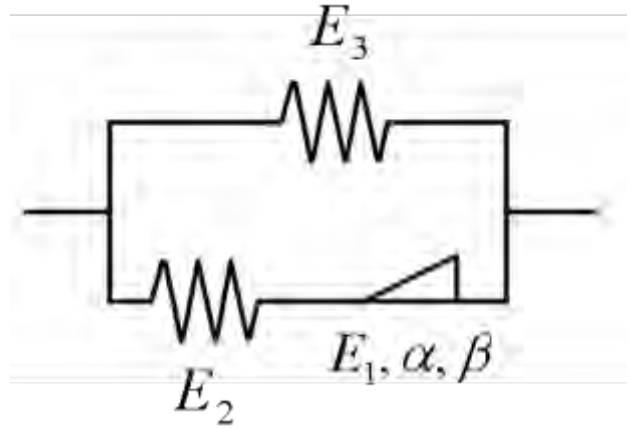


Figure 8. Fractional order viscoelastic function, diagram of equivalent dynamic system

This formulation has substantial advantages for soft tissues. It is more computationally efficient than the Green-Rivlin formulations and provides satisfying theoretical characteristics. It is more compact, directly models power law behaviors with fewer parameters. The formulation is capable of optimizing parameters well at either peak or for long time durations in which relaxation occurs preferentially at short or long times (**Figure 9**). The single stress optimizations used provide good values for multi step stress predictions which have been previously difficult for typical linear or quasilinear viscoelasticity (**Figure 10**).

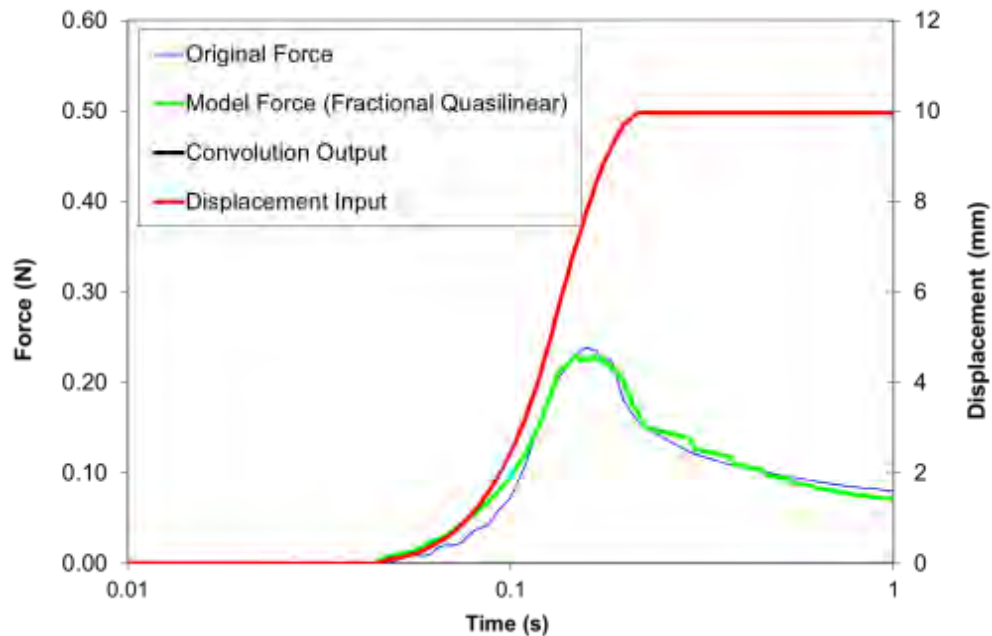


Figure 9. Fractional viscoelastic model for brain tissue showing good fit for both short time (ramp) and long time (relaxation)

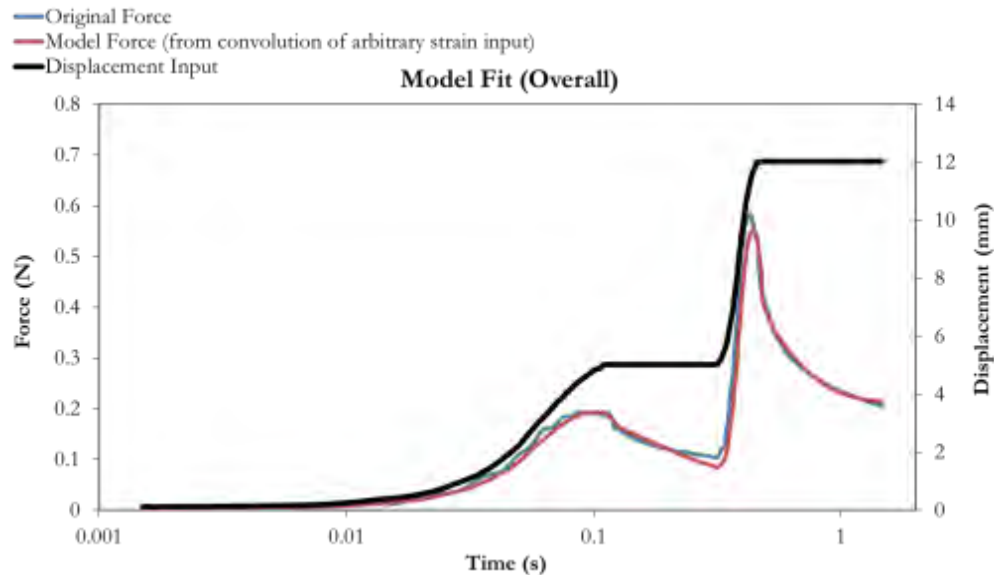


Figure 10. Multi step fractional viscoelastic model fit, previously only possible with Green-Rivlin models (Takhounts, 2002)

2. *Computational model (strain map) of ferret correlates well with ferret injury giving injury criterion for stress/strain that correlates well with the actual injuries seen in the ferret model (Panzer, 2012, 2013)*

Model

Model geometry was based on a CT scan ($0.1875 \times 0.1875 \times 0.625$ mm voxel size) of an adult male ferret (mass = 1.2 kg) from the group of specimens tested by Rafaels et al. (2012). The CT data was segmented into soft tissue (Figure 11, A) and bone (Figure 11, B) using Avizo 7.0 (Visualization Sciences Group, Berlin, Germany). The initial “rough” phase of tissue segmentation was done by automatically distinguishing the tissue type of each voxel based on a threshold of -200 to 300 Hounsfield Units for soft tissues and above 300 Hounsfield Units for bony tissues. A second “fine” phase of segmentation was done by manually cleaning each slice of the CT (removing voids and speckles associated with automated segmentation) and smoothing out features too small for modeling. Surface meshes were generated from the segmented tissues in the CT scan (Figure 11, C) and exported into Hypermesh (v11.0; Altair Engineering, Troy, MI) for finite element mesh generation. The ferret surface geometry was oriented such that the ferret’s mid-sagittal plane was on the global YZ-plane, and the line formed between the ferret rhinion (lower end of suture between the nasal bones) and opisthion (midpoint of the lower border of the foramen magnum) was parallel to the global Y-axis.

Panzer et al. (2012) demonstrated that tetrahedral meshes were not suitable for blast modeling with nearly incompressible biological tissues. Therefore, automated mesh generation algorithms (based on tetrahedral elements) were not used to discretize the ferret head. Instead, the mesh was created manually (a tedious and time-consuming task). This process involved the accumulation of an extensive series of solid meshes created by extruding the surface of a previously created solid mesh. Element extrusions were designed to conform to the anatomical surface geometry and to preserve nodal connectivity throughout the model, but this caused their topology to become increasing

complex. For this reason, the brain mesh was generated first to ensure that its mesh consisted of high quality elements. Following the brain, mesh creation progressed to the skull and vertebra, and finally the soft tissue mesh. The complex anatomy of the structures within the ferret head resulted in compromises between the model geometry and the element size and quality, mainly in the complex soft tissues around the jaw and ear canal. Finally, the ferret head mesh was smoothed using the GETMe algorithm (Vartziotis and Wipper, 2011) to maximize the overall quality of the mesh. Surface and edge nodes were constrained during the smoothing process using quadratic functions (Yin and Teodosiu, 2008).

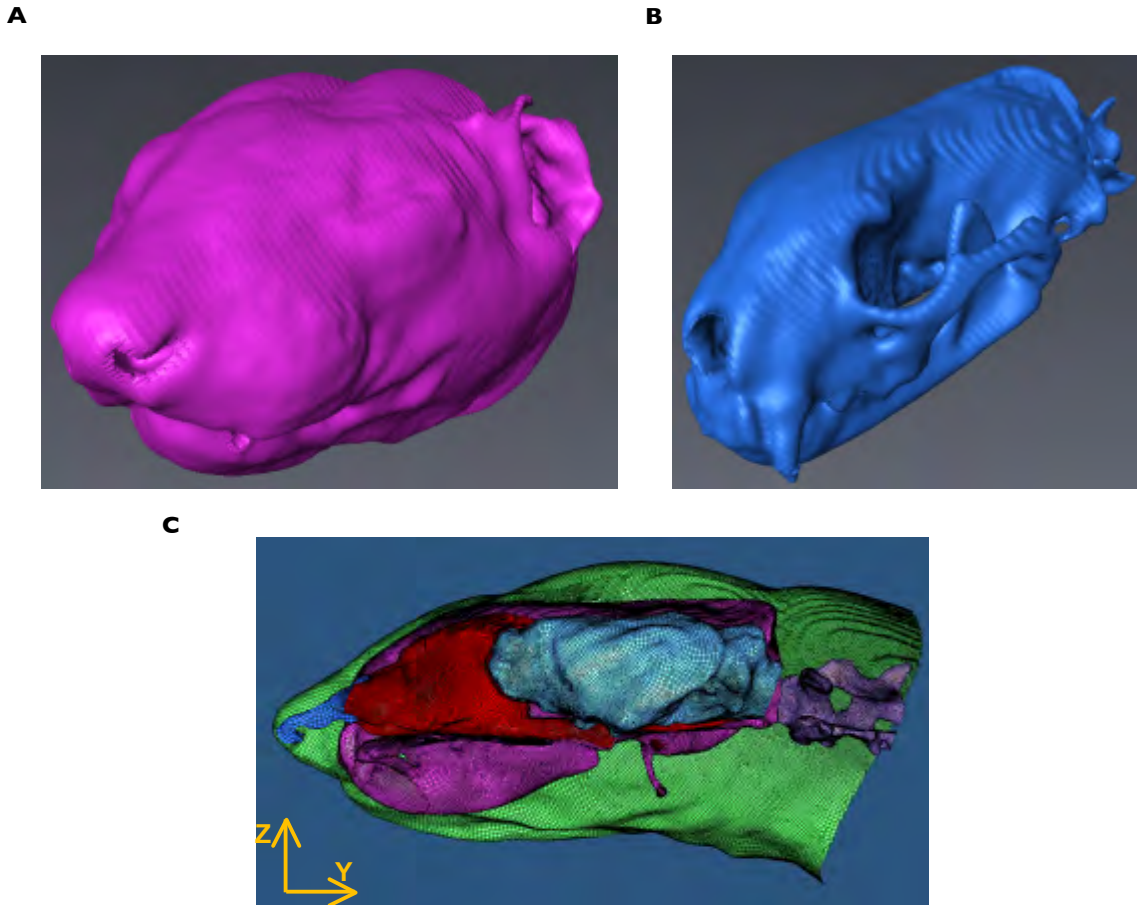


Figure 11:: Isosurface representations of segmented tissues of the ferret CT for exterior soft tissue (A) and skull (B). A medial view of the surface meshes for the interfaces of various tissue types generated from the segmented CT (C).

The final ferret head mesh consisted of CNS (brain and spinal cord), CSF, skull, vertebrae, and soft tissue. Only one side of the head was meshed because the blast loading in this study and the geometry of the ferret was symmetric about the mid-sagittal plane. The CSF layer was selected with a thickness of approximately 0.5 mm, and provided a fluid interface between the CNS and the skull and vertebra.

The peak principal strain distribution in the ferret brain was consistent for all levels of shock tube simulations, and differed greatly from the distribution of peak pressure. The highest values of tissue strain were observed in the hindbrain, midbrain and spinal cord (**Figure 12**). Peak principal strains in the hindbrain and midbrain were 40 – 75% higher than in the parietal or frontal lobes. Unlike the

distribution of peak pressure, there was relatively low strain in the frontal and parietal cortex. In contrast, the human head model had the highest strains at the CSF interface.

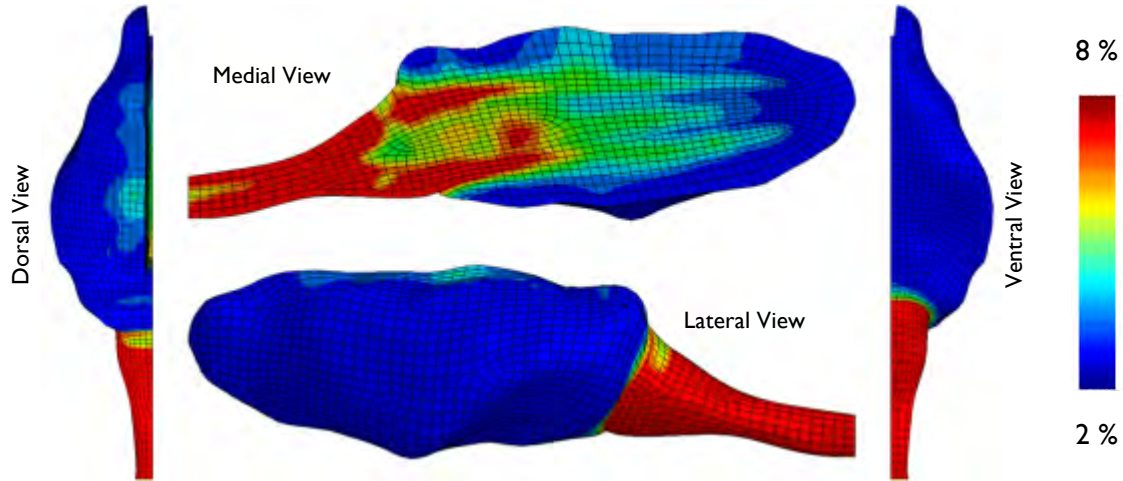


Figure 12: Typical distribution of the peak principal strain predicted in the ferret brain.

3. Comparison with blast injury results

For the shock tube tests of Rafaels et al. (2012), gross examination found subdural and subarachnoid hemorrhages in the non-surviving specimens, often in areas on and adjacent to the brainstem (Figure 13). In all specimens that presented with some degree of hemorrhage, the most frequent sites of injury were on and around the brainstem, followed by the ventral surface of the brain and the area around the dorsal junction between the cerebrum and the cerebellum. Remarkably, these injury sites correspond with the predicted areas of high strain in the ferret FE model. Petechial hemorrhages were located on the frontal lobe of five of the 64 specimens. These injuries correlated with the sites of high brain pressure response.

Histological staining was done on coronal slices of the injured ferrets for the presence of axonal injury (α -amyloid precursor protein; α -APP) and neurofilament damage (a monoclonal mouse anti-neurofilament-midsized-antibody; RM014). Positive staining for α -APP and RM014 was found throughout the cerebrum and brain stem. Common sites for positive results from both stain types in the midbrain included the corpus callosum, corona radiata, at the border of ventricles, and at the interfaces between gray and white matter in the midbrain (Figure 13, A). The sensory and motor tracts of the brain stem (Figure 13, C) and the cerebellum (Figure 13, E) were also areas of common positive staining. The hippocampus and thalamus were areas that were only positive for α -APP, and the cerebellar peduncle was only positive for RM014.

Post-hoc comparison of the histology results with the FE model results at the same level of coronal section showed excellent correlation between the peak predicted strain distributions and the common areas of positive staining. The FE model predicted large strains to occur in areas that correspond with the corpus callosum and the corona radiata (Figure 13, B), the cerebral peduncle, the sensory and motor tracts, and the thalamus (Figure 13, D), and the cerebellum (Figure 13, F). Peak pressure distribution did not correlate with the histological results.

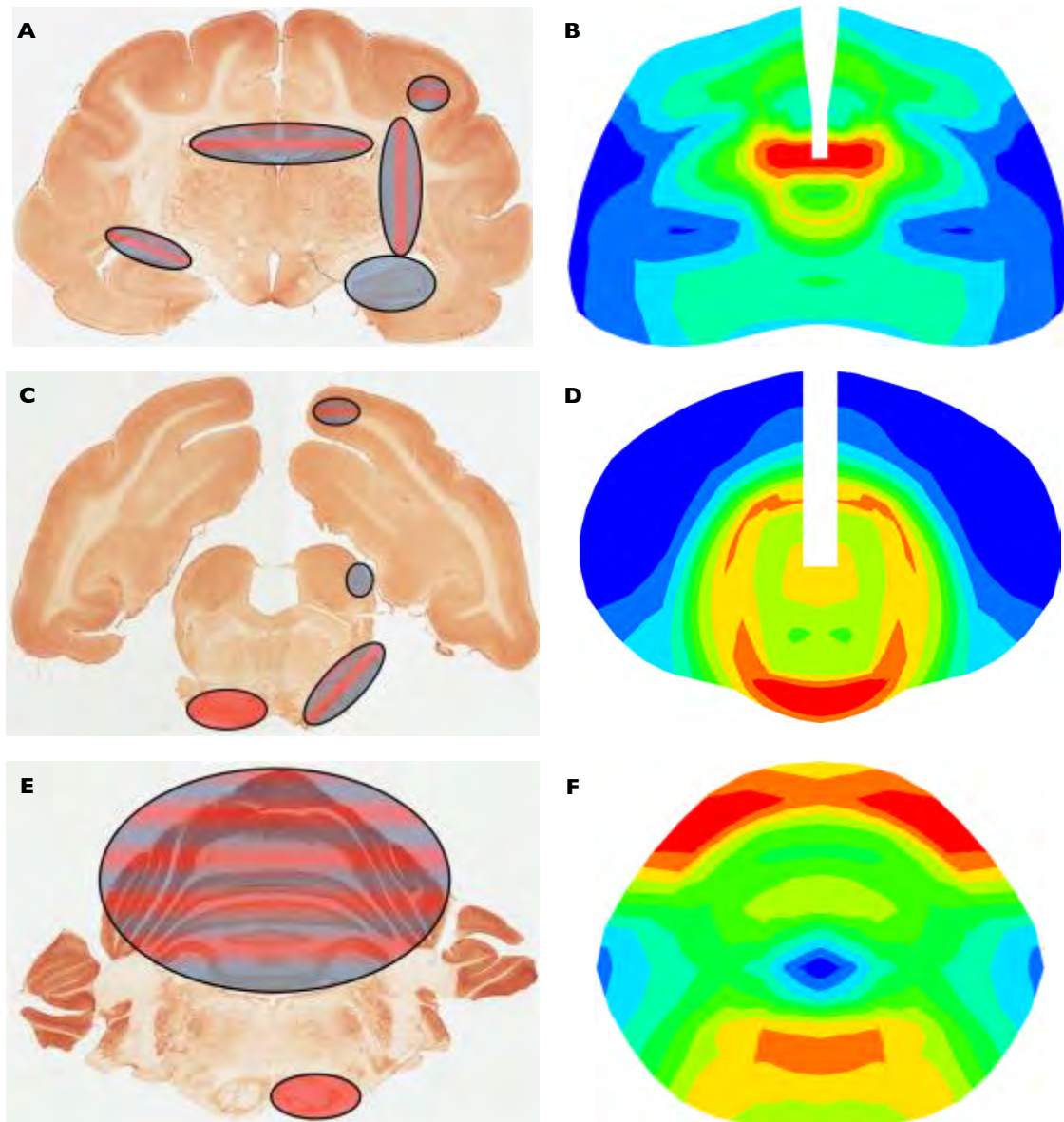


Figure 13: A post-hoc comparison of the frequent areas of positive staining for β APP (blue regions), RM014 (red regions), or both (blue and red striped regions) in blasted ferrets (left) to the peak predicted strain distributions in the ferret FE model (right). Coronal section taken at the midbrain (A and B), 8 mm inferior to bregma (C and D), and at the cerebellum (E and F) (Photos adapted from Rafaels, 2011).

Isolines were generated from the contour plots using values corresponding to the 50% injury risk of the Weibull model fits. For example, the 50th percentile peak principle strain metric having a value of 1.61% corresponded to the 50% risk of apnea .

The isolines were plotted for blast pressure and duration load, below, and compared with the 50% risk curves developed by Rafaels et al. (2012). The phenomenological-based risk curve for mild bleeding had no significant duration dependence (only pressure dependence), and a similar finding

was reached with both the pressure-based and strain-based injury risk curves (below, A and B). Both pressure-based and strain-based risk curves were within the 95th percentile confidence bands of the phenomenological risk curve. However, only the strain-based injury risk curves were in good agreement with the injury data for moderate bleeding and apnea, and within the confidence bands of the phenomenological-based risk curves. The pressure-based injury risk curves did not capture the durational dependence of the moderate bleeding or apnea injury responses of the *in vivo* data. The poor correlations of the curves based on the peak brain pressure metric to the injury data for moderate brain bleeding and apnea response suggest that the injury mechanisms at the tissue-level are not associated with peak ICP.

Principal results include:

4. *Measured brain material properties strongly depend on boundary conditions (in vivo vs excised tissue).*

This study assessed *in vivo* and *in vitro* brain mechanical properties using shear wave elasticity imaging (SWEI) in a minimally invasive technique to track acoustic radiation force impulse (ARFI) induced shear waves in a porcine brain model. Results from this study suggest that the new techniques for estimation of the ARFI shear wave speed, elastic shear modulus and viscoelasticity of the white matter are robust across experimental condition and variation in acoustic input. Experimental white matter testing using ARFI with *in vitro* brains at 20° C yielded a shear modulus of $3.03 \pm 0.87 \text{ kPa}$ while brains in a water bath at 37° C yielded a shear modulus of $1.06 \pm 0.37 \text{ kPa}$. This dramatic difference in material properties has implications when modeling brains *in vivo*. We have further developed a novel viscoelastic modeling technique based on fractional calculus (Urbanczyk, 2012) that extends current concepts in quasilinear viscoelasticity across many orders of strain rate.

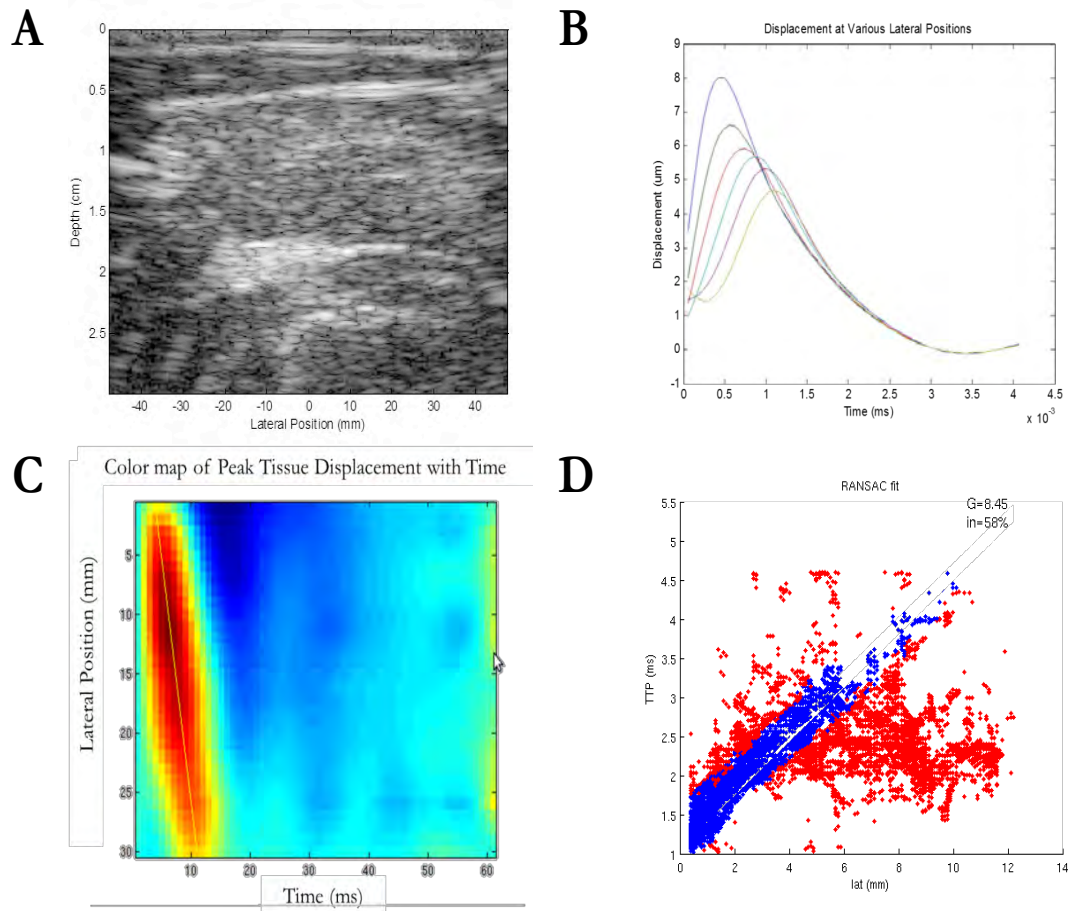


Figure 3: B-mode ultrasound image of porcine brain *in vivo* (A). ARFI imaging uses high-intensity, short-duration pulses to generate local displacements in tissue on the order of $10\mu\text{m}$ (B). The colormap allows us to visualize peak displacements as a function of time and lateral position (C). An iterative method with a 3D fit-plane regression is used to reconstruct shear wave velocity (D) (Urbanczyk, 2012)

5. Human and ferret models have been developed and hypotheses investigated on blast phenomenology.

We developed a detailed model of the human head (Figure 14) for the simulation of the brain's response to a wide range of real-world threats. For our model, the mesh could be spatially resolved to capture the high-frequency waves associated with blast: the shock wave from a free-field blast has relevant frequency content up to 40 kHz. We found that when wave propagation is considered important in an FE model, the mesh should be six to ten elements per wavelength in order to reduce numerical dispersion. At ten elements per wavelength, the current air and head mesh sizes could effectively propagate pressure waves with frequencies up to 18 kHz in air, and 140 kHz in brain tissue without accumulating significant numerical dispersion.

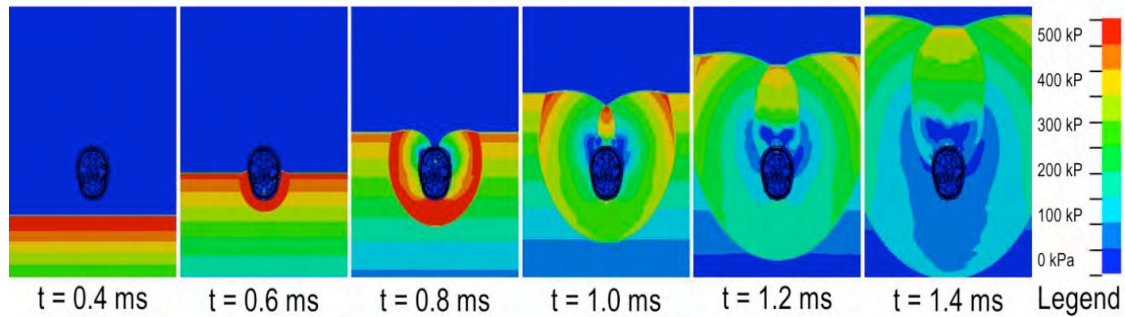


Figure 14. The time progression of overpressure showing the impingement of the simulated blast wave on the head model (pressure in head not shown) (Panzer, 2012)

a. *Brain Response to Blast*

Over the wide range of blast conditions simulated, the maximum pressure levels within the brain were primarily dependent on the overpressure conditions of the blast wave. The insensitivity of pressure response to the blast duration was likely because the speed of sound in the skull and brain are much higher than that of air. The higher sound speed propagated pressure away from the impact site faster than it was loaded, as evidenced by the 0.8 - 1.2 ms pressure pulse in the brain compared to the 1.0 – 8.0 ms pressure pulse of the blast. The length of the overpressure pulse in the brain tissue is likely an important consideration for *ex vivo* tissue studies attempting to replicate the internal conditions of blast exposure.

The deviatoric response of the brain was driven largely by skull deformation and not head motion (i.e., rigid body inertia), confirming previous computational results. Strain developed mainly in the cerebral cortex as the tissue deformed relative to the vibrating skull. Decreasing the radial coupling between the brain and the skull (via CSF cavitation) increased the lag between the brain and skull and augmented strain levels. It is important to consider that maximum stresses and strains occurred after the initial shock wave passed through the head. Many FE models did not run the simulation past 2 ms (Moore et al., 2009; Nyein et al., 2010; Taylor & Ford, 2009), only capturing the response of the brain during the incident wave and not the response caused by the coupling between the brain and the flexing skull. If high-rate strain response from skull deformation following blast exposure is the primary mechanism for blast TBI, then it is critical that models are simulated long enough to capture these effects.

The skull deformation was primarily of the 1st mode of flexure, which had a natural frequency of approximately 305 Hz when the brain coupled with the skull and 169 Hz when CSF cavitation caused the brain to decouple. No evidence of localized skull flexure (skull ripple), as initially reported by Moss (Moss, 2010), was seen in the simulations despite the plane-strain model being more susceptible to this type of deformation than an ellipsoid. The difference may be from the inclusion of a skin layer over the skull. The skin likely attenuates pressure waves at the skull, and disperses the loading area so that the shock load is not concentrated locally on the skull. Regardless of these differences, it is apparent that skull deformation plays an integral role in the loading of the brain during blast exposure. There is a need for empirical data on the deformation of human skulls exposed to blast loading to validate the skull mechanics in computational models.

Minimizing skull deformation may be an important consideration for improving helmet design in blast. The results of this study suggest that reducing the total impulse transferred to the head will reduce the amount of strain developed in the brain. Military helmet design strategies similar to those used in helmets designed to mitigate blunt impact forces (increased helmet-head standoff, energy-dissipative padding, etc.) are likely to reduce the skull deformation in blast. In a parametric study on helmet padding design for blast brain response, Panzer et al., (2010) found that low-density crushable helmet padding best dissipated the energy transferred from the helmet to the head, and this resulted in lower brain strain.

b. Effects of cerebrospinal fluid (CSF) cavitation

CSF cavitation has long been hypothesized as a cause of brain injury in both automotive head impacts and blast impacts. However, it remains unclear whether CSF cavitation occurs during these impact events and at what tensile pressure levels. In laboratory conditions and devoid of nucleation sites, the cavitation pressure of water (by stretching) ranged from -100 kPa (aerated tap water) to -20 MPa (de-gassed distilled water). Fluid cavitation pressure is dependent on a number of factors including temperature, surface tension, dissolved gas, presence of particles and nucleation sites. Since the constituents of CSF differ from water, the pressure level at which CSF cavitation will occur may not be the same as water. Most lab studies on cavitation include dissolved gases and electrolytes. CSF, like plasma, also includes dissolved proteins albeit far fewer than plasma. Additionally, structures in the subarachnoid space may provide some tensile support that would alter the effective cavitation threshold of the CSF.

The results of this study indicate that the presence of CSF cavitation at -100 kPa has a substantial impact on the response of the brain in more severe blast conditions (Figure 15). Wardlaw et al., (2010) reported on the possibility for CSF cavitation to occur in blast using a 3D ellipsoid head model. In conclusions similar to this study, they found that the periodic formation of CSF cavitation and collapse was related to skull deformation. However, they did not quantify the effect of CSF on the mechanics of the brain. This project found that in addition to creating localized regions of high pressure when the CSF cavitation collapsed (the mechanism for traditional cavitation damage), the presence of CSF cavitation allowed the brain to decouple from the skull resulting in an increase in brain strain. CSF cavitation also occurred early in the simulation because of the inertial and deformational effects between the brain and skull, and not during the negative pressure phase of the blast as previously hypothesized.

CSF cavitation may also play a role in damaging deeper neural tissues. The periventricular tissues experienced higher levels of strain when CSF cavitation occurred in addition to the elevated levels of pressure from cavitation collapse. Periventricular white matter changes are commonly seen on MRI scans of persons with Alzheimer's disease and diffuse radiation injury of the brain. MRI changes in periventricular areas are also seen in vascular disease, even in the absence of clinical signs of disease. Migraine headaches are also associated with these periventricular changes. In this model, results show greater potential for tissue damage at anatomic locations that are with relatively poor blood supply compared to other brain regions.

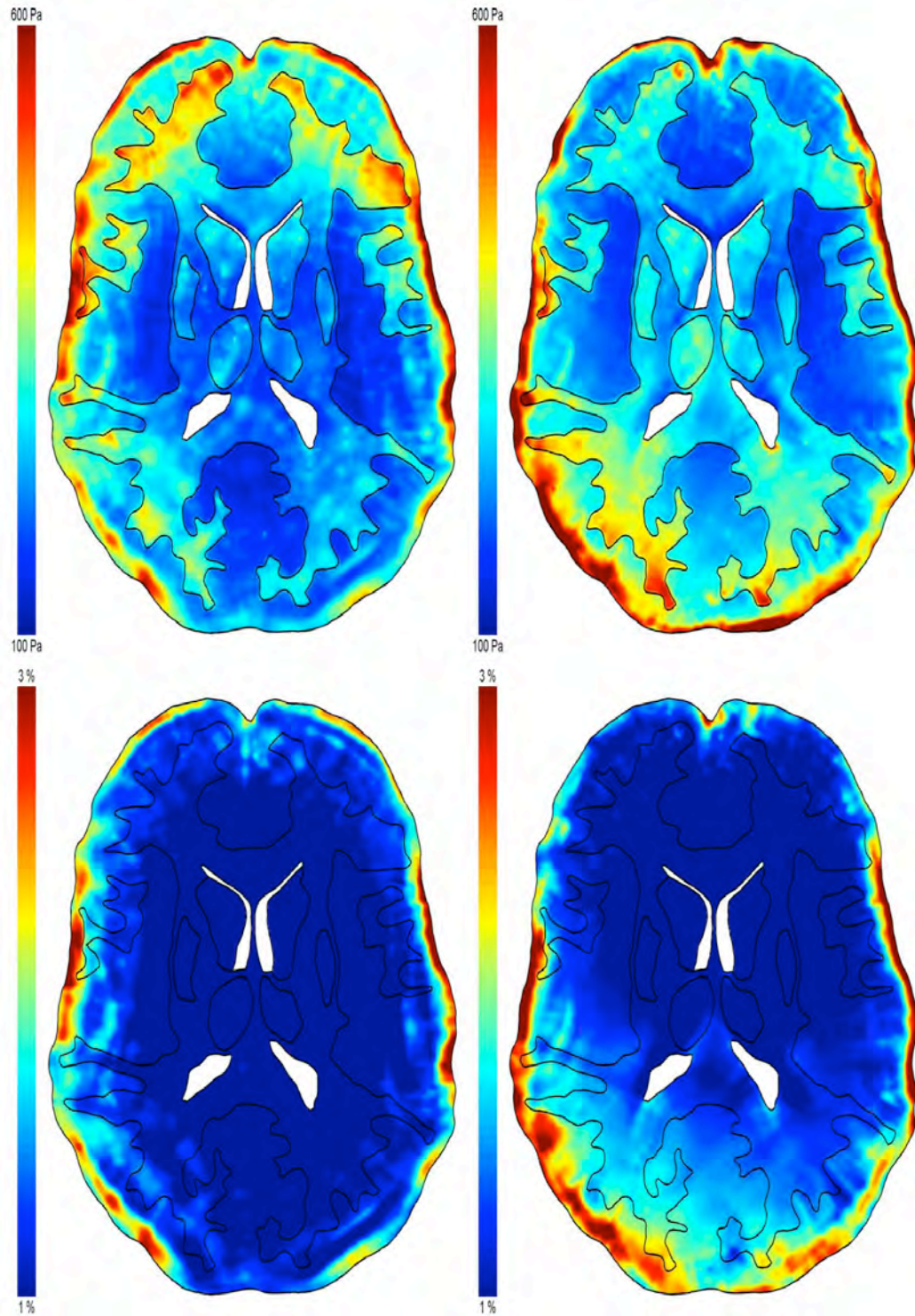


Figure 15. Comparison of the distributions of peak von Mises stress (top) and shear strain (bottom) between the non-cavitating (left) and cavitating (right) models for the 500 kPa / 4 ms blast condition (Panzer, 2012)

c. *Potential Injury Mechanisms*

All pressures measured in the brain in various experimental efforts and computational efforts were much lower than the hydrostatic threshold for cell death (approximately 100 MPa) measured in bacterial and mammalian cells, even in the most severe conditions simulated. This would indicate that either pressure is not an injury mechanism for brain tissue in blast, or that a pressure-based injury criterion will include rate effects that would decrease the tissue threshold from the hydrostatic criterion.

Maximum pressure levels within the brain were primarily dependent on the overpressure conditions of the blast wave, even in the presence of CSF cavitation, implying that if pressure was the only injury mechanism of brain tissue, then TBI should not depend on blast duration or impulse. This would be unlike short-duration pulmonary blast injury criteria where injury risk is strongly associated with both peak overpressure and duration. Furthermore, our recent experimental results using a thoracic-protected ferret model exposed to a wide range of blast conditions has shown strong exposure duration dependence for moderate/severe meningeal bleeding, apnea, and fatality. By considering these animal tests along with the findings of this study, it would suggest that brain tissue pressure was not the sole injury mechanism for moderate to fatal brain injuries. The model predicted brain tissue strain would increase with blast impulse, which agrees with the results found by Rafaels if the brain injury mechanism was strain-based. However, peak strain levels predicted in the tissue were typically much lower than strain levels thought to be associated with injury thresholds. Bean and Meaney found electrophysiological impairment in axons of a guinea pig optic nerve model at a threshold of 18% strain. Elkin and Morrison reported a cortical cell death threshold between 10 and 20% strain in organotypic hippocampal slice cultures in addition to finding an increase of injury with strain rate. Given the relatively low levels of strain for nearly all blast conditions simulated, a rate-dependent, strain-based injury mechanism is the likely source of brain injury.

An additional point to note is that this discussion on injury mechanism only considers moderate and severe TBI based on our work (Rafaels, 2011). This study is extending models to a wide range of peak overpressures and durations (or impulses) to investigate the hypothesis that the injury mechanisms responsible for gross injury of brain tissue in blast are not the same as mechanisms that are responsible for mild TBI. This is especially important in the context of regional differences in both material properties and characteristic injury thresholds shown by Duke researchers and MURI partners at Penn and Columbia.

[A2] Use computational methods for interspecies scaling of the blast wave through the mammalian brain.

Interspecies Scaling:

We have made substantial progress in understanding physical scaling of blast, applicable from cell cultures through human scales, including publications on the validation of the numerical models for blast in Panzer et al (2012), Panzer et al (2011), and experimental scaling results in Bass et al (2012), Rafaels et al (2012), currently unpublished animal results by Yu et al, Wood et al and Rafaels et al and recent results presented at the National Neurotrauma society meeting (Panzer et al, 2012a).

Animal models are essential for elucidating physical and physiological consequences of blast. Such animal model tests have been conducted on a wide size range of animal species (Figure 16), from mice through pig, though most of the research has focused on rodents such as mice. For these experimental models, scaling from the animal model to the human is the essential conundrum, especially with small rodent models in which there are considerable anatomical and physical differences with humans. Failure to understand the relative scaling may make experimental models inapplicable to the actual human blast scenarios and pathophysiology. This scaling may involve many variables, accounting for large differences in comparative neuroanatomy with vast differences in gray matter/white matter ratios (Bell, 2008), and critical differences in underlying physiology (e.g. Bass, 2012). Interspecies differences in CNS tissue layer may also be relevant as we do not adequately understand the implications of murine cortical biomechanical properties compared to a ferret or human six layer cortex.



Figure 16: Relative brain size of typical blast TBI animal model species (adapted from the Wisconsin Brain Collection and Panzer, 2012)

All animal TBI models can only approximate the intra-cranial biophysics and subsequent pathophysiology of blunt or blast injury to humans. Animal models are limited by possible differences in biomechanical properties of neuronal tissues, physiological differences, and obvious anatomical differences. To mitigate the risk of substantial anatomical differences between humans and animal models, human cadaveric models may be used to determine anatomical response, though cadavers may have altered postmortem biomechanical properties and lack post-injury physiological response. In the last year, this project has collected high rate intracranial pressure and response data from human cadavers to validate human models and to provide physical scaling principles (Wood, unpublished).

To make use of injury risk assessments and pathophysiological correlates in animal models, scaling is essential. Such scaling derives the physical relationship between an exposure to an experimental animal model and an equivalent exposure to a human, perhaps in terms of blast wave

characteristics such as pressure, duration or impulse. These scaled mechanical parameters may be associated with an animal injury to determine the equivalent blast exposure for a human. Scaling is a vital component for establishing robust and functional human blast injury criteria and helping define exposure tolerances for occupational safety and personal protection design. The fundamentals of this crucial scaling relation for blast TBI are unknown and are urgently needed.

The most widely used scaling law for blast was developed at the Lovelace Foundation for pulmonary injuries using a mathematical lumped-mass model of a mammalian thorax and abdominal cavity (Bowen, 1965). Bowen used a simple dimensional analysis to compare the internal lung pressure response between animals (and by assuming both tissue density and tissue moduli were constant across species). Bowen's model reduced to a simple dimensional scaling procedure for the positive-phase overpressure duration based on the cube root of the ratio between body masses:

$$\Delta t_{\text{scaled}} = \lambda \Delta t \quad \text{where} \quad \lambda = \left(\frac{M_{\text{ref}}}{M} \right)^{1/3} \quad \text{Equation 1}$$

where Δt and M are the positive-phase duration and body mass of the exposed animal model, and Δt_{scaled} and M_{ref} are the positive-phase duration and body mass of the human. This method scales the duration of the blast and not the amplitude of the overpressure, and is essentially a length scaling between species assuming a spherical body shape. Remarkably, the scaling law developed for pulmonary blast injuries is identical to those developed for automotive blunt impacts.

This approach was thought to account for the variation of chest wall thickness between species for short duration blast (< 30 ms), where overpressure duration has a substantial effect on the peak overpressure tolerance (Bass, 2008). *The physical or physiological mechanism of this pulmonary blast scaling is still unknown.* Bowen found this pulmonary scaling law did not apply equally to all mammals, and that species appeared to fall into two distinct groups described as “small” animals and “large” animals. “Small” animals (mouse, rat, guinea pig, rabbit) had a significantly lower pulmonary blast tolerance than “large” animals (monkey, cat, dog, goat). This difference was not reflected in the pulmonary scaling law and was attributed to average lung volume to body mass ratio. Differences in pulmonary scaling between large and small animals may depend in part on physiological differences. Murine respiratory rates are extremely high relative to humans. Further, murine lungs default to open whereas mammalian lungs tend to collapse. This physiological difference allows mice to breathe rapidly with less energy expenditure. Based on the pulmonary blast injury scaling laws, Bowen was later able to compile Lovelace's “large” animal blast injury data into a human primary blast pulmonary injury criteria based on a reference mass of a 70 kg human. This injury criteria was later modified to include a greater number of experimental results for short duration blast (Bass, 2008), long duration (Rafaels, 2011), and repeated blast exposure (Panzer, 2012b).

For human blast brain injury criteria, the establishment of a definitive scaling law has been hampered by the lack of test data across a wide range of species in comparable blast conditions save the rabbit and ferret data of Rafaels, the recent porcine test data of Shridharani (2012), and unpublished cadaver response data of Wood et al from this project. We are further seeking human blast-only epidemiology data in situations where the torso is protected from past and current conflicts to verify these animal models. *It is important to consider the potential for exposure scaling when designing animal injury models; experimental tests should be representative of real-world exposures.* For instance, most rodent models have been tested in compressed air driven shock tubes, resulting in blast exposures with relatively low peak incident overpressures (less than 250 kPa) but large overpressure durations (greater than 10 ms). If the applicable scaling law for blast TBI is the Bowen pulmonary or automobile brain scaling from Equation 1, the corresponding scaled blast duration for a 70 kg human would be seven times that of a 200 gm rat, making the equivalent human exposure for typical rodent blast TBI experiments large charge sizes of greater than 20,000 kg TNT or nuclear blasts. In contrast, real-world exposure of typical IEDs composed of stacked artillery shells produces overpressure durations less typically than 10 ms.

As with the pulmonary scaling law, there is a strong likelihood that factors associated with neuroanatomy and physiology will be important for blast brain injury scaling. These factors include mass (body, head, or brain), skull dimension or thickness, the ratio of grey to white matter, relative sizes of brain structures such as the amygdala and hippocampus, position and sizes of ventricles, thickness of the cerebrospinal fluid, etc. Furthermore, human blast brain injuries may not scale from all species, and scaling may be limited to animal models whose brains share anatomical features with humans (lissencephalic versus gyrencephalic brains). Ideally, scaling would be based on physical or physiological factors required to injure the brain such as equivalent stress or strain on similar brain structures.

In addition to brain mass other mechanical and structural factors likely contribute to brain injury response from blast. Skull dimensions or thickness likely have an effect as resonant frequency decreases with skull size. Absolute and relative skull thickness is also known to vary between species and will effect blast wave transmission to the brain tissue. Structural differences within the brain such as grey/white matter ratio and relative brain structure size can change the overall mechanical behavior of the tissue and therefore the biomechanical response to blast. Of special interest is the surface structure of the brain (lissencephaly, gyrencephaly) and scaling may be limited to animal models with similar features to the gyrencephalic human brain.

This project has combined physiological data (bleeding and apnea results) from multiple species with physical and finite element modeling data presented at the recent National Neurotrauma Society Meeting (Panzer, 2012) and slated for presentation at the upcoming Biomedical Engineering Society Meeting (Wood, 2012) to produce estimated intraspecies scaling. These principles assume that injurious stress levels are invariant across species. This assumption is being tested using mouse and ferret cell models.

The work of Duke (Panzer, 2012 and Wood, 2012) focuses on the development of a framework for scaling blast dose in an animal model to a human for equivalent biomechanical response. Scaled finite element modeling of a simplified replica skull/CSF/brain model has investigated differences in peak pressure and strain in the brain according to brain size for responses to blast pressure, duration and brain mass as

$$\frac{X_2}{X_1} = \left(\frac{P_2}{P_1}\right)^{\alpha} \left(\frac{T_2}{T_1}\right)^{\beta} \left(\frac{M_2}{M_1}\right)^{\gamma}$$

Results (Figure 17) have shown that increases in blast pressure lead to increases in both brain pressure and strain. However, increasing blast duration results in an increase of brain strain only. These simulations have shown that smaller heads exhibit a slightly higher brain pressure but dramatically higher stress/strain behavior for the same blast condition. The increase in brain strain was found to be roughly 50% when halving the head size. A scaling model fit determined a duration dependence upon brain mass to approximately the 0.25 power as seen below.

$$T_2 = T_1 \left(\frac{M_2}{M_1}\right)^{0.248}$$

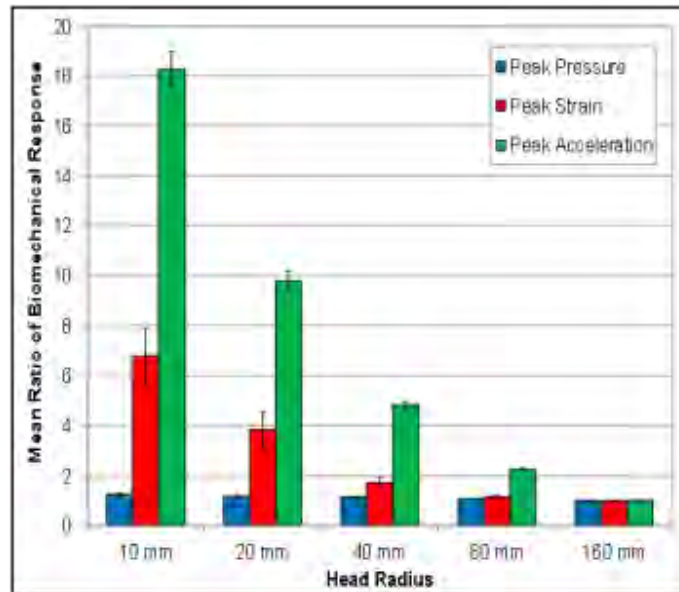


Figure 17: Mean biomechanical response of the brain relative to 160 mm model over all conditions (Panzer, 2012)

Based upon typical brain mass for common blast testing animal models the appropriate duration scaling factor by species (Figure 18) and scaled apnea response for human exposure (Figure 19) are shown. *It is important to emphasize that much of the animal model blast research, under the assumptions of this work, would explore scaled duration ranges typical of nuclear blasts, not high explosive blasts.* This is also true for the simple biomechanical pulmonary biomechanical scaling (Bass, 2012).

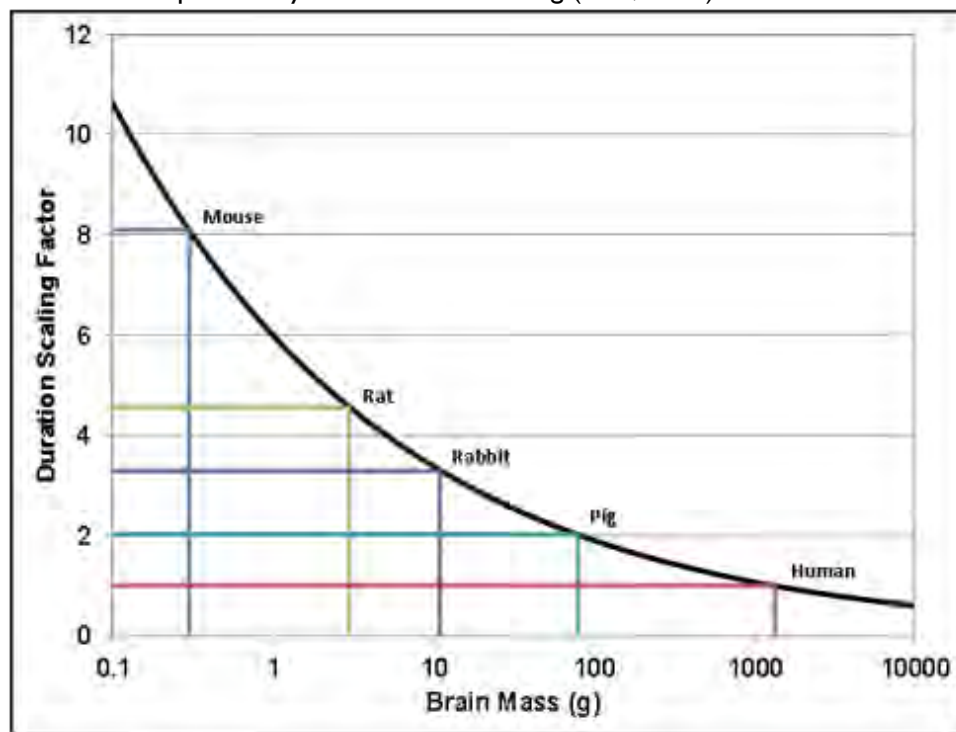


Figure 18: Duration scaling factor by species for common blast animal models (Panzer, 2012)

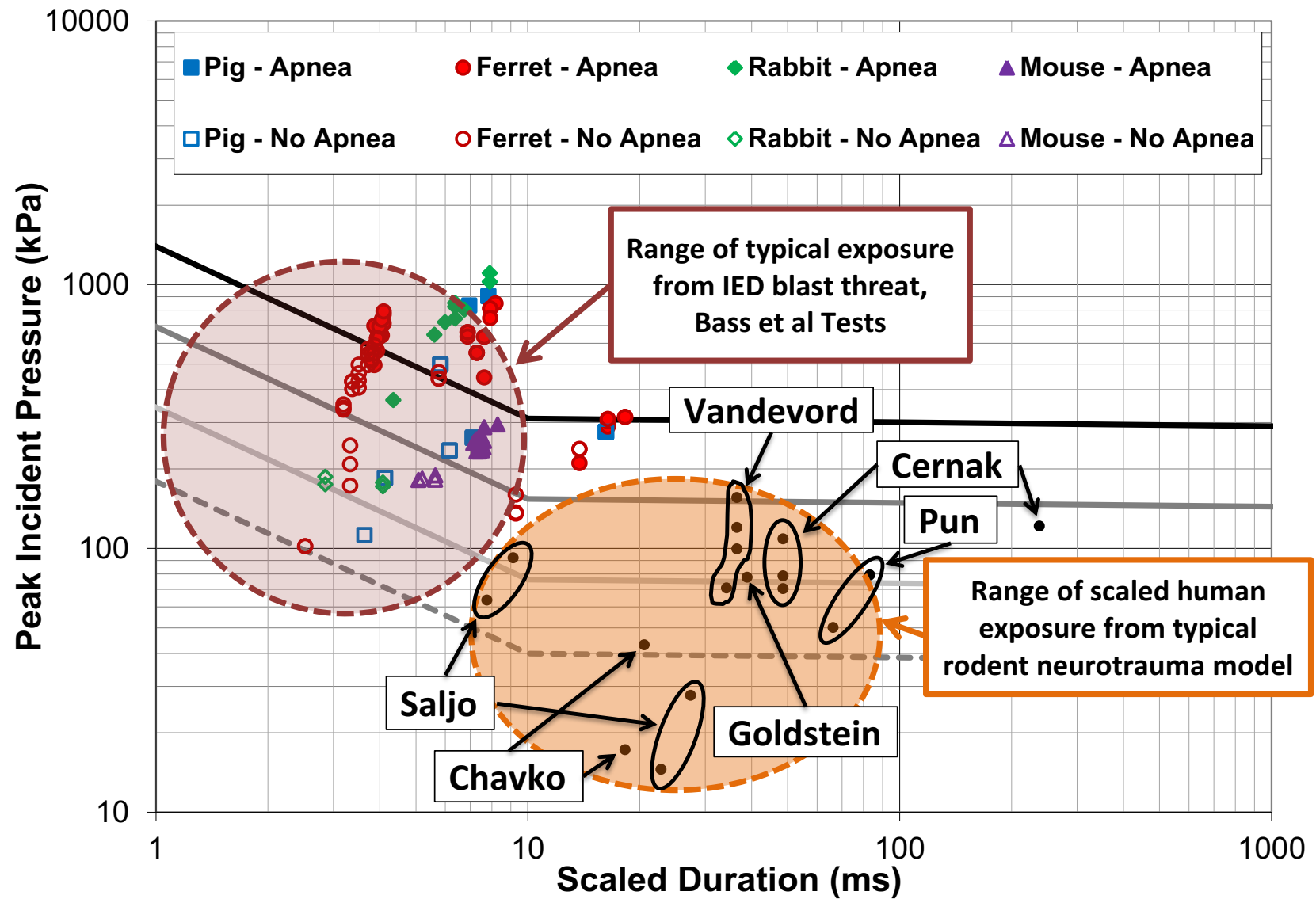


Figure 19. Apnea response scaled for human exposure (Wood, 2012, Panzer, 2012)

Additional scaling metrics based upon physiological function are being explored in this project based on evidence from cellular response through animal model response based upon available epidemiological data. There are large differences in physiological rates and processes among mammals. Some simple metrics include life span, heart rate and metabolic rate which vary greatly among mammals commonly used as blast animal models. Differences in life span and heart rate may change the rate by which injury acts or is exhibited within a species. It has long been known that these physiological metrics are closely interrelated. Life span can be defined by a total number of heart beats which does not significantly vary across mammalian species. Therefore, life span can be closely correlated with resting heart rate, which is inversely proportional to body mass. In fact heart rate and body weight are nearly linearly related. These metrics may prove important for injury as the injury time scale will vary relative to the important time scales for circulation and life span of the model animal.

Basal metabolic rate and oxygen consumption may provide useful scaling parameters as they describe the rate by which small-scale cellular processes take place throughout the body and within the brain. As injury response from blast is theorized to stem from not only instantaneous mechanical damage but also secondary response of cellular processes, metabolic rate may be very important in describing differences in injury across species. Extensive literature exists describing basal metabolic rate and its relation to body mass. For mammalian species this relationship is scaled well with body mass and an exponent of approximately $3/4$. Further study has established a similar allometric scaling relationship between brain mass and basal metabolic rate with an exponent of approximately $2/3$.

However, the metabolic rate in the brain specifically cannot be scaled so simply. Relative to the entire body the brain maintains high metabolic activity even during periods of rest. Differences in the size of brain structures such as the cerebral cortex and brain size relative to body size further complicate the scaling of brain metabolic rate. Hofman et al. (1983) and others have attempted to derive scaling procedures for brain metabolism as a function of brain mass relative to body mass and encephalization (cerebral cortex size). It may be valuable to attempt scaling injury metrics based upon the brain metabolic rate since it is clear that there is no simple relationship between absolute or relative brain metabolism across species.

As seen in Figure 19, there is great concern that the bulk of current testing focuses on scaled blast conditions that vary greatly from those typically seen in combat, especially in rodent models. The widespread usage of proper scaling laws for blast TBI is vital to ensure research is useful to our understanding of injury thresholds and risk.

Further development of these models is continuing to support the cellular and network work and provide appropriate scaling for excitation of these networks.

[A3] Build devices for studying the effects of blast loading at the synaptic, network, and circuit level.

The MURI collaboration has developed shock tubes capable of providing realistic blast shock for cell cultures with appropriate matched boundary conditions to small animals to large animals (Panzer, 2012). This is a strength of this collaboration. The devices designed for this project are currently in use at Duke (4 laboratories), Penn and Columbia and collaborations are being established outside the core MURI institutions to promulgate these devices. This work was reported in Panzer et al (2012)

A substantial amount of blast-related neurotrauma research has focused on understanding the mechanisms and effects caused by direct impingement of the blast wave on the body (known as a primary blast injury). In vivo animal models are used to elucidate the pathological effects of BINT, with the most common species being small rodents (mice or rat). Previous studies have reported a wide array of histological and gross pathological perturbations following blast exposure to in vivo models. Structural and/or morphological changes have been reported using a variety of histochemical and microscopy techniques in neuronal and glial cells following blast exposure (Kaur et al., 1995; Cernak et al., 2001; Mochhala et al., 2004; Long et al., 2009; Garman et al., 2011; Pun et al., 2011). The blood-brain barrier defects resulting in increased permeability were found post-blast (Garman et al., 2011; Risling et

al., 2011). In more severe BINT, gross pathological findings typically present as mild or moderate subarachnoid and/or subdural hemorrhaging (Kaur et al., 1995; Bauman et al., 1997; Säljö et al., 2008; Long et al., 2009; Cheng et al., 2010; Rafaels et al., 2011). More recently, the clinical manifestation of apnea immediately following blast exposure is being reported in many animal models exposed to blast waves (Long et al., 2009; Cheng et al., 2010; Garman et al., 2011; Rafaels et al., 2011).

Much of the BINT research is in the discovery period. Most primary blast models use shock tubes (compressed gas) or blast tubes (explosive charges) to generate the blast overpressures time histories (Bass et al., 2011). Test methodologies and analyses are not thoroughly established, and it is difficult to compare results across studies because of the vast differences in methods and resulting blast exposure. One major limitation to current in vivo BINT models is the unknown scaling between the animal model and the human response (Bass et al., 2011). A vital component in establishing a human blast injury criterion is the methodology of scaling the characteristics of a blast (pressure, duration, impulse) associated with an animal injury to the equivalent blast exposure for a human. The scaling law widely used for pulmonary blast injury models was developed at the Lovelace Foundation, and scaled the blast overpressure duration by the cube root of the ratio between body masses of species (Bowen et al., 1968; Bass et al., 2008). This simplified dimensional procedure only considers the scaling of the duration (and impulse) of the blast overpressure, and not its amplitude. Remarkably, the scaling law developed for pulmonary blast injuries is identical to those developed independently for automotive blunt impacts (Eppinger and Marcus, 1984) despite the vast differences in the total momentum in each loading type. Injurious short-duration blasts generally have lower total momentum. Current scaling results are discussed above.

a. Shock tube design

A gas-driven shock tube is the most common device used to generate blast overpressure conditions for neurotrauma research (e.g. Celander et al., 1955; Cernak et al., 2001; Chavko et al., 2007; Rafaels et al., 2011), because of its ability to produce repeatable blast waveforms that closely resemble free-field blast waves in a controlled laboratory environment. However, most shock tube methodologies expose small rodent models to blast overpressures with long durations (> 4 ms). Considering this, we designed a set of shock tubes for generating short positive-phase durations (0.3 – 3 ms) but relatively high peak incident overpressures (up to 650 kPa) for direct exposure to in vivo rodent injury models. The capabilities of the designed shock tube allow for scaled equivalent human durations to range from 1.8 to 18 ms for a rat injury model, and 3.9 to 39 ms for a mouse injury model, which are more representative of real-world conditions than long-duration shock tube tests. However, if BINT scaling is different than pulmonary injury scaling, then the designed shock tube fills a gap in the range of blast conditions tested in current methodologies.

A number of factors are important for designing a shock tube to produce the blast characteristics desired, the most critically being driver gas type, diaphragm burst pressure, and the ratio between driven length and driver length (Bass et al., 2011). For the current shock tube design, the diameter also needed to be large enough for exposing a rodent head to a well-defined plane wave, but small enough for bench-top application. The rule-of-thumb for shock tube design is to use a driven length to diameter ratio greater than 10 to ensure the shock wave is planar (cf. Bass et al., 2011), and in the case of the 630 mm design, this ratio is approximately 8. This likely explains the significant increase in inter-test variability with the 630 mm tube. Shock tube repeatability and reproducibility was an important consideration for the design, because multiple institutions are currently using this equipment (Figure 20).

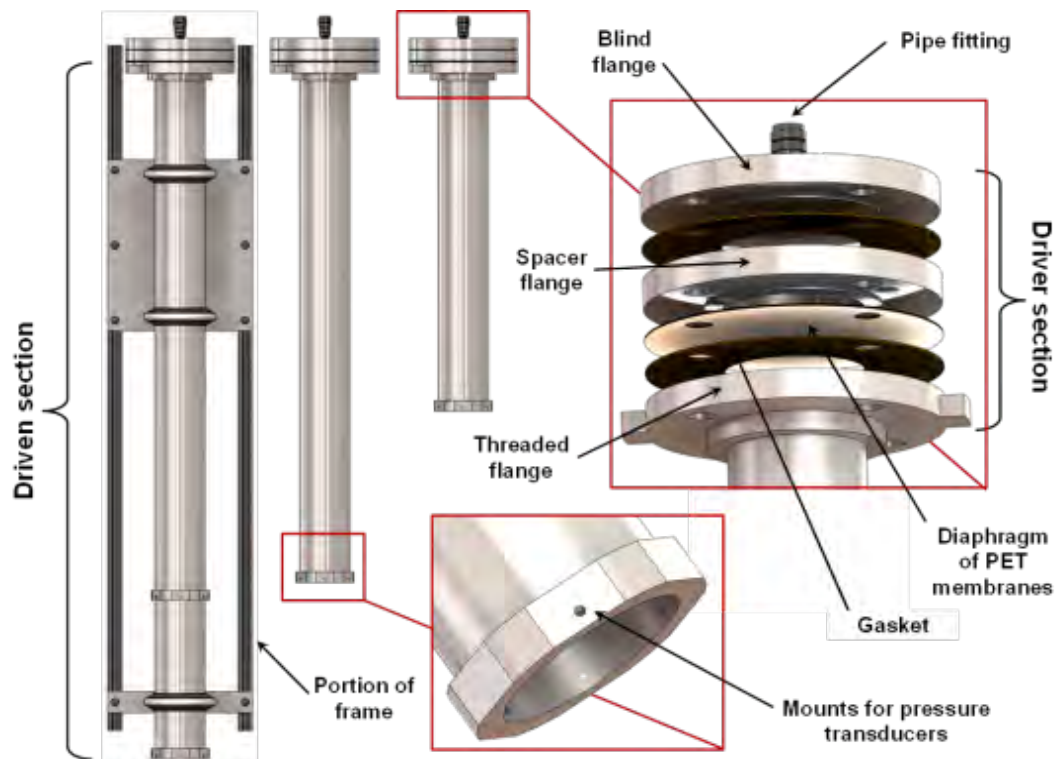


Figure 20. Shock Tube Design (Panzer, 2012)

One of the issues we have experienced with using the shock tube is the batch-to-batch variability of the PET membrane thickness. The thickness of a batch of PET film has a variability of $\pm 10\%$ (personal communication; Grafix Plastics Inc, Cleveland, OH), and this variability can compound when multiple membranes are used to build the diaphragm. For instance, a 1.27 mm diaphragm (5 x 0.254 mm sheets) test condition averaged burst pressures of 4887 kPa (± 62 kPa SD) for one batch of film and 6005 kPa (± 27 kPa SD) for another using the same test conditions. This issue did not affect the response of the shock tube (peak pressure and duration were well correlated with burst pressure), but it did affect our ability to precisely control the blast conditions using stated diaphragm thickness. We have implementing quality assurance protocols to assess individual diaphragm batches.

b. In vitro injury models

In vitro models are an important tool for elucidating the pathobiology of TBI caused by mechanical disruption of central nervous system (CNS) tissue by allowing researchers to reduce the complexity of in vivo TBI models, and improve access to the biological and mechanical parameters associated with the tissue. However, for in vitro models to be effective in improving our understanding of the injury sequelae, they must accurately represent the in vivo post-injury response to mechanical loading. Morrison et al. (2011) provides a comprehensive review on in vitro models for TBI and their recapitulation of in vivo pathobiology (Morrison III et al., 2011).

A large number of in vitro TBI models were developed for understanding the response of CNS tissue to mechanisms caused by blunt head impact or inertial loading. Many of these models focused on applying a disruption to the CNS tissue in shear (e.g., LaPlaca and Thibault, 1997; LaPlaca et al., 2005), or in stretch (e.g., Cargill and Thibault, 1996; Morrison III et al., 1998; Morrison III et al., 2003; Morrison III et al., 2006). The fastest deformation capabilities of these in vitro models can apply strains to tissue at rates up to 50 s⁻¹ (Morrison III et al., 2003; Cater et al., 2006). However, these rates are too slow for replicating conditions caused by

blast loading, where strains are typically very low (less than 10%) but strain rates may be very high (100 to 1000 s⁻¹) (Panzer et al., 2011c). Thus, new in vitro injury models are needed to study the pathobiological effects of TBI caused by blast exposure.

A fluid-filled receiver was designed to replicate the in vivo boundary conditions for in vitro cellular and organotypic samples subjected to an overpressure pulse caused by a blast wave (Figure 21). This in vitro injury methodology is the first to replicate the loading conditions and boundary conditions that are relevant for studying BINT, and not overly compress the injury model against a material with higher impedance. Additionally, this methodology allows for the direct measurement of the overpressure applied to the specimen. This capability will allow for the future development of injury criteria that can be applied to computational models for injury risk assessment.

The rationale for this design was to surround the sample with materials with similar bulk properties and impedance so that the applied pressure wave propagated through the tissue rather than reflected off the tissue. This is an important aspect of the methodology because reflecting the applied wave off the sample will have the unintended consequence of large tissue deformations not associated with blast. Furthermore, the receiver was designed to mitigate and attenuate possible pressure wave reflections that may return to the tissue in an effort to reduce the possibility of additional tissue disruption from repeated loading. The receiver design could be modified in future studies to produce more complex waveforms to simulate additional types of blast overpressures in more complex operational environments.

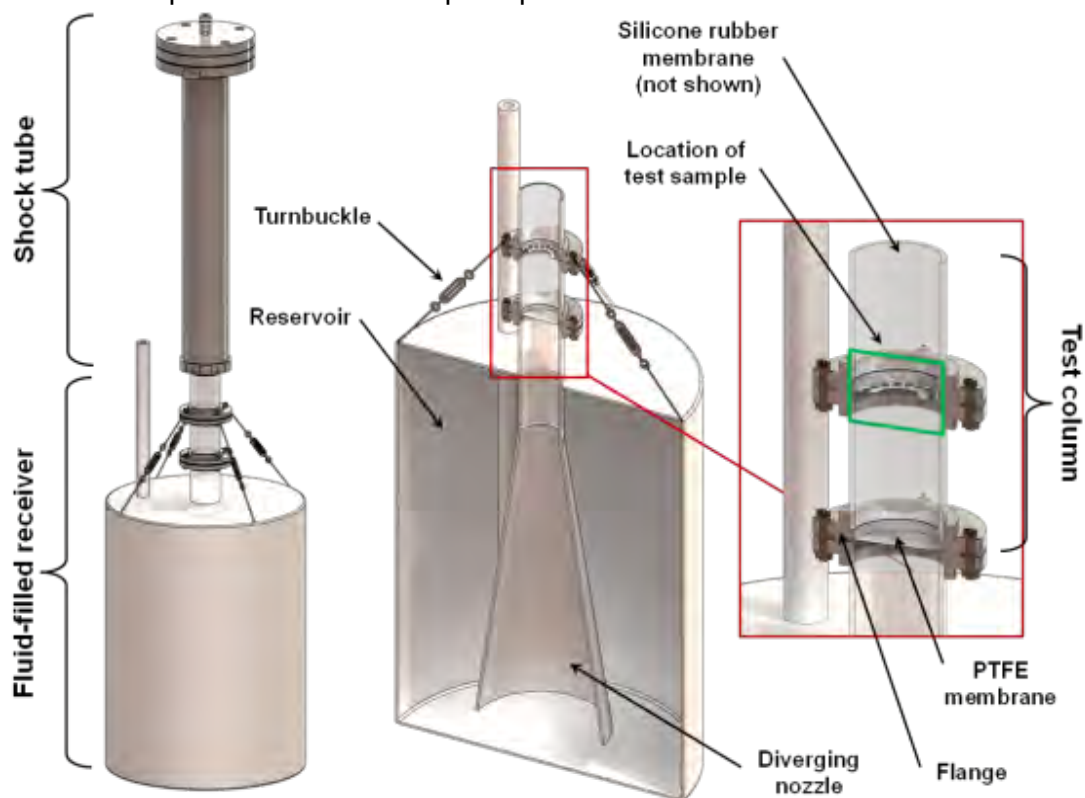


Figure 21. Shock Tube Receiver Design for testing Cell and Slice Cultures (Panzer, 2012)

One of the advantages of the fluid-filled receiver is that it is not limited to a specific in vitro culture model. Many types of tissues, including organotypic slices and cell cultures, are currently being used with the receiver for in vitro blast injury modeling. Furthermore, the

dimensions of the receiver can be modified in the future to tailor the applied overpressure pulse to match specific intracranial pressure traces seen in animal or cadaveric blast models. This may be particularly important when considering more complex intracranial pressure pulses caused by the interaction of the blast with the head and its surroundings (including helmets and other protective equipment). Work is ongoing to extend the available blast conditions with appropriate gas choice (Figure 22).

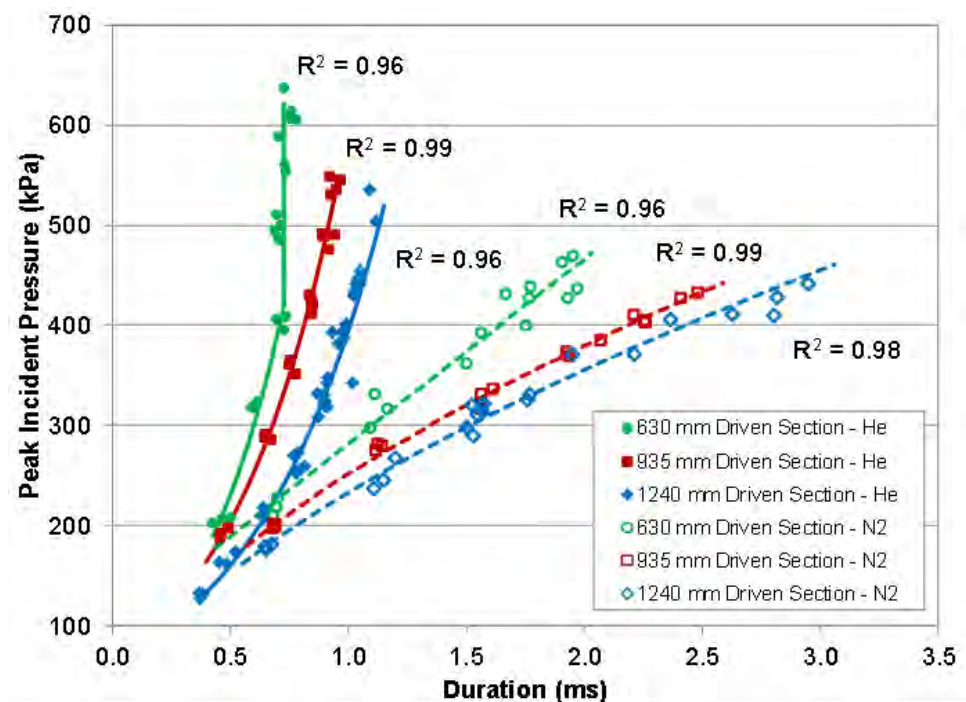


Figure 22. Shock Tube Incident Pressure Results (Panzer, 2012)

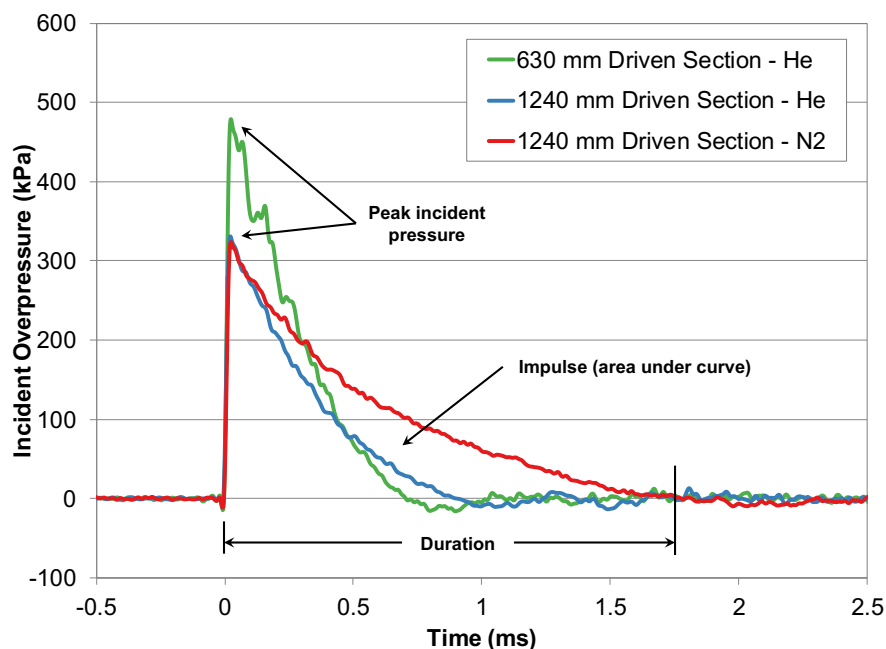


Figure 23. Shock Tube Incident Pressure Time History Results (Panzer, 2012)

Task D. Correlate changes at the synapse and circuit level to corresponding neurobehavior deficits in animals.

[DI] We use knowledge from Thrust A to scale models of blast wave transmission into animals.

One of the keys to this is appropriate neurobehavioral model that replicates typical features of human behavior and may be correlated with cellular response. To do this we have two thrusts. We have developed a ferret assay for blast including blast injury criteria in ferrets (Rafaels, 2012) in terms of peak pressure and scaled duration (Figure 24). The assay is behaviorally appropriate and similar to neurobehavioral deficits seen in humans (e.g. Capehart, 2012). The second thrust is to identify human epidemiological data that we can use to validate our animal, cadaver and numerical models. Suitable datasets have been identified from large blasts in World War I and I and recent conflicts. Data analysis of these is ongoing.

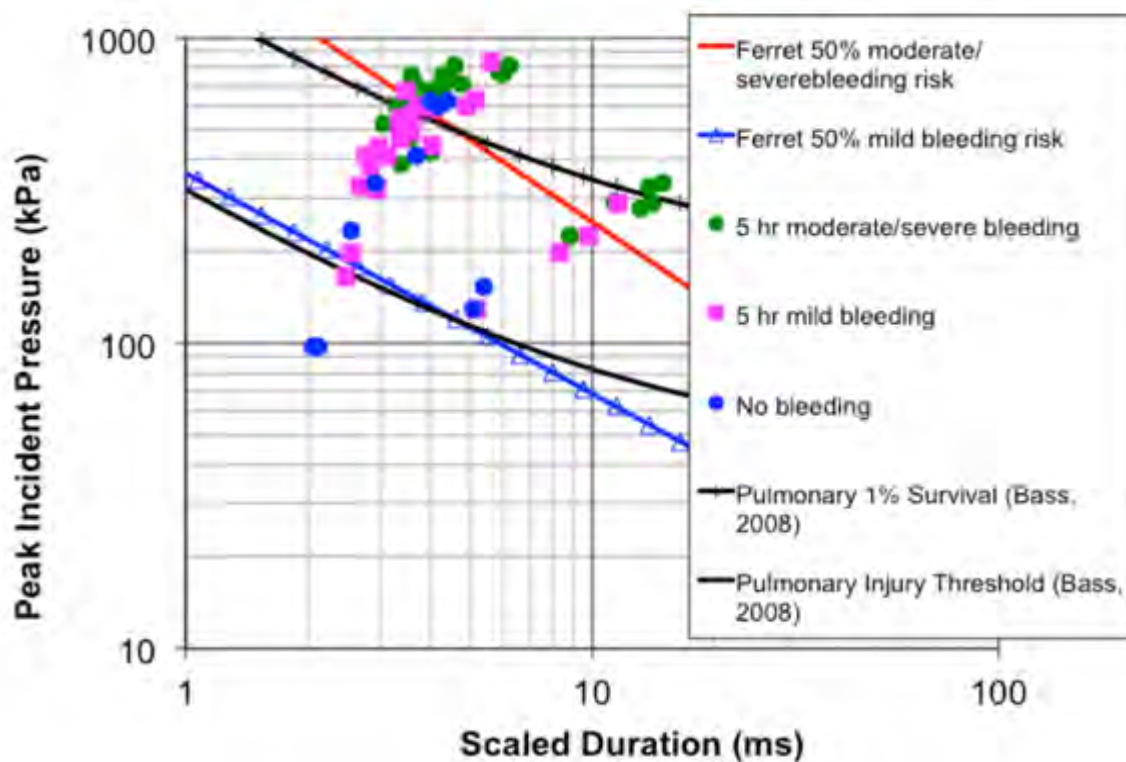


Figure 24. Ferret mild/moderate blast TBI injury risk function (Rafaels, 2012)

In addition to previous oculomotor behavioral tests, a novel ferret behavioral assay for neurocognitive research was developed. A custom software interface was created in MATLAB to obtain directional control of an off-the-shelf remotely controlled toy ball. The ball was programmed to accurately simulate the random motion and escape speed of small rodent prey.

A commercial robotic ball game (Sphero; Orbotix, Boulder, CO) was adapted to accept direction from MATLAB (MathWorks, Natick, MA) code. We created a custom interface from MATLAB to handle the heavy processing components of real-time motion tracking as well as determination of proper Sphero response. The desired Sphero heading is passed through from MATLAB to an iPad application using a TCP/IP socket chat server written in Python. These commands are then transmitted to the Sphero via

Bluetooth with the Sphero Software Development Kit (Orbotix, Boulder, CO). MATLAB code was written to emulate the movements of a mouse in order to actively evade capture by a ferret. By tracking the locations of the Sphero and ferret in real-time, as well as window-averaged velocities, the program can determine a Sphero trajectory which gives it the best chance of evading the ferret and avoiding impact with the walls of the enclosure. The escape trajectories are based on animal escapology principles.

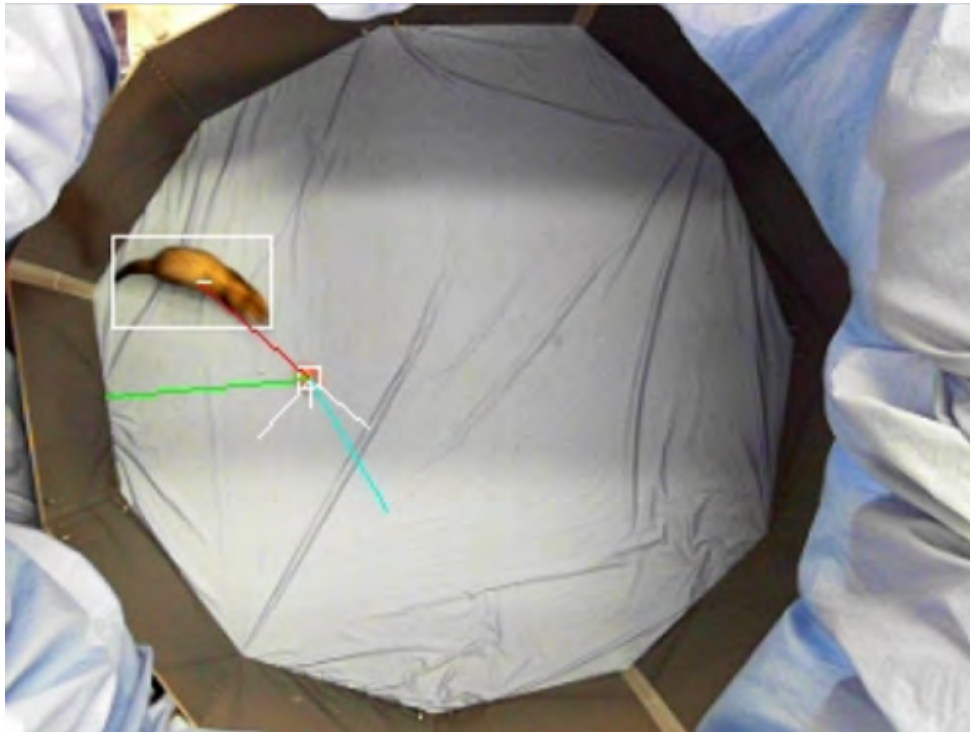


Figure 25. Sample real-time output from MATLAB code, detailing tracking of Sphero and Ferret, as well as ferret velocity, closest wall distance, and components making up Sphero heading determination.

When the ball was activated, the ferret responded to it by appearing to attack the ball (trajectories notes in real time in Figure 25). Repeated trials resulted in similar results. Rubbing the exterior of the ball with bacon-flavored reward treats (Marshall Bandit ferret treats) enhanced the ferret's attention to rapidly catching the ball. We further observed the ferret removing small pieces of bacon from the ball. After eating the bacon, the ferret would resume stalking and attacking the ball in a behaviorally appropriate manner. Trajectories and speed of approach may be assessed in this assay.

Discussion: This novel behavioral assay consists of a behaviorally appropriate task for a predator, tracking prey. Such behavior is comparable to human ocular tracking and is not seen in prey species such as mice. In this assay, we collect a substantial amount of quantitative information on ferret behavior. The ferret's natural instincts to track and attack small rodents will cause a ferret to track and chase a moving mouse-sized ball. This assay does not require animal training or behavioral conditioning. The ferret's natural curiosity, desire to play, and predatory instincts combine to create an irresistible game that provides valuable data on animal behavior.

The ferret Predatory Response including Tracking and Attacking Behavior(PRiTAB) assay represents a significant improvement on previous research with ferret-prey behavior. Our assay provides a simulated

prey that incorporates a random element in its movements, thus providing a more realistic simulation of normal ferret prey. The MATLAB code is easily modifiable to simulate different behavior and could be used to simulate other animal behaviors (e.g. change velocity of the simulated prey). These alterations could be used to investigate how the ferret behaves in novel situations. The commercial off-the-shelf components create an inexpensive option for investigators who wish to simulate small animal behavior. The software interface between Sphero and MATLAB is believed to be the first of its kind. This interface could be adapted as a teaching tool in university coursework on robotics and controller systems.

Although most current ferret behavioral assays require training regimens, this novel assay can be conducted with untrained animals. In addition to engaging the ferret's predatory instincts, this assay also resonates with the ferret's propensity to play. Ferrets are known for playfulness and their husbandry should include enrichment activity. This behavioral test provides simultaneous enrichment and behavioral data.

Our results successfully demonstrated a behavioral assay that can evaluate multiple neurologic and cognitive functions in an experimental animal. The PRiTAB assay provides a global assessment of the animal's ability to react to a novel stimulus and engage in species-appropriate behavior toward it. The assay evaluates oculomotor functions (saccades and smooth pursuit), neurologic function (motor control, balance and coordination), and cognitive function (reaction time, pre-motor/motor planning). This assay also may measure the ferret's interest in play and thus provide a measure of apathy, an important clinical finding in subcortical brain trauma

The main strength of this assay is a real-world representation of the ferret's normal tasks without any pre-assay training requirements. As an obligate carnivore, the ferret is a skilled hunter. Ferrets also engage in group play. This assay measures multiple functions as an integrated response to behavioral stimuli. If changes in the assay are observed after blast exposure, then the assay will provide a sensitive measure of multiple neurologic and cognitive functions.

The PRiTAB assay can be applied to various clinical scenarios that require an integrated response from oculomotor, cognitive, and motor functions. Other clinical areas that may benefit from this assay include:

- blunt head trauma
- cerebrovascular accident (stroke)
- neurologic and cognitive side-effects of anti-cancer chemotherapeutic agents
- measuring the sedating or cognitive side-effects of prescription medications
- measuring the intoxicant effects of alcohol

Next steps in our research include reporting results from this assay in studies of blast brain trauma and possibly other clinical conditions. This assay provides a novel capability to compare behavioral outcomes to the blast overpressure and duration.

We believe the PRiTAB analysis fits the MURI criteria for innovative research results that could apply to scientific fields outside of blast brain injury. The PRiTAB is applicable to a wide range of animals that demonstrate either predation (i.e. carnivores) or a drive towards curiosity or play. This assay may reveal differences between species' response to the novel behavioral stimulus.

References

- Bass, C. R., Rafaels, K. A., & Salzar, R. S. (2008). Pulmonary Injury Risk Assessment for Short-Duration Blasts. *The Journal of Trauma and Acute Care Surgery*, 65(3), 604-615. doi: 10.1097/TA.1090b1013e3181454ab3181454.
- Bauman, R. A., Elsayed, N., Petras, J. M., & Widholm, J. (1997). Exposure to sublethal blast overpressure reduces the food intake and exercise performance of rats. *Toxicology*, 121(1), 65-79. doi: 10.1016/s0300-483x(97)03656-1
- Bell, M. K. (2008). Standardized model is needed to study the neurological effects of primary blast wave exposure. *Mil Med*, 173(6), v-viii.
- Bowen, I., & Fletcher, E. R., DR. (1968). Estimate of Man's Tolerance to the Direct Effects of Air Blast: Lovelace Foundation for Medical Education and Research.
- Cargill, R. S., 2nd, & Thibault, L. E. (1996). Acute alterations in $[Ca^{2+}]_i$ in NG108-15 cells subjected to high strain rate deformation and chemical hypoxia: an in vitro model for neural trauma. *J Neurotrauma*, 13(7), 395-407.
- Celander, H., Clemedson, C.-J., Ericsson, U. A., & Hultman, H. I. (1955). The Use of a Compressed Air Operated Shock Tube for Physiological Blast Research. *Acta Physiologica Scandinavica*, 33(1), 6-13. doi: 10.1111/j.1748-1716.1955.tb01188.x
- Cernak, I., Wang, Z., Jiang, J., Bian, X., & Savic, J. (2001). Ultrastructural and Functional Characteristics of Blast Injury-Induced Neurotrauma. *The Journal of Trauma and Acute Care Surgery*, 50(4), 695-706.
- Chavko, M., Koller, W. A., Prusaczyk, W. K., & McCarron, R. M. (2007). Measurement of blast wave by a miniature fiber optic pressure transducer in the rat brain. *Journal of Neuroscience Methods*, 159(2), 277-281. doi: 10.1016/j.jneumeth.2006.07.018
- Cheng, J., Gu, J., Ma, Y., Yang, T., Kuang, Y., Li, B., & Kang, J. (2010). Development of a rat model for studying blast-induced traumatic brain injury. *Journal of the Neurological Sciences*, 294(1-2), 23-28. doi: 10.1016/j.jns.2010.04.010
- Garman, R. H., Jenkins, L. W., Switzer, R. C., 3rd, Bauman, R. A., Tong, L. C., Swauger, P. V., . . . Kochanek, P. M. (2011). Blast exposure in rats with body shielding is characterized primarily by diffuse axonal injury. *J Neurotrauma*, 28(6), 947-959. doi: 10.1089/neu.2010.1540
- Kaur, C., Singh, J., Lim, M. K., Ng, B. L., Yap, E. P. H., & Ling, E. A. (1995). The response of neurons and microglia to blast injury in the rat brain. *Neuropathology and Applied Neurobiology*, 21(5), 369-377. doi: 10.1111/j.1365-2990.1995.tb01073.x
- LaPlaca, M. C., Cullen, D. K., McLoughlin, J. J., & Cargill li, R. S. (2005). High rate shear strain of three-dimensional neural cell cultures: a new in vitro traumatic brain injury model. *Journal of Biomechanics*, 38(5), 1093-1105. doi: 10.1016/j.jbiomech.2004.05.032
- LaPlaca, M. C., Lee, V. M., & Thibault, L. E. (1997). An in vitro model of traumatic neuronal injury: loading rate-dependent changes in acute cytosolic calcium and lactate dehydrogenase release. *J Neurotrauma*, 14(6), 355-368.
- Long, J. B., Bentley, T. L., Wessner, K. A., Cerone, C., Sweeney, S., & Bauman, R. A. (2009). Blast overpressure in rats: recreating a battlefield injury in the laboratory. *J Neurotrauma*, 26(6), 827-840. doi: 10.1089/neu.2008.0748
- Moochhala, S. M., Md, S., Lu, J., Teng, C.-H., & Greengrass, C. (2004). Neuroprotective Role of Aminoguanidine in Behavioral Changes after Blast Injury. *The Journal of Trauma and Acute Care Surgery*, 56(2), 393-403.
- Moore, D. F., Jerusalem, A., Nyein, M., Noels, L., Jaffee, M. S., & Radovitzky, R. A. (2009). Computational Biology — Modeling of Primary Blast Effects on the Central Nervous System. *Neuroimage*, 47(S2), T10-T20.

- Nyein, M. K., Jason, A. M., Yu, L., Pita, C. M., Joannopoulos, J. D., Moore, D. F., & Radovitzky, R. A. (2010). In silico Investigation of Intracranial Blast Mitigation with Relevance to Military Traumatic Brain Injury. *Proceedings of the National Academy of Sciences*, 107(48), 20703-20708.
- Panzer, M. B., 'Dale' Bass, C. R., Rafaels, K. A., Shridharani, J., & Capehart, B. P. (2012). Primary blast survival and injury risk assessment for repeated blast exposures. *The Journal of Trauma and Acute Care Surgery*, 72(2), 454-466 410.1097/TA.1090b1013e31821e38270.
- Pun, P. B., Kan, E. M., Salim, A., Li, Z., Ng, K. C., Moochhala, S. M., . . . Lu, J. (2011). Low level primary blast injury in rodent brain. *Front Neurol*, 2, 19. doi: 10.3389/fneur.2011.00019
- Risling, M., Plantman, S., Angeria, M., Rostami, E., Bellander, B. M., Kirkegaard, M., . . . Davidsson, J. (2011). Mechanisms of blast induced brain injuries, experimental studies in rats. *NeuroImage*, 54, Supplement 1(0), S89-S97. doi: 10.1016/j.neuroimage.2010.05.031
- Saljo, A., Arrhen, F., Bolouri, H., Mayorga, M., & Hamberger, A. (2008). Neuropathology and pressure in the pig brain resulting from low-impulse noise exposure. *J Neurotrauma*, 25(12), 1397-1406. doi: 10.1089/neu.2008.0602
- Taylor, P. A., & Ford, C. C. (2009). Simulation of Blast-Induced Early-Time Intracranial Wave Physics leading to Traumatic Brain Injury. *Journal of Biomechanical Engineering*, 131(6), 061007.

Shear shocks Occur In Brain In Vivo Under Blast Loading (Urbanczik, 2014)

In collaboration with MURI partners, we have made a fundamental discovery on the biomechanics of wave transmission in the brain which may have downstream implications in other neurotrauma and human injury scenarios. We have found that blast loading produces shear waves of sufficient amplitude to create shear shocks (Pinton, Urbanczyk, Bass, unpublished). Experimental data collected in late 2013 and early 2014, for the first time, capture shear shock wave propagation in the brain using this high-frame rate ultrasound imaging and displacement tracking system (Figure 26). Positive and negative velocity profiles that are characteristic of cubic nonlinearity are visible in between each peak. Initial data suggests that transverse shock development is largely affected by input strain, and output displacement is secondarily modulated by the frequency at which the input is applied. In multi-cycle pushes, at higher frequencies we also see faster collapse of later shear waves onto earlier shear waves. This is likely related to preferential attenuation of higher frequencies and the brain's viscoelasticity. However, factorial assessment of important parameters continues with frequency sweep, strain sweep, and strain rate sweep experiments.

Experimental results from preliminary shock tube tests show the blast excitation occurred simultaneously to the ultrasound acquisition and the scanner acquired 5000 frames of raw echo data. The continued development of this high-rate ultrasound acquisition occurred in concert with the shear shock results. The middle three B-mode ultrasound images below, show the brain at rest ($t=0$), the brain at maximum compression ($t=69$ ms) and at maximum dilation ($t=104$ ms). A dramatic range of motion is apparent from these snapshots. The right plot shows the particle velocity at a point 3 cm deep and 0 cm laterally. For the 0 cm lateral position, the time curve of wave propagation across the brain under blast loading shows very sharp changes in displacement amplitude, similar to those seen in external vibration results, and to the cubic profile of the analytical shear shock solution.

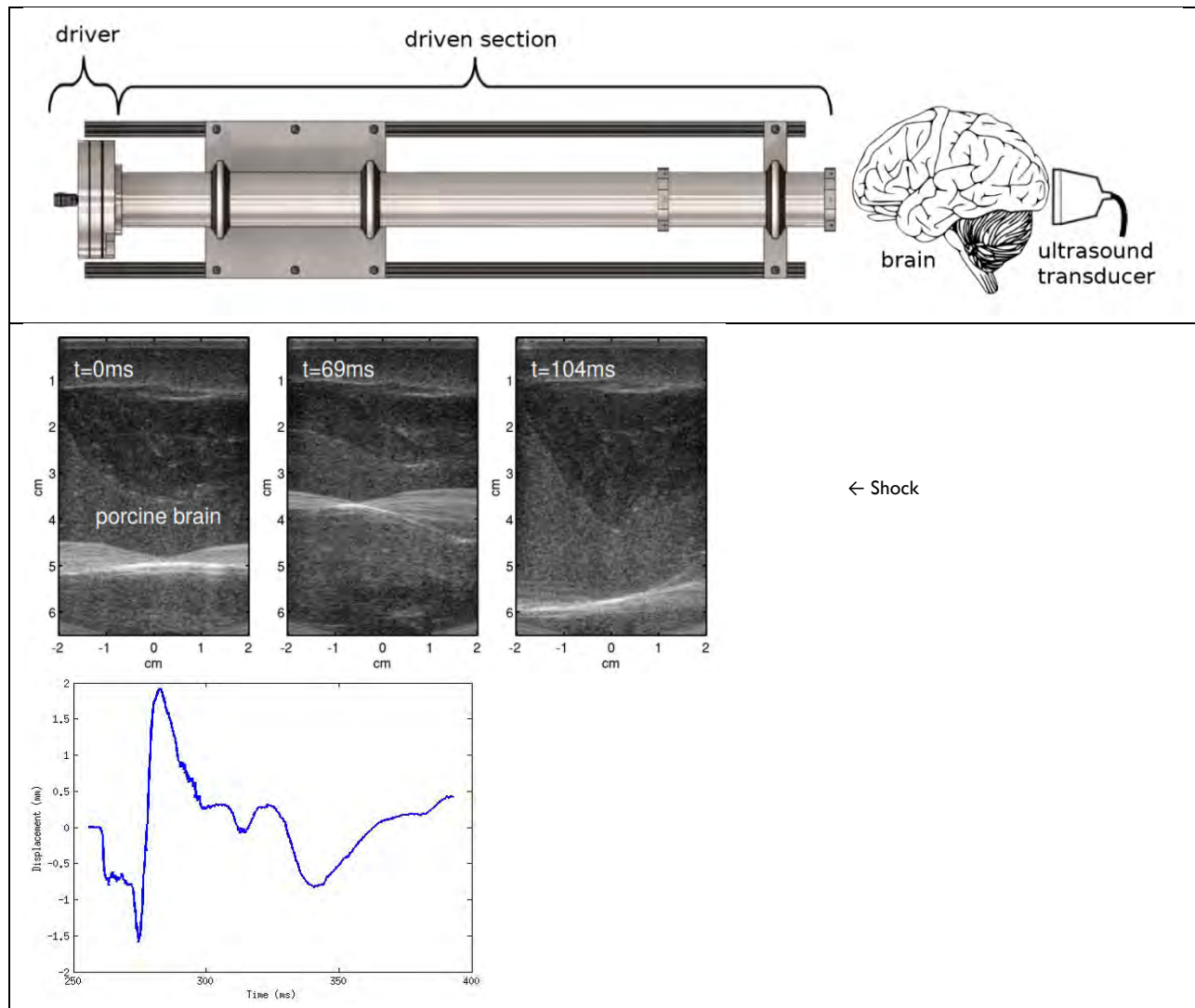
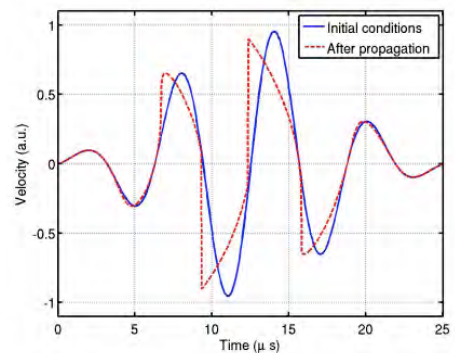


Figure 26: Shock tube setup (based on Panzer, 2012a) developed by the MURI collaboration. Three B-mode ultrasound snapshots of porcine brain embedded in graphite/gelatin phantom. (Left) At rest. (Center) Maximum compression. (Right) Maximum extension. And a temporal plot of shear shock wave propagation at a depth of 2.2 cm and 0 cm laterally.

Little is currently known about the primary damage mechanism associated with traumatic brain injury. We hypothesize that sharp stress and strain gradients, associated with shock propagation and reflection, generate areas of substantial wave construction and shearing effects far from the impact site, likely stretching and damaging neurons. In biological tissues, low shear elasticity allows for high particle velocities relative to wave speed. Due to high Mach numbers in soft solids smooth shear waves can quickly develop into shocks. This could occur, for example, when shear waves are focused by the skull's quasi-spherical geometry.

Nonlinear behavior of longitudinal waves in fluids and solids has been analytically derived and experimentally observed. In contrast, nonlinear behavior of transverse (ie. shear) waves in fluids and solids has only been theoretically predicted. The first measurement of shear shock waves in a soft solid (Catheline et al., 2003) generated a surge of theoretical and numerical interest in modeling these waves.



Much of this interest has come from the acoustics and ultrasound community where the nonlinear behavior of waves in fluids is well established from a theoretical and an experimental point of view. For medical applications nonlinear ultrasound propagation has been extensively characterized in the context of shock wave lithotripsy for the treatment of kidney stones (Cleveland and Sapozhnikov, 2005), high intensity focused ultrasound for thermal ablation of tumors (Curra et al., 2000) and more recently in harmonic ultrasound imaging (Pinton et al., 2011). Methods that have been used in nonlinear acoustics can therefore be applied to the relatively unexplored domain of nonlinear shear waves. Note that with the exception of one report in *ex vivo* liver there is currently no characterization of nonlinear elastic parameters in biological soft tissue.

We are developing high frame rate diagnostic ultrasound and SWEI as a powerful and informative means to non-invasively assess pathological change. The modality's ability to track large, fast displacements in real-time, makes it especially appealing for the study of closed head injury including blunt, ballistic, or blast trauma. We have developed ultrasound methods that combine high rate imaging (up to 10,000 frames/sec) with high resolution tracking (better than 1mm) to accurately measure deformation of tissue and nonlinear properties at frequencies within the spectrum of shear shock wave propagation (1000 – 100,000 Hz). We are refining the experimental approach and signal processing using ultrasound, to image and track brain tissue motion during mechanical excitation of the head. Because of the viscoelastic nature of the brain, we emphasize characterization of linear and nonlinear elastic properties of *ex-vivo* and *in-vivo* brain tissue elastic material properties by examining a wide range of frequencies, strains, and strain rates.

In ongoing studies, we have used high rate SWEI imaging to capture and help characterize the nonlinear elastic properties of brain during mechanical excitation by measuring tissue displacement with high frame rate ultrasound. For *in vitro* imaging of cadaveric porcine brain, a two part, layered construction allows whole brain samples to be embedded in the gel. Imaging protocols include: (1) *in-vitro* imaging of heterogeneous tissue mimicking gelatin phantoms (2) *in-vitro* imaging of cadaveric porcine specimens embedded in gelatin. A rigid polycarbonate plate cast into the gel during phantom construction was fixed to a VTS-80 external vibration generator (Vibration Test Systems, Aurora, OH, USA) and data acquisition was synced through a function generator and a customized Verasonics Vantage research ultrasound scanner (Verasonics Inc., Redmond, WA, USA). A schematic diagram of the experimental setup is shown below. Large shear driving amplitudes were used to generate shear shock waves.

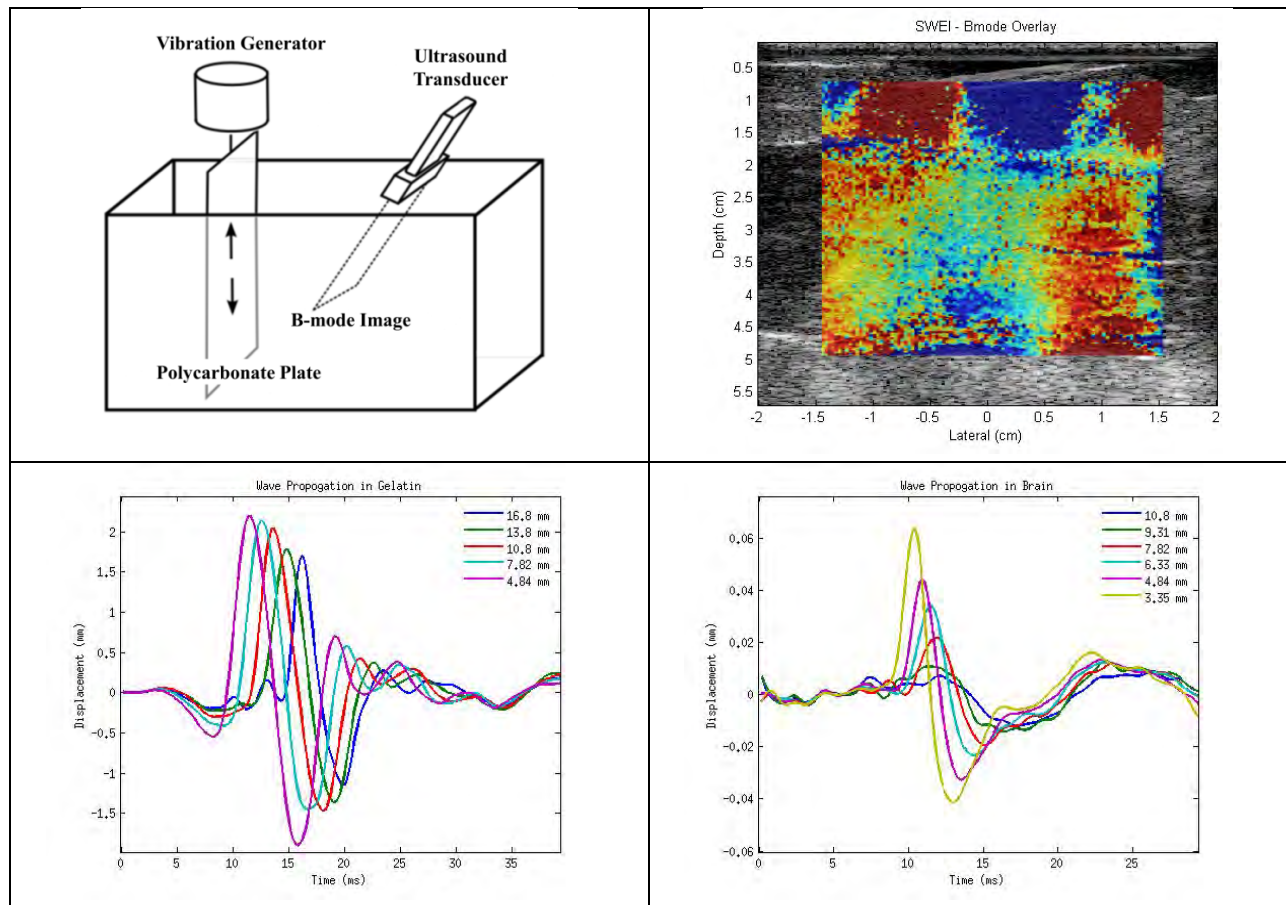


Figure 27: Schematic diagram of external mechanical vibration setup for in-vitro ultrasound imaging in tissue mimicking phantoms and brain embedded in gelatin. Overlay of shear wave propagation across Bmode imaging window shows two shear waves in frame. Clearly visible in the gelatin background and quickly slowing and dispersing in the porcine brain (center). Uniaxial displacement estimates of brain and gelatin background during shear wave passing.

Brain tissue properties (Urbanczyk, 2014)

Duke, in collaboration with the MURI partners has continued to develop brain tissue properties, including the properties in vivo using several techniques including ultrasound based techniques developed by collaborators at Duke. These properties include the effect of rate and in vivo confinement. These results add to validation data including porcine, ferret, mouse and rabbit and human cadaver response have been studied in this project (Shridharani, 2012, Wood, 2013, Yu, 2013 unpublished).

Current diagnostic imaging modalities vividly demonstrate changes in brain anatomy and function with severe injuries (Munkeby & Lyng, 2004; Pickett, Arden, & Brison, 2001), but in milder cases clinical imaging shows little or no pathology and is often uncorrelated with clinical outcome (Hammoud & Wasserman., 2002). Neuroimaging techniques such as MRI and CT do not have the spatial or temporal resolution necessary to delineate local structural alterations, or micro-elasticity variations and neither can be used to measure material property changes, only to visualize anatomic changes. MRI and CT also have practical limits of expense and radiation exposure. Subtle vascular changes and dynamic changes in tissue properties associated with pathological states are not accessible using current clinical imaging techniques. Recently, successful preliminary studies with magnetic resonance

elastography (MRE) have been used *in vivo* to estimate brain tissue elasticity. However, this technique has met with limitations related to low spatial resolution, long acquisition time, the need for external mechanical coupling, transmission through multiple tissue layers and establishment of standing wave patterns for imaging. (Green et al., 2008; Kruse et al., 2008; Sack et al., 2008). These limits may be overcome using ultrasound shear wave elasticity imaging (SWEI) proposed in this study. SWEI is an acoustic radiation force impulse (ARFI)-based ultrasound imaging technique able to sensitively, non-invasively and non-destructively assess qualitative and quantitative stiffness *in vivo* (Doherty, Trahey, Nightingale, & Palmeri, 2013; Sarvazyan, Rudenko, Swanson, Fowlkes, & Emelianov, 1998; Urbanczyk, Palmeri, & Bass, 2014). SWEI is used clinically in liver and heart tissue (Hsu, Fahey, Dumont, Wolf, & Trahey, 2007; Palmeri, Wang, Dahl, Frinkley, & Nightingale, 2008) and shows substantial benefit over previous methods to sensitively and specifically evaluate pathophysiological changes in brain material properties *in vivo*, without disruption to living physiology.

SWEI Experimental Studies (Urbanczyk, 2014)

In the following experimental studies we implemented SWEI, as a high rate image capturing system of internal brain motion during injury and used it study differences in tissue stiffness with several environmental variables (temperature, transducer orientation, confinement) and physiological variables (intracranial pressure, spatial location). Shear waves were generated with focused acoustic radiation force (ARF) and radiofrequency (RF) data was collected using a customized Siemens ACUSON™ S2000 scanner (Siemens Medical Systems, Ultrasound group, Issaquah, WA, USA). The system has been modified to allow for user control of acoustic beam sequences and intensities. Local displacements were calculated with a Loupas phase-shift estimator (Loupas, Peterson, & Gill, 1995). Shear wave speeds were calculated as the inverse slope along the vector with the largest sum of local displacements.

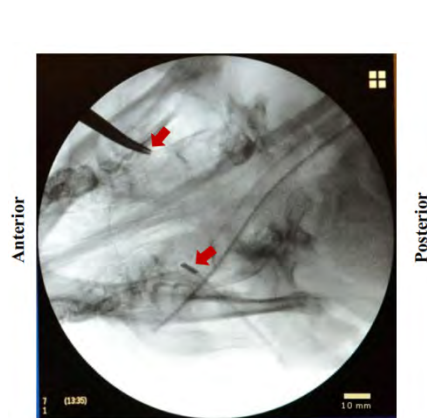


Figure 28: Fluoroscopic image of in vivo instrumentation within porcine animal subject skull. Red arrows indicates placement of Millar pressure sensor and location of catheter ultrasound probe.

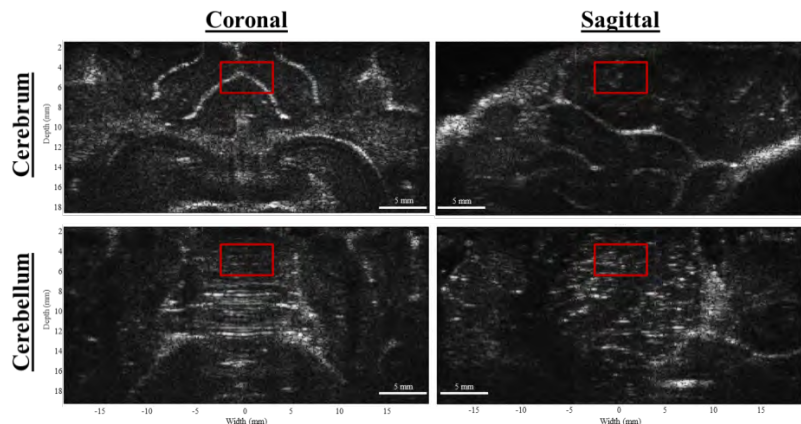


Figure 29: B-mode images of porcine brain displays the geometric complexity including presence of gyri, sulci, and fluid filled ventricles. We characterize stiffness properties within 4mm x 4mm region of interest (red boxes) through which we track shear wave propagation

Key Findings

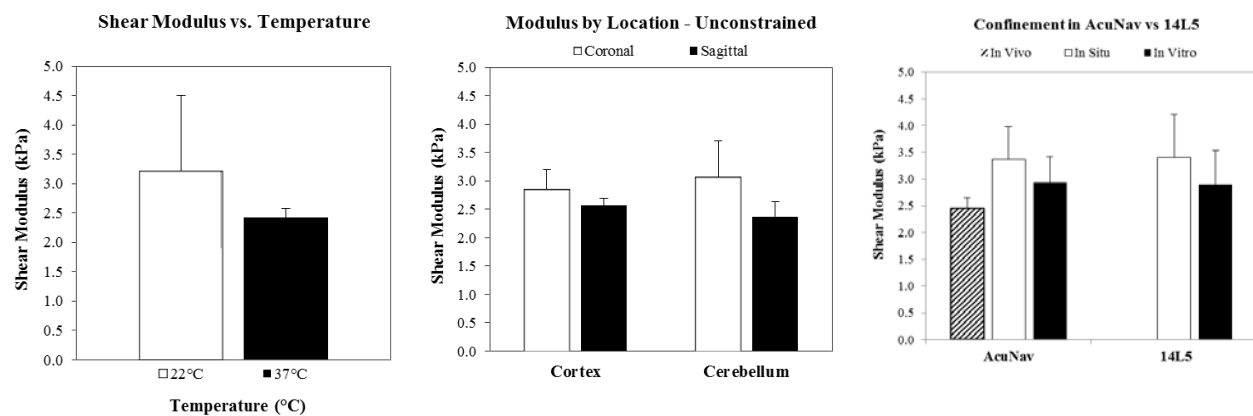
Shear modulus is significantly decreased in cortex at physiological temperature, compared to ambient temperature - Experiments on *in vitro* brains yielded a statistically significant decrease in stiffness values with variation in temperature ($p < 0.001$). Testing at 22° C produced a shear modulus of 3.36 ± 0.28 kPa while brains maintained at 37° C yielded a shear modulus of 2.42 ± 0.06 kPa, suggesting that samples must

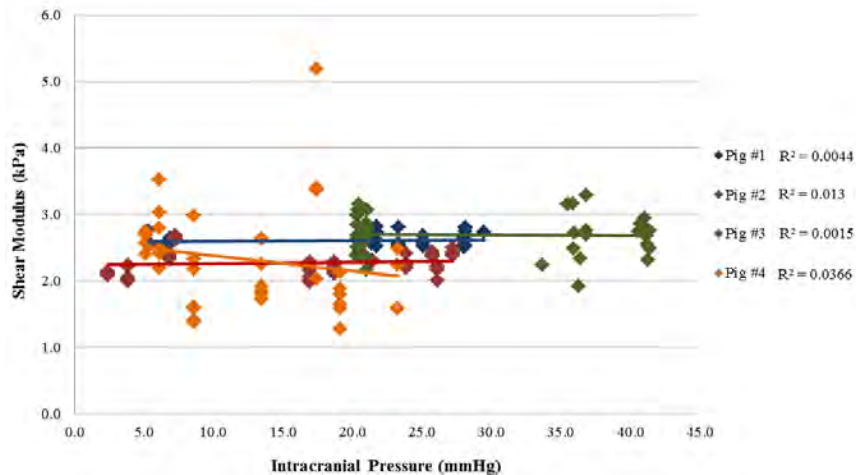
be tested at physiological temperature to obtain material properties in a lab setting with a tight confidence interval.

Shear modulus does not vary between white matter tracts in the cerebral and cerebellar brain lobes, nor between sagittal and coronal imaging planes within brain regions - To study variation by brain region and directionality, we examined stiffness for the cerebral lobe and the cerebellar lobe independently *in vitro*. Average elasticity values along the anterior-posterior axis (sagittal) were compared to those along the left-right axis (coronal). We found no statistical effect on tissue stiffness related to imaging plane for either cerebral or cerebellar brain regions ($p=0.71$, $p=0.35$). Since the differences between coronal and sagittal values within brain regions were not significant, we pooled displacement data from both directions to compare tissue stiffness between spatial locations. Shear modulus values were 2.73 ± 0.63 kPa and 2.76 ± 1.11 kPa for the cerebrum and cerebellum, respectively and were not statistically significantly different ($p=0.94$).

Removing the brain from confinement within the skull increases tissue stiffness - We pooled data by spatial location to examine the effects of external confinement by the skull. The average shear modulus for cerebral specimens partially constrained within the skull was 3.33 ± 0.22 kPa and for unconstrained specimens was 2.69 ± 0.17 kPa. We also examined confinement effects in three conditions: *in vivo*, *in situ* (partially constrained), and *in vitro* (unconstrained). The mean shear moduli were 2.44 ± 0.41 kPa, 3.36 ± 1.22 kPa, 2.94 ± 0.93 kPa for *in vivo*, *in situ*, and *in vitro* constraining conditions. *In situ* and *in vitro* conditions showed a 37% and 22% increase in stiffness, respectively, over the *in vivo* condition. From the *in situ* to *in vitro* setting, there was a stiffness decrease of 14% and 19% seen in datasets using different transducers. Major frequency contributions, from the first harmonic, were 250 – 500 Hz.

Intracranial pressure variation under external constraint does not affect the shear modulus of the cerebral brain - Under closed-skull, physiological conditions, *in vivo* imaging of sagittal plane cortex produced average shear moduli of 2.49 ± 0.18 kPa at normal, baseline ICP levels. Linear regression of tissue stiffness values versus normalized ICP for mild increase (1-3 times) and moderate increase (3-5 times) yielded correlation coefficients that were neither statistically different from each other nor statistically different from a horizontal line. Absolute shear modulus values and linear correlation coefficients are presented in. It is clear from the data that changes in intracranial pressure did not modulate *in vivo* shear modulus.





This experimental study is the first to use ultrasound imaging to examine the effects of several environmental and physiological parameters on shear modulus in both the laboratory (*in vitro*) and surgical (*in vivo*) setting. Results suggest that skull confinement affects nonlinear material brain behavior: with a 22% increase in shear modulus from *in-vivo* to *in-situ* and 37% from *in-vivo* to *in-vitro*. Decreased testing temperature showed 23% increased stiffening of brain tissue response, but modulation of intracranial pressure under fully constrained conditions did not significantly affect brain tissue stiffness. Our results underline the importance of temperature and skull derived boundary conditions on brain stiffness and suggests that physiological ranges of ICP do not significantly affect *in situ* brain tissue properties. SWEI allowed for brain material properties to be characterized in a physiological setting, which provides a stronger basis for assessing brain injury in computational models.

Development of interspecies scaling for blast barotrauma (Wood, 2014).

Following the development of the first interspecies scaling for neurotrauma (Wood, 2013, Panzer, 2014), we developed a similar scaling for barotrauma to allow the consideration of animal neurotrauma models and human epidemiology without thoracic protection. The goals of this effort were to establish a scaling procedure overpressure mediated trauma using simple scaling methods to determine equivalent cross-species and human exposure in models of blast barotrauma. Though previous pulmonary scaling was developed by Bowen at the Lovelace foundation based on theoretical principles now known to be flawed in part, no group assessed the existing blast data to determine scaling for fatality and injury endpoints. As with neurotrauma, it is important to note that scaling may be different for different injury endpoints (e.g. apnea, death, tracheal injury, alveolar injury, etc.) and therefore injury scaling must be considered specific to the injury response.

A database of blast animal model data was created which includes 14 different species and over 12,000 tests. This body of data was filtered for this study through the use of several exclusion criteria. Only studies reporting fatality data from a simple Friedlander type pressure wave were included. Studies with thoracic protection were excluded along with multiple blast exposure data, except in cases that resulted in no injury. Studies were excluded which did not provide sufficient methodological detail to recreate the blast dosage, mainly peak overpressure and duration. In some cases, especially with free-field explosives where only charge size and standoff distance was reported, blast data was calculated through the use of CONWEP to calculate exposure level (1). Orientation and the presence of a reflecting surface behind the animal were not considered as their effects were previously found to be insignificant in large animals (2, 3). Only species with sufficient data to fit a single species fatality risk model were included, resulting in a dataset of 4193 total tests with 5 different species which were used to develop pulmonary fatality risk in this study. A list of studies and number of tests per species are

presented in Table 1 and Table 2, respectively. Injuries reported varied from minor petechiae (4) and hemorrhage (5) to rapid fatality resulting from major lung hemorrhage (6).

Ambient pressure scaling was employed for both peak pressure and duration for body mass scaled durations longer than 30ms as described by Bowen (6) but was not used for scaled durations less than 30ms as discussed by Bass (2). This accounts for the effects of high altitude testing or the modification of ambient pressure during testing, and this scale factor approaches one at normal sea level ambient pressure.

$$P_{P,scaled} = P \left(\frac{P_{sea\ level}}{P_{ambient}} \right) \quad \Delta t_{P,scaled} = \Delta t \left(\frac{P_{ambient}}{P_{sea\ level}} \right)^{1/2} \quad (1)$$

A simple duration scaling model was used to account for interspecies body mass differences. This scaling uses a ratio of body masses between the test subject and a reference human body mass. This allows the blast dosage to be transformed to an equivalent human biomechanical input. The scale factor, α , was optimized to best fit the experimental data.

$$\Delta t_{scaled} = \Delta t \left(\frac{mass_{reference}}{mass} \right)^{\alpha} \quad (2)$$

To describe the fatality risk a nonlinear logistic regression model was constructed that was dependent upon peak incident pressure and scaled duration (2, 6).

$$P = P^* (1 + a \Delta t^{-b}) \quad (3)$$

where P^* , a , and b are model parameters to be fit by the data. This form describes the decreasing peak pressure tolerance as duration increases while at short durations. As durations increase, the peak pressure tolerance approaches a constant, P^* .

Fatality risk models were fit to the five individual species to determine the long duration peak pressure threshold, P^* , for each species. Values of P^* fell into two distinct groups, large and small species (6). As human body size and pulmonary system anatomy suggest it would fall within the large animal group, a mean P^* value for the three large species was used as the human P^* . To correct for differences in peak pressure tolerance, the pressure values for each test were scaled according to a ratio of the human P^* value and that for the species.

$$P_{P^*,scaled} = P \left(\frac{P_{human}^*}{P^*} \right) \quad (4)$$

Regression was then performed on the complete set of data from five species to simultaneously determine the fatality risk model and duration scaling model. Nonlinear regression and statistical analyses were performed for the following logistic regression model

$$\pi = \frac{e^F}{1 + e^F} \quad F = f \{ \ln [P^* (1 + a \Delta t^{-b})] - \ln(P) \} \quad (5)$$

where f , a , and b are fitted model parameters and π is the probability of fatality.

The area under the receiver operating characteristic curve (AUC) was used to assess model goodness-of-fit. AUC measures sensitivity versus (1-specificity) of the fit and values greater than 0.8 are considered good model discrimination.

Unscaled fatality and survival data is shown in Figure 30. It is important to note that when all of the injury data across different species is plotted against pressure and duration exposure without incorporating any interspecies scaling the data appears unorganized, and there is no clear delineation between injury and non-injury cases. Many injury points fall well below levels of non-injury and likewise,

non-injury points appear at high exposure levels for some species relative to others. Without interspecies scaling, model fit statistics in Table I show poor model parameter fits with large standard error values, additionally the AUC value of 0.78 indicates only fair specificity and sensitivity of the unscaled model.

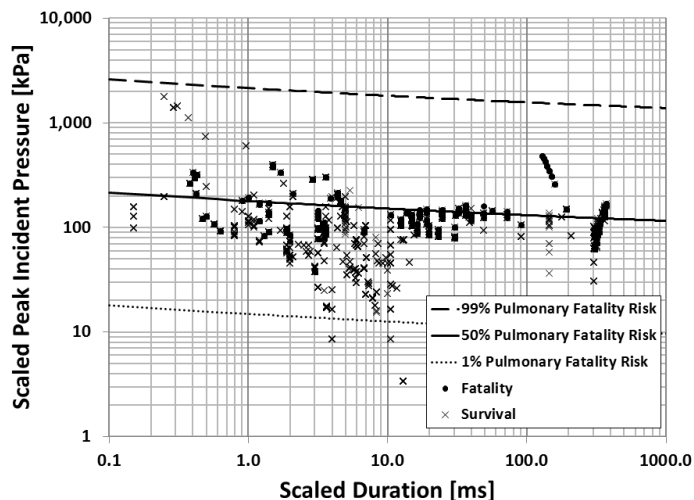


Figure 30: Unscaled pulmonary injury data across five species lacks separation between injury and non-injury cases

When each of the five species were fit with individual fatality models to determine long term pressure tolerance (P^*) values, there was a clear grouping of small species (mouse, rabbit) and large species (dog, goat, sheep). Figure 2 shows the small species grouped around a pressure value of 90kPa and the large species around approximately 145kPa. Since human pulmonary anatomy most closely resembles that of the large species (7) a mean of those P^* values (143.4kPa) was used as the human reference value. P^* is equivalent to the lowest peak pressure capable of 50% fatality from exposure. This means that, independent of duration, peak pressure values less than P^* will always produce less than 50% fatality, regardless of blast duration. As the duration decreases, the risk will decrease.

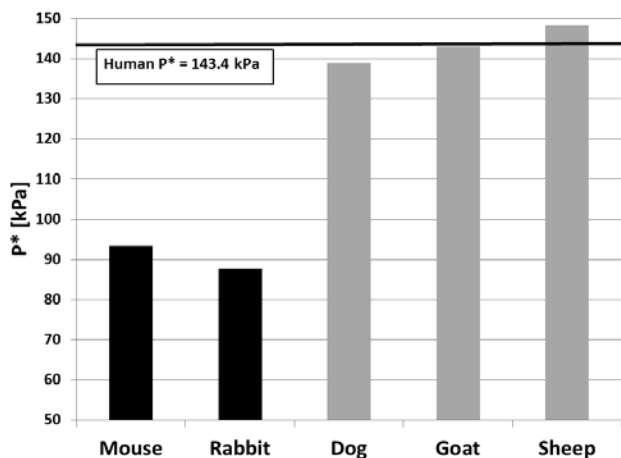


Figure 31: Long duration 50% fatality values, P^* , for individual species

From five species 4193 data points were fit with an interspecies scaling and fatality risk model. This dataset included 2866 survival and 1327 fatality cases. The results of the nonlinear regression are presented in Table I. The optimized duration scaling according to Equation 2 resulted in an α of 0.351. The use of interspecies scaling improved the model fit, supporting the need for interspecies scaling to describe fatality risk. An AUC of 0.88 indicates good specificity and sensitivity of the model. The fatality risk model is shown in Figure 32 along with the fatality data. Not only does the interspecies scaling organize the injury data to see a clear delineation between fatality and survival levels across all species, model loglikelihood data shows that this holds true individually for large and small species. Values in Table I for average loglikelihood show that contribution, per test, to the overall loglikelihood is consistent across species. The model best fits the sheep data as shown by the low average loglikelihood of 0.105. The other four species have similar values indicating that the model does not fit either small or large species better than the other.

Table I. Species data with regression model coefficients and goodness of fit [coefficient \pm SE]

		Mouse	Rabbit	Dog	Goat	Sheep	
	# of Tests	1828	392	409	255	1309	
	Reported Mass [kg\pmSD]	0.023 \pm 0.004	2.08 \pm 0.55	16.36 \pm 1.30	24.16 \pm 4.17	47.76 \pm 8.75	
	P* [kPa]	93.4	87.7	138.9	143.1	148.3	
	Avg. loglike	0.555	0.567	0.531	0.578	0.105	
	P*	a	-b	f	α	loglike	AUC
Unscaled	71.84 \pm 74.04	1.49 \pm 2.55	0.13 \pm 0.13	1.85 \pm 0.08	0	2202.6	0.78
Full Model	143.4	3.53 \pm 0.23	1.06 \pm 0.04	4.41 \pm 0.20	0.351	1737.3	0.88

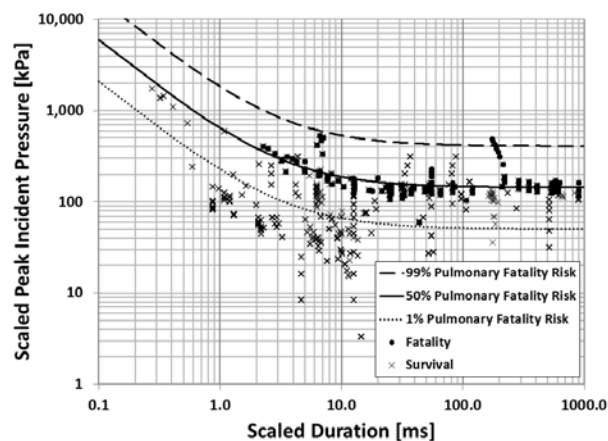


Figure 32: Regression model for fatality due to pulmonary trauma in five large and small species ($\alpha=0.351$).

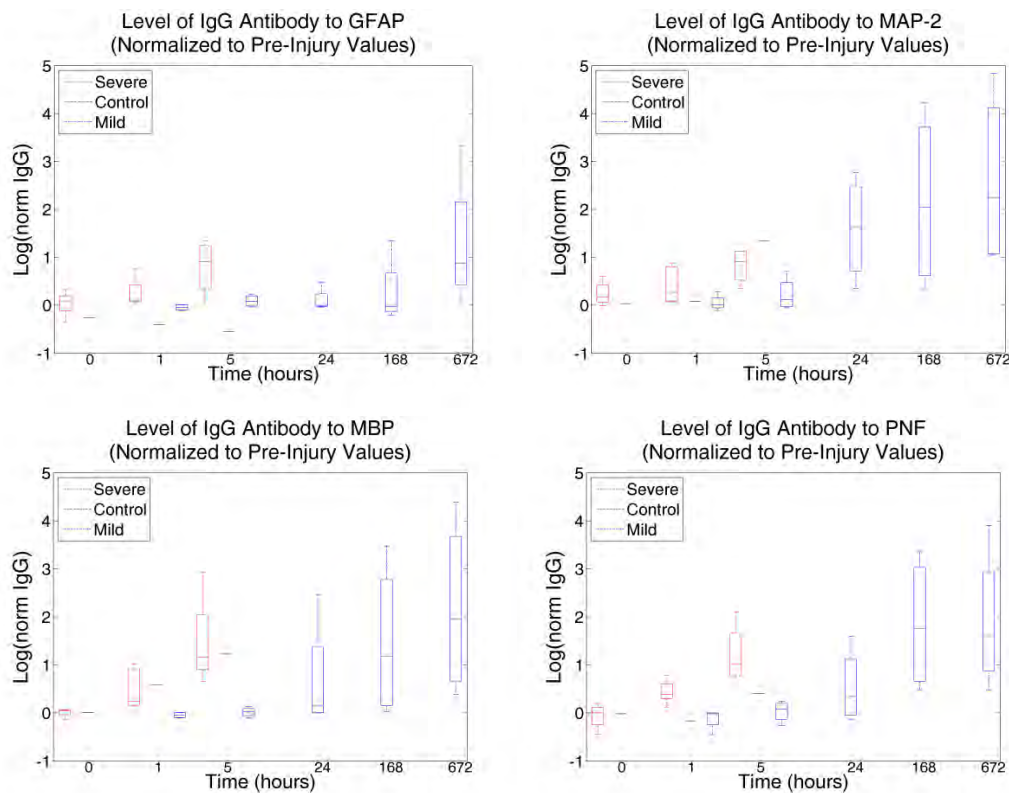
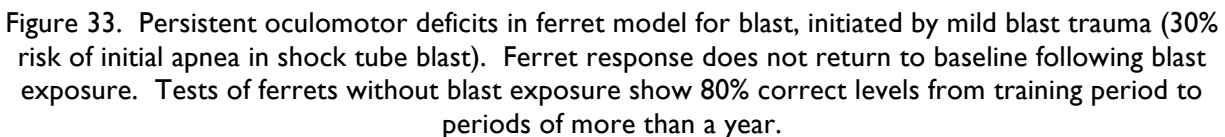
Table 2: Published blast animal model work used

Reference	Species Used	Reference	Species Used
Bowen 1968 (6)	Sheep	Richmond 1961 (8)	Mouse, Rabbit, Dog, Goat
Celander 1955 (5)	Mouse	Richmond 1962a (9)	Mouse, Rabbit
Cernak 2011 (10)	Mouse	Richmond 1962b (11)	Mouse, Rabbit
Clifford 1984 (12)	Sheep	Richmond 1966 (13)	Mouse, Rabbit, Dog, Goat
Damon 1964 (14)	Mouse	Richmond 1968 (15)	Dog, Goat, Sheep
Damon 1966 (16)	Dog, Goat	Richmond 1981 (17)	Sheep
Damon 1970 (18)	Dog, Sheep	Richmond 1982 (19)	Sheep
DASA 1656 1965 (20)	Goat	Rubovitch 2011 (21)	Mouse
Dodd 1989 (22)	Sheep	Woods 2013 (23)	Mouse
Mundie 2000 (24)	Sheep	Yang 1996 (25)	Sheep
Phillips 1988 (26)	Sheep	Young 1985 (27)	Sheep

Task D. Correlate changes at the synapse and circuit level to corresponding neurobehavioral deficits in animals.

[D1] We use knowledge from Thrust A to scale models of blast wave transmission into animals,

One of the keys to this is appropriate neurobehavioral model that replicates typical features of human behavior and may be correlated with cellular response. To do this we have two thrusts. We have developed a ferret assay for blast including blast injury criteria in ferrets (Rafaels, 2012) in terms of peak pressure and scaled duration. The assay is behaviorally appropriate and similar to neurobehavioral deficits seen in humans (e.g. Capehart, 2012). The second thrust is to identify human epidemiological data that we can use to validate our animal, cadaver and numerical models. We have gathered a dataset from large blasts in World War I and recent conflicts. We have seen persistent oculomotor deficits from blast in this animal model as shown below and testing is ongoing for various blast input conditions out to durations of a month.



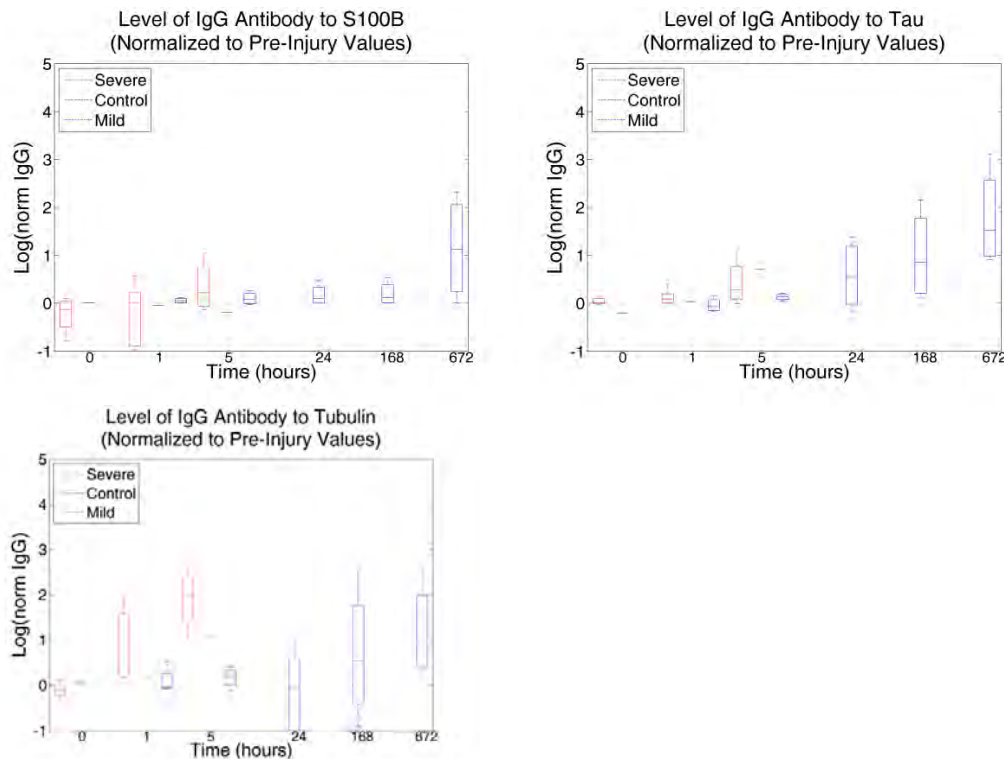


Figure 34: Autoantibodies normalized to pre-injury levels for: GFAP, MAP-2, MBP, NFP, S100B, Tau, and Tubulin. Increases are evident with severity of injury and time.

REFERENCES

- Abou-Donia, M.B., et al., Autoantibodies to nervous system-specific proteins are elevated in sera of flight crew members: biomarkers for nervous system injury. *J Toxicol Environ Health A*, 2013. 76(6): p. 363-80.
- Bass CR, Rafaels KA, Salzar RS. Pulmonary Injury Risk Assessment for Short-Duration Blasts. *The Journal of trauma*. 2008;65(3):604-15.
- Bowen IG, Fletcher ER, Richmond DR. Estimate of Man's Tolerance to the Direct Effects of Air Blast. Albuquerque, NM: Lovelace Foundation for Medical Education and Research, 1968 October 1968. Report No.: Contract No.: DA-49-146-XZ-372.
- Catheline, S., Gennisson, J., Tanter, M., and Fink, M. (2003). Observation of shock transverse waves in elastic media. *Physical Review Letters*, 91(16):164301.
- Celander H, Clemendson C-J, Ericsson UA, Hultman HE. A Study on the Relation between the Duration of a Shock Wave and the Severity of the Blast Injury Produced by It. *Acta Physiologica Scandinavica*. 1955;33(1):14-8.
- Cernak I, Merkle AC, Koliatsos VE, Bilik JM, Luong QT, Mahota TM, Xu L, Slack N, Windle D, Ahmed FA. The Pathobiology of Blast Injuries and Blast-Induced Neurotrauma as Identified Using a New Experimental Model of Injury in Mice. *Neurobiol Dis*. 2011;41(2):538-51.
- Chavko M, Prusaczyk WK, McCarron RM. Lung Injury and Recovery After Exposure to Blast Overpressure. *The Journal of Trauma and Acute Care Surgery*. 2006;61(4):933-42. 10.1097/01.ta.0000233742.75450.47.
- Cleveland, R. and Sapozhnikov, O. (2005). Modeling elastic wave propagation in kidney stones with application to shock wave lithotripsy. *The Journal of the Acoustical Society of America*, 118:2667.

- Clifford CB, Jaeger JJ, Moe JB, Hess JL. Gastrointestinal lesions in lambs due to multiple low-level blast overpressure exposure. *Mil Med.* 1984;149(9):491-5. Epub 1984/09/01.
- Crosfill M, Widdicombe J. Physical characteristics of the chest and lungs and the work of breathing in different mammalian species. *The Journal of physiology.* 1961;158(1):1-14.
- Curra, F. P., Mourad, P. D., Khokhlova, V. A., Cleveland, R. O., and Crum, L. A. (2000). Numerical simulations of heating patterns and tissue temperature response due to high-intensity focused ultrasound. *IEEE Transactions on Ultrasonics Ferroelectrics and Frequency Control*, 47(4):1077–1089.
- Damon E, Richmond D, White C. The effects of ambient pressure on the tolerance of mice to air blast. Albuquerque, NM: Lovelace Foundation, 1964.
- Damon E, Yelverton J, Luft U, Mitchell K, Jones R. The Acute Effects of Air Blast on Pulmonary Function in Dogs and Sheep. Lovelace Foundation for Medical Education and Research, 1970 Contract No.: DASA2461.
- Damon EG, Gaylord CS, Hicks W, Yelverton JT, Richmond DR. The Effect of Ambient Pressure on Tolerance of Mammals to Air Blast. Albuquerque, NM: Lovelace Foundation, 1966.
- DASA. Biomedical Program 500-Ton Explosion. Washington, DC: Defense Atomic Support Agency, 1965 Contract No.: DASA-1656.
- Dodd K, Yelverton J, Richmond D, Morris J, Ripple G. Nonauditory Injury Threshold for Repeated Intense Freefield Impulse Noise. Walter Reed Army Instit of Research, 1989 1 Jan 1989. Report No.: Contract No.: ADA224108.
- Doherty, J., Trahey, G., Nightingale, K., & Palmeri, M. (2013). Acoustic Radiation Force Elasticity Imaging in Diagnostic Ultrasound. *IEEE Transactions on Ultrasonics, Ferroelectrics, and Frequency Control*, 60(4), 685–701.
- Donnelly, D.J. and P.G. Popovich, Inflammation and its role in neuroprotection, axonal regeneration and functional recovery after spinal cord injury. *Exp Neurol*, 2008. 209(2): p. 378-88.
- Hammoud, D. A., & Wasserman, B. A. (2002). Diffuse axonal injuries: pathophysiology and imaging. *Neuroimaging Clinics of North America*, 12(2), 205–216.
- Hsu, S. J., Fahey, B. J., Dumont, D. M., Wolf, P. D., & Trahey, G. E. (2007). Challenges and implementation of radiation-force imaging with an intracardiac ultrasound transducer. *IEEE Trans Ultrason Ferroelectr Freq Control*, 54(5), 996–1009.
- Hyde DW. CONWEP 2.1.0.8, Conventional Weapons Effects Program. Vicksburg, MS: US Army Corps of Engineers, 2004.
- Kruse, S., Rose, G. H., Glaser, K. J., Manduca, A., Felmlee, J. P., & Ehman, R. L. (2008). Magnetic resonance elastography of the brain. *NeuroImage*, 39(1), 231–237.
- Loupas, T., Peterson, R. B., & Gill, R. W. (1995). Experimental evaluation of velocity and power estimation for ultrasound blood flow imaging, by means of a two-dimensional autocorrelation approach. *IEEE Transactions on Ultrasonics, Ferroelectrics and Frequency Control*, 42(4), 689–699. doi:10.1109/58.393111
- Mundie TG, Dodd KT, Lagutchik MS, Morris JR, Martin D. Effects of Blast Exposure on Exercise Performance in Sheep. *The Journal of Trauma and Acute Care Surgery.* 2000;48(6):1115-21.
- Munkeby, B., & Lyng, K. (2004). Morphological and hemodynamic magnetic resonance assessment of early neonatal brain injury in a piglet model. *Journal of Magnetic Resonance Imaging*, 20(1), 8–15. doi:10.1002/jmri.20084
- Palmeri, M. L., Wang, M. H., Dahl, J. J., Frinkley, K. D., & Nightingale, K. R. (2008). Quantifying hepatic shear modulus in vivo using acoustic radiation force. *Ultrasound in Medicine & Biology*, 34(4), 546–58. doi:10.1016/j.ultrasmedbio.2007.10.009

- Panzer, M. B., Matthews, K. A., Allen, W. Y., Barclay Morrison III, D. F. M., and Bass, C. R. (2012a). A multiscale approach to blast neurotrauma modeling: part i—development of novel test devices for in vivo and in vitro blast injury models. *Frontiers in neurology*, 3.
- Phillips YY, Mundie TG, Yelverton JT, Richmond DR. Cloth ballistic vest alters response to blast. *The Journal of trauma*. 1988;28(1 Suppl):S149-52. Epub 1988/01/01.
- Pickett, W., Ardern, C., & Brison, R. J. (2001). A population-based study of potential brain injuries requiring emergency care. *CMAJ : Canadian Medical Association Journal*, 165(3), 288–92.
- Pinton, G., Dahl, J., and Trahey, G. (2011b). Sources of image degradation in fundamental and harmonic ultrasound imaging: A nonlinear, full-wave, simulation study. *IEEE Trans. Ultrason. Ferroelectr. Freq. Control*.
- Pinton, G., Gennisson, J., Tanter, M., and Coulouvrat, F. (2014). Adaptive motion estimation of shear shock waves in soft solids and tissue with ultrasound. *IEEE Trans. Ultrasonics Ferroelect. Freq. Control*. (In Press).
- Pulendran, B., Learning immunology from the yellow fever vaccine: innate immunity to systems vaccinology. *Nat Rev Immunol*, 2009. 9(10): p. 741-7.
- Rafaels KA, 'Dale' Bass CR, Panzer MB, Salzar RS. Pulmonary Injury Risk Assessment for Long-Duration Blasts: A Meta-Analysis. *The Journal of Trauma and Acute Care Surgery*. 2010;69(2):368-74
10.1097/TA.0b013e3181e88122.
- Rafaels, K., et al., Survival risk assessment for primary blast exposures to the head. *J Neurotrauma*, 2011. 28(11): p. 2319-28.
- Richmond D, Clare V, Goldizen V, Pratt D, Sanchez R, White C. Biological Effects of Overpressure II: A shock tube utilized to produce sharp-rising overpressures of 400 milliseconds duration and its employment in biomedical experiments. *Aerospace Medicine*. 1961;32(11):997-1008.
- Richmond D, Goldizen V, Clare V, Pratt D, Sherping F, Sanchez R, Fischer C, White C. The biologic response to overpressure III: Mortality in small animals exposed in a shock tube to sharp-rising overpressures of 3 to 4 msec duration. *Aerospace Medicine*. 1962;33:1-27.
- Richmond D, Yelverton J, Fletcher E, Phillips Y, Jaeger J. Damage-risk criteria for personnel exposed to repeated blasts. DTIC Document, 1982.
- Richmond DR, Damon EG, Bowen IG, Fletcher ER, White CS. Air-Blast Studies with Eight Species of Mammals. Albuquerque, NM: Lovelace Foundation for Medical Education and Research, 1966.
- Richmond DR, Damon EG, Fletcher ER, Bowen IG, White CS. The Relationship between Selected Blast-Wave Parameters and the Response of Mammals Exposed to Air Blast. *Annals of the New York Academy of Sciences*. 1968;152(1):103-21.
- Richmond DR, Goldizen VC, Clare VR, White CS. The Overpressure-Duration Relationship and Lethality in Small Animals. Albuquerque, NM: Lovelace Foundation for Medical Education and Research, 1962.
- Richmond DR, Yelverton JT, Fletcher ER. The biological effects of repeated blasts. DTIC Document, 1981.
- Rubovitch V, Ten-Bosch M, Zohar O, Harrison CR, Tempel-Brami C, Stein E, Hoffer BJ, Balaban CD, Schreiber S, Chiu W-T, et al. A mouse model of blast-induced mild traumatic brain injury. *Experimental Neurology*. 2011;232(2):280-9.
- Sack, I., Beierbach, B., Hamhaber, U., Klatt, D., & Braun, J. (2008). Noninvasive measurement of brain viscoelasticity using magnetic resonance elastography. *NMR in Biomedicine*, 21, 265–271.
doi:10.1002/nbm
- Sarvazyan, A., Rudenko, O., Swanson, S., Fowlkes, J., & Emelianov, S. (1998). Shear Wave Elasticity Imaging: A New Ultrasonic Technology of Medical Diagnostics. *Ultrasound Med. Biol.*, 24(9), 1419–1435.

- Urbanczyk, C., Palmeri, M., & Bass, C. (2014). Material characterization of in vivo and in vitro porcine brain using shear wave elasticity imaging. *Ultrasound in Medicine and Biology*.
- Woods AS, Colsch B, Jackson SN, Post J, Baldwin K, Roux A, Hoffer B, Cox BM, Hoffer M, Rubovitch V, et al. Gangliosides and Ceramides Change in a Mouse Model of Blast Induced Traumatic Brain Injury. *ACS Chemical Neuroscience*. 2013.
- Yang Z, Wang Z, Tang C, Ying Y. Biological effects of weak blast waves and safety limits for internal organ injury in the human body. *The Journal of trauma*. 1996;40(3 Suppl):S81-4.
- Young AJ, Jaeger JJ, Phillips YY, Yelverton JT, Richmond DR. The influence of clothing on human intrathoracic pressure during airblast. *Aviation, space, and environmental medicine*. 1985;56(1):49-53. Epub 1985/01/01.
- Zhang, Z., et al., Human traumatic brain injury induces autoantibody response against glial fibrillary acidic protein and its breakdown products. *PLoS One*, 2014. 9(3): p. e92698.
- Zurek, J. and M. Fedora, The usefulness of S100B, NSE, GFAP, NF-H, secretogin and Hsp70 as a predictive biomarker of outcome in children with traumatic brain injury. *Acta Neurochir (Wien)*, 2012. 154(1): p. 93-103; discussion 103.

Spinout Investigations

IS THERE A BRAIN MICROBIOME?

An outgrowth of the physical investigations of this MURI is the question of whether the physical insults from blast or blunt trauma interact with commensal microorganisms in the brain. We have found strong evidence that these exist in animal models with implications for pathophysiology of neurotrauma.

The microbiome is comprised of symbiotic microorganisms that play key roles in host physiology. Microbiome research primarily focuses on gut flora with little investigation into immune-privileged sites. To address this knowledge gap, microbial DNA was isolated from brain tissue and whole blood of healthy mice and assessed by 16S rRNA gene phylogenetic microarray (PhyloChip G3). Here we present evidence of bacteria found in both blood and brain tissue. Moreover, a significant separation was observed between sample types based on presence/absence and abundance metrics of the detected operational taxonomic units. Six bacterial families were found exclusive to brain tissue whereas 15 families were found exclusive to blood, revealing a distinct brain microbiome that is separate and identifiable from matched blood controls. The discovery of flora within the brain of healthy mice may suggest a role for microbiota in neurological health and could serve as a new frontier for microbiome research.

Introduction

Humans and other mammals host complex microbial communities and together exist in a co-evolutionary symbiosis. The collective genomes of indigenous microbiota that inhabit the complex ecosystems on and within the body has been termed the “microbiome”¹. In humans, the diversity and number of microorganisms that make up the microbiome is immense, estimated to at least match or outnumber human cells^{2,3}. The spatial distribution of unique communities of commensal bacteria varies throughout the body and depends largely on the microenvironment of each location⁴. Analysis of skin, oral cavity, oropharynx, gastrointestinal tract, blood, and sexual organs have revealed distinct dominant bacterial taxa at each location⁵⁻⁸.

Because a substantial proportion of the symbiotic bacteria reside in the gastrointestinal system, a large focus has been placed on studying the biological significance of gut microbiota^{9,10}. As the primary site of host-microorganisms interaction, the enteric microbiome has been implicated in basal metabolism, diet, and defense against opportunistic pathogens¹¹. More recently, research has revealed a bidirectional communication between the gut and brain, not only ensuring gastrointestinal homeostasis but also influencing neurological function such as learning, memory, emotion, and decision making processes¹²⁻¹⁴. The host microbiome has further been implicated in psychiatry and neurobehavior including anxiety and stress response¹⁵⁻¹⁷, depression¹⁵, neurodevelopmental disorders^{18,19}, social behaviors¹², and other central nervous system (CNS) disease states²⁰. The ability of the flora in the gastrointestinal tract to communicate with the brain and subsequently modulate behavior has been termed the “gut-brain axis”^{12,15,17}. Proposed mechanisms of gut-brain communication have centered on the vagus nerve^{21,22}, immune system signaling and modulation^{20,23}, immune, and endocrinology based mechanisms of signaling²⁴. Even with an increasing body of evidence, these proposed communication mechanisms are indirect and have yet to unequivocally demonstrate the ability of microbiota to influence behavioral changes.

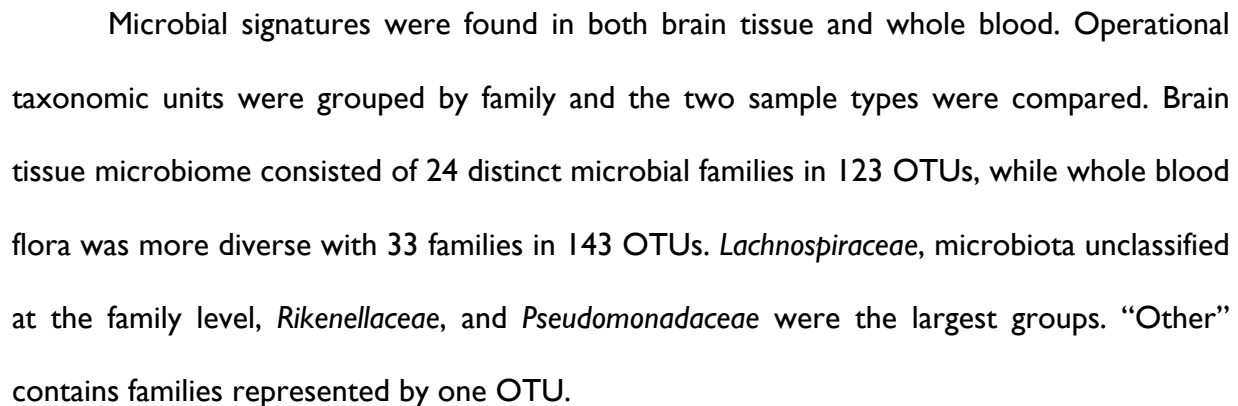
Despite the growing understanding of the microbiome-host interaction, the identification and characterization of the full microbiome within the diversity of bodily niches remain incomplete. The CNS has rarely been assessed even with the recent attention on microbial driven neurological modulation. The vast majority of research on microbiome composition focuses on non-CNS environments, with most neurobehavioral changes hypothesized to stem from the enteric gut microbiota. The brain has long been thought to be a sterile organ protected by the blood brain barrier except in cases of disease and injury²⁵, although the existence and composition of the gut microbiome appears to influence blood-brain barrier permeability²⁶. Only recently has the assumption of a sterile brain in non-diseased states been challenged. In testing a novel sequencing 16S pipeline, Lluh et al. assessed a variety of mouse organs including the brain, revealing the presence of bacteria²⁷. During investigation of microbial diversity in diseased humans brains, Branton et al. found alpha-Proteobacteria to predominate, independent of host disease status²⁸.

In order to complement and extend these studies, the purpose of the current work was to utilize the high-density 16S rRNA gene oligonucleotide profiling microarray, the Phylochip G3, to directly identify any bacterial signature within the mouse brain. If present, we aimed to characterize these signatures and compare them to any bacterial signatures within the blood. Given the rich microbial diversity found across tissues throughout the body and the potential role of bacteria conferring neurological function via the gut-brain axis, we hypothesized the existence of a previously unappreciated bacterial microbiota in the normal brain that is separate and distinct from the microbiota found in blood. The existence of brain microbiota would establish a direct link between microflora and the brain, perhaps suggesting a direct yet unexplored role of CNS bacteria in influencing normal physiology and development of pathophysiology.

Microbiota found in both whole blood and brain tissue

Microarray profiling of whole blood and brain tissue revealed the presence of bacteria in both tissue types with 197 unique operational taxonomic units (OTUs) above the thresholds for inclusion within this analysis. These OTUs were grouped by family to determine relative presence or absence in brain and whole blood (Figure 35). Brain tissue contained 24 unique bacterial families in 123 OTUs. The diversity of microbiota was greater in whole blood with

Figure 35: The microbiome of brain tissue and whole blood - A comparison of OTUs by family



Distinct bacteria found exclusive to each sample type

The microbiome of brain tissue was distinctly different from that found in blood with several bacterial families exclusive to one of the sample types. Microarray incidence scores were used to determine bacterial families found only in the brain tissue and not in whole blood, and similarly, families limited only to blood and not brain tissue, for at least one sample. As shown in

Table 3, the differentiation between brain and blood occurs at the Class level with the exception of gamma- and delta-proteobacteria.

Table 3 Bacterial families found exclusively in one sample type

Bacteria Exclusive to Brain Tissue			
Phylum	Class	Order	Family
Bacteroidetes	Bacteroidia	Bacteroidales	<i>Prevotellaceae</i>
Cyanobacteria	Oscillatoriothycideae	Oscillatoriales	<i>Phormidiaceae</i>
Proteobacteria	Gammaproteobacteria	Chromatiales	<i>Chromatiaceae</i>
	Deltaproteobacteria	Syntrophobacterales	<i>Desulfobacteraceae</i>
			<i>Syntrophobacteraceae</i>
Verrucomicrobia	Verrucomicrobiae	Verrucomicrobiales	<i>Verrucomicrobiaceae</i>
Bacteria Exclusive to Blood			
Phylum	Class	Order	Family
Actinobacteria	Actinobacteria	Actinomycetales	<i>Intrasporangiaceae</i>
Cyanobacteria	Synechococcophycideae	Synechococcales	<i>Synechococcaceae</i>
Firmicutes	Bacilli	Bacillales	<i>Alicyclobacillaceae</i>
	Clostridia	Clostridiales	<i>Veillonellaceae</i>
Proteobacteria	Alphaproteobacteria	Rhizobiales	<i>Bradyrhizobiaceae</i>
		Rhodospirillales	<i>Rhodospirillaceae</i>
		Sphingomonadales	<i>Sphingomonadaceae</i>
	Betaproteobacteria	Burkholderiales	<i>Alcaligenaceae</i>
			<i>Aquabacteriaceae</i>
			<i>Burkholderiaceae</i>
			<i>Comamonadaceae</i>
	Gammaproteobacteria	Chromatiales	<i>Sinobacteraceae</i>
	Deltaproteobacteria	Desulfobacterales	<i>Desulfobulbaceae</i>
Tenericutes	Mollicutes	Acholeplasmatales	<i>Acholeplasmataceae</i>
	Erysipelotrichi	Erysipelotrichales	<i>Erysipelotrichaceae</i>

Six bacterial families representing Proteobacteria (*Chromatiaceae*, *Desulfobacteraceae*, *Syntrophobacteraceae*), Cyanobacteria (*Phormidiaceae*), Bacteroidetes (*Prevotellaceae*), and Verrucomicrobia (*Verrucomicrobiaceae*) were present in brain but absent from blood (OTU 65, 179, 84, 1, 168, 212). Genera results were reported as *Phormidium* (*Phormidiaceae*), and

Prevotella (Prevotellaceae); the species were reported as unclassified. Genera data for other families was unknown.

Whole blood samples contained 15 bacterial families exclusive to only the blood. These consisted of Proteobacteria (*Alcaligenaceae*, *Aquabacteriaceae*, *Bradyrhizobiaceae*, *Burkholderiaceae*, *Comamonadaceae*, *Desulfobulbaceae*, *Rhodospirillaceae*, *Sinobacteraceae*, *Sphingomonadaceae*), Tenericutes (*Acholeplasmataceae*, *Erysipelotrichaceae*), Firmicutes (*Alicyclobacillaceae*), Actinobacteria (*Intrasporangiaceae*), and Cyanobacteria (*Synechococcaceae*) within a total of 24 OTUs (191, 205, 129, 204, 34, 44, 151, 36, 48, 45, 49, 179, 160, 119, 207, 18, 37, 15, 33, 46, 109, 133, 144, 78). Classified genus and species data are listed in Table 4. The families in Table 4 listed with * indicate families represented by more than one OTU.

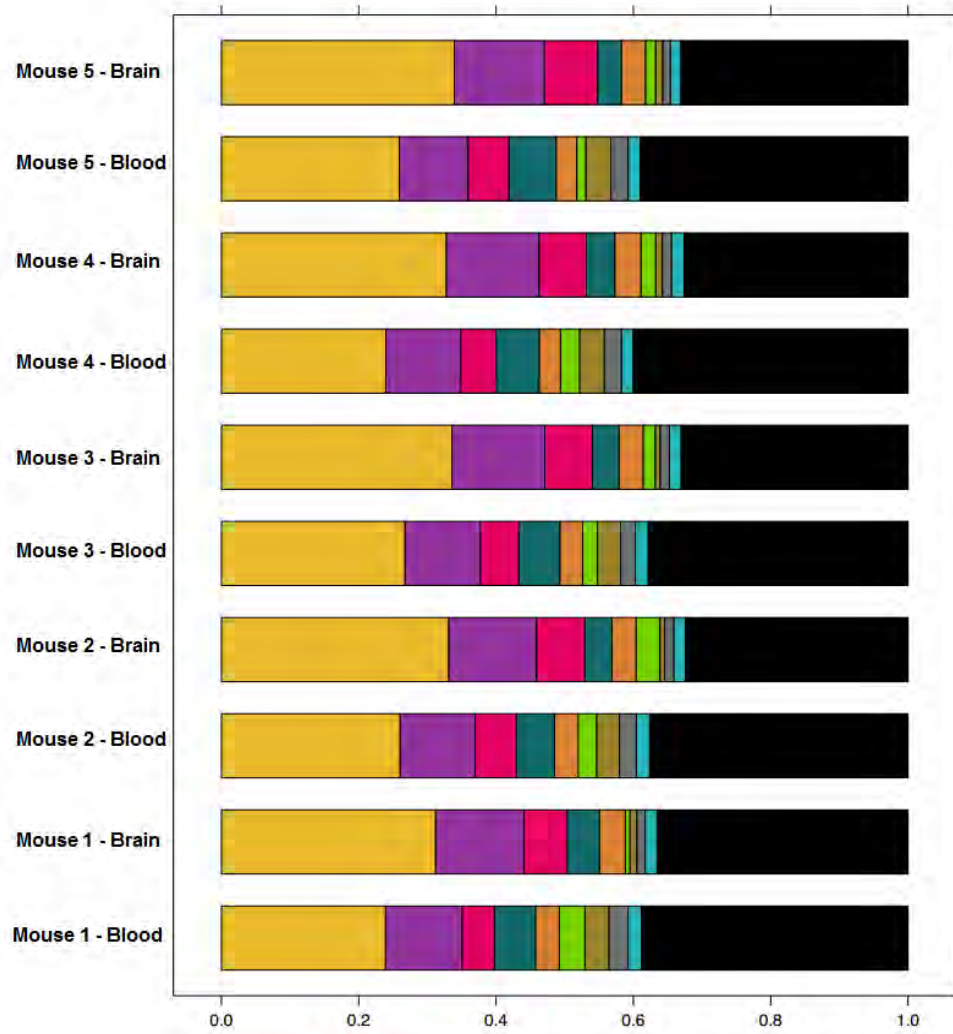
Table 4 Genus and Species Data - Bacteria Exclusive to Blood

Bacteria Exclusive to Blood		
*represented by >1 OTU		
Family	Genus	Species
<i>Acholeplasmataceae</i>	<i>Candidatus Phytoplasma</i>	unclassified
<i>Alcaligenaceae</i>	unclassified	unclassified
<i>Alicyclobacillaceae</i>	<i>Alicyclobacillus</i>	unclassified
<i>Aquabacteriaceae</i>	<i>Aquabacterium</i>	unclassified
<i>Bradyrhizobiaceae</i> *	<i>Bradyrhizobium</i>	<i>elkanii</i>
<i>Burkholderiaceae</i> *	<i>Burkholderia</i>	unclassified
	<i>Ralstonia</i>	unclassified
<i>Comamonadaceae</i> *	unclassified	unclassified
<i>Desulfobulbaceae</i>	unclassified	unclassified
<i>Erysipelotrichaceae</i>	<i>Allobaculum</i>	<i>sp ID4</i>
<i>Intrasporangiaceae</i>	<i>Janibacter</i>	unclassified
<i>Rhodospirillaceae</i>	unclassified	unclassified
<i>Sinobacteraceae</i> *	unclassified	unclassified
<i>Sphingomonadaceae</i> *	<i>Novosphingobium</i>	unclassified
	<i>Sphingomonas</i>	unclassified
<i>Synechococcaceae</i>	<i>Prochlorococcus</i>	unclassified
<i>Veillonellaceae</i>	<i>Dialister</i>	unclassified

Whole community microbiome profiles were consistently separated between brain and blood samples

In addition to the absolute presence or absence of specific bacteria, the relative amounts of different bacteria also contribute to the tissue-specific microbial signature. Abundance metric results from microarray hybridization score (HybScore) data were compared across tissue type and subjects, revealing consistent differences between blood and brain. Figure 2 displays the nine families with the largest total HybScore as a proportion of the grand total of all detected OTUs for each subject. The “Other” category includes the sum of all HybScores for families outside the top nine. Family level abundance patterns were significantly different between brain and blood samples based on a two-tailed heteroskedastic t-test for all top families ($p < 0.05$) except for *Lactobacillaceae* and *Plantomycetaceae*. For all brain samples, the top nine families

represent a greater percentage of each samples' total Hybscore compared to their respective blood control.

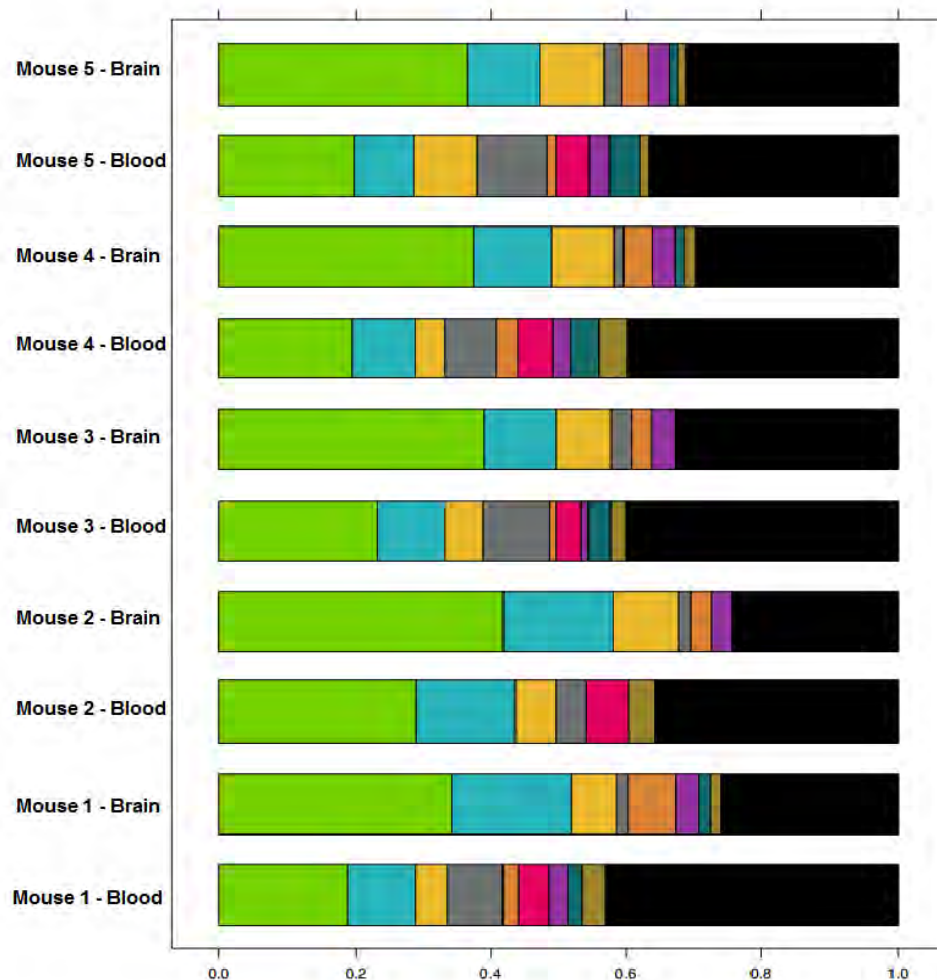


	Domain	Phylum	Class	Order	Family
	Bacteria	Firmicutes	Clostridia	Clostridiales	Lachnospiraceae
	Bacteria	Bacteroidetes	Bacteroidia	Bacteroidales	Rikenellaceae
	Bacteria	Proteobacteria	Gammaproteobacteria	Pseudomonadales	Pseudomonadaceae
	Bacteria	Proteobacteria	unclassified	unclassified	unclassified
	Bacteria	Proteobacteria	Gammaproteobacteria	unclassified	unclassified
	Bacteria	Firmicutes	Bacilli	Lactobacillales	Lactobacillaceae
	Bacteria	Proteobacteria	Alphaproteobacteria	Sphingomonadales	Sphingomonadaceae
	Bacteria	Proteobacteria	Gammaproteobacteria	Enterobacteriales	Enterobacterceae
	Bacteria	Planctomycetes	Planctomycea	Planctomycetales	Planctomycetceae
	Other				

Figure 36 Family-level proportional abundance

Relative abundance of the top nine bacterial families across brain and blood samples. (“Other” contains families outside the top nine and unclassified bacteria). The color of each block corresponds to the family listed above. The size of each block corresponds to the total HybScore in a specific family relative to the total abundance level in the sample (eg. *Lachnospiraceae* abundance represent 23.9% of the total HybScores in Mouse I – Blood compared to 31.2% of the total in Mouse I – Brain). Abundance patterns were significantly different between brain and blood for all top families except *Lactobacillaceae* and *Planctomycetaceae*, indicating separation in brain and blood flora abundance.

Microbiome composition between brain tissue and blood were again separated when assessing bacterial family richness patterns. Figure 2 shows the top nine most diverse families and an “Other” category containing all other families. The size of each color block represents the number of detected OTUs in that family relative to the total number of OTUs detected in that sample. A significant difference in proportion was detected using a two-tailed heteroskedastic t-test between brain and blood samples for all top families ($p < 0.05$) except for the *Rikenellaceae* family. Similar to the previous proportional abundance metric, the top families comprised a greater proportion of total detected OTUs in all brain samples compared to the respective blood results. There is a noticeable increase in the proportion of *Lachnospiraceae* OTUs in brain tissue versus blood, whereas *Sphingomonadaceae* comprises a sizable proportion of whole blood family richness unmatched in the brain tissue.



	Domain	Phylum	Class	Order	Family
	Bacteria	Firmicutes	Clostridia	Clostridiales	Lachnospiraceae
	Bacteria	Bacteroidetes	Bacteroidia	Bacteroidales	Rikenellaceae
	Bacteria	Proteobacteria	Gammaproteobacteria	Pseudomonadales	Pseudomonadaceae
	Bacteria	Proteobacteria	unclassified	unclassified	unclassified
	Bacteria	Proteobacteria	Gammaproteobacteria	unclassified	unclassified
	Bacteria	Proteobacteria	Alphaproteobacteria	Sphingomonadales	Sphingomonadaceae
	Bacteria	Planctomycetes	Planctomycea	Planctomycetales	Planctomycetceae
	Bacteria	Proteobacteria	Alphaproteobacteria	unclassified	unclassified
	Bacteria	Proteobacteria	Gammaproteobacteria	Enterobacteriales	Enterobacteriaceae
	Other				

Figure 37 Family-level richness

Bacterial family proportional richness between brain and blood samples showing the top nine most diverse families (“Other” contains families outside the top nine and unclassified bacteria). Family is indicated by the block color while the block size represents the number of OTUs in a specific family relative to the total OTUs for that sample (eg. *Lachnospiraceae* OTUs represent 18.6% of all observed OTUs in Mouse 1 – Blood compared to 34.5% of all OTUs in

Mouse 1 – Brain). A significant difference was detected between brain and blood samples for all top families except *Rikenellaceae*. This figure suggests a separation in bacterial family diversity between sample types, further contributing to the microbial signature of the two tissue types.

To further characterize the bacterial composition by tissue type, we analyzed the effect of sample type on microbiome composition using ordination analysis given the presence of the 197 detected OTUs present in at least one sample. A principal coordinate analysis (PCoA) based on abundance data displayed significant separation based on sample type ($p = 0.007$, Adonis test; Figure 4). A similar PCoA analysis based on incidence data revealed similar microbiota separation between the two tissue types ($p = 0.011$, Adonis test; Figure 5). Each data point denotes the total microbial community for a sample. Both analyses revealed separation into two distinct clusters, one for brain and one for whole blood. Taken together, the microbial composition results significantly diverged with respect to tissue type and remained relatively consistent across the different experimental subjects.

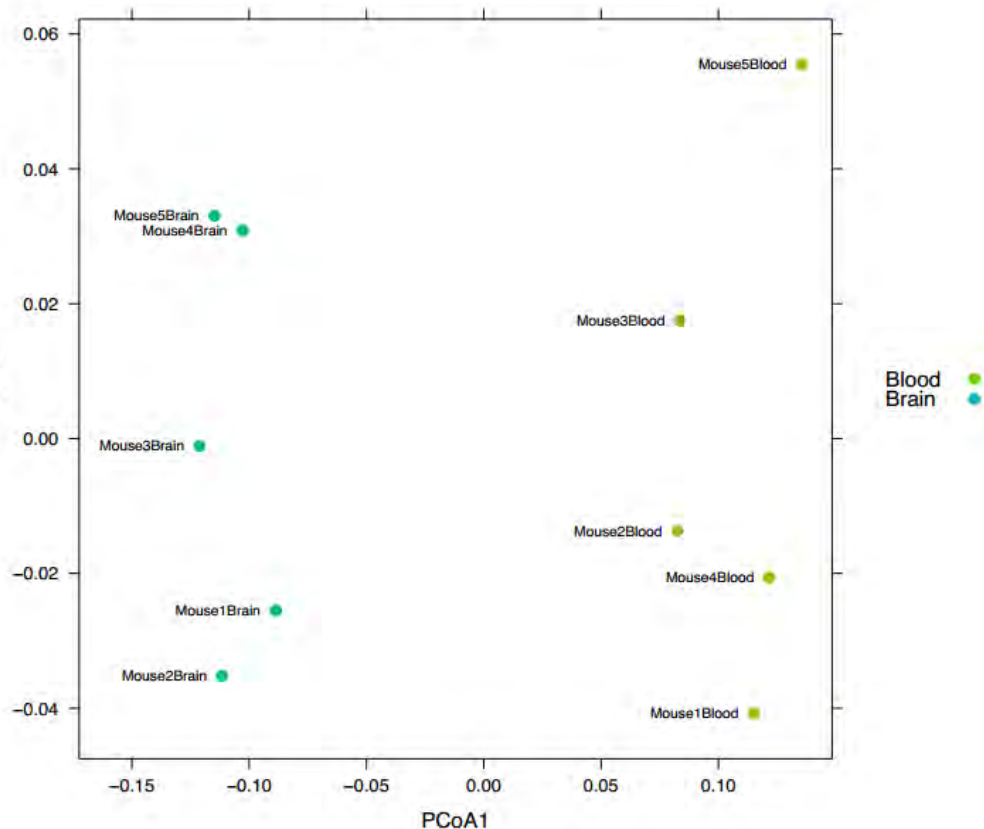


Figure 38 Principal coordinate analysis on weighted UniFrac abundance

PCoA of observed microbial taxa from blood vs brain tissue indicate a significant microbiome abundance difference between the two sample types (Adonis test, $p = 0.007$). Axis 1, the horizontal axis, explained 86% of the variation and axis 2, the vertical axis, explained 7% of observed variation. The clear separation in sample clusters indicate similarity in community composition within the same sample types and dissimilarity between brain and blood microbiota.

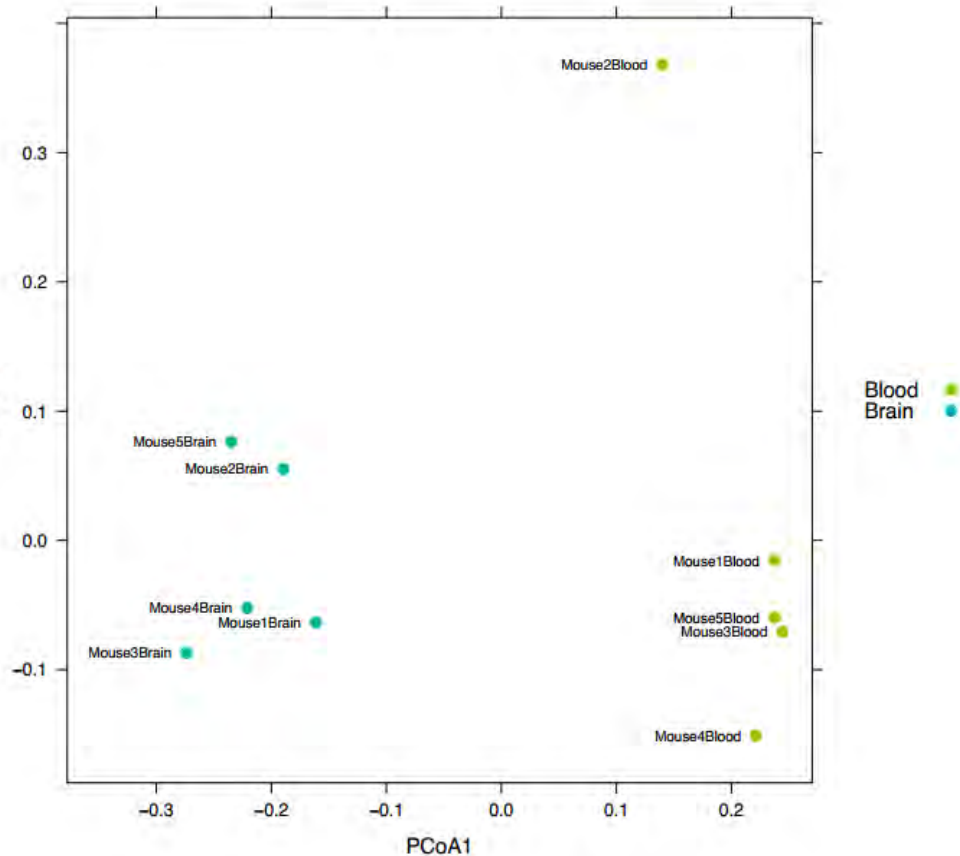


Figure 39 Principal coordinate analysis on unweighted UniFrac (incidence data)

PCoA of unweighted UniFrac given the presence or absence of 197 taxa demonstrates a significant microbiome difference between brain and blood sample types (Adonis test, $p = 0.011$). A clear separation between sample types and clustering partition is evident. Axis 1, the horizontal axis, explained 46% of the variation and axis 2, the vertical axis, explained 18%.

Analysis based on OTUs with significant abundance differences across sample types confirm microbiota separation across brain and blood samples

A parametric Welch test was performed to identify taxa that were significantly increased or decreased across the two sample types. We found 167 out of the 197 OTUs with significantly different abundance patterns. A PCoA based on the abundance of the 167 taxa significantly separated the microbiome, again indicating that the microbiome of the brain and blood are different, and explaining 97% of the difference between the two tissue types.

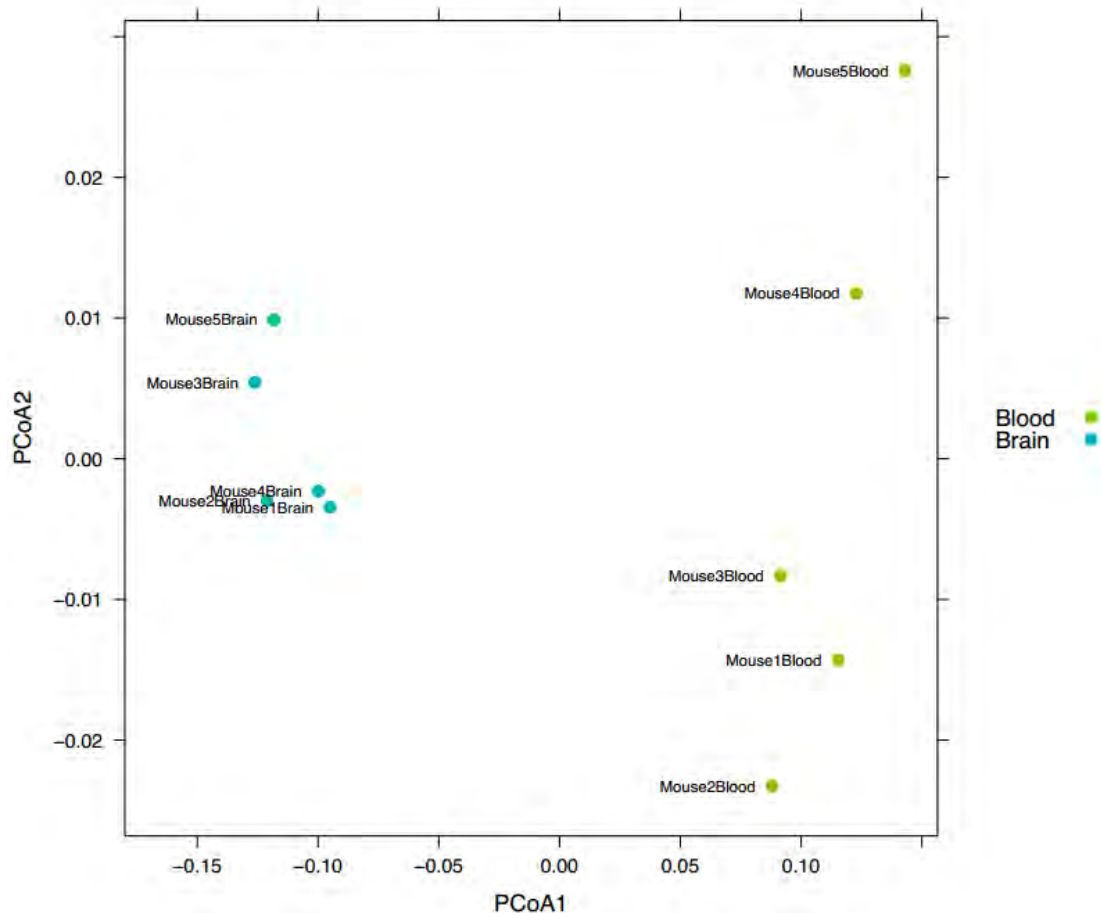


Figure 40 Principal coordinate analysis on weighted UniFrac abundance, 167 taxa

PCoA plot based on weighted UniFrac distance between samples given the abundance of 167 OTUs with significant abundance differences across the sample types. Results indicate differences in microbial signatures across the two sample types. Blood and brain sample results were separated across axis I, representing 97% of the variation between the samples.

Comparison to prior brain microbiome results

The top bacterial phyla and families are presented in comparison with two prior studies, Lluch et al. 2015²⁷ which reported bacterial signatures in mice and Branton et al. 2012²⁸ which detailed human brains. Our results are in good accordance with the same top bacteria phyla and sharing common bacterial families (Table 5). The study by Branton utilized human tissue and did not report results at the family taxonomic level.

Table 5 Comparison of brain microbiome with previous studies

	Brain Microbiome – Most prevalent bacterial phyla and families		
	Current Study (mouse)	Lluch 2016 (mouse)	Branton 2012 (mouse)
Phylum	Firmicutes	Proteobacteria	Proteobacteria
	Bacteroidetes	Bacteroidetes	Actinobacteria
	Proteobacteria	Firmicutes	-
	Actinobacteria	Actinobacteria	-
Family	Lachnospiraceae	Bifidobacteraceae	-
	Rikenellaceae	Sphingomonadaceae	-
	Pseudomonadaceae	Burkholderacaceae	-
	Lactobacillaceae	Lachnospiraceae	-
	Sphingomonadaceae	Moraxallaceae	-
	Enterobacteriaceae	Porphyromonadaceae	-
	Planctomycetaceae	Campylobacteraceae	-

Discussion

In this work, we utilized genomic sequences of 16S rRNA to investigate the microbial composition of brain tissue and whole blood from healthy adult mice and demonstrated the presence of bacteria within both tissue types. Our results demonstrate a diverse murine brain bacterial community comprised of 123 detected OTUs from 24 bacterial families. Additionally, these results demonstrate unique microbial profiles for the two tissue types and the presence of previously unclassified bacteria in both brain and blood.

Sequence analysis revealed microbiota within brain tissue, and the community profile of brain bacteria was found to be distinct from the microbial diversity, richness, and abundance in whole blood from the same animal. When the whole microbiota profile was assessed, ordination analyses based on both presence/absence and abundance metrics showed a significant separation of brain from blood microbiota, and, importantly, similar separation was observed for all studied mice. Cluster analysis also revealed two distinct groupings for each sample type, further confirming a differential presence in the brain environment compared to blood. Furthermore, certain bacterial families were identified as unique either brain tissue or whole blood (Table 1), indicating that bacteria that comprise the brain microbiota are not simply a subset derived from other bodily microenvironments. Taken as a whole, the evidence we report supports the idea of a discrete brain microbiome comprised of bacteria both common and exclusive to those found in blood.

To our knowledge, we make the second report of a brain microbiome within healthy wild-type mice and the third report overall of microbiota found in the brain of healthy mammals^{27,28}. Lluch and colleagues used an optimized 16S rDNA-targeted metagenomics sequencing pipeline to analyze genetic sequences from various murine tissues, discovering tissue-specific bacteria in many organs including the brain²⁷. Sequence analysis revealed brain microbiota belonging to many shared families to the current study, as was described (Table 5). Similarly, results revealed a substantial number of unknown or uncharacterized bacteria living within healthy murine brain

tissue. Unlike this publication, our results present a prospective systematic investigation of the presence, abundance, and community composition of bacteria from blood and brain samples across multiple animals. The Lluh et al publication was intended to demonstrate the feasibility of a novel 16S screening method. The presence of bacteria within brain tissue was mentioned in one figure and was not otherwise discussed in detail.

Branton et al. investigated the microbial diversity in pathologically normal and abnormal brains from people with HIV/AIDS and other disease controls using deep sequencing²⁸. At the class level, alpha proteobacteria associated sequences were predominant, independent of host disease status. Given the methodological discrepancy between profiling human and murine tissue and the spectrum of host disease status, direct comparison between Branton et al. and the current study is difficult. Nevertheless, our results when combined with these prior studies, are highly suggestive of a normal brain microbiome

Our results establishing a consistent brain microbial population across several healthy subjects raises the question about the assumed physiologic role for these bacteria. Mounting evidence has shown that the unique microbiomes within different organs exert important physiologic, not pathologic, effects on the host organ. The presented results raise the possibility that the brain's own microbiome may contribute to normal CNS function, with alterations leading to neurologic or psychiatric signs and symptoms, or neuropathologic findings. Breakdown of the blood-brain barrier (BBB) can occur in brain tumors, head trauma, burns, or sepsis²⁹⁻³¹. BBB disruptions have been reported to persist in some persons with traumatic brain injury (TBI), and are suggested as a potential risk for dementia³⁰. Given our results of two distinct microbiomes in the blood and healthy brain tissue, increased BBB permeability may alter the brain microbiome with unknown consequences. Similar to altered microbiome composition in the immune system³², gut⁸, or lungs³³ leading to altered physiology, this dysbiotic brain microbiome could lead to various clinical or neuropathologic outcomes³⁴. If such links were to be established, the implications of a brain microbiota role could have profound effects on clinical medicine, neuroscience research, and animal models of human disease.

Due to the ubiquitous presence of bacteria, environmental contamination is an appreciable concern and a possible limitation to the study. However, our PCoA results are both internally consistent across tissue types and are generally consistent with prior results exploring the brain and blood microbiomes. All specimens of the same compartment, whether brain tissue or whole blood, consistently separated with abundance and incidence analysis, supporting the reliability of the presented observations. True contamination would otherwise appear randomly from sample to sample. In view of two prior studies complementing the current results, contamination appears less likely to explain the findings.

A limitation of any microarray profiling technique is the inability to distinguish between living and dead microbes. Live culturing would aid in this regard but it too has limited purpose due to the difficulty in replicating growth environment along with likely presence of viable but nonculturable bacteria^{35,36}. Furthermore, cultures taken at a single point in time cannot differentiate between long-term colonizing bacteria versus transient species.

Reliance on bacterial culture techniques can inform but may not provide a complete understanding of a microbiome³³. Cultures typically focus on clinically important (i.e. pathogenic) organisms and do not properly evaluate a host-microbiome environment in its entirety³⁷. Several microbiome studies have utilized 16S sequencing technologies to corroborate and extend bacterial culture results, enhancing confidence in 16S-based results from heretofore unexamined tissues. Wolfe et al reported bacteria on 16S analysis in urine samples that failed to grow bacteria under usual clinical conditions³⁸. In a subsequent study, Hilt et al utilized

enhanced culture techniques to demonstrate cultivable bacteria in urine specimens reported as “sterile” with standard clinical laboratory techniques, and then showed a correlation between enhanced culture results and 16S analysis of the urine specimens³⁹. An interesting use of 16S sequencing is demonstrating the presence of bacteria in culture-negative samples taken from hospitalized inpatients^{40,41}. The results from Rampini et al compare conventional culture methods to 16S analysis to PCR-amplified culture-negative clinical specimens, and found more than 90% agreement between the two methods⁴¹. Other tissues believed to be sterile, where the term sterile is synonymous with “lack of known pathogenic organisms”, and later found to display a distinct organ-specific microbiome include placenta^{37,42} and lung³³.

The aggregate impact of our results combined with other studies demonstrating bacteria in supposedly sterile tissues raises an important question about “sterility” in tissue assumed to be devoid of microbiota. Perhaps a better distinction is not sterile compared to non-sterile, but instead the probability of developing an infection against which the body mounts an inflammatory response^{8,33}.

The current study is the first to characterize a separate and distinct microbiome within the murine brain compared to the microbiota composition of animal-matched blood samples. Bacterial signatures from the brain were significantly different from those found in blood by all assessed metrics. Certain families of bacteria were found exclusive to either the brain or blood, perhaps indicating a yet unknown physiologic role for brain flora. The emerging links between the mammalian enteric microbiota and neurobehavioral modulation has already been suggested as a major paradigm shift in the field of neuroscience⁴³. Here however, rather than gut bacteria, the discovery of normal brain flora establishes a direct association between potential symbiotic bacteria and the CNS, unveiling and supporting the novel concept of brain bacteria within healthy mammals. The exact role of the brain microbiome is unidentified and serves as a new frontier for microbiome research investigating the intimate links between microbiota and neuroscience.

Methods

Sample Collection and Preparation

All animal procedures in this study followed the Guide for the Care and Use of Laboratory Animals and were approved by the Duke University Institutional Animal Care and Use Committee (IACUC). Five C57Bl/6J mice (Jackson Laboratories, Bar Harbor, Maine) age 12 weeks were used for this study. Prior to blood and tissue sample collection, animals were housed with free access to food and water in a 12 hour light-dark cycle at a housing temperature of 22 °C. Mice were allowed two weeks to acclimate to housing conditions before sample preparation.

We collected blood via aseptic cardiac puncture as previously described^{44,45}. Mice were anesthetized with 4.3% isoflurane in oxygen at a FiO₂ of 30% in an anesthesia induction box for 90 s. The trachea was then intubated with 20 gauge teflon catheter, and the lung mechanically ventilated with a 0.7 ml tidal volume at 110 breaths per minute. The concentration of isoflurane was reduced to 1.6% to maintain anesthesia. Body temperature was regulated at 37.0 °C with a heating pad and a heating lamp connected to a temperature controller unit. The thorax and adjacent regions were shaved and triple disinfected with 10% Betadine antiseptic solution. A sterile 22G needle was inserted into the left ventricle of the heart. 0.1 to 0.2 cc of whole blood was drawn and immediately snap frozen in liquid nitrogen. The entire blood content of each animal was stored at -80 °C until shipment on dry ice. After blood collection, animals were euthanized via transcardial perfusion of 60 mL sterilized saline. Sterile saline

perfusion was maintained using a syringe pump set at 5 mL/minute. Blood flush was complete when the saline ran clear and the liver blanched. Following decapitation, the calvaria was removed using sterilized forceps. All instruments were sterilized using a glass bead sterilizer and washed with 70% sterile ethanol after each contact with the specimen. 0.2 g of brain tissue was aseptically excised and snap frozen in liquid nitrogen before storage at -80 °C until shipment on dry ice.

DNA extraction and PCR amplification

Bacterial DNA from whole blood samples were extracted with BiOstic Bacteremia DNA Isolation Kit (MO BIO Laboratories, Carlsbad, CA) and brain tissue with Ultra Clean Tissue and Cells DNA Isolation Kit (MO BIO Laboratories, Carlsbad, CA). Bacterial 16S rRNA gene regions were subject to 35 cycles of amplification using the degenerate forward primer 27F.I (5'-AGRGTTCGATCMTGGCTCAG-3') and the non-degenerate reverse primer 1492R (5'-GGTTACCTTGTTACGACTT-3'). PCR amplification products were concentrated using a solid-phase reversible immobilization method for the purification of PCR products and quantified by electrophoresis using an Agilent 2100 Bioanalyzer. Phylochip Control Mix was added to each amplified product for scaling and normalization. 500 ng of amplicons were fragmented into 50 – 200 bp and biotin labeled (Affymetrix WT Double Stranded DNA Terminal Labeling) in preparation for hybridization. Negative controls (sterile water) were included at each of the prior steps to control for possible environmental contamination.

Microarray hybridization

Tissue from each specimen comprised one sample for a total of 10 samples (n = 5 mice, matched brain tissue and whole blood from each animal for a total of 10 samples). Each sample was hybridized to one commercially available PhyloChip microarray chip, version G3 (Second Genome, San Bruno, CA) at Second Genome. The microarray contains 1.1 million oligonucleotide probes to detect over 50,000 taxa of known bacterial and archaeal operational taxonomic units (OTUs). DNA probes are contained in 59,959 clusters of 17 nucleotides. The 27,938 detectable microbial OTUs represent 147 phyla, 1123 classes, 1219 orders, and 1464 families. Hybridization was performed according to manufacturer protocol (Affymetrix, Santa Clara, CA) and as previously described⁴⁶. Arrays were washed, stained, and scanned using a GeneArray scanner (Affymetrix). Each scan was captured using standard Affymetrix software (GeneChip Microarray Analysis Suite). Samples were processed in a Good Laboratory Practices compliant service laboratory at Second Genome.

Microarray scoring

To calculate the summary fluorescence intensity (FI) for each feature on each array, the central 9 pixels of individual image features were ranked by intensity and the 75th percentile was used⁴⁶. Probe FIs were background-subtracted and scaled to the PhyloChip Control Mix. Array FI is collected as integer values ranging from 0 to 65,536. Fluorescence intensity observed from perfectly matching (PM) probes were compared to mismatching (MM) probes and were considered positive if the FI from PM probe is at least 1.5 times greater than the intensity of the MM control ($PM/MM \geq 1.5$), PM minus MM is at least 50 times greater than the array specific noise N^{47} ($PM-MM \geq 50*N$), and ≥ 0.95 where r represents the response score⁴⁶.

Only PM FI from probes observed as positive in at least 3 samples were exported from all experiments then rank-normalized and used as input to empirical probe-set discovery. Probes were clustered into probe-sets based on both correlations in FI across all biological samples and taxonomic relatedness. Where multiple clustering solutions were available, higher correlation coefficients were favored over lower, taxonomic relatedness at the species level was favored over higher ranks, and sets composed of more probes were favored over less. All probe sets contained ≥ 5 probes, with average pair-wise correlation coefficients ≥ 0.85 . The empirical OTU (eOTU) tracked by a probe set was taxonomically annotated from the combination of the 9-mers contained in all probes of the set. Hybridization score (HybScore) is the mean of the ranked probe FIs within each set and is used to compare relative changes in a taxon's population abundance between samples. HybScore values are in the range of 0 to 16000 and changes by 1000 indicate a two-fold increase in FI. The proportion of probes for an eOTU that are observed as positive in a sample (number of positive probe pairs divided by the total number of probe pairs in a probe set) is referred to as the positive fraction (pf). An eOTUs was considered present in a sample where $pf \geq 0.8$, and only eOTUs passing the pf cutoff are included for further analysis.

Data reduction and statistical analysis

Data was filtered leaving only OTUs present in at least one sample, or to taxa significantly increased in abundance in either brain tissue or blood compared to the other. The parametric Welch test was used to calculate p-values for the abundance filter. Furthermore, q-values were determined using the Benjamini-Hochberg procedure to correct p-values, controlling for false discovery rates as described previously⁴⁶.

After data filtering for inclusion criteria, the values used for each taxa-sample intersection were determined using two metrics. In the first case, the abundance metrics are used directly (AT). Abundance values (HybScores) for all eOTUs with a probe score below are utilized even those where $pf < 0.8$. Binary metrics were created in the second case (absence, 0; presence, 1) (BT). A non-paired, heteroskedastic Student's t-test assuming unequal variances was used to test for differences in microbial richness and hierarchical summarization between brain and blood sample categories.

To evaluate sample-to-sample distance all profiles were inter-compared in a pairwise fashion to determine a dissimilarity score and stored it in a distance dissimilarity matrix. The distance functions were chosen to allow similar biological samples to produce only small dissimilarity scores. The Unifrac distance metric utilizes the phylogenetic distance between OTUs to determine the dissimilarity between communities⁴⁶. Unifrac was used for presence/absence, whereas Weighted Unifrac (WUnifrac) was used for abundance data.

Two-dimensional ordinations and hierarchical clustering maps of the samples were created to graphically summarize the inter-sample relationships. Principal Coordinate Analyses (PCoA) is a method of two-dimensional ordination plotting used to visualize complex relationships between samples. PCoA uses the dissimilarity values to position the points relative to each other. The Adonis test is utilized for finding significant differences among discrete categorical or continuous variables. In this randomization/Monte Carlo permutation test, the samples are randomly reassigned to the various sample categories, and the between-category differences are compared to the true between-category differences. Adonis utilizes the sample-to-sample distance matrix directly, not a derived ordination or clustering outcome

References

- 1 Hooper, L. V. & Gordon, J. I. Commensal host-bacterial relationships in the gut. *Science* 292, 1115-1118 (2001).
- 2 Ley, R. E., Peterson, D. A. & Gordon, J. I. Ecological and evolutionary forces shaping microbial diversity in the human intestine. *Cell* 124, 837-848, doi:10.1016/j.cell.2006.02.017 (2006).
- 3 Sender, R., Fuchs, S. & Milo, R. Are We Really Vastly Outnumbered? Revisiting the Ratio of Bacterial to Host Cells in Humans. *Cell* 164, 337-340, doi:10.1016/j.cell.2016.01.013 (2016).
- 4 Costello, E. K. et al. Bacterial community variation in human body habitats across space and time. *Science* 326, 1694-1697, doi:10.1126/science.1177486 (2009).
- 5 Paise, S. et al. Comprehensive description of blood microbiome from healthy donors assessed by 16S targeted metagenomic sequencing. *Transfusion* 56, 1138-1147, doi:10.1111/trf.13477 (2016).
- 6 Stumpf, R. M. et al. The primate vaginal microbiome: comparative context and implications for human health and disease. *American journal of physical anthropology* 152 Suppl 57, 119-134, doi:10.1002/ajpa.22395 (2013).
- 7 Human Microbiome Project, C. Structure, function and diversity of the healthy human microbiome. *Nature* 486, 207-214, doi:10.1038/nature11234 (2012).
- 8 Cho, I. & Blaser, M. J. The human microbiome: at the interface of health and disease. *Nature reviews. Genetics* 13, 260-270, doi:10.1038/nrg3182 (2012).
- 9 Eckburg, P. B. et al. Diversity of the human intestinal microbial flora. *Science* 308, 1635-1638, doi:10.1126/science.1110591 (2005).
- 10 Marchesi, J. R. et al. The gut microbiota and host health: a new clinical frontier. *Gut*, doi:10.1136/gutjnl-2015-309990 (2015).
- 11 Butel, M. J. Probiotics, gut microbiota and health. *Medecine et maladies infectieuses* 44, 1-8, doi:10.1016/j.medmal.2013.10.002 (2014).
- 12 Montiel-Castro, A. J., Gonzalez-Cervantes, R. M., Bravo-Ruiseco, G. & Pacheco-Lopez, G. The microbiota-gut-brain axis: neurobehavioral correlates, health and sociality. *Frontiers in integrative neuroscience* 7, 70, doi:10.3389/fnint.2013.00070 (2013).
- 13 Borre, Y. E. et al. Microbiota and neurodevelopmental windows: implications for brain disorders. *Trends in molecular medicine* 20, 509-518, doi:10.1016/j.molmed.2014.05.002 (2014).
- 14 Mayer, E. A., Knight, R., Mazmanian, S. K., Cryan, J. F. & Tillisch, K. Gut microbes and the brain: paradigm shift in neuroscience. *The Journal of neuroscience : the official journal of the Society for Neuroscience* 34, 15490-15496, doi:10.1523/JNEUROSCI.3299-14.2014 (2014).
- 15 Foster, J. A. & McVey Neufeld, K. A. Gut-brain axis: how the microbiome influences anxiety and depression. *Trends in neurosciences* 36, 305-312, doi:10.1016/j.tins.2013.01.005 (2013).
- 16 Dinan, T. G. & Cryan, J. F. Regulation of the stress response by the gut microbiota: implications for psychoneuroendocrinology. *Psychoneuroendocrinology* 37, 1369-1378, doi:10.1016/j.psyneuen.2012.03.007 (2012).
- 17 Cryan, J. F. & O'Mahony, S. M. The microbiome-gut-brain axis: from bowel to behavior. *Neurogastroenterology and motility : the official journal of the European*

- Gastrointestinal Motility Society 23, 187-192, doi:10.1111/j.1365-2982.2010.01664.x (2011).
- 18 Hsiao, E. Y. et al. Microbiota modulate behavioral and physiological abnormalities associated with neurodevelopmental disorders. *Cell* 155, 1451-1463, doi:10.1016/j.cell.2013.11.024 (2013).
 - 19 de Theije, C. G. et al. Altered gut microbiota and activity in a murine model of autism spectrum disorders. *Brain, behavior, and immunity* 37, 197-206, doi:10.1016/j.bbi.2013.12.005 (2014).
 - 20 Ochoa-Reparaz, J., Mielcarz, D. W., Begum-Haque, S. & Kasper, L. H. Gut, bugs, and brain: role of commensal bacteria in the control of central nervous system disease. *Annals of neurology* 69, 240-247, doi:10.1002/ana.22344 (2011).
 - 21 Bravo, J. A. et al. Ingestion of *Lactobacillus* strain regulates emotional behavior and central GABA receptor expression in a mouse via the vagus nerve. *Proceedings of the National Academy of Sciences of the United States of America* 108, 16050-16055, doi:10.1073/pnas.1102999108 (2011).
 - 22 Bravo, J. A. et al. Communication between gastrointestinal bacteria and the nervous system. *Current opinion in pharmacology* 12, 667-672, doi:10.1016/j.coph.2012.09.010 (2012).
 - 23 Ochoa-Reparaz, J. et al. A polysaccharide from the human commensal *Bacteroides fragilis* protects against CNS demyelinating disease. *Mucosal immunology* 3, 487-495, doi:10.1038/mi.2010.29 (2010).
 - 24 Lyte, M. Microbial endocrinology in the microbiome-gut-brain axis: how bacterial production and utilization of neurochemicals influence behavior. *PLoS pathogens* 9, e1003726, doi:10.1371/journal.ppat.1003726 (2013).
 - 25 Farrall, A. J. & Wardlaw, J. M. Blood-brain barrier: ageing and microvascular disease--systematic review and meta-analysis. *Neurobiology of aging* 30, 337-352, doi:10.1016/j.neurobiolaging.2007.07.015 (2009).
 - 26 Braniste, V. et al. The gut microbiota influences blood-brain barrier permeability in mice. *Science translational medicine* 6, 263ra158, doi:10.1126/scitranslmed.3009759 (2014).
 - 27 Lluch, J. et al. The Characterization of Novel Tissue Microbiota Using an Optimized 16S Metagenomic Sequencing Pipeline. *PloS one* 10, e0142334, doi:10.1371/journal.pone.0142334 (2015).
 - 28 Branton, W. G. et al. Brain microbial populations in HIV/AIDS: alpha-proteobacteria predominate independent of host immune status. *PloS one* 8, e54673, doi:10.1371/journal.pone.0054673 (2013).
 - 29 Davies, D. C. Blood-brain barrier breakdown in septic encephalopathy and brain tumours. *Journal of anatomy* 200, 639-646 (2002).
 - 30 Hay, J. R., Johnson, V. E., Young, A. M., Smith, D. H. & Stewart, W. Blood-Brain Barrier Disruption Is an Early Event That May Persist for Many Years After Traumatic Brain Injury in Humans. *Journal of neuropathology and experimental neurology* 74, 1147-1157, doi:10.1097/NEN.0000000000000261 (2015).
 - 31 Hu, J., Zhang, Y., Ding, S. & Li, H. Dynamic Observation on Opening of the Blood-Brain Barrier in the Primary Stage of Severely Scalded Rabbits, a Multimodal Study. *J Burn Care Res* 37, e279-286, doi:10.1097/BCR.0000000000000172 (2016).
 - 32 Honda, K. & Littman, D. R. The microbiota in adaptive immune homeostasis and disease. *Nature* 535, 75-84, doi:10.1038/nature18848 (2016).

- 33 Dickson, R. P., Erb-Downward, J. R., Martinez, F. J. & Huffnagle, G. B. The Microbiome and the Respiratory Tract. *Annu. Rev. Physiol.* 78, 481-504, doi:10.1146/annurev-physiol-021115-105238 (2016).
- 34 Washington, P. M., Villapol, S. & Burns, M. P. Polypathology and dementia after brain trauma: Does brain injury trigger distinct neurodegenerative diseases, or should they be classified together as traumatic encephalopathy? *Experimental neurology* 275 Pt 3, 381-388, doi:10.1016/j.expneurol.2015.06.015 (2016).
- 35 Oliver, J. D. Recent findings on the viable but nonculturable state in pathogenic bacteria. *FEMS Microbiol Rev* 34, 415-425, doi:10.1111/j.1574-6976.2009.00200.x (2010).
- 36 Relman, D. A. Detection and identification of previously unrecognized microbial pathogens. *Emerging infectious diseases* 4, 382-389, doi:10.3201/eid0403.980310 (1998).
- 37 Segal, L. N., Rom, W. N. & Weiden, M. D. Lung microbiome for clinicians. New discoveries about bugs in healthy and diseased lungs. *Ann Am Thorac Soc* 11, 108-116, doi:10.1513/AnnalsATS.201310-339FR (2014).
- 38 Wolfe, A. J. et al. Evidence of uncultivated bacteria in the adult female bladder. *Journal of clinical microbiology* 50, 1376-1383, doi:10.1128/JCM.05852-11 (2012).
- 39 Hilt, E. E. et al. Urine is not sterile: use of enhanced urine culture techniques to detect resident bacterial flora in the adult female bladder. *Journal of clinical microbiology* 52, 871-876, doi:10.1128/JCM.02876-13 (2014).
- 40 Aguilera-Arreola, M. G. et al. Cultivation-independent approach for the direct detection of bacteria in human clinical specimens as a tool for analysing culture-negative samples: a prospective study. *Springerplus* 5, 332, doi:10.1186/s40064-016-1949-3 (2016).
- 41 Rampini, S. K. et al. Broad-range 16S rRNA gene polymerase chain reaction for diagnosis of culture-negative bacterial infections. *Clinical infectious diseases : an official publication of the Infectious Diseases Society of America* 53, 1245-1251, doi:10.1093/cid/cir692 (2011).
- 42 Aagaard, K. et al. The placenta harbors a unique microbiome. *Science translational medicine* 6, 237ra265, doi:10.1126/scitranslmed.3008599 (2014).
- 43 Kelly, J. R. et al. Breaking down the barriers: the gut microbiome, intestinal permeability and stress-related psychiatric disorders. *Frontiers in cellular neuroscience* 9, 392, doi:10.3389/fncel.2015.00392 (2015).
- 44 Hoff, J. Methods of Blood Collection in the Mouse. *Laboratory animals* 29 (2000).
- 45 Parasuraman, S., Raveendran, R. & Kesavan, R. Blood sample collection in small laboratory animals. *Journal of pharmacology & pharmacotherapeutics* 1, 87-93, doi:10.4103/0976-500X.72350 (2010).
- 46 Hazen, T. C. et al. Deep-sea oil plume enriches indigenous oil-degrading bacteria. *Science* 330, 204-208, doi:10.1126/science.1195979 (2010).
- 47 DeSantis, T. Z., Stone, C. E., Murray, S. R., Moberg, J. P. & Andersen, G. L. Rapid quantification and taxonomic classification of environmental DNA from both prokaryotic and eukaryotic origins using a microarray. *FEMS microbiology letters* 245, 271-278, doi:10.1016/j.femsle.2005.03.016 (2005).

IN VS. OUT: CONTROVERSIES IN SHOCK TUBE BLAST EXPERIMENTS AND STAGING - CONTINUED

The recognition of the importance of blast-related neurotrauma in current military operations constitutes a critical need for examining primary blast injury [1, 2]. To elucidate the pathophysiology of blast in humans, many animal models of blast traumatic brain injury (TBI) have been established. These include small animal models of mouse [3-5], rat [6-8], and rabbit [9, 10], and other larger animals including swine [11, 12] and sheep [13-15]. To simulate blast in a laboratory setting, gas-driven shock tubes have been extensively used and provide the advantage of replicating primary blast in a controlled and repeatable manner [16]. However, many studies fail to consider the issues of proper shock tube use, limiting considerations to simple 'inside vs. outside' controversies [17]. Due to variation in experimental shock tube methodologies, ambiguity and inconsistencies confound the proper characterization of primary blast exposure. These variations include the direction of the impinging wave front, immobilization of the head and body of the test animal, use of thoracic protection, appropriate scaling of blast inputs, and placement of the test specimen relative to the location of shock initiation and shock tube exit, amongst others [17, 18]. Each factor can alter the biomechanical loading of the specimen thus potentially altering injury type and severity. As such, subsequent blast sequelae and histopathological findings cannot be compared across the diversity of injury models performed with inconsistent protocols. This issue is not widely recognized by funding agencies and thus, there exists no push for standardization. Without some consensus view, blast research will continue to employ disjointed injury models without any corroboration or validation.

Standardizing blast procedures begins with understanding the desired loading condition. The ideal planar wave is characterized by a Friedlander curve as depicted in Figure 1. Friedlander-type blasts represent a realistic free field high explosive blast exposure as measured from a stationary location and serves as the ideal comparison for laboratory conducted tests [17]. Often, shock tube testing is performed without regard to whether the profile represents an ideal waveform or a complex waveform, nor the details of the time history beyond the peak pressure. For a Friedlander profile, the pressure profile follows a sharp rise of less than 1 ms duration, followed by an exponential decay to a relatively short negative phase before returning to ambient pressure. Considering the numerous methodologic inconsistencies in published blast injury models, this study focused on assessing overpressure waves at locations inside, at the exit, and outside the shock tube into the free field. As most injury tolerance is a function of some combination of peak overpressure, overpressure duration, and impulse for ideal waveforms, these three metrics must be considered together and were used to assess the experimentally and numerically derived pressure behavior [19]. By characterizing blast wave profile progression at multiple distances, locations of planar and deteriorated waveforms can be established. Placing test subjects in locations that encounter an ideal planar wave reduces complex loading and allows for better characterization of loading condition. Deviation from an ideal waveform can lead to applied impulse that is larger than that expected for an ideal waveform and difficult to characterize inputs.

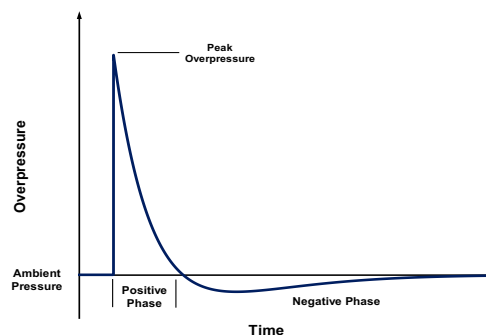


Figure 1. Graphical representation of a planar Friedlander waveform [17]

Little agreement has been reached on valid placement locations for shock tube tests, and there is a distinct lack of experimental validation. In order to provide clarification on this issue, the goals of this study were to (1) characterize blast wave profile evolution using pressure transducers at predetermined landmarks corresponding to common specimen placements, (2) identify locations of ideal waveform impingement during shock tube experiments, (3) validate shock tube experiments with finite element numerical simulations, and (4) consider the benefits and limitations of various specimen placements.

METHODOLOGY

Shock tube

Shock waves were generated using a 305mm diameter, cylindrical shock tube (Figure 2) consisting of a 305mm long driver section, and a 3.05m long driven section (10:1 driven to driver length ratio). The bursting diaphragm was composed of two polyethylene terephthalate (PET) sheets of total thickness 0.508mm. Nitrogen was the driver gas. All factors were kept constant for the entire test battery.

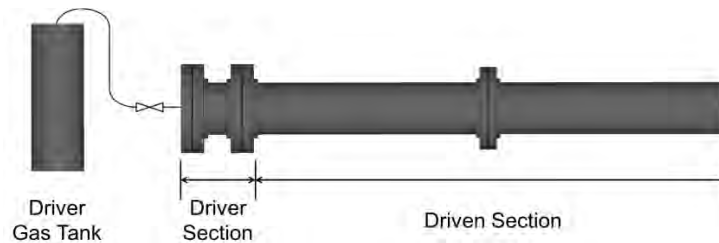


Figure 2. Shock tube schematic

Pressure measurements

Pressure profiles were acquired at predetermined landmarks as shown in Figure 3. Each point represents a pressure transducer (PT; Endevco 8530B-200; San Juan Capistrano, CA) measuring incident pressure. Replicates of three trials were tested for each location. Standoff distances were determined by number of tube diameter lengths (D_T) from the exit of the shock tube: Standoff A (61cm inside; $-2D_T$), Standoff B (30.5cm inside; $-D_T$), Standoff C (0cm/exit; $0D_T$), Standoff D (2.5cm outside; $D_T/12$), Standoff E (15.25cm outside; $\frac{1}{2}D_T$), Standoff F (30.5cm outside; D_T), Standoff G (61cm outside; $2D_T$), and Standoff H (91.5cm; $3D_T$). For each standoff, measurements were taken at various radial distances starting at the tube central axis. Marked in red, Location 1 (tube central axis) through Location 5 (Shock tube wall) are equally spaced apart. Locations 1 through 3 marked in blue measured pressure from the spherical expansion of the shock front in the free field. Location 3 increased in radial distance equally with increased standoff, and Location 2 marked the midpoint of Location 1 and 3.

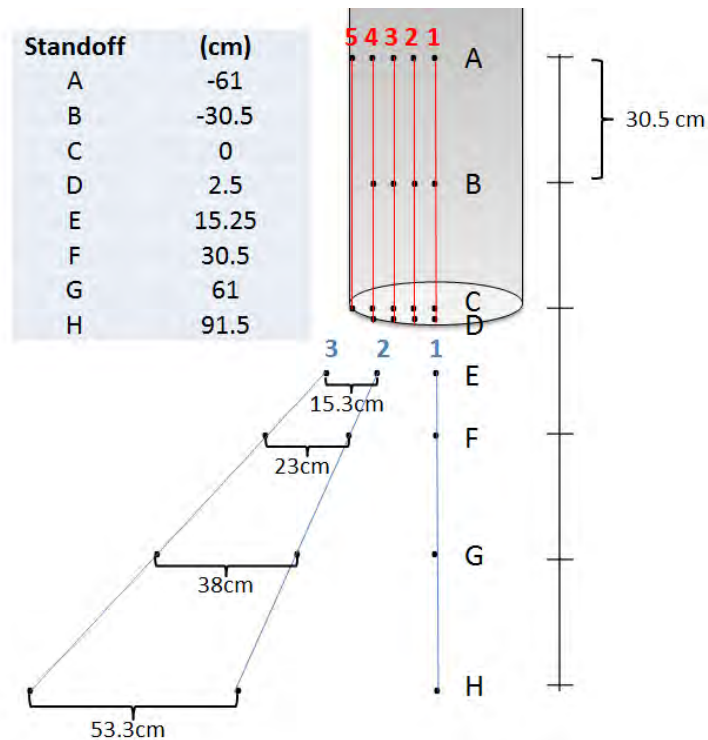


Figure 3. Pressure transducer locations varied in both standoff and radial distance from the central axis. Locations A through H mark standoff distance from tube exit (positive standoffs are downstream from exit, negative standoffs are upstream). Locations across the tube diameter are marked Location 1 through 5 (red) for standoffs A through D, and Location 1 through 3 (blue) for standoffs E through H.

Wedge (Figure 4A) and pie-shaped (Figure 4B) mounting fixtures were machined to allow a blast wave to pass undisturbed across a PT, permitting incident profile measurement. PTs are mounted flush with the housing surface at a right angle, incident to the oncoming wave. The wedge is a 15cm x 15cm x 1.25cm aluminum plate with a 30 degree wedge. The flat surface is placed horizontally in the plane of the tube axis. The wedge is fixed onto a horizontal support and can be moved along the center-axis along Standoffs A through D. Four PTs are mounted approximately 3.8cm apart, accounting for locations 1 through 4. Shock tube wall mounted sensors account for location 5. The pie plate is a 23 cm diameter aluminum plate with a 30 degree bevel. A single pressure transducer is mounted in the center. The flat surface is placed horizontally in the plane of the tube axis and moved through the different locations across and downstream of the shock tube exit.

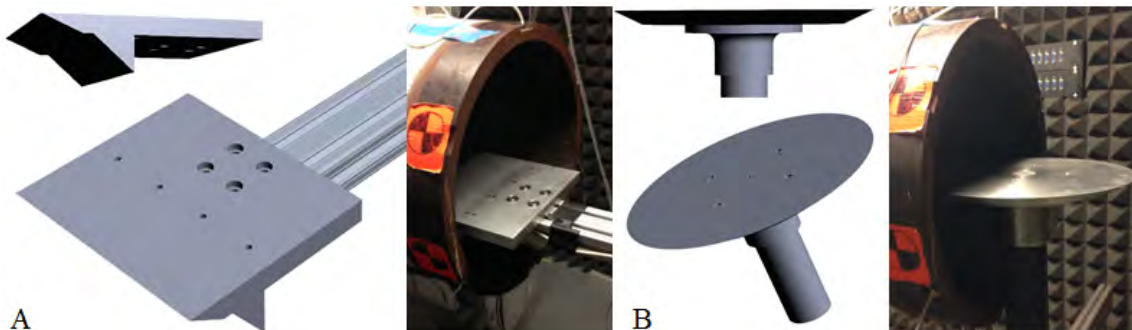


Figure 4. (A) Wedge pressure transducer housing fixture (B) Pie plate pressure transducer housing fixture

Finite element model

A finite element number model of free field blast was established to validate experimental shock tube results. To observe the full response field during the blast, a 2D, symmetric shock tube model was built in LS-DYNA (Livermore Software Technology Corporation; Livermore, CA). The model consists of over 250,000 plane elements and includes a high pressure nitrogen driver section (Figure 5, red) with an initially ambient driven mesh (Figure 5, blue) and ambient free field (Figure 5, green). A reflecting plane of symmetry was assumed, and a 2mm mesh was chosen as it has been shown to sufficiently capture blast waves in simulation while still maintaining computational efficiency [20]. The model uses the DYNA arbitrary Lagrangian Eulerian (ALE) formulation with 2nd order accurate Van Leer advection and builds upon existing shock tube FE models [16]. Initial conditions in the driver section were set to mimic an empirical burst pressure levels.

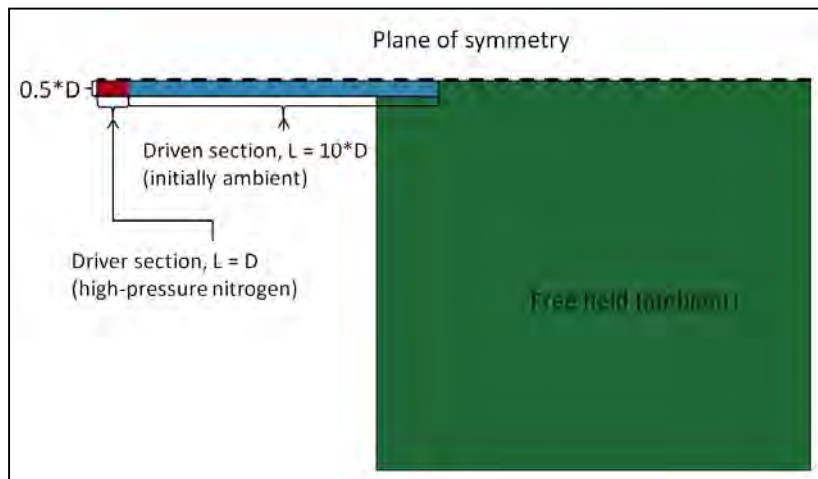


Figure 5. Finite element ALE model of shock tube with high-pressure nitrogen driver section (red) and 10 diameters length driven section (blue) to match the experimental setup.

Sampling and Statistics

All data was sampled at 1 Mhz with a 500 kHz anti-alias hardware filter and post-processed using an 8-pole Butterworth filter with a cut-off frequency of 40 kHz [21]. Matlab R2012b (Mathworks; Natick, MA) was used to process the raw data. Statistical comparisons were performed using JMP Pro 10.0.2 (SAS Institute Inc; Cary, NC). The interactions between dependent variables pressure, duration, and impulse were considered correlated, and thus univariate analysis of variance comparisons were conducted to assess shock tube parameters. The effects of sensor standoff and location across the diameter on generated blast response (pressure, duration, and impulse) was analyzed using ANOVA to see general effects and Tukey post hoc analysis of means comparisons to assess specific effects. Normalized experimental and numerical simulation data was compared using ANCOVA. Results were considered significant at $p < \alpha = 0.05$.

Results

Shock Tube Characterization

Blast wave peak overpressure, positive duration, and impulse from all PT locations are provided in Table I (Appendix). For Standoff A through D, results showed no significant differences across the five radial distances for peak overpressure, duration, and impulse. Thus, measurements across the tube diameter were nominally similar at all standoffs inside the tube and $D_T/12$ past the exit. This trend was not found across Locations 1 through 3 for Standoffs E, F, G, and H. Significant differences were found in all standoffs past $\frac{1}{2}D_T$ from the exit of the shock tube.

Peak overpressure across the shock tube diameter grouped by standoff is shown in Figure 6. Across Locations 1 through 5, Standoffs A through D and Location 1 for Standoff E exhibited no significant differences. Peak overpressure for the given experimental tube conditions were approximately 160kPa. Peak overpressure declined into the free field at standoffs F, G, and H, at a distance of greater than one D_T from the shock tube exit.

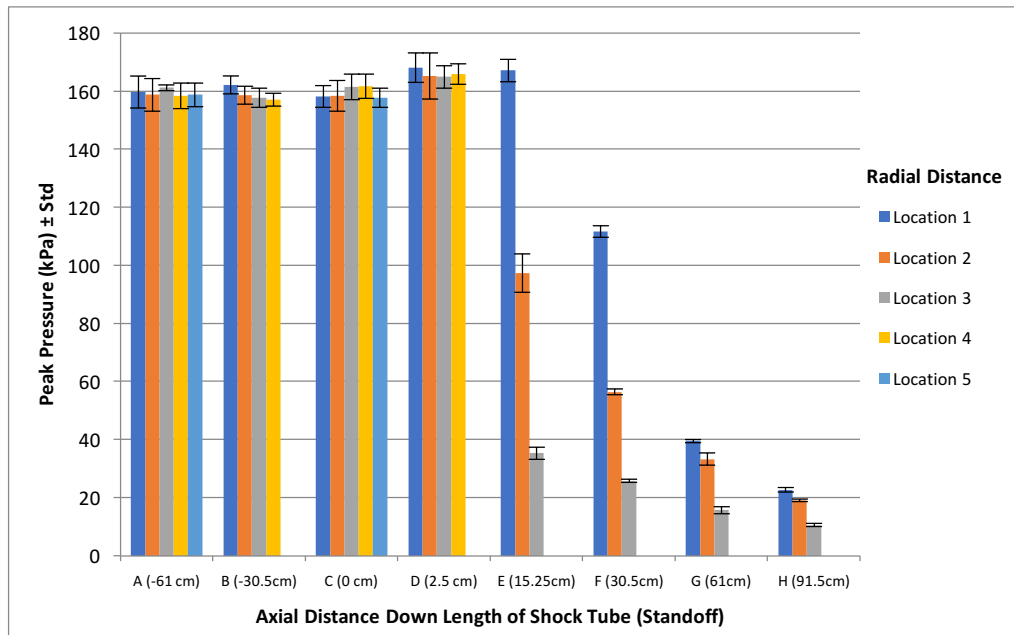


Figure 6. Peak overpressure measured at various radial distances grouped by standoff

Positive overpressure duration across the tube diameter by standoff is shown in Figure 7. At Standoff A, the furthest inside the tube, positive duration was found to be significantly different from all other standoff distances. A positive duration of approximately 6ms was measured at A. Standoff B saw a positive duration of approximately 4ms and was also significantly different from all other standoffs. Durations were not found to be significantly different at Standoffs C and D, the shock tube exit and $D_T/12$ outside the exit. These standoffs saw durations of approximately 2.6ms. Duration increased with distance into the free field starting one D_T outside the exit. This trend is most notable at Location 1, down the the length of the shock tube central axis.

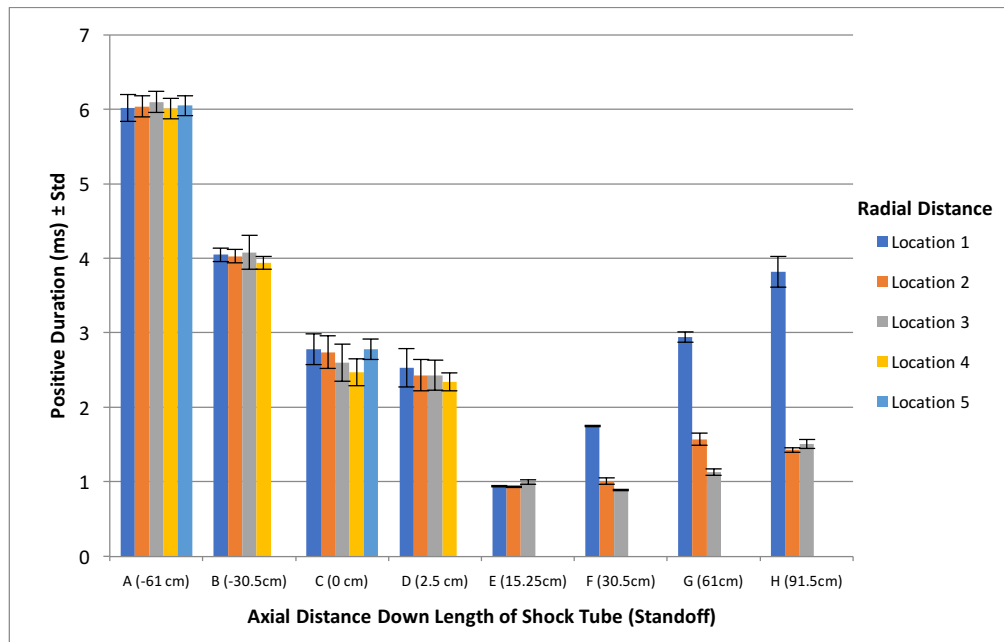
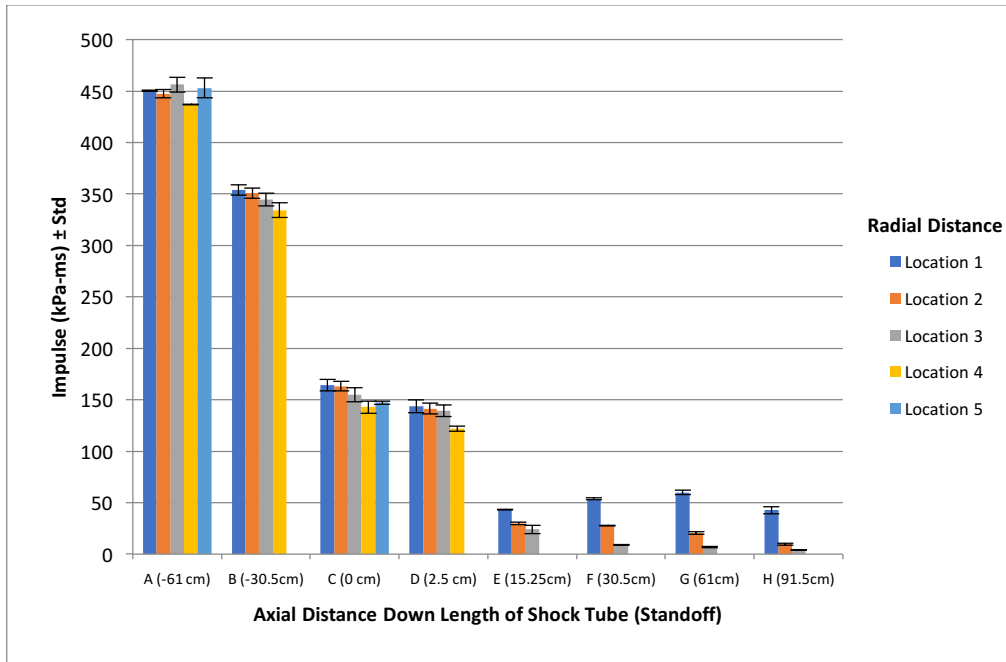


Figure 7. Positive duration measured at various radial distances grouped by standoff

Impulse results across the tube diameter by standoff are shown in Figure 8. Similar to the duration results, impulse at standoffs A and B showed significant differences from each of the rest of the standoff locations. Impulses of approximately 450 and 350 kPa-ms were measured at A and B, respectively. At Standoff C and D, impulse was not found to be significantly different. This range of standoffs produced impulse of 140 to 150 kPa-ms. Further outside the shock tube, impulse was significantly different at Location 1 than at Location 2 and 3, the more lateral PT locations.



Chapter 2

Figure 8. Impulse measured at various radial distances grouped by standoff

Incident pressure-time histories along the tube central axis (Location 1) show distinct waveform evolution as the shock front travels down the length of the driven section and expands into the free field (Figure 9). Beginning with Standoff A at $2D_T$ inside the exit, the curve shows a sharp rise but a fairly slow return to ambient conditions. Of note is the slight plateaued peak in the trace. Standoff B, one D_T inside the exit, displays a similar profile but with a slightly faster decay. By the time the blast front reaches the exit of the tube, Standoff C, the pressure profile is Friedlander-like with a sharp rise and a quick exponential decay. Standoff D, 2.5cm past the exit of the shock tube, retains this this profile and is indistinct from the exit pressure profile. When pressure wave reaches $\frac{1}{2}D_T$ at Standoff B, the curve shows deviation from the ideal Friedlander-like profile. A large negative duration develops as the peak overpressure diminishes. By Standoff H, at $3D_T$ outside, the peak is drastically reduced and duration lengthened for the given peak as shown by the complex profile in gray.

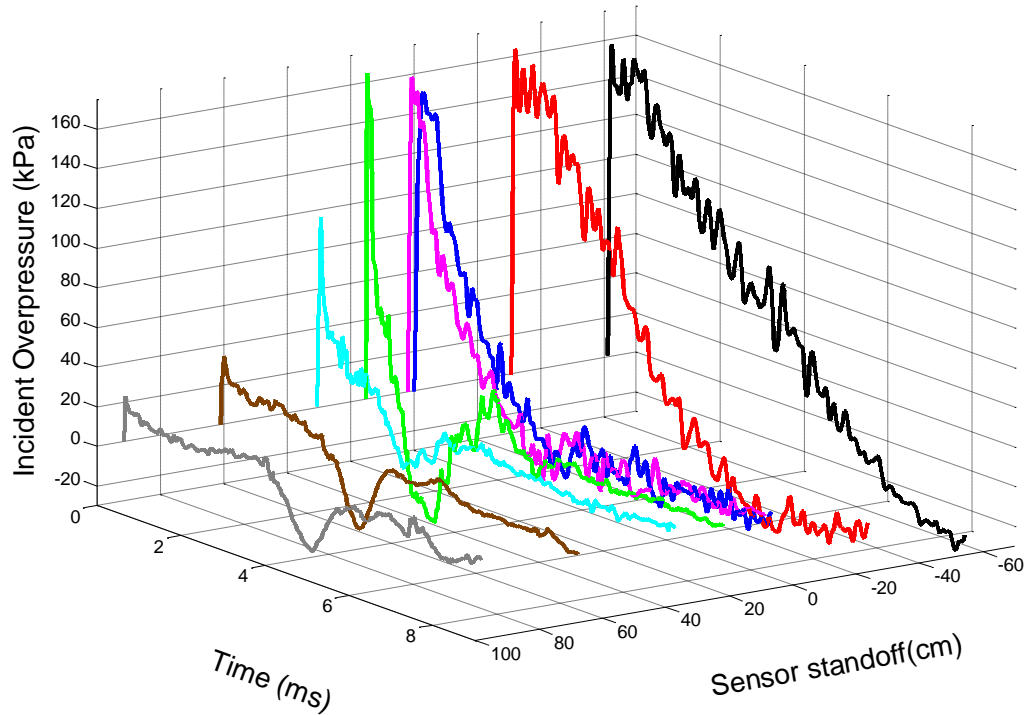


Figure 9.

Experimentally derived pressure-time profiles along the tube central axis (Location 1) for Standoff A (black; $-2D_T$), Standoff B (red; $-D_T$), Standoff C (blue; $0D_T$), Standoff D (magenta; $D_T/12$), Standoff E (green; $1/2D_T$), Standoff F (cyan; D_T), Standoff G (brown; $2D_T$), and Standoff H (gray; $3D_T$).

3.2 Numerical Simulation – Finite Element Model

To compare relative exposure at each location, both numerical and experimental results were normalized to their respective peak pressure, duration, and impulse at the tube wall exit (Standoff C, Location 5 from experimental setup). This location is conserved across experimental tests and not affected by variation in wedge or pie plate positioning. Results show excellent agreement with experimental tests in the free field, overestimating the peak pressure inside the tube by on average 6% (Figure 10, left) and underestimating peak pressures outside the tube by on average 4%. Duration results were underestimated in the simulation by approximately 2% inside the tube and 20% outside. Overall impulse was overestimated by on average 13% inside and 8% outside the tube. No statistical differences were found between normalized data for all across three metrics.

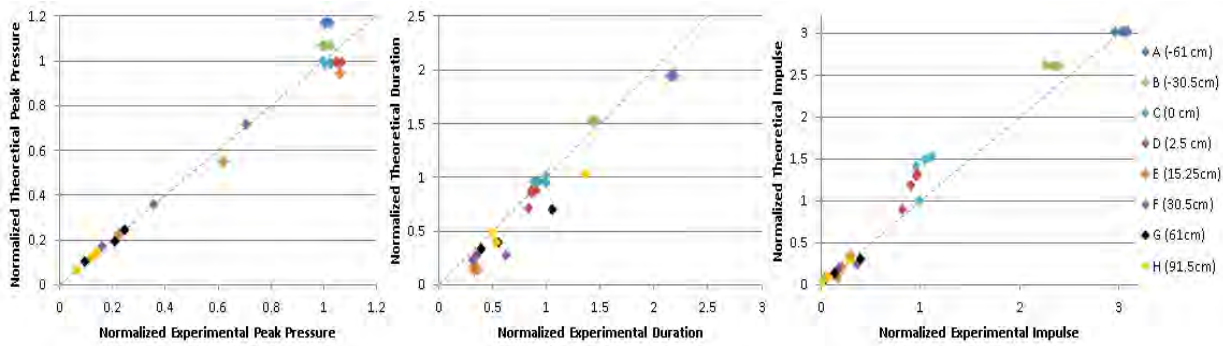


Figure 10. One-to-one comparison of experimental and finite element results. Left - peak positive overpressure. Middle - overpressure duration. Right - impulse.

Simulation shock tube pressure-time history at exit is shown in Figure 11 and . As the shock exits, the expansion wave generated at the edge of the tube moves inward and meets at the tube centerline at approximately one half of a diameter. The pressure pulse after this point is greatly diminished due to geometric spreading of the shock energy.

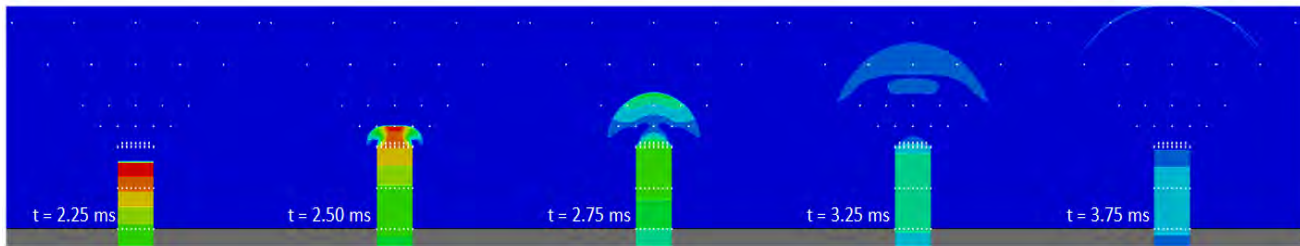


Figure 11. Shock tube time-history with experimental pressure locations shown as white dots (locations analogous to those in Figure 3).

Simulation incident pressure-time histories along the tube central axis (Location 1) show distinct waveform evolution down the driven section of the shock tube (Figure 12). Pressure profile trends show a good match with experimentally derived curves (Figure 9).

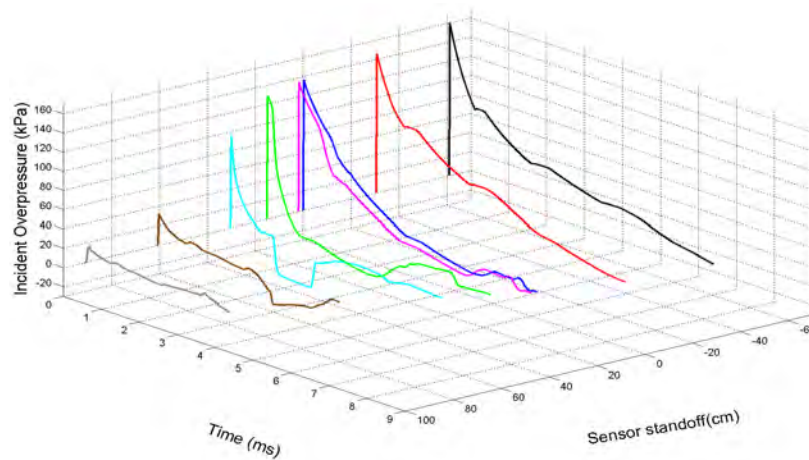


Figure 12. Numerically derived pressure-time profiles along the tube central axis (Location 1) for Standoff A (black; $-2D_T$), Standoff B (red; $-D_T$), Standoff C (blue; $0D_T$), Standoff D (magenta; $D_T/12$), Standoff E (green; $\frac{1}{2}D_T$), Standoff F (cyan; D_T), Standoff G (brown; $2D_T$), and Standoff H (gray; $3D_T$).

DISCUSSION

The shock tube performance characteristics with the chosen setup clearly demonstrate a distinct range of locations at which test subjects would experience ideal loading conditions. First, pressure data across the diameter of the shock

tube suggest that the shock wave was planar by Standoff A, a distance of $8D_T$ down the driven section. Overpressure, impulse, and duration across the diameter of the tube showed no significant differences at this standoff. On average in this planar regime, the relative error for these measurements across Locations 1 through 5 was within 5% of the mean. At Location 1 down the central axis, peak pressure is unchanged until Standoff F, $1D_T$ past the exit, where peak pressure begins to decrease. Moving out radially for Standoffs F, G and H, we see increased waveform complexity and a decrease in all blast parameter values. Deviations away from the central axis occur due to the spherical expansion of the shock front from the exit of the tube as noted visually in the simulations and reconfirmed by the data. For lateral positioning, specimens must be placed as close as possible to the shock tube central long axis.

Analysis of standoff locations of non-planarity, where pressure, duration, and impulse drop off significantly, determine inside vs. outside placement validity. A consistent overpressure is maintained over the range of $-2 D_T$ to $1D_T$ outside the tube. This indicates that subjects along the major axis within $1 D_T$ outside the tube will experience similar peak overpressure values. Across the tube diameter, no significant differences of blast parameters were found between Standoff C, the tube exit, and standoff D, $D_T/12$ past the exit. Pressure-time histories for both standoffs are also indistinct (Figure 9), and similar to the intended Friedlander type loading curve. Consequently, specimens tested outside the shock tube in this regime will see the same loading condition as those measured directly at the exit as the shock maintains planarity. Thus, placing specimens outside is indeed an appropriate experimental shock tube experiment method. The drop off of duration and impulse past Standoff E at $\frac{1}{2}D_T$ downstream indicate that a test specimen should ideally be placed before this standoff. Further out into the free field, Standoffs G and H exhibit complex pressure profiles that are difficult to characterize (Figure 9). Similarly at these standoffs, for a given peak pressure at more than $1D_T$, duration and impulse can increase relative to values immediately outside the exit (Figure 7 and 8). Injuries from impinging pressure waves here and farther out are more momentum dominated events not representative of common primary blast exposure. For testing specimens outside the shock tube, this study recommends the standoff to be minimized, allowing a maximum standoff of $\frac{1}{2}D_T$.

Loading conditions for subjects placed at distances inside the shock tube must also be considered. Though pressure was not shown to vary with standoff distance inside the shock tube, positive duration and impulse were significantly different between Standoffs A, B, and C (Figure 7 and 8). Impulse measurements at $2D_T$ inside the exit were a twofold increase over impulse measured at $1D_T$ inside, and nearly a threefold increase over impulse measured at the exit. The pressure-time histories at $1 D_T$ and $2D_T$ inside the exit can be characterized by a more complex decay than a Friedlander-type pressure trace as seen at the tube exit (Figure 1, Figure 9). A relatively slow decay to ambient conditions results in a longer duration and a subsequent increase in impulse.

Upon rupture of the diaphragm separating the high pressure driver from the rest of the shock tube, a compression wave is sent upstream into the driven section and an expansion wave towards the driver. A shock front is formed as the tail of the compression wave moves faster than the lead end. With a sufficiently short driver, the expansion wave reflects off the back wall of the driver and can reach the shock, attenuating the pressure. The attenuation due to the expansion fan results in Friedlander-like waves. If the shock front reaches the test

subject or PT before the expansion fan catches it, blast waves can plateau, are not attenuated, and can deliver excessive impulse. Using a driver gas with a high speed of sound or a short driver section allows placement closer to the test driver. Still, a conservative estimate is to test at least $8-10 D_T$ down from the driver. Any closer and the shock front will not have sufficient distance to fully develop a Friedlander-type pressure profile. [17]

The higher impulse loading condition from testing deeper inside the tube must be considered if a clinical and realistic blast model is to be established. For the given shock tube setup conditions for this study, approximate similar exposure levels from the resulting unscaled peak overpressure and duration according to the Conventional Weapons Effect Program (CONWEP) are as follows (Table 2)[22]:

Table 2. CONWEP determined exposure levels for standoffs of this study

Standoff (cm)	Overpressure (kPa)	Duration (ms)	Equivalent Exposure	
			TNT (kg)	Distance (m)
-61 (A)	160	6	1	2.6
-30 (B)	160	4	5	4.4
0 (C)	160	2.5	16	6.5

Equivalent exposures at Standoff A and B are fairly large charge sizes at close distances. As many blast injury models study mild to moderate injury, Standoff C provides the appropriate loading condition [19]. Some blast models may indeed desire a large impulse loading condition. However, failure to scale the biomechanical response across species leads to unrealistic injury. Moreover, many injury models are conducted on smaller animals such as mice. Even with a simple scaling technique, such as the cube-root of mass [13], scale factors may be 10-15 times the experimental positive duration value. Neglecting these factors and not considering specimen placement ultimately lead to scaled exposures outside the realm of clinical interest.

The confinement effect of the tube wall on the test subject is another consideration for placement inside vs. outside the shock tube [16]. The impinging wave front will reflect off the specimen onto the shock tube wall. Shock reflections off these boundaries generate higher pressures that would otherwise be experienced by an object in the free field. Complex waveforms may interact with the specimen and measuring instruments, confounding the exact state of exposure level. Since the shock at exit is preserved within $\frac{1}{2}D_T$, testing within this outside region and allowing reflections to dissipate into the free field may be beneficial if an ideal blast is desirable. Confinement effects can be mitigated with a sufficiently large shock tube diameter. However, the minimum 8 to 1 driven to driver ratio may result in large and impractical shock tubes to be used in a laboratory setting.

We have shown that specimen placement both inside and outside the shock tube is appropriate within a certain range. This study well characterizes overpressure for a single shock tube setup configuration, but can be scaled to all shock tube sizes by diameter lengths. Numerical simulations provided good validation against experimentally derived blast results as shown through blast parameters and wave profiles. Further configurations include using other

driver gases and testing further upstream than $2D_T$ to fully characterize compression wave generation, progression, and attenuation.

Important conclusions of this study include:

1. Specimen placements interior and exterior to the shock tube exit are appropriate with the following conditions:
 - a. Inside: At least 8-10 shock tube diameters down the driven section
 - b. Outside: Minimize standoff as close to the exit as possible. At most $\frac{1}{2}$ a tube diameter away from the exit.
2. A higher impulse loading condition is found for specimens placed inside the shock tube. This must be considered when developing a realistic and clinically relevant blast injury model that is properly scaled from humans to the test animal species.
3. Confinement effects may generate complex loading scenarios for large specimens placed inside a shock tube. Using a sufficiently large shock tube or placing specimens outside minimize these effects and allow exact measurement of loading input.

References

- [1] Elder, G.A. and Cristian, A., Mt Sinai J Med, 76(2009), 111-8.
- [2] Okie, S., N Engl J Med, 352(2005), 2043-7.
- [3] Celandier, H., Clemenson, C.J., Ericsson, U.A., et al., Acta Physiol Scand, 33(1955), 6-13.
- [4] Cernak, I., Merkle, A.C., Koliatsos, V.E., et al., Neurobiol Dis, 41(2011), 538-51.
- [5] Rubovitch, V., Ten-Bosch, M., Zohar, O., et al., Exp Neurol, 232(2011), 280-9.
- [6] Saljo, A., Bao, F., Haglid, K.G., et al., J Neurotrauma, 17(2000), 719-26.
- [7] Svetlov, S.I., Prima, V., Kirk, D.R., et al., J Trauma, 69(2010), 795-804.
- [8] Garman, R.H., Jenkins, L.W., Switzer, R.C., 3rd, et al., J Neurotrauma, 28(2011), 947-59.
- [9] Richmond, D.R., Bowen, I.G. and White, C.S., Aerosp Med, 32(1961), 789-805.
- [10] Rafaels, K., Bass, C.R., Salzar, R.S., et al., J Neurotrauma, 28(2011), 2319-28.
- [11] Shridharani, J.K., Wood, G.W., Panzer, M.B., et al., Front Neurol, 3(2012), 70.
- [12] Saljo, A., Arrhen, F., Bolouri, H., et al., Journal of Neurotrauma, 25(2008), 1397-1406.
- [13] Bowen, I.G., Fletcher, E.R., Richmond, D.R., et al., Ann N Y Acad Sci, 152(1968), 122-46.
- [14] Clifford, C.B., Jaeger, J.J., Moe, J.B., et al., Mil Med, 149(1984), 491-5.
- [15] Yang, Z., Wang, Z., Tang, C., et al., J Trauma, 40(1996), S81-4.
- [16] Panzer, M.B., Matthews, K.A., Yu, A.W., et al., Front Neurol, 3(2012), 46.
- [17] Bass, C.R., Panzer, M.B., Rafaels, K.A., et al., Ann Biomed Eng, 40(2012), 185-202.
- [18] Wood, G.W., Panzer, M.B., Shridharani, J.K., et al., Inj Prev, 19(2013), 19-25.
- [19] Bass, C.R., Rafaels, K.A. and Salzar, R.S., J Trauma, 65(2008), 604-15.
- [20] Panzer, M.B., Myers, B.S. and Bass, C.R., Comput Methods Biomech Biomed Engin, 16(2013), 612-21.
- [21] Bass, C.R., Davis, M., Rafaels, K., et al., Int J Occup Saf Ergon, 11(2005), 347-61.
- [22] Hyde, D.W., CONWEP 2.1.0.8, Conventional Weapons Effects Program, (US Army Corps of Engineers, Vicksburg, MS, 2004)

Section 2: Columbia University Final Report

Theme: Thresholds for blast induced cell death and dysfunction

As a MURI partner, Columbia had two primary responsibilities over the duration of this project:

In collaboration with Duke, develop and use methodologies for measuring:

- *The threshold for cell death in organotypic representations of the brain*
- *The threshold for neuronal network dysfunction*
- *The loading required to cause structural and glial changes in organotypic representations of the brain*

In collaboration with Penn, assess circuit level changes in neuronal activity and function after blast exposure by:

- *Measuring paired-pulse ratios after blast in organotypic slice cultures*
- *Measuring activation thresholds for neural circuit activation*
- *Measuring LTP induction thresholds following blast exposure in hippocampal slice cultures*
- *Investigating cellular mechanisms responsible for functional changes*
- *Measuring LTP and cell death following repetitive primary blast exposure in hippocampal slice cultures*

Task A: Examine the multiscale physics of blast wave transmission to the brain.

[A3] Build devices for studying the effects of blast loading at the synaptic, network, and circuit level.

We have developed novel and robust methods for exposing isolated tissues to pressure transients that mimic the human intracranial pressure transients experienced during blast. These methods have been standardized and are now published so that others may also use them so that experiments are standardized across locations, both within and outside of this MURI. No other groups have been able to accomplish this important milestone which we believe will hasten progress for understanding the physics and biological mechanisms of blast TBI.

Shock tube: Shock waves were generated with a 76 mm diameter aluminum shock tube with an adjustable-length driver section (25 mm - 190 mm) pressurized with helium or nitrogen and a 1240 mm long driven section. Piezoresistive pressure transducers (Endevco, San Juan Capistrano, CA) were flush-mounted at the exit of the shock tube and within the fluid-filled blast receiver, at the location of the culture, and were oriented perpendicular to the direction of propagation to record side-on (incident) pressure. Transducer outputs were amplified (50X gain) and low-pass filtered (corner frequency of 40 kHz, Alligator Technologies, Costa Mesa, CA) before being digitized at 125 kHz. Peak overpressure, overpressure duration, and impulse were calculated with custom MATLAB scripts (Mathworks, Natick, MA). For in-air and in-fluid pressure histories, peak overpressure was defined as the maximum pressure of the positive overpressure phase, duration was defined as the length of time of the positive overpressure phase, and impulse was defined as the integral over time under the pressure history trace for the duration of the positive overpressure exposure (i.e. area).

Sample receiver: A fluid-filled receiver was designed to work in conjunction with the shock tube. The receiver (Figure 41) consisted of an enclosed 57 L high-density polyethylene (HDPE) reservoir filled

with water. Extending from the top of the reservoir was a 152 mm long, 51 mm diameter polycarbonate tube (6 mm wall thickness) attached to a 400 mm long, 8-degree diverging HDPE nozzle. The polycarbonate tube was sealed and secured to the top of the reservoir, and was positioned so that the diverging nozzle was 48 mm from the bottom of the reservoir. A 25 mm diameter open tube (HDPE) was installed in the reservoir to equalize the initial pressure in the receiver with the atmosphere, and to adjust the internal fluid levels during setup. The top surface of the test column was positioned directly under the center of the open end of the shock tube with a gap no more than 2 mm.

During in vitro testing, cultures are positioned in the center of the test column between the top set of aluminum flanges (approximately 76 mm from the top surface of the fluid column). The planar shock wave impinges the top surface of the fluid-filled receiver positioned at the end of the tube. The pressure wave in the test column propagates through the test sample (i.e., tissue culture) rather than reflecting off it because materials with similar impedances were selected to surround the sample. This aspect of the design was important because it minimize large strains in the sample. The pressure wave passes through the diverging nozzle into the reservoir causing the wave to attenuate and disperse. This design feature limits large pressure waves reflecting back through the test sample, and effectively loading the sample more than once during each test.

All membrane materials used in the fluid-filled receiver (including those containing the tissue samples) were tested for impedance matching with water to ensure that they would not create wave reflections during the test. The top surface of the test section had a thin (0.254 mm) silicone rubber membrane stretched over the surface and secured tightly using a hose clamp to prevent fluid from leaking and/or splashing from the column during the shock tube test. Between the bottom section of the test column and the portion of the polycarbonate tube attached to the reservoir was a thin membrane (0.254 mm) of PTFE. The purpose of this membrane was to create a barrier between the water in the reservoir and the fluid in the test column to reduce the bulk motion of the fluid in the column. Bubbles were carefully evacuated from the receiver and test column prior to each test to ensure that pockets of air did not affect the pressure wave.

One of the strengths of our multi-scale approach to bTBI is that the tissue culture experiments provide the opportunity to eliminate confounding injury modes (i.e. secondary (penetration, tearing) or tertiary (inertial loading, large deformation) from primary blast injury. We are the only group that we are aware of who has this capability to apply primary blast injury to living tissue in isolation of other blast injury mechanisms.

However, achieving primary blast injury in isolation from other modes requires extreme attention to detail and independent validation. To this end, high-speed (2100 fps) video analysis revealed that the tissue cultures placed within the receiver experienced substantial bulk motion during blast loading. Based on its timing, this bulk motion was caused not by the shock wave, but by the plug of cold gas traveling behind the shock wave. Closer analysis revealed that the motion was due to the flexion of the polyethylene lid of the drum forming the receiver. The subsequent bulk motion could potentially lead to inertial loading of the tissue and tissue deformation.

To eliminate this bulk motion and any of its possible confounds, the lid of the receiver was redesigned in 1/2 " polyvinyl chloride (PVC) making the new lid much stiffer than the old lid. We also took this opportunity to use off-the-shelf Schedule 80 PVC components, including pipe and pipe flanges, to simplify construction of the fluid-filled column (Figure 41). This approach had three additional benefits: 1) with the thicker wall of the pipe, pressure transducers could be mounted directly to the column, 2) pipe and flanges could be solvent welded, eliminating leaks even during blast-loading, and 3) the sample could be filmed more clearly over the course of the blast event.

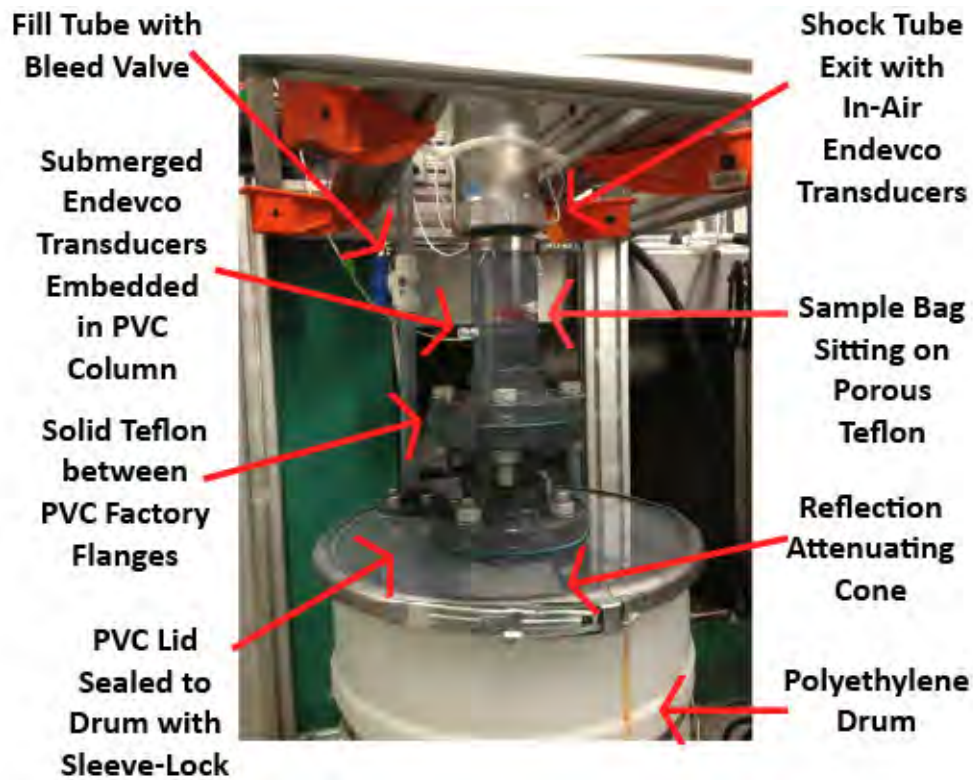


Figure 41. Redesigned receiver lid and fluid column using off the shelf components resulting in a stiffer design and the use of Endevco pressure transducers in the fluid column.

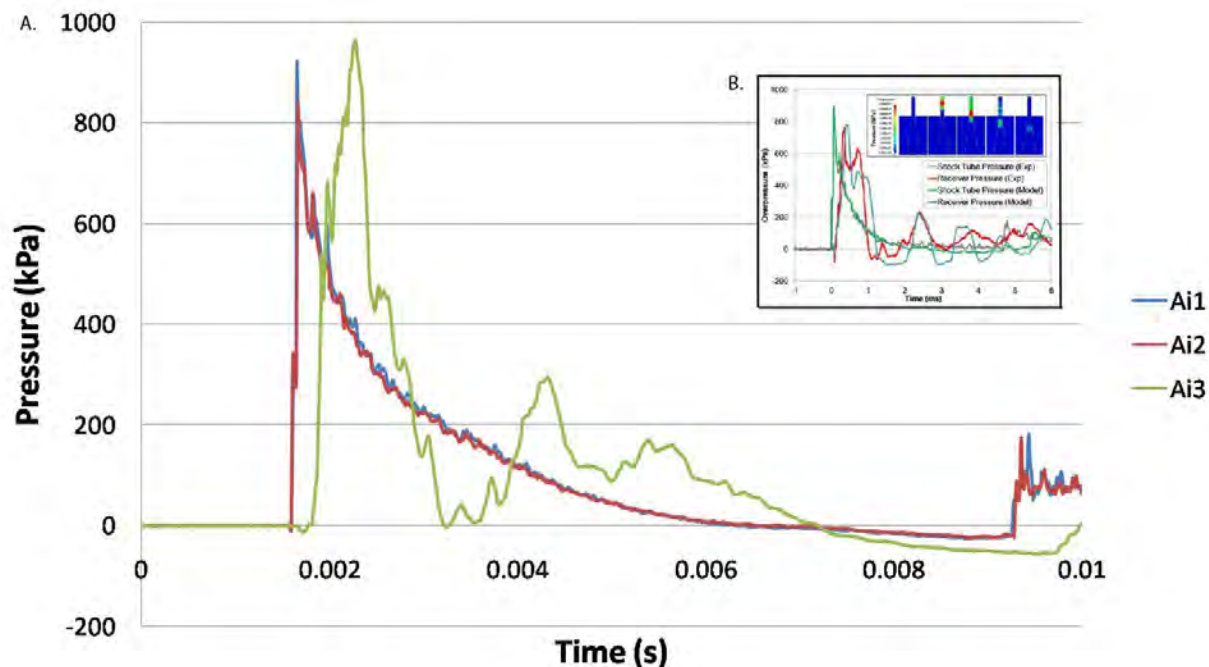


Figure 42. Pressure histories from the array of new Endevco sensors for multiple regions within the receiver. Ai1 and Ai2 represent in-air transducers located at the end of the shock tube. Ai3 represents a submerged transducer trace at the level of the tissue. The experimental data agrees well with the numerical simulations (inset).

Task B. Define the threshold for alterations in synaptic function, neural connectivity, and neuronal loss after scaled blast loading. In particular,

[B1] We use technologies developed by Task A to define the minimum blast input conditions necessary to cause changes in structure and function.

The exact physical and biological mechanisms of bTBI are still elusive, and a major goal of this MURI is to identify what in the brain sustains damage when exposed to a shock wave. We have identified candidates of the brain that serve as the mechanotransducer of the injury event into a biological response. The damage is caused in part by direct interaction of the shock wave with the cells which make up the brain, i.e. neurons, but also other cells including microglia and astrocytes, and endothelial cells.

Threshold for altered blood-brain barrier (BBB) function after blast: One of the advantages of an in vitro model is that the tolerance of separate CNS components can be tested in isolation from others. In this way, we can determine which element(s) of the CNS is(are) most vulnerable to primary blast-injury, allowing us to focus our efforts appropriately. The BBB is a specialized, cerebrovascular structure which separates the brain from the systemic circulatory system and circulating neurotoxic compounds, e.g. glutamate, iron. Given the fine structure of the BBB, only 300 nm thick with a combined surface area of 20 m² lining 600 km of brain capillaries, (Huber et al. 2001; Pardridge 2007) damage to the barrier could be a primary mechanism of blast-induced TBI by

allowing plasma components to flood the brain parenchyma. Infiltration of circulating compounds could alter synaptic activity, affect network function, or cause overt neuronal death.

Continuing with the in vitro approach, which allows for the study of primary blast injury in isolation of other confounding mechanisms, as well as isolating tissues and structures of interest, we have utilized an in vitro model of the BBB consisting of bEnd.3 cells.

The integrity of the BBB is quantified by measuring the flux of specific ions and molecules across the barrier. Transendothelial electrical resistance (TEER) is a measure of the flux of ions across the BBB; hydraulic conductivity is a measure of the flux of water across the BBB, and solute permeability is a measure of the flux of larger (neutral) molecules of different molecular weights (sizes) across the BBB.

Blast-induced deficits in TEER: An initial investigation was conducted to identify a threshold for this disruption as determined by a significant decrease in TEER measured acutely between 2 to 10 minutes after blast exposure. Using helium as the driver gas, TEER acutely decreased in a dose-dependent manner at increasing severities of blast from: 231 to 571 kPa peak incident overpressure, 0.60 to 1.06 ms duration, and 40 to 186 kPa*ms impulse (Figure 43A). Following the 469 kPa peak overpressure blast, TEER significantly ($p < 0.05$) decreased to 78 ± 8 % of pre-exposure levels compared to 102 ± 3 % in sham controls (Figure 43A). TEER continued to decrease at greater blast levels, while exposure to lower severity blasts with peak overpressure ranging from 231 to 377 kPa, duration of 0.60 to 0.89 ms, and impulse of 40 to 96 kPa*ms did not significantly reduce TEER.

The scientific contribution of this study is that these are the first data to identify a threshold for BBB damage from purely a primary blast injury. An implication is that if in vivo studies observe BBB breakdown at lower exposures, then it is probable that secondary or tertiary blast injury mechanisms are contributing to the observed pathology. (Goldstein et al. 2012a)

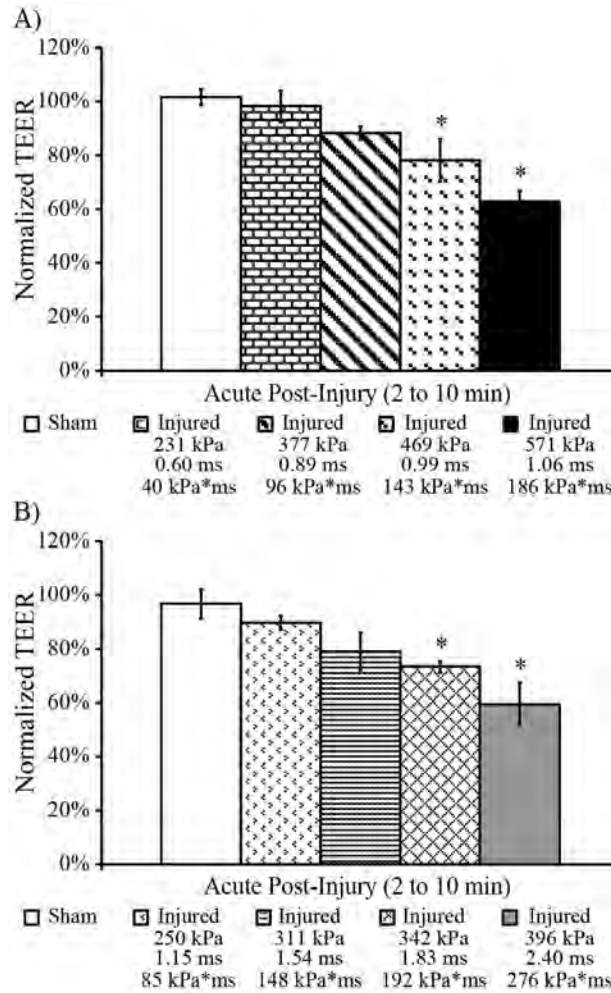


Figure 43 Dose-dependent TEER response in endothelial monolayers following exposure to a range of blast loading conditions. A) Following the 469 kPa peak overpressure blast (helium driver gas), TEER significantly and acutely decreased in injured cultures to 78 ± 8 % of pre-exposure levels. B) Following the 342 kPa peak overpressure blast (nitrogen driver gas), TEER significantly and acutely decreased in injured cultures to 73 ± 2 % of pre-exposure levels. (* $p < 0.05$; \pm SEM; Sham $n \geq 8$; Injured $n \geq 6$ per blast condition).

We next sought to identify the most influential biomechanical blast parameter driving damage to the barrier. Changing the driver gas to nitrogen enabled generation of a different combination of parameters that included generally lower peak overpressures at longer durations and higher impulses compared to helium as the driver gas. TEER acutely decreased in a dose-dependent manner as the blast severity increased from: 250 to 396 kPa peak incident overpressure, 1.15 to 2.40 ms duration, and 85 to 276 kPa*ms impulse (Figure 43B). Following the 342 kPa peak overpressure blast, TEER significantly decreased to 73 ± 2 % of pre-exposure levels compared to 97 ± 5 % in sham controls (Figure 43B). TEER continued to decrease as the blast severity increased, while exposure to milder blasts with peak overpressure ranging from 250 to 311 kPa, duration of 1.15 to 1.54 ms, and impulse of 85 to 148 kPa*ms did not significantly reduce TEER.

Taken together, the scientific contribution of these two sets of data is that they indicate the BBB can be damaged at lower pressures if the duration and/or impulse are increased. Using helium, the BBB was damaged at a peak overpressure of 469 kPa, duration of 0.99 ms, and impulse of 143 kPa ms (Figure

43A), whereas with nitrogen, the BBB was damaged at a lower peak overpressure of 342 kPa, a longer duration of 1.83 ms, and a larger impulse of 192 kPa ms. These are the first studies to demonstrate that the threshold for BBB disruption is a peak overpressure greater than 311 kPa and an impulse greater than 96 kPa ms.

To determine which blast parameter was most critical to BBB disruption, the correlation between changes in TEER and each of the three biomechanical injury parameters – peak overpressure, duration, and impulse – measured in the open-tube configuration (air) and in the sample receiver (fluid) was determined. As evidenced by the high R^2 values of 0.92 (Figure 44A) and 0.88 (Figure 44D) for measurements in both the air and fluid, changes in TEER were overall most strongly correlated with impulse. A significant decrease in TEER after blast was observed at an air impulse as low as 143 kPa*ms, indicating functional deficits at TEER levels approximately 80 % of pre-injury values (Figure 43A, B). TEER was also strongly correlated with peak overpressure measured in the fluid, as indicated by a high R^2 value of 0.93 (Figure 44E). Weaker associations were evident between TEER and air peak overpressure, air duration, and fluid duration, which were all associated with comparatively lower R^2 values of 0.52, 0.52, and 0.34, respectively (Figure 44B, C, F).

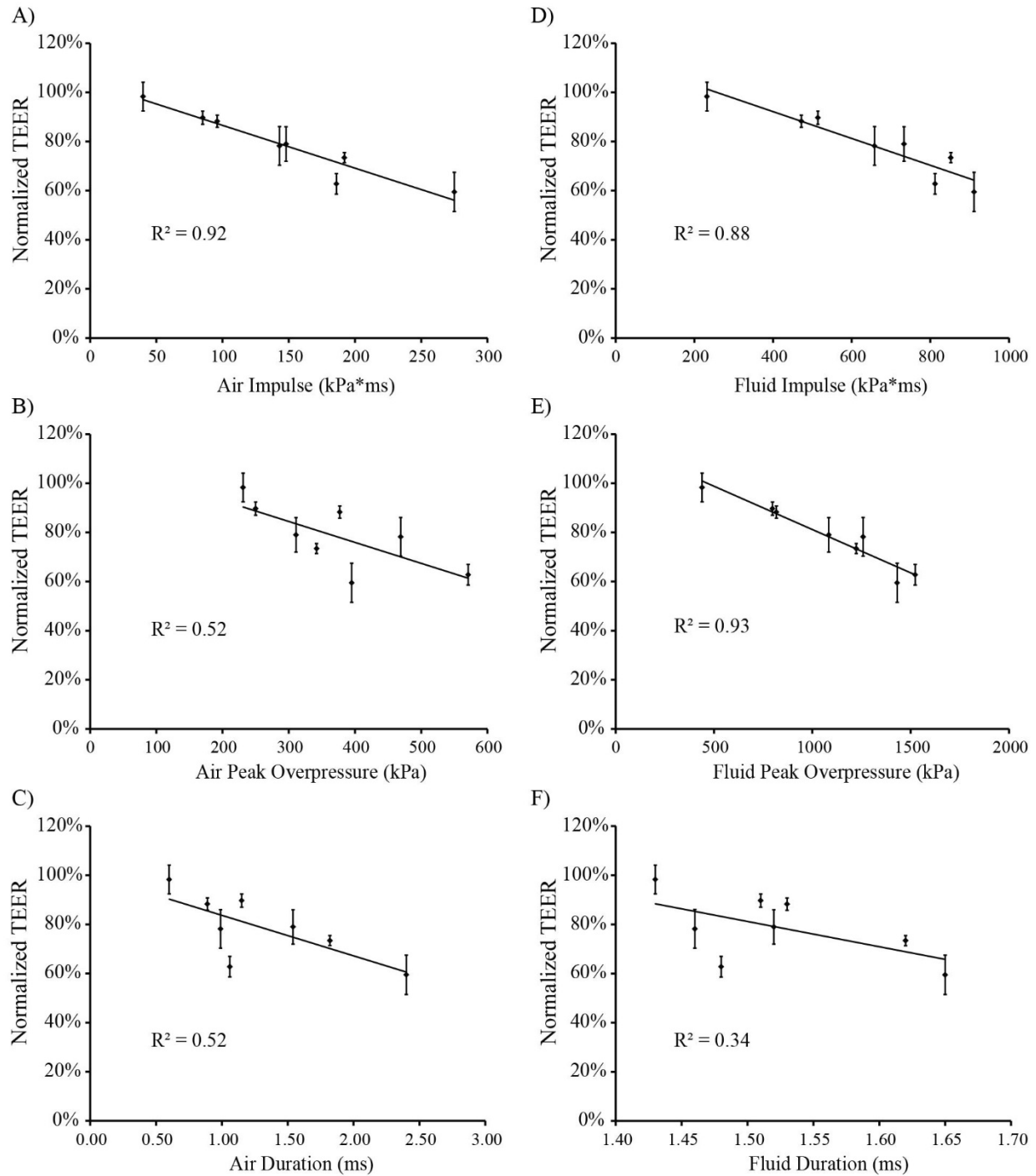


Figure 44 Correlations established for changes in TEER with different blast injury parameters measured in the open-tube configuration (air) and in the sample receiver (fluid). Linear functions were fit to the data for each association. A) Correlation between TEER and air impulse, showing $R^2 = 0.92$. B) Correlation between TEER and air peak overpressure, indicating a weaker association with $R^2 = 0.52$. C) Correlation between TEER and air duration, indicating a weaker association with $R^2 = 0.52$. D) Correlation between TEER and fluid impulse, showing $R^2 = 0.88$. E) Correlation between TEER and fluid peak overpressure, showing $R^2 = 0.93$. F) Correlation between TEER and fluid duration, indicating a weaker association with $R^2 = 0.34$.

Blast-induced increases in hydraulic conductivity: A major function of the BBB in vivo is to exclude water flux by the presence of tight junctions, and measuring blast-induced modulation of hydraulic conductivity is important for linking exposure to the neuropathological conditions associated with vessel hyper-permeability. (Elliott et al. 2007; Fenstermacher 1984; Garcia et al. 2011; Olson et al. 1997; Victorino et al. 2003) Hydraulic conductivity, L_p , was measured between 30 minutes to 2 hours post-injury to quantify water flux through the BBB model. After exposure to blast with a peak overpressure of 571 kPa, duration of 1.06 ms, and impulse of 186 kPa*ms (helium driver gas), hydraulic conductivity was significantly increased to $11.4 \pm 3.5 \times 10^{-7}$ cm/s/cmH₂O compared to $2.9 \pm 0.4 \times 10^{-7}$ cm/s/cmH₂O in sham controls (Figure 45). Similarly, blast with a peak overpressure of 396 kPa, duration of 2.40 ms, and impulse of 276 kPa*ms (nitrogen driver gas) significantly increased hydraulic conductivity to $7.5 \pm 1.9 \times 10^{-7}$ cm/s/cmH₂O (Figure 45). Blasts with peak overpressures of 469 or 342 kPa, durations of 0.99 or 1.83 ms, and impulses of 143 or 192 kPa*ms did not cause significant increases in hydraulic conductivity.

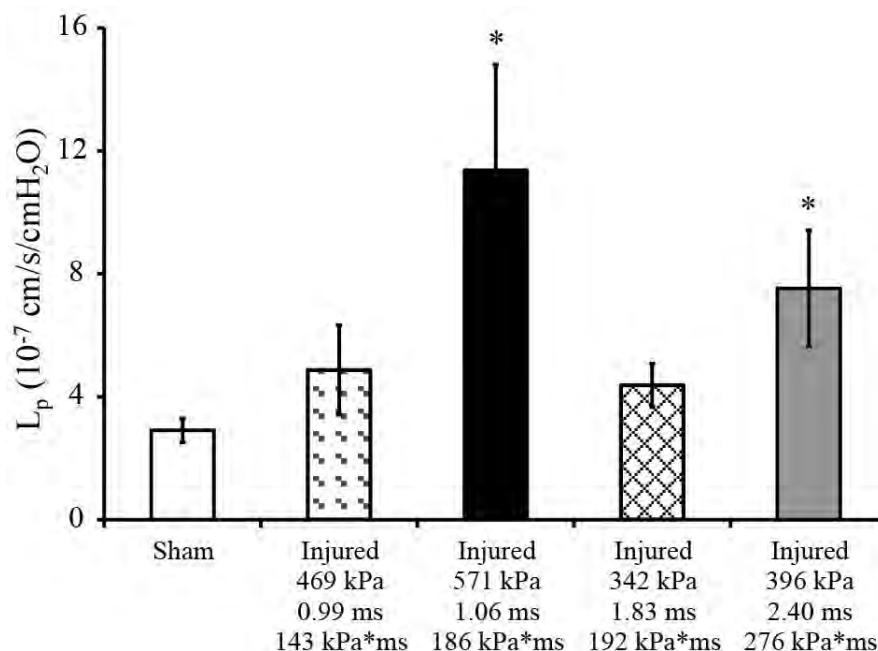


Figure 45 Hydraulic conductivity of blast exposed endothelial monolayers. Between 30 minutes to 2 hours after injury, cultures exposed to the 571 and 396 kPa blasts exhibited a significant increase in hydraulic conductivity to $11.4 \pm 3.5 \times 10^{-7}$ cm/s/cmH₂O and $7.5 \pm 1.9 \times 10^{-7}$ cm/s/cmH₂O, respectively, compared to $2.9 \pm 0.4 \times 10^{-7}$ cm/s/cmH₂O in sham controls. (* $p < 0.05$; \pm SEM; Sham $n = 23$; Injured $n \geq 6$ per blast condition).

These results are scientifically important as they are the first to quantify a blast-induced increase in water flux across an in vitro BBB model. It is possible that our relatively long measurement time window, coupled with temporal variations in blast-induced BBB opening, account for why our hydraulic conductivity results did not mirror the acute TEER dose-dependent response observed (between 2 to 10 minutes after exposure) with increasing impulse levels. A previous study comparing the progression of BBB opening in different rat models of TBI demonstrated that impact acceleration resulted in immediate BBB opening followed by rapid closing of the barrier, whereas lateral cortical impact was associated with prolonged BBB opening for up to 4 hours. (Beaumont et al. 2000) Therefore, we anticipate that more precisely defining the time point at which hydraulic conductivity is measured after

injury will allow for improved mechanistic understanding of the high incidence of brain edema following bTBI. (Ling et al. 2009; Mac Donald et al. 2011)

Blast-induced increases in solute permeability: Solute permeability provides a method of assessing the transport properties of an endothelial monolayer representing the BBB, serving as a quantitative measure of the diffusive permeability of a blast-injured BBB to a range of molecular weights (different sized dextrans). Between 30 minutes to 2 hours of exposure to blast with a peak overpressure of 571 kPa, duration of 1.06 ms, and impulse of 186 kPa*ms (helium driver gas), a trend of increased solute permeability was observed. The permeability of exposed cultures at the 10 kDa group significantly increased to $2.5 \pm 0.3 \times 10^{-6}$ cm/s compared to $1.2 \pm 0.2 \times 10^{-6}$ cm/s in shams (Figure 46).

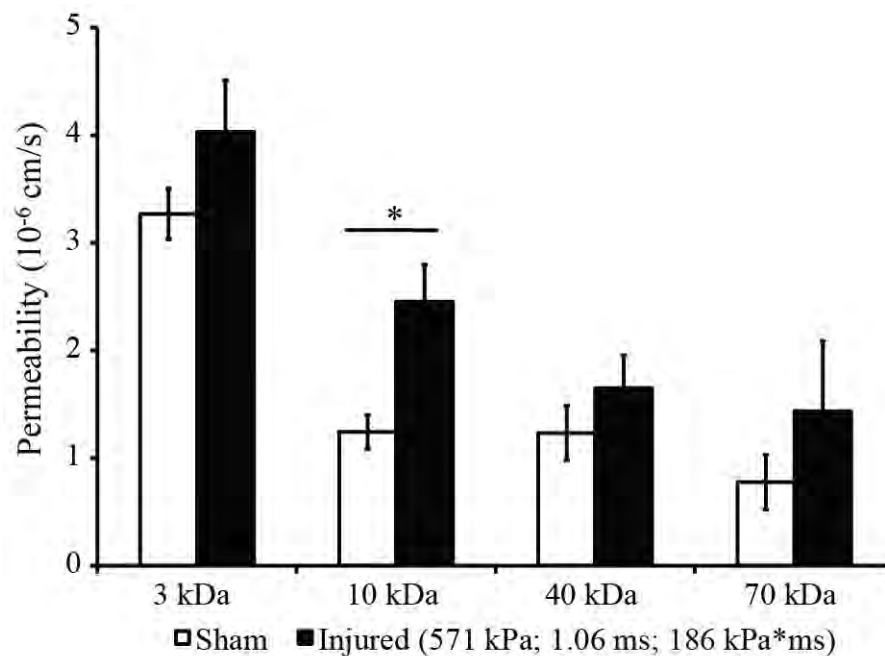


Figure 46 Increased solute permeability of 3, 10, 40, and 70 kDa dextran molecules after blast exposure. Injured cultures exhibited a significant increase in solute permeability to $2.5 \pm 0.3 \times 10^{-6}$ cm/s compared to $1.2 \pm 0.2 \times 10^{-6}$ cm/s in shams for the 10 kDa molecular weight tracer. (* p < 0.05; \pm SEM; Sham n = 6; Injured n = 6).

Solute permeability data for the blast-injured BBB are scientifically significant as they provide quantitative indication of the sizes of molecules potentially able to penetrate a compromised barrier. Such insight holds further implications for a size-range of neurotoxic serum constituents that may infiltrate the brain, potentially leading to alterations in synaptic function, neural connectivity, and neuronal loss.

Structural disruption of the BBB: The BBB is a selective barrier comprised of specialized brain endothelial cells characterized by complex tight junctions, highly regulated permeability, and polarity. (Hue et al. 2013d; Simon et al. 2010) BBB dysfunction and the disruption of tight junctions is a known phenomenon following TBI. (Blyth et al. 2011; Morganti-Kossmann et al. 1999; Vilalta et al. 2008) Intercellular tight junctions are formed by plasma membrane proteins including occludin, claudins and zonula occludens accessory proteins (ZO-1 and ZO-2). (Kniesel and Wolburg 2000)

In sham cultures, ZO-1 immunostaining revealed high levels of ZO-1 protein on the surface of cells and at the junctions between cells, indicating wide-spread expression of tight junction proteins (Figure 47). Visual examination of immunofluorescence images of the bEnd.3 cultures confirmed confluent cell monolayers exhibiting characteristic, elongated spindle-shape morphology for sham controls (Figure 47), (Brown et al. 2007; Omid et al. 2003) bearing very close resemblance to the cell architecture of confluent bEnd.3 monolayers shown by light microscopy and tight junction immunostaining in previous studies. Between 1 to 2 hours of exposure, a blast with peak overpressure of 571 kPa, duration of 1.06 ms, and impulse of 186 kPa*ms (helium driver gas) substantially decreased ZO-1 staining and altered tight junction morphology (Figure 47). Similarly, a blast with peak overpressure of 396 kPa, duration of 2.40 ms, and impulse of 276 kPa*ms (nitrogen driver gas) substantially compromised ZO-1 staining (Figure 47). The morphology of tight junctions in both injury groups was more punctate and discontinuous, leaving regions between cells devoid of well-formed tight junctions.

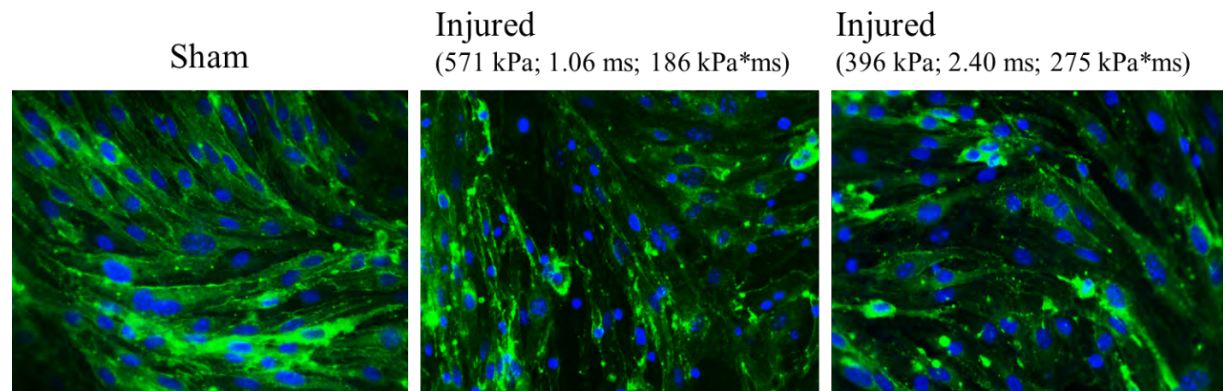


Figure 47 Immunostaining for ZO-1 (green), a marker for tight junctions. After two levels of blast, the morphology of ZO-1 staining and its overall expression changed. The punctate staining suggests physical breakdown of tight junctions which provides a structural and mechanistic explanation for the changes in BBB function reported above. Note that the cell density, indicated by the blue nuclei, is not altered after blast, ruling out the possibility that the functional changes were due to cell loss.

ZO-1 immunostaining was then quantified as the percent area of staining exhibiting fluorescence above a threshold, normalized to the total number of bEnd.3 cells in the field of view. Consistent with the qualitative imaging data, the area-percentage of ZO-1 immunostaining per cell was significantly decreased in the 571 kPa injured cultures to $0.25 \pm .02 \%$ and in the 396 kPa injured cultures to $0.18 \pm .01 \%$, compared to $0.31 \pm .02 \%$ in sham controls (Figure 48). Previous characterization of our bTBI model has confirmed cell viability following similar exposure levels, showing the absence of any significant cell death post-injury.

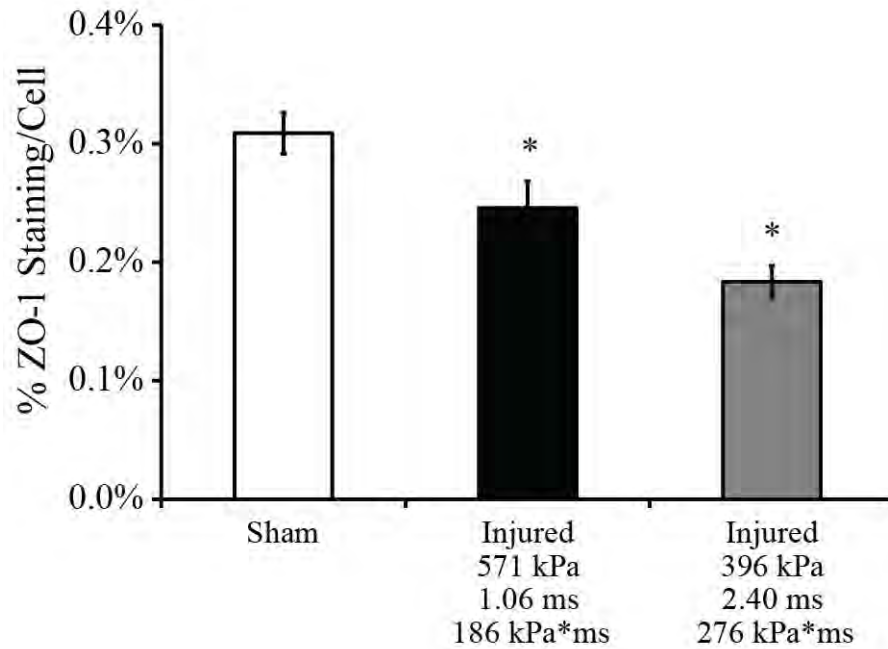


Figure 48 Quantitative analysis of ZO-1 immunostaining was decreased after two levels of blast compared to the sham group, supporting the qualitative interpretation of the imaging data. * indicates $p < 0.05$ compared to uninjured sham group; data presented as mean \pm SEM; Sham $n = 50$; Injured $n \geq 20$.

The average number of cells in each immunofluorescence image was quantified to determine the degree of cell detachment between 1 to 2 hours of exposure to the 571 and 396 kPa peak overpressure blasts. In sham controls, the average cell count per field of view was 90 ± 2 , while corresponding cell counts for cultures injured at the 571 and 396 kPa overpressure levels were 87 ± 3 and 79 ± 2 , respectively (Figure 49). Significant, but minimal, cell detachment compared to sham was only observed for cultures exposed to the highest level blast (396 kPa overpressure, 2.40 ms duration, and 276 kPa*ms impulse, nitrogen driver gas). These results confirm that the blast-induced changes in BBB integrity we observed were due to functional barrier disruption and not to the loss of cells in the monolayer cultures.

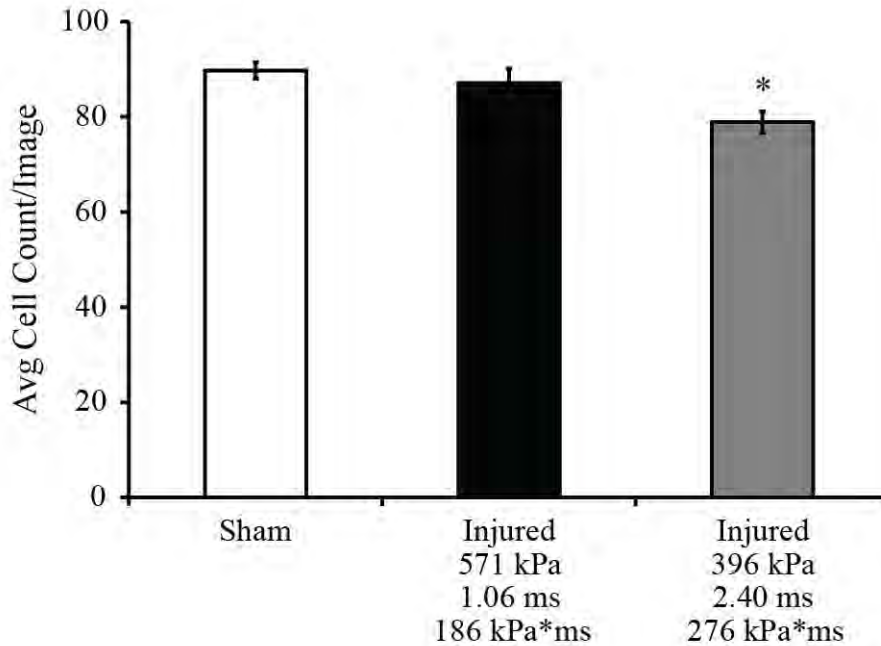


Figure 49 Average cell count per immunostained image to quantify cell detachment between 1 to 2 hours of blast exposure. The cell count was significantly reduced by 12 % in cultures exposed to a blast with a 396 kPa peak overpressure, 2.40 ms duration, and 276 kPa*ms impulse (nitrogen driver gas). (* $p < 0.05$; \pm SEM; Sham $n = 50$; Injured $n \geq 20$ per blast condition).

Time course of BBB disruption: The temporal recovery of TEER was measured after a blast with a peak overpressure of 571 kPa, duration of 1.06 ms, and impulse of 186 kPa*ms (helium driver gas). This level was selected because it was shown to cause a robust decrease in TEER based on the dose-dependent response in the in vitro BBB model without significant loss of cells (Figure 43A). TEER of the injured cultures, normalized to age-matched and time point-matched sham controls, decreased in the acute phase 30 minutes after injury (Figure 50). TEER remained significantly depressed for 2 days after exposure as compared to pre-injury levels (Figure 50). Injured cultures recovered over time, and exhibited full-recovery to pre-injury TEER levels at 3 days post-blast (Figure 50).

The significance of these data is the demonstration of an intrinsic capacity for spontaneous recovery of the endothelial monolayer after blast injury if given sufficient time to repair itself. These are the first data to suggest an underlying mechanism of repetitive blast-TBI relating to cumulative and/or prolonged damage to the BBB and interference with endogenous repair processes, and hold further implications for mandatory resting periods for exposed personnel.

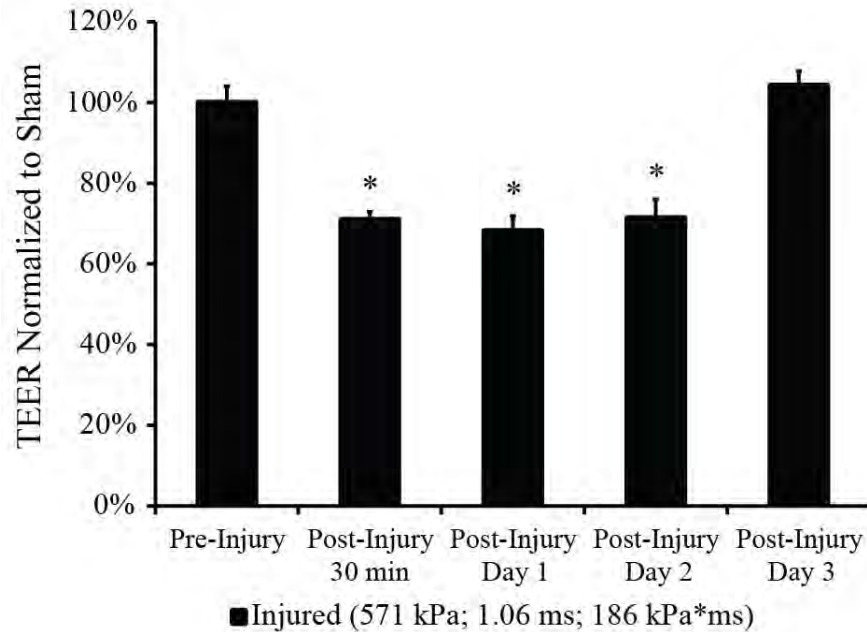


Figure 50 TEER time-course of blast-exposed endothelial monolayers normalized to age-matched sham controls. Depressed TEER of injured cultures fully recovered to pre-injury levels at 3 days post-blast. (* $p < 0.05$; \pm SEM; $n = 3$).

Recent studies have demonstrated increased susceptibility to breakdown of the cerebral vasculature and neuropathological outcomes associated with repetitive traumatic brain injury. (Ahlers et al. 2012; Fujita et al. 2012; Kamnaksh et al. 2012; Rosenfeld and Ford 2010) We hypothesized that exposure to two consecutive blast injuries would result in exacerbated damage of the in vitro BBB model compared to exposure to a single blast of the same severity. However, contrary to our hypothesis, repeated mild or moderate primary blast delivered within 24 or 72 hours was not additive as described below.

Severity-dependent TEER response after repeated blast injury: The in vitro BBB model was subjected to two blasts delivered 24 hours apart at a severity level previously determined to result in mild functional disruption of the endothelial monolayer (377 kPa peak overpressure, 0.89 ms duration, and 96 kPa*ms impulse). In the single injury group receiving one mild blast (injury 1), TEER decreased significantly compared to sham to 91 ± 3 % (mean \pm SEM), and was not significantly different at 92 ± 6 % following the second sham injury time point (Figure 51A). In the double injury group receiving two mild blasts delivered 24 hours apart, TEER was significantly decreased compared to sham to 84 ± 4 % after injury 1 and 78 ± 4 % after injury 2 (Figure 51A). There was no significant difference in TEER between the double and single injury groups following the second injury time point, indicating mild effects of repeated exposure to a mild intensity blast. Sham control TEER levels remained high at 102 ± 2 % and 99 ± 6 % following the first and second sham exposures, respectively (Figure 51A).

When the blast severity was increased to a level previously determined to result in moderate functional disruption of the endothelial monolayer (402 kPa peak overpressure, 0.92 ms duration, and 118 kPa*ms impulse), more dramatic compromises in BBB integrity were observed. In the single injury group receiving one moderate blast, TEER decreased significantly compared to sham to 52 ± 7 % after the initial injury and remained significantly depressed at 71 ± 4 % after the second sham injury time point; compared to after the first injury, TEER was slightly increased (not significantly) after the second sham

injury due to spontaneous recovery of the monolayer (Figure 51B). In the double injury group (24 hour inter-injury interval), TEER was significantly decreased to 54 ± 7 % after injury 1 and similarly to 44 ± 7 % after injury 2 (Figure 51B), demonstrating sustained, but not additive, disruption of the monolayer with repeated injuries. TEER of the double injury group was significantly more depressed than the single injury group after the second injury time point due to persistent damage in the double injury group and partial recovery in the single injury group. TEER of sham controls was consistently high at 94 ± 3 % and 101 ± 5 % following the first and second sham injuries, respectively (Figure 51B).

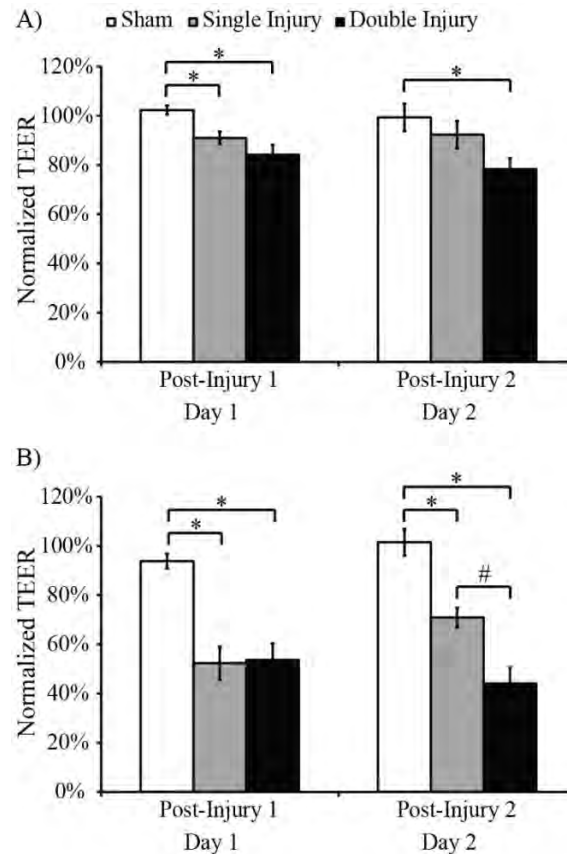


Figure 51 Acute TEER response of in vitro BBB model to repeated mild and moderate blast injuries. A) Mild, sustained disruption of the BBB following repeated mild blast with a 377 kPa peak overpressure, 0.89 ms duration, and 96 kPa*ms impulse. B) Pronounced, sustained disruption of BBB following exposure to repeated moderate blast with a 402 kPa peak overpressure, 0.92 ms duration, and 118 kPa*ms impulse. (*, # p < 0.05; \pm SEM; Sham n = 12; Single Injury n \geq 11; Double Injury n = 12).

Augmented brain pathology is considered a defining characteristic of repetitive brain injury, (Wang et al. 2011a) and our results extend this understanding to repeated, primary blast exposure in an in vitro BBB model. The significant difference in TEER which we observed between cultures exposed to two moderate injuries demonstrated sustained, but not cumulative, effects associated with the subsequent insult. It is important to note, however, that our results demonstrated persistent injury to the BBB following multiple insults, which is distinct from additive damage to the barrier.

Blast-induced increases in solute permeability: Despite slightly elevated permeability of the 3 kDa dextran in the single and double injury groups after exposure to moderate blast compared to

sham, there was no significant difference among the experimental groups for the 3, 10, or 40 kDa molecular weight tracers (Figure 52). As a positive control, endothelial monolayers were exposed to a single blast with a 571 kPa peak overpressure, 1.06 ms duration, and 186 kPa*ms, previously found to significantly increase permeability of 10 kDa dextrans through the barrier. Following acute exposure to the same blast level in this study, solute permeability significantly increased to $1.77 \pm 0.25 \times 10^{-6}$ cm/s compared to $0.90 \pm 0.05 \times 10^{-6}$ cm/s in sham controls (data not shown), which is in agreement with our previous data following a single primary blast injury. (Hue et al. 2013d)

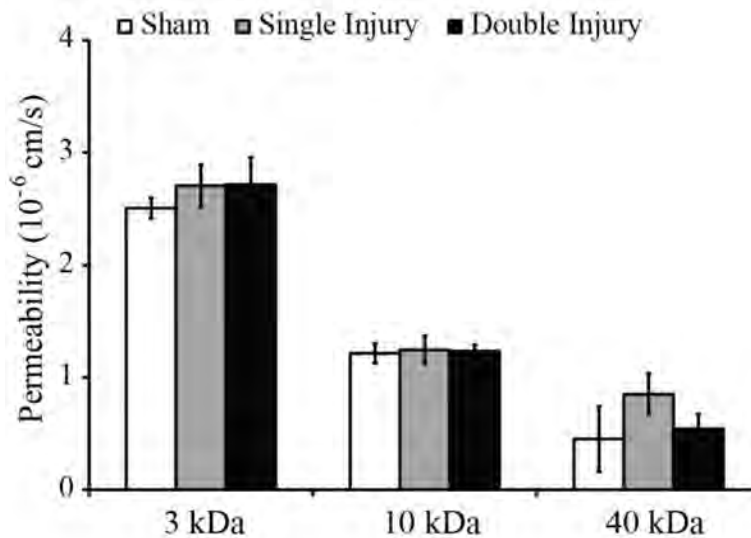


Figure 52 Unaltered solute permeability after repeated blast injury in BBB cultures. Following exposure to moderate levels of blast with a 402 kPa peak overpressure, 0.92 ms duration, and 118 kPa*ms impulse, no significant difference in solute permeability was observed between sham and the single or double injury groups. (* $p < 0.05$; \pm SEM; Sham $n = 10$; Single Injury $n = 10$; Double Injury $n \geq 9$).

A detailed understanding of blast-induced disruption of cerebral vascular integrity is of scientific and clinical importance because greater adhesion and infiltration of immune cells, including macrophages, can promote neurovascular inflammation and degeneration in vivo. (Abdul-Muneer et al. 2013) Interestingly, exposure to moderate blast (402 kPa) in the current study did not increase solute permeability, even after repeated exposure over a 24 hour interval. These data suggest that repeated blast exposure at mild or moderate levels may not be sufficient to permit an influx of larger solutes (≥ 3 kDa) through the barrier compared to the changes of ion-flux measured by TEER.

BBB tight junction disruption after repeated blast: Wide-spread and integral expression of tight junction proteins was indicated by high levels of ZO-1 and claudin-5 staining in sham control cultures (Figure 53A, E). As described previously, visual inspection of bright field and immunostained images of sham control cultures confirmed the formation of confluent monolayers exhibiting spindle-shape morphology that was characteristic of bEnd.3 cells and the brain endothelial cell phenotype. (Effgen et al. 2012c; Hue et al. 2013d) After moderate blast exposure, tight junction protein-staining for the single and double injury groups appeared less intense and slightly more punctate in morphology as compared to sham controls. The area-percentage of ZO-1 immunostaining per cell was significantly decreased to 0.09 ± 0.01 % in the single injury group and to 0.08 ± 0.01 % in the double injury group, as compared to 0.15 ± 0.02 % in sham controls (Figure 53D). Levels of ZO-1

immunostaining were not significantly different between the single and double injury groups, showing no cumulative disruption of the ZO-1 tight junction protein. Similarly, the area-percentage of claudin-5 immunostaining per cell was significantly decreased to 0.15 ± 0.01 % in the single injury group and to 0.18 ± 0.02 % in the double injury group, as compared to 0.24 ± 0.02 % in sham controls (Figure 53H). Levels of claudin-5 immunostaining were not significantly different between the single and double injury groups.

These results are scientifically important because they suggest that the effects of repeated blast on the integrity of the BBB are not associated with significantly worse tight junction damage over consecutive insults within a 24 hour time frame.

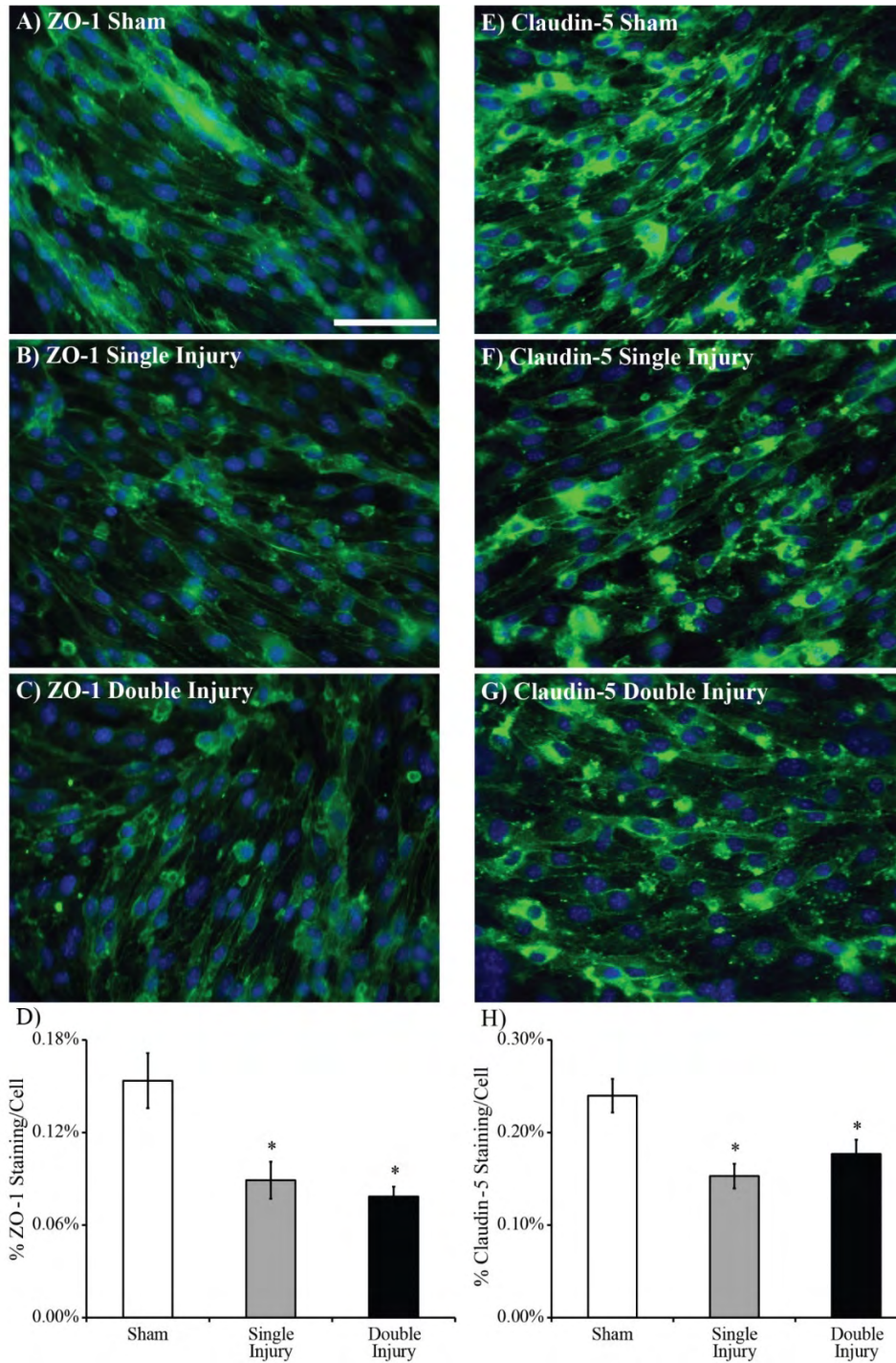


Figure 53 Immunostaining of tight junction proteins ZO-1 (green) and claudin-5 (green) following repeated moderate blast injury with a 402 kPa peak overpressure, 0.92 ms duration, and 118 kPa*ms impulse. **A, E)** ZO-1 and claudin-5 staining was high in sham cultures, together indicating the presence of well-formed tight junctions. **B, F)** Exposure to a single blast injury compromised ZO-1 and claudin-5 staining as compared to sham controls. **C, G)** Exposure to repeated blast injury compromised ZO-1 and claudin-5 staining as compared to sham controls, but not compared to the single injury group. **D, H)** Quantified ZO-1 and claudin-5 staining in the single and double injury groups was significantly reduced as compared to sham, consistent with qualitative depictions in immunofluorescence images. (* $p < 0.05$; \pm SEM; Sham $n = 6$ cultures (30 images); Single Injury $n = 6$

cultures (30 images); Double Injury n = 6 cultures (30 images) for ZO-1 or claudin-5; Scale bar = 70 μm).

Delayed TEER recovery after repeated blast: Temporal recovery of TEER in cultures exposed to moderate, repeated blast injury was delayed compared to cultures exposed to a single blast. TEER of the single injury group was significantly depressed compared to age-matched shams for up to one day after the initial injury delivered on day 1, but was no longer significantly different by day 2 due to recovery of the monolayer (Figure 54). Recovery of TEER in the double injury group was delayed such that TEER remained significantly lower compared to age-matched shams up to day 3 after exposure to the initial insult (Figure 54).

The scientific significance of these results is that the time course for changes in TEER suggests that repeated blast exposure delays recovery of the damaged BBB. We are the first to report delayed recovery of TEER following repeated, pure primary blast injury, and our time course for in vitro barrier recovery is reasonably similar to that observed in vivo (approximately 3 days) (Garman et al. 2011; Readnower et al. 2010) at comparable blast exposure levels.

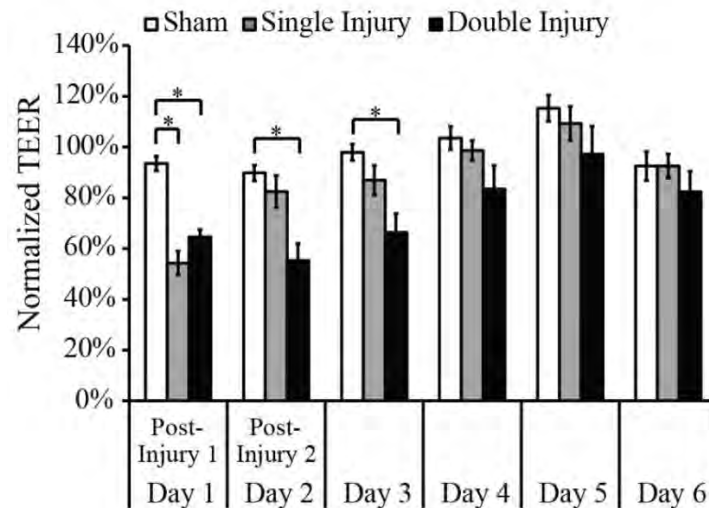


Figure 54 Endothelial monolayers exhibited delayed recovery in TEER following exposure to repeated moderate blast with a 402 kPa peak overpressure, 0.92 ms duration, and 118 kPa*ms impulse. TEER in the single injury group remained significantly depressed compared to shams for up to 1 day following the initial injury. TEER of the double injury group remained significantly depressed compared to shams for 3 days following the first injury. (* $p < 0.05$; \pm SEM; Sham n = 6; Single Injury n = 6; Double Injury n = 6).

Increased hydraulic conductivity after repeated blast: Hydraulic conductivity, L_p , was measured 15 to 30 minutes after the second blast or sham injury to quantify water flux through the BBB model. In the single injury group, L_p was slightly elevated but not significantly different compared to sham at 24 hours following exposure to one mild blast – i.e. immediately after the second sham injury time point (Figure 55). In the double injury group, L_p was significantly elevated to $2.14 \pm 0.54 \times 10^{-7}$ cm/s/cmH₂O compared to $0.83 \pm 0.18 \times 10^{-7}$ cm/s/cmH₂O in sham controls immediately after a second blast – i.e. the same measurement time point as the single injury group (Figure 55). However, there was no significant difference in hydraulic conductivity between the single and double injury groups. These results suggest that L_p spontaneously recovers over time similarly to the observed changes in TEER.

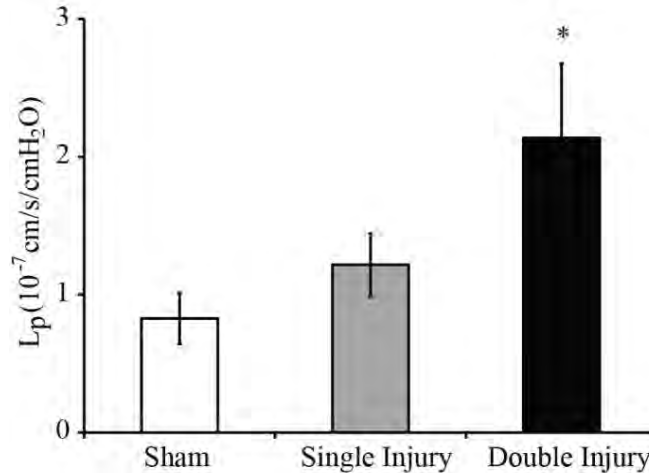


Figure 55 Increased hydraulic conductivity following repeated blast injury in BBB cultures. Hydraulic conductivity of endothelial monolayers exposed to consecutive moderate blasts with a 402 kPa peak overpressure, 0.92 ms duration, and 118 kPa*ms impulse was significantly increased to $2.14 \pm 0.54 \times 10^{-7}$ cm/s/cmH₂O compared to $0.83 \pm 0.18 \times 10^{-7}$ cm/s/cmH₂O in sham controls. Hydraulic conductivity in cultures sustaining two blast injuries was not significantly different from sham controls or the single injury group when measured at the same time point (i.e. after the second sham injury). (* $p < 0.05$; \pm SEM; Sham $n = 11$; Single Injury $n = 12$; Double Injury $n = 12$).

Independent effects of repeated blast on TEER with prolonged interval: To

investigate the interval-specific effects of repeated blast injury in the BBB cultures, the time between injuries was extended to 72 hours. After the first exposure to moderate blast, TEER of injured cultures decreased by 25 to 30 % compared to sham controls (Figure 56). Injured cultures recovered at a similar rate over time, exhibiting full recovery of TEER by day 3. Following the second injury time point on day 4, TEER of the double injury group was significantly decreased by a consistent 25 to 30 % in comparison to age-matched shams; this change in TEER was not significantly different than the change in TEER after the first injury (Figure 56). The similar decrease in TEER between the double injury group and sham cultures following both the initial (day 1) and subsequent (day 4) injuries suggests that the effects of multiple injuries on the BBB are independent given enough recovery time between the two injuries.

These data are significant because they suggest that with an extended inter-injury interval from 24 to 72 hours, the BBB response to repeated blasts may be independent given a sufficient delay between consecutive injuries. Overall, such findings support the existence of a window of heightened vulnerability (Fujita et al. 2012; Prins et al. 2013; Vagnozzi et al. 2008) of the BBB to repetitive primary blast injury, which holds implications for a minimum mandatory rest-period for blast-injured service members prior to returning to duty.

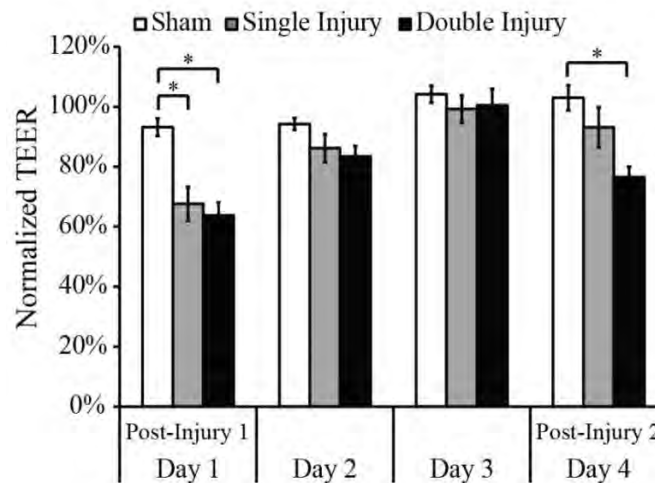


Figure 56 Independent effects of blast on BBB cultures over an extended 72 hour inter-injury interval between consecutive moderate blasts with a 402 kPa peak overpressure, 0.92 ms duration, and 118 kPa*ms impulse. The consistently similar 25 to 30 % difference in TEER between the double injury and sham groups after the first (day 1) and second (day 4) injuries suggests that the effects of repeated injuries are independent given a sufficiently prolonged inter-injury interval. (* $p < 0.05$; \pm SEM; Sham $n = 6$; Single Injury $n = 6$; Double Injury $n = 6$).

Blood-brain barrier (BBB) dysfunction and modulated recovery after blast in vitro:

The BBB has also emerged as a promising therapeutic target for the treatment of TBI caused by explosive blast. Given that BBB integrity is compromised in various disorders of the central nervous system including bTBI, (Abdul-Muneer et al. 2013; Hatashita and Hoff 1990; Hue et al. 2013a; McDonald 1994; Shlosberg et al. 2010; Tanno et al. 1992; Yeoh et al. 2013) mechanistic studies will aid in the development of more effective therapies to enhance repair of the damaged BBB and to potentially protect brain homeostasis and neuronal activity. (Forster et al. 2006; Shlosberg et al. 2010) In addition, outcomes of these studies will provide important mechanistic insight that may lead to identification of new therapeutic targets for mitigating the damaging effects of bTBI.

Glucocorticoids, a subclass of anti-inflammatory steroid hormones known as corticosteroids, are important to the clinical management of central nervous system disorders associated with a compromised BBB, such as edema and brain tumors. (Cucullo et al. 2004; Kaal and Vecht 2004) Dexamethasone (DEX) is one of the most commonly used corticosteroids and promotes BBB formation and enhances barrier tightness by inducing glucocorticoid receptor signaling activity and increasing expression of tight junction proteins such as occludin and zonula occludens (ZO)-1. (Beato et al. 1987; Forster et al. 2006; Holgate and Polosa 2008; Romero et al. 2003)

We hypothesized that treatment with DEX after primary blast exposure potentiates functional recovery of a brain endothelial monolayer representing the BBB. We report, for the first time, that treatment with DEX after blast exposure enhances functional recovery of the BBB in vitro, as measured by changes in TEER, hydraulic conductivity, and immunostaining of tight junction proteins including ZO-1. By inhibiting treatment effects using the glucocorticoid receptor antagonist, RU486, we provide further supporting evidence that enhanced functional recovery of the blast-injured monolayer was mediated by glucocorticoid receptor signaling activity. (Forster et al. 2006; Heiss et al. 1996)

Potentiated TEER recovery with DEX treatment after blast: In vitro BBB cultures were exposed to blast with a 571 kPa peak overpressure, 1.06 ms duration, and 186 kPa*ms impulse, which is a level we have previously demonstrated to be above the threshold for causing barrier disruption. (Hue et al. 2013a) Following blast exposure (day 0), TEER of injured cultures decreased acutely to approximately 80 % of pre-exposure levels compared with 102 ± 1 % in sham controls (Figure 57). One day following blast exposure (day 1), TEER increased in a dose-dependent manner after DEX treatment at a concentration range of 0-10 μ M, with no significant increases after a 100 μ M treatment (Figure 57). TEER of cultures treated with 10 μ M DEX decreased to 80 ± 4 % acutely after blast, followed by recovery to 117 ± 5 % 1 day after injury (Figure 57). Because 10 μ M DEX produced a maximal TEER increase, that concentration was selected for all subsequent experiments.

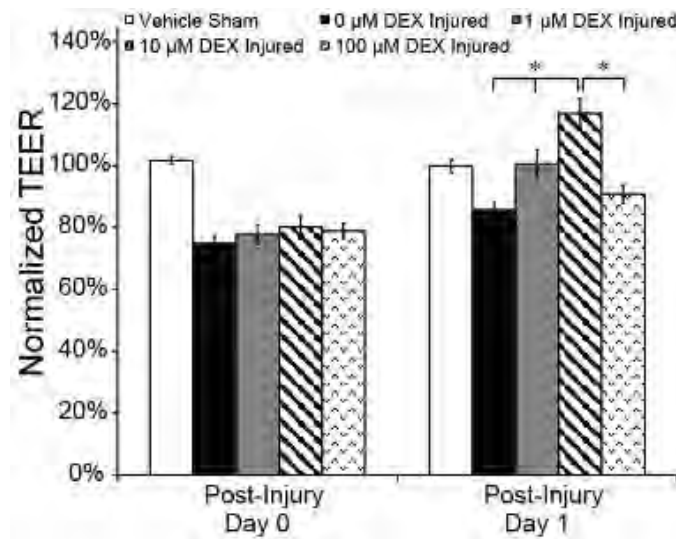


Figure 57 Dose-dependent TEER response effected by DEX treatment after blast injury. Cultures were exposed to blast with a 571 kPa peak overpressure, 1.06 ms duration, and 186 kPa*ms impulse. Post-injury treatment with 10 μ M DEX resulted in the greatest TEER recovery 1 day after blast exposure. (* $p < 0.05$; \pm SEM; $n \geq 9$ per treatment group).

TEER of vehicle-treated injured cultures required 3 days to fully recover in TEER, compared with 1 day in DEX-treated (10 μ M) injured cultures, demonstrating faster BBB recovery due to treatment (Figure 58). Treatment-induced TEER recovery was permanent up to 3 days post-injury, which was the last time point tested. Vehicle-treated shams maintained consistently high TEER levels up to 3 days after sham-injury. TEER of DEX-treated shams increased from 102 ± 1 % to 119 ± 2 % 1 day after sham-blast, with elevated TEER levels sustained up to 3 days after injury (Figure 58).

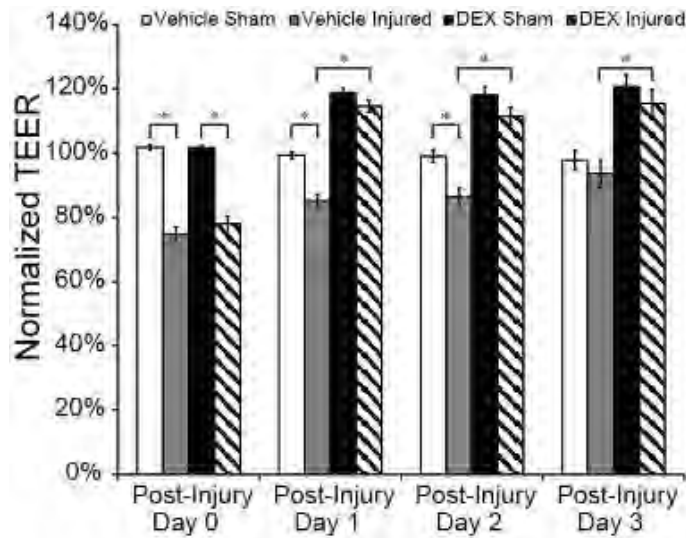


Figure 58 Potentiated TEER recovery induced by DEX treatment after blast injury. TEER of vehicle-treated injured cultures required 3 days to fully recover, whereas TEER of DEX-treated injured cultures fully recovered 1 day after blast exposure. (* $p < 0.05$; \pm SEM; $n \geq 10$ per exposure condition).

The scientific contribution of these data is that they are the first to demonstrate that treatment with DEX after blast exposure potentiates functional recovery, as measured by TEER, of the BBB *in vitro*. We have previously demonstrated an intrinsic capacity for spontaneous recovery of the endothelial monolayer after single and multiple blast injuries if given sufficient time (days) for self-repair. However, we have demonstrated that glucocorticoid treatment can potentially reduce prolonged damage to the BBB and brain by potentiating recovery of TEER (measure of BBB integrity) 1 day after injury. These results may hold promising implications for reducing mandatory resting periods for personnel exposed to blast.

Reduced hydraulic conductivity (L_p) with DEX treatment after blast: L_p was significantly decreased – indicating a tighter barrier – in DEX-treated injured and sham cultures compared with vehicle-treated injured cultures from days 1-3 after blast (Figure 59A-C). L_p of vehicle-treated injured cultures was elevated compared with that of vehicle-treated shams on days 1-2 after blast (not-significant), with recovery to sham levels by day 3. However, L_p fully recovered in DEX-treated injured cultures by day 1 after blast, and remained significantly decreased compared with vehicle-treated injured cultures from days 1-3 after injury (Figure 59A-C). Overall, these results support the post-injury time course of TEER recovery (Figure 58), demonstrating potentiated and sustained recovery of BBB integrity in DEX-treated injured cultures for 3 days after blast.

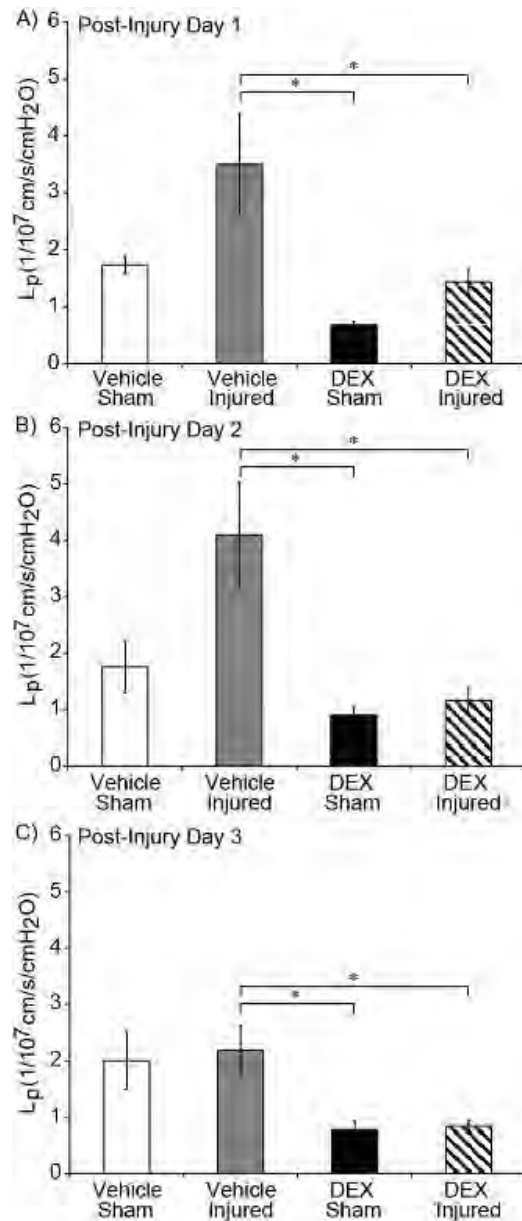


Figure 59 Decreased hydraulic conductivity (L_p) due to DEX treatment after blast injury. L_p was significantly reduced – indicating a tighter barrier – in DEX-treated cultures compared with vehicle-treated injured cultures on day 1 post-injury (A), day 2 post-injury (B), and day 3 post-injury with recovery of vehicle-treated injured cultures to vehicle-treated sham levels (C). (* $p < 0.05$; \pm SEM; $n \geq 7$ per exposure condition in A, B, and C).

These results are scientifically important as they are the first to quantify decreased water flux – i.e. a tighter barrier – across an in vitro BBB model due to DEX treatment after blast injury. Treatment with DEX mitigates heightened paracellular water flux after injury, in addition to restricting the transport of ions (measured by TEER). Because increased water flux can contribute to brain edema in vivo – a common outcome of TBI – these data hold implications for mitigating the damaging consequences of blast exposure. These results also suggest that L_p spontaneously recovers over time in vehicle-treated injured cultures, similarly to the observed changes in TEER.

Inhibition of DEX-induced potentiated BBB recovery: Co-treatment with DEX and the glucocorticoid receptor antagonist, RU486, inhibited TEER recovery attributed to DEX treatment alone (Figure 60A). DEX-treated injured cultures recovered 1 day after injury, compared with 3 days in injured cultures receiving both DEX and RU486. The recovery time course of injured cultures receiving the inhibitor matched that of vehicle-treated injured cultures (Figure 58). In addition, sham cultures treated with RU486 maintained high TEER levels for the duration of the time course, confirming that RU486 alone did not negatively affect TEER. Co-treatment with DEX and RU486 also inhibited the reduction in L_p (tightening of the barrier) effected by DEX treatment alone (Figure 60B). L_p of DEX-treated injured cultures recovered 1 day after injury, whereas L_p of injured cultures receiving DEX and RU486 remained significantly elevated at levels comparable to vehicle-treated injured cultures 1 day post-injury (Figure 59A).

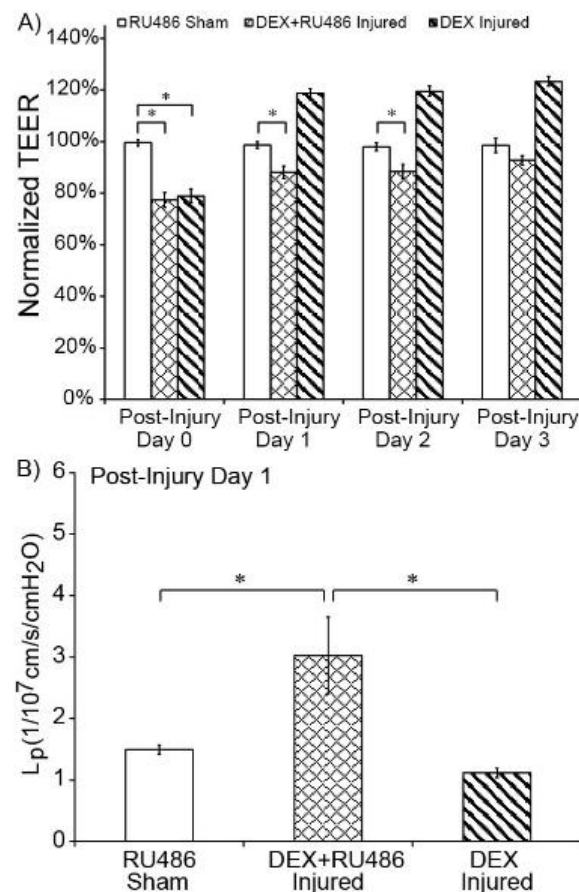


Figure 60 Inhibition of DEX-induced potentiated BBB recovery. Co-treatment with DEX and RU486 inhibited potentiated TEER recovery attributed to DEX treatment alone (A). TEER of DEX-treated injured cultures recovered 1 day after injury, compared with 3 days in injured cultures receiving both DEX and RU486. Co-treatment with DEX and RU486 inhibited the reduction in L_p attributed to DEX treatment alone (B). L_p of DEX-treated injured cultures recovered 1 day after injury, whereas L_p of injured cultures receiving DEX and RU486 remained significantly elevated compared with sham and DEX-treated injured groups. (* $p < 0.05$; \pm SEM; $n = 9$ per exposure condition in A; $n \geq 11$ per exposure condition in B).

These data are scientifically important as they confirm that the effects of DEX treatment are mediated by signaling activity of the glucocorticoid receptor. Co-treatment with the glucocorticoid receptor antagonist, RU486, effectively blocked all changes in TEER and L_p effected by DEX treatment alone. In

addition, cultures receiving the inhibitor had a similar recovery time-course in TEER and L_p as vehicle-treated injured cultures. These results lend mechanistic insight into a specific cell signaling pathway, that when activated, leads to potentiated recovery of the BBB after blast exposure. This may help to identify novel therapeutic targets for mitigating the damaging consequences of blast on the BBB and brain in injured service members.

Increased tight junction immunostaining with DEX treatment after blast:

Characteristic morphology and localized staining of the tight junction protein, ZO-1, at the cytoplasmic membrane surface were detected in vehicle-treated shams (Figure 6IA). ZO-1 staining was reduced in vehicle-treated injured cultures, which was consistent with our previously reported results (Figure 6IB). (Hue et al. 2014b; Hue et al. 2013a) ZO-1 immunofluorescence was visibly stronger at the cell periphery in DEX-treated injured cultures, suggesting that increased ZO-1 is a structural correlate to potentiated recovery of the BBB after blast exposure (Figure 6IC). Co-treatment with DEX and RU486 inhibited DEX-induced increases in ZO-1 after injury (Figure 6ID). The quantified area-percentage of ZO-1 immunostaining per cell confirmed qualitative trends observed in the immunofluorescence images (Figure 6IE), further supporting the critical role of ZO-1 in mediating DEX-induced tightening of the BBB. (Romero et al. 2003)

Consistent with studies characterizing bEnd.3 cells, (Brown et al. 2007; Song and Pachter 2003) staining of the transmembrane tight junction protein, occludin, was widespread throughout the cytoplasm without distinct localization to the cell periphery (characteristic of primary brain endothelial cultures) (Song and Pachter 2003). No visual differences in occludin staining were found among the different exposure conditions (Figure 6IF-I), and this was confirmed by the quantified area-percentage of occludin staining per cell (Figure 6IJ). It is likely that diffuse occludin staining throughout the cytoplasm hampered sensitivity for detecting tight junction-specific changes due to injury or treatment.

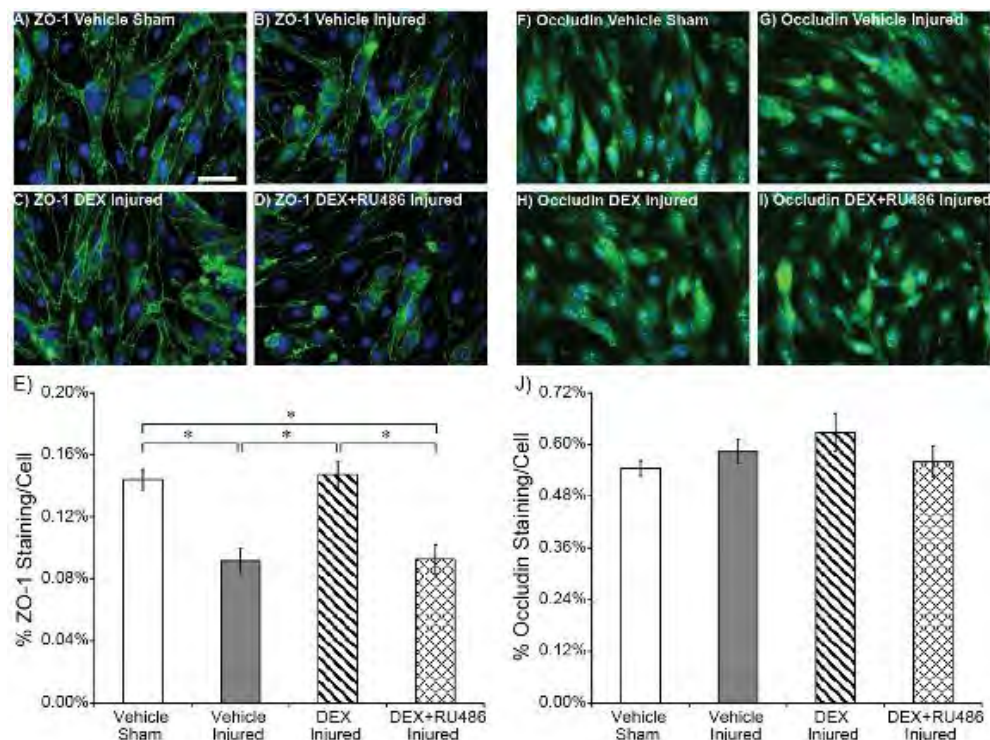


Figure 6I Increased tight junction immunostaining due to DEX treatment after blast injury. Characteristic staining of the ZO-1 tight junction protein was present in vehicle-treated shams (A), with compromised ZO-1 staining after injury (B), enhanced ZO-1 staining in DEX-treated injured cultures (C), and inhibition of increased ZO-1 in cultures treated with DEX and RU486 (D). Quantified ZO-1 staining per cell was consistent with qualitative changes depicted in immunofluorescence images (E). No changes in occludin immunostaining were visually apparent among the different exposure conditions (F-I), and the absence of any significant differences was confirmed by quantified occludin staining per cell (J). (* $p < 0.05$; \pm SEM; $n \geq 6$ cultures (≥ 30 images) per exposure condition for ZO-1 and occludin; Scale bar = 50 μ m).

These data are scientifically significant as they suggest that increased ZO-1 is a structural correlate to potentiated BBB recovery with DEX treatment after blast injury. The disruption of tight junction proteins (occludin, claudins, zonula occludens) is a known phenomenon following TBI, (Blyth et al. 2011; Morganti-Kossmann et al. 1999; Vilalta et al. 2008) and has been demonstrated specifically after primary blast TBI. (Abdul-Muneer et al. 2013; Hue et al. 2014b; Hue et al. 2013a) Our results suggest that enhanced ZO-1 expression and morphology play a critical role in restoring BBB function and integrity after blast-induced injury to tight junctions of the BBB. Future studies will more quantitatively assess whether changes in other tight junction proteins such as claudin-5 occur with DEX treatment after blast.

BBB breakdown after blast exposure *in vivo*:

Several studies have demonstrated brain microvascular and BBB breakdown resulting from blast exposure by increased extravasation of IgG, Evans blue (EB), and sodium fluorescein (NaFl) in the brain parenchyma (Abdul-Muneer et al. 2013; Garman et al. 2011; Logsdon et al. 2014; Lucke-Wold et al. 2014; Readnower et al. 2010; Skotak et al. 2013; Yeoh et al. 2013). Despite this evidence, there is limited quantitative understanding of the extent of BBB opening and the time course of damage after blast injury. Detailed characterization of blast-induced BBB damage may hold important implications for serum constituents that may potentially cross the compromised barrier and contribute to neurotoxicity, neuroinflammation, and persistent neurologic deficits. To help shed necessary insight on the extent of BBB disruption after blast injury, we characterized the pore-size of BBB opening and its time course for spontaneous recovery after exposure to blast injury by measuring extravasation of NaFl (376 Da), EB (69 kDa when bound to serum albumin) and dextrans (3, 70, and 500 kDa). We utilized a previously described *in vivo* blast injury model with high-speed video to control and report the biomechanics of injury and minimize head motion associated with blast exposure (Gullotti et al. 2014a). We report that BBB opening was sufficient to permit significant extravasation of molecules less than approximately 70 kDa in the acute period after blast, with recovery of BBB integrity by 1 day post-injury. We are the first to quantify the time course and pore-size of BBB opening after blast exposure, and our data hold important implications for the influx of serum constituents into the brain that may initiate secondary pathological cascades after bTBI.

***In vivo* blast-induced traumatic brain injury model:**

Our bTBI model consists of a 76 mm-diameter shock tube that was previously described in detail (Gullotti et al. 2014a), with a 25 mm-length driver section pressurized with helium gas, and a 1,240 mm-long driven section (Panzer et al. 2012a). The body of the mouse was secured within a rigid pipe to protect the torso but expose the head 15 mm away from the shock tube exit where the shock wave is still nearly planar (Figure 62) (Gullotti et al. 2014a; Panzer et al. 2012a). The head was further restrained using an adjustable, metal nose bar to minimize motion of the head during blast exposure. Pressure transducers (Meggitt Sensing Systems, Irvine, CA, USA; Endevco 8530B-1000) were flush-mounted at the shock tube exit, as well as inside the mouse holder in close proximity to the animal torso.

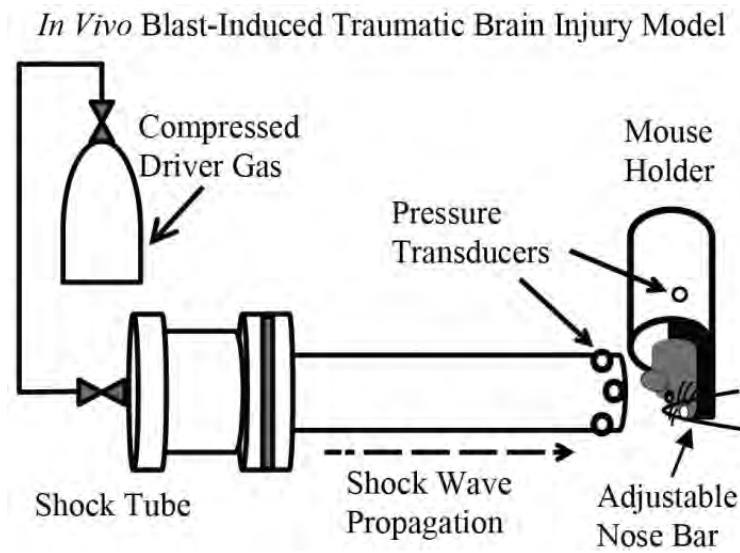


Figure 62: *In vivo* blast-induced traumatic brain injury (bTBI) model consisting of a shock tube and custom-designed mouse holder (Gullotti et al. 2014a). Pressure transducers were flush-mounted at the exit of the tube and within the mouse holder. The mouse head was aligned 15 mm away from the exit of the tube. An adjustable nose bar was used to restrain the mouse head and minimize head motion during blast exposure. (Figure not drawn to scale.)

Kinematic analysis of blast-induced head motion:

Animals were exposed to a shock wave with a 272 ± 6 kPa peak overpressure, 0.69 ± 0.01 ms duration, and 65 ± 1 kPa*ms impulse. Consistent with our previous study (Gullotti et al. 2014a), head motion was generally characterized by rapid head movement in the direction parallel to the incident shock wave, followed by a slower and prolonged movement in the reverse direction, and a slow lateral evolution of the head as it reached its final position. The peak displacement, velocity, and acceleration of the head were all dramatically greater in the direction parallel to the incident shock wave (x component) than in the perpendicular direction (y component) (Table 6). Blast-induced head motion of a representative mouse, using head restraint, is presented in Figure 63. The peak pressure measured inside of the animal holder, adjacent to the torso, was 24 ± 1 kPa, which was well below reported thresholds for pulmonary injury (Bass et al. 2008). We also note that after injury, we did not observe any gross macroscopic pulmonary injury.

Table 6: Kinematic Analysis of Head Motion^a

	Displacement (m)	Velocity (m/s)	Acceleration (m/s ²)
Maximum Total	0.003 ± 0.0001	7.07 ± 0.33	16349 ± 819
Maximum X	0.003 ± 0.0001	6.93 ± 0.33	16493 ± 819
Maximum Y	0.001 ± 0.0001	1.75 ± 0.10	6977 ± 380

^a(Mean \pm SEM; n = 20 independent high-speed videos of mouse blast exposure)

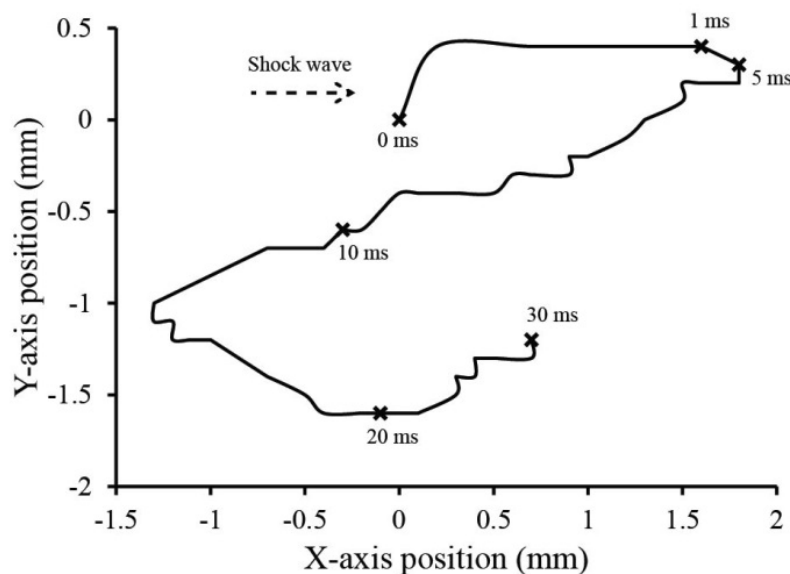


Figure 63: Head motion induced by blast exposure for a representative mouse (with head restraint). After blast exposure, the mouse head returned to rest at 31 ms. The direction of the oncoming shock wave is represented by the dashed arrow.

These results are scientifically important as we have quantified mouse head accelerations and shock wave parameters to more fully describe our blast conditions and enable more direct comparisons with future studies. Although our careful efforts to restrain the head reduced overall motion, accelerations remained appreciable. Angular acceleration of the head (without blast exposure) has been postulated to result in widespread pathological and morphological changes to the cerebrovasculature throughout the

brain (Maxwell et al. 1992). For example, controlled angular head accelerations of approximately $1 - 2 \times 10^5 \text{ rad/s}^2$ resulted in extravasation of blood from vessels throughout the brain as well as subdural and intracerebral hematomas in non-human primates (Adams et al. 1981; Gennarelli et al. 1981; Gennarelli et al. 1982; Maxwell et al. 1992). After blast exposure in mice, Goldstein et al. (2012) reported peak average angular head acceleration of $9.54 \times 10^5 \text{ rad/s}^2$, which was associated with microvascular pathology and abnormal BBB ultrastructure (Goldstein et al. 2012a). Peak angular head acceleration associated with BBB opening in our current study was estimated to be $7 \times 10^5 \text{ rad/s}^2$ (peak linear acceleration of $16,349 \text{ m/s}^2$), within the range of head accelerations reported in non-blast and blast models of TBI. Importantly, our results also highlight the more general challenge of interpreting the effects of blast in the majority of *in vivo* bTBI models, in which inertial contributions of head motion can be minimized but not completely eliminated.

Blast-induced blood-brain barrier opening in vivo:

In contrast to sham controls, blast resulted in widespread extravasation of NaFl and 3 kDa dextran in the acute period (day 0) after exposure (Figure 64A, B). EB was also visible in several injured brain sections in the acute period after exposure, when compared with EB-injected sham animals (Figure 64C). However, there was no qualitative indication of extravasation of the 70 or 500 kDa dextrans acutely after injury except for scattered, localized regions of fluorescence (Figure 64D-E). At 1 day after blast exposure, there were no visible differences in extravasation of the different-size dextrans or EB between injured and sham samples (Figure 65A-D), suggesting that the BBB had recovered. Qualitatively as the molecular mass increased, accumulation of dextran in injured samples was less widespread.

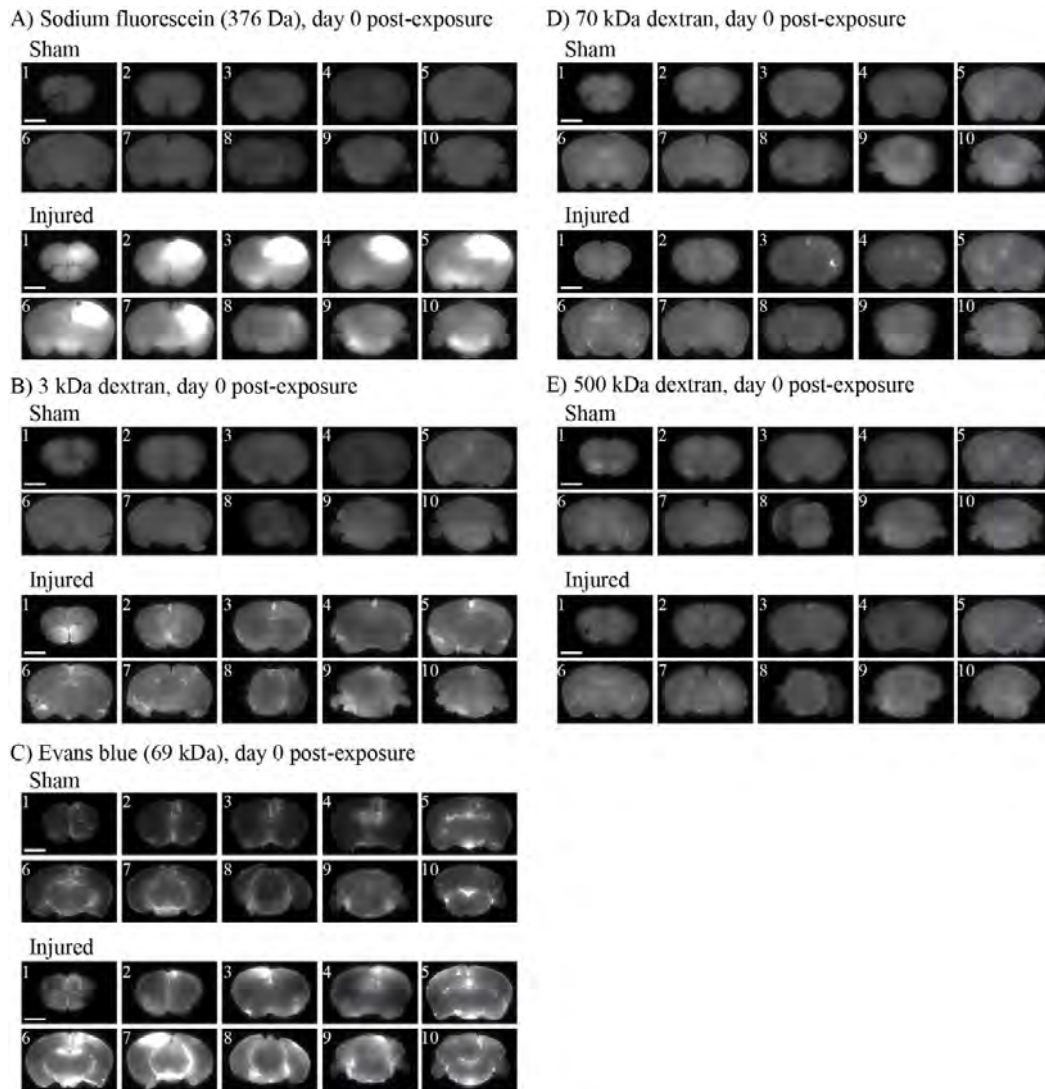


Figure 64 Blood-brain barrier opening in the acute post-injury period (day 0). Sections from a representative sham or injured brain are presented for each tracer. (A) Strong, widespread fluorescence of NaFI throughout the entire blast-injured brain on day 0. (B) Widespread fluorescence of 3 kDa dextran throughout the entire blast-injured brain on day 0. (C) Regions of strong EB fluorescence in several injured brain sections on day 0. (D, E) No qualitative differences in fluorescence of 70 or 500 kDa dextrans between sham and injured brains on day 0. (Scale bar = 3 mm)

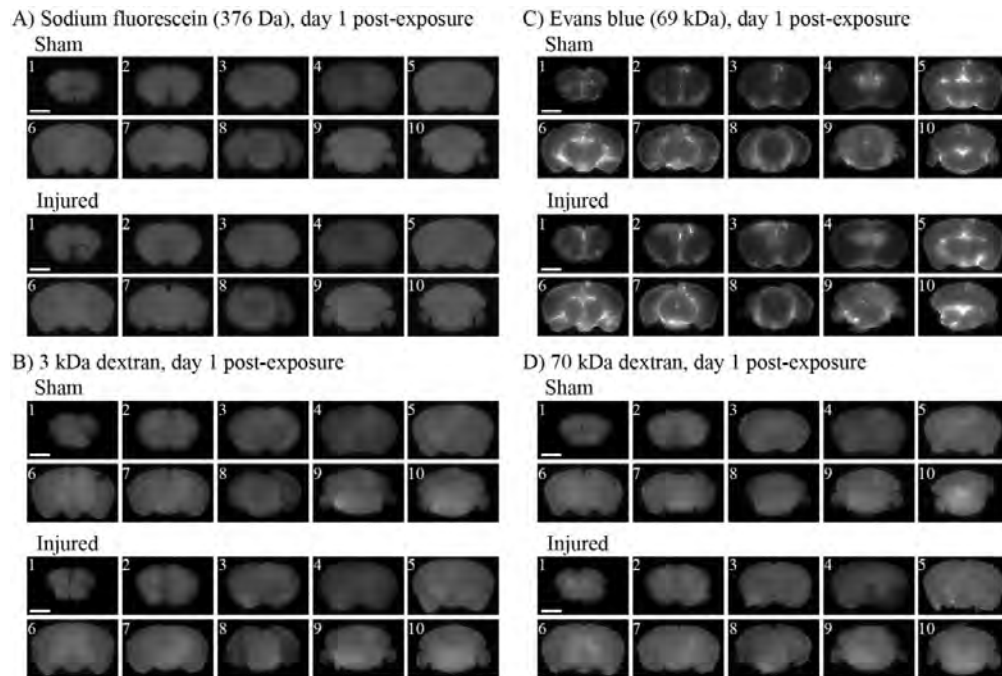


Figure 65 Blood-brain barrier opening 1 day post-injury. Sections from a representative sham or injured brain are presented for each tracer. (A, B, C, D) No qualitative differences in fluorescence of NaFl, 3 or 70 kDa dextrans, or EB on day 1 after injury. (Scale bar = 3 mm)

These results are scientifically important as they define the pore-size and recovery time course of BBB opening after blast injury using a range of different-sized tracers. BBB function recovered 1 day after blast exposure in mice, which was in close agreement with a recent *in vivo* bTBI study (Logsdon et al. 2014). More specifically, the qualitative images support that molecules less than approximately 70 kDa can penetrate the BBB in the acute period after blast injury at conditions tested in this study, but are excluded by 1 day after exposure when the BBB has recovered.

Quantification of blast-induced blood-brain barrier opening:

Quantitative analysis of the mean fluorescence intensity of each brain section confirmed qualitative visual trends. The mean fluorescence intensity of NaFl was significantly increased in the acute period after exposure (day 0) in all injured brain sections (Figure 66A). The mean fluorescence intensity of 3 kDa dextran was significantly increased in the acute period after exposure (day 0) in all injured brain sections except in section 10 (S10; $p = 0.061$) (Figure 66B). Mean fluorescence intensity of EB was also significantly greater in injured brain sections 3, 7, and 8 (S3, S7, and S8) in the acute period after blast (Figure 66C). Fluorescence intensity of 70 or 500 kDa dextrans was not altered in the acute post-injury period (Figure 66D-E). At 1 day after blast exposure, mean fluorescence intensity was unaltered for NaFl and only significantly higher in injured samples in section 4 (S4) for 3 kDa dextran, section 3 (S3) for EB, and section 6 (S6) for 70 kDa dextran (Figure 67A-D). The quantitative results support that blast-induced BBB opening permits the influx of molecules less than approximately 70 kDa in the acute post-injury period, with spontaneous recovery of the BBB 1 day after exposure.

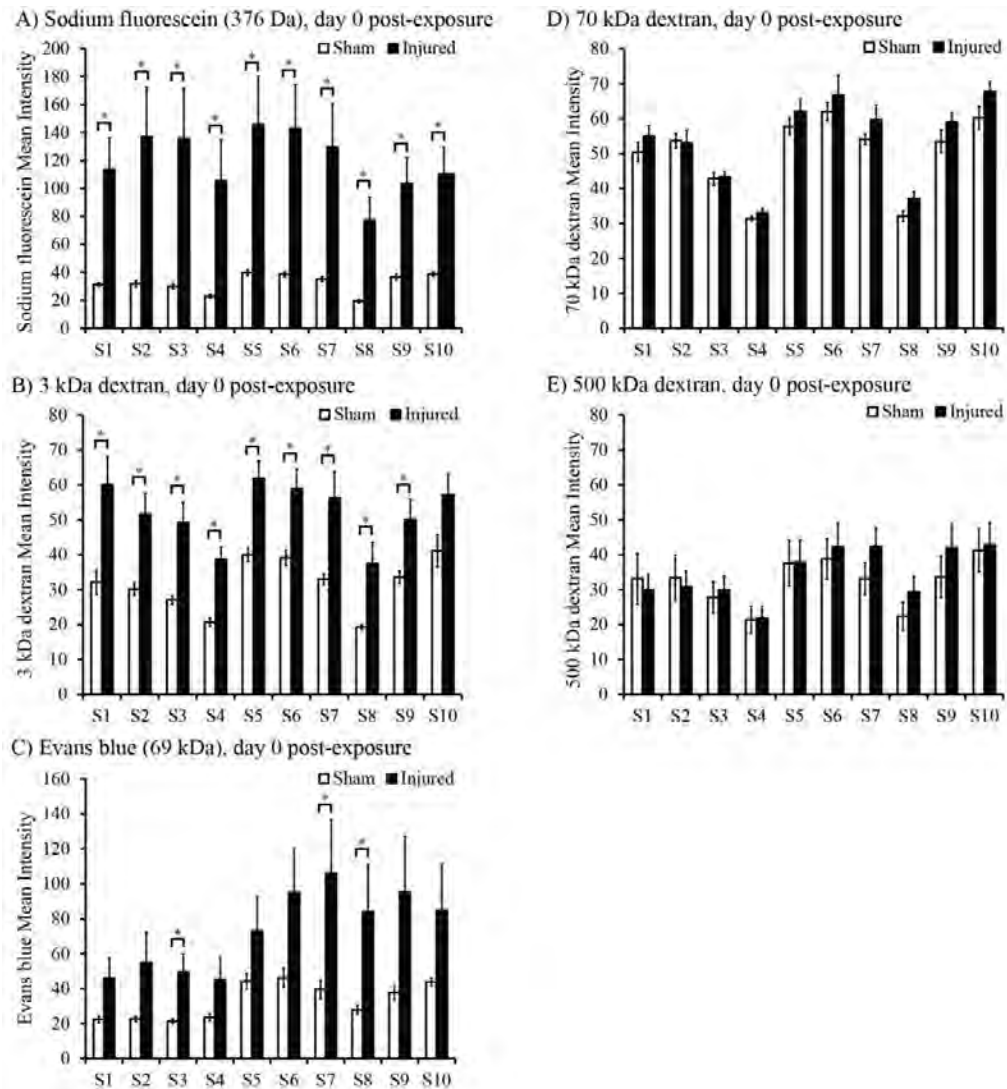


Figure 66: Quantification of blood-brain barrier opening in the acute post-injury period (day 0). (A) Mean fluorescence intensity of NaFl significantly increased throughout injured brain sections after blast exposure on day 0 ($n \geq 3$ animals per exposure condition). (B) Mean fluorescence intensity of 3 kDa dextran significantly increased throughout injured brain sections after blast exposure on day 0 ($n = 7$ animals per exposure condition). (C) Mean fluorescence intensity of EB significantly increased in several injured brain sections (S3, S7 and S8) after blast exposure on day 0 ($n \geq 6$ animals per exposure condition). (D, E) No changes in fluorescence of 70 or 500 kDa dextrans after injury on day 0 ($n \geq 5$ animals per dextran tracer and exposure condition). (* $p < 0.05$; \pm SEM)

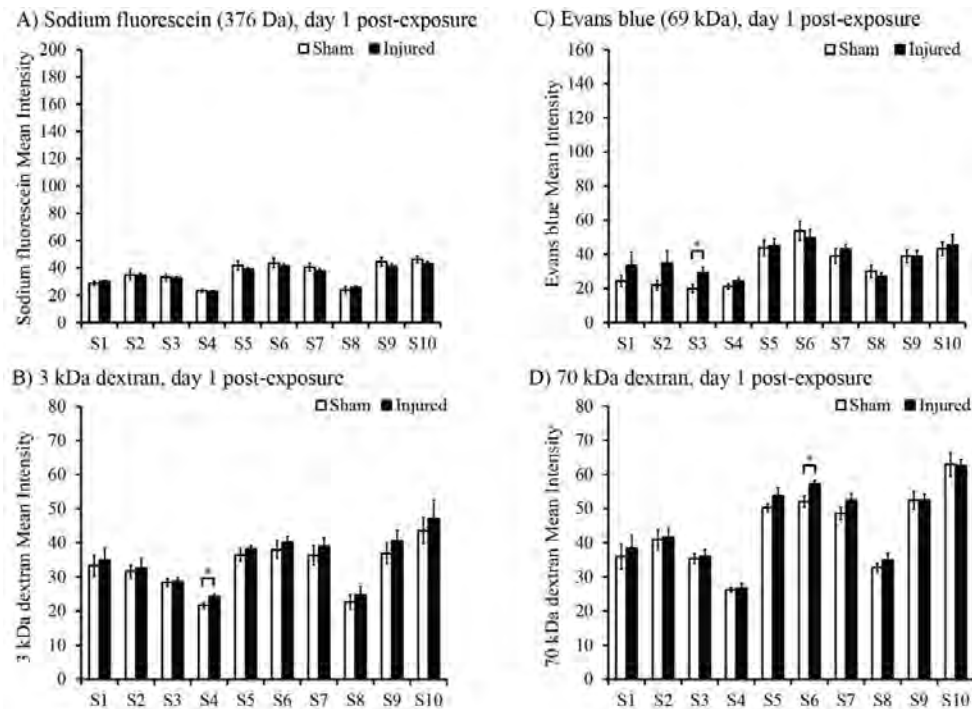


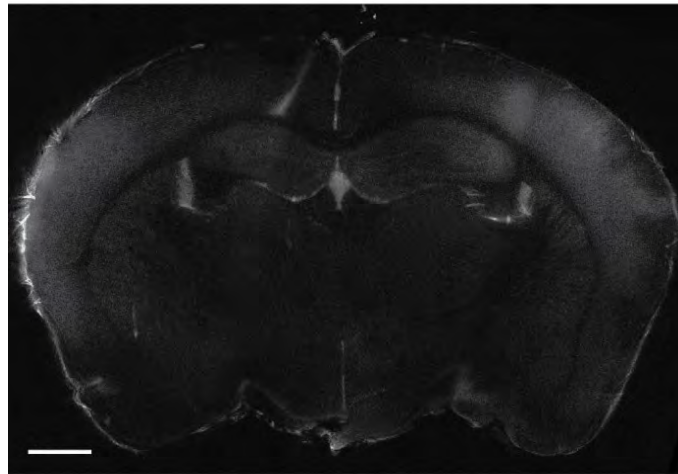
Figure 67: Quantification of blood-brain barrier opening 1 day post-injury. (A, B, C, D) Minimal to no differences in mean fluorescence intensity of NaFl ($n \geq 3$ animals per exposure condition), 3 and 70 kDa dextrans ($n = 6$ animals per dextran tracer and exposure condition), and EB ($n = 6$ animals per exposure condition) on day 1 after blast exposure, strongly supporting the recovery of BBB integrity. (* $p < 0.05$; \pm SEM)

These results are of scientific importance because they are the first to quantitatively demonstrate that BBB opening was sufficient to permit significant extravasation of molecules less than approximately 70 kDa in the acute period after blast, with recovery of BBB integrity by 1 day post-injury. Our results hold important implications for the influx of serum constituents into the brain that may initiate secondary pathological cascades after bTBI.

Microscopic evaluation of blood-brain barrier damage after blast:

In the acute period (day 0) after sham exposure, there were no regions of EB fluorescence indicative of any BBB disruption in a representative sham sample, as determined by high-resolution confocal microscopy (section 5; -1.6 mm from Bregma) (Figure 68A). By contrast, there was widespread EB fluorescence throughout a corresponding blast-injured brain section that appeared to be strongest in the right motor (MO) and somatosensory cortex (SS), as well as in the left piriform (PIR), entorhinal (ENT), and perirhinal (PERI) cortex (Figure 68B). Although specific anatomical regions of EB extravasation and fluorescence intensity varied across injured samples, overall BBB breakdown appeared to be diffuse but strongest in the cerebral cortex, which was consistent with previous findings (Garman et al. 2011; Logsdon et al. 2014; Lucke-Wold et al. 2014; Readnower et al. 2010).

A) Sham, Evans blue, day 0 post-exposure



B) Injured, Evans blue, day 0 post-exposure

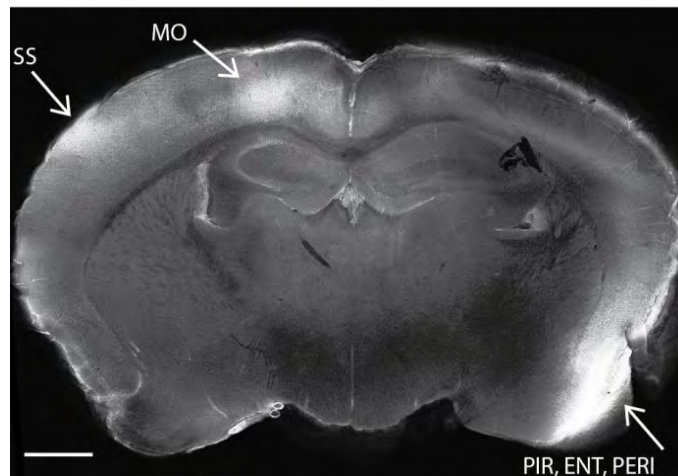


Figure 68: Confocal microscopy of Evans blue (EB) fluorescence in the acute period (day 0) after blast exposure. (A) No regions of strong EB fluorescence in sham exposed brain section. (B) Widespread EB fluorescence indicating BBB breakdown in an example injured brain section, with strongest regions of fluorescence in the right motor (MO) and somatosensory (SS) cortex, as well as in the left piriform (PIR), entorhinal (ENT), and perirhinal (PERI) cortex (white arrows). Anatomical regions of BBB damage as well as fluorescence intensity varied across injured samples, but were generally strongest in the cerebral cortex. (Scale bar = 1 mm)

Our data are significant as they support that BBB breakdown after blast injury is diffuse in nature without preferential susceptibility in specific anatomical brain regions. A number of studies describing cerebrovascular compromise after blast injury also report the diffuse nature of BBB breakdown. In some cases, damage in general anatomical regions was observed, revealing diffuse staining predominantly in the prefrontal and outer layers of the cortex (Garman et al. 2011; Logsdon et al. 2014; Lucke-Wold et al. 2014; Readnower et al. 2010). Consistent with these previous findings, BBB breakdown in the current study was observed in the cerebral cortex under microscopic evaluation but was generally more widespread and diffuse throughout the brain.

Comparison of primary to tertiary blast injury

Blast is also multiphasic in its physical injury mechanisms. The biomechanics of blast-induced injury are complex but classified into four mechanisms: primary blast due to the interaction of the supersonic shock wave with biological tissues; secondary blast due to ejecta causing penetrating injuries; tertiary blast due to blunt impact or rapid acceleration / deceleration leading to injurious deformation within the brain; and quaternary blast due to remaining mechanisms including burning, poisoning, infection, and electromagnetic waves (Effgen et al. 2014b; Keyes 2005). Therefore we compared the response of organotypic brain slice cultures to isolated primary blast injury (shock wave alone) versus isolated tertiary blast injury (stretch alone).

Histology and immunohistochemistry

After injury or sham exposure, cultures were fixed with neutral buffered 10% formalin (Sigma), dehydrated in a gradient of alcohols followed by xylene before embedding in paraffin. Samples were cut into 6 μ m thick sections and mounted on slides. Paraffin was removed, and sections for histology were stained with hematoxylin & eosin (H&E; Gill's Hematoxylin 3 and Eosin Y, Thermo Fisher Scientific, Waltham, MA), dehydrated with a gradient of alcohols, and mounted for routine pathological analysis (N=4 for each group).

Separate, adjacent sections were stained with an antibody for microtubule associated protein 2 (MAP-2; anti-MAP2 AB5622, Millipore; 1:100) to visualize dendrites, antibodies for phosphorylated neurofilament heavy (NF-H; SMI-31, BioLegend, San Diego, CA; N=3; 1:500) and non-phosphorylated NF-H (SMI-32, BioLegend; N=3; 1:500), an antibody for glial fibrillary acidic protein (GFAP) to visualize activated astrocytes (anti-GFAP Ab7260, Abcam, Cambridge, MA; N=4; 1:2000), and an antibody for IBA1 to visualize activated microglia (anti-IBA1, Wako Pure Chemical Industries, Richmond, VA; N=4; 1:400). Paraffin was removed. Antigen retrieval was performed for samples stained for GFAP, IBA1, SMI-31, and MAP-2 by microwaving in citrate buffer (0.01 M, pH 6.0, Fisher Scientific) for 20 minutes and cooling to room temperature for 30 minutes before being washed. Antigen retrieval was performed for samples stained for SMI-32 by warming for 25 minutes in a low pH retrieval solution (DAKO, Carpinteria, CA) before cooling to room temperature for 20 minutes. GFAP, IBA1, SMI-31, and MAP-2 samples were blocked with 10% normal goat serum (Vector Laboratories, Burlingame, CA) for 25 minutes and then incubated overnight at 4°C with the primary antibody. SMI-32 samples were blocked with 5% horse serum for 25 minutes and then incubated overnight at 4°C with the primary antibody. GFAP, IBA1, SMI-31, and MAP-2 samples were incubated with biotinylated anti-rabbit IgG secondary antibody (1:200 for GFAP, IBA1, and MAP-2) or with horse anti-mouse secondary antibody (1:200 for SMI-31 and SMI-32; Vector Laboratories) for 30 minutes at room temperature. All samples were washed, incubated with ABC reagent (A 1:50, B 1:50) for 30 minutes at room temperature, washed, added to 3,3'-diaminobenzidine solution (DAKO) for 1 minute (with the exception of GFAP: 30 seconds), and counterstained with hematoxylin. Samples were dehydrated with a gradient of alcohols and mounted. As negative controls, additional sections received the same staining protocol without the primary antibodies.

Samples were analyzed semi-quantitatively by an individual blinded to the identity of the sections. To evaluate H&E stained sections, a four-point rating scale of 0-3 was devised to assess (0: none, 1: rare, 2: occasional, 3: frequent) pathological findings such as shrunken neurons, vacuolization, neuronal loss, and dark neurons. For MAP-2 immunohistochemistry, a rating scale of 0-3 corresponded to intensity and consistency of dendritic staining (0: uniform staining, 1: patchy loss of staining, 2: extensive loss of staining, 3: complete loss of staining). Samples stained with SMI-31 for phosphorylated NF-H were

visually inspected for loss of axons, axonal swellings and discontinuities, and graded on a four-point scale of 0-3 (0: uniform staining, 1: patchy loss of staining, 2: extensive loss of staining, 3: complete loss of staining). Samples stained with SMI-32 for non-phosphorylated NF-H were visually inspected for presence of non-phosphorylated and injured axons and graded on a scale from 0-3 (0: uniform staining, 1: patchy loss of staining and beading, 2: extensive loss of staining and significant beading, 3: complete loss of staining). Relative presence of microglia and macrophages was evaluated and graded on a scale from 0-3 (0: no IBA1 expression; 1: minimal number of IBA1 positive cells; 2: moderate number of IBA1 positive cells with varying presence of activated microglia (amoeboid shape) and macrophages; 3: high number of IBA1 positive cells with large number of activated microglia and macrophages). Presence of activated astrocytes was evaluated with GFAP and graded on a scale of 0-3 (0: no GFAP expression; 1: minimal number of GFAP positive astrocytes; 2: moderate number of GFAP positive astrocytes; 3: large number of GFAP positive astrocytes).

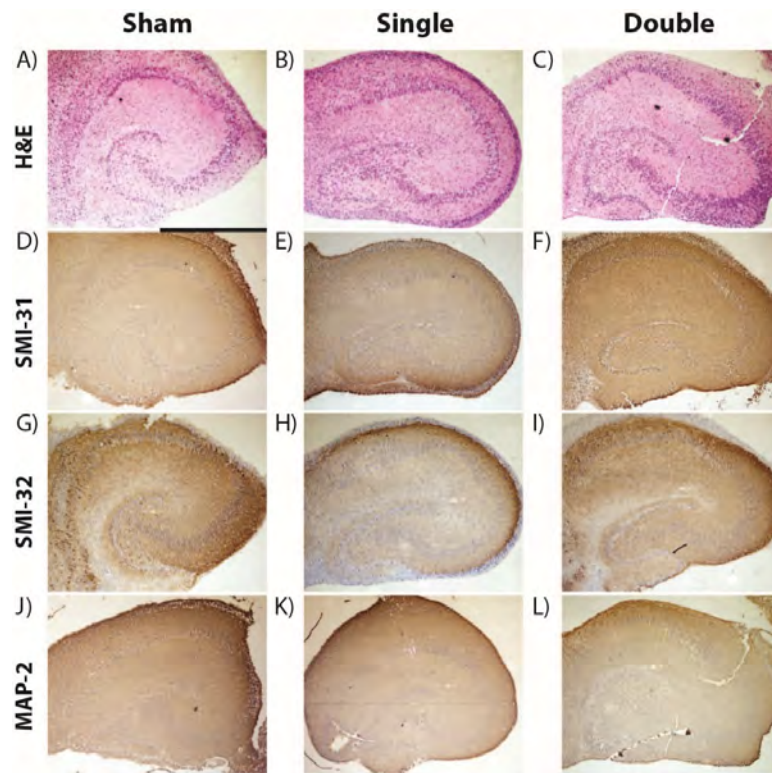


Figure 69 Histological and immunohistochemical evaluation of neurons, axons, and dendrites in OHSCs following exposure to single and repetitive Level 2 primary blast. (A-C) H&E staining of OHSCs receiving the sham (A, scale bar=1 mm), a single Level 2 blast (B), or two Level 2 blasts 24 hours apart (C) revealed intact principal cell body layers. (D-F) SMI-31 staining of OHSCs receiving the sham (D), a single Level 2 blast (E), or two Level 2 blasts 24 hours apart (F) showed the majority of axons were undisturbed by primary blast. (G-I) SMI-32 staining of OHSCs receiving the sham (G), a single Level 2 blast (H), or two Level 2 blasts 24 hours apart (I) revealed minimal damage to axons. (J-L) MAP-2 staining of OHSCs receiving the sham (J), a single Level 2 blast (K), or two Level 2 blasts 24 hours apart (L) showed the

Single and repetitive primary blast did not alter histology or structure of axons or dendrites.

Samples stained with H&E were evaluated for loss of neurons, vacuolization, and dark or shrunken neurons. No histological damage was observed in samples receiving the sham, single Level 2, or repetitive Level 2 blasts with the 24h interval (representative images shown in Figure 69). Staining with MAP-2 and SMI-31 was uniform and did not suggest a significant loss of dendrites or axons, respectively (Figure 69D-F & J-L). Staining with SMI-32 was consistent with neuronal cell bodies and dendrites in the hippocampus and did not show appreciable differences between groups suggesting no de-phosphorylation of NF-H or axonal damage (Figure 69G-I).

Microglia activation was increased after Level 2 primary blast exposure; however, astroglial response was unaffected by blast exposure.

Samples stained with GFAP did not show any significant differences in activated astrocytes with either single or repetitive primary blast as compared to the sham (Figure 70A-C). The number of IBA1 positive cells (microglia and macrophages) was increased by Level 2 primary blast exposure (Figure 70D-I). This response was significantly higher for the double injury group as compared to the sham (Figure 70J).

Tertiary blast or stretch injury

The stretch-injury device and loading mechanism have been previously characterized in detail. (Morrison et al. 2006b; Morrison et al. 2003b) In brief, culture medium was aspirated, and each culture well was placed on the injury-device, which was pre-warmed to 37°C. An equibiaxial stretch injury was achieved by displacing the well and silicone tissue substrate over a hollow, cylindrical indenter. (Morrison et al. 2006b; Morrison et al. 2003b) Tissue strains were verified via image analysis of high-speed video with custom MatLab code (Natick, MA). Cultures received 0, 1, or 2 mild stretch injuries 24, 72, or 144 hours apart. All samples not scheduled to receive a stretch injury at a given time point were exposed to the sham injury. The average equibiaxial strain was $12.9\% \pm 0.3\%$ (\pm SEM; N=492). The average strain rate was $5.3 \text{ s}^{-1} \pm 0.2 \text{ s}^{-1}$ (\pm SEM; N=492). For sham injury, samples were clamped on the injury device, but the device was not fired.

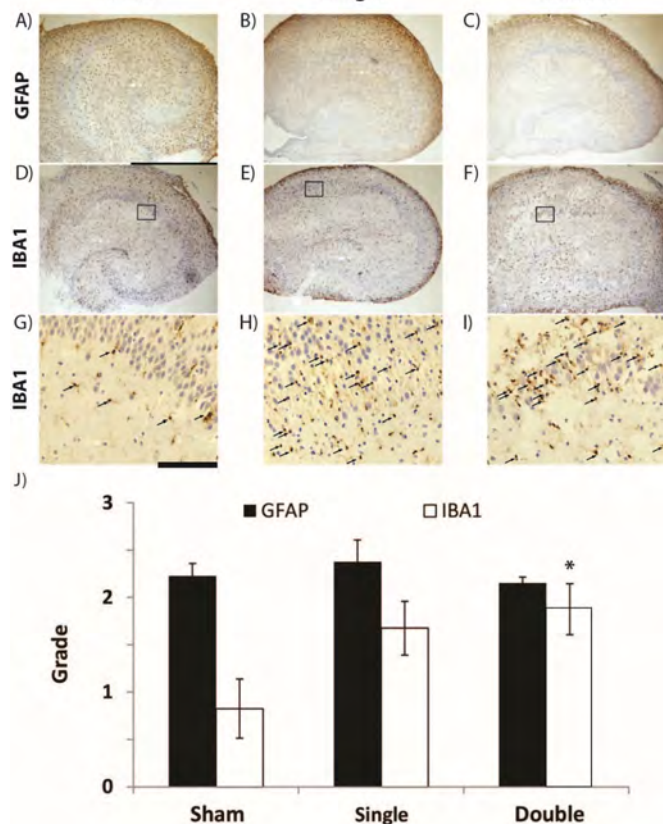


Figure 70 Immunohistochemical evaluation of OHSC glial response following exposure to single and repetitive Level 2 primary blast. (A-C) GFAP staining of OHSCs receiving the sham (A, scale bar=1 mm), a single Level 2 blast (B), or two Level 2 blasts 24 hours apart (C) did not reveal an increase in astrogliosis. (D-F) IBA1 staining of OHSCs receiving the sham (D), a single Level 2 blast (E), or two Level 2 blasts 24 hours apart (F) suggested an increase in activated microglia with primary blast. (G-I) Under higher magnification (scale bar = 100 μ m) of the indicated regions in D-F, activated microglia (arrows) were observed in a region of the CA1 following sham (G), single (H), and repetitive (I) injury. Semi-quantification of the samples (J) suggests there was a nearly significant increase in microglia response to a single primary blast ($p=0.058$) and a significant increase in microglia response

Cell injury and astrogliosis was more vulnerable to additional stretch injury; astroglial vulnerability persisted for 72 hours following mild stretch.

Increased cell loss and shrunken cell bodies were observed along principal cell layers of the hippocampus, primarily in the CA1, of repetitively injured OHSCs with the 24-hour inter-injury interval (Figure 71C & E). Semi-quantitative analysis of H&E stained sections revealed a significant increase in pathology in repetitive injured samples as compared to sham for the 24-hour interval, which was not observed for the 72- or 144-hour intervals (Figure 72A).

All samples stained with SMI-31 to visualize pNF-H had consistent and complete staining throughout OHSCs (images not shown). There was no significant difference in semi-quantitative data for any group and the 3 different inter-injury intervals for SMI-31 staining (Figure 72B).

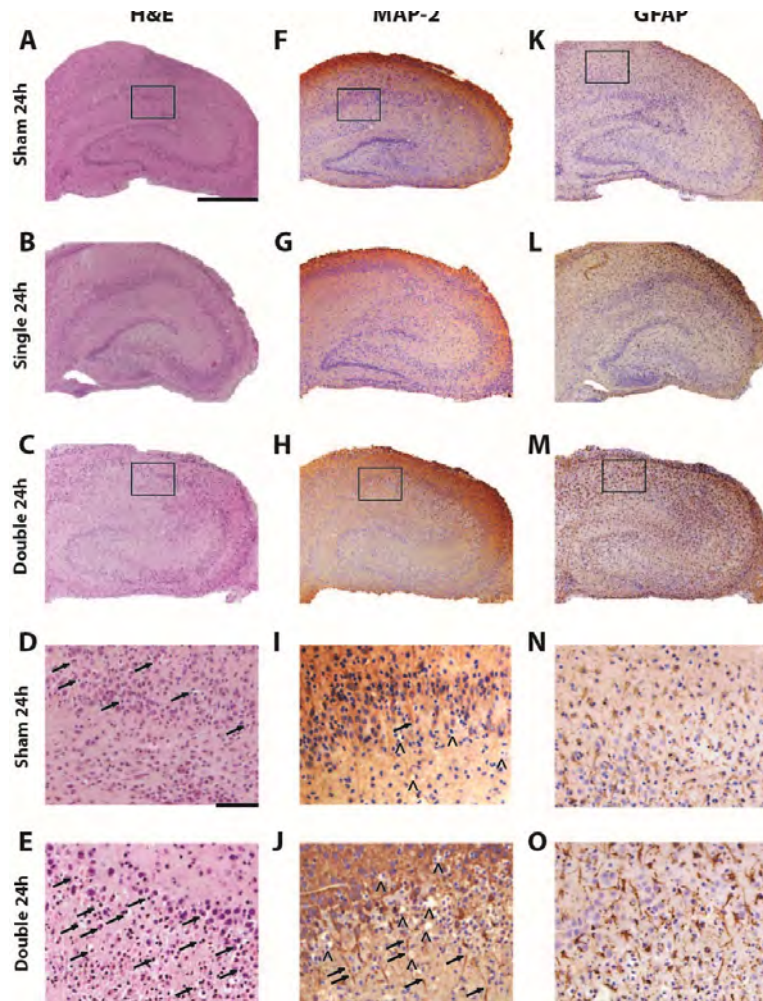


Figure 71 Images from the 24-hour inter-injury interval. **A-E)** A subset of samples was stained with H&E. Sham (**A**) and single injury (**B**) samples had minimal cell loss, and double injury samples (**C**) had significant cell loss. **D)** Region in **A** with occasional shrunken cell bodies (arrow) in the CA1 of sham samples. **E)** Region in **C** with high density of shrunken cell bodies (arrow) in the CA1 after repetitive injury. **F-J)** Samples stained with an antibody to MAP-2. Sham (**F**) and single injury (**G**) had robust immunoreactivity for MAP-2, whereas samples that received 2 mild stretch injuries (**H**) had decreased MAP-2 immunoreactivity in the principal cell layers. **I)** Region in **F** shows mostly uniform immunoreactivity for MAP-2 with occasional discontinuities in dendrites (arrow) and small regions with absence of MAP-2 staining (^) in the CA1. **J)** Region in **H** shows many discontinuities in dendrites (arrow) and larger regions with absence of MAP-2 staining (^) in the CA1 after repetitive injury. **K-O)** A subset of samples was stained with an antibody to GFAP. Sham (**K**) and single injury (**L**) samples had a low density of GFAP-positive cells, whereas samples with 2 injuries (**M**) had a high density of GFAP-positive cells with increased staining. **N)** Higher magnification shows a moderate density of GFAP-positive cells in the CA1. **O)**

Loss of MAP-2 staining, discontinuities in dendrites, and areas of darker staining were observed along the principal cell layers of the hippocampus of repetitively injured OHSCs with the 24-hour interval (Figure 71H & J). Semi-quantitative analysis of MAP-2 staining to visualize dendrites revealed a significant increase in grade, i.e. increased pathology, in samples that were repetitively injured as compared to the shams for the 24-hour interval (Figure 72C).

An increase in density of GFAP-positive cells and GFAP immunoreactivity was observed in samples that received repetitive injury with either a 24- (Figure 71M & O) or 72-hour interval (not shown). Semi-quantitative analysis of GFAP staining revealed a significant increase in astrogliosis in these samples as compared to their time-matched controls. There was no significant difference in GFAP grade among experimental groups for the 144-hour interval (Figure 72D).

IBA1 staining for microglia and macrophages did not appear different among samples (images not shown). Semi-quantitative analysis of IBA1 stained samples confirmed there was no significant difference between each experimental group and its time-matched control for any of the inter-injury intervals (Figure 72E).

These results are especially important because they suggest that different physical injury mechanisms affect different cell types. After blast, microglia were activated whereas after stretch, microglia were not activated. Conversely, after blast, astrocytes were not activated, but after stretch, astrocytes were activated. Multiple mild stretch injuries caused significantly more damage to the tissue than repetitive blast. This differential response may have implications for treatment strategies depending on the injury.

[B4] We measure blast conditions necessary to cause acute and delayed neuronal loss.

As described above, we developed an *in vitro* model for blast that generates a shock wave in-air that interacts with a fluid-filled sample receiver, serving as a surrogate for the skull-brain complex. Fluid in the receiver translates pressure to cultured surrogates (Effgen et al. 2012b; Hue et al. 2013b). This blast injury model delivers military-relevant, reproducible isolated primary blast (Panzer et al., 2012).

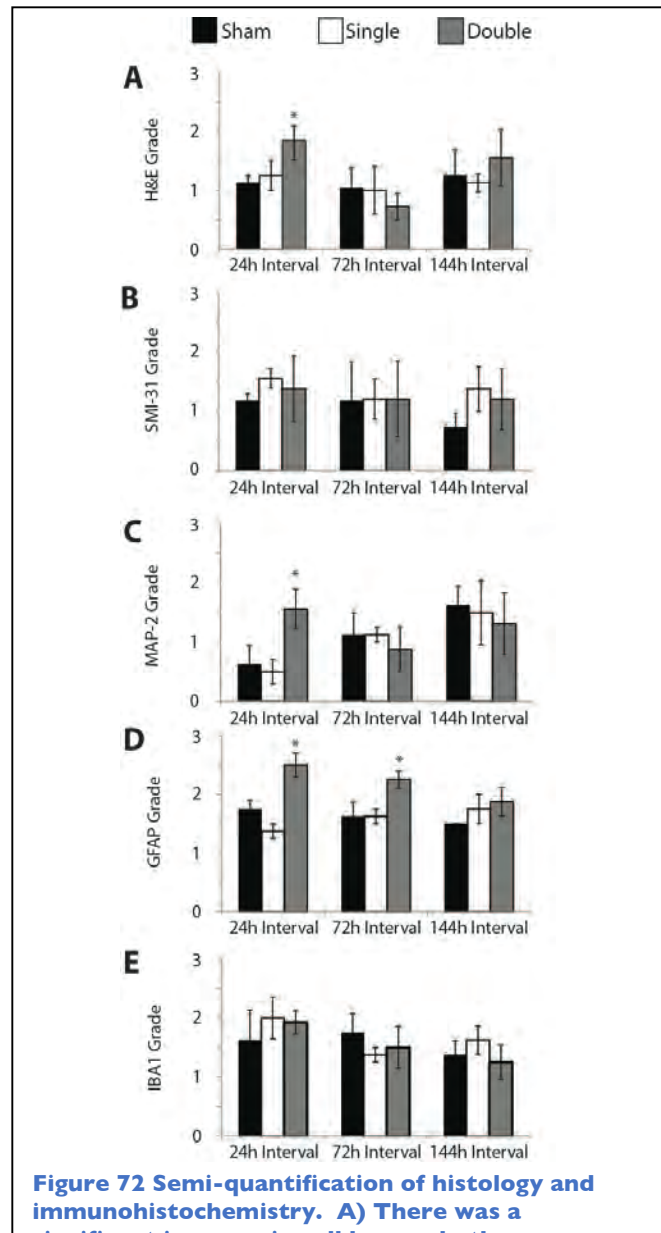


Figure 72 Semi-quantification of histology and immunohistochemistry. A) There was a significant increase in cell loss and other pathology identified by H&E in the double injury group for the 24-hour interval as compared to sham ($N \geq 4$, \pm SEM, $*p < 0.05$). **B)** For SMI-31, there was no significant difference among sham, single, or double injury groups for any inter-injury interval. **C)** There was a significant loss of MAP-2 staining, corresponding to an increase in MAP-2 grade, for the double injury group with the 24-hour interval as compared to sham ($N \geq 4$, \pm SEM, $*p < 0.05$). **D)** There was a significant increase in GFAP-positive cells in the repetitively injured groups as compared to the time-matched shams for both the 24- and 72-hour inter-injury intervals ($N \geq 4$, \pm SEM, $*p < 0.05$). **E)** For IBA1,

Primary Blast Exposure Levels						
In-Air				In-Fluid		
Level	Peak Pressure	Duration	Impulse	Peak Pressure	Duration	Impulse
1	106 ± 2.2	0.25 ± 0.001	9.2 ± 1.6	134 ± 1.9	1.5 ± 0.01	88.8 ± 0.20
2	92.7 ± 2.6	1.4 ± 0.01	38.5 ± 0.7	270.1 ± 14.6	2.6 ± 0.2	295.1 ± 56.1
3	190 ± 2.1	1.2 ± 0.01	73.1 ± 1.3	516 ± 30.7	1.3 ± 0.03	254 ± 35.2
4	336 ± 8.3	0.84 ± 0.01	86.5 ± 1.4	598 ± 14.5	1.85 ± 0.3	440 ± 12.5
5	377 ± 8.3	0.89 ± 0.01	95.5 ± 1.5	817 ± 22	1.53 ± 0.04	472 ± 15.5
6	469 ± 21	0.99 ± 0.005	143 ± 1.5	1258 ± 26	1.46 ± 0.02	658 ± 22.4
7	364 ± 2.8	1.6 ± 0.01	151 ± 1.3	956 ± 42.8	3.6 ± 0.1	1285 ± 43.4
8	534 ± 3.6	1.0 ± 0.01	184 ± 2.1	991 ± 53	2.1 ± 0.2	686 ± 22.5
9	424 ± 6.4	2.3 ± 0.3	248 ± 3.4	1510 ± 90.4	2.8 ± 0.1	1420 ± 86.6

Figure 73 The peak pressure, impulse, and duration of the shock wave in-air were characterized using pressure transducers located at the exit of the shock tube (In-Air). Primary blast levels were enumerated from 1 to 9 in order of increasing impulse in-air. The peak pressure, impulse and duration of the pressure wave in the fluid of the receiver resulting from the primary blast levels tested were characterized using pressure transducers located in the receiver at the sample location (Effgen et. al., 2012).

Immediately prior to injury, organotypic hippocampal slice cultures (OHSC) were imaged for both bright-field and propidium iodide (PI) fluorescence, which is a dead cell stain. Cultures with greater than 5% cell death in any region of interest of the hippocampus (DG, CA3, CA1) prior to experimentation were excluded from the study. At the time of injury, samples were encapsulated in a sample bag with equilibrated medium (5% CO₂, 37° C). Care was taken to prevent entrapment of air bubbles in the sample bags. Sham exposed cultures underwent the same procedures except for blast-loading.

Time course of blast-induced cell death: OHSC received a Level 9 (424 kPa peak pressure, 248 kPa-ms impulse, 2.3 ms duration; see Figure 73) primary blast injury or the sham injury and were evaluated for resultant cell death every 24 hours following exposure. Sham-injured cultures were handled identically to the blast-injured samples but the shock tube was not fired. Dead cells were imaged with propidium iodide (PI) staining, and cell death was quantified as a percent area fluorescence of a region of interest (ROI; DG, CA3, CA1) above an intensity threshold. This level of primary blast injury was selected for its relevance to real-world blast exposure and, of the exposure levels tested, delivered the greatest impulse.

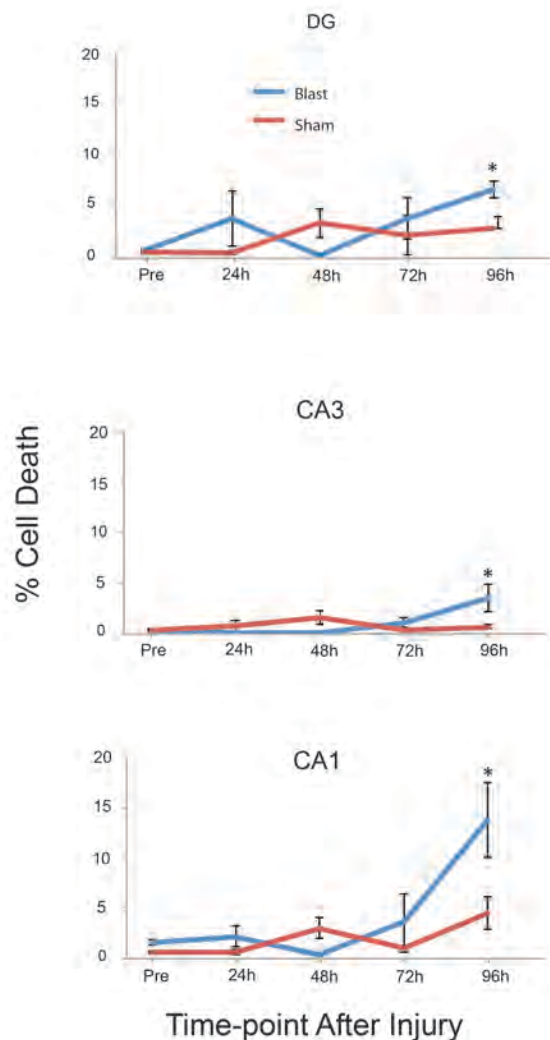


Figure 74 Blast-induced cell death time course.

OHSC were exposed to the most severe primary blast tested (424 kPa, 248 kPa-ms, 2.31 ms). Cell death increased significantly for blast-injured OHSC as compared to time-matched controls on but not prior to day 4 following exposure (\pm SEM, $*p < 0.05$, $n \geq 5$).

This is the first study to demonstrate *in vitro* that primary blast exposure does not result in acute (<1 day following exposure) cell death. Cell death increased slowly over the course of 4 days following exposure in all 3 ROI and increased significantly as compared to time-matched sham-injured controls on but not prior to day 4 (

Figure 74). Therefore, for subsequent experiments cell death was evaluated only on day 4 following exposure. This delay suggests that cell death is initiated by slowly developing secondary messenger cascades initiated by the mechanical stimulus. Similarly, stretch injury of OHSC, which simulates inertia-driven injury, results in protracted cell death over several days following stretch (Cater et al. 2007; Cater et al. 2006a; Morrison et al. 2006a; Morrison et al. 2003a). Inertia-driven TBI is characterized by relatively high strain at low strain rate as compared to primary blast injuries, which are characterized by low strain at high strain rate (Panzer et al. 2012b). The different biomechanics of these injuries resulted in a similar delayed progression of cell death. Future studies will be necessary to determine the cell death pathways and secondary messengers influential in

blast-induced cell death.

Previously, our group has demonstrated that a single, severe, primary blast exposure does induce minimal cell death in OHSC (Effgen et al. 2014b). We continued to characterize the cell death response to multiple primary blast injuries. Propidium iodide (PI) fluorescence was used to quantify cell death prior to the first exposure time point to assess culture health and 72 hours following the second exposure time point. A subset of samples was subsequently exposed to an excitotoxic injury to serve as a positive control for cell death, with these positive control cultures imaged 24 hours following the excitotoxic injury (see 'Excitotoxic injury' below). OHSCs were stained with PI and imaged using previously published methods. (Effgen et al. 2012a; Effgen et al. 2012d; Vogel et al. 2015) Following pre-injury imaging, cultures were immediately injured. Cell death was determined for all regions of interest (ROI) of OHSCs (dentate gyrus, DG; cornu ammonis I, CA1; cornu ammonis 3, CA3), as previously described, using MetaMorph (Molecular Devices, Downingtown, PA). (Cater et al. 2006b; Effgen et al. 2012d; Effgen et al. 2014a; Morrison et al. 2006c; Vogel et al. 2015) Any OHSC with 5% or greater cell death in any ROI at the pre-injury time point was excluded from the study.

As a positive control for cell death, a subset of OHSCs were exposed to glutamate as previously described. (Effgen et al. 2014a) These samples received two blasts (Level 4) 24 hours apart and were subjected to an excitotoxic injury (10 mM glutamate in serum-free medium for 3 hours) 72 hours following the second blast exposure (i.e. immediately after measuring blast-induced cell death). After 3 hours, the glutamate-containing medium was changed to fresh, full serum medium. Cultures were imaged for resultant cell death 24 hours following glutamate exposure.

Blast-induced cell death tolerance of the hippocampus *in vitro*: To identify a threshold for cell death resulting from primary blast, OHSC were exposed to a range of blast severities (Figure 73). Cell death increased significantly following exposure to Level 8 (534 kPa, 184 kPa-ms, 1.04 ms) as well as Level 9 (424 kPa, 248 kPa-ms, 2.31 ms) primary blasts indicated by increased PI fluorescence (Figure 75 & Figure 76). These levels were the 2 most severe tested as denoted by impulse in the open-tube configuration. Previously, finite element analysis was used to predict that sample-level strain in the receiver would be less than 5% (Panzer, 2012). PI is not a cell-specific dead cell stain, and further studies are necessary to determine cell-type preferential vulnerability to blast-loading (Figure 76).

The scientific contribution of these results is that isolated primary blast in the absence of higher order blast loading (such as inertia-loading) can result in neurodegeneration.

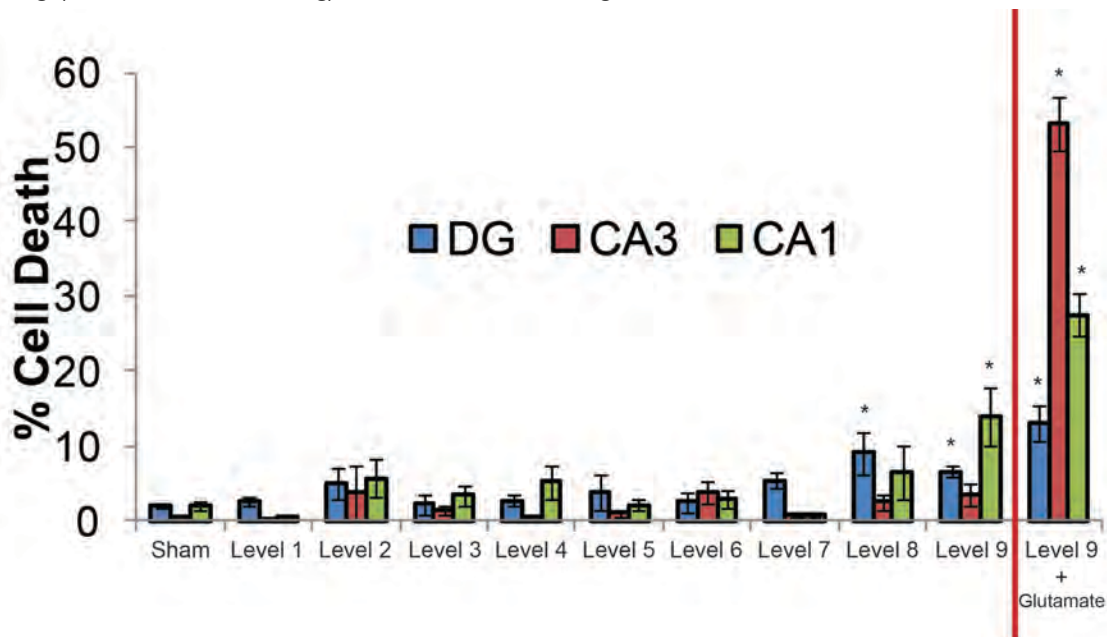


Figure 75 Tolerance of organotypic hippocampal slice cultures (OHSC) to primary blast. OHSC were exposed to a range of relevant primary blast exposure levels. Cell death did increase as compared to sham-injured controls with the greatest amount of cell death in the CA1;

Although isolated primary blast does have the potential to induce cell death, the maximum cell death for the most severe exposure tested (424 kPa, 248 kPa-ms, 2.31 ms) was observed in the CA1 and was less than 14% (Figure 75). Furthermore, for all blast exposure levels studied, there was no significant increase in cell death in the CA3. To confirm tissue health and the potential for a more severe observable injury in the organotypic slice cultures, additional OHSC were exposed to an excitotoxic injury (glutamate) following blast (Level 9). Following a 3 hour 10 mM glutamate exposure, OHSC appeared darker, and, as indicated by PI, cell death in the CA1 was greater than 30% and greater than 50% in the CA3 (Figure 76). Therefore, following a Level 9 blast the majority of cells in all ROI of

OHSC were still viable and susceptible to further excitotoxic insult. The scientific importance of these results is that while isolated primary blast exposure can result in cell death, primary blast exposure in the absence of higher order blast injury, such as inertia-loading (tertiary blast injury), results in mild structural damage. Furthermore, there exists a threshold between 151 and 184 kPa-ms for significant increases in cell death in any ROI as compared to sham-injured controls.

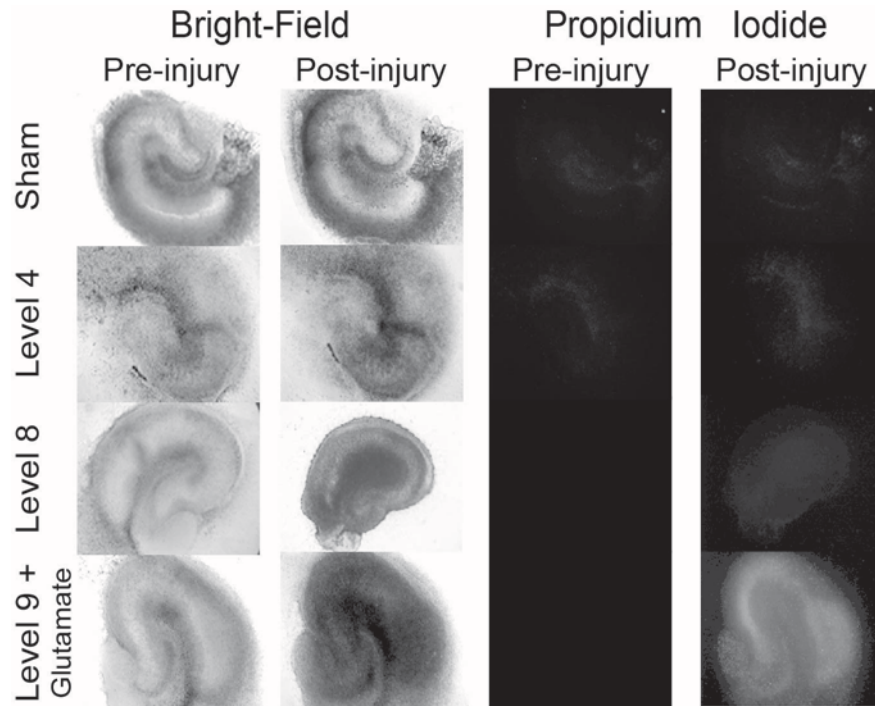


Figure 76 Bright-field and propidium iodide fluorescence images of OHSC exposed to blast. Representative bright-field and fluorescent images of OHSC exposed to blast below (336 kPa, 86 kPa-ms, 0.84 ms) and above (524 kPa, 184 kPa-ms, 1.04 ms) the threshold for blast-induced cell death demonstrate that blast-induced injury is mild. Excitotoxic exposure following blast resulted in significant cell death in all ROI.

Repetitive blast exposure of organotypic hippocampal slices: OHSC were exposed to the lowest level of primary blast capable of inducing significant cell death in any region (534 kPa, 184 kPa-ms, 1.04 ms; Level 8) to determine whether two injuries delivered 24 hours apart produced more cell death. OHSC were exposed to 0, 1, or 2 Level 8 blast exposures 24 hours apart on days 0 and 1. All samples not scheduled to receive a blast at a given time point were sham-injured. OHSC receiving 2 sham injuries (Sham) had less than 5% cell death in all ROI on day 4. OHSC receiving a single injury and sham injury 24 hours apart had very little additional cell death as compared to sham. However, our investigation of OHSC tolerance to a range of blast severities (Figure 75) demonstrated significantly increased cell death in the DG following a single Level 8 exposure. This difference is attributable to additional sample manipulation and multiple media changes in delivery of 2 exposures (sham and blast) in a 24 hour period. Cell death increased minimally for OHSC receiving 2 blasts (Figure 77).

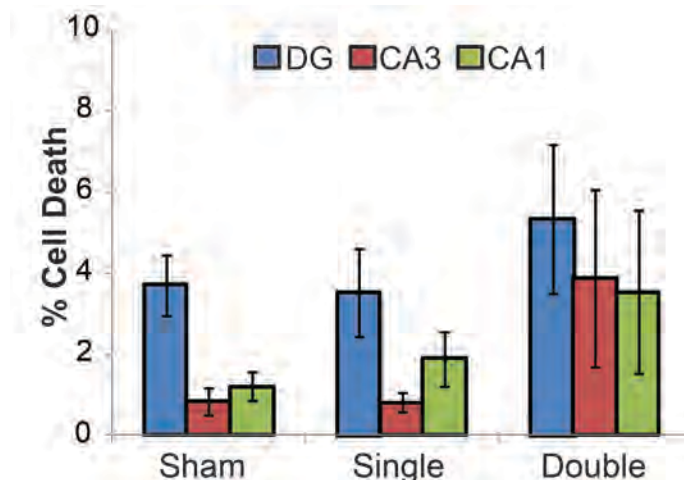


Figure 77 24-hour repetitive blast exposure. OHSC received either 0, 1, or 2 blast injuries 24 hours apart. Cell death increased minimally in all 3 ROI as compared to samples receiving a single or no blasts (\pm SEM, $*p < 0.05$, $n \geq 9$).

Repetitive blast did not increase cell death: Cell death increased minimally ($< 5\%$) in all ROI after sham injury (**Error! Reference source not found.**). Cell death increased minimally following single and repetitive primary blast (Levels 1, 2, 4) with an inter-injury interval of 24 hours. Given that multiple, primary blasts (Levels 1, 2, 4) did not result in significant cell death, we investigated the potential for repetitive exposure to our highest primary blast level (Level 9) to cause cell death. Three Level 9 blasts delivered within 10 minutes did not increase cell death, either. However, cell death increased substantially and significantly following glutamate exposure (after blast), which served as the positive control (Double Level 4+ Glutamate; $>37\%$ cell death in all ROI).

Repetitive mild stretch injury (tertiary blast) increased cell death

We also have extensive previous experience with in vitro injury models that simulate tertiary blast, i.e. stretching of brain tissue up to 50% Lagrangian strain at rates up to 50 /s (Cater et al. 2006c; Morrison III et al. 2006). After a single mild stretch injury (12% equi-biaxial at 5/s), little cell death was induced. Cell death was less than 5% in all ROI in all sham-injured groups (**Error! Reference source not found.**). Similarly, among samples that received a single mild stretch and a subsequent sham injury (24, 72, or 144 hours later), cell death was less than 5%, as designed by choosing a mild level of stretch. Cell death increased significantly following two injuries delivered 24 hours apart as compared to that of samples receiving a single mild stretch or no stretch injury (sham). Cell death was below 5% in samples that received 0, 1, or 2 mild stretch injuries 72 or 144 hours apart, and there was no significant difference in cell death between samples receiving 0, 1, or 2 injuries for either inter-injury interval (72 or 144 hours). Subsequent excitotoxic exposure, which served as a positive control, increased cell death significantly in all ROI for all inter-injury interval groups. The positive control suggested that OHSCs contained viable cells that were not killed by stretch injury and that a lack of cell death in repetitively injured OHSCs for the 72- and 144-hour intervals was not due to a lack of living cells in the samples.

These results further support the hypothesis that primary and tertiary blast injuries are fundamentally different. Blast does not kill brain cells, whereas stretch does kill brain cells.

[C2 & C3] We use organotypic culture preparations to define when synaptic changes lead to corresponding changes in neural circuit activation and the ability to induce long term potentiation (LTP).

Animal studies investigating the effects of primary blast injury have produced mixed results. Some studies have demonstrated losses in motor function in tests like the rotarod test (Cernak et al. 2011; Wang et al. 2011b). However, others have reported no overall decline in motor skills (Elder et al. 2012; Goldstein 2012; Vandevord et al. 2012). Similar results have been found with studies focused on cognition. Following primary blast exposure, animal performance on cognitive maze tests was significantly decrease (Saljo et al. 2009; Vandevord et al. 2012), however others have shown that it does not change at all (Elder et al. 2012; Goldstein 2012). It is clear that patterns of neurological deficit following blast are very complex. These mixed results may be due to the fact that current models of primary blast injury are extremely varied, where factors like head immobilization, thorax protection, and blast parameter scaling vary across studies (Effgen et al. 2014b).

One way to further elucidate the source of variability in *in vivo* behavioral results is to study changes in neuronal function *in vitro*. Recordings of neuronal electrophysiological activity provide a correlate to behavioral testing, where changes in neuronal function can be studied in simpler culture models as opposed to an entire animal brain. To this end, the limited number of functional studies investigating primary blast has produced mixed results, similar to their *in vivo* counterparts (Connell et al. 2011; Effgen et al. 2014b; Goldstein 2012).

The military relevance of determining a working threshold for blast-induced functional deficits is to enhance military training safety, as well as improve helmet technology. Current helmets are better designed for protection against penetrating modes of blast, and less so against impact or inertially-driven injuries. If primary blast injury mechanisms prove to be substantial in the injury cascade, knowledge of an injury threshold will better inform helmet designers moving forward.

Electrophysiological activity within the OHSC was recorded using 60-channel MEAs (8×8 electrode grid without the corners, 30 μ m electrode diameter, 200 μ m electrode spacing) at either 1 hour, 1 day, 2 days, 4 days, 6 days, or 10 days following blast injury (60MEA200/30iR-Ti-gr, Multi-Channel Systems, Reutlingen, Germany) (Effgen et al. 2014b; Vogel III et al. 2016). The MEAs were prepared and slices were placed onto the arrays as previously described (Effgen et al. 2014b; Vogel III et al. 2016). OHSCs were perfused with artificial cerebral spinal fluid (norm-aCSF) containing 125 mM NaCl, 3.5 mM KCl, 26 mM NaHCO₃, 1.2 mM KH₂PO₄, 2.4 mM CaCl₂, 1.3 mM MgCl₂, 10mM 4-(2-hydroxyethyl)-1-piperazineethanesulfonic acid (HEPES), and 10 mM glucose (pH = 7.40), which was bubbled with 5% CO₂/95% O₂ and warmed to 37°C, as previously described (Yu and Morrison III 2010). Recordings were acquired with an MEA1060-BC amplifier and data acquisition system (Multi-Channel Systems).

Primary blast exposure minimally alters spontaneous event activity: Spontaneous recording were evaluated for three different measures: event rate (Hz, **Error! Reference source not found.A**), event magnitude (μ V, **Error! Reference source not found.B**), and event duration (ms, **Error! Reference source not found.C**). In the case of event rate and event magnitude, both measures tended to decrease with increased blast exposure. However, neither of the two measures reached significance. Event duration had no distinguishable trend with blast exposure. We conducted a principal component analysis (PCA, **Error! Reference source not found.D**), which attempted to reveal variance that may exist internally within each of these measures (rate, magnitude, and duration) and further help identify blast induced changes. However, when looking at the first principal component (PC1), which captured over 95% of the overall variance, there were no significant changes. This data is important because it supports that primary blast does not affect the ability of neurons to fire spontaneously, suggesting the deficits in LTP and synchrony were not due to an inability of blasted

cultures to fire action potentials. Instead, the molecular mechanisms required for LTP must be disrupted.

Primary blast exposure minimally altered stimulus-response evoked recordings:

To measure evoked responses, stimulation was delivered to either the mossy fiber or Schaffer collateral regions of the hippocampus and the response was recorded from all other electrodes simultaneously. To generate stimulus response curves, two rounds of stimuli of 20 rectangular current pulses delivered 10 s apart with each pulse incrementally increasing from 0-200 μA in 10 μA steps were applied to either mossy fibers (MF) or Schaffer collaterals (SC). The response was measured as the peak to peak magnitude and plotted versus the stimulus intensity. S/R data was compiled and fit to a sigmoidal function using a custom analysis algorithm operated through MATLAB (Mathworks, Natick, MA). Three parameters were measured from this fit: I_{50} , R_{\max} , and m (Figure 78) (Yu and Morrison 2010).

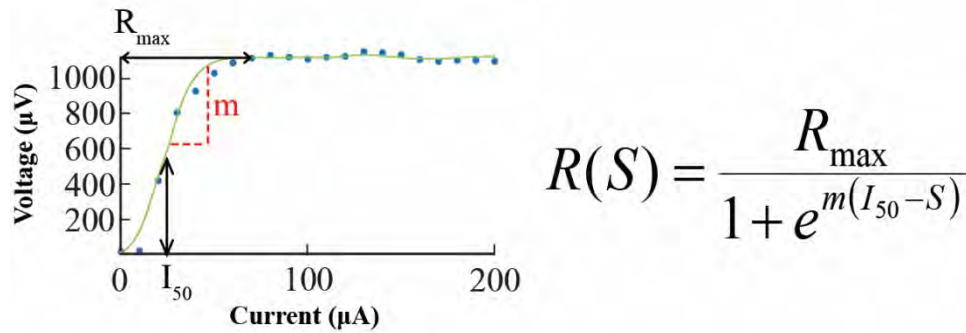


Figure 78 Analyzed stimulus-response curve for a sample electrode and the associated equation used to fit R_{\max} , I_{50} , and m parameters. R_{\max} represents the maximum response read by the electrode. I_{50} represents the current necessary to generate a half-maximal response. The parameter m represents the slope of the sigmoidal curve of the S/R relationship, which reflects the uniformity of excitability.

I_{50} is a measure of the current necessary to evoke a half-maximal response from the tissue slice, which also represents excitability. R_{\max} is a measure of the maximal response from the tissue during stimulation, physiologically is proportional to the number of neurons firing. The slope of the sigmoidal curve of the S/R relationship is quantified as m and can be thought of as the uniformity in excitability of the stimulated neurons [Yu et. al., 2010]. These parameters were evaluated in all regions of interest following stimulation across the mossy fiber (MF) or SC pathways. For MF stimulation (Figure 79), we found that only a Level 4 blast caused a significant change in m (Figure 79C) within the DG and CA3 regions. Level 9 exposure reduced m , however it was not significant. We also performed a PCA using R_{\max} , I_{50} and m as input variables and found the first principal component decreased (Figure 79D) following level 4 and level 9 blast exposures, but the changes were not significant.

For SC stimulation (Figure 80), we found that only a Level 9 blast caused a significant change in R_{\max} (Figure 80A), within the DG, and in I_{50} (Figure 80B), within the CA3. A principal component analysis found the first principal component significantly decreased (Figure 80D) following level 9 blast exposure in the DG, but the decreases in the CA3 and CA1 were not significant.

Taken together, these data are scientifically important because they data demonstrate that there are subtle changes in simple evoked function within hippocampal slices occurring around the Level 4 threshold; however, the SR protocol does not have the high level of sensitivity to detect functional changes previously demonstrated with LTP.

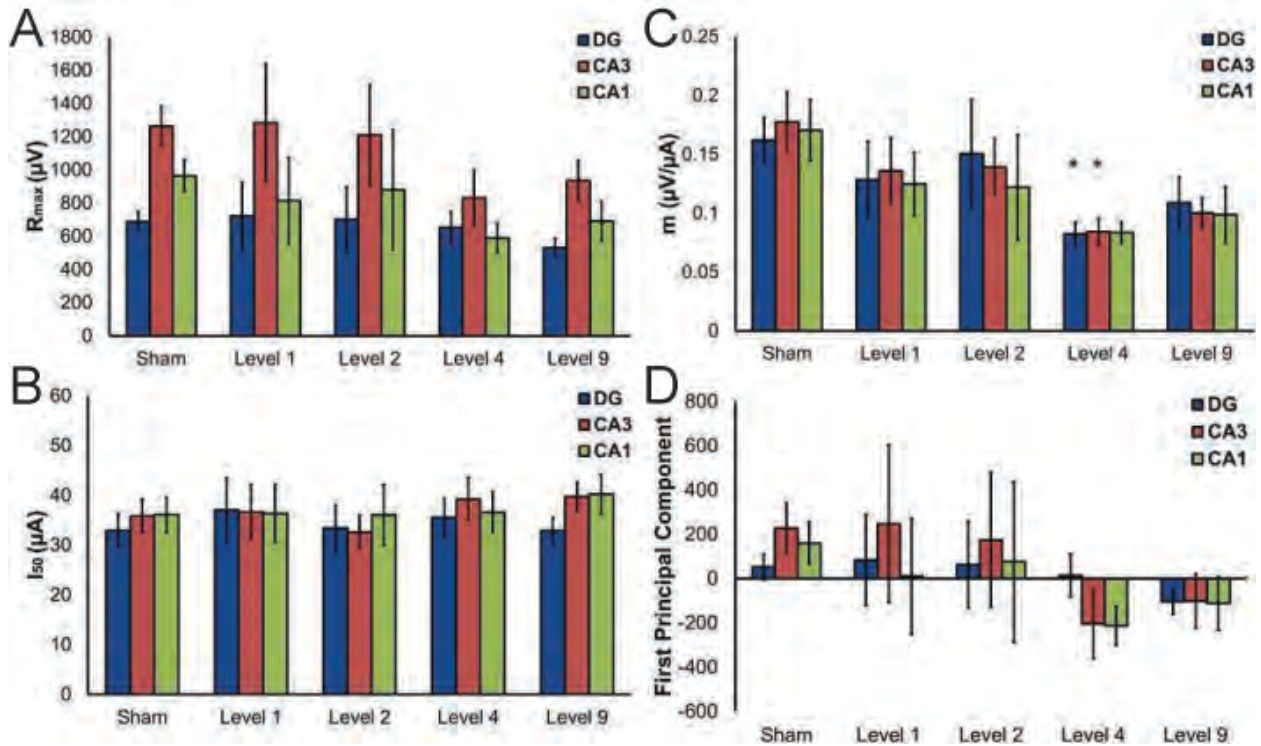


Figure 79 Primary blast exposure minimally altered stimulus-response evoked recordings when stimulating across the MF pathway. A) There was no change in R_{max} as a result of primary blast injury. B) There was no change in I_{50} as a result of primary blast. C) Blast injury (Level 4) significantly decreased the parameter m within the DG and CA3 regions. Level 9 exposure decreased m , however it was not significant. D) Level 4 and 9 blast exposures decreased the first principal component of the PCA, however they were not significant. (* $p < 0.05$; \pm SEM; $n \geq 5$ slices)

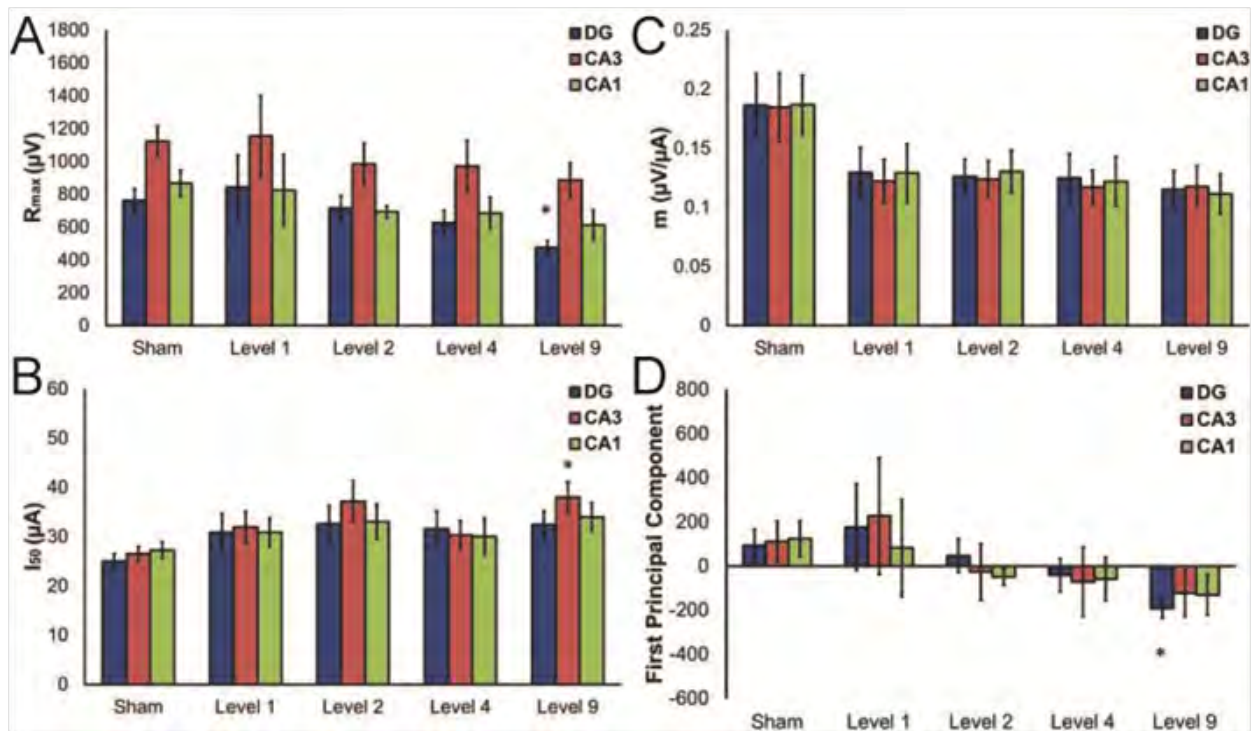


Figure 80 Primary blast exposure minimally altered stimulus-response evoked recordings when stimulating across the SC pathway. A) Level 9 blast exposure significantly decreased R_{max} within the DG only. B) Level 9 blast exposure significantly increased I_{50} within the CA3 only. C) Blast injury decreased the parameter m within across all blast levels, however it was not significant. D) Level 9 blast exposure significantly decreased the first principal component of the PCA within the DG, but the changes in CA3 and CA1 were not significant. (* $p < 0.05$; \pm SEM; $n \geq 5$ slices)

Primary blast exposure did not alter paired-pulse response: We also studied paired-pulse (PP) response, where two successive I_{50} current stimuli were injected into the slice, while increasing the inter-stimulus interval (ISI) with each sweep. We measured the effect of primary blast on the ratio between the peak-to-peak magnitudes of the second response to the first response. Paired pulse ratio (PPR) was measured in all regions of interest following stimulation across the mossy fiber (MF) or SC pathways. Previous studies have demonstrated that the ISIs can be divided into four different temporal bins based on their physiological response: Short-term (25ms), Early-mid (35, 50, 70, 100ms), Late-mid (140, 200, 300, 500ms) and Long-term (1000, 2000ms). For MF stimulation (Figure 81), we found no significant changes as a result of primary blast exposure in any regions across any temporal bin. We also performed a PCA using each bin as the input variables and found no significant changes within the first principal component (Figure 81D) following level 4 and level 9 blast exposures, but the changes were not significant. For SC stimulation (Figure 82), we again found no significant changes in any temporal bins or the PCA as a result of primary blast. This data demonstrates that the specific mechanisms involved with PP response were not significantly altered by primary blast.

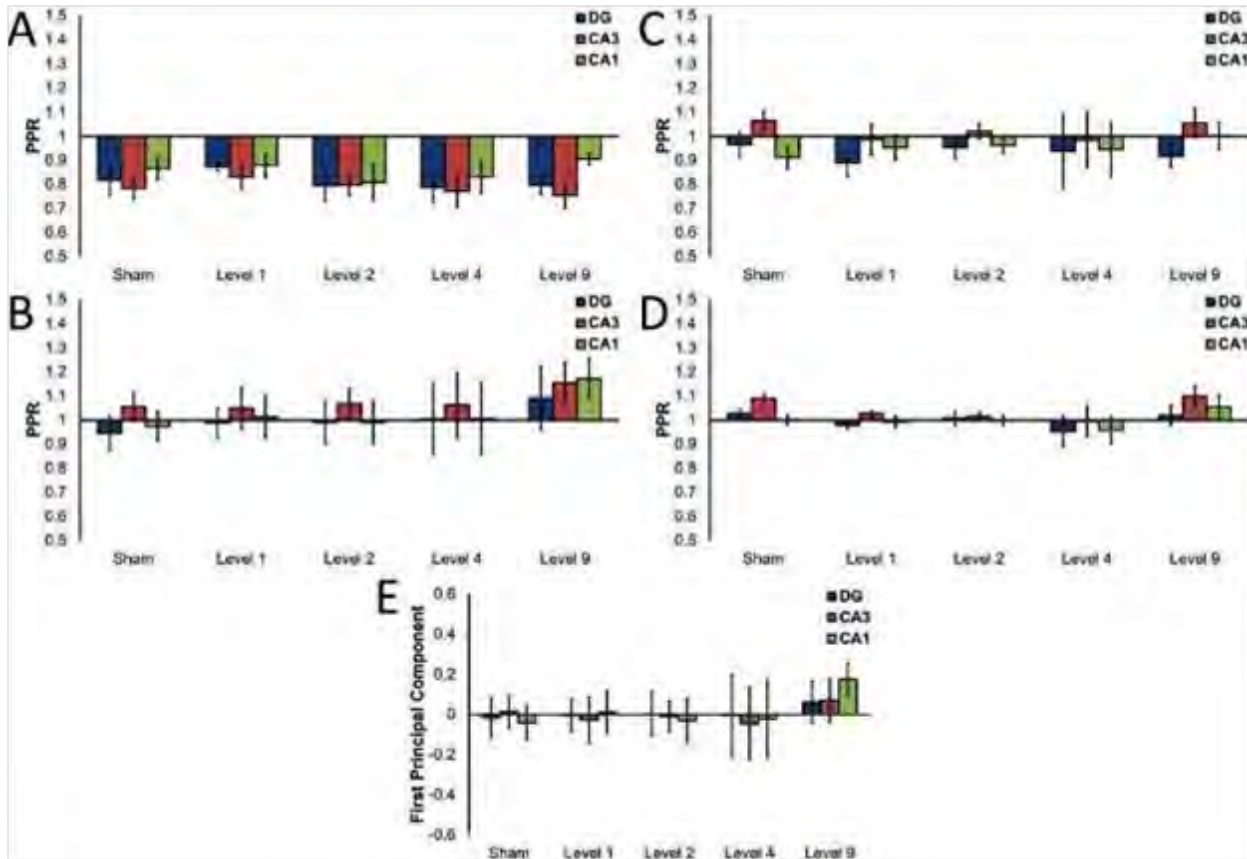


Figure 8 | Primary blast exposure did not affect paired-pulse response when stimulating across the MF pathway. A) Short-term (ISI = 25ms) paired-pulse ratios did not change with increased blast exposure. B) Level 9 blast exposure increased PPRs for the early-mid temporal bin (35, 50, 70, 100ms); however these changes were not significant. C) Blast exposure did not affect late-mid (140, 200, 300, 500ms) PPRs. D) Long-term (1000, 2000ms) paired-pulse ratios did not change with increased blast exposure. E) Level 9 blast exposure increased the first principal component in the CA1 during the long-term (1000, 2000ms) temporal bin; however the changes were not significant. (\pm SEM; $n \geq 5$ slices)

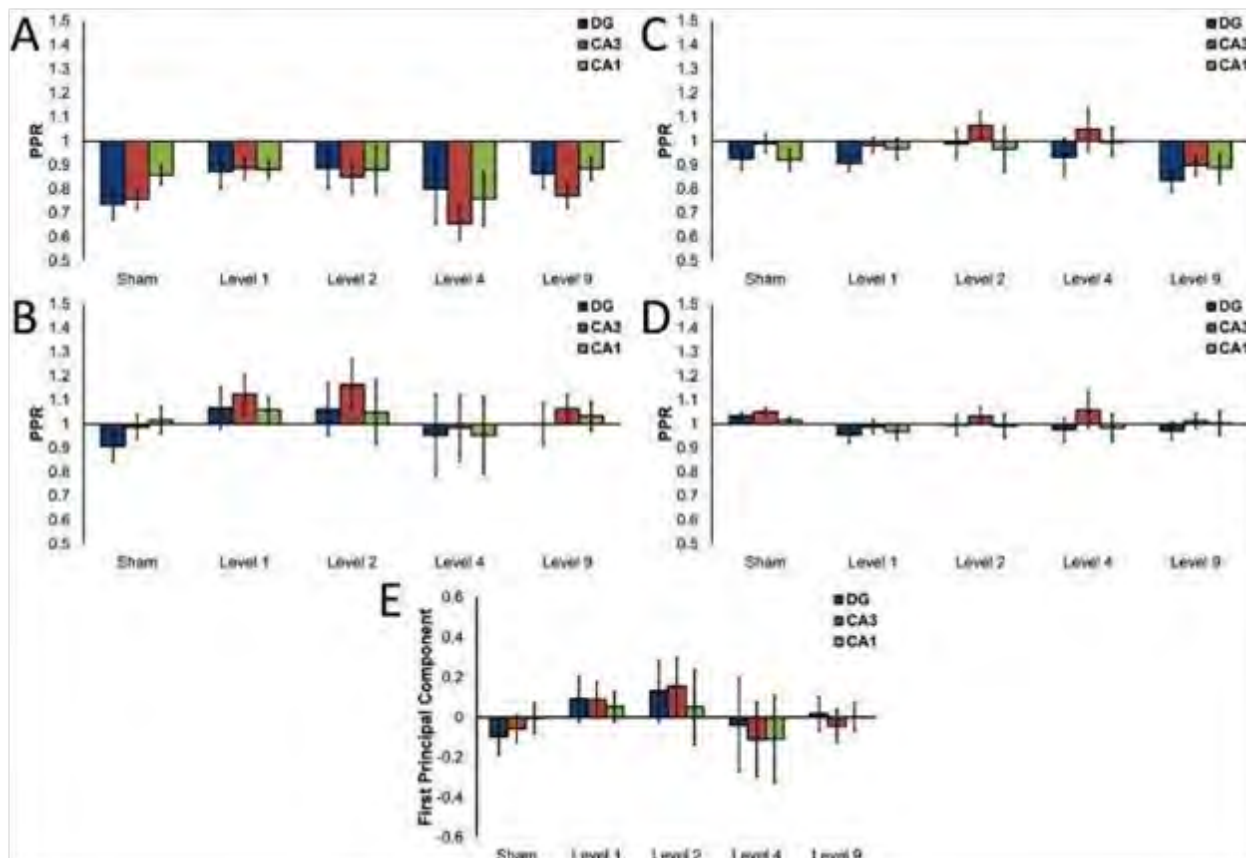


Figure 82 Primary blast exposure did not affect paired-pulse response when stimulating across the SC pathway. A) Short-term (ISI = 25ms) paired-pulse ratios did not change with increased blast exposure. B) Early-mid temporal bin (35, 50, 70, 100ms) did not change with increased blast exposure. C) Blast exposure did not affect late-mid (140, 200, 300, 500ms) PPRs. D) Long-term (1000, 2000ms) paired-pulse ratios did not change with increased blast exposure. E) Blast exposure did not affect the first principal component during the long-term (1000, 2000ms) temporal bin. (\pm SEM; $n \geq 5$ slices)

Long-term Potentiation

Following SR evaluation, the ability to induce long-term potentiation (LTP) was measured. Baseline response was evoked by stimulating at I_{50} once every minute for 30 minutes. LTP was then induced by stimulating across the SC pathway with a high frequency stimulus, which consisted of three trains of 100 Hz pulses applied for 1 second at I_{50} , with each train separated by 10 seconds (Hu et al. 2007; Swant and Wagner 2006). Immediately following LTP induction, post-LTP responses were evoked by stimulating at I_{50} once every minute for 60 minutes. LTP induction was calculated as percent potentiation above baseline based on the last 10 minutes of recording in each recording window. To ensure only stable responses were included for analysis, electrodes were discounted if the coefficient of variance (pre or post-induction) was greater than 20% (Heuschkel et al. 2002). LTP induction was averaged among electrodes within the CA1 and analyzed by ANOVA followed by Dunnett post hoc tests with statistical significance set as $p < 0.05$, as compared to time-matched shams (SPSS v22, IBM).

Primary blast exposure completely erased long-term potentiation: OHSC were exposed to a single primary blast of varying intensity (Figure 73) and functional changes were measured 4-6 days following injury using a microelectrode array (MEA). Long-term potentiation (LTP) was

induced using a high-frequency (100Hz) stimulation protocol (Figure 83). Potentiation was measured in the CA1 following stimulation across the Schaffer collateral (SC) pathway at one hour post-induction. Level 4 and Level 9 blast injury significantly ($p < 0.05$) reduced potentiation to $-0.7 \pm 12.7\%$ and $-1.9 \pm 10.4\%$, respectively. Sham ($50.0 \pm 8.6\%$) and Level 1 blast exposure groups ($41.4 \pm 15.3\%$) had potentiation similar to levels found in literature (D'Ambrosio et al. 1998). Level 2 blast exposure reduced potentiation ($17.6 \pm 8.8\%$), however it was not significant. This data demonstrates the presence of primary blast threshold for functional changes between 39 and 87 kPa-ms impulse.

These data are scientifically important because blast is capable of disrupting complex electrophysiological function of the brain like learning without affecting simpler measures of activity (described below). These data are especially important because they show that it is possible to reproduce in an in vitro model the subtle deficits reported by military personnel after blast exposure, including difficulties with learning and memory.

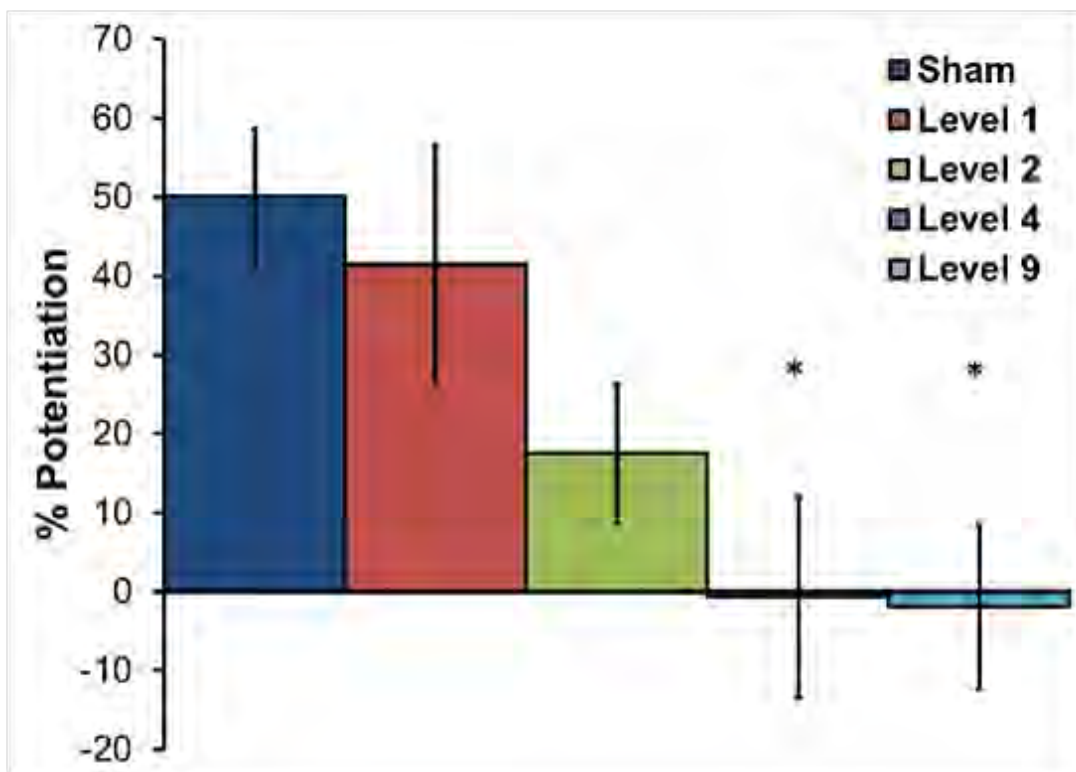


Figure 83 Primary blast exposure erased long-term potentiation in OHSC. Level 4 and 9 blasts significantly decreased potentiation ($-0.7 \pm 12.7\%$ & $-1.9 \pm 10.4\%$, respectively), as compared to sham exposure ($50.0 \pm 8.6\%$). Level 1 ($41.4 \pm 15.3\%$) and 2 ($17.6 \pm 8.8\%$) blasts were decreased, but were not significantly changed. (* $p < 0.05$; \pm SEM; $n \geq 5$ slices)

Primary blast exposure disrupts global synchronization within OHSC: Four to six days following exposure, spontaneous activity was recorded within the OHSC for three minutes. Field potential events were identified in each electrode over the course of the recording. Spontaneous network synchronization was quantified using previously published methods based on correlation matrix analysis and surrogate resampling for significance testing (Li et al. 2007; Li et al. 2010; Patel et al. 2012). Similar to the LTP data, Level 4 and 9 blast exposures caused a significant decrease (Figure 84) in global synchronization index (0.047 ± 0.025 & 0.052 ± 0.022 , respectively), as compared to sham exposure (0.212 ± 0.033). Again, Level 1 (0.241 ± 0.086) and 2 (0.178 ± 0.075) blast exposures did not

significantly change global synchronization index. Similar to the LTP data, a functional injury threshold exists between 39 kPa-ms and 87 kPa-ms impulse. Previous research into hippocampal global synchronization changes following inertial injury proposed that alterations in K⁺-Cl⁻ co-transporters (namely KCC2 and NKCC1) may be the root cause [Kang et. al., 2014]. These possibilities will be explored in the upcoming year.

These data are scientifically important because they show that our in vitro model is capable of reproducing deficits in subtle neuronal function, similar to subtle deficits reported by military personnel exposed to blast. Synchronization is thought to underlie many higher order behaviors including memory encoding and retrieval, which our results suggest is impaired after primary blast.

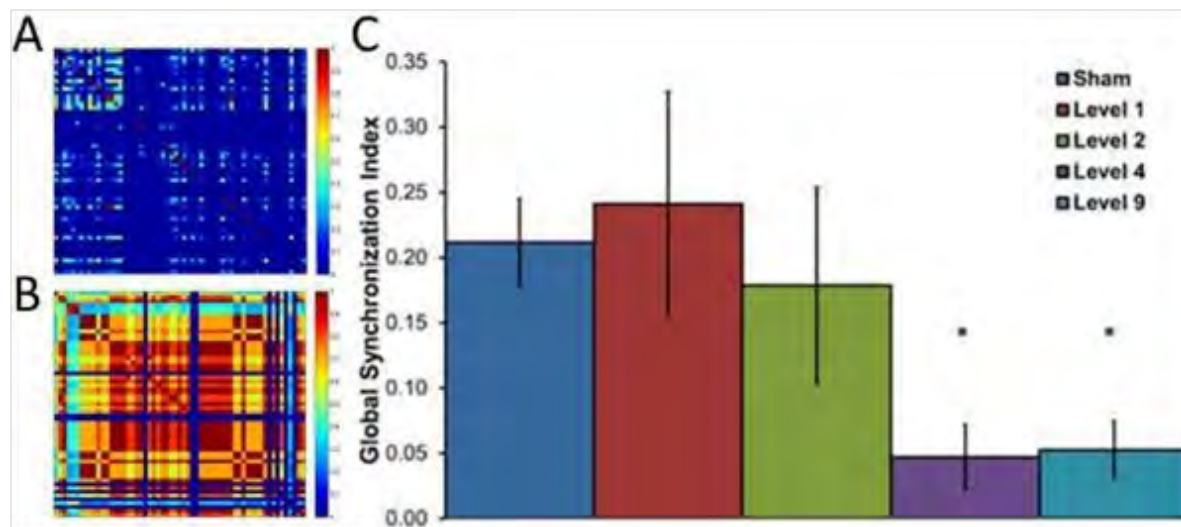


Figure 84 Primary blast exposure significantly decreased global synchronization index (GSI) across OHSC. A) A sample heat map showing correlation scores between each electrode pair in a poorly synchronized slice. These correlation scores would be analyzed in combination with surrogate resampling for significance testing in order to determine GSI. The color bar ranges from more correlated (1, red) to less correlated (0, blue). B) A sample heat map showing correlation scores between each electrode pair in a highly synchronized slice. C) Level 4 and 9 blasts significantly decreased GSI (0.047 ± 0.025 & 0.052 ± 0.022 , respectively), as compared to sham exposure (0.212 ± 0.033). Level 1 (0.241 ± 0.086) and 2 (0.178 ± 0.075) blasts were decreased, but were not significantly changed. (* $p < 0.05$; \pm SEM; $n \geq 7$ slices)

Chemically-induced LTP (chemLTP)

In separate sets of cultures, LTP was chemically induced with two distinct protocols. Baseline electrical activity was recorded for 30 minutes as above. The first chemLTP protocol replaced electrical LTP induction with a 3 minute perfusion with a modified aCSF solution (gly-aCSF) (Lu et al. 2001): norm-aCSF containing 200 μ M glycine and 0 mM MgCl (reduced from 1.3mM). The perfusate was then switched back to norm-aCSF and washed out for 20 minutes prior to post-induction electrical stimulation. Percent potentiation was calculated by comparing the average of the final 10 minutes of post-induction responses to the average of the final 10 minutes of pre-induction responses, as above. The gly-aCSF solution activates synaptic N-methyl-D-aspartate (NMDA) receptors, allowing Ca²⁺ ions to enter the dendritic spine, similar to electrically-induced LTP (Lu et al. 2001).

The second chemLTP protocol replaced electrical LTP induction with a 20 minute perfusion with a modified aCSF solution (cAMP-aCSF) (Otmakhov et al. 2004): norm-aCSF containing 1 mM MgCl

(reduced from 1.3mM), 50 μ M forskolin, 50 μ M picrotoxin, and 100 nM rolipram. Forskolin, rolipram, and picrotoxin stocks were dissolved in dimethyl sulfoxide (DMSO) with a final DMSO concentration in cAMP-aCSF of 0.07%. The perfusate was then switched back to norm-aCSF and washed out for 20 minutes prior to post-induction stimulation for 60 minutes. Percent potentiation was calculated as above. The cAMP-aCSF solution acts to upregulate the cAMP-PKA pathway through inhibition of phosphodiesterase-4 (rolipram) and activation of adenylate cyclase (forskolin), which results in elevated cAMP levels and consequently PKA activation (Otmakhov et al. 2004) [ENREF 13](#). Picrotoxin, a GABA_A inhibitor, reduced inhibition and enhanced stability of the potentiated signal, while not inducing LTP on its own (Otmakhov et al. 2004).

Chemically-induced LTP was averaged among electrodes within the CA1 and analyzed by ANOVA followed by Dunnett *post hoc* tests with statistical significance set as $p < 0.05$, as compared to time-matched shams (SPSS v22, IBM).

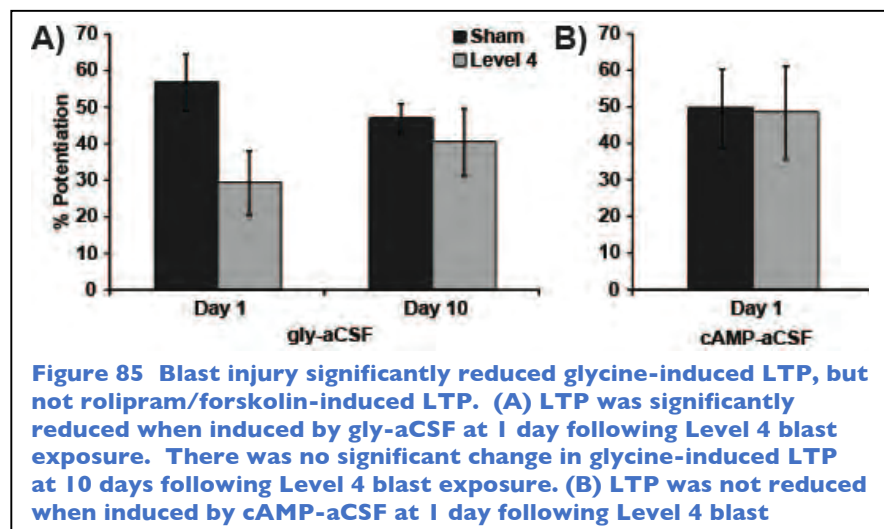
Primary blast exposure reduced potentiation when induced with gly-aCSF

To further explore blast-induced deficits in LTP, we investigated the effect of blast injury on chemical induction of LTP using gly-aCSF. We observed that potentiation (Figure 85A) was significantly reduced in Level 4 blast-exposed cultures measured at 1 day after injury when induced with gly-aCSF. When measured at 10 days following Level 4 blast exposure, gly-aCSF-induced potentiation (Figure 85A) recovered and was not significantly different from time-matched, sham-exposed cultures. These findings matched the time course of blast-induced LTP deficits when induced electrically. To verify that the shorter treatment duration with gly-aCSF did not confound results, we extended gly-aCSF treatment from 3 to 20 minutes and observed that Level 4 blast exposure significantly decreased potentiation ($27 \pm 13\%$) as compared to sham ($78 \pm 15\%$) exposure (data not shown).

Primary blast exposure did not reduce potentiation when induced with cAMP-aCSF

In contrast, potentiation (Figure 85B) was not significantly reduced at 1 day following a Level 4 blast exposure using a chemLTP induction protocol that upregulated the cAMP/PKA pathway (cAMP-aCSF). To

verify the extended treatment duration with cAMP-aCSF did not confound results, we shortened cAMP-aCSF treatment from 20 to 3 minutes and observed that blast exposure did not significantly reduce potentiation ($48 \pm 11\%$) as compared to sham ($42 \pm 17\%$) exposure (data not shown). These results suggested that modulation of the cAMP/PKA pathway may act therapeutically against primary blast-induced LTP loss.



Western Blotting

For each condition tested by western blotting, 8 slices from 2 different animals were collected for protein extraction. Groups receiving chemLTP induction (gly-aCSF or cAMP-aCSF) were treated, switched back to normal aCSF after respective treatment times, incubated for appropriate induction times, and then lysed. Slices were rinsed twice with ice-cold PBS and immediately placed in chilled lysis buffer A (40 mM HEPES, 120 mM NaCl, 1 mM EDTA, 1% Triton X-100, 10 mM sodium pyrophosphate, 50 mM sodium fluoride, 0.5 mM sodium orthovanadate, 10 mM β -glycerophosphate, Sigma). Samples were sonicated (Sonicator 3000, Misonix, NY, USA), incubated on ice and then centrifuged to remove cellular debris. Protein concentrations were determined by the bicinchoninic acid assay (BCA) according to the manufacturer's instructions (Thermo Fisher Scientific, Waltham, MA, USA), and 50 μ g of protein per sample were loaded in a 4-12% Bis-Tris gel (Life Technologies). Proteins were separated by electrophoresis (150V, 1.5h) and transferred (100mA, 40mins) to a nitrocellulose membrane (Life Technologies) using a semi-dry apparatus (Fisher Scientific, NY, USA). The membrane was blocked in Tris-buffered saline (TBS, pH 7.4) with 1% bovine serum albumin (BSA) for 1 hour. Membranes were incubated overnight at 4°C with primary antibodies (total GluRI [Millipore, #04-855], phosphorylated GluRI-Ser⁸³¹ [Millipore, #04-823], phosphorylated GluRI-Ser⁸⁴⁵ [Millipore, #04-1073], total CaMKII [Sigma, #SAB4503250], phosphorylated CaMKII-Thr²⁸⁶ [Abcam, #ab5683], total NMDA NR2B [Millipore, MAB5778], total PSD-95 [Thermo Fisher, MA1-046], phosphorylated stargazin-Ser239/240 [Millipore, AB3713], β -actin [Sigma, #A1978]) in TBS with Tween (TBS-T, 0.1% Tween-20, pH 7.4) and 0.25% BSA. Following the primary antibody incubation, membranes were washed 3 x 10 min in TBS-T. To detect protein bands, the membranes were labeled with a corresponding secondary antibody (Donkey anti-Rabbit Alexa Fluor 488 or Goat anti-Mouse Alexa Fluor 647, Life Technologies). Fluorescence was detected using a CRi Maestro 2 Imaging System (Perkin Elmer). The bands were quantified using ImageJ software. Average fluorescence was quantified from, at minimum, 4 lysates per exposure group (8 slices per lane, 32 slices in total) and analyzed by ANOVA with statistical significance set as $p < 0.05$, as compared to treatment-matched shams (SPSS v22, IBM). A post-hoc Bonferroni analysis revealed statistical significant differences between injury-matched treatments for each antibody, with significance set as $p < 0.05$.

Phosphorylated GluRI-Ser831 and total GluRI expression was significantly reduced by primary blast injury

Blast prevented a significant increase in phosphorylation of AMPAR-GluRI subunits at the Serine-831 site at 24 hours post-injury as compared to shams, when LTP was induced with gly-aCSF (Figure 86A). There was no observed effect of blast with vehicle-treated cultures or with the cAMP-aCSF treatment. Treatment with either gly-aCSF or cAMP-aCSF significantly increased GluRI-Ser831 phosphorylation over vehicle-treated sham cultures, i.e. no induction of LTP; however, only cAMP-aCSF significantly increased GluRI-Ser831 phosphorylation over vehicle-treated blast-cultures.

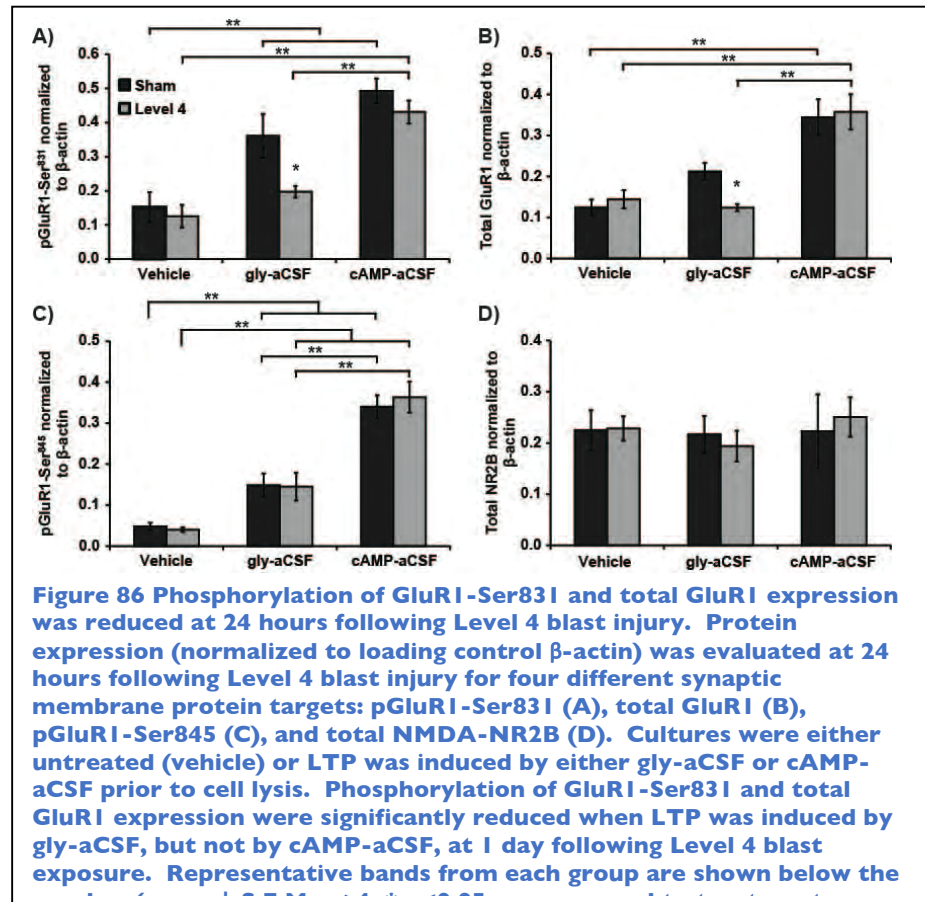
Blast also significantly decreased the expression of total GluRI subunits (Figure 86B) as compared to shams, when LTP was induced with gly-aCSF. Although this deficit was not observed with vehicle-treated cultures or with the cAMP-aCSF treatment, it is important to note that there was an increase in total GluRI expression for both sham and blast-exposed cultures receiving cAMP-aCSF treatment, as compared to the vehicle-treated cultures.

We observed no significant change in the phosphorylation state of AMPAR-GluRI subunits at the Serine-845 site (Figure 86C) between blast and sham cultures for any chemical treatment; however, both chemical treatments significantly increased GluRI-Ser845 phosphorylation over vehicle treated cultures. There also was no significant change to NMDAR-NR2B subunits (Figure 86D) as a result of either injury exposure or chemical treatment.

Primary blast injury did not affect total CaMKII nor phosphorylated CaMKII-Thr286

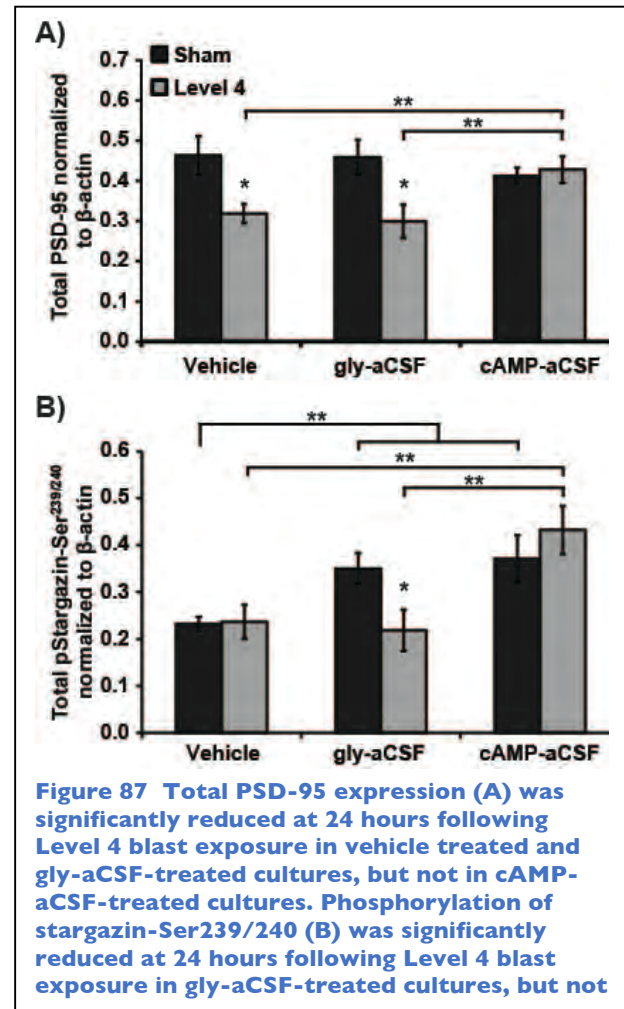
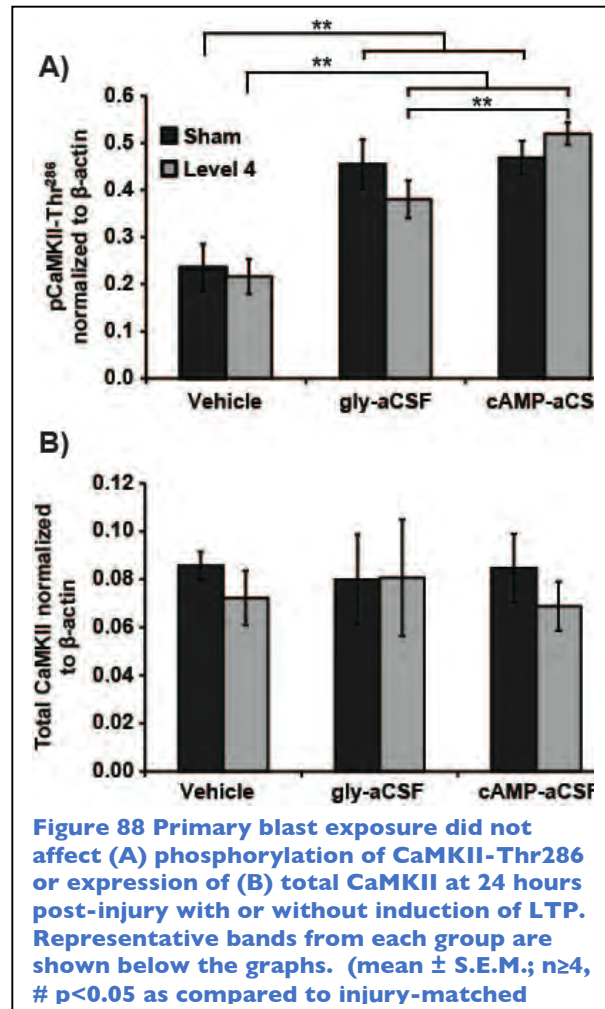
Another important target in the LTP pathway is CaMKII as CaMKII phosphorylation is necessary for the induction of some forms of LTP (Bliss and Collingridge 1993; Mayford et al. 1995; Sanhueza et al. 2011). We observed that phosphorylation of CaMKII at the Threonine-286 (Thr-286) site was not affected by injury (Figure 88A). There was an expected increase in phosphorylation with both chemLTP treatments. We also observed that total expression of CaMKII (Figure 88B) was not altered as a result of injury ($p > 0.33$) or chemical treatment ($p = 1.0$).

Primary blast injury significantly reduced PSD-95 and pStargazin-Ser239/240



We also examined two key proteins responsible for receptor integration at the synapse: PSD-95 and stargazin. We found that blast decreased expression of total PSD-95 for both vehicle and gly-aCSF treated cultures as compared to shams, but not for cAMP-aCSF treated cultures (Figure 87A). We observed that blast exposure reduced the phosphorylation of stargazin (Ser239/240) after gly-aCSF treatment, but not for vehicle or cAMP-aCSF treated cultures (Figure 87B).

Roflumilast Treatment

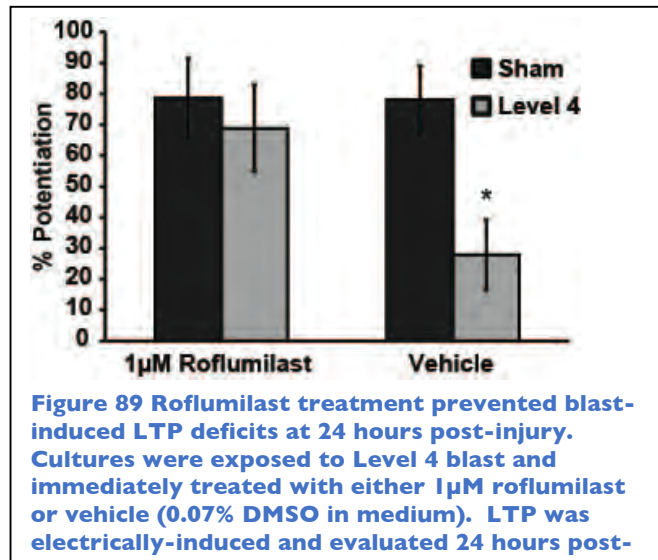


The intracellular levels of cAMP are controlled by a balance between reactions that produce cAMP and those that degrade cAMP. Phosphodiesterases-4 (PDE4) is an enzyme that specifically degrades cAMP. To test the ability of a PDE4 inhibitor to rescue LTP after blast exposure, 1 μ M Roflumilast (SML1099, Sigma-Aldrich; dissolved in 0.07% DMSO) in full serum media was delivered to sham and Level 4-exposed cultures immediately after blast exposure. For comparison, DMSO vehicle was also delivered to a second set of cultures that had received either sham or Level 4 blast exposure. The cultures' ability to generate LTP through high frequency electrical stimulation was evaluated at 24 hours post-exposure. Potentiation was averaged in CA1 region of the hippocampus and analyzed by ANOVA with statistical significance set as $p < 0.05$, as compared to similarly-treated shams.

Roflumilast treatment immediately following exposure prevented blast-induced LTP deficits

Roflumilast treatment immediately following blast exposure prevented a deficit in electrically-induced LTP at 24 hours post-injury (Figure 89). Level 4 blasted cultures that were treated with vehicle (0.07% DMSO in aCSF) immediately following injury were unable to potentiate at 24 hours post-exposure, as compared to sham-vehicle treated cultures. This indicated that PDE4 inhibitors have the potential to prevent primary blast-induced LTP loss.

[C4] We evaluate if acute alterations in circuit behavior recover over time, and therefore define the blast conditions (number & severity) to cause persisting changes in neural circuit function and cell death.



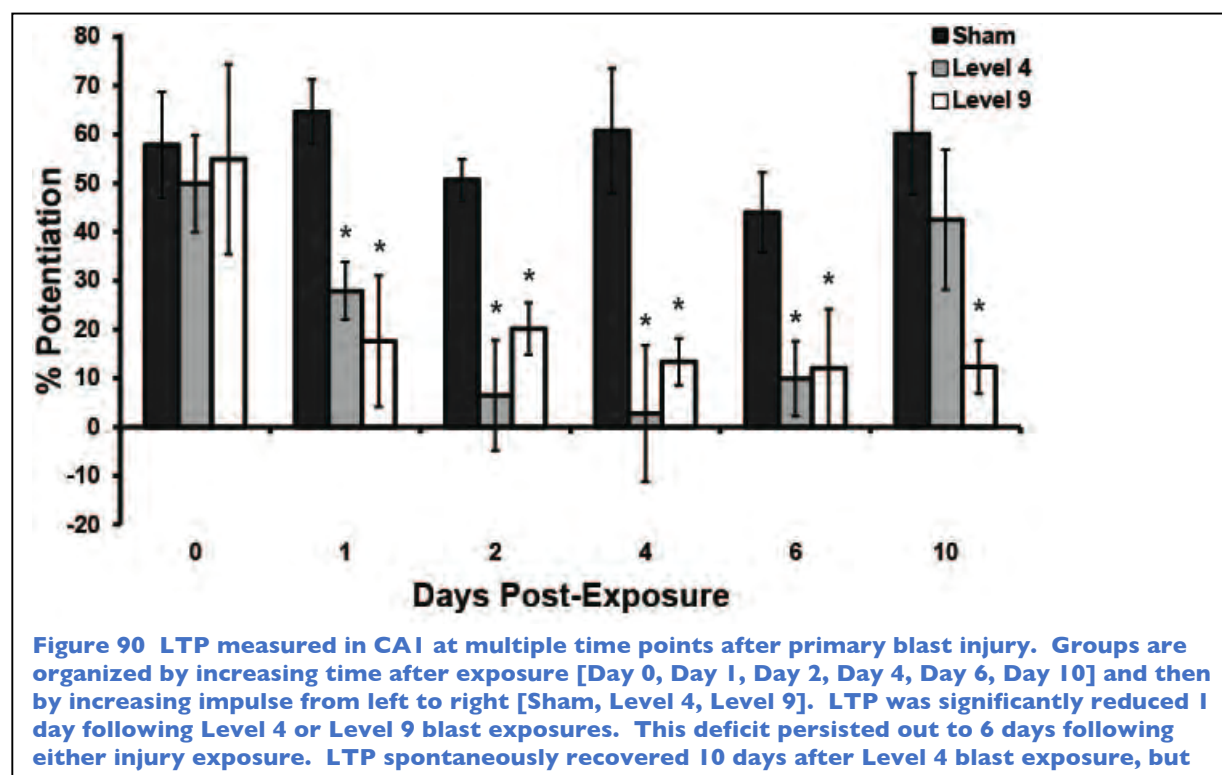
LTP deficits after blast were delayed and recovery was severity dependent

OHSC were exposed to a single blast of either mild (Level 4) or moderate (Level 9) severity and LTP was induced using a high-frequency (100 Hz) stimulation protocol at various time points following injury: 60 minutes (Day 0), 1 day, 2 days, 4 days, 6 days, or 10 days. Cell death remained minimal at all time points after injury, which agreed with previous studies using this injury model (data not shown). Potentiation was measured in CA1 following stimulation across the Schaffer collateral (SC) pathway at one hour post-induction. Neither blast level significantly reduced potentiation at 1 hour post injury. However, both blast intensities induced significant ($p < 0.05$) deficits in potentiation (Level 9: $17.6 \pm 13.5\%$; Level 4: $27.9 \pm 5.9\%$) at 1 day post-injury, as compared to sham ($64.6 \pm 6.6\%$). This deficit persisted out to 6 days following both blast exposure levels. At 10 days post-injury, potentiation remained significantly depressed ($12.3 \pm 5.5\%$) for Level 9 injured cultures; however, Level 4 injured cultures were able to partially recover ($42.5 \pm 14.4\%$), as compared to sham ($60.1 \pm 12.4\%$).

These data are scientifically important for multiple reasons. First, it demonstrates that a therapeutic window may possibly exist during which pharmaceuticals could be administered before functional deficits begin. Second, it demonstrates that an injury threshold exists below which a period of rest after exposure can facilitate spontaneous LTP recovery, but above which the recovery does not occur. Although this temporal history has not been investigated following blast injury, previous studies following non-blast injury have observed spontaneous LTP recovery between 1 and 2 weeks post-injury (Norris and Scheff 2009; Reeves et al. 1995), while others observed no recover out to 8 weeks post-injury (Sanders et al. 2000).

Potentiation (**Error! Reference source not found.**) was not reduced when measured 1 hour (Day 0) after Level 4 or Level 9 blast exposures, as compared to sham. When measured at 24 hours (Day 1) post-blast exposure, potentiation was significantly reduced in cultures exposed to either a Level 4 or Level 9 exposure. This deficit was maintained at Day 2, Day 4, and Day 6 post-Level 4 and Level 9 blast exposure. At 10 days after Level 4 blast, potentiation had partially recovered and was no longer

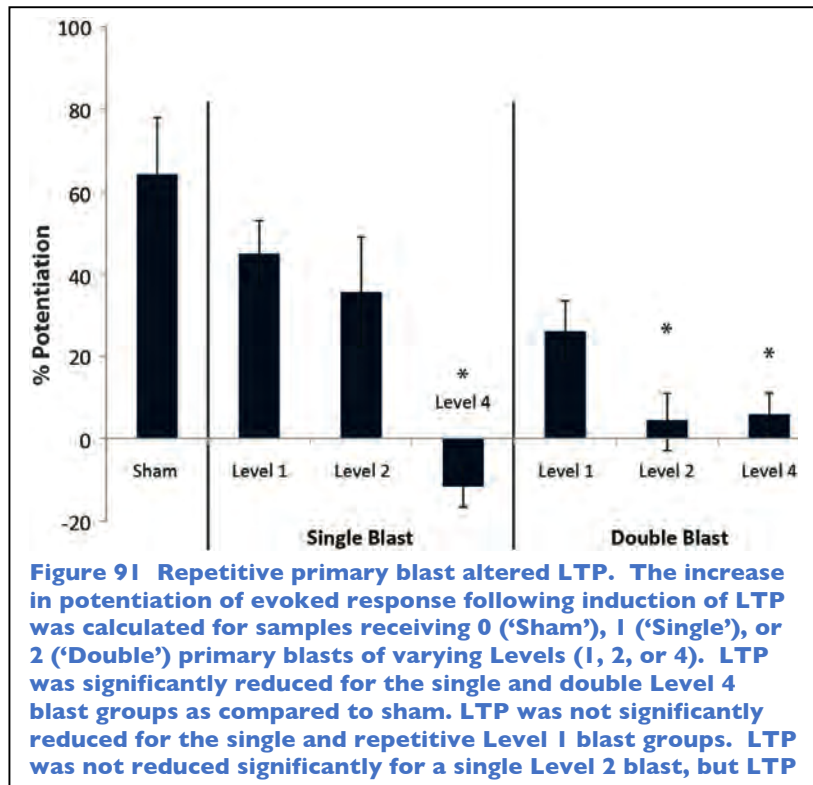
significantly different from time-matched sham-exposed cultures; however, potentiation remained significantly depressed in the Level 9 exposed cultures at the same time point.



Some US service members experience multiple blast exposures while on active duty, including breachers, who have the role of using explosives to break perimeters like locked buildings (Tate et al. 2013). During training, breachers can experience as many as 20 explosive detonations over 5 days of practical training (Tate et al. 2013). Symptoms of repetitive blast have been referred to informally as “breachers brain” and are similar to those of people who have suffered multiple non-blast concussions (DeKosky et al. 2010; Tate et al. 2013).

It has been suggested from experimental models that mimic inertia-driven TBI that an initial mild TBI (mTBI) initiates a period of both increased susceptibility and heightened vulnerability to subsequent brain injury (DeRoss et al. 2002; Giza and Hovda 2001; Guskiewicz et al. 2003; McCrea et al. 2005). Clinical studies suggest that athletes who have had one concussion are at a higher risk for multiple concussions particularly in the same season of play (Guskiewicz et al. 2005; Guskiewicz et al. 2003; Wall et al. 2006). Furthermore, studies suggest multiple concussions result in more significant verbal, memory, and motor deficits than a single concussion (Guskiewicz et al. 2005; Guskiewicz et al. 2003; Matser et al. 1998; Matser et al. 1999; Wall et al. 2006). Potentially the most severe clinical outcome of multiple concussions is the phenomenon termed second impact syndrome (SIS). SIS is a catastrophic brain injury thought to be the result of a second concussion occurring while the patient is symptomatic from an initial concussion (Signoretti et al. 2011).

Experimental models of repetitive blast have been used to investigate the phenomenon of “breachers brain” and synergy from multiple blast exposures. Exposure of mice to single and repetitive complex blast (3 blasts within 30 minutes) with a custom shock tube (142 kPa) resulted in a decline in neuromotor function and reflexes. Deficits in performance of animals receiving multiple blasts were greater and more persistent than that of single blast. Repetitively injured animals also had increased damage to neurons, cell permeability, and cell death (Arun et al. 2012; Wang et al. 2011b).



These studies suggest that repetitive blast exposure results in increased brain injury as noted not only by persistent neuromotor dysfunction but also by neurodegeneration. However, it is still unclear whether or not primary blast alone can result in worse outcomes for soldiers who experience multiple blasts without concomitant head motion.

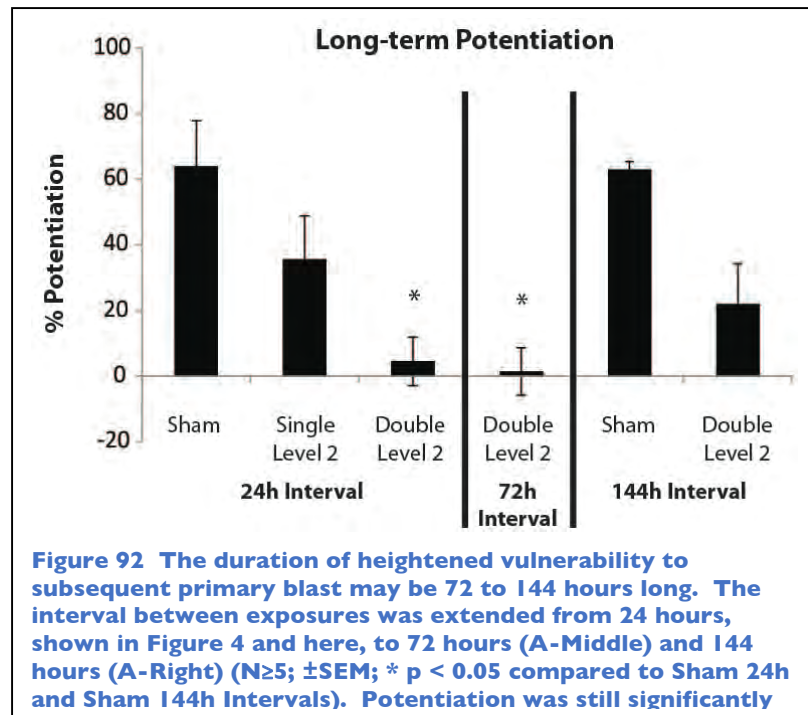
Long-term potentiation was significantly depressed following repetitive primary blast without altering basal evoked response

Potentiation was roughly 64% in the CA1 in sham-injured samples (**Error! Reference source not found.**). LTP decreased, non-significantly, following both a single and double Level 1 primary blast with a 24-hour interval between exposures. LTP was not significantly reduced following a single Level 2 primary blast exposure; whereas it was significantly reduced as compared to sham after two exposures of Level 2 primary blast delivered 24 hours apart. LTP decreased significantly following both a single and double Level 4 primary blast with a 24-hour interval between exposures as compared to the sham.

There were no statistically significant changes in any S-R parameter (I_{50} , R_{max} , m) in any of the three ROI (DG, CA3, CA1) after sham, single, or repetitive Level 2 blast exposures applied with a 24 hour interval between injuries (data not shown).

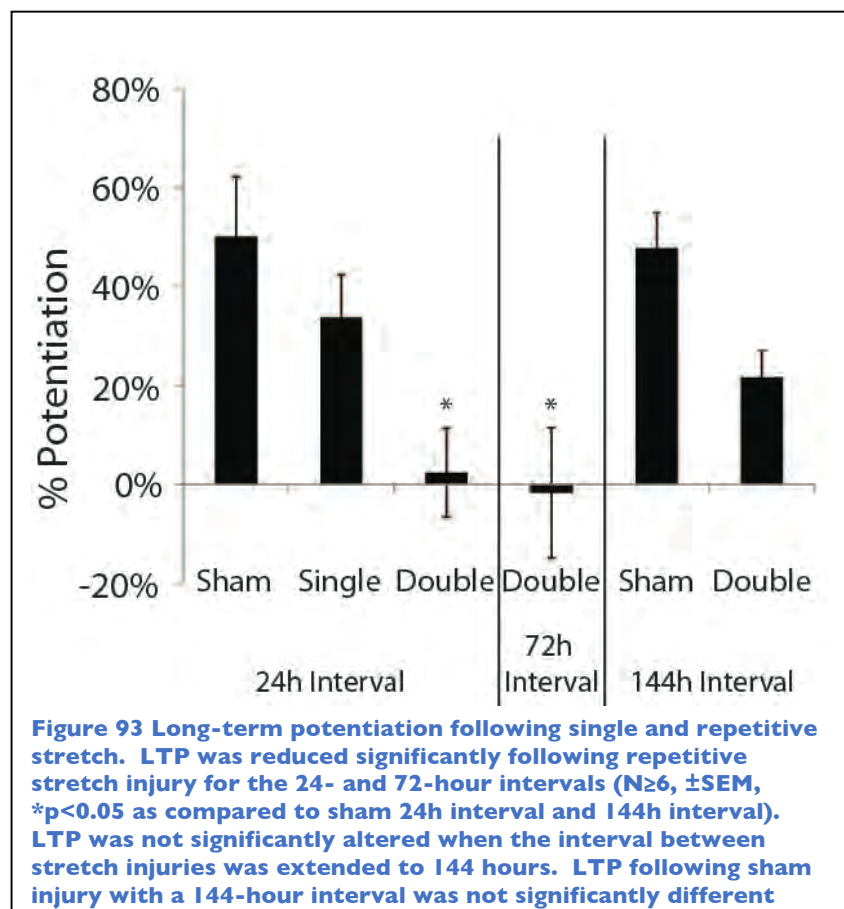
Heightened vulnerability of LTP to subsequent primary blast persisted for at least 72 hours

Increasing the interval to 72 hours did not mitigate the deficit in LTP, which was still significantly depressed by both Level 2 primary blast exposures (Figure 92). When the interval was increased to 144 hours, potentiation was decreased but was not significantly lower than sham from the 24-hour interval study or its own time-matched sham (Figure 92: Sham 144h Interval). LTP was not decreased when the inter-sham interval was extended to 144 hours, indicating that the extended experimental duration did not negatively impact induction of LTP. Similarly, cell death did not increase with the extended duration of the experiment. All samples appeared otherwise healthy with less than 5% cell death in all ROI (data not shown).



Long-term potentiation was more vulnerable to additional injury up to 72 hours following an initial mild stretch.

Potentiation following the sham exposure (24h interval) was over 50% (Figure 93). LTP was not significantly reduced by a single mild stretch injury but was significantly reduced by repetitive mild stretch injury (24h Interval). When the inter-injury interval was extended to 72 hours, LTP was still significantly depressed compared to that of the 24-hour interval sham group. When the inter-injury interval was extended to 144 hours, LTP was no longer significantly reduced as compared to the sham group for the time-matched controls (144h



interval) or shams of the 24-hour interval. Samples that received two sham injuries 144-hours apart did not have significantly different LTP as compared to that the 24-hour interval sham group, suggesting that the extended time course of the experiment was not detrimental to potentiation.

Future Areas of Research

Future work is warranted to assess the mechanism of LTP loss specific to single and repetitive primary blast exposure. Studies to identify the mechanism for LTP loss from primary blast exposure may aid in identifying therapeutic targets to prevent LTP loss and injury from primary blast exposure. Additional studies should explore the therapeutic potential of phosphodiesterase inhibitors to preserve memory function after blast exposure.

In military theater, the soldier may experience a complex combination of primary and tertiary blast exposure. Future studies to investigate more complex loading conditions may be necessary to understand pathologies from complex blast loading. *In vivo* studies of blast exposure deliver both primary and tertiary blast loading to the animal brain, so there is precedent for study of complex blast experimentally. (Goldstein et al. 2012b; Gullotti et al. 2014b; Hue et al. 2015) *In vitro* models of complex blast where primary and tertiary loading can be independently modified may help to understand the interaction of these distinct mechanical stimuli that results in pathology.

Primary blast exposure loads the body prior to tertiary blast exposure. It is possible that an initial primary blast exposure may alter the brain's response to subsequent tertiary blast exposure. Future studies could investigate how primary blast may alter the tolerance of OHSCs to tertiary blast.

Future studies are necessary to identify the biochemical mechanism responsible for heightened vulnerability. Improved understanding of this mechanism will help to identify biomarkers for concussion and heightened vulnerability. These biomarkers can be used to accurately and objectively diagnose mTBI and monitor a patient's recovery through the period of heightened vulnerability. Accurate diagnosis and patient monitoring is essential to remove the injured soldier from active duty to prevent synergistic injury response in the event of additional concussion. Better understanding of this mechanism can also identify targets for therapeutic intervention to prevent injury from multiple concussions.

Given that the findings in this study are limited to the hippocampus, we could replicate these studies for other regions of the brain *in vitro*. Additionally, we could design complex *in vitro* models incorporating the hippocampus and other brain regions and an *in vitro* model of the BBB. We have previously investigated the effect of single and repetitive primary blast exposure on an *in vitro* model of the BBB, (Hue et al. 2014a; Hue et al. 2013c) and we have also generated tolerance criteria of cortical slice cultures to stretch injury. (Elkin and Morrison 2007) The results from these *in vitro* studies could be used to design and interpret results from *in vitro* studies using complex biological tissue explants.

- Abdul-Muneer PM, Schuetz H, Wang F, Skotak M, Jones J, Gorantla S, Zimmerman MC, Chandra N, Haorah J (2013) Induction of oxidative and nitrosative damage leads to cerebrovascular inflammation in an animal model of mild traumatic brain injury induced by primary blast. *Free Radic Biol Med* 60: 282-91
- Adams JH, Graham DI, Gennarelli TA (1981) Acceleration induced head injury in the monkey. II. Neuropathology. *Acta neuropathologica Supplementum* 7: 26-8
- Ahlers ST, Vasserman-Stokes E, Shaughnessy MC, Hall AA, Shear DA, Chavko M, McCarron RM, Stone JR (2012) Assessment of the effects of acute and repeated exposure to blast overpressure in rodents: Toward a greater understanding of blast and the potential ramifications for injury in humans exposed to blast. *Front Neurol* 3: 32
- Arun P, Abu-Taleb R, Valiyaveetil M, Wang Y, Long JB, Nambiar MP (2012) Transient changes in neuronal cell membrane permeability after blast exposure. *Neuroreport* 23: 342-6
- Bass CR, Rafaels KA, Salzar RS (2008) Pulmonary injury risk assessment for short-duration blasts. *J Trauma* 65: 604-15
- Beato M, Arnemann J, Chalepakis G, Slater E, Willmann T (1987) Gene regulation by steroid hormones. *J Steroid Biochem* 27: 9-14
- Beaumont A, Marmarou A, Hayasaki K, Barzo P, Fatouros P, Corwin F, Marmarou C, Dunbar J (2000) The permissive nature of blood brain barrier (bbb) opening in edema formation following traumatic brain injury. *Acta neurochirurgica Supplement* 76: 125-9
- Bliss TVP, Collingridge GL (1993) A synaptic model of memory: Long-term potentiation in the hippocampus. *Nature* 361: 31-39
- Blyth BJ, Farahvar A, He H, Nayak A, Yang C, Shaw G, Bazarian JJ (2011) Elevated serum ubiquitin carboxy-terminal hydrolase L1 is associated with abnormal blood-brain barrier function after traumatic brain injury. *J Neurotrauma* 28: 2453-2462
- Brown RC, Morris AP, O'Neil RG (2007) Tight junction protein expression and barrier properties of immortalized mouse brain microvessel endothelial cells. *Brain Res* 1130: 17-30
- Cater HL, Gitterman D, Davis SM, Benham CD, Morrison B, 3rd, Sundstrom LE (2007) Stretch-induced injury in organotypic hippocampal slice cultures reproduces in vivo post-traumatic neurodegeneration: Role of glutamate receptors and voltage-dependent calcium channels. *Journal of Neurochemistry* 101: 434-47
- Cater HL, Sundstrom LE, Morrison B, 3rd (2006a) Temporal development of hippocampal cell death is dependent on tissue strain but not strain rate. *J Biomech* 39: 2810-8
- Cater HL, Sundstrom LE, Morrison B, III (2006b) Temporal development of hippocampal cell death is dependent on tissue strain but not strain rate. *J Biomech* 39: 2810-2818
- Cater HL, Sundstrom LE, Morrison III B (2006c) Temporal development of hippocampal cell death is dependent on tissue strain but not strain rate. *J Biomech* 39: 2810-2818
- Cernak I, Merkle AC, Koliatsos VE, Bilik JM, Luong QT, Mahota TM, Xu L, Slack N, Windle D, Ahmed FA (2011) The pathobiology of blast injuries and blast-induced neurotrauma as identified using a new experimental model of injury in mice. *Neurobiol Dis* 41: 538-51
- Connell S, Gao J, Chen J, Shi R (2011) Novel model to investigate blast injury in the central nervous system. *Journal of neurotrauma* 28: 1229-1236
- Cucullo L, Hallene K, Dini G, Dal Toso R, Janigro D (2004) Glycerophosphoinositol and dexamethasone improve transendothelial electrical resistance in an in vitro study of the blood-brain barrier. *Brain Res* 997: 147-51

- D'Ambrosio R, Maris DO, Grady MS, Winn HR, Janigro D (1998) Selective loss of hippocampal long-term potentiation, but not depression, following fluid percussion injury. *Brain research* 786: 64-79
- DeKosky ST, Ikonomic MD, Gandy S (2010) Traumatic brain injury-- football, warfare, and long-term effects. *N Engl J Med* 363: 1293-1296
- DeRoss AL, Adams JE, Vane DW, Russell SJ, Terella AM, Wald SL (2002) Multiple head injuries in rats: Effects on behavior. *The Journal of Trauma Injury, Infection, and Critical Care* 52
- Effgen GB, Gill E, Morrison BI (2012a) A model of repetitive, mild traumatic brain injury and a novel pharmacological intervention to block repetitive injury synergy. Paper presented at the International Research Council on Biomechanics of Injury, Dublin, Ireland, Sept 2012
- Effgen GB, Hue CD, Vogel E, 3rd, Panzer MB, Meaney DF, Bass CR, Morrison B, 3rd (2012b) A multiscale approach to blast neurotrauma modeling: Part ii: Methodology for inducing blast injury to in vitro models. *Front Neurol* 3: 23
- Effgen GB, Hue CD, Vogel E, 3rd, Panzer MB, Meaney DF, Bass CR, Morrison B, 3rd (2012c) A multiscale approach to blast neurotrauma modeling: Part ii: Methodology for inducing blast injury to in vitro models. *Front Neurol* 3: 23
- Effgen GB, Hue CD, Vogel EW, III, Panzer MB, Meaney DF, Bass CR, Morrison B, III (2012d) A multiscale approach to blast neurotrauma modeling: Part ii: Methodology for inducing blast injury to in vitro models. *Front Neurol* 3: 23
- Effgen GB, Vogel EW, III, Lynch KA, Lobel A, Hue CD, Meaney DF, Bass CR, Morrison B, III (2014a) Isolated primary blast alters neuronal function with minimal cell death in organotypic hippocampal slice cultures. *J Neurotrauma* 31: 1202-10
- Effgen GB, Vogel III EW, Lynch KA, Lobel A, Hue CD, Meaney DF, C.R. B, Morrison III B (2014b) Isolated primary blast alters neuronal function with minimal cell death in organotypic hippocampal slice cultures. *J Neurotrauma* 31: 1202-1210
- Elder GA, Dorr NP, De Gasperi R, Gama Sosa MA, Shaughnessy MC, Maudlin-Jeronimo E, Hall AA, McCarron RM, Ahlers ST (2012) Blast exposure induces post-traumatic stress disorder-related traits in a rat model of mild traumatic brain injury. *Journal of neurotrauma* 29: 2564-2575
- Elkin BS, Morrison BI (2007) Region-specific tolerance criteria for the living brain. *Stapp* 51: 127-138
- Elliott MB, Jallo JJ, Gaughan JP, Tuma RF (2007) Effects of crystalloid-colloid solutions on traumatic brain injury. *J Neurotrauma* 24: 195-202
- Fenstermacher J (1984) Volume regulation of the central nervous system. *Edema*: 383-404
- Forster C, Waschke J, Burek M, Leers J, Drenckhahn D (2006) Glucocorticoid effects on mouse microvascular endothelial barrier permeability are brain specific. *J Physiol* 573: 413-25
- Fujita M, Wei EP, Povlishock JT (2012) Intensity- and interval-specific repetitive traumatic brain injury can evoke both axonal and microvascular damage. *J Neurotrauma* 29: 2172-80
- Garcia AN, Vogel SM, Komarova YA, Malik AB (2011) Permeability of endothelial barrier: Cell culture and in vivo models. *Methods Mol Biol* 763: 333-354
- Garman RH, Jenkins LW, Switzer RC, Bauman RA, Tong LC, Swauger PV, Parks SA, Ritzel DV, Dixon CE, Clark RSB, et al. (2011) Blast exposure in rats with body shielding is characterized primarily by diffuse axonal injury. *J Neurotrauma* 28: 947-959

- Gennarelli TA, Adams JH, Graham DI (1981) Acceleration induced head injury in the monkey.I. The model, its mechanical and physiological correlates. *Acta neuropathologica Supplementum* 7: 23-5
- Gennarelli TA, Thibault LE, Adams JH, Graham DI, Thompson CJ, Marcincin RP (1982) Diffuse axonal injury and traumatic coma in the primate. *Ann Neurol* 12: 564-74
- Giza CC, Hovda DA (2001) The neurometabolic cascade of concussion. *Journal of Athletic Training* 36: 228-235
- Goldstein LE, A.M. Fisher, C.A. Tagge, X. Zhang, L. Velisek, J.A. Sullivan, C. Upreti, J.M. Kracht, M. Ericsson, M.W. Wojnarowicz, C.J. Goletiani, G.M. Maglakelidze, N. Casey, J.A. Moncaster, O. Minaeva, R.D. Moir, C.J. Nowinski, R.A. Stern, R.C. Cantu, J. Geiling, J.K. Blusztajn, B.L. Wolozin, T. Ikezu, T.D. Stein, A.E. Budson, N.W. Kowall, D. Chargin, A. Sharon, S. Saman, G.F. Hall, W.C. Moss, R.O. Cleveland, R.E. Tanzi, P.K. Stanton, A.C. McKee (2012) Chronic traumatic encephalopathy in blast-exposed military veterans and a blast neurotrauma mouse model. *Science Translational Medicine* 4: 134-160
- Goldstein LE, Fisher AM, Tagge CA, Zhang XL, Velisek L, Sullivan JA, Upreti C, Kracht JM, Ericsson M, Wojnarowicz MW, et al. (2012a) Chronic traumatic encephalopathy in blast-exposed military veterans and a blast neurotrauma mouse model. *Sci Transl Med* 4: 134ra60
- Goldstein LE, Fisher AM, Tagge CA, Zhang XL, Velisek L, Sullivan JA, Upreti C, Kracht JM, Ericsson M, Wojnarowicz MW, et al. (2012b) Chronic traumatic encephalopathy in blast-exposed military veterans and a blast neurotrauma mouse model. *Sci Trans Med* 4: 134ra60
- Gullotti DM, Beamer M, Panzer MB, Chen YC, Patel TP, Yu A, Jaumard N, Winkelstein B, Bass CR, Morrison B, et al. (2014a) Significant head accelerations can influence immediate neurological impairments in a murine model of blast-induced traumatic brain injury. *J Biomech Eng* 136: 091004
- Gullotti DM, Beamer M, Panzer MB, Chen YC, Patel TP, Yu A, Jaumard N, Winkelstein B, Bass CR, Morrison BI, et al. (2014b) Significant head accelerations can influence immediate neurological impairments in a murine model of blast-induced traumatic brain injury. *J Biomech Eng* 136: 091004
- Guskiewicz KM, Marshall SW, Bailes J, McCrea M, Cantu RC, Randolph C, Jordan BD (2005) Association between recurrent concussion and late-life cognitive impairment in retired professional football players. *Neurosurgery*: 719-726
- Guskiewicz KM, McCrea M, Marshall SW, Cantu RC, Randolph C, Barr W, Onate JA, Kelly JP (2003) Cumulative effects associated with recurrent concussion in collegiate football players. *American Medical Association* 290: 2549-2555
- Hatashita S, Hoff JT (1990) Brain edema and cerebrovascular permeability during cerebral ischemia in rats. *Stroke* 21: 582-8
- Heiss JD, Papavassiliou E, Merrill MJ, Nieman L, Knightly JJ, Walbridge S, Edwards NA, Oldfield EH (1996) Mechanism of dexamethasone suppression of brain tumor-associated vascular permeability in rats. Involvement of the glucocorticoid receptor and vascular permeability factor. *J Clin Invest* 98: 1400-8
- Heuschkel MO, Fejtl M, Raggenbass M, Bertrand D, Renaud P (2002) A three-dimensional multi-electrode array for multi-site stimulation and recording in acute brain slices. *J Neurosci Methods* 114: 135-148

- Holgate ST, Polosa R (2008) Treatment strategies for allergy and asthma. *Nature reviews Immunology* 8: 218-30
- Hu D, Cao P, Thiels E, Chu CT, Wu G, Oury TD, Klann E (2007) Hippocampal long-term potentiation, memory, and longevity in mice that overexpress mitochondrial superoxide dismutase. *Neurobiology of Learning and Memory* 87: 372-384
- Huber JD, Egleton RD, Davis TP (2001) Molecular physiology and pathophysiology of tight junctions in the blood-brain barrier. *Trends Neurosci* 24: 719-25
- Hue CD, Cao S, Bass CR, Meaney DF, Morrison BI (2014a) Repeated primary blast injury causes delayed recovery, but not additive disruption, in an in vitro blood-brain barrier model.
- Hue CD, Cao S, Dale Bass CR, Meaney DF, Morrison B, 3rd (2014b) Repeated primary blast injury causes delayed recovery, but not additive disruption, in an in vitro blood-brain barrier model. *J Neurotrauma* 31: 951-60
- Hue CD, Cao S, Haider SF, Vo KV, Effgen GB, Vogel E, 3rd, Panzer MB, Bass CR, Meaney DF, Morrison B, 3rd (2013a) Blood-brain barrier dysfunction after primary blast injury in vitro. *J Neurotrauma*
- Hue CD, Cao S, Haider SF, Vo KV, Effgen GB, Vogel E, 3rd, Panzer MB, Bass CR, Meaney DF, Morrison B, 3rd (2013b) Blood-brain barrier dysfunction after primary blast injury in vitro. *J Neurotrauma* 30: 1652-1663
- Hue CD, Cao S, Haider SF, Vo KV, Effgen GB, Vogel EW, III, Panzer MB, Bass CR, Meaney DF, Morrison B, III (2013c) Blood-brain barrier dysfunction after primary blast injury in vitro. *J Neurotrauma* 30: 1652-1663
- Hue CD, Cao S, Haider SF, Vo KV, Effgen GB, Vogel Iii E, Panzer MB, Bass CD, Meaney D, Morrison Iii B, 3rd (2013d) Blood-brain barrier dysfunction after primary blast injury in vitro. *J Neurotrauma*
- Hue CD, Cho FS, Cao S, Nicholls RE, Vogel EW, III, Sibindi C, Arancia O, Bass CR, Meaney DF, Morrison B, III (2015) Time course and size of blood-brain barrier opening in a mouse model of blast-induced traumatic brain injury *J Neurotrauma*: DOI:10.1089/neu.2015.4067
- Kaal EC, Vecht CJ (2004) The management of brain edema in brain tumors. *Current opinion in oncology* 16: 593-600
- Kamnaksh A, Kwon SK, Kovesdi E, Ahmed F, Barry ES, Grunberg NE, Long J, Agoston D (2012) Neurobehavioral, cellular, and molecular consequences of single and multiple mild blast exposure. *Electrophoresis* 33: 3680-92
- Keyes DC (2005) Medical response to terrorism: Preparedness and clinical practice. Lippincott Williams & Wilkins
- Kniesel U, Wolburg H (2000) Tight junctions of the blood-brain barrier. *Cell Mol Neurobiol* 20: 57-76
- Li X, Cui D, Jiruska P, Fox JE, Yao X, Jefferys JGR (2007) Synchronization measurement of multiple neuronal populations. *J Neurophysiol* 98: 3341-3348
- Li X, Ouyang G, Usami A, Ikegaya Y, Sik A (2010) Scale-free topology of the ca3 hippocampal network: A novel method to analyze functional neuronal assemblies. *Biophysical journal* 98: 1733-1741
- Ling G, Bandak F, Armonda R, Grant G, Ecklund J (2009) Explosive blast neurotrauma. *J Neurotrauma* 26: 815-25

- Logsdon AF, Turner RC, Lucke-Wold BP, Robson MJ, Naser ZJ, Smith KE, Matsumoto RR, Huber JD, Rosen CL (2014) Altering endoplasmic reticulum stress in a model of blast-induced traumatic brain injury controls cellular fate and ameliorates neuropsychiatric symptoms. *Frontiers in cellular neuroscience* 8: 421
- Lu W, Man H, Ju W, Trimble WS, MacDonald JF, Wang YT (2001) Activation of synaptic nmda receptors induces membrane insertion of new ampa receptors and ltp in cultured hippocampal neurons. *Neuron* 29: 243-254
- Lucke-Wold BP, Logsdon AF, Smith KE, Turner RC, Alkon DL, Tan Z, Naser ZJ, Knotts CM, Huber JD, Rosen CL (2014) Bryostatin-1 restores blood brain barrier integrity following blast-induced traumatic brain injury. *Mol Neurobiol*
- Mac Donald CL, Johnson AM, Cooper D, Nelson EC, Werner NJ, Shimony JS, Snyder AZ, Raichle ME, Witherow JR, Fang R, et al. (2011) Detection of blast-related traumatic brain injury in u.S. Military personnel. *N Engl J Med* 364: 2091-100
- Matser JT, Kessels AGH, Jordan BD, Lezak MD, Troost J (1998) Chronic traumatic brain injury in professional soccer players. *Neurology* 51: 791-796
- Matser JT, Kessels AGH, Lezak MD, Jordan BD, Troost J (1999) Neuropsychological impairment in amateur soccer players. *Journal of the American Medical Association* 282: 971-973
- Maxwell WL, Whitfield PC, Suzen B, Graham DI, Adams JH, Watt C, Gennarelli TA (1992) The cerebrovascular response to experimental lateral head acceleration. *Acta Neuropathol* 84: 289-96
- Mayford M, Wang J, Kandel ER, O'Dell TJ (1995) Camkii regulates the frequency-response function of hippocampal synapses for the production of both ltd and ltp. *Cell* 81: 891-904
- McCrea M, Barr W, Guskiewicz KM, Randolph C, Marshall SW, Cantu RC, Onate JA, Kelly JP (2005) Standard regression-based methods for measuring recovery after sport-related concussion. *Journal of the International Neuropsychological Society* 11: 58-69
- McDonald WI (1994) Rachelle fishman-matthew moore lecture. The pathological and clinical dynamics of multiple sclerosis. *J Neuropathol Exp Neurol* 53: 338-43
- Morganti-Kossmann MC, Hans VH, Lenzlinger PM, Dubs R, Ludwig E, Trentz O, Kossmann T (1999) Tgf-beta is elevated in the csf of patients with severe traumatic brain injuries and parallels blood-brain barrier function. *J Neurotrauma* 16: 617-28
- Morrison B, 3rd, Cater HL, Benham CD, Sundstrom LE (2006a) An in vitro model of traumatic brain injury utilising two-dimensional stretch of organotypic hippocampal slice cultures. *J Neurosci Methods* 150: 192-201
- Morrison B, Cater HL, Wang CC-B, Thomas FC, Hung CT, Ateshian GA, Sundstrom LE (2003a) A tissue level tolerance criterion for living brain developed with an in vitro model of traumatic mechanical loading. *Stapp Car Crash Journal* 47: 93-105
- Morrison B, III, Cater HL, Benham CD, Sundstrom LE (2006b) An in vitro model of traumatic brain injury utilising two-dimensional stretch of organotypic hippocampal slice cultures. *J Neurosci Meth* 150: 192-201
- Morrison B, III, Cater HL, Benham CD, Sundstrom LE (2006c) An in vitro model of traumatic brain injury utilising two-dimensional stretch of organotypic hippocampal slice cultures. *J Neuroscience Methods* 150: 192-201

- Morrison B, III, Cater HL, Wang CC-B, Thomas FC, Hung CT, Ateshian GA, Sundstrom LE (2003b) A tissue level tolerance criterion for living brain developed with an in vitro model of traumatic mechanical loading. *Stapp* 47: 93-105
- Morrison III B, Cater HL, Benham CD, Sundstrom LE (2006) An in vitro model of traumatic brain injury utilising two-dimensional stretch of organotypic hippocampal slice cultures. *JNeurosciMeth* 150: 192-201
- Norris CM, Scheff SW (2009) Recovery of afferent function and synaptic strength in hippocampal ca1 following traumatic brain injury. *J Neurotrauma* 26: 2269-2278
- Olson JE, Banks M, Dimlich RV, Evers J (1997) Blood-brain barrier water permeability and brain osmolyte content during edema development. *Acad Emerg Med* 4: 662-73
- Omid Y, Campbell L, Barar J, Connell D, Akhtar S, Gumbleton M (2003) Evaluation of the immortalised mouse brain capillary endothelial cell line, b.End3, as an in vitro blood-brain barrier model for drug uptake and transport studies. *Brain Res* 990: 95-112
- Otmakhov N, Khibnik L, Otmakhova N, Carpenter S, Riahi S, Asrican B, Lisman J (2004) Forskolin-induced ltp in the ca1 hippocampal region is nmda receptor dependent. *J Neurophysiol* 91: 1955-1962
- Panzer MB, Matthews KA, Yu AW, Morrison B, 3rd, Meaney DF, Bass CR (2012a) A multiscale approach to blast neurotrauma modeling: Part i - development of novel test devices for in vivo and in vitro blast injury models. *Front Neurol* 3: 46
- Panzer MB, Matthews KA, Yu AW, Morrison B, 3rd, Meaney DF, Bass CR (2012b) A multiscale approach to blast neurotrauma modeling: Part i - development of novel test devices for in vivo and in vitro blast injury models. *Front Neurol* 3: 46
- Pardridge WM (2007) Blood-brain barrier delivery. *Drug Discov Today* 12: 54-61
- Patel TP, Ventre SC, Meaney DF (2012) Dynamic changes in neural circuit topology following mild mechanical injury in vitro. *Annals of biomedical engineering* 40: 23-36
- Prins ML, Alexander D, Giza CC, Hovda DA (2013) Repeated mild traumatic brain injury: Mechanisms of cerebral vulnerability. *J Neurotrauma* 30: 30-8
- Readnower RD, Chavko M, Adeeb S, Conroy MD, Pauly JR, McCarron RM, Sullivan PG (2010) Increase in blood-brain barrier permeability, oxidative stress, and activated microglia in a rat model of blast-induced traumatic brain injury. *J Neurosci Res* 88: 3530-3539
- Reeves TM, Lyeth BG, Povlishock JT (1995) Long-term potentiation deficits and excitability changes following traumatic brain injury. *Exp Brain Res* 106: 248-256
- Romero IA, Radewicz K, Jubin E, Michel CC, Greenwood J, Couraud PO, Adamson P (2003) Changes in cytoskeletal and tight junctional proteins correlate with decreased permeability induced by dexamethasone in cultured rat brain endothelial cells. *Neurosci Lett* 344: 112-6
- Rosenfeld JV, Ford NL (2010) Bomb blast, mild traumatic brain injury and psychiatric morbidity: A review. *Injury* 41: 437-43
- Saljo A, Svensson B, Mayorga M, Hamberger A, Bolouri H (2009) Low-level blasts raise intracranial pressure and impair cognitive function in rats. *Journal of neurotrauma* 26: 1345-1352
- Sanders MJ, Sick TJ, Perez-Pinzon MA, Dietrich WD, Green EJ (2000) Chronic failure in the maintenance of long-term potentiation following fluid-percussion injury in the rat. *Brain Research* 861: 69-76

- Sanhueza M, Fernandez-Villalobos G, Stein IS, Kasumova G, Zhang P, Bayer KU, Otmakhov N, Hell JW, Lisman J (2011) Role of camkii/nmda receptor complex in the maintenance of synaptic strength. *J Neurosci* 31: 9170-9178
- Shlosberg D, Benifla M, Kaufer D, Friedman A (2010) Blood–brain barrier breakdown as a therapeutic target in traumatic brain injury. *Nat Rev Neurol* 6: 393-403
- Signoretti S, Lazzarino G, Tavazzi B, Vagnozzi R (2011) The pathophysiology of concussion. *Pm R* 3: S359-68
- Simon MJ, Kang WH, Gao S, Banta S, Morrison B (2010) Tat is not capable of transcellular delivery across an intact endothelial monolayer in vitro. *Ann Biomed Eng* 39: 394-401
- Skotak M, Wang F, Alai A, Holmberg A, Harris S, Switzer RC, Chandra N (2013) Rat injury model under controlled field-relevant primary blast conditions: Acute response to a wide range of peak overpressures. *J Neurotrauma* 30: 1147-60
- Song L, Pachter JS (2003) Culture of murine brain microvascular endothelial cells that maintain expression and cytoskeletal association of tight junction-associated proteins. *In vitro cellular & developmental biology Animal* 39: 313-20
- Swant J, Wagner JJ (2006) Dopamine transporter blockade increases ltp in the ca1 region of the rat hippocampus via activation of the d3 dopamine receptor. *Learn Mem* 13: 161-167
- Tanno H, Nockels RP, Pitts LH, Noble LJ (1992) Breakdown of the blood-brain barrier after fluid percussive brain injury in the rat. Part 1: Distribution and time course of protein extravasation. *J Neurotrauma* 9: 21-32
- Tate CM, Wang KKW, Eonta S, Zhang Y, Carr W, Tortella FC, Hayes RL, Kamimori GH (2013) Serum brain biomarker level, neurocognitive performance, and self-reported symptom changes in soldiers repeatedly exposed to low-level blast: A breacher pilot study. *J Neurotrauma* 30: 1620-1630
- Vagnozzi R, Signoretti S, Tavazzi B, Floris R, Ludovici A, Marziali S, Tarascio G, Amorini AM, Di Pietro V, Delfini R, et al. (2008) Temporal window of metabolic brain vulnerability to concussion: A pilot 1h-magnetic resonance spectroscopic study in concussed athletes--part iii. *Neurosurgery* 62: 1286-95; discussion 1295-6
- Vandevord PJ, Bolander R, Sajja VSSS, Hay K, Bir CA (2012) Mild neurotrauma indicates a range-specific pressure response to low level shock wave exposure. *Annals of biomedical engineering* 40: 227-236
- Victorino GP, Newton CR, Curran B (2003) The impact of albumin on hydraulic permeability: Comparison of isotonic and hypertonic solutions. *Shock* 20: 171-175
- Vilalta A, Sahuquillo J, Rosell A, Poca MA, Riveiro M, Montaner J (2008) Moderate and severe traumatic brain injury induce early overexpression of systemic and brain gelatinases. *Intensive Care Med* 34: 1384-1392
- Vogel EW, III, Effgen GB, Patel TP, Meaney DF, Bass CR, Morrison B, III (2015) Isolated primary blast inhibits long-term potentiation in organotypic hippocampal slice cultures. *J Neurotrauma*: DOI:10.1089/neu.2015.4045
- Vogel III EW, Effgen GB, Patel TP, Meaney DF, Bass CR, Morrison III B (2016) Isolated primary blast inhibits long-term potentiation in organotypic hippocampal slice cultures. *J Neurotrauma* 33: 652-661

- Wall SE, Williams WH, Cartwright-Hatton S, Kelly TP, Murray J, Murray M, Owen A, Turner M (2006) Neuropsychological dysfunction following repeat concussions in jockeys. *J Neurol Neurosurg Psychiatry* 77: 518-20
- Wang Y, Wei Y, Oguntayo S, Wilkins W, Arun P, Valiyaveetil M, Song J, Long JB, Nambiar MP (2011a) Tightly coupled repetitive blast-induced traumatic brain injury: Development and characterization in mice. *J Neurotrauma* 28: 2171-83
- Wang Y, Wei Y, Oguntayo S, Wilkins W, Arun P, Valiyaveetil M, Song J, Long JB, Nambiar MP (2011b) Tightly coupled repetitive blast-induced traumatic brain injury: Development and characterization in mice. *Journal of neurotrauma* 28: 2171-2183
- Yeoh S, Bell ED, Monson KL (2013) Distribution of blood-brain barrier disruption in primary blast injury. *Ann Biomed Eng*
- Yu Z, Morrison B (2010) Experimental mild traumatic brain injury induces functional alteration of the developing hippocampus. *Journal of Neurophysiology* 103: 499-510
- Yu Z, Morrison III B (2010) Experimental mild traumatic brain injury induces functional alteration of the developing hippocampus. *JNeurophysiol* 103: 499-510

Section 3: University of Pennsylvania Final Report

Theme: Synapses, wiring in neural networks after blast; extensions to neurobehavior

As a MURI partner, Penn has three primary responsibilities:

1. In collaboration with Duke and Columbia, develop methodologies for measuring circuit activation, wiring, and activity patterns, including:
 - a. algorithms for calcium imaging based maps of electrical activity
 - b. corroborating these methods with models and measures of electrical activity
 - c. extending these methods into acute brain slice cultures
2. In collaboration with Duke, assess neurobehavioral impairments and neural circuit changes in mice and other species after blast exposure by:
 - a. use an in vivo model (mouse) to generate samples for studying network alterations after blast exposure
 - b. identify thresholds for synaptic level changes, adaptations, and alterations in network topology
 - c. correlating changes at the micro scale to the macroscale
3. Integrate activities among participating members

Imaging for single cell precision estimates of electrical activity

Along with advances in animal and *in vitro* models of injury, a substantial new set of tools appeared recently for formulating principles of information flow among neural networks. These tools include measuring relative neural connectivity maps and understanding key points of control for complex networks. Key in this progress is a new emerging set of fluorescent reagents that provide stable, long term optically-based recording of dissociated neurons, ensembles of neurons within acute brain slices, and the living cortex. Collectively, these new tools allow for the direct visualization of the nervous system at an unprecedented scale – it allows one to estimate the input/output connectivity maps among neurons, assess the relative strength of connections among neurons in a network, and to define the network scaling principles used in the design of the network.

In the past year, we critically analyzed fluorescence based imaging methods for mapping neural network properties, and used this analysis to design experiments for measuring changes in network behavior following mild and moderate stretch injury to cortical neuronal networks *in vitro*. We first developed an *in silico* model of neural network activity, conducting a parametric analysis to understand advantages and drawbacks of choices that are commonly used in optical imaging of neural activity. Our network model used a weighted pseudo-randomized network connection topology, and individual synapses, populated with AMPA and NMDA receptors, were assumed to follow a stochastic activation pattern per a recent report (Figure 95A). Integration of current from individual synaptic release events, which could include a random vesicular release event (i.e., synaptic noise), showed development of spontaneous network activity that would vary temporally (Figure 95B). Within individual neurons, these periodic bursts of activity would slightly precede or follow neighboring neurons, would show some modest diversity in the spontaneous timing of bursts. Repeat simulations of the same network topology yielded slightly different patterns of activity, owing to the stochastic synaptic activation scheme. Inhibitory neurons in the network provided modulation of the activity pattern, as reducing the relative strength of the inhibitory neuronal tone led to a progressive synchronization of network activity (Figure 22C), resembling a common technique to synchronize the electrical activity of cortical neuron cultures *in vitro*.

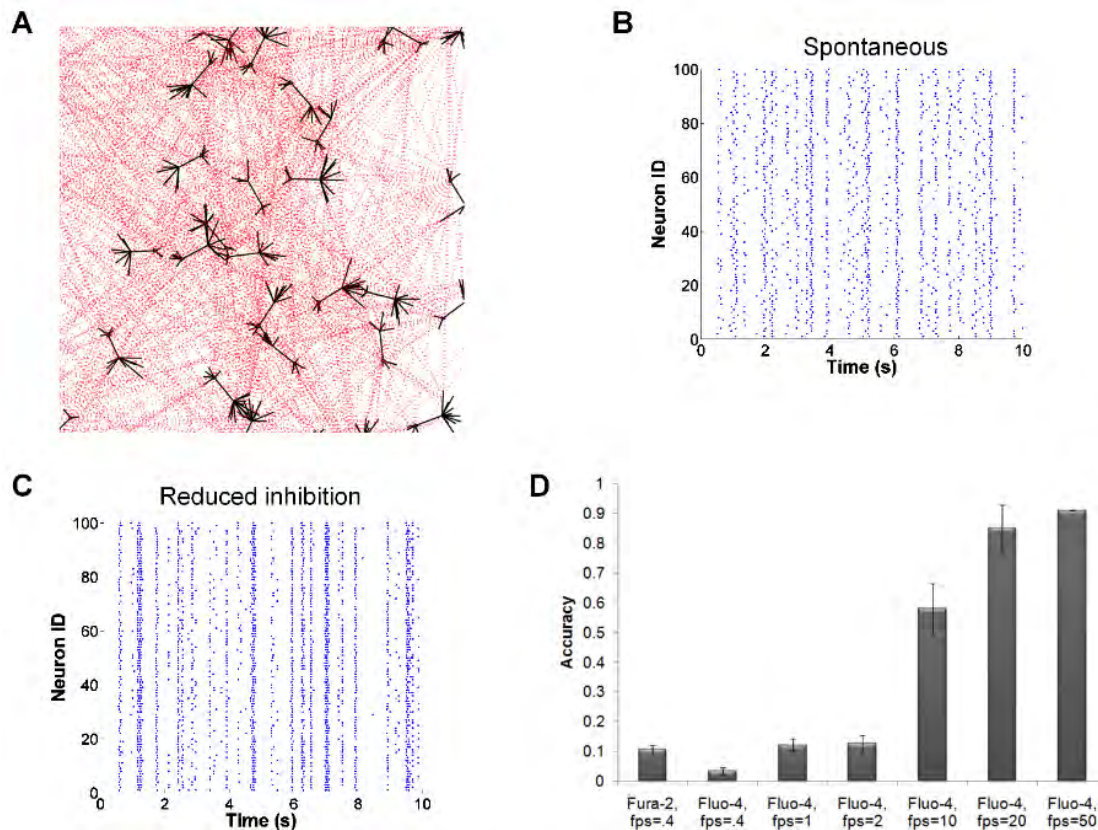


Figure 94- Overview of optimal imaging acquisition requirements for mapping neural circuit activity.

In silico neural network yields estimates of optimal imaging parameters necessary to achieve accurate spike detection

Using estimates of calcium binding for different calcium indicator dyes, we investigated how well fura-2 and fluo-4 capture underlying electrical activity. Under the most ideal conditions, without hardware noise, we found neither Fura-2 nor Fluo-4 provided accurate estimates of precise timing of action potential firing when sampled at relatively low rates. Although Fura-2 offers approximately double the accuracy in detecting action potentials within networks under very low framing rate conditions (.4

frames per second), the predicted accuracy was still less than 10% (Figure 22D). Fluo-4 offers the ability, with its single emission wavelength, to capture fluorescence imaging data at a much faster rate limited only by the imaging hardware⁽⁵⁹⁾. Across typical imaging rates available in commercial interline CCD and EMCCD camera, we find that image acquisition rate will substantially improve the fidelity between increases in calcium indicator fluorescence changes and action potential activity (Figure 22D). Optimal image acquisition rates with the Fluo-4 indicator exceed 80% accuracy in capturing action potentials ($85\% \pm 7.8\%$) at reasonable framing rates, and approach 60% ($58\% \pm 8.52$) even at 10 frames per second.

Optical imaging of network activity in vitro reveals network modules and minimum acquisition requirements

After establishing the necessary acquisition speeds to accurately detect activity, we next considered both the number of neurons and length of imaging time necessary to accurately estimate network synchronization, a key parameter often used to determine network modules. Across multiple cultures ($n=8$), we found that the phase difference in the calcium transients was not spatially sensitive, suggesting a randomized network topology often associated with dissociated cortical networks. The periodic bursting behavior observed with neural networks, when acquired at high framing rates (20 Hz), yielded a synchronization index for the entire culture and also produced measures of smaller subclusters of neurons with highly coordinated firing activity (Figure 96A,B). To obtain accurate measures of synchronization, we needed imaging data from at least 40 individual neurons to achieve less than 5% error (Figure 96C). Similarly, we found that at least 2.5 minutes of imaging spontaneous calcium activity in the dissociated cultures was necessary to achieve reasonably stable estimates of the synchronization index (Figure 96D).

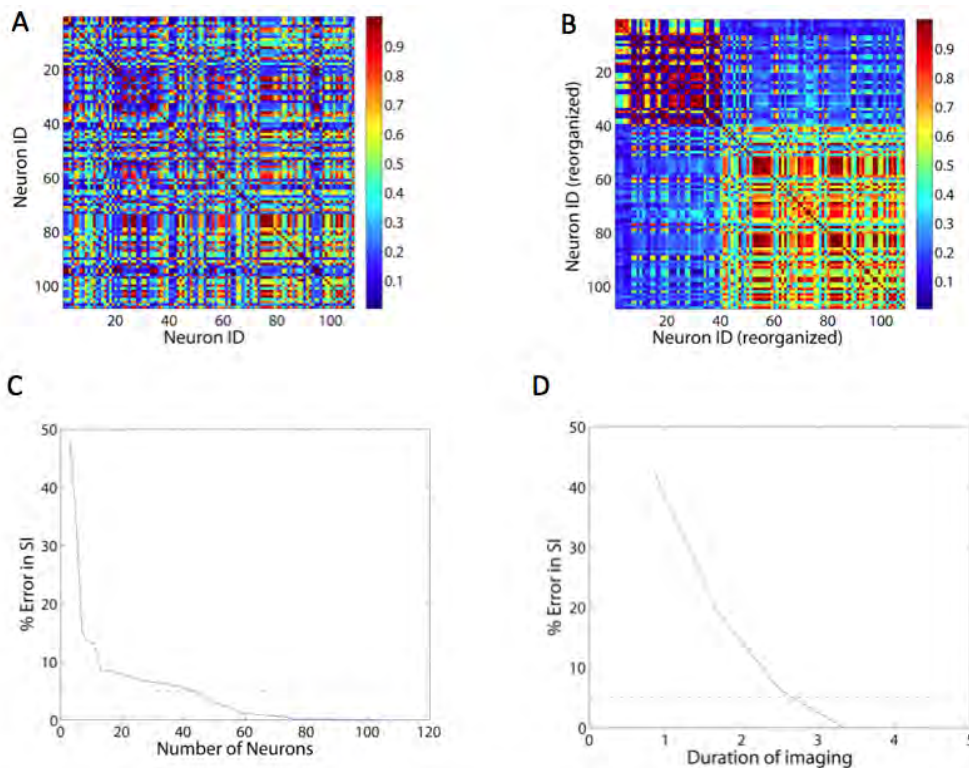


Figure 95- Neural circuit topology needs a minimum number and duration of imaging

Mechanical injury to cortical neurons changes network dynamics and functional connectivity

Upon establishing the necessary imaging conditions to capture accurate measures of network behavior, we next studied the response of cortical neurons to two distinct levels of mechanical injury. Neither level of mechanical injury causes neuronal death 24 hours following injury. One level of mechanical injury ($35\% \pm 5\%$) will cause a delayed proteolysis of the voltage gated sodium channel, as measured by immunoblotting. For this injury level, we observe a consistent and immediate decrease in spontaneous activity, consistent with a recent report that excitatory transmission is altered following mechanical injury in cultured neurons (Figure 97A, 97B). Our detailed analysis of calcium transients on an individual neuron basis revealed a significant decrease in network synchronization (Figure 97C). These changes in spontaneous activity and synchronization persisted for 6 hours. Functional connectivity was also reduced, and the network topology showed signs of damage or rewiring as the previously integrated network, consisting of a single interconnected module, broke off into multiple sub-modules suggesting a loss in long-range connectivity. Finally, excitatory tone was decreased relative to uninjured control cultures, consistent with a broad loss in activity and synchronization (Figure 97C)

Broadly, these data show that mechanical injury to cortical neurons will incur immediate and broad disruptions in network behavior. However, finite element models suggest a wide range of *in vivo* brain deformations occur during concussion. As such, we also tested a less severe injury level ($10\% \pm 4\%$). Distinct from studies at the moderate injury level, we observed no change in the network synchronization or excitatory tone (Figure 97D-F). Interestingly, the frequency of network-wide spontaneous oscillations significantly increased acutely after injury and returned to pre-stretch levels by 1 hr.

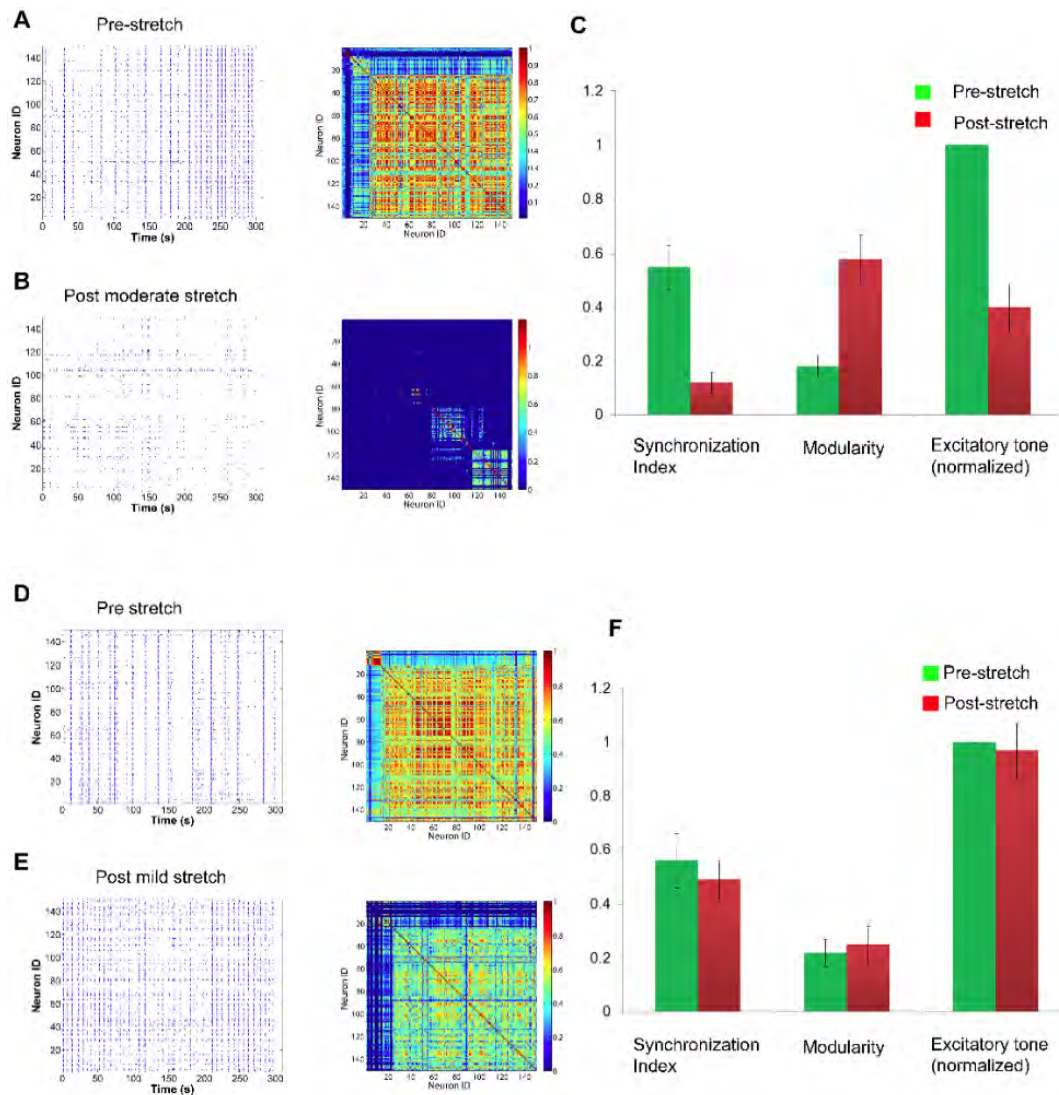


Figure 96- Moderate and mild stretch injury to cortical neurons alters network connections and synaptic strength

Future activities: There are two main areas where we will apply these technologies. First, we will use these methods to assess activity patterns in vitro after blast exposure in both dissociated cortical neuron cultures and organotypic brain slice cultures (Columbia). Second, we will develop the necessary tools to use the genetically encoded calcium indicator in acute slice cultures from the living brain, permitting us to measure changes in the network of different brain regions after blast exposure. We have preliminary data showing good transfer of this technology into living animals.

Blast-induced behavioral changes in mice

As part of our overall effort to merge the changes in neural circuitry after blast exposure across many length scales, we also started a series of tests in mice to answer one broad question: When does blast-induced damage to circuits influence neurobehavior?

With the expertise of the Abel lab at Penn, we have a direct means to compare across species and to use neurobehavior tests that are centered on important brain structures that may be damaged following

primary blast loading. We select behavior tests in animals that focus on the following traits: locomotor activity and sleep/wake cycle, motor coordination, learning and memory, and depression-like behavior. In the first phase of the project, we used the blast tube developed at Duke and assayed for changes in motor coordination, learning, and memory in mice after blast exposure.

Motor Coordination: Our analysis examines the cerebellar system, motor coordination, fatigue and ataxia using the accelerating rotarod treadmill (Ugo Basile, Stoelting Co., Wood Dale, IL) and hindpaw footprint analysis. The Rotarod test measures the ability of a mouse to maintain its balance on a rotating rod, whereas the hindpaw footprint test evaluates the walking pattern of the mice. We started our testing with the RotaRod apparatus

Learning and Memory (mice). Learning and memory will be assayed using three tests, novel object recognition, the Morris water maze and fear conditioning. In the past year, we focused on assessing novel object recognition and fear conditioning at Penn, with plans to assess Morris water maze deficits in the upcoming year. The novel object recognition task relies on the natural exploratory activity of rodents toward novel objects and they provide a nonaversive single-trial learning paradigm that we use to determine the effects of blast loading on memory storage. In contextual fear conditioning tasks, animals learn in a single trial to fear a new environment because of its association with an aversive unconditioned stimulus (US), usually foot shock. In addition to allowing good temporal resolution, fear conditioning involve distinct neuroanatomical substrates: contextual conditioning is dependent on both hippocampus and amygdala function. Animals are monitored for freezing activity one day following the fear conditioning stimulus.

Mice were exposed to one of two blast exposure levels (1 membrane = 10 mil, 2 membrane = 20 mil membrane, corresponding with peak open tube pressures of 176 kPa or 253.1 kPa respectively). Righting times were evaluated after blast exposure, and animals were subject to the following neurobehavioral testing paradigm:

- One day after injury, they were evaluated in the zero maze
- One, two and three days after injury, they were subject to the RotaRod test
- Four and five days postinjury, they were tested in the spatial object recognition test
- Eight and nine days after injury, they were subject to the fear conditioning test

For the zero maze test, mice prefer the closed portion of the maze. We observed no significant changes in the difference between time spent in the closed portion of the maze among three groups – the sham exposure and two different blast conditions. These data suggest no overt changes in anxiety of animals at these testing levels (Figure 98A).

The Rotarod test has two measures: the time until the first foot fault, and the time until the animal drops from the rotating rod. Increasing times over successive days in sham exposed animals suggest the animals are successfully improving their motor coordination and motor memory. This is normal behavior. In blast injured mice, there is a significant deficit appearing for foot fault and modest decrease in fall time one day after the highest blast exposure. There is no significant difference on the second and third day of testing. These data suggest a transient impairment after blast exposure (Figure 98B, C).

For fear conditioning, animals were placed in the fear conditioning chamber and exposed to the stimulus for 2 seconds out of a 5 minute testing period. One day later, animals were placed in the same chamber and monitored for a five minute period and assessed for any freezing behavior. We observed a freezing behavior in sham animals that was not different from animals exposed to either open field blast pressure (Figure 98D). We are exploring if these measures will differ using one second monitoring periods, which are an alternative measure used by some laboratories.

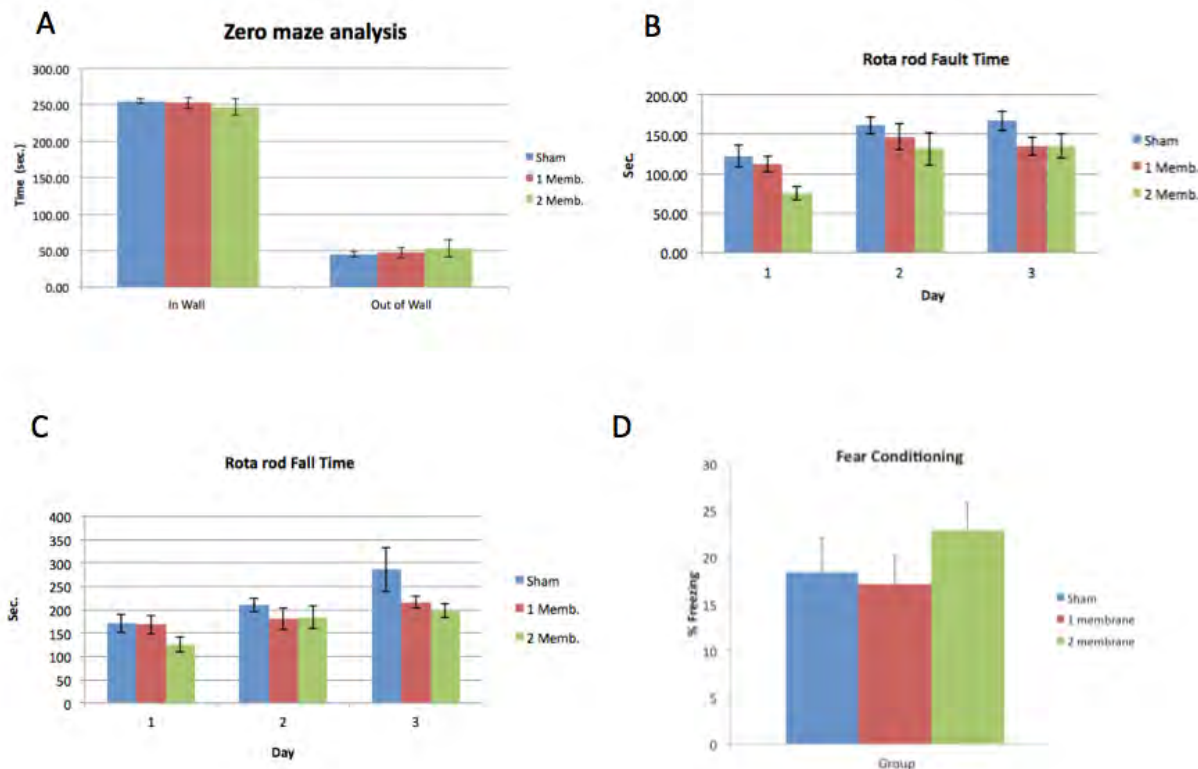


Figure 97- Neurobehavioral impairments in mice exposed to blast loading

The analysis of the final test (spatial object recognition) was not completed at the time of progress report submission, but will be included in subsequent reports. Similarly, histological evaluation of these animals is ongoing, and will be included in the progress report for next year.

The complex kinematics of blast induced head motions

In collaboration with the Duke investigators, we characterized the gross head motions that occurred in a murine model of blast-induced brain injury. We identified key methodological features that contribute to the type and severity of injury in the mouse, measured the relative motion of the mouse head during a blast event, and tested if this model creates an injury with immediate neurological impairment. Our analysis showed that the external signs of damage caused by blast input are influenced by the position of the animal at the shock tube exit, and that significant head motions and accelerations occur during a typical blast event. We show this model creates immediate neurological impairment, with no sign of pulmonary trauma. These data highlight that shock tube based models must be developed carefully to avoid inertial (acceleration) effects, and designed to minimize other external injuries that can complicate the interpretation from these animate models of bTBI. The results of this analysis are presented in more detail in the subsequent paragraphs.

To maintain consistency across the projects, we used the traditional shock tube design developed by the Duke group in the first year of the project. We used pressure transducers with sufficient dynamic response (Endevco, model 8350, San Juan Capistrano, CA) to record the pressure at the exit of the shock tube. We used three equally spaced transducers along the perimeter of the blast tube to evaluate

wave symmetry, and acquired pressure data using a Matlab based data acquisition program sampling at 250kHz per channel. We placed a fourth pressure transducer within the holder cavity, an area adjacent to the animal torso, to assess the potential indirect transfer of any blast wave along its axis. To eliminate aliasing artifact, we conditioned each pressure transducer signal with an inline filter conditioning box (Gator Technologies, Florida) set to provide a 20 kHz cutoff frequency Bessel filter.

We used a high-speed video acquisition system to record head motion either from the side or front of the blast tube, corresponding to lateral or frontal view of the animal head. We identified a region of interest within the field of view to reduce the memory storage requirements per frame, thereby maximizing the framing rate available during testing. For all reported tests, we kept the framing rate between 22-24 kHz. Fiduciary markers in the field of view provided a calibration measure for displacement in the x and y (frontal view) or x and z (lateral view) direction.

A Matlab based video capture algorithm automatically tracked markers on the animal head during the blast sequence. The two fiduciary markers used in the tracking algorithm were used to measure the movement of the head center during blast. We tracked both the net displacement and the x and y displacement components over the entire duration of the experiment that included a pre-triggering period (5 milliseconds) and the movement for the first 30 milliseconds during and following the blast event. Preliminary analysis of video recordings showed negligible head movement beyond 30 milliseconds after blast. We used data smoothing algorithms and numerical calculations of the first and second derivatives of these displacements to calculate the velocity and acceleration measured in the plane of view. Similar to displacement, we calculated the net magnitude, as well as the x and y components, of the velocity and acceleration measures.

Animal preparation and injury. Male, C57BL6 mice aged 12-14 weeks were obtained from Charles River laboratories and allowed to acclimate in the colony before testing. We carefully adhered to the animal welfare guidelines established by the University of Pennsylvania's Institutional Animal Care and Use Committee. Animals used to characterize the head motion during blast were euthanized with a lethal dose of sodium pentobarbital immediately prior to placement in the animal holder. All animals were tested within 30 minutes of euthanization to minimize the influence of rigor mortis on head motions. In separate tests to measure the neurological impairments after blast exposure, animals were placed in an anesthesia induction chamber (4% Isoflurane induction) for 5 minutes, and then transported into the testing room for injury. Animals remained on anesthesia during placement and position of the animal prior to exposure. Immediately prior to testing, anesthesia was discontinued. Immediately after injury, the animal was removed from the holder and brought to a recovery area.

Animal neurological impairment immediately after blast was measured using a righting time response. To measure righting time, we placed animals on their back, and measured the time for the animals to turn over and right themselves onto their forepaws and hindpaws. Once animals regained the ability to right themselves, they were monitored for several minutes to establish their movement and exploratory behavior before they were returned a warmed recovery cage and monitored for future status.

Free field blast events show a characteristic rapid increase in pressure that corresponds with the initial arrival of the shock wavefront, followed by a rapid, exponential decay that can include a modest negative pressure phase when compared to atmospheric pressure. Our design successfully re-creates these three phases of the free field blast event. This blast waveform is repeatably produced for test conditions that span peak pressures of 100 to 700 kPa. Pressures around the perimeter of the tube varied less than 3 % within individual tests, and less than 5% across tests using the same membrane thickness

With the animal holder positioned at the blast exit, we observed a consistent and significant increase in the peak pressure recorded for each test. The magnitude of the peak pressure varied across each test more significantly in comparison to tests where the holder was not used. The peak pressure varied with position of the pressure sensor along the perimeter. The sensor located most distant from the animal holder was closest to the recorded free field pressures, while the second and third pressure sensors were significantly higher but close to each other in magnitude, likely due to the similar position of each sensor relative to the animal holder. In comparison to the pressure transducer measurements along the perimeter of the shock tube exit, the pressure transducer recordings within the animal holder tube were significantly less than the free field equivalent.

Positioning an animal within the holder assembly led to a similar increase in peak pressures for all three transducers located at the blast tube exit. Similar to results with only the animal holder assembly, we observed the largest increase for locations close to the external surfaces of the animal holder, and the least influence on pressures recorded opposite the holder. We observed a significant difference between the peak pressures at the blast tube exit in comparison to the same measures without an animal in place. In comparison, we observed a significant reduction in the pressure measured at the approximate torso location when an animal was placed in the assembly. In all tests, this peak torso pressure was well below the threshold pressure associated with pulmonary trauma.

High speed recording of the head motion during blast exposure showed three general phases of motion: a rapid, nearly vertical downward motion, followed by a slightly longer upward motion, and then a slowly tracking lateral motion as the head rotated and slowed into its near final position. Starting from its rest position, tests across different test subjects showed a relatively consistent peak downward displacement. Moreover, the first and second phase of movement was confined to within a relatively narrow corridor of head displacement. The third phase of motion had the most variability. Using an algorithm to minimize errors associated with calculating velocities and accelerations from video measurements, we found peak vertical accelerations (y) were significantly larger than lateral (x) accelerations. Moreover, we observed a significant acceleration and deceleration component to the vertical motion, and did not detect a significant difference between these two components. We observed similar changes in the velocities tracked over successive tests; the vertical velocities were significantly larger than the horizontal velocities, and the peak downward velocity was not significantly different from the upward velocity.

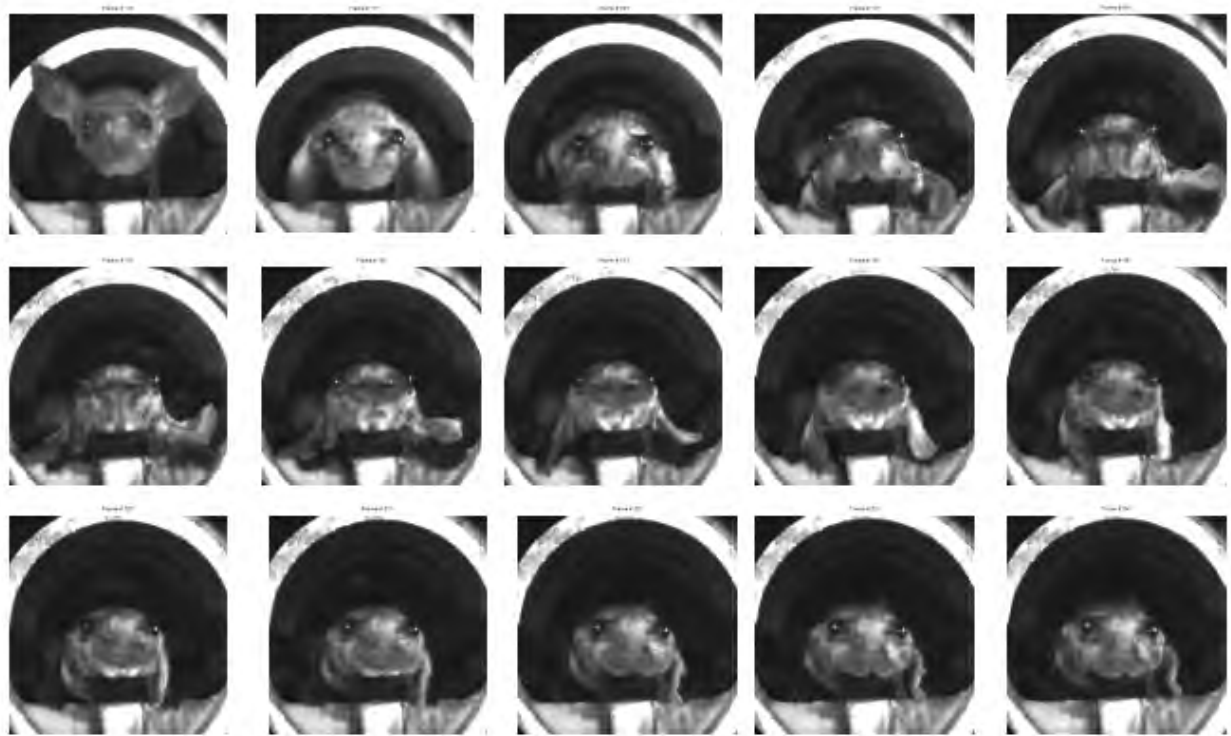


Figure 98 - High speed montage of a typical head motion recording during the blast event. Animals received a blast wave in the dorsal-ventral direction, which caused a corresponding downward and then upward motion of the head. High speed filming of the event (22,000 frames per second) revealed the extent of downward movement, speed, and peak acceleration during the blast event.

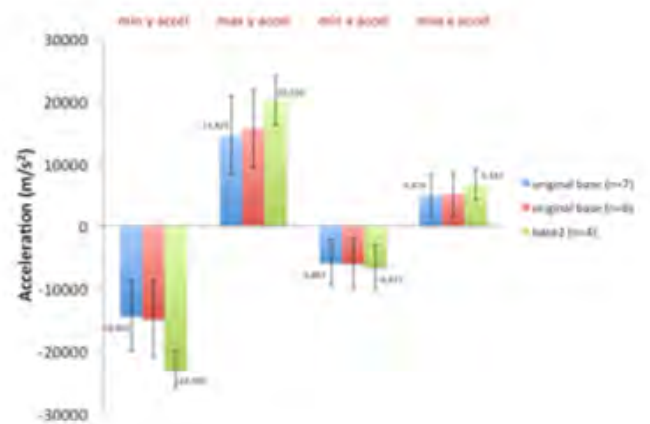
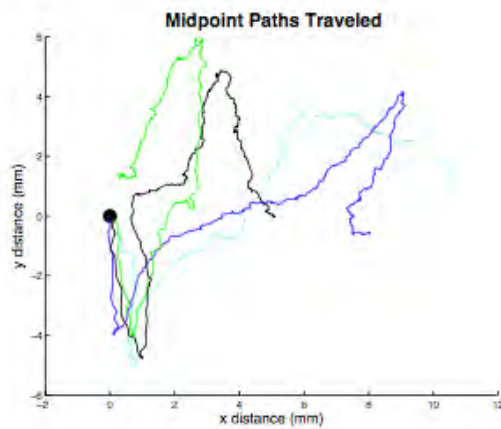


Figure 99 - Significant inertial loading accompanies blast exposure. For the configuration shown in Figure 99, the recorded displacements during blast shows a complex trajectory downward and laterally during and following the blast exposure period. An aggregate path of the trajectory shows the most consistent displacement across tests occurs within the first 3 milliseconds of loading; more variation follows this period when the head is rebounding from the initial loading phase. Estimates of the velocities and accelerations show that the significant accelerations occur in the dorsal-ventral axis, nearly 7 times the magnitude in the lateral direction.

We next considered if these blast loading levels were sufficient to cause any overt impairment. Due to the external damage observed when the animal was placed along the centerline axis of the blast tube, we only considered the impairments caused when the animal was located at the edge of the blast tube. Animals exposed to a single blast event showed a significant increase in their righting time when compared to sham animals. None of the animals experienced obvious signs of pulmonary distress. Animals were ambulatory one day following injury, appearing only slightly lethargic compared to sham mice. Normal grooming behavior recovered within 2-3 days post injury.

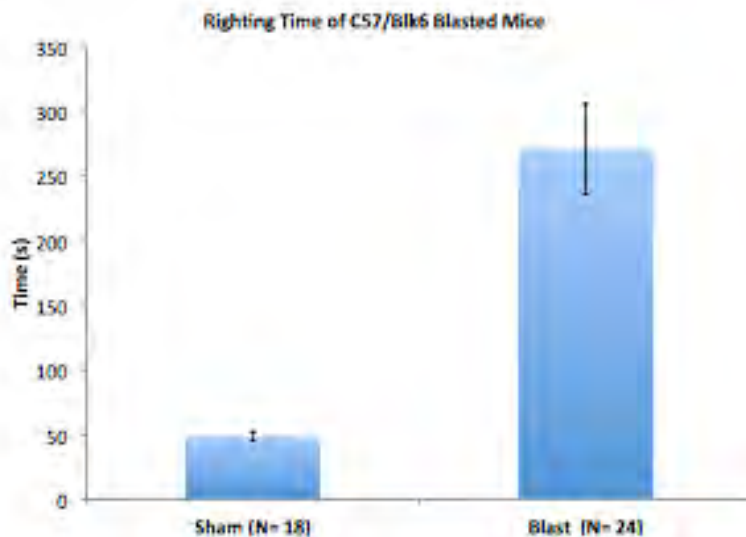


Figure 100 - Righting time following blast exposure. For the exposure conditions studied in Figures 99 and 100, we recorded the time for an animal to right itself after blast exposure. A significant increase in righting time appeared when compared to control animals.

Collectively, these data show it is possible to reproducibly create a Friedlander type blast wave with a portable shocktube design. We find the position of the animal at the tube exit influences the external damage occurring from the blast wave. Importantly, we measure significant head motions occur from a single blast event, with the primary acceleration loading along the direction of travel for the blast wave. At the conditions studied, we report a transient neurological impairment in righting time without any sign of pulmonary trauma.

Blast induced traumatic brain injury models are increasing in number and include both rodent and higher order species. Results from swine models show a complex biomechanical response in the animals that includes the transfer of the blast wave into the brain parenchyma, head motion, and highlight the possibility that that blast wave may also damage other organ systems. However, these larger animal models show relatively little, if any, head acceleration during the blast exposure. A similar modest acceleration profile occurs in human surrogate and manikin testing. Together, these data suggest that the contribution of tissue pressure relative to tissue deformation in blast exposure will change significantly across brain size. This enhanced role of acceleration in a small animal model of bTBI indicates that injury patterns must be interpreted cautiously, and suggests the primary effect of blast wave transmission in larger structures is the transmission of the pressure wave, rather than an induced acceleration, throughout the brain. Our efforts to focus on the influence of blast wave exposure on the head, and we successfully protected the remainder of the animal body from any significant trauma by encasing the animal in a rigid, insulated enclosure.

Our efforts concentrated on studying this murine model of bTBI from two perspectives: how the blast wave would influence the biomechanical loading experience by the head, and whether this device creates appropriate input loading conditions. For pulmonary injury associated with blast loading, a well known scaling relationship indicates the peak pressure between two model systems each with a mass of $M1$ and $M2$ should scale with the one-third power of mass. In comparison, the duration of the pressure exposure should scale with the $1/4$ power of mass.

These relationships are based on the principles that the model organ systems have similar mechanical properties, shape, and an equal tolerance to damage at the microscopic scale. Each of these is not well proven when scaling from human to murine systems. Nevertheless, our tube design can produce very brief shockwaves with a very high onset rate, and the durations studied here will scale to an equivalent live explosive duration of 3-5 milliseconds in humans. Our design is flexible to provide either shorter or longer durations by adjusting the gas density and chamber volume, thereby providing more flexibility to studying these pressure and duration (as well as impulse) scaling principles in the future.

Our results also show that blast may introduce significant head accelerations that must be considered when interpreting the resulting neurological impairment. A recent report showed similar inertial motions in a murine model of bTBI. Our measures did not account for the possible rotational accelerations that occur during the blast event, primarily because the instrumentation to measure rotational accelerations is too cumbersome to place directly on the animal for testing. However, using estimates of possible rotation points about the cervical spine, we find that estimates of rotational acceleration (distance from head center to midcervical spine: 1.2 cm; peak rotational acceleration = peak / radius = $\sim 1,100 \text{ krad/s}^2$; scaled human rotational acceleration $\sim 10 \text{ krad/s}^2$) well exceed the scaled estimates for concussion in humans derived from field studies. We use these estimates with caution, however, as we do not know the exact rotation point during the head movement. Nevertheless, these measures highlight the importance to study different blast exposure conditions to minimize the inertial movement. Future studies will evaluate the influence of animal orientation on the resulting head movement, with the expectation that we will minimize head motions while still maintaining a sufficient external shock wave loading to the head. Once developed, this methodology will allow us to directly compare the difference in tolerance and neurobehavior between the motion/no motion scenarios with blast exposure.

Task B. Define the threshold for alterations in synaptic function, neural connectivity, and neuronal loss after scaled blast loading;

[B1] We develop and use technologies to define the minimum mechanical input necessary to cause changes in synaptic structure and function

[B2] We extend these technologies to define conditions necessary to cause changes in neural circuit connectivity

Our goal of understanding the multiscale consequences of blast loading to the brain requires us to understand exactly how these loading conditions will cause changes to the connection nodes (i.e., the synapses) and the connectivity of the neural circuits we study. However, new methodologies are required to obtain this information. We also break this down into three distinct components – understanding how the synapse may change shape, identifying the receptors at the synapse that will respond to the mechanical forces during blast exposure, and determining if there are changes in the wiring of the circuit post blast exposure. Based on the macroscopic head motions that occur during blast loading (see above), we are realizing that blast loading can create both deformation and pressure components of mechanical loading at the cellular scale. Therefore, our methods need to be scalable across both approaches. Shown below is our work in defining how mechanical inputs (deformation)

cause changes to synapse morphology and activate some subtypes of glutamate receptors. Future work in the coming year expands this to include the pressure loading observed during blast.

Synapse morphology – is there a threshold for changes in the shape of synapses?

With the possibility that some, but not all, synaptic glutamate receptors will respond to the mechanical forces during blast exposure, we also explored whether we would detect a change in the shape of synaptic spines after mechanical stimulation. Knowing if spine shape changes would be a critical parameter that could influence the activity of neural networks. As a result, we designed our methodology of determining synapse shape to occur in parallel with imaging activity of the neural circuit dynamics.

We examined four potential technologies, given the constraint that we wanted to establish a live cell imaging protocol simultaneously with our spine labeling technique. The simplest protocol was using biolistic transfection to label a small number of neurons within the network with a fluorescent eGFP, filling the cytosol and showing the spine morphology. We did not achieve consistent labeling with this approach. Second, we used the genetically engineered Brainbow mice that would produce a spectrum of colors within individual neurons, and we could use spectral imaging to identify a small subpopulation of neurons labeled with a combination of CFP/YFP/RFP. We did not achieve sufficient expression of the proteins to identify the individual synapses in these images. Third, we expressed a red cytosolic protein (mTomato) in combination with the fluorescent dye to detect calcium transients (Fura) and observed that we also did not achieve an effective, consistent transduction of a small percentage of neurons within the field of view. Achieving high transduction rates limited the ability to discriminate among neurons. Our final labeling technique used a small concentration of diO in the media to label the plasma membrane of a small percent of cells in the field of view, producing excellent high-resolution images of single neuron dendritic fields with clearly observable synaptic structures. We also achieved simultaneous labeling of this network with Fura-2AM, an indicator that we could use to detect electrical activity patterns following mechanical stimulation.

We applied this labeling approach to measure the corresponding relationship between spine shape changes and neural circuit dynamics. As a preliminary study, we used a device designed by the Columbia group to study the effect of biaxial stretch insult. We double-labeled neurons with diO to track spine shape and Fura-2AM to track calcium dynamics, as an indicator of electrical activity. We compared spontaneous patterns of activity with the Fura-2AM – measured by the magnitude and frequency – to the same measures when we blocked inhibitory neuron activity with bicuculline methiodide. Normally, in control cultures, blocking inhibitory neurons increases the magnitude of the Fura-2AM oscillations and the relative frequency of the oscillations. Stretch progressively reduced the peak magnitude and the relative frequency of the observed oscillation. However, these changes were not uniform across the population. Stretch also increased the relative amount of distinct patterns observed in the circuit and altered directed connectivity. Grouping the data across two broad categories – either stretch levels < 15% or levels > 15% - shows that the spines lengthen in both groups, but they lengthen slightly more under smaller strain levels. At higher stretch levels, we begin to observe spine retraction. We can reverse some, but not all, of the spine lengthening response by blocking the NMDA receptor.

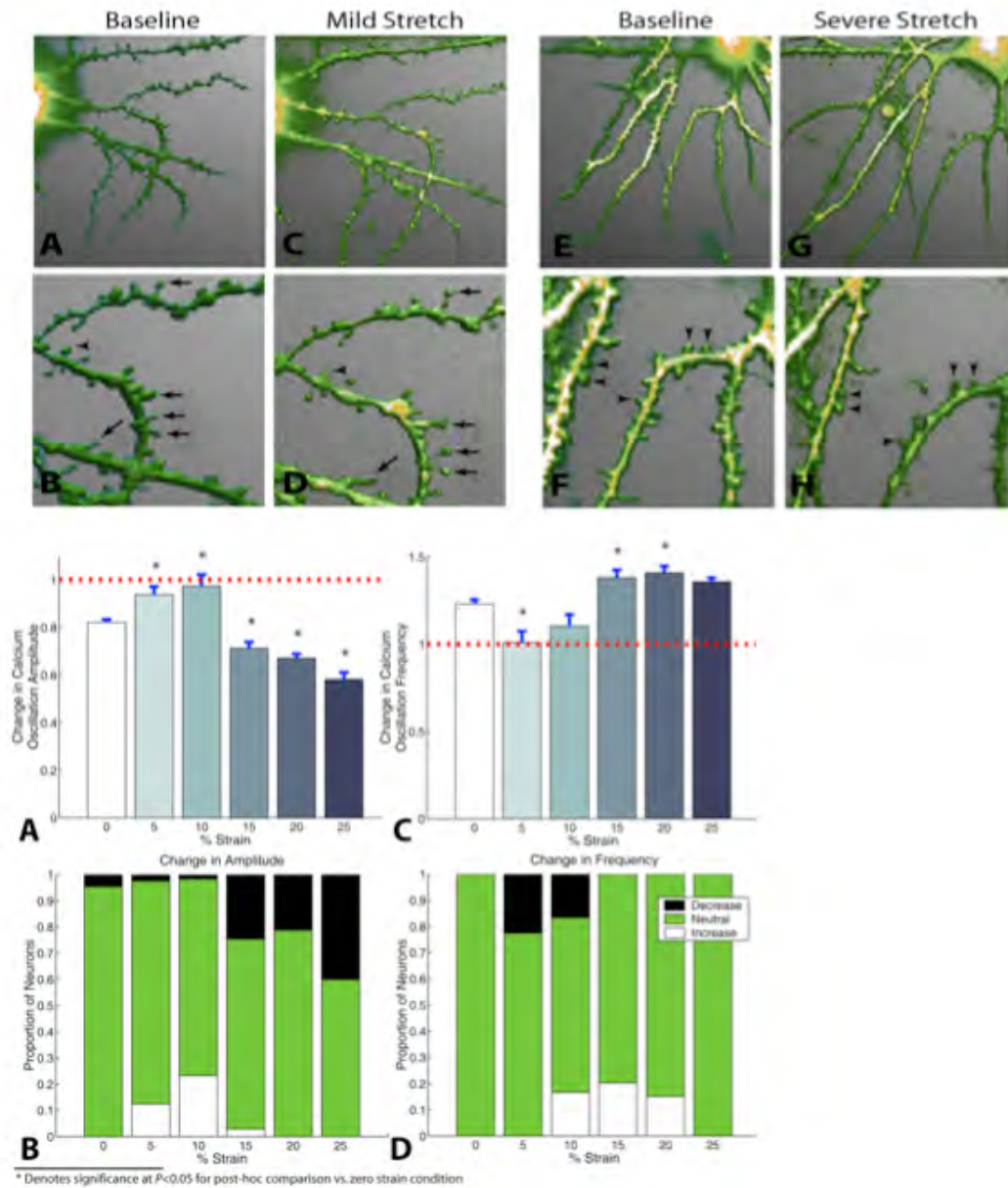


Figure 101 - Simultaneous imaging of spine shape and circuit activity. Spine shape was identified using a diO labeling technique that randomly labeled a small number of neurons within an intact neural circuit. In the same network, Fura-2AM or Fluo-4 AM revealed the increases in cytosolic calcium that appear with bursts of electrical activity. We observed that stretch of these cultures would cause a lengthening of some spines, and a retraction of other spine structures. In parallel, we observed a change in both the magnitude of calcium oscillations and the relative frequency of these oscillations.

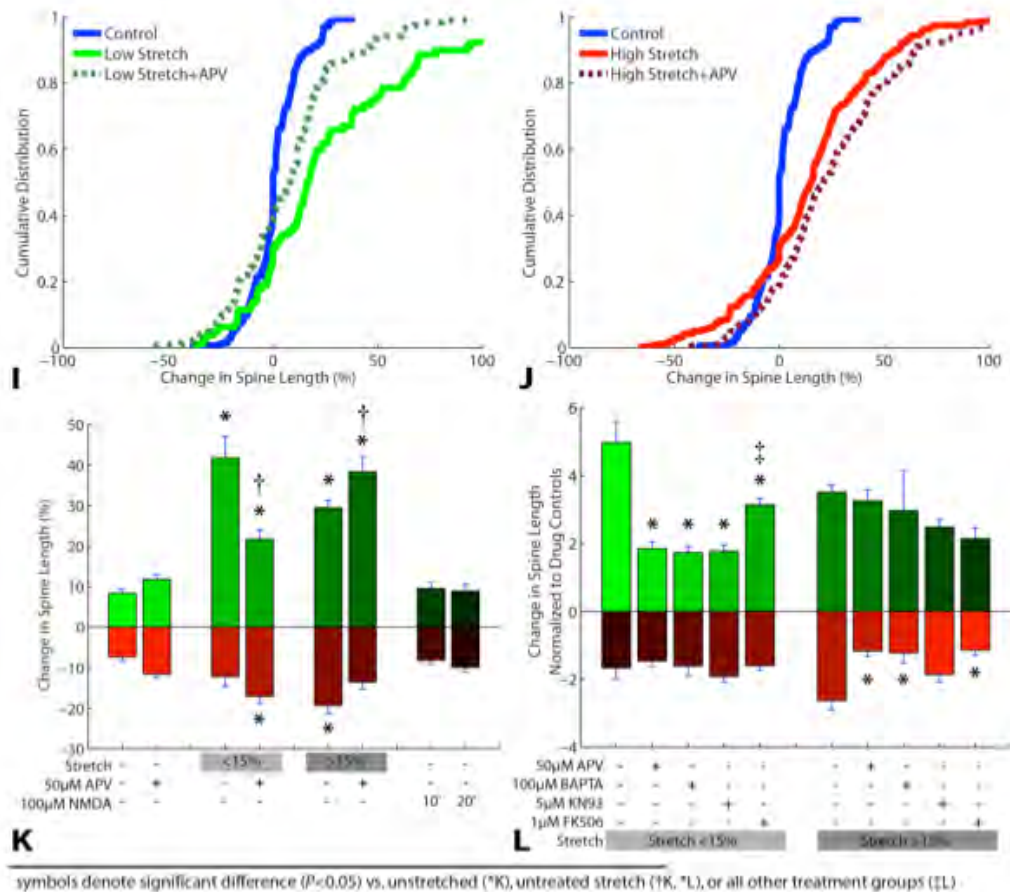


Figure 102 -A threshold stretch level distinguishes different modalities of spine shape changes. Below 15% applied stretch, the predominant response is a proportional increase in the length of the spines across labeled neurons. Above this threshold level, we observed a shift to a balance of spine extension and spine retraction, and this occurred in parallel with changes in the activity of the circuit evidenced by high speed calcium imaging.

We are now applying these same technologies to understand the spine lengthening/contraction changes after blast exposure. We use a modified shock tube/receiver design from the Duke group that allows us to rapidly return dissociated cultures to the viewing stage. We use a smaller shock tube (2" diameter), and loading profiles below the threshold for neuronal loss observed in organotypic slice cultures. In naïve, uninjured cultures, we see no effect on spine shape when we move the cultures from the incubator to the microscope stage, to the receiver, and then back to the microscope stage. Intriguingly, at 135kPa peak blast loading, we observe no detectable change in the shape of the synapses but we see a modest increase in the spontaneous firing frequency. At higher blast loadings (200kPa peak), we observe a significant retraction in the synapse length that corresponds with a reduction in the spontaneous firing patterns. We are very excited by these data, as these show that the blast profile is capable of creating immediate changes in the synapse shape and activity patterns at levels not associated with neuronal death.

Mechanically-activated glutamate receptors – are there mechanosensors at the synapse?

We used recombinant receptor systems to test if the common glutamate receptors found in glutamatergic synapses would respond directly to an applied mechanical force. In vivo forces during

blast injury are composed of both deviatoric and dilatational components. We used an existing system to study the response to deviatoric (shear) loading. This loading is reproduced using a custom-designed system that applies a non-biaxial loading to cell monolayers, mimicking a pure shear loading.

We expressed three different types of glutamate receptors – AMPA receptors, NMDA receptors, and metabotropic glutamate (mGLUR) receptors – in HEK293 cells. For NMDA and mGLUR receptors, we measured the primary calcium transient that occurs when the receptor is activated to determine if either receptor would activate in response to the applied mechanical force. One formulation of AMPA receptors (GluR1/GluR1 homomer) is also calcium permeable, and we used a similar approach to test if the receptor is activated directly following stretch. For the calcium impermeable formulations of the AMPA receptor (GluR1/GluR2), we used a sodium-sensitive fluorescent indicatory dye (SBFI) to test for any primary response to the mechanical injury. In all cases, we used a receptor agonist (glutamate, NMDA, AMPA, DPHG) to confirm that our measurement of receptor activation was appropriate.

Our results show that only NMDA receptors respond to the mechanical impulse. However, this response was not universal among the different NMDAR formulations. In some formulations of the receptor (NR1/NR2A), we did not see a detectable increase in fluorescence above baseline values. In other formulations (NR1/NR2B; NR1/NR2A/NR2B), we did observe a significant response after mechanical stimulation. The most robust response was from the NR1/NR2B NMDA receptor. After expressing NMDA receptor mutants lacking phosphorylation domains and/or intracellular domains on the receptor, we determined that one single phosphorylation residue in the NR2B subunit will significantly reduce this mechanical response, and that eliminating nearly the entire intracellular domain of the NR2B subunit will eliminate the response to mechanical stimulation, but will leave unchanged the response to agonist (NMDA) stimulation.

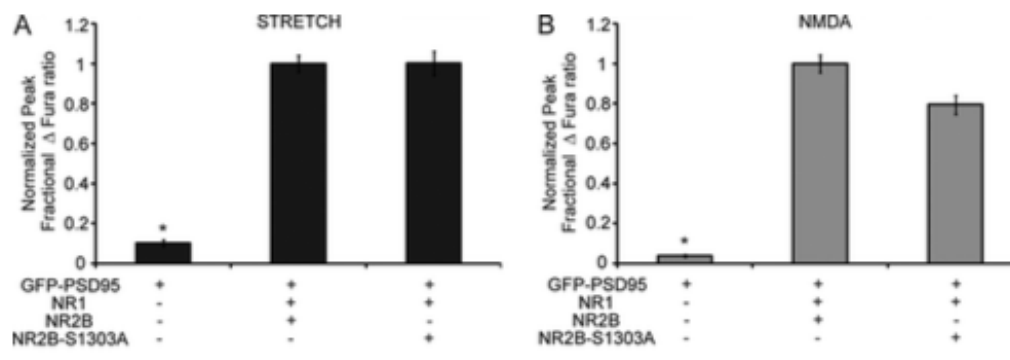


Figure 103 -Only NR2B-containing NMDARs respond to direct mechanical stimulation. The response to the mechanical stimulus is immediate, and is mediated partly by a single phosphorylation site (Y1323) on the NR2B subunit.

Studying the response of either AMPA or mGLUR receptors showed that none of these recombinant receptor populations responded to the mechanical stimulation. In each formulation, we did observe a significant increase in response to agonist stimulation. However, we recorded no significant response above the baseline when they were exposed to mechanical stimulation.

We are working now on extending these results to test if any of these receptor systems will respond to the dynamic pressures that occur during a blast exposure. We used the Duke receiver design from the first year, adopted it for use on a microscope, and are currently testing to determine if one or more subtype of NMDARs, AMPARs, or mGLURs are responsive to this loading condition.

Task C. Identify the transition point between synaptic/cellular changes and larger scale circuit dysfunction, leading to blast thresholds for circuit function.

[C1] We use dissociated culture preparations to define when synaptic changes lead to corresponding changes in individual neuron function,

[C2] We use both dissociated and organotypic culture preparations to define when synaptic changes lead to corresponding changes in neural circuit activation,

[C3] We define if there is a different threshold for neural circuit changes (LTP/LTD) when connectivity is altered in a network

The multiscale representation of neural circuitry: Incorporating mechanosensing effects and single neuron phenotype profiles

With our systems coming together for probing the neural circuit at different scales, we identified the need to develop new in silico tools to help interrogate the effects of changes at the synaptic scale into changes in the circuit dynamics. In parallel, we sought the need to establish the aggregate properties of single neurons – i.e., if they have a predominant NMDAR, AMPAR, or mGLUR profile that is predominant in their calcium signaling during normal neurotransmission. Here, we integrate our past work with new studies to define how the selective mechanoactivation of some, but not all, NMDARs contribute to early changes in network properties of neural circuits after mild mechanical injury. We use an integration of in silico and in vitro approaches to find an important new role for the NR2B containing NMDA receptors: these receptors are a major mediator of network asynchrony, and blocking these receptors both enhances network synchrony and facilitates the re-integration of single neurons into functional neural circuits after mild traumatic brain injury in vitro.

To examine the spectrum of possible circuit dynamics in vitro, we built an integrate-and-fire model of spontaneous network activity. Population of pyramidal-like neurons were assembled into a network following the topology measured in in vitro cultures. Dendritic spines in this model were populated with AMPARs and NR2A- and NR2B- NMDA receptors (Fig 105A). Synaptic transmission was simulated by vesicular release of glutamate onto the spine head, and the activation of these receptors was modeled using a stochastic diffusion-reaction scheme⁴ (Fig 105D). The resulting current, summed at the soma, was used to update the cell membrane potential. Calcium influx through NMDARs was modeled by computing membrane potential dependent relief of Mg²⁺ block of activated glutamate bound and open receptors (Fig 105C).

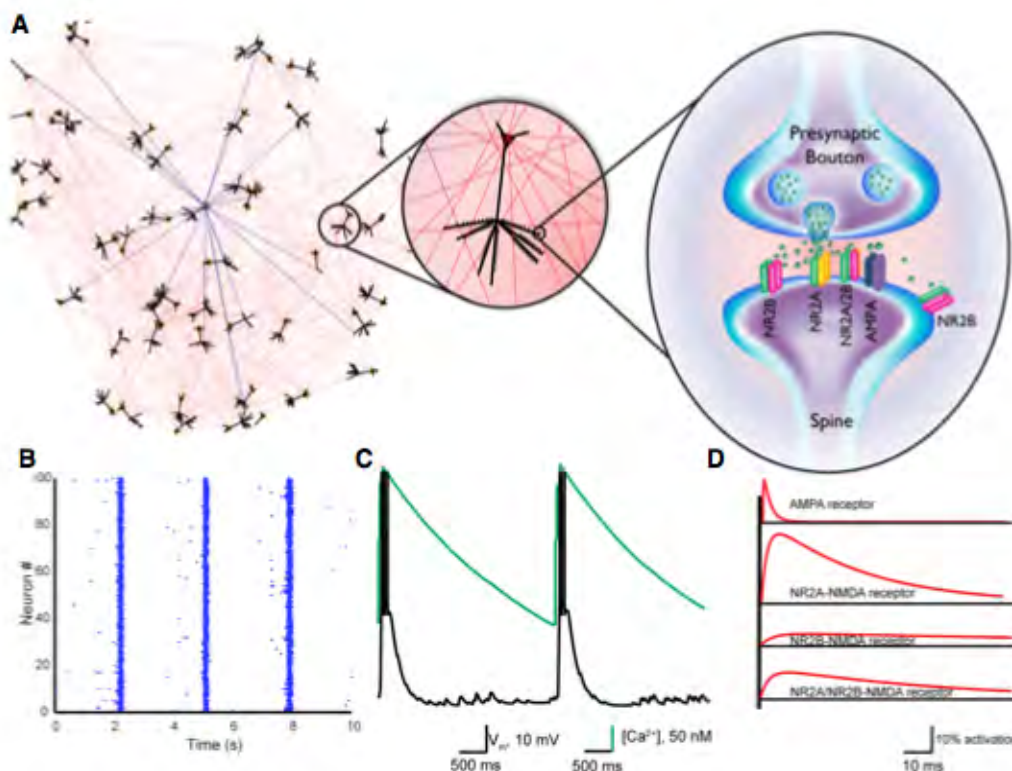


Figure 104 -Overview of multi-scale computational model of neural networks. A: Schematic of model architecture: networks -> neurons -> spines. B: Raster plot of simulated network activity. C: Membrane potential (black) and calcium transient (green) of a representative neuron. D: Activation of excitatory receptors at a prototypical dendritic spine.

Our next objective was to develop and test new methods for assaying the individual neuronal response to tonic electrical activity. Our approach was based on identifying if there were substantial differences in the pathways responsible for calcium influx in individual neurons across a neural circuit. In past studies, we used calcium imaging of the population to characterize the general receptor expression profile for AMPA receptors, NMDA receptors, and voltage-gated calcium channels. We now extended this into single neuron profiles, establishing a protocol to progressively activate and then reversibly block different calcium influx pathways in primary cortical neurons. We found we could successfully block the NR2B and NR2A-containing NMDARs separately, and could use the blockade of voltage gated calcium channels (nimodipine) as a surrogate measure of single neuron AMPAR strength. We found the relative magnitude of AMPAR strength was correlated to enhanced functional connectivity in the circuit. Additionally, we found the relative magnitude of NMDAR calcium influx to the overall calcium influx for a given neuron was inversely proportional to the functional connectivity. These trends generally follow the developmental trends observed in dissociated cultures: NMDARs are the first to appear at synapses, followed by a progressive increase in the insertion of AMPARs.

We then tested cultures for changes in neural circuit dynamics by assessing by measuring the calcium activity of a population of neurons with the genetically encoded calcium indicator, GCaMP3 (AAV2/I-hSynapsin I). Five minutes of time-lapse imaging of a neuronal population (150-200 neurons in field of view; 20 Hz framing rate) was performed pre- and post-injury. At levels that do not cause neuronal death, we observed that mild injury caused widespread changes in network topology, synchrony, and excitatory transmission (Fig 106 A-C). Alternatively, even milder mechanical injury (10% stretch)

produced very little changes in network topology or synchrony, however, there was a brief period of heightened spontaneous activity following injury, suggesting there is a graded response to injury (Fig 106 D-F).

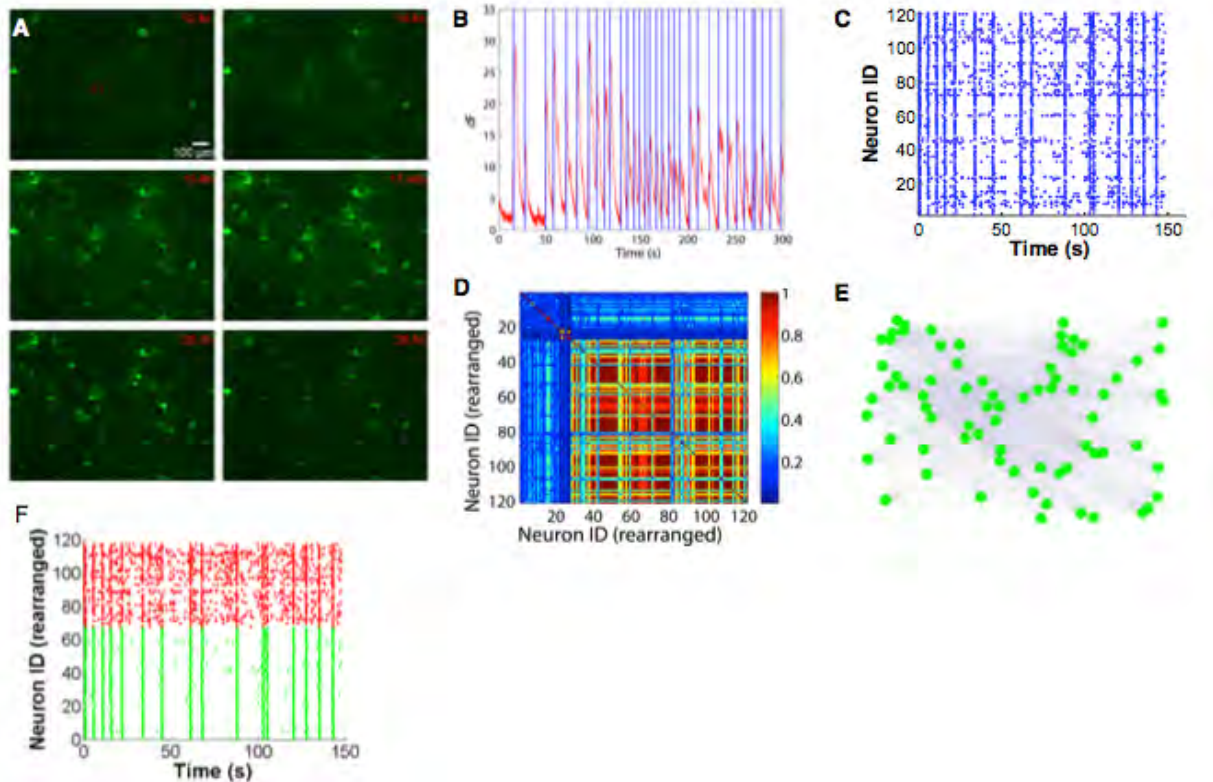


Figure 105 -Measurement of network properties using calcium imaging. A: Example of a network-wide oscillation. B: Fluorescence trace of a sample neuron (red) and automated detection of onset of transients (blue). C: Calcium activity of the network is compactly represented in a raster plot. D: Synchronization cluster analysis revealed detailed information about how groups of neurons are synchronized. E: Functional connectivity was determined by surrogate resampling. F: Functional connectivity was used to determine network topology. The network consists of two modules (red and green). Activity of neurons within a module is similar and distinct from the activity in a different module.

To investigate the mechanisms of network change following injury, we first explored if the injured networks showed a change in the relative activation of NMDAR subtypes. We measured the fractional drop in the amplitude of calcium fluorescence of spontaneously active neurons with successive application of Ro 25-6981 (NR2B specific antagonist), APV (non-specific NMDAR antagonist), and nimodipine (voltage-gated calcium channel (VGCC) antagonist) (Fig 107A). The main sources of calcium in uninjured neurons are NR2As and VGCCs. Acutely (1-hr) following dynamic stretch injury, NR2B receptors become a significant source of Ca^{2+} , likely due to partial loss of its native Mg^{2+} block (Fig 107B) ($n=8$, pre-stretch NRB content $20\% \pm 2.8\%$, post-stretch NRB content $35\% \pm 8.5\%$, $*p<0.05$).

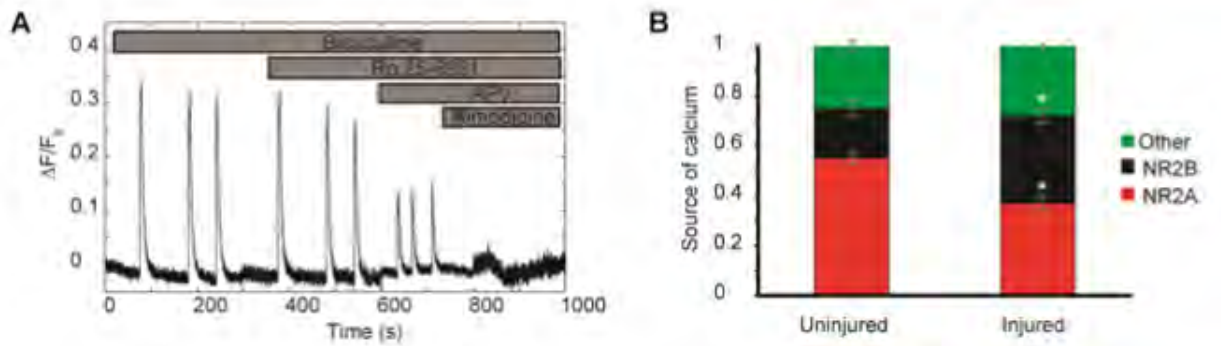


Figure 106 -Source of calcium determined by the drop in fluorescence upon successive application of NMDAR subtype antagonists (A). Injury enhances calcium influx through NR2B containing NMDARs during synaptic transmission (B). * $p < 0.05$ relative to control, uninjured cultures.

To investigate the effects of enhanced NR2B activity on network dynamics, we used our multi-scale model of network activity. Under physiologic conditions, vesicular release of glutamate onto a dendritic spine showed consistent AMPAR and NR2A- activation, with nearly no NR2B-NMDAR activation (**A, left**). In simulated injury condition, we found significant activation of NR2B- **B** NMDARs receptors and large variability between repeated simulations (**A, right**). We used the activation profile of these receptors at a single spine to simulate the activity patterns of a population of neurons (**B, left**). Our simulations predicted that the selective loss of NR2B Mg^{2+} block significantly decreases network synchrony (**B, right**). (Fig 108) Consistent with our in silico predictions, blocking NR2B containing NMDARs of mechanically injured neurons significantly rescued synchrony (0.37 ± 0.15 post-stretch to 0.81 ± 0.22 post- stretch with Ro 25-6981, $p < 0.05$) and restored network integration (Fig 108).

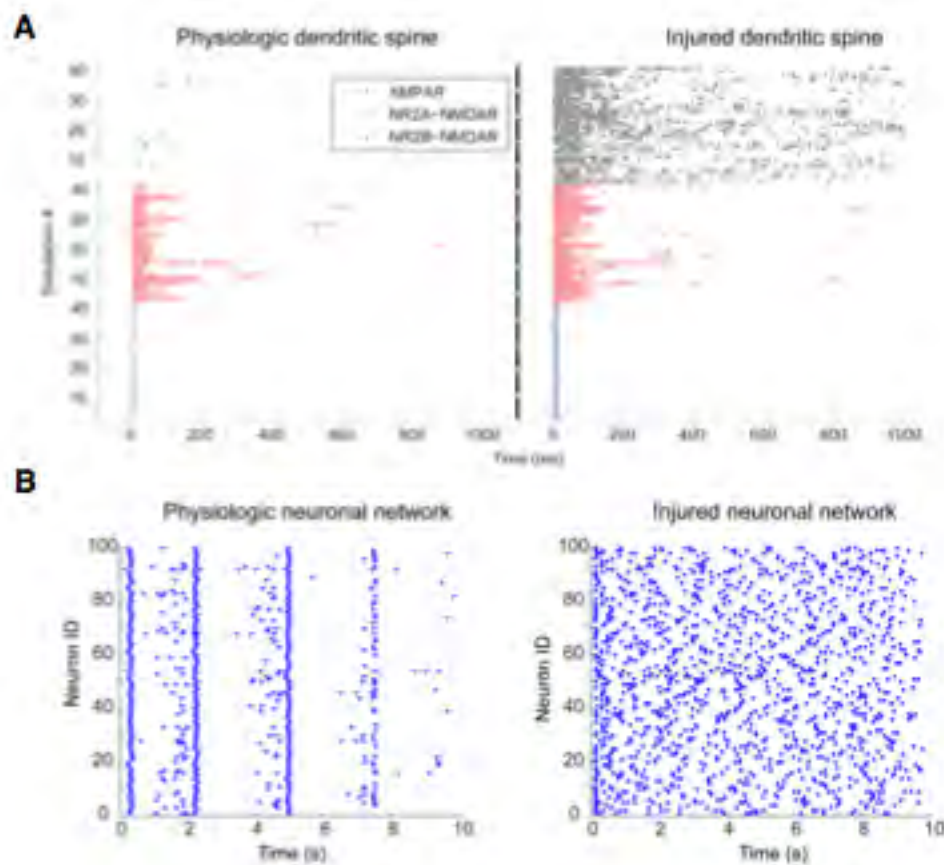


Figure 107 -Simulation of NR2B-NMDAR activation *in silico* shows that the fluctuation in receptor opening dynamics at a single synapse are variable across single release events. Incorporating these into models of the *in vitro* circuit (B) shows that the change in physiology of the NMDAR will lead to a significant increase in the disorder of the neural circuit.

Task D. Correlate changes at the synapse and circuit level to corresponding neurobehavior deficits in animals. To accomplish this task,

[D1] We use knowledge from Thrust A to scale models of blast wave transmission into animals,

[D2] We verify that the scaling of thresholds for synaptic, connectivity and neuronal loss is correct for these experimental models, and

[D3] We exercise these animal models at the threshold levels for multi-scale dysfunction in synapses and circuits, and correlate these circuit-scale alterations to changes in neurobehavior.

These tasks are based on developing an understanding of how the blast wave focuses its effects within brain subregions, and developing neurobehavior testing protocols that allow us to scan across the spectrum of behaviors associated with different brain regions. Therefore, we needed to develop and use a battery of neurobehaviors in each animal, and to evaluate these behaviors in total. In the subsequent paragraphs, we define these developments and apply this analysis to our dataset of behaviors collected to date.

The complex consequences of blast exposure - Rapid Neurobehavior phenotyping

Mouse models, with specific genetic mutations or disease/treatment paradigm, are often subjected to a series of behavior experiments to characterize the phenotypic effect of a transgene or an intervention. Each behavior experiment is designed to test the function of a brain region in isolation. Although many behavior tests are available, it is uncommon to see a battery of tests applied within a single study. A large reason for this absence of a test battery is the sheer amount of time required to analyze the behavior testing, as well as postprocessing of any recorded behaviors for more subtle signs of damage. As a result, data produced are inconsistent and lack a clear behavior basis for some of the procedures and calculations used to collect and analyze data. Developing a battery of tests applied to each animal may also reveal subtle behavioral deficits associated with subgroups of animals, as well as correlations in deficits across different behavior scoring paradigms.

One major obstacle in acquiring an accurate test battery is that the scoring is done manually, making it time-intensive and liable to subjectivity. Using fear conditioning as an example, manual scoring involves watching animals live or posthoc from video and assessing freezing time with a stopwatch. In the entirely manual mode, there is no video recording of the experiment and therefore no ability to return to a given experiment and mine the data more deeply. With video recording of the experiment, one then faces the choice of continuing a manual scoring method – which can be highly variable across personnel – or to invest in an automated scoring platform. Several automated activity monitoring methods exist, but they either lack robustness or rely on specialized expensive equipment. For example, San Diego Instruments uses a concentrated number of infrared photo beams to measure beam breaks, while Clever Systems and Kinder analysis rely on proprietary software for segmenting the mouse in a fear conditioning chamber and tracking movement of the central part (centroid) of the animal to calculate freeze time. Large deviations in the centroid position are recorded as motion and small deviations are scored as freeze events. However, this method requires setting an arbitrary threshold and is not robust enough to distinguish between true freezing events and micro-motions, both of which cause very small changes in the centroid position. The end result is gross over-estimation of freeze percentage, limiting the use of these software.

Furthermore, each behavior experiment is full of rich data that is often ignored during manual scoring - for example, in a spatial object recognition (SOR) task, an observer manually records the total duration that a mouse interacts with an object. However, with automated tools, the same SOR video can be used

to analyze mouse's motor function (total distance traveled, speed, gait, etc.), the level of general anxiety (amount of time spent in the periphery vs. center), and exploratory tendencies. One can choose even more sophistication – e.g., we can determine exactly how a mouse interacts with a 3-dimensional object, whether it focuses on just one side of the object, or explores the object through different directions to build a more complete internal representation of the object. These automated measurements can augment existing manual scoring methods, provide assessment of higher-level brain function and allow us to extract more meaningful behavior phenotypes, especially when the effects of disease/treatment are subtle and not localized to a brain region.

In the past year, we developed a geometrical model framework for automated analysis of commonly used neurobehavior tasks, including, open field test, SOR, NOR, social interaction, T-maze, zero-maze, fear conditioning, and Morris water maze. We identified and incorporated technical changes to improve automated scoring of neurobehavior videos. We used a video recording of all tests performed in series – Rotarod, spatial object recognition, open field, and fear conditioning. We developed a Matlab-based tool that performs an automated analysis of each test, using a standardized scoring routine. Motion detection utilizes estimation of camera noise (red line) for setting threshold for discriminating between strict freezing events and motion or micro-movements from large ambulatory motion. These are used across all experiments to discriminate motion versus static position. To track the position and attention of the mouse, we segment the mouse shape by background subtraction with a median filter, apply landmarks on the segmented image, and use a custom algorithm to identify the head from the tail. We model the mouse's field of vision pointing in the direction of the head from the centroid. We use this model of vision tracking for the animal to discriminate when the animal interacts with a novel object, or interacts with spatial objects placed in a cage. Developing maps of this interaction time and profile allows us to detect if there are differences in animal behavior among different test groups. The same algorithm applies to social interactions, where a mouse can be placed in one of two chambers, with the second chamber containing a companion mouse (or empty). We find this algorithm is capable of detecting differences in the elevated zero maze among four testing groups, across fear conditioning tests, and can show significant differences in ambulation across SOR and open field tests, and fear conditioning tests.

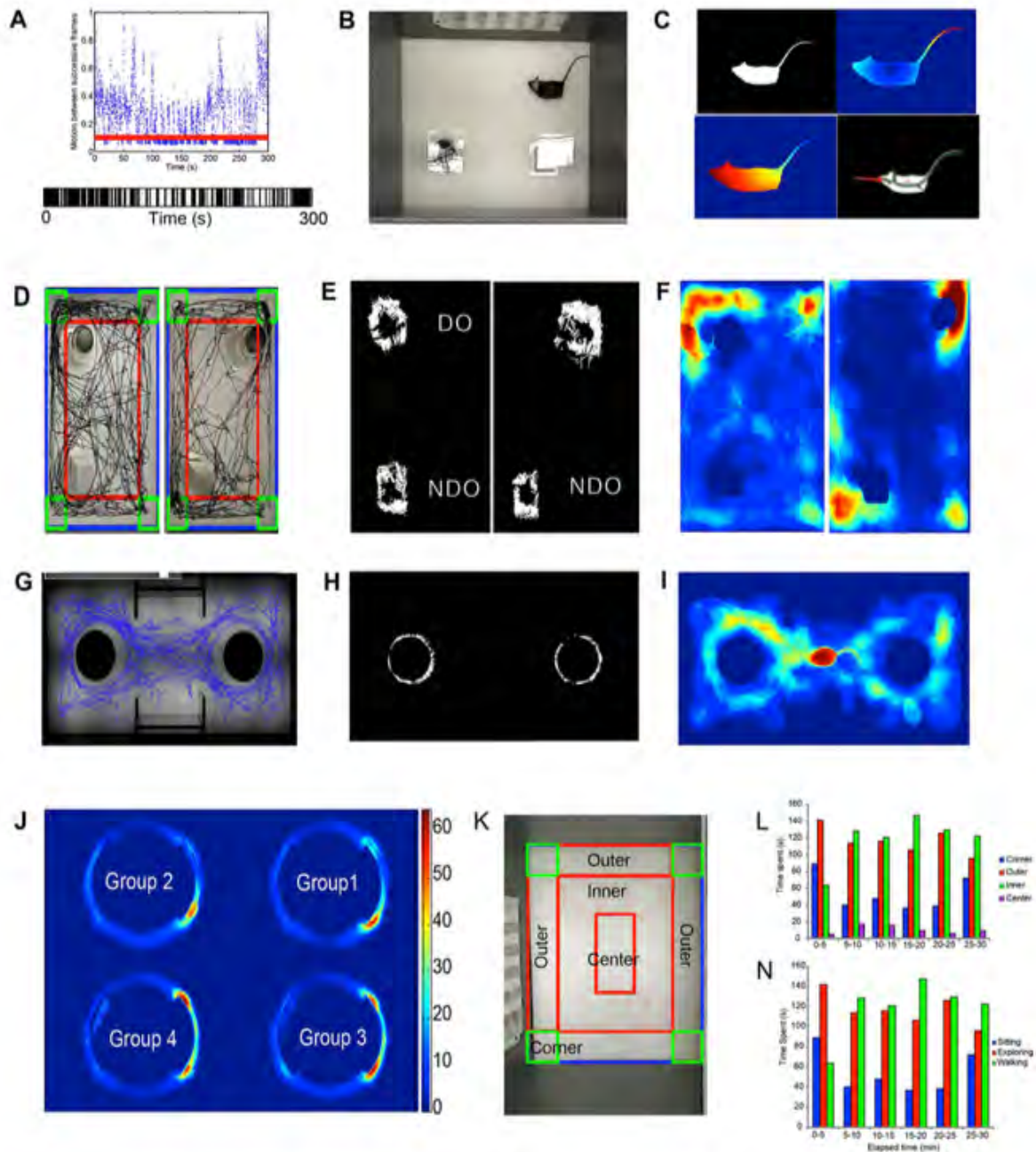


Figure 109 -Summary of automated behavior analysis algorithms. From video recordings of an animal in a confined box (B), measures of the animal motion extracted by using a wireframe model of the animal (Panel C) are discriminated from random camera noise. Bar codes defining periods of motion (black) and rest (white) are analyzed to detect patterns of movement. In an object recognition algorithm, the use can generate an automated map of the time and extent of interaction an animal has with either object, scoring the preference of the animal to explore the displaced object or the novel object. Similarly, the path of the animal in a social interaction test will reveal if the animal has a preference towards interacting with a littermate. Heat maps (F,I) indicate the relative position of the animal over the five minute monitoring period. In the elevated zero maze, the sham animals show a general preference to remain within the closed portion of the maze (between 2 o'clock and 5 o'clock), while blast exposure significantly shifts this preference (Group 1, Group 2). With this automated analysis, one can analyze automatically the position of the animal in the open field test, a measure of the general exploratory behavior of the animals.

Equally useful is our ability now to combine this test battery from the automated analysis into a single evaluation of the response following blast exposure. We assemble a matrix of test results from the test battery, and use a principal components analysis to determine the key components of behavior that discriminate the group exposed to blast versus naïve animal groups. Using our automated analysis, we extracted 14 relevant parameters to describe each mouse's performance in tasks related to motor function, spatial and associative memory, fear/anxiety, and reaction to novelty. We found that bTBI causes early deficits in motor memory and fear conditioning. We drew associations among these tested behaviors in naïve animals. Since these behaviors had little overlap when considering their anatomical substrate (eg, Rotarod is primarily an indicator of cortical and cerebellar function, while fear conditioning involves both the hippocampus and amygdala; spatial object recognition centered principally in the hippocampus), we did not observe much cross-correlation among these behaviors in naïve mice. However, the correlation among the behaviors was strengthened following blast exposure. We are now exploring if this convergence in behavior associations is caused by a more diffuse brain injury from blast, or if it suggests a broad connection among behaviors with linked anatomic substrates.

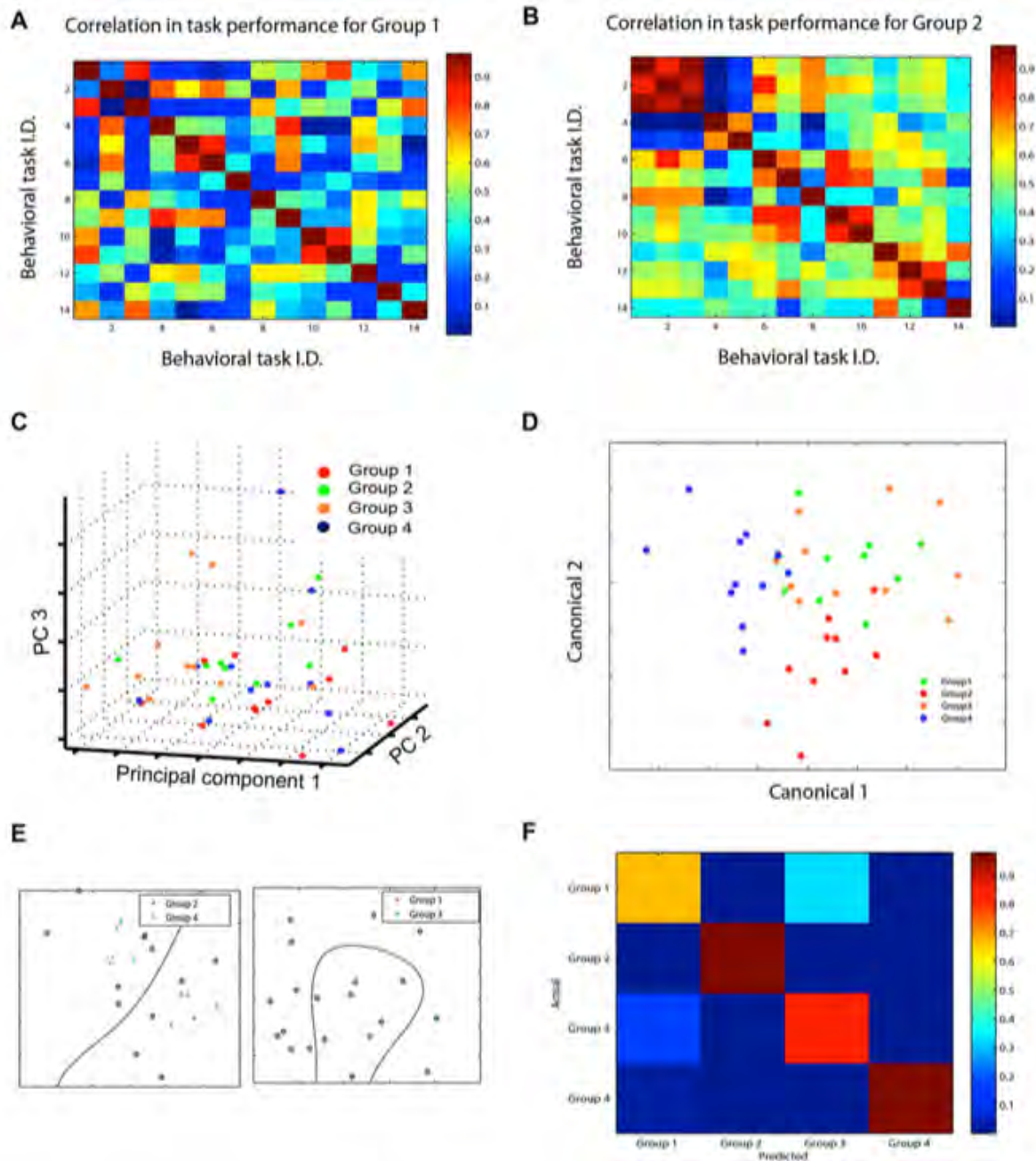


Figure 110 -Principal component-based analysis of behavior testing reveals behavior phenotypes. With an aggregate of the 14 separate behavior tasks extracted from each animal, we can use these to develop correlations in the sham state (group 1) and the injured state (Group 2, B). We also develop the principal components from these aggregate measures to determine significant differences among testing groups. Using a canonical analysis technique to define distinct performance corridors among these testing groups, we can define significant group differences between blast injured (group 4, group 1) and sham (group 2, group 3) animal groups.

Our toolkit, centered around assessing mice in task related experiments, will complement existing automated software for monitoring mice behavior in their home-cages. We reveal, for the first time, a novel neurobehavior phenotype for blast exposure based on an aggregate performance across several neurobehavior tests.

Creating a murine model of 'pure blast' injury

Last year we developed a framework for analyzing the head motions/accelerations caused by the blast loading from our shocktube. Our results clearly showed a complex head motion created by the blast wave. In the past year we used these findings to identify a method for creating 'pure blast' loading in the mouse.

Shock tube design: We used the shock tube design provided by the Duke partner, in use for both both in vitro and in vivo studies. The shock tube design, developed in detail in a separate publication, provides controllable and reproducible input that mimics the common Friedlander wave described for free-field blast events.

Mouse holder design: In some past configurations, the animal is placed immediately outside the tube, permitting the investigator to visually observe the animal status prior to and immediately following blast exposure. We studied this configuration in depth, designing an animal holder that would position the center of the mouse head at a prescribed distance (15 mm) from the exit of the tube, as well as different radial distances from the tube's centerline axis to examine the reproducibility, distance dependence, and potential complication factors with animal misalignment. A stock, threaded aluminum tube (Part no. 44705K233, MMC) was cut to length, inserted into a threaded flange (Part no. 4568K273, MMC), and filled with a urethane material to provide a flat surface for mounting the mouse in a prone position. Resting on a thin trapezoidal extension of the holder, the head was exposed to the shockwave while the rest of the body was encased by the aluminum tube. The interior surfaces of the holder were lined with a blast absorbing material (Sorbothane, Part no. 8514K362, MMC), and the animal was secured in place to minimize any indirect transfer of the blast wave along the animal torso.

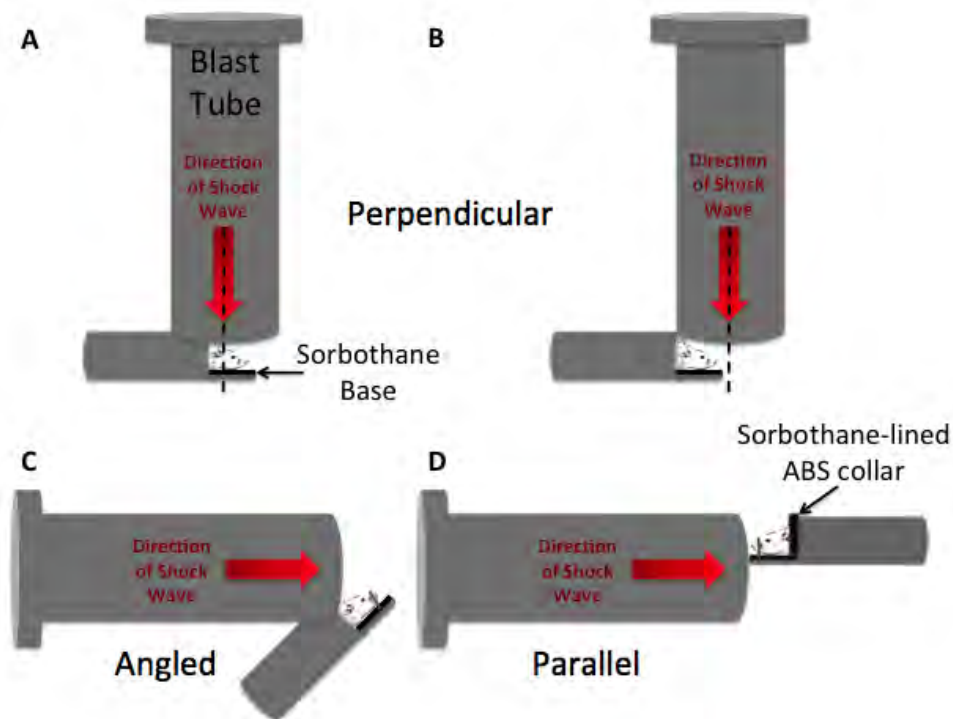


Figure 111 - Diagrams representing the different animal orientations relative to the blast tube. All orientations held the distance from the exit of the tube to the center of the mouse head constant.

In two of our configurations (Figure 111), a thin metal rod was positioned on the holder to secure the snout and limit the lateral motion of the head. The thickness and positioning of the material were chosen to limit the obstruction of the shockwave path to the brain.

Collar design: In some experiments, we exposed the mouse to a shockwave traveling parallel to its body's long-axis. To restrain head motion, we designed a custom cervical collar that fit around the neck and sized this collar to permit normal breathing. The design was wedge-shaped to accommodate variation in the anatomy of different test subjects. The position of the collar relative to the mouse was adjustable to ensure a secure fit for each mouse. Lastly, the top surface of the animal holder was replaced with clear PETG tubing (Part no. 9245k51, MMC) to visualize the torso and verify that collar positioning did not obstruct breathing.

Animal orientation: Animals were oriented in one of three different positions relative to the direction of blast wave propagation (Figure 111): (1) **perpendicular** to the blast wave exiting from the shock tube, with the head center either (a) aligned with the center of the tube axis or (b) aligned within the inner periphery of the shock tube, (2) **angled** 45 degrees from the shock tube axis with the nose pointing away from the tube exit, and (3) **parallel** to the axis of the shock tube with the nose pointing towards the tube exit.

Pressure recording: We used pressure transducers with sufficient dynamic frequency response (Endevco, model 8530B-200, San Juan Capistrano, CA, USA) to record the pressure at the exit of the shock tube. We used three equally spaced transducers along the perimeter of the blast tube to evaluate wave symmetry, and acquired pressure data using a MATLAB based data acquisition program sampling at 200kHz per channel. We placed a fourth pressure transducer within the animal holder cavity, located in an area adjacent to the animal torso, to assess the potential indirect transfer of any blast wave along its axis. To eliminate aliasing artifact, we conditioned each pressure transducer signal with an inline filter conditioning box (Alligator Technologies, USBPGF-S1, Costa Mesa, CA, USA) set to provide a 20 kHz cutoff frequency linear phase filter.

High Speed Video: We used a high-speed video acquisition system (Phantom v4.2 camera, Vision Research, Wayne, NJ, USA) to record head motion either from the side or front of the blast tube, corresponding to a lateral or frontal view of the animal head. For all reported tests, the framing rate was set to either 10 kHz (resolution: 256x128; N=1) or 22 kHz (resolution: 128x128; N=17). Fiduciary markers in the field of view provided a calibration measure for lengths and displacements in the x and y (frontal view) or y and z (lateral view) direction.

A MATLAB based image processing algorithm was used to manually track the fiduciary markers on the head during the blast sequence. The two fiduciary markers defined in the tracking algorithm were used to measure the movement of the head center during blast. We tracked both the displacement vector, and the x and y displacement components, over the entire duration of the experiment that included a pre-triggering period (5 milliseconds) and the movement for the first 30 milliseconds during and following the blast event, since preliminary testing showed negligible head movement after that timepoint. We used data smoothing algorithms (zero-phase 8th order Butterworth filter, 1kHz cutoff frequency for vertical (y-axis) data and 6th order, 500 Hz cutoff frequency for horizontal (x-axis) data) on the tracked displacement data. We next applied a first order Euler's approximation to calculate the velocity and, in turn, the acceleration in the x-y or y-z laboratory coordinate system based on these displacement data. Similar to displacement, we calculated the resultant magnitude, as well as the x and y components, of the velocity and acceleration.

Animal preparation and injury: Male, C57BL6 mice aged 12-14 weeks were obtained from either Charles River laboratories (Wilmington, MA, USA) or Taconic (Hudson, NY, USA) and allowed to acclimate in the colony before testing. We carefully adhered to the animal welfare guidelines established by the University of Pennsylvania's and Columbia University's Institutional Animal Care and Use Committee (IACUC), and used procedures that were approved by those IACUC committees. Animals used to characterize the head motion during blast were euthanized immediately prior to placement in the animal holder. All animals were tested within 40 minutes of euthanization to minimize the influence of changes in tissue properties due to rigor mortis. In separate tests to measure the neurological impairments after blast exposure, animals were placed in an anesthesia induction chamber (5% isoflurane) for 2 minutes, and then transported into the testing room. Animals remained on 2% isoflurane anesthesia for 3 minutes during placement and positioning prior to exposure. Immediately prior to testing, anesthesia was

discontinued. Immediately after injury, the animal was removed from the holder and brought to a recovery area.

Neurological impairment immediately after blast was measured using a righting time response. To measure righting time, we placed the mouse on its back and measured the time elapsed until it turned over and righted onto all four paws. Recording time started when the animal was removed from the animal holder following blast or sham exposure. Once animals regained the ability to right themselves, they were monitored for several minutes while they established their movement and exploratory behavior before they were returned to a warmed recovery cage and monitored for future status.

Statistical analyses: We used an analysis of variance model to compare peak velocities and accelerations across different testing configurations. We used Student's t-testing to compare pressure data as well as righting times between sham and injured animals in each testing configuration. Finally, we used logistic regression techniques to determine the survivability curve in the perpendicular, angled, and parallel test setups. For all tests, significance was set at $p < 0.05$.

Free field blast events show a characteristic rapid increase in pressure that corresponds with the initial arrival of the shock wavefront, followed by a rapid, exponential decay that can include a modest negative pressure. Our design successfully re-created the sharp rise and rapid decay, but did not include the significant negative pressure phase commonly found with large explosions (Figure 112). This blast waveform was repeatable for test conditions that spanned peak pressures of 120 to 500 kPa (Table 1). Peak overpressures around the perimeter of the tube varied less than 15 % within individual tests, and less than 7% across tests using the same membrane thickness.

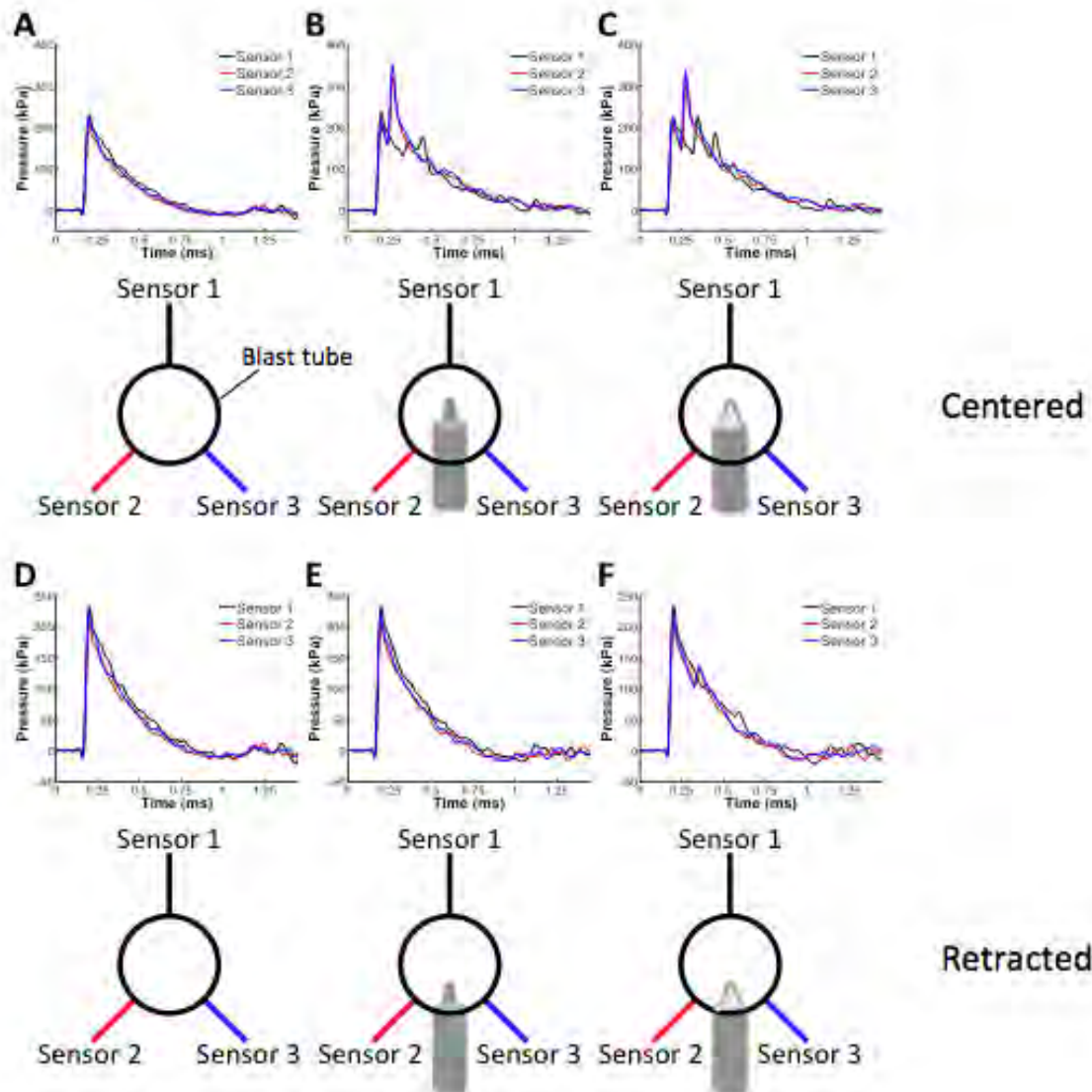


Figure 112 - Representative pressure traces gathered from the three sensors at the exit of the blast tube with the mouse holder in different positions. All tests were conducted in the perpendicular position.

With the animal holder positioned in the centered perpendicular orientation at the blast exit, we observed a consistent secondary reflected pressure spike recorded for each test (0.508 mm membrane thickness; Figure 112). Due to this wave reflection, the magnitude of the peak pressure averaged across all three transducers was significantly larger ($p < 0.01$) with the animal holder in place (259 ± 15 kPa) when compared to tests in which the holder was not used (215 ± 13 kPa). Readings from the pressure sensor located most distant from the animal holder (Sensor 1) did not differ from free field pressures ($(229 \pm 16$ kPa (with holder) vs. $(227 \pm 4$ kPa (free field); $p = 0.57$), while the second and third pressure sensors closest to the animal holder (Sensor 2, Sensor 3) displayed higher peak pressures (292 ± 19 kPa (Sensor 2) and 257 ± 20 kPa (Sensor 3)) that were significantly different ($p < 0.01$) from the free field pressure for each sensor position (201 ± 3 kPa (Sensor 2) and 218 ± 6 kPa (Sensor 3)). In comparison to the pressure transducer measurements along the perimeter of the shock tube exit, the pressure

transducer recordings within the animal holder tube were significantly less (219 ± 15 kPa (average across perimeter sensors) vs. (156 ± 8 kPa (within holder); $p < 0.01$).

Table 1			
Membrane Thickness (in)	Peak Overpressure (kPa)	Duration (ms)	Impulse/Area (kPa*ms)
0.01	139 ± 5	$0.39 \pm .04$	18 ± 2
0.02	215 ± 13	$0.65 \pm .04$	46 ± 5
0.03	275 ± 24	$0.80 \pm .03$	77 ± 7
0.04	329 ± 31	$0.91 \pm .05$	106 ± 9
0.05	390 ± 24	$0.98 \pm .04$	135 ± 11
0.55	415 ± 41	$1.02 \pm .04$	148 ± 12
0.06	448 ± 29	$1.07 \pm .02$	163 ± 12

Positioning an animal within the holder assembly led to no differences in peak pressures for all three transducers located at the blast tube exit when compared to pressures recorded with only the animal holder in place (Figure 112). Although peak pressure was not significantly affected, the presence of the animal's head led to a small transient increase in pressure during the decay phase of the waveform measured by Sensor 1. We observed a significant reduction in the pressure measured at the approximate torso location when an animal was placed in the assembly (156 ± 8 kPa (empty holder) vs. 12 ± 3 kPa (animal in position)). In all tests, peak torso pressure was well below the threshold pressure associated with pulmonary trauma.

These data show that placing the animal holder in the blast wave path creates a more complex blast loading profile. We next tested if we could adjust the position of the animal holder at the exit of the shock tube to minimize the effect of the holder. Placing the holder near the periphery of the shock tube (Figure 112) substantially reduced reflections of the shockwave, and the measured peak pressures averaged across the sensors (224 ± 10 kPa) were not significantly different from the peak pressures measured in the free field condition (215 ± 13 kPa). One additional benefit was that the new position of the holder in the periphery of the blast wave path eliminated the overt damage to the mouse ear that occurred when the mouse was aligned with the centerline axis of the blast tube (data not shown).

These tests confirmed it was possible to place the animal holder at the exit of the blast tube and minimally interfere with the input blast wave. We next tested if the position of the mouse at the tube exit significantly influenced the head motion occurring during the blast event. When the head was oriented perpendicular to the blast wave (Figure 111), it showed three general phases of motion during the blast event: a rapid, nearly vertical downward motion, followed by a slightly longer upward motion, and then a slowly tracking lateral motion as the head rotated and slowed into its near final position (Figure 113). Starting from its rest position, trials across different test animals showed a relatively consistent peak downward displacement (Figure 113). When the animal was placed at an angle of 45° to the direction of the shock wave, video footage revealed significant flexion movement of the animal head into the supporting sorbothane layer, followed by an extension of the head beyond the initial position (Figure 113). When the animal was placed parallel to the direction of the shockwave, we supported the

occiput with a custom-designed cervical collar. In this configuration, very minimal head displacement was observed (Figure 113).

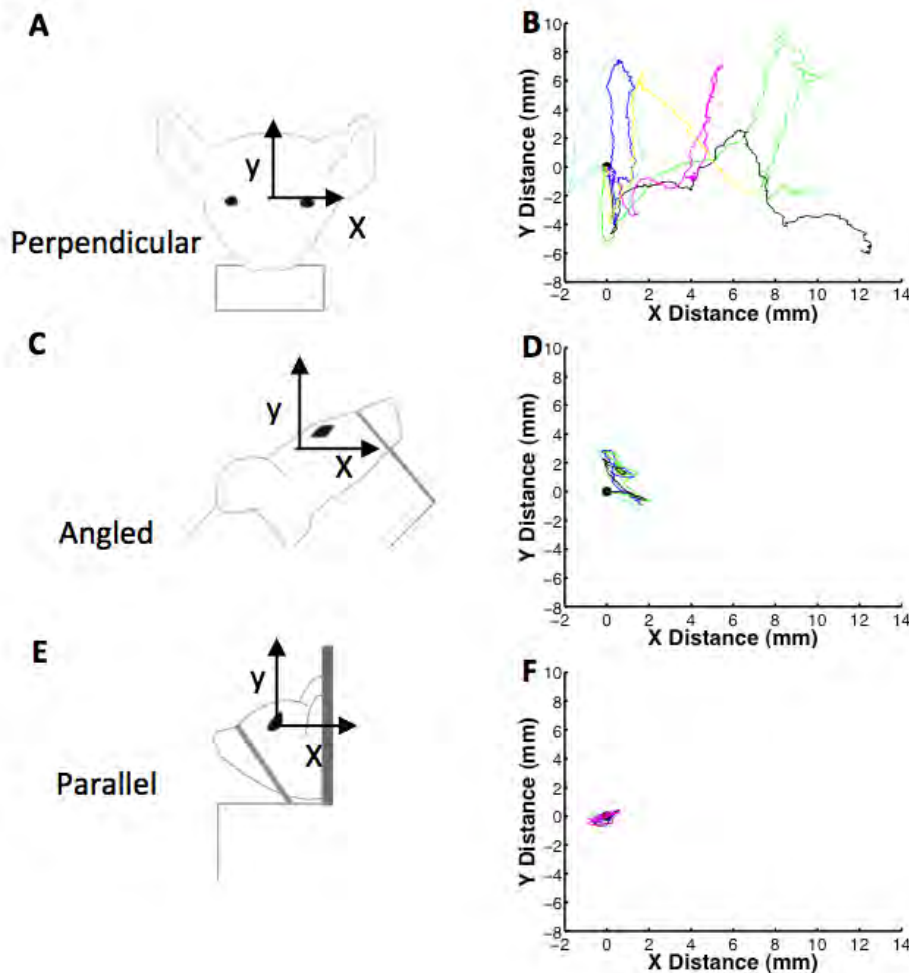


Figure 113 - Displacement that occurs during each blast event for the perpendicular (B), angled (D) and parallel (F) orientations.

Across the three positions studied, we used the displacement data to determine if there were significant differences in the accelerations occurring across these tests. See Figure 114 for illustrations of the filtering process as well as representative velocity and acceleration traces for the perpendicular configuration. In the perpendicular configuration, peak vertical accelerations ($a_y = 15,900 \pm 5,400 \text{ m/s}^2$) were significantly larger than peak lateral accelerations ($a_x = 870 \pm 470 \text{ m/s}^2$; $p < 0.01$). In the angled configuration, the vertical head acceleration magnitude (a_y) was significantly less than the perpendicular configuration ($3,960 \pm 970 \text{ m/s}^2$ (angled) vs. $15,900 \pm 5,400 \text{ m/s}^2$ (perpendicular); $p < 0.01$). The parallel configuration produced peak vertical accelerations that were comparable to those of the angled orientation, but significantly smaller than in the perpendicular orientation, and peak horizontal accelerations that were significantly smaller than in both the perpendicular and angled configurations ($a_y = 3,940 \pm 1,210 \text{ m/s}^2$; $a_x = 1,240 \pm 110 \text{ m/s}^2$). Both the angled and parallel orientations produced significantly lower peak resultant accelerations than the perpendicular orientation ($5,320 \pm 620 \text{ m/s}^2$ (angled) and $4,110 \pm 1180$ (parallel) vs. $16,830 \pm 5,720 \text{ m/s}^2$ (perpendicular); $p < 0.05$; Figure 115G).

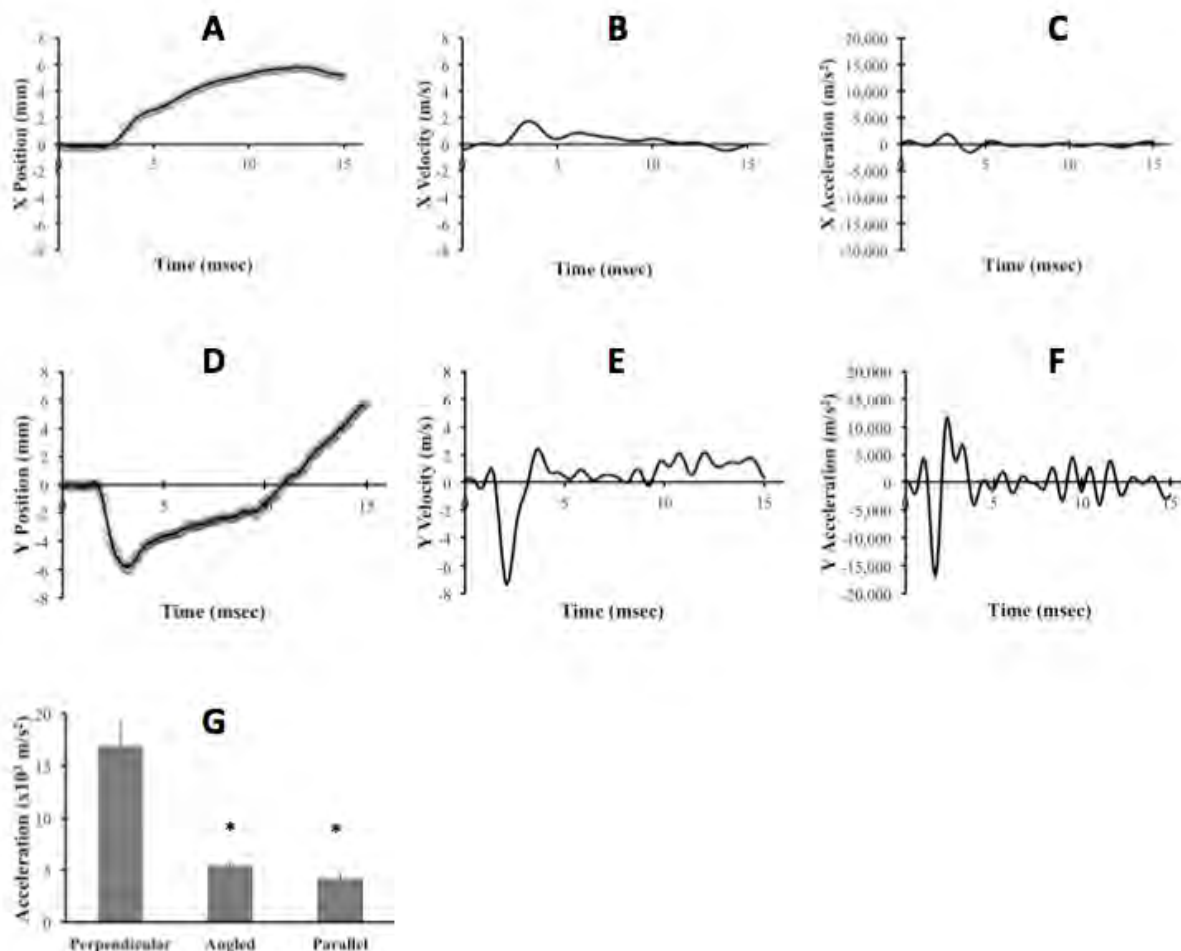


Figure 114 - Horizontal (A-C) and vertical (D-F) components of motion resulting from a blast exposure with the mouse aligned perpendicular to the incoming blast wave, and positioned along the periphery of the shock tube.

These tests demonstrated that it was possible to develop a blast testing protocol to examine two different biomechanical scenarios: (1) a blast wave transmitting an intracranial pressure change and a significant head acceleration (perpendicular orientation), and (2) a blast wave that only transmitted an intracranial pressure change, with minimal head acceleration (parallel orientation). We explored the effect of these two kinematic scenarios by measuring the survivability and threshold for neurological impairment in these conditions. We found that the perpendicular orientation – with significant head acceleration – showed a significantly lower 50% survival threshold in mice when compared to the parallel orientation (246 ± 4 kPa (perpendicular) vs. 396 ± 10 kPa (parallel); Figure 115). Similarly, for the same blast input (.508 mm membrane thickness; 215 ± 13 kPa), we observed that significantly reducing the head acceleration (parallel configuration) led to a significant reduction in righting time (307 ± 74 seconds (perpendicular) vs. 60 ± 5 seconds (parallel); Figure 115). Finally, we tested if pressure alone – with no significant acceleration – could alter neurological impairment. Using the survival dataset as a guide, we found a blast overpressure level (415 ± 41 kPa) in the parallel configuration that produces a significant alteration in the righting time reflex immediately after exposure (Figure 115). Across all tests, none of the animals exposed to blast loading showed

signs of pulmonary trauma during necropsy. Moreover, all animals were ambulatory by one day following injury, appearing only slightly lethargic with less active exploratory behavior compared to sham mice. Normal grooming behavior recovered within 2-3 days post injury.

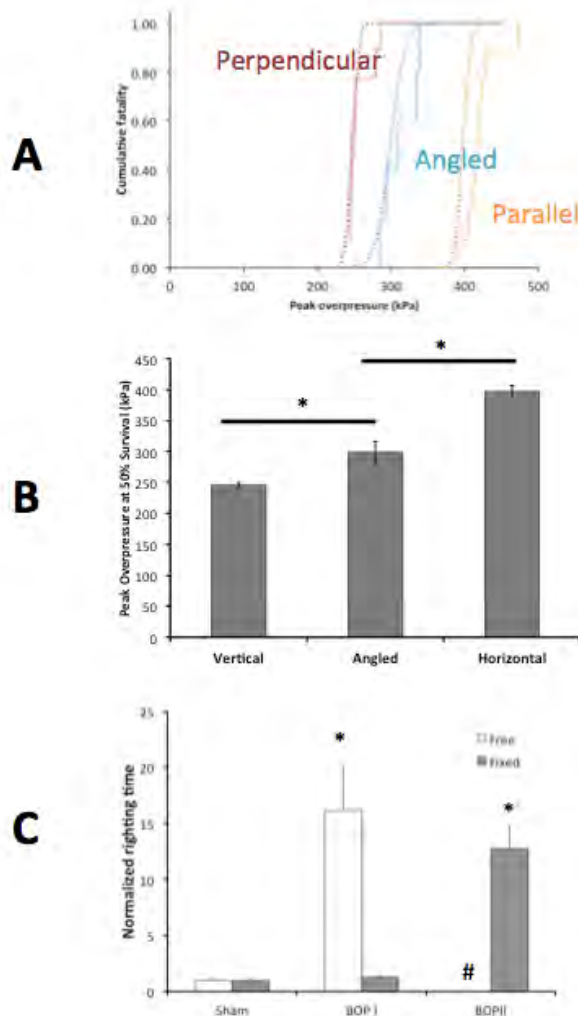


Figure 115 - Induced head acceleration influences survival and immediate neurological impairment following blast exposure.

Behavioral assessments motivate the study of hippocampal function in ‘pure blast’

With the development of a model to isolate the effects of primary blast from other biomechanical inputs (e.g., head acceleration; see above) we explored two specific configurations in more detail. We first tested for behavioral impairments across two levels of blast input where acceleration was minimized (parallel configuration). Two blast inputs were tested – 215 +/- 13 kPa and 415 +/- 41 kPa peak pressure.

Neurobehavior assay development: We ordered a sequence of tests to profile behavior: elevated zero-maze (day 1 post-blast), rotarod (days 1-3), open-field (day 4), spatial object recognition (SOR) (days 4,5), and fear conditioning (days 8,9). Standard protocols were used for all tests.

Elevated Zero-Maze (Day 1): The elevated zero maze was used to examine anxiety-related behavior. The apparatus comprised of an elevated annular platform with two opposite, enclosed quadrants and two open quadrants. Mice were placed in the walled region and left undisturbed for 5 minutes. The latency to first exit from the walled region and the cumulative time spent the open region were recorded. In addition, a risk assessment measure was calculated.

Rotarod performance (Days 1-3): Motor coordination and motor learning was assessed on days 1,2, and 3 following blast injury. Animals were placed on a rotarod apparatus (model: ENV-577M, MedAssociates Inc., Georgia, VT) that accelerates linearly from 4 to 40 RPM over a five-minute session. Three trials, separated by an hour each, were conducted each day. Two measures were recorded for each rotarod test: the time lapsed until first fault, and the total time the animal remained on the rotating rod before falling. Fault is defined as making a complete revolution around the rotarod. If an animal did not fault, we used fall time for fault.

Open field test (Day 4) Individual mice were released in the corner of a rectangular (30cmx40cm) open field arena. Mice were left undisturbed and videotaped with a camera mounted on the ceiling above the center of the open field arena for 30 minutes. At the end of testing, mice were returned to their home cage.

Spatial Object Recognition (SOR; Days 4, 5): Spatial object recognition was used to determine the effects of blast loading on memory storage. On the day of training (d4), mice were placed in the training arena for a total of 10-minute session. The first session consisted of context habituation without objects in the arena. During the next 3 sessions, mice were allowed to explore the arena with two distinct objects (a glass bottle and a metal tower). Each session lasted 10 minutes. Testing occurred 24 hours after the four training sessions in which one of the two objects was displaced. The mouse's preference for the displaced object over the non-displaced object was measured for all sessions.

Fear Conditioning (Days 8, 9): Contextual fear conditioning was performed to develop a complementary measure of hippocampal and amygdala function. On the training day (d8), the mouse was placed in the conditioning chamber for 2:28 minutes before the onset of a foot shock (2-sec 1.5 mA). Contextual conditioning was assessed 24 hours later by placing the mouse back in the same chamber for 5 minutes.

Our results show that this configuration of primary blast injury causes a complex behavioral impairment. No impairment in neurological severity scores were recorded after injury (data not shown). We did not observe a significant difference in either the time to first exit, the time in the walled region or the total distance traveled during the elevated zero maze test (Figure

116). A transient impairment in Rotarod fault and fall time was observed for the moderate injury level, but this was not observed for the severe category.

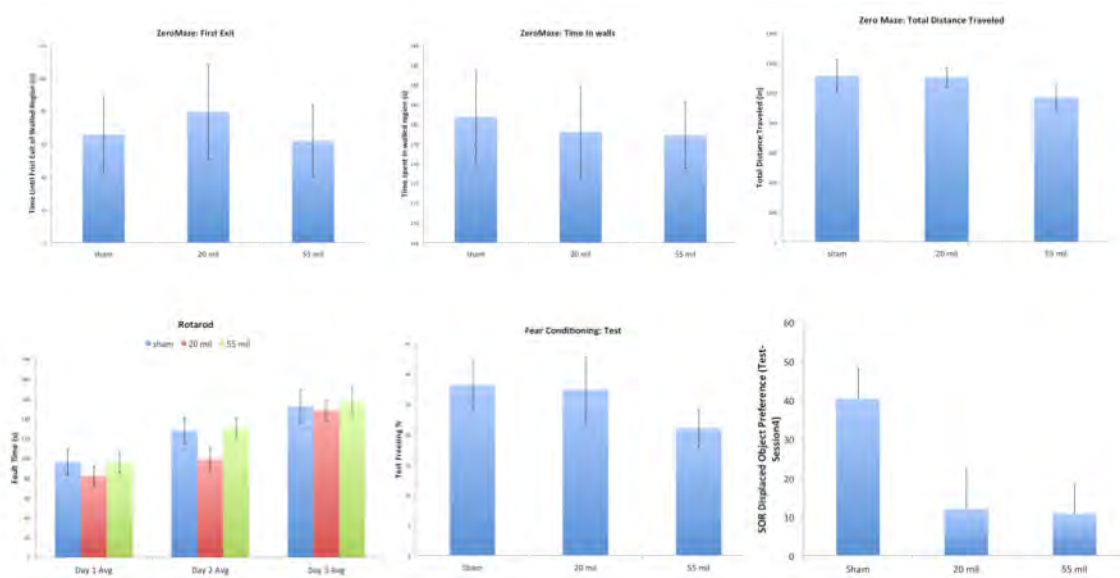


Figure 116 - Behavioral impairments in a model of pure blast injury

The most significant changes in neurobehavior appeared for the hippocampal dependent functions that we examined 5-8 days following injury. The most severe blast overpressure level produced significant changes in the fear conditioning response (Figure 117). Across both injury levels, we saw a consistent change in the spatial object recognition tests, with the deficits at both levels significantly different from sham exposed animals.

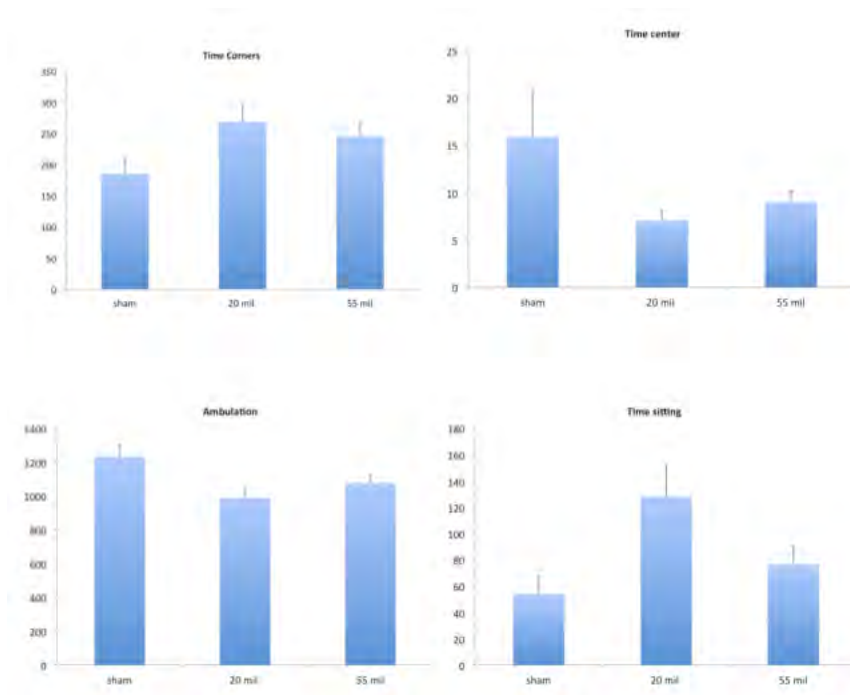


Figure 117 - Impairments in hippocampal function appear in bTBI

We further explored the behavioral changes in animals subject to the spatial object recognition test. Consistent with the change in the preference for the displaced object, there was little behavioral changes that separated the moderate and severe blast overpressure levels. Animals showed the same general ambulatory activity, distance traveled, and time either in the corners or the center. Similar to previous work collected with this model, we observed a general trend for the animals to stay in the corners that was an indicator of heightened anxiety.

Based on these data, we conclude that a primary blast overpressure is capable of creating significant neurobehavioral deficits, even in the absence of head accelerations that can be induced by the blast wave/wind. We feel this is an important juncture in the MURI research because it establishes unique biomechanical conditions that cause impairment. These data also do not agree with recent publications indicating that eliminating head motions or, alternatively, placing the animal head in a region outside the blast wind corridor will lead to the elimination of neurological impairment. It is important to note that these past publications did not study these blast over pressure conditions, so the most straightforward explanation is that previous studies did not achieve a critical threshold loading necessary to cause impairment. Future studies will indicate if our impairments persist at lower blast over pressure loading levels.

Defining the electrophysiological substrate of ‘pure blast’ injury

Motivated by these impairments in hippocampal behavior, we proceeded to the next scale and measured alterations in hippocampal circuit function after blast injury. With no difference in impairment after either moderate or severe blast overpressure, we selected the moderate level because of select deficit in spatial object recognition and no significant change in fear conditioning. The spatial object recognition test is associated most centrally with dorsal

hippocampal function, while the contextual fear conditioning test is often associated with hippocampal and cortical regions.

To test for alterations in the hippocampal circuitry, we isolated acute coronal hippocampal slices from blast exposed and sham animals, using the moderate blast overpressure conditions noted above (215 +/- 13 kPa). Extracellular hippocampal field recordings were collected in acute slices perfused in aCSF or modified aCSF supplemented with 6 μ M CNQX. We used a common formulation of aCSF ((in mM): 130 NaCl, 3KCl, 1.25 NaH₂PO₄, 26 NaHCO₃, 10 glucose, 1 MgCl₂, 2 CaCl₂). Recordings were collected from two brain regions: (1) stimulating the perforant path and recording in the dorsal blade of the dentate, and (2) stimulating the Schaffer collaterals and recording in stratum radiatum of CA1. Recording electrodes were prepared daily, and stimulation protocols were kept consistent across all recordings. Input output curves were generated in the presence of the baseline aCSFs solution, and then collected again in aCSF supplemented with 6 μ M CNQX to identify the NMDAR component of the input/output curve. Following the recording of input/output curves for a given slice, we used a paired pulse stimulation (25, 50, 75, and 100 ms interstimulus intervals) to identify if there were changes in presynaptic glutamate release in blast-exposed animals. We collected acute slice samples five days following blast injury, the same timepoint we observed impairments in spatial object recognition.

We first observed that blast injury does not alter circuit excitability in the dentate gyrus (Figure 118). Experiments were performed in normal aCSF (n=7 for sham, n=6 for blast). Data from sham animals was very consistent. Across the entire input/output curve, acute slices from blast injured animals did not differ significantly from sham animals.

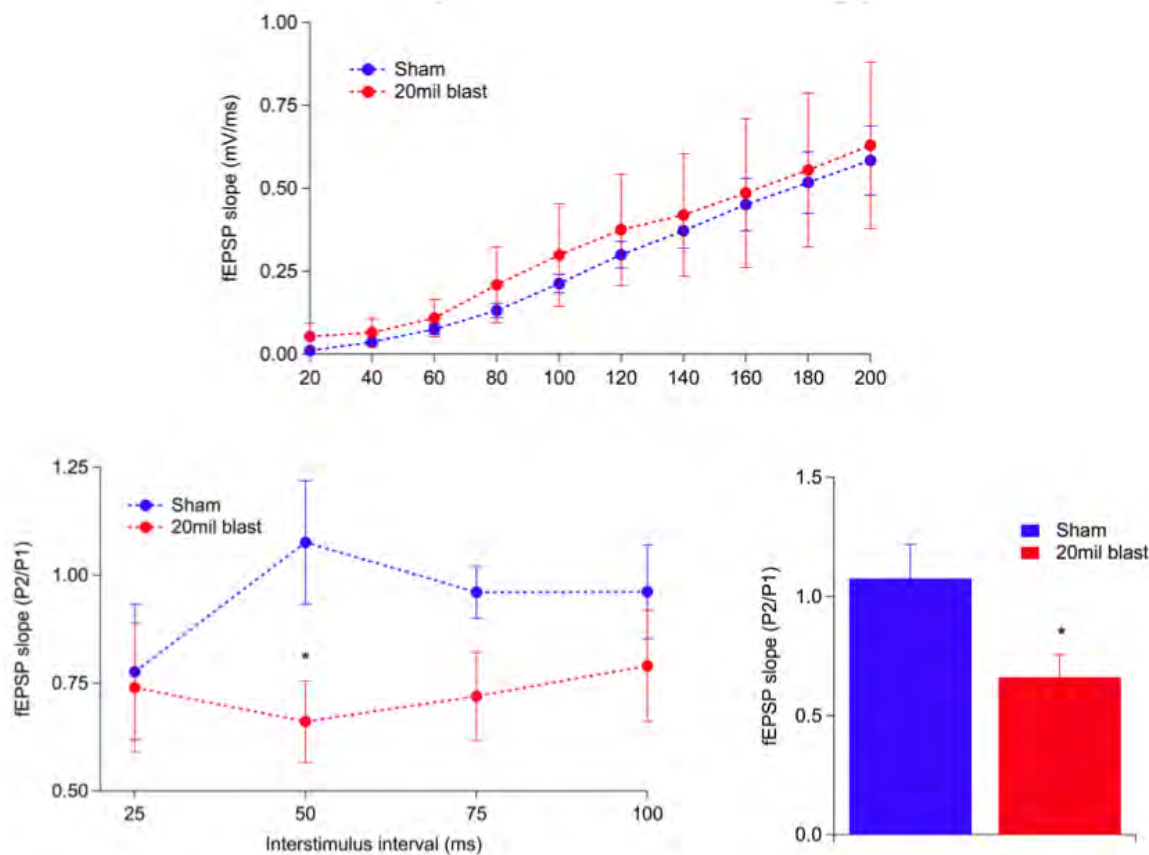


Figure 118 - Slice recordings in blast injured animals 5d following injury. Recording in the dentate gyrus, with stimulus from the Mossy fibers.

In contrast, blast injury increased neurotransmitter release probability in perforant path fibers projecting into the dentate gyrus (Figure 118). We observed a significant paired pulse depression in slices from blast injured animals using a 50ms interstimulus interval (n=5 for sham and blast). The presence of a paired pulse depression suggests an increased neurotransmitter release probability from fibers of the perforant path onto granule cells of the dentate following blast injury. These results should provide motivation for additional investigation of injury induced alterations in this brain region.

We observed a significant shift in circuit function when measuring changes in the area CA1. Experiments were performed in normal aCSF (n=13 for sham, n=14 for blast), and the significant reduction in the I/O curve following blast injury (Figure 119) suggests a functional impairment in the connectivity between CA3 and CA1 regions of hippocampus following blast.

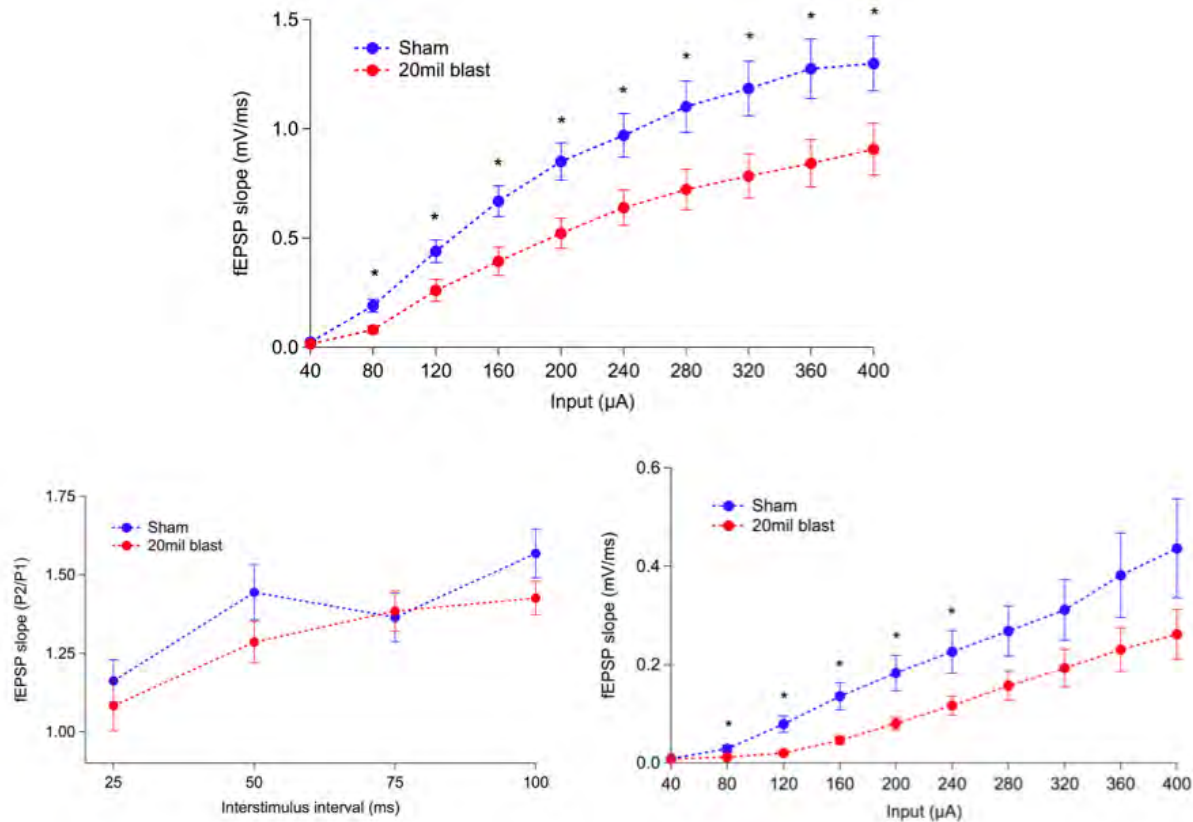


Figure 119 - Slice recordings in blast injured animals 5d following injury. Recordings in the CA1 region with stimulation of the incoming Schaffer collaterals.

In contrast, we did not see a corresponding impairment in neurotransmitter release when measuring paired pulse changes in CA1 (Figure 119). Using a stimulating electrode for the Schaffer collaterals projecting into CA1, we did not observe significant differences between sham and blast injured animals across any of the tested paired pulse intervals ($n=13$ for sham and blast). These data suggest that the downward shift in the I/O curve following blast injury is due to post-synaptic changes or loss of pre-synaptic fibers, rather than pre-synaptic neurotransmitter release.

Finally, we observed a significant reduction in NMDA receptor mediated field potentials in area CA1, coincident with a reduction in the I/O curves from the same region (Figure 119). Using a saturating dose of CNQX to block all AMPA receptor activation, these changes were significant across nearly all stimulation intensities. These data indicated that blast injury decreases NMDAR-mediated, evoked field potentials at lower input stimuli.

Overall, our data indicate a very specific change to a subregion of the hippocampus. Rather than broadly affecting all circuitry, the blast overpressure (with minimal head acceleration) affects selectively neurotransmitter release in the dentate gyrus and field potentials in CA1. We are now testing if these changes in field potentials are accompanied by changes in neuronal degeneration using standard neuronal degeneration staining. Moreover, we are exploring

methods to measure changes in long-term potentiation and long-term depression across these acute slice preparations.

Genotype manipulation and high throughput analysis uncovers a neuronal transcription factor mediating anxiety induced by blast exposure

In an application of the high throughput behavioral phenotyping that we developed as part of last year's progress, we tested for the effects of deleting an important neuronal transcription factor (Ets-like kinase I; Elk-1). Neuronal transcription factors are a largely understudied class of proteins that can play a significant role in deficit recovery following bTBI. The Ets-like kinase I (Elk-1) is a prime candidate because it serves a range of functions spanning development, plasticity, and degeneration. Given these pleotropic effects, we hypothesized that Elk-1 is an important intermediary in post-bTBI deficits.

Statistical differences in task-related performance of animals in four experimental groups (wildtype littermate sham, wildtype littermate blast-injured, Elk-1 knockout sham, and Elk-1 knockout blast) were assessed via one-way ANOVA and Tukey's post-hoc test. Shapiro-Wilk test was used to assess normality and nonparametric tests (Kruskal-Wallis and Mann-Whitney U) were employed when needed. A repeated-measures (RM) ANOVA was performed when the same measurement was obtained for an animal over multiple trials as in rotarod or habituation. Group sizes were: WT sham $n = 13$, WT blast $n = 13$, Elk-1 KO sham $n = 11$, Elk-1 KO blast $n = 12$. alpha-level 0.05, $*p < 0.05$ and $**p < 0.01$ indicated significance. For a given level of analysis, a Bonferroni correction for multiple comparisons was used. All values reported are mean \pm s.e.m. unless otherwise noted. Significance of time in all RM-ANOVA, $p < 0.001$ unless otherwise noted.

Behavior pattern analysis: Each animal was subjected to a battery of behavior tasks and 14 performance metrics were computed (see Figure 120). Principal component analysis (PCA) visualized the dataset in a lower dimensional space and identified a combination of the original variables that explained the largest possible variation. Following PCA, a MANOVA identified a linear combination of the original variables with the largest separation between groups. Relationships between group means were visualized in a distance dendrogram. Additionally, the ability to use a pattern of behavior to correctly identify group membership was assessed by multiclass support vector machine (SVMlight).

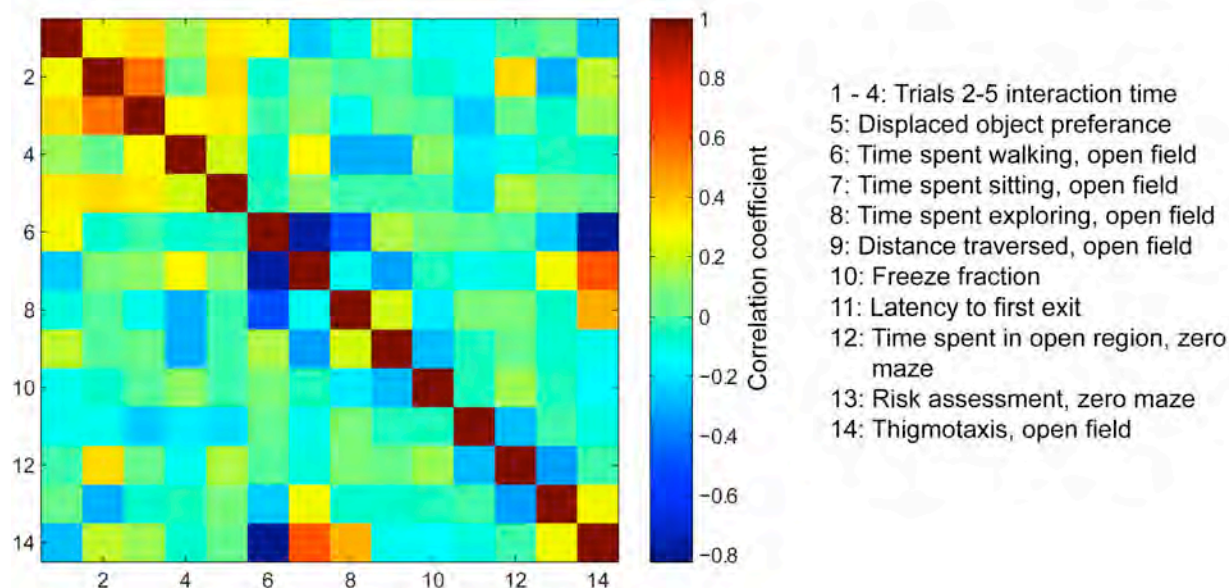


Figure 120 - Summary of behavioral endpoints used in the pattern analysis of blast deficits. Key is the absence of correlation among these parameters prior to their use in a canonical analysis.

To characterize the spectrum of behavior changes that result from bTBI and to investigate the potential role of Elk-1, we first developed a set of automated algorithms for scoring task-related behavior in mice. Although several proprietary software packages (e.g., Clever Systems, EthoVision, San Diego Instruments) allow automated scoring of mouse behavior, an open-source platform provides transparency, accessibility, and potential for growth through collaboration. A complete list of behavior tasks appears in Table I.

Comparison of automated and manual analysis of behavior tasks

After confirming the robustness of our automated algorithms and calibrating them on a small subset of the recorded tests, we tested the accuracy of the automated video analysis in 4 specific behavior tasks: fear conditioning, SOR, elevated zero-maze, and open field test. For each task, 20 videos were manually analyzed and scored using the automated approach, resulting in 2 data points for each video. The mean biases of the automated approach relative to manual measurements were 5.24% for freezing time in fear conditioning task (Figure 121), 1.07s for latency to first-exit in elevated zero maze (Figure 121), -0.37s for amount of time spent in the open region in elevated zero maze (Figure 121), 0.003 for thigmotaxis in open-field (Figure 121), and 2.98% for object interaction time in SOR (Figure 121).

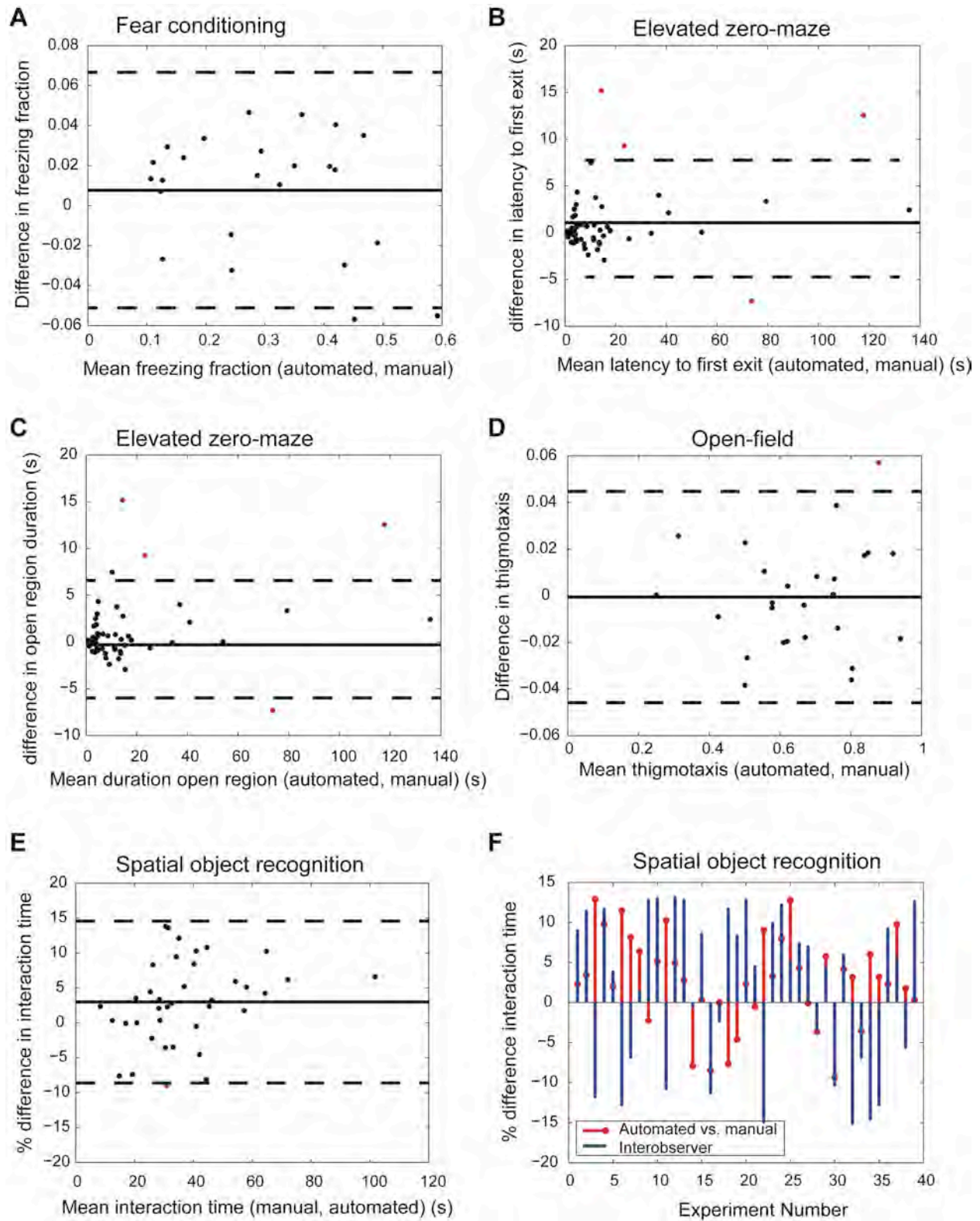


Figure 121 - Correlation of automated and manual scoring for behavioral analysis.

Forty SOR videos were manually scored for object interaction time in SOR experiments by two independent expert human observers, user A and user B. User A calibrated the automated approach using 3 videos chosen at random as described in Supplemental Methods (Figure 121). All videos were then automatically processed using the definition of interaction provided by User A. We compared the percent difference in interaction time between automated and User A, and between User A and User B (Figure 121). The limits of agreement (bias \pm 1.96*std) between automated and User A was [-8.62%, 14.6%], compared to [-17%, 21.8%] for User A vs. User B.

Real-time animal tracking and object interaction scoring is possible with our implementation (see Supplemental Video). Our automated system consistently identified the correct coordinates of the nose and scored object interaction. In a few instances, the animal was sitting in a corner in a curled posture, and the algorithm did not correctly identify the head and tail coordinates. However, objects are rarely placed in the corners and mislabeled events span less than 2-3 consecutive frames. In our experience, manual correction took less than 1 minute for a 10-minute video and improved sensitivity to nearly 98%.

Blast-injury increases generalized anxiety in wildtype animals while Elk-1 knockout mice are resistant to post-blast anxiety.

Our collective results from open-field and elevated zero-maze tests show that bTBI significantly increases anxiety-like behavior. Uninjured animals placed in an open-field arena showed a typical spatiotemporal response to novel environment, spending most of their time along the periphery (thigmotaxis) during the first 5 minutes and gradually entering the central zone of the arena during the next two 5-minute intervals. We quantified thigmotaxis, an index of anxiety, by determining the ratio of time spent along the periphery relative to time spent in the center over any five-minute interval. Following bTBI, wildtype animals show increased thigmotaxis during the second 5-minute interval compared to sham (mean \pm SEM: 0.820 \pm 0.033 blast vs. 0.588 \pm 0.039 sham, p = 0.0013, Figure 122). In addition, blast-injured mice spent significantly more time sitting in an open-field compared to uninjured shams, another measure of anxiety (95.81s \pm 9.19s blast vs. 62.56s \pm 8.83s sham, p = 0.0484, Figure 122). The total distance traveled and time spent walking or exploring were not significantly different between sham and injured wildtype animals.

In contrast to wildtype littermates, blast-injured Elk-1 KO animals did not show a significant difference in thigmotaxis or total time spent sitting compared to uninjured sham Elk-1 KO (thigmotaxis: 0.626 \pm 0.028 blast vs. 0.638 \pm 0.026 sham, p > 0.05; sitting: 82.3s \pm 9.69s blast vs. 73.4s \pm 9.82s sham, p > 0.05). Moreover, blast-injury in Elk-1 KO group resulted in significantly less thigmotaxis compared to blast-injured WT (0.626 \pm 0.028 Elk+blast vs. 0.820 \pm 0.033 WT+blast, p = 0.0081).

An alternative test for anxiety-like behavior is the elevated zero maze. We found increased risk assessment activity in WT blast group relative to uninjured sham (49.8s \pm 4.08s blast vs. 36.8s \pm 3.41s sham, p = 0.0312, Figure 122). No significant difference was found between WT blast and

WT sham groups in latency to first exit or time spent in unprotected open regions (Figure 122). We observed a very significant decrease in latency to first exit in Elk-I KO blast-injured mice relative to 3 other groups ($5.63s \pm 1.14s$ Elk+blast vs. $40.82s \pm 6.87s$ WT sham, $46.8s \pm 4.08s$ WT blast, $35s \pm 4.9s$ Elk sham, $p < 0.001$, Figure 122). Similar to decreased latencies to exit, a decrease in risk assessment behavior appeared in Elk-I KO blast-injured mice (Figure 122). The cumulative distance traveled in the zero maze, as well as the peak instantaneous speed, were not statistically different between the 4 groups (ANOVA, $p > 0.05$).

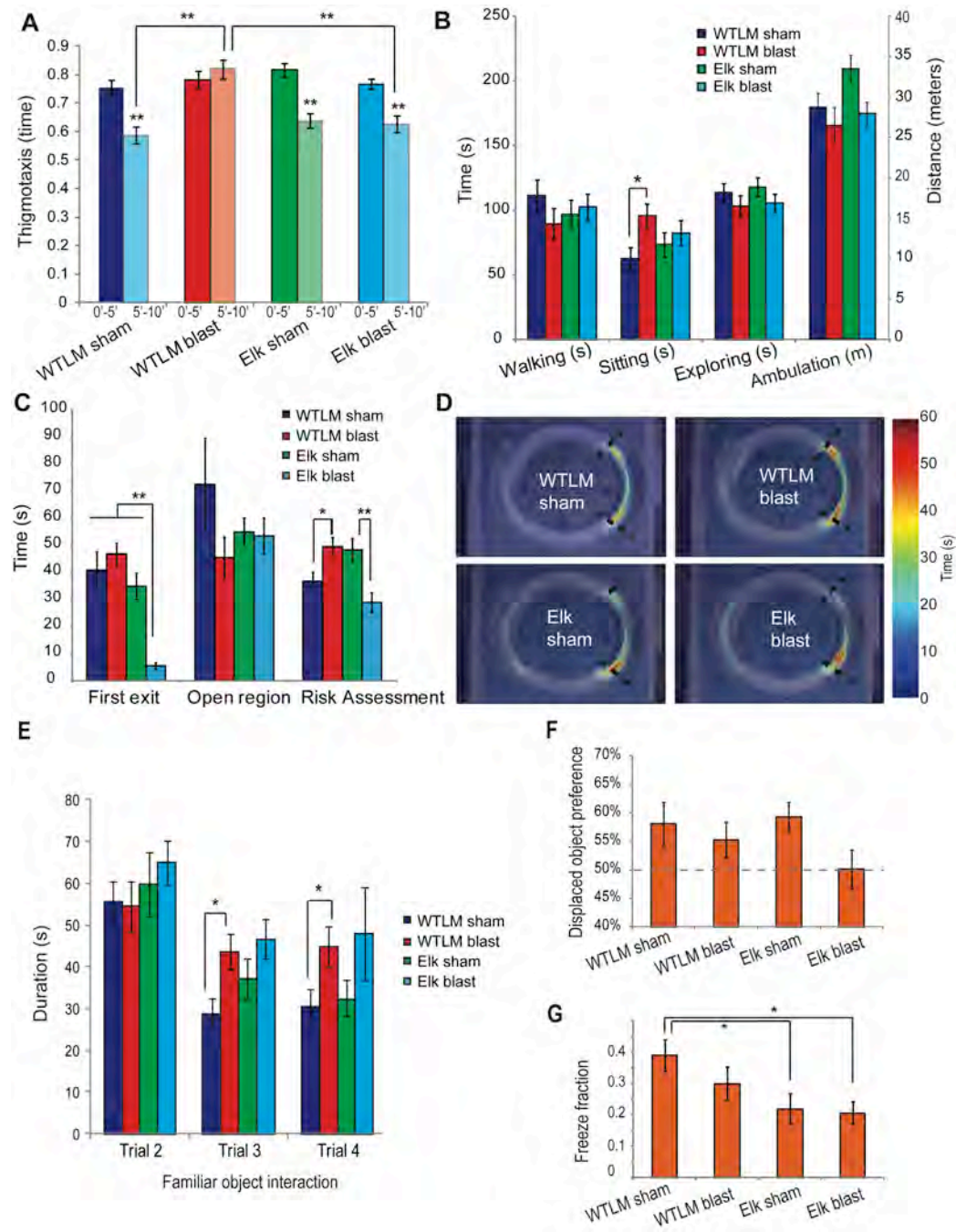


Figure 122 - Role of Elk1 in mediating outcome after bTBI

Blast-injury to wildtype mice impairs object habituation but Elk-1 deletion recovers normal behavior

Habituation is one form of nonassociative learning that is readily measured in the SOR test where exploration of the objects during consecutive training trials decreases before one of the objects is displaced. Therefore, we analyzed the duration of interaction with the object in trials 2-4 of the SOR test in mice that received bTBI. Uninjured wildtype mice habituated to the SOR arena as the duration of interaction significantly decreased over time (RM-ANOVA, $p=0.0062$, Figure 122). In contrast, blast-injured wildtype animals failed to show a significant decline in object exploration from trial 2 to trials 3 and 4 (RM-ANOVA $p>0.05$). Direct comparison between sham and blast-injured wildtype animals showed a significant deficit in object habituation during trial 3 (blast: $42.8s \pm 4.12s$, sham: $26.1s \pm 5.03s$, $p=0.0036$).

In contrast to WT, blast-injured Elk-1 KO animals did not show a deficit in habituation compared to sham (multivariate RM-ANOVA, $p>0.05$). Both sham and injured Elk-1 KO groups spent equally large amounts of time interacting with the non-displaced object in trial 2 (first exposure to objects in the arena) and significantly less time in trials 3 and 4 (Trial 3: Elk-1 KO sham, $37.1s \pm 2.36s$ compared to Elk-KO injured, $46.6s \pm 2.26s$, $p = 0.2366$).

Blast-injury impairment of spatial and associative memory only in Elk-1 knockout mice.

We assessed spatial memory by calculating the percent of total object interaction time spent exploring the displaced object in the SOR test during trial 5. Typically, by trial 4, mice spend nearly equal time interacting with the two objects. Upon displacing an object in trial 5, both wildtype sham and blast-injured animals spent significantly more time ($>50\%$) interacting with the displaced object. Preference for the displaced object was not different between sham and injured wildtype animals (wildtype sham $58.1\% \pm 3.8\%$ vs. wildtype injured $55.2\% \pm 3.2\%$, $p>0.05$). Similarly, Elk-1 KO sham animals showed a preference for the displaced object in trial 5. However, the preference for the displaced object was abolished in blast-injured Elk-1 KO group (Elk-1 KO sham $59.3\% \pm 2.6\%$ vs. Elk-1 KO injured $50.1\% \pm 3.4\%$, $p=0.0034$) (Figure 122).

We next tested contextual fear memory, a distinct hippocampus-dependent form of associative memory. We found no statistical difference in total freeze fraction between sham and blast-injured wildtype animals (sham: 0.390 ± 0.049 , 0.3 ± 0.053 , $p = 0.18$) suggesting that associative memory is not altered following blast-injury (Figure 122).

Compared to wildtype mice, Elk-1 KO showed significantly less freezing behavior (wildtype sham freeze fraction: 0.3904 ± 0.0494 , Elk-1 KO sham: 0.2198 ± 0.0492 , $p = 0.0213$). However, the impairment in associative memory was not worsened by blast-injury (Elk-1 KO blast: 0.2069 ± 0.035 , $p > 0.05$ compared to Elk-1 KO sham) (Figure 122).

Blast-injury impairs motor coordination and motor learning.

We assessed motor coordination and learning in rotarod task by measuring latency to fault. On first exposure to the rotarod (day 1), wildtype blast-injured animals had significantly lower fault time compared to wildtype sham (wildtype blast 79.8 ± 10.8 s vs. wildtype sham 117.9 ± 10.5 s, $p=0.0145$) (Figure 122). Interestingly, Elk-1 KO animals were resistant to blast-induced deficits in motor coordination (Elk sham: 127.3 ± 13.5 vs. Elk blast: 104.2 ± 12.2 , $p=0.2097$).

An improved performance on the rotarod during subsequent trials 2 and 3 indicates acquisition of motor memory. All four groups showed an improvement in latency to fault over days 1-3, but the increase in performance was greater for uninjured shams than blast-injured animals regardless of genotype (RM-ANOVA, within subjects time $p<0.0001$, between subjects sham vs. blast $p = 0.0037$, wildtype vs. KO $p = 0.8712$).

Multivariate analysis reveals the relative effects of genotype, injury and genotype*injury on behavior outcome.

A summary of behavioral alterations in WT blast, Elk-1 knockout sham and Elk-1 knockout blast relative to WT sham animals are provided in Table 2. Given the complex phenotypic spectrum, we applied principal component analysis (PCA) followed by MANOVA to identify a linear combination of the original behavior variables with the largest separation between groups (Figure 123; see Figure S1B for variable list). A significant difference appeared in overall group mean centroids, Wilk's lambda $p = 0.0011$. Genotype alone did not have an effect on multivariate group mean differences (WT vs. Elk-1 KO, $p=0.0825$), however, injury severity (sham vs. blast, $p=0.0007$) and genotype*injury ($p=0.0018$) were both significant. We projected these multivariate behavior scores for each mouse onto a canonical subspace and color-coded each group (Figure 123). Inspection of the group mean centroids and 95% confidence bounds revealed intersecting groups with no significant difference from each other (WT sham vs. Elk sham), and non-intersecting groups that are significantly different (e.g., Elk-1 KO sham vs. Elk-1 KO injured). Using this canonical representation, a dendrogram constructed from pair-wise Mahalanobis distances between each pair of group means identified the hierarchical similarity among groups - WT sham and Elk-1 KO sham were phenotypically most similar; blast-injury affects the two genotypes differently, wildtype injured mice are most affected, and Elk-1 KO injured have milder phenotypic alterations (Figure 123).

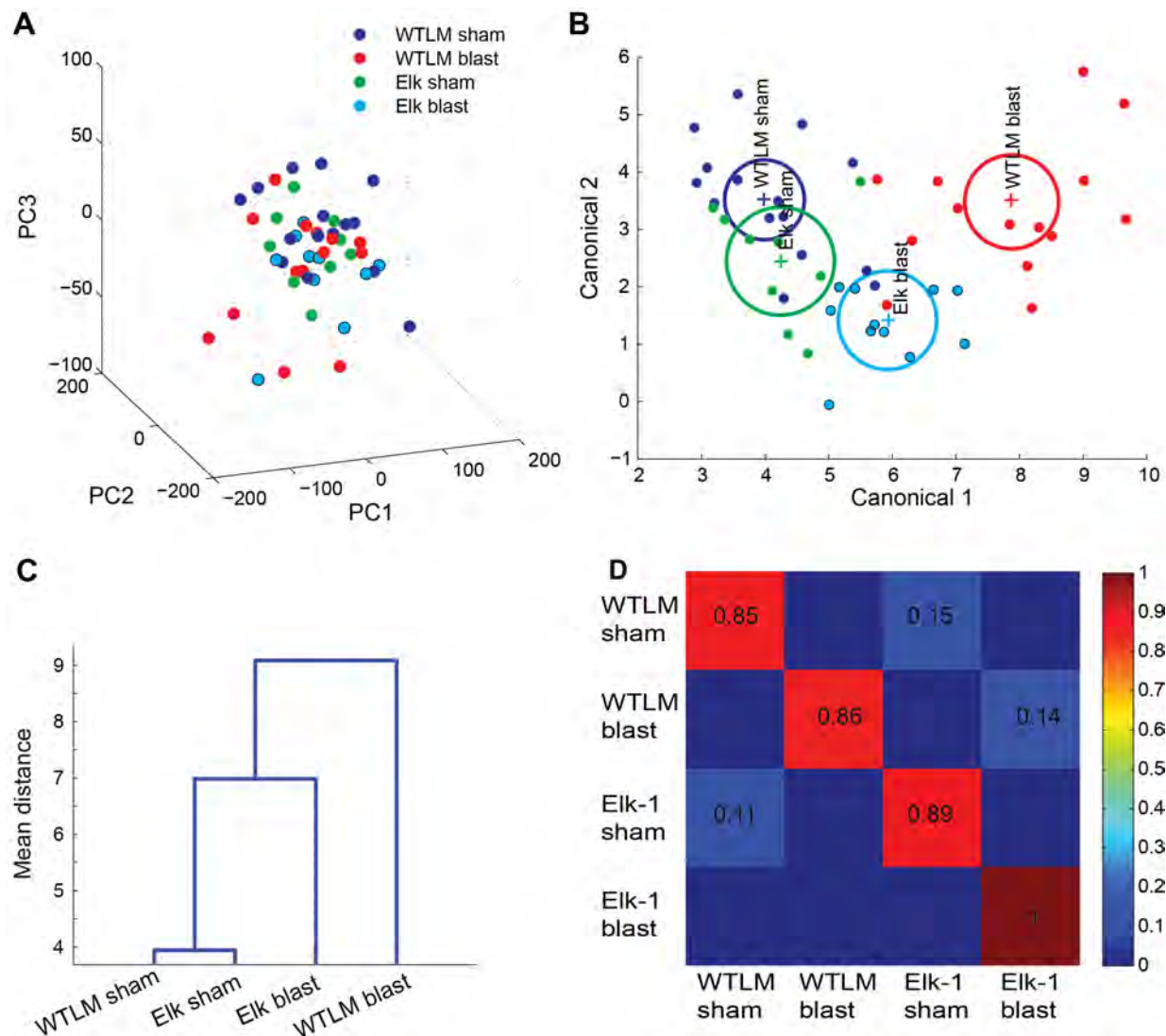


Figure 123 - Analysis of behavioral deficits reveals a close phenotype between sham groups, but the Elk I KO shows a partial recovery of deficits displayed in the canonical space.

Finally, we tested whether patterns of task-related behaviors could accurately predict injury severity or animal genotype. We trained and tested a linear multiclass support vector machine using the 14 behavior attributes. The results of a leave-one-animal-out cross-validation are shown in a confusion matrix (Figure 123). Classification accuracy for wildtype sham and blast-injured groups was the largest, while there was some confusion in accurately classifying animals into WT sham and Elk-I KO sham groups - 85% of true wildtype sham animals were correctly classified as wildtype sham, while 15% were falsely classified as Elk-I KO. However, the overall classification accuracy was 90.2%, suggesting that automated behavioral assessment can successfully phenotype animals.

In vitro blast model – development and testing

Motivated by our multiscale approach, we next developed a portable shocktube for use on dissociated cultures of neurons/astrocytes. The initial receiver/shock tube design, modeled for

used with organotypic slice cultures, was too large for use with the microscope mounted imaging system that we developed to estimate functional network connectivity. Instead, we prototyped and built a second generation portable shocktube that satisfied the following criteria: (1) provides for the imaging of neuronal networks in the existing live cell confocal microscope, (2) minimizes the complex waveforms that can be created with wave reflections, (3) permits the imaging of an acute response (<1 minute after insult) and postacute (1 hr, 1 day, 3 days, 7 days) response to blast exposure, (4) provides shocktube impulse waveforms that are within the range of those used in vivo with our mouse model and also in vitro with the organotypic slice cultures.

Figure 124 shows the schematic of our design, complete with photographs of the working prototype. Also shown is the integration of this device into the existing microscopy system. Similar to the existing tube designs, we used the rupture of a Mylar membrane within a confined chamber. The chamber has an adjustable volume, using a series of commercially available flanges. The choice of gas is flexible, providing a method to vary the impulse and peak pressure independently in the blast exposure.

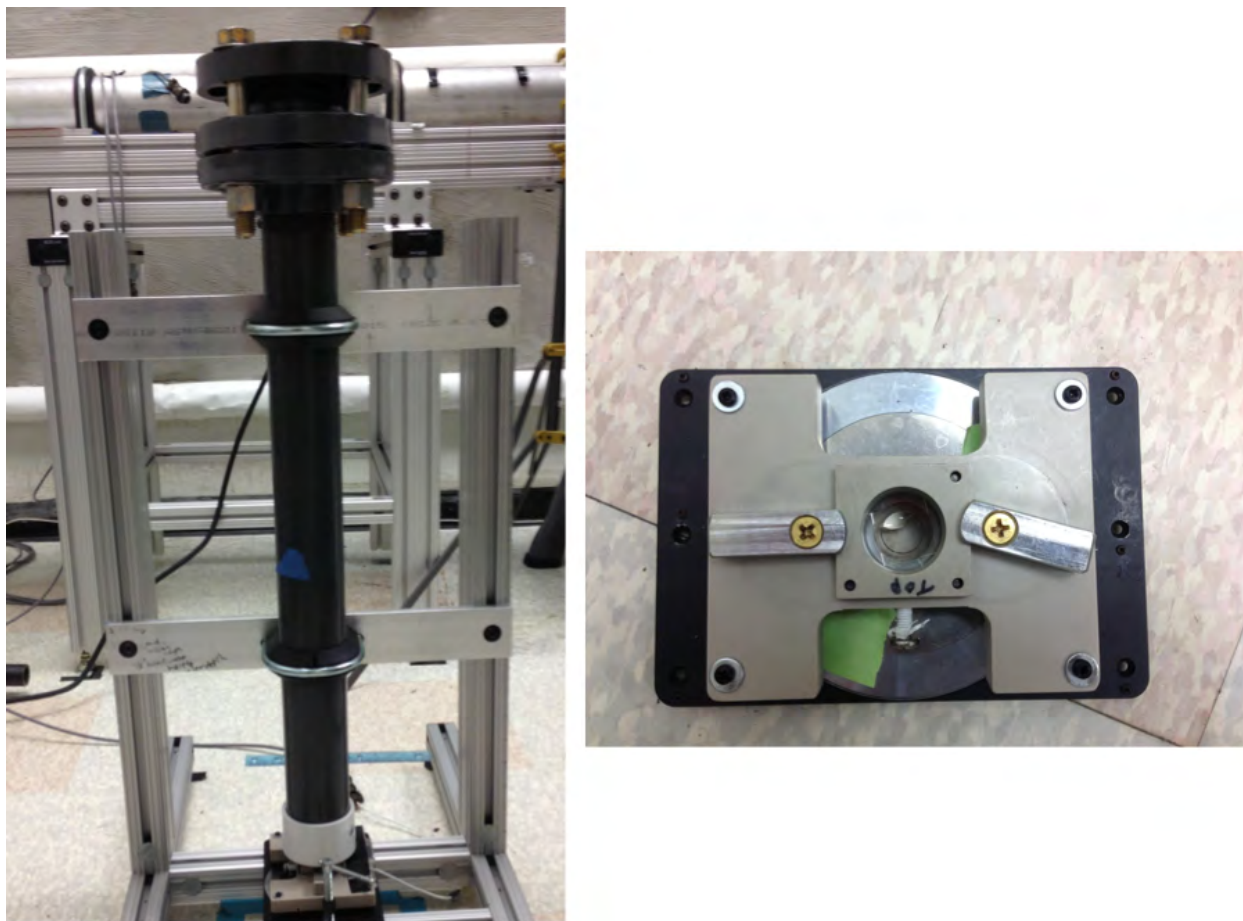


Figure 124 - Overview of in vitro blast tube setup

Examples of the free field pressures possible with this shock tube design are shown in Figure 125. Additionally, the table below shows the range of possible free field pressures that can be

achieved with the device. Repeatability is excellent, with variance in both the peak pressure and impulse less than 6% across all conditions.

		Pressure	Duration	Impulse
2 mil (He)	Tube	138.62 ± 11.19	1.82 ± .15	56.65 ± 4.03
	Device	473.19 ± 28.72	0.67 ± .04	58.69 ± 11.57
4 Mil (He)	Tube	303.43 ± 23.08	2.23 ± .61	117.95 ± 6.4
	Device	724.19 ± 65.75	.54 ± .01	86.54 ± 9.58

We spent considerable effort to minimize reflections and potential complications in the blast pressure pulse within the cell culture chamber. Normally the presence of a reflection surface can create very complex and highly variable changes in the pressure within the chamber. Our concern was largely centered on achieving a simple, repeatable waveform that would correlate to the free field pressure. Using pressure transducers within the chamber, at the exit of the shocktube, and additional sensors with a free field allowed us to systematically compare the fluctuations and the variance in these changes over time (Figure 125). Our recorded pressures within the chamber showed the wave transmitted with some reflections and decay within the chamber. However, the secondary pressure oscillations within the fluid were restricted to less than 10% of the peak pressure achieved in the initial loading phase.

Given this consistency, we next tested the response of dissociated cultures to the peak loading conditions achievable with the in vitro system. We used mixed neuron/astrocyte cultures derived from embryonic rats, transduced these cultures with a genetically encoded calcium indicator GCaMP6f to specifically express a calcium sensitive protein in the neurons, and then tested to measure the primary calcium transient in response to the blast input. As a comparison, we also labeled both neurons and astrocytes with a calcium sensitive fluorescence indicator (Fluo-4) that provided the same temporal sensitivity as the GCaMP6f indicator.

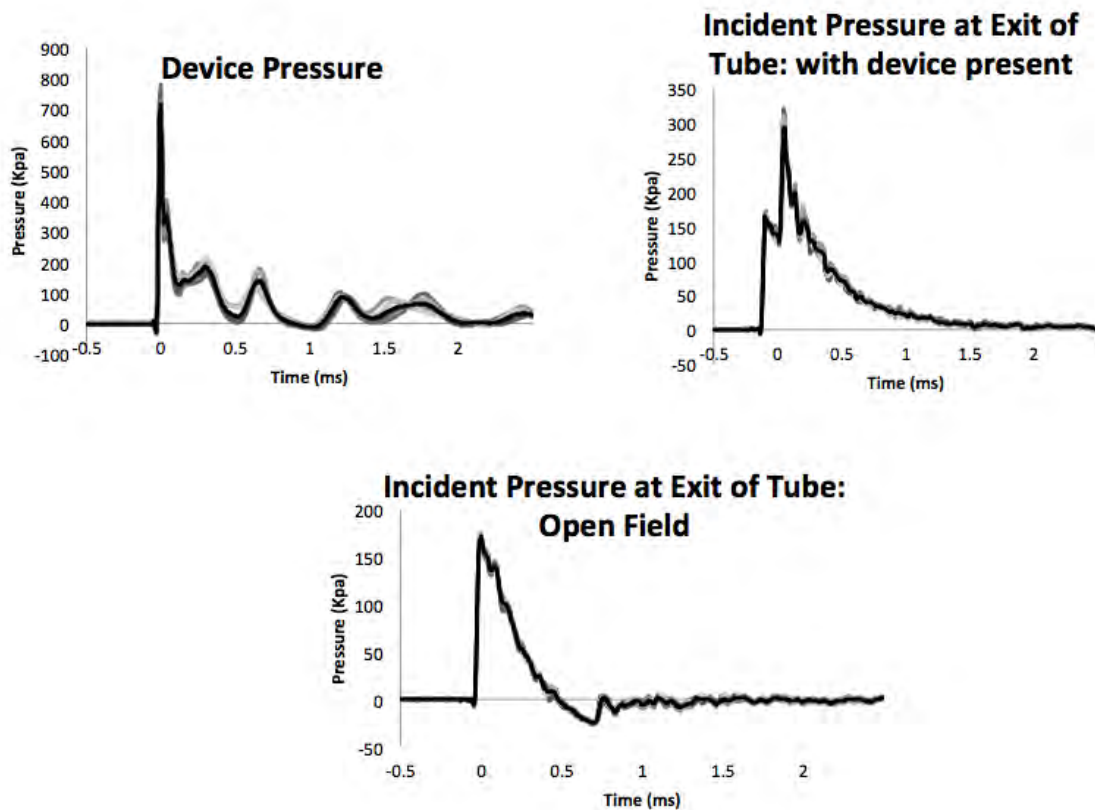
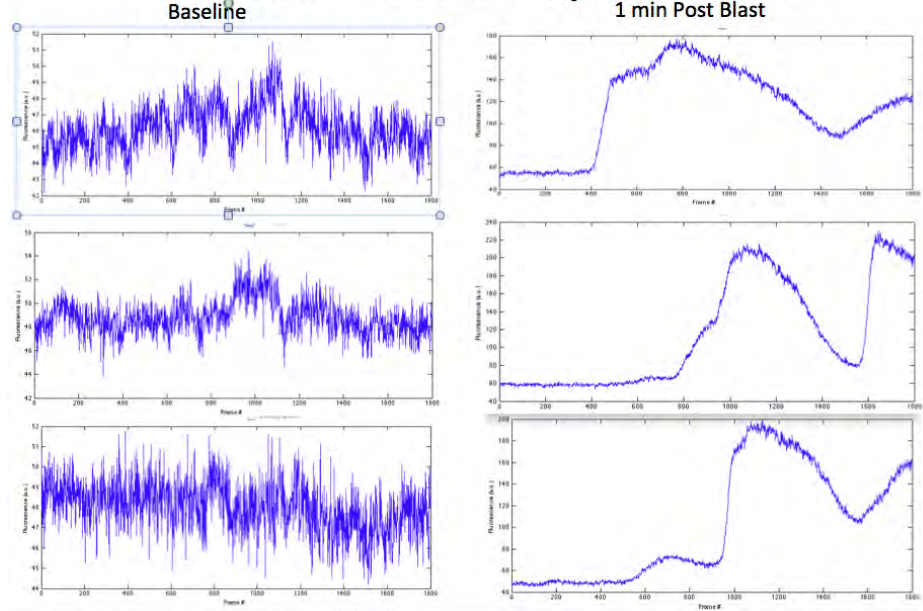


Figure I25 - Pressure traces within the chamber, at the tube exit, and in the free field.

Neurons within the network prior to blast exposure displayed periodic increases in cytosolic calcium. We found these transient increases in cytosolic calcium were due to spontaneous electrical activity, as we could block these changes with either treatment with tetrodotoxin or CNQX, antagonists toward the α -subunit of the sodium channel and AMPA receptors, respectively. Following blast exposure at low levels (86 ± 9.58 kPa msec), we did not see any evidence of primary calcium transients in the cultures. Moreover, we did not see any evidence of a primary response throughout the astrocyte network. The lack of a response was not due to a decline in culture viability within the device, as we observed changes in cytosolic calcium with the addition of NMDA (neuronal stimulation) and/or glutamate.

Time Course Astrocyte Calcium



Time Course Neuronal Calcium

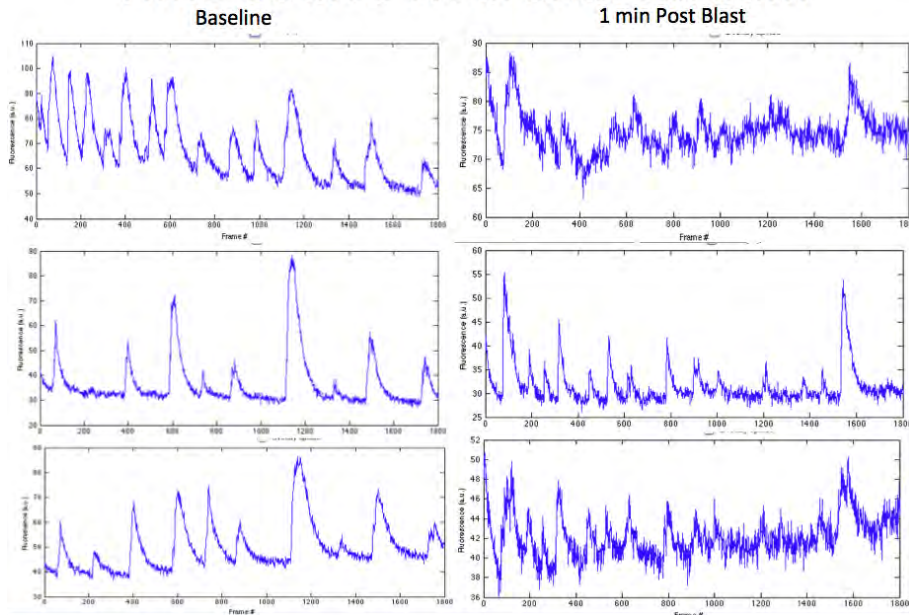


Figure 126 - Representative responses of astrocytes (top) and neurons (bottom) to in vitro blast overpressure

At higher blast exposure levels, neurons again showed little primary response. However, the astrocytes began to show an immediate response to the blast exposure with a calcium transient that showed a more gradual increase over the initial 5 minute period following blast injury.

Together, these pilot data suggest strongly that there is a threshold blast exposure level for both neurons and glia responding to the primary blast input. Moreover, these data suggest the astrocytes are the first cell type to respond to the blast pressure impulse. We are actively

exploring (a) the relative thresholds for both neurons and astrocytes in responding to the initial blast exposure, (b) the change in this threshold when we examine blast exposures of different durations and peak pressures, and (c) the change in this threshold when we use multiple exposures over several days, using the protocol outlined for the in vitro BBB studies from the Columbia partner.

Year 4 progress: University of Pennsylvania

In the fourth year, the Penn group:

- concentrated our efforts to examine the relative effects of unconstrained and constrained blast, where the primary loading conditions to the brain involve a mixture of blast+acceleration or only acceleration (constrained)
- assessed completely the behavior phenotype in unconstrained and constrained blast
- measured the electrophysiological impairment in hippocampal circuitry after blast exposure in both constrained and unconstrained conditions
- characterized the complete blast-induced pathology caused by unconstrained and constrained blast
- developed, prototyped and tested a new in vitro blast TBI model

Extending in vitro BBB damage thresholds to *in vivo*.

We have worked with our Columbia partner in evaluating the relative presence or absence of BBB damage in mice exposed to blast. Our goal is to determine the change in threshold for damage to the BBB when we move our testing from in vitro monolayers into the living brain.

Animal preparation and injury: Male, C57BL6 mice aged 12-14 weeks were obtained from either Charles River laboratories (Wilmington, MA, USA) or Taconic (Hudson, NY, USA) and allowed to acclimate in the colony before testing. We carefully adhered to the animal welfare guidelines established by the University of Pennsylvania's and Columbia University's Institutional Animal Care and Use Committee (IACUC), and used procedures that were approved by those IACUC committees. Animals were placed in an anesthesia induction chamber (5% isoflurane) for 2 minutes, and then transported into the testing room. Animals remained on 2% isoflurane anesthesia for 3 minutes during placement and positioning prior to exposure. Immediately prior to testing, anesthesia was discontinued. Immediately after injury, the animal was removed from the holder and brought to a recovery area.

We used Evans blue dye tracer to indicate damage to the blood brain barrier. Fifteen minutes prior to blast injury, mice received a single injection of Evans blue dye into the tail vein. Over the circulation time of 15 minutes, past work has shown that this dye complexes nearly completely with serum albumin protein. Without any injury, animals that are euthanized and perfused with a 4% paraformaldehyde solution showed no significant staining in coronal sections. Animals receiving a direct cortical impact injury show widespread labeling of Evans blue throughout the parenchyma following perfusion, indicating that the serum crossed the blood-brain barrier and entered the interstitial space.

Our previous work showed that a blast exposure delivered to the dorsal head surface would lead to significant changes in righting time deficit, and changing the direction of loading to strike the nose first

would lead to a significant shift in the righting time. We focused on examining a specific loading condition (225 kPa peak; .69 msec duration; 114 kPa*msec impulse) and testing if the primary changes in BBB permeability, as evidenced by % Evans blue dye staining in tissue sections, would differ across the two loading conditions.

Measuring blood-brain barrier extravasation in the living brain: One hour following exposure to the blast pulse, animals were euthanized with an overdose of sodium pentobarbital (65 mg/kg) and perfused with 4% paraformaldehyde. Brains were removed from the cranial vault and sectioned on a freezing stage microtome. Coronal sections 1 mm apart were generated for each brain. Each individual coronal section was placed in PBS buffer within an individual plastic well of a multiwell plate, and a series of wells was generated across each animal set. The set of wells was imaged on an IVIS imaging system (Perkin-Elmer), and image threshold intensity subtraction was used to eliminate background and measure the % of each tissue section that showed Evans Blue dye extravasation.

Results show that dye extravasation appeared in some, but not all, coronal planes. Perhaps most surprisingly, we did not notice a difference in extravasation patterns among the two blast wave conditions and sham when examining the front (rostral) portion of the brain. Within the region spanning the hippocampus (sections 5-7), we observed significant dye extravasation for both loading directions. Towards the caudal portion of the brain (section 9), significant leakage also appeared one hour following injury. Together, these data show that the loading conditions associated with neurological impairments in mice also cause breakdown of the blood-brain barrier in parts of the brain.

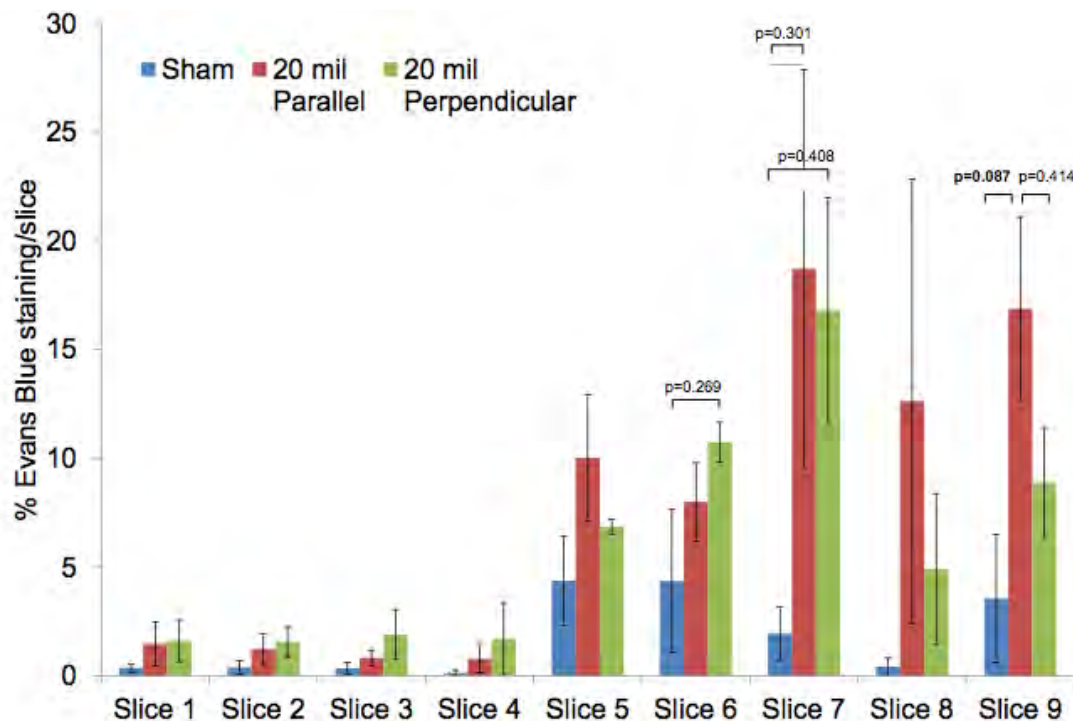


Figure 127 - Animals exposed to a direct blast loading in either the parallel or perpendicular direction were examined for changes in blood-brain barrier breakdown. Coronal sections of the brain (1 mm spacing) showed a significant elevation in some, but not all, of the brain sections relative to sham exposure animals.

Collectively these data show that a primary consequence of blast loading to cells of the brain – leakage of an intact BBB in vitro – is also preserved when examining the consequences of blast loading to the living brain. We are very encouraged by the conservation of these injury mechanisms across our testing platforms. We are now exploring if the intracranial pressures within the brain are sufficiently different than the external free field conditions of blast applied to the brain. With these measurements in hand, we will develop an empirical comparison between the thresholds for BBB damage after in vivo and in vitro loading in the next year.

Compromise of the BBB – serum response of cultures of the BBB

These in vivo and past in vitro data show clearly that blast loading can cause changes to the integrity of the blood brain barrier. We next explored how this release of serum into the interstitial space within the brain would affect the signaling within neurons and astrocytes of the brain, and also the activity and network structure of networks in vitro.

Primary mixed cultures. We generated mixed cultures of primary neurons and glial cells from embryonic rat pups (E17), plating cells onto treated Mattek glass dishes at a density of 500,000 cells/ml. Seven days prior to testing, cells were transduced with a genetically encoded calcium indicator (GCaMP6). On the day of testing, virus particles were rinsed from the culture and the cells were placed on a custom, live cell imaging platform with constant temperature and humidity control.

Serum isolated from rats and diluted down to different effective concentrations in the cell media elicited a strong, robust response in both neurons and astrocytes (Figure 129). The minimal concentration necessary to elicit a response in culture was 1:500 of the initial serum concentration. At this dilute concentration, there was an initial transient that quickly recovered back to baseline values. Moreover, the relative activity of neurons within the mixed culture showed no significant change in the activity pattern 15 minutes following stimulation at this level. In comparison, serum diluted 1:50 in the cell culture media caused a strong, initial calcium transient in astrocytes that was quickly followed by a sustained calcium elevation in neurons within the culture. We did not see a significant difference when we replaced rat serum with commercially available horse serum in the nature or timecourse of these calcium transients.

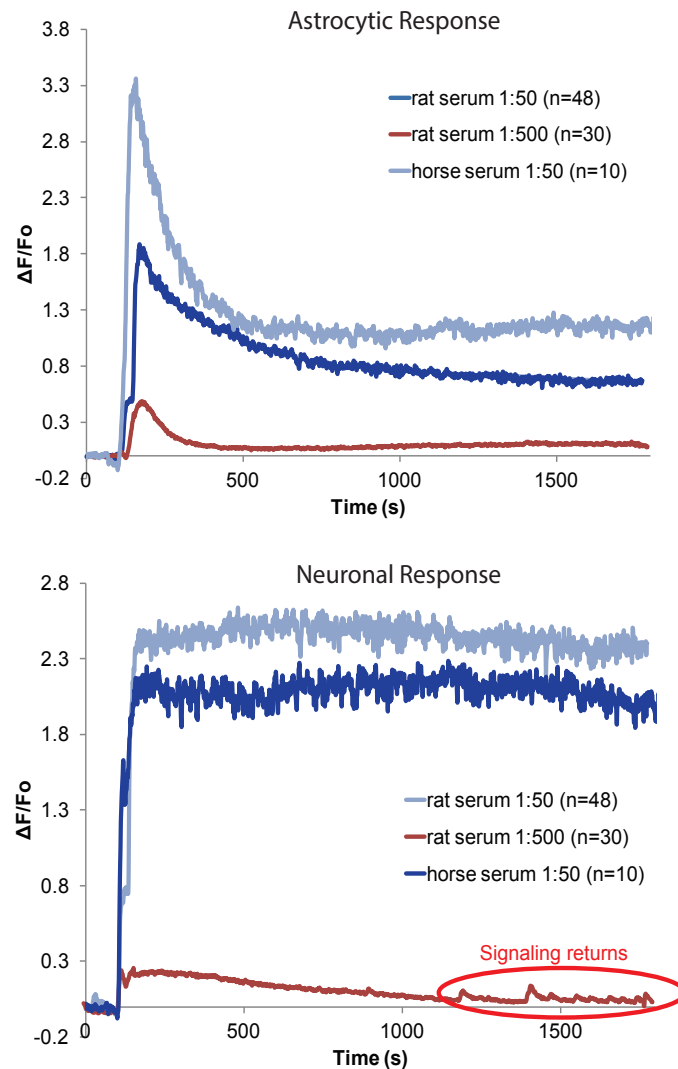


Figure I28 - Response of mixed neuronal/glial cell cultures to serum exposure.

Given the complex composition of serum, we then proceeded to characterize the prominent mechanisms responsible for the immediate changes in cytosolic calcium within both neurons and astrocytes. We examined if glutamate receptors were responsible for some of the changes within neurons, and found a primary contributor to the calcium transient was the activation of NMDA receptors. We also explored if metal ions contained in serum – some of which are well known modulators of neurotransmitter receptors and also mediators of neuronal degeneration – were responsible for some of the changes observed in the acute response. We found a broad spectrum cation channel blockade (LOE) also reduced the primary response in neurons, and this reduction was enhanced with the additional blockade of internal IP3 receptors (2-APB). In comparison, the most effective reduction of astrocyte calcium transients was a combination a broad spectrum cation channel blockade and IP3 receptor inhibition (Figure I30)

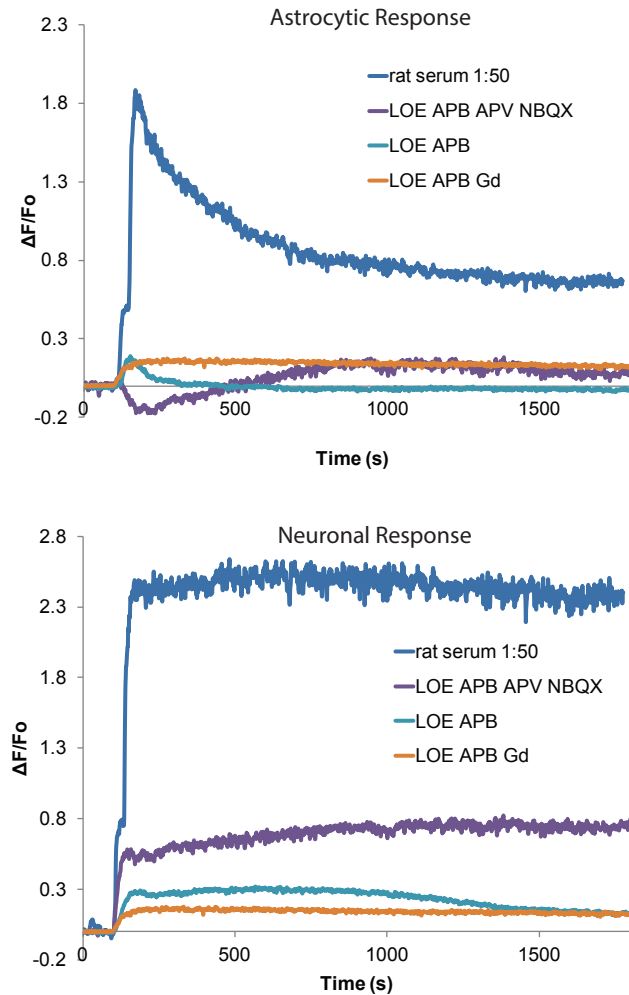


Figure 129 – Mechanisms of acute calcium elevation in neurons and astrocytes differ following serum exposure

We next tested if these significant and persisting changes in neuronal/glial signaling would persist and change the activity/structure of the network over a 24 hour time period. Applying serum continuously, even at a 1:50 dilution, would lead significant neuronal degeneration 24h later. We tested different exposure times – 8h, 4h, 2h, and 1h – and found that a two hour exposure was the maximum exposure to avoid cell death at 24h. We then tested if this limited exposure to serum would affect network topology one day later.

Activity of the network was significant reduced while serum was applied to the mixed neuronal/glial cell culture. Once serum was removed, activity started to recover in the cultures but was still significantly reduced compared to control cultures. One day following the initial exposure of network to serum, we did not observe a significant reduction in either the synchrony, functional connectivity, or spontaneous activity of the network. We did observe an improvement in the activity of the network if the initial calcium transient was reduced with compounds to target NMDA receptor activation, cation channels, or IP3 receptors

A final outcome measure tested in these studies is whether the remodeling capacity of the network changes following serum exposure. Using the two hour serum exposure protocol that did not affect the topology or the survival of neurons/glia cells within the network at 24h, we examined if the changes within the network from sustained (15 min) stimulation of the network were altered. In control cultures, applying bicuculline methiodide to block inhibitory neurotransmission results in a periodic bursting of the network that differs significantly from control cultures. In addition, removing this 15 minute blockade leaves a persisting effect on the culture – both the spontaneous activity, functional connectivity, and synchronization are all significantly different. In serum treated cultures, we found that bicuculline treatment was unable to change synchronization, connectivity, and activity of the cultures. Therefore, this brief serum exposure led to a loss in the remodeling capacity of the network one day later (Figure 131). The data are intriguing because they may provide a mechanistic consequence of disruption of the blood-brain barrier on the function of networks, separate from any neuronal degeneration that could appear in the network following more sustained exposure.

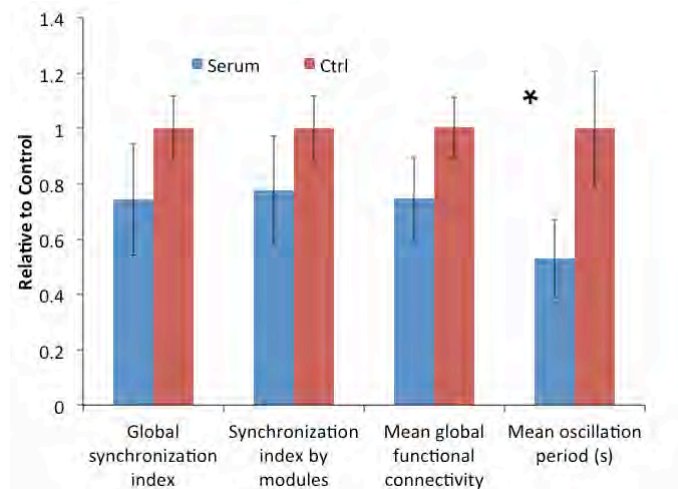


Figure 130 – Remodeling of the neural network differs following serum exposure

Measuring the relative behavioral differences in blast from different directions

Our work shows that blast loading causes primary breakdown of the blood-brain barrier, and that serum affects the remodeling ability of neuronal networks in vitro. Our work using behavioral phenotyping last year provides us with an automated, validated, and fast methodology to screen several different behavioral assays in a short period of time. With our background in establishing connections among the mechanisms of primary blast injury, we now returned to the in vivo system and examined the relative difference in neurobehavior that occurs when the blast wave direction is changes.

The behavior protocol that we followed in the tests is outlined in Figure 132. Animals are first evaluated for impairments in open field navigation, cortical/motor coordination, anxiety (elevated zero maze), motor learning, novel object recognition, and fear conditioning. Animals were exposed to either a blast wave striking the dorsal head surface (perpendicular) or the tip of the nose first (parallel). Videotape recordings of each behavioral test was converted into digital format, and the automated processing of the behavior for each test was scored, automatically recorded, and then randomly checked by manual scoring in 10% randomly selected tests.

DAY	1	2	3	4	5	6	7	8	9
AM	Zero Maze			Spatial Object Recognition		Break		Fear Conditioning	
PM	Rotorod								

Figure 131 – Schedule of tests used to evaluate the neurobehavioral impairments of ‘pure blast’ loading

The composite neurobehavior results are shown in Figure 133. Briefly, we see significant cortical motor impairments (Rotarod) in the perpendicular direction when compared to sham animals, and we also observe an alteration in the open field measures related to anxiety. Perhaps most significantly, we observe a consistent alteration in novel object recognition across both directions. Using an independent component analysis that we developed last year, we assembled a canonical representation of the 14 dimensional behavior response space and found that sham, perpendicular, and horizontal direction exposed animals were distinct in this reduced canonical space. These collective data show that the aggregate behavioral response of animals exposed to either a perpendicular or parallel blast were statistically different, although these two groups did share a common set of core behavioral deficits after blast exposure.

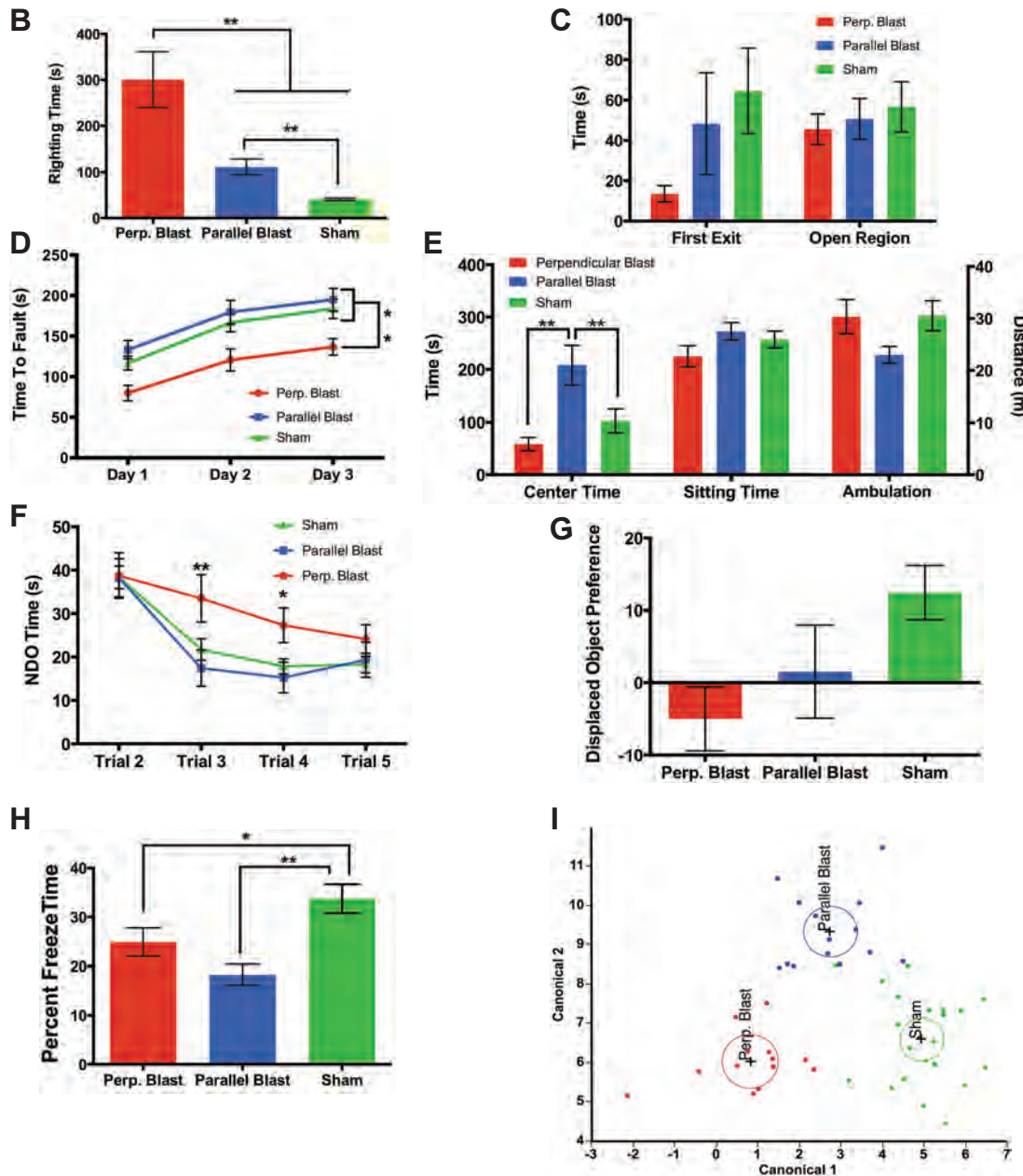


Figure 132 – Composite neurobehavior results of parallel and perpendicular blast loading

The resulting histological changes for these loading scenarios showed no demonstrable change in the macroscopic brain structures, and no observable evidence of neuronal loss using Nissl staining. The most significant change was glial reactivity, evident with GFAP immunohistochemistry, in the hippocampus and cerebellum (Figure 134).

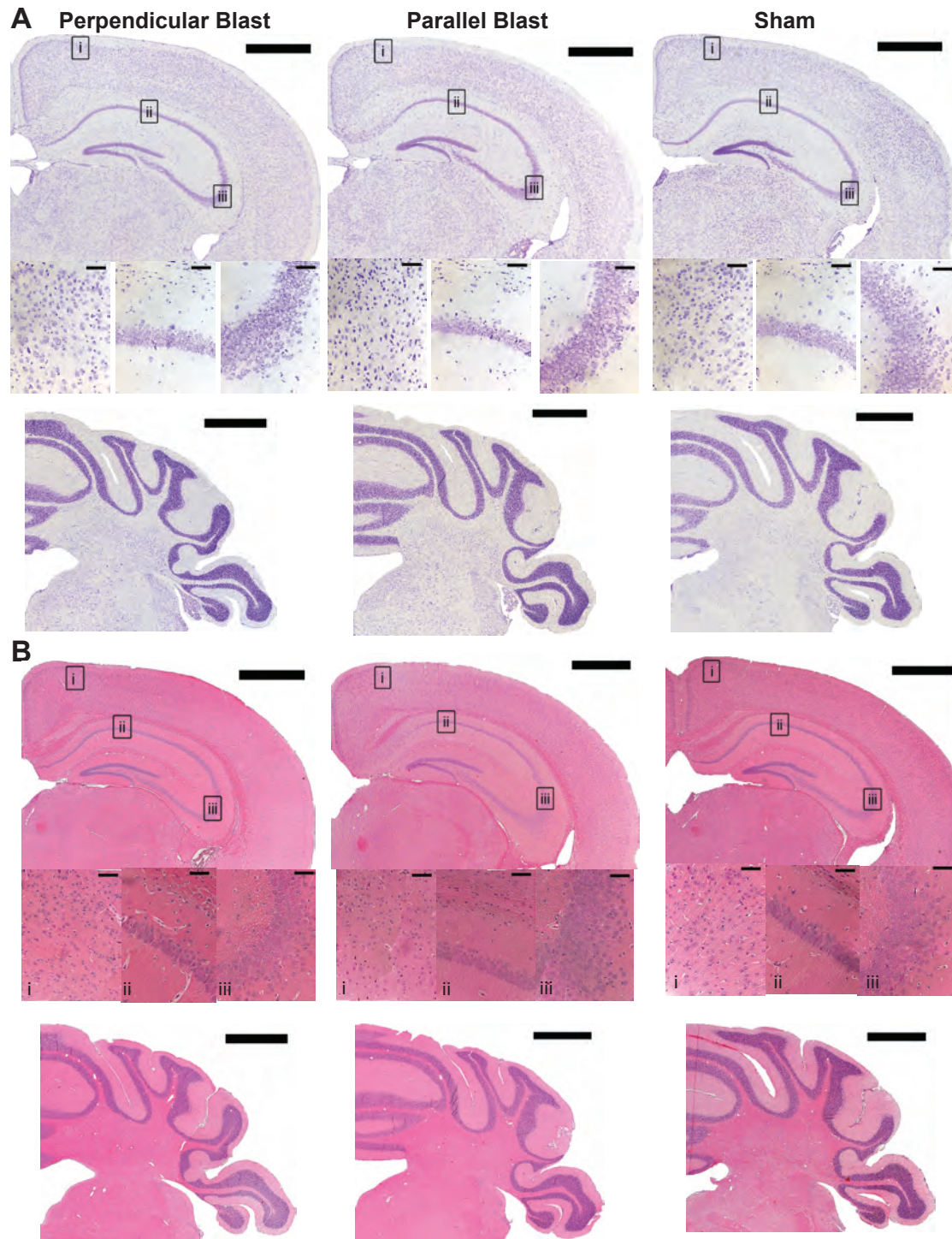


Figure 133 - Representative images of histological changes following blast exposure in the parallel and perpendicular direction.

We then extended these results by studying the response of animals exposed to blast loading in a ‘head constrained’ condition. Our work last year showed that blast loading can cause significant head motion/accelerations that may not be evident in most testing conditions. Currently, there is

considerable debate in the literature on the potential for primary blast loading alone – with minimal to no head acceleration – to cause any behavioral changes in animals.

We repeated these same behavioral tests, but now focused our analysis on the differences appearing when we exposed animals to two different blast exposure levels – a first level using the same exposure conditions in the perpendicular/parallel testing describe above, and a second level significantly above this exposure level and just below the survivable blast dose for mice of this age, weight, and gender. Both exposures are delivered with the animal aligned parallel to the blast tube axis, with the blast wave first striking the tip of the nose before progressing across the head surface.

Righting time is significantly impaired across both loading levels, with the highest loading level (415 kPa peak over pressure) showing the longest righting time. Animals showed an aversion to explore the center portion of the open field test for both loading levels when compared to sham injured animals, a reduction in ambulation, and increase in thigmotaxis. The percent preference for the novel object in the NOR test was significantly different for both loading levels when compared to sham, but they were not different from each other. Fear conditioning deficits only appeared at the highest loading level (415 kPa). Finally, an independent component analysis of the aggregate behavioral data showed that all three experimental conditions could be separated from each other, with the 415 kPa condition showing the greatest distinction from the sham condition.

To our knowledge, this is the first evidence that we know which establishes that primary blast affects neurobehavior. We next considered if these behavioral deficits also corresponded with deficits in the hippocampal circuitry. To examine this question, we examined acute slice preparations of the hippocampus and used field recording protocols to evaluate if there were presynaptic release changes, postsynaptic changes, or alterations in the LTP that would occur in animals after exposure to blast loading at either 215 or 415 kPa peak overpressure. These data also allow us to compare these results from the living animal to similar measures from the organotypic slice culture work presented by Columbia in their progress report (see Section 2).

Acute changes in hippocampal circuitry following blast exposure

We used acute slice preparations from the hippocampus, isolated from a blast injured animal 5 days following blast exposure. Both loading levels in the ‘pure blast’ configuration created hippocampal impairment by causing deficits in spatial object recognition. However, only the highest loading condition created impairment in the fear conditioning test. We sought to assess whether there were consistent changes in hippocampal circuitry across both levels, and if there were differential changes that appeared at the higher loading level.

All experiments were performed on adult male (12-16 weeks old) C57BL/6J mice. Animal care and use was in accordance with the guidelines specified by the Institutional Animal Care and Use Committee of the University of Pennsylvania. Animals were decapitated under isoflurane anaesthesia and their brains were quickly isolated into ice-cold oxygenated (95% O₂ / 5% CO₂) sucrose based artificial cerebrospinal fluid (ACSF) comprising of (in mM) 202 sucrose, 3 KCl, 2.5 NaH₂PO₄, 26 NaHCO₃, 10 glucose, 1 MgCl₂ and 2 CaCl₂. Coronal sections (350 µm thick) were cut using a vibratome (VT1200S, Leica Microsystems, Buffalo Grove, IL) and transferred to oxygenated ACSF (comprising, in mM, of 130 NaCl, 3 KCl, 1.25 NaH₂PO₄, 26 NaHCO₃, 10 glucose, 1 MgCl₂, and 2 CaCl₂) maintained at 34-36°C. Prior to recording, slices were transferred to room temperature (22-24°C) in an interface chamber perfused with oxygenated ACSF (2-4 ml min⁻¹). Field potentials were recorded in the CA1 region of the dorsal

hippocampus (1.58 – 2.30 mm posterior to Bregma) from either hemisphere by an Axoclamp 900A amplifier interfaced with pClamp 10 data acquisition software (Molecular Devices, Sunnyvale, CA). The stimulating electrode (#CBDPG75, Frederick Haer Corporation, Bowdoin, ME) was placed in the stratum radiatum (SR) at the boundary between the CA1 and CA2 regions, approximately two-thirds of the length of the SR from the cell body layer (stratum pyramidale; SP). The recording electrode was similarly placed in the SR in CA1 at approximately two-thirds the length of the SR from the SP and 700-1100 μm from the stimulating electrode. Both electrodes were gradually positioned at a depth at which the maximum amplitude of the measured parameter (slope of the initial linear portion of the response) was obtained. Recording electrodes were fabricated from borosilicate glass capillaries (#IB150F-4, World Precision Instruments, Sarasota, FL) to have a tip resistance of 2-6 $\text{M}\Omega$ and filled with ACSF. The electrical stimulus was 100 μs in duration and the recorded signals were low pass filtered at 2kHz.

Field potential recordings and paired pulse recordings: Field potentials in CA1 were recorded five days after treatment (sham or injury). Input-output curves were first obtained for all slices for stimulus intensities in the range of 40-400 μA . The stimuli were incremented by 40 μA , and were 8s apart. The stimulation pattern was repeated thrice and the slopes in the three repetitions were averaged. The stimulus intensity at which the half-maximum slope was obtained was then used to examine paired-pulse facilitation. The pair of stimuli was delivered 25, 50, 75 and 100 ms apart. For each inter-stimulus interval, the slopes in three trials (separated by 8s) were averaged and the ratio of the second to the first slope was calculated. Data from all the slices obtained from an animal were averaged and statistically analyzed using two-way nested ANOVA. A p-value of less than 0.05 ($p < 0.05$) was considered significant.

Role of NMDA receptors in field I/O recordings: Contribution of the NMDA receptors to the field potential were isolated through perfusion of 6 μM CNQX in reduced magnesium ACSF (mACSF) comprising of (in mM): 130 NaCl, 3 KCl, 1.25 NaH_2PO_4 , 26 NaHCO_3 , 10 glucose, 0.5 MgCl_2 , and 2 CaCl_2 . The stimulus intensity for half-maximum slope was used to determine the baseline during drug perfusion. The stimulus was delivered every 30s until the decreased slope stabilized at its final value (typically 20-30 minutes). Input-output curves were determined as described above.

In animals exposed to either blast condition, we observed no difference in the field I/O curves for the dentate gyrus across the stimulation corridor. In contrast, we did observe a significant difference in the paired pulse ratio for 50 millisecond inter-stimulus ratio. (Figure 135)

The most significant change in the field I/O curves appeared for the CA1 region of the acute slice, where we observed changes for both exposure levels. Unlike the dentate gyrus, we did not see evidence of presynaptic release changes. Neither condition produced changes in paired pulse facilitation ratios. The reduction in the field I/O curves was not different across exposure levels. (Figure 135)

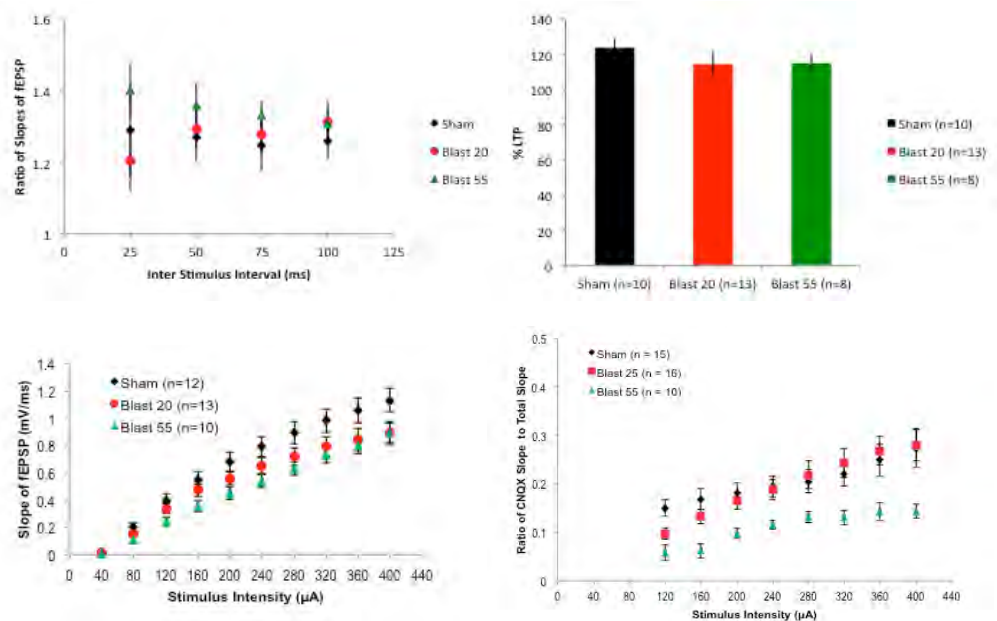


Figure 134 – Summary of acute hippocampal slice activity 5 days following blast exposure.

One potential cause for the neurobehavioral deficits is an alteration in the long term potentiation response that can be triggered in acute slice preparations. Normally, these LTP changes are evaluated in slices prepared from younger animals, and we needed to modify our procedures accordingly to account for mice aged 12-14 weeks. In slices derived from sham animals, we used a 100 Hz x 3 burst stimulation protocol test evaluate changes in the field I/O slope that occurred within one hour of stimulation. Repeated tests across sham cultures showed a 20% potentiation in the field I/O response to this burst stimulation. Animals exposed to either the low (215 kPa) or high (415 kPa) exposure level did not show a significant reduction in this LTP response, suggesting that behavioral deficits observed in these tests could not be attributed a change in the remodeling response of the hippocampal circuitry.

One possible additional change to the hippocampal circuitry is an alteration in the balance of glutamate receptors activated postsynaptically. One method to assess these changes is by blocking either AMPA receptors (w/ CNQX) or NMDA receptors (w/ APV) during the stimulation of the perforant path. In sham cultures, we found that blocking the AMPA receptors during Schaffer collateral stimulation would lead to a significant reduction in the resulting field I/O curve. Subsequent blockade of the NMDA receptors would block the remainder of the field I/O curve, indicating that AMPA and NMDA receptors together are the primary postsynaptic receptors that contribute to activation of the hippocampal circuitry in CA1. Although the lowest level of primary blast exposure (215 kPa) led to a significant reduction in the field I/O curve, we did not observe a change in the relative proportion of AMPA/NMDA currents. In comparison, the highest blast exposure level significantly reduced the relative contribution of the NMDA receptors to the overall field I/O curve. These data, combined with earlier paired pulse facilitation data, shows a dose dependent change in the circuitry of the CA1 region. Further, the data show the primary change is in the postsynaptic receptor population. These data will

be examined more in the future to test how these changes recover, or are different, following repeated blast exposure.

In Vivo Imaging of CAI Networks

Anaesthesia and Initial Setup for Stereotaxic Procedures:

An adult mouse (6-8 weeks old), under isoflurane anaesthesia, is placed onto a stereotaxic frame to immobilize its head. Isoflurane (1-2%) is continuously administered throughout the procedure through the nose cone. Depth of anaesthesia is determined using the paw pinch test and the percentage of inspired isoflurane is adjusted as necessary. Eyes are lubricated with lubricant eye drops to minimize corneal drying. The animal is placed on a heating pad to maintain its body temperature in the physiological range (36° - 37° C).

Virus Injection into Dorsal CAI:

Meloxicam (5mg kg⁻¹) is administered subcutaneously prior to the start of the procedure. Following the initial setup the scalp is swabbed thrice, alternately with betadine (10%) and ethanol (70%) and incised parallel to the midline with a scalpel. A local anaesthetic (bupivacaine) is administered and the periosteum cleared. A motorized burr (0.5 mm) is used to drill a small hole in the skull at the coordinates of interest to expose the dura. The injection coordinates are -1.8 mm from bregma, ± 1.4 mm from laterally from midline and -1.3 mm dorso-ventral from dura. Injections are done only in one hemisphere, either the left or right. Typically a batch of 5 animals is divided so that 3 animals are injected on the right side and 2 on the left or vice versa. The needle of a Hamilton syringe controlled by an automatic micromanipulator is gradually lowered to the necessary depth and allowed to settle for ~ 2 minutes prior to injection (1µl of desired concentration of the titre at a rate of 0.25 µl min⁻¹) of the virus. After injection the needle is left in for ~ 2minutes and then gradually and carefully removed. The scalp is sutured (22mm 0.5c sutures) and the animal is allowed to recover.

Cannula Insertion:

Approximately one week (7-10 days) after injection a cannula for in vivo imaging is inserted around the site of the injection. Meloxicam (5mg kg⁻¹) is administered subcutaneously prior to the start of the procedure. The animal is prepared for craniotomy as above and the scalp is disinfected with three alternate swabs of betadine (10%) and ethanol (70%). The scalp is incised and the periosteum is cleared subsequent to administration of bupivacaine. A motorized trephine (1.8 mm outer diameter) is used to drill a larger hole encompassing that created for injection into the skull. Drilling is intermittent; with rinses with sterilized saline to prevent overheating of the bone and tissue. The bone piece and then the dura are carefully removed with a pair of forceps. The cortex is gently aspirated down to the alveus under continuous perfusion of saline with a 25 -G (initial, crude) and 27-G (final, delicate) blunt needle (bent to ~ 45°) attached to a vacuum pump. After reaching the desired depth, the underlying tissue is cleared with saline and suction, and the bleeding allowed to stem. In case of excessive bleeding,

gel foam is applied to stem it. Clots are gently removed with a 30-G needle tip and the tissue cleared with saline and suction. Once the bleeding stops, the hole is filled with saline and a cannula (~ 1.8 mm outer diameter) is gently lowered until contact with the underlying tissue is established. In case of bleeding or the presence of air bubbles, the cannula is removed and replaced after allowing the bleeding to stop and refilling the hole with saline. The skull is dried with cotton swabs and melted agarose (1%) is applied to the sides of the cannula to fill the gap between it and the skull. The skull is then dried with hydrogen peroxide and air. Dental cement is applied around the cannula over the exposed skull secure it to the skull. Once the acrylic hardens, the animal is allowed to recover (Fig 136). Meloxicam (5mg kg^{-1}) is administered subcutaneously for two days post operation.



Figure 135- Animal with a cannula implanted into the right hippocampus.

Mounting baseplates:

Baseplates are mounted 1-2 weeks after insertion of the cannula. Animals are placed on a stereotaxic frame under isoflurane anaesthesia and the baseplate of the microscope is glued to the skull with dental cement at the height at which the stratum pyramidale is in best focus (Fig 137). The coverslip at the end of the cannula is gently cleaned with water and a cannula sleeve containing a GRIN lens is placed in it. The camera attached to the base plate is gently lowered over the grin lens until the plane of sharpest focus is observed. The base plate is then cemented to the skull and the camera removed. Meloxicam (5mg kg^{-1}) is administered subcutaneously prior to the start of the procedure.



Figure 136 - Animal with a base plate mounted over the cannula. The ink darkened dental cement eliminated stray background.

Imaging: Imaging is performed in awake, behaving or un-anaesthetized mice. Imaging is performed 2-3 weeks after inserting the cannula. Animals are anaesthetized briefly to mount the camera on the baseplate and are allowed to completely recover. They are then placed in an open field and allowed to explore. Subsequent to the behavioral task, the animal is once again briefly anaesthetized and sodium fluorescein dye (FITC, 1% solution; 0.05 ml) is injected through the tail vein to obtain a vascular map of the region of interest. Subsequent to injection the animal is allowed to recover and replaced in its home cage.

Results

For calcium imaging of CA1 network activity during behaviour we used the genetically encoded calcium indicator (GECI) GCaMP6f. To confine GCaMP6f expression to pyramidal neurons we chose the CamKII α promoter. The gene encoding the indicator was delivered to the cells in a rAAV vector (AAV9, CamKII, GCaMP6f, WPRE, SV40). We chose AAV9 as it is known to have a high specificity for neurons. To confirm that AAV9 does indeed have a high specificity for neurons and to determine its spread we injected animals with different dilutions (1:10, 1:100, 1:1000, 1:10,000 and 1:20,000) of the titre and performed immunohistochemistry for GFP after 4 weeks (Fig 138). Our results confirm that AAV9 has a high specificity for neurons with the area of infection depending on the concentration. At the higher dilutions (1:10 and 1:100) virus was expressed throughout the cross section of the hippocampus, in the habenum and in the cortex along the needle track throughout the dorsal hippocampus. At the very low concentrations (1:10,000 and 1:20,000) expression was confined along the needle track. At the middle concentration (1:1000) staining was confined to and around the targeted layer of the hippocampus beyond the needle track. Further, high magnification images showed GFP expression in only the cytosol (red staining) and very little green fluorescence compared with the 1:10 and 1:100 dilutions indicating that the virus was not enucleated and cells were alive (GCaMP6f has a low baseline). Consequently, we decided to dilute the titre to 1:1000 for in vivo imaging. These animals were injected using the coordinates provided by Ziv et al in their Nature Neuroscience paper using the Inscopix imaging system. They did not specify if their dorso-ventral coordinate was from the surface of the skull or the dura. Based on our images we realized that these coordinates were from the surface of the skull and in our coordinate

system of injection (wherein dura is 0) this results in transfection in the dentate gyrus. We therefore corrected the coordinate by measuring the thickness of the skulls of several animals in the age group of interest and subtracting the same. We then confirmed the subtracted coordinate (1.2-1.3 mm) with other published reports and now use it.

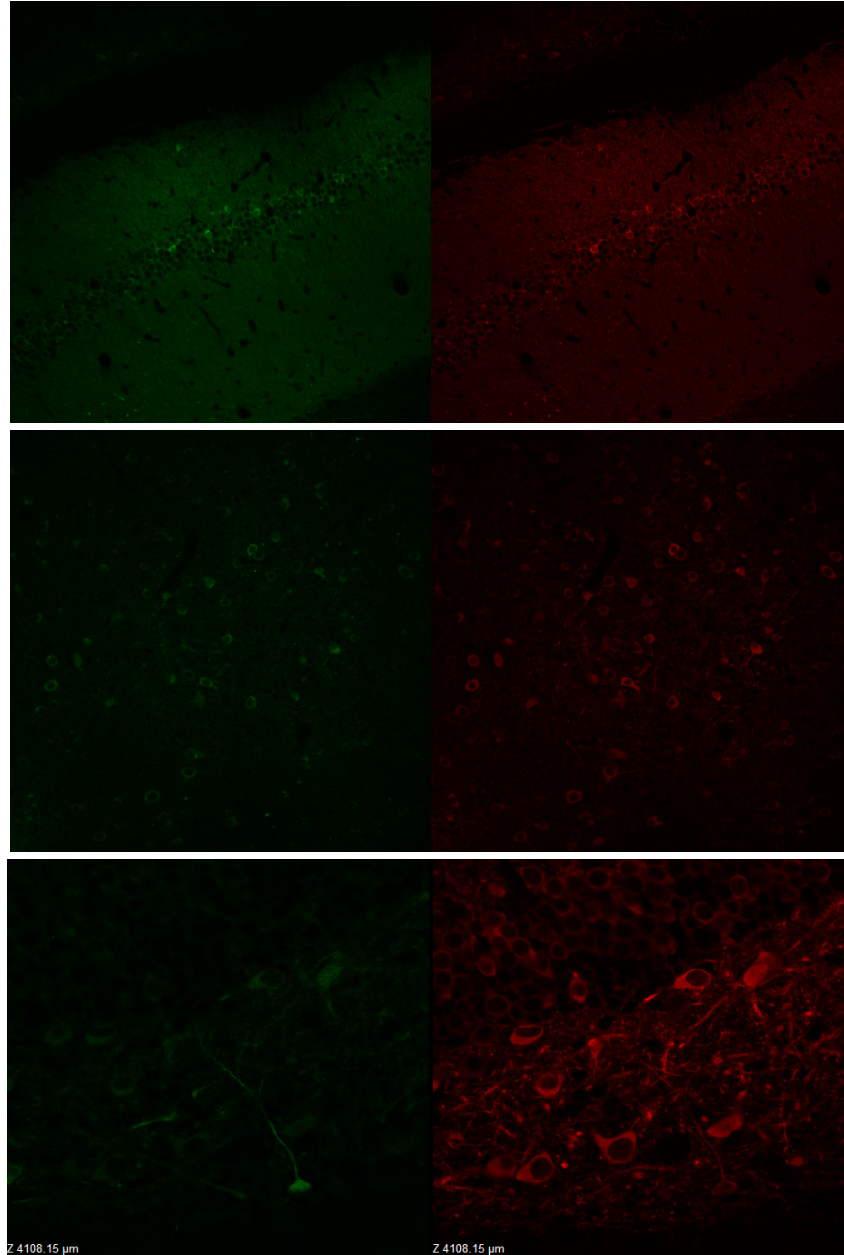


Figure 137 - Expression of GCamp6f under the CamKII promoter using AAV9. The green channel is endogenous GCamp6f (GFP) signal and the red (Cy3) is the signal from the bound GFP antibody. GFP antibody was used to stain for GCamp6f. First panel: 1:10 dilution of the virus titre. Second: 1:1000. Magnification on both sets 20x. Third: Higher magnification (60x) 1:1000.

After verifying GCamp6f expression under the CamKII promoter in the hippocampus with the AAV9, we started our in vivo procedures. In an attempt to reduce experimental costs we

innovated techniques to manufacture all the necessary components. For the cannulas, we purchased a hypodermic tube (15g) which we cut into ~ 4mm pieces and apply slow drying epoxy on one edge and glue to a glass coverslip (#1). The glass is then cut and polished with the help of two high speed Dremmels. For the base plates, we incorporated its design into CAD and now use a 3-D printer to mass print them. These manufacturing procedures reduced the cost by over \$200 per animal and enabled us to increase the number of animals we can implant and prepare for imaging. We have successfully injected, implanted and mounted baseplates. Initially, many of the animals dislodged the entire preparation (base plate and cannula) when the camera was first placed on them, while some of them dislodged it over the next couple of days when in their home cages. We identified several potential reasons and set about modifying the procedure to ensure that the animals retained the base plates. First, we realized that the depth of the normal cages for housing mice was small so that once the base plates were mounted they were continuously jostled due to impact with the grill covering the cage and containing food and water. Consequently, once the base plates are mounted we house the mice in larger cages designed for rats. Second, we noticed that in all the dislodged preparations, prior to dislodgement, there was fluid seeping under the dental cement from under the skin at the edges of the cement. We therefore modified the procedure so that during the cannula implantation step, prior to sealing the cannula to the skull with dental cement, we first dry the skull with hydrogen peroxide followed by air and glue the skin with Vetbond to the edges of the skull. Third, we noticed that once the base plates were mounted and the animals recovered from anaesthesia they would paw the skin surrounding the cement. We reasoned that the dental acrylic was probably irritating the skin and decided to administer a dose of meloxicam prior to the start of the base plate mounting procedure as well. Last, we observed that camera and its cable exerted a torque on the preparation when the base plate was freshly mounted. We therefore decided to wait a few days (at least two) after base plate mounting to image. With these measures the animals retained their base plates until euthanasia (6 weeks in most animals; 8 weeks in a couple).

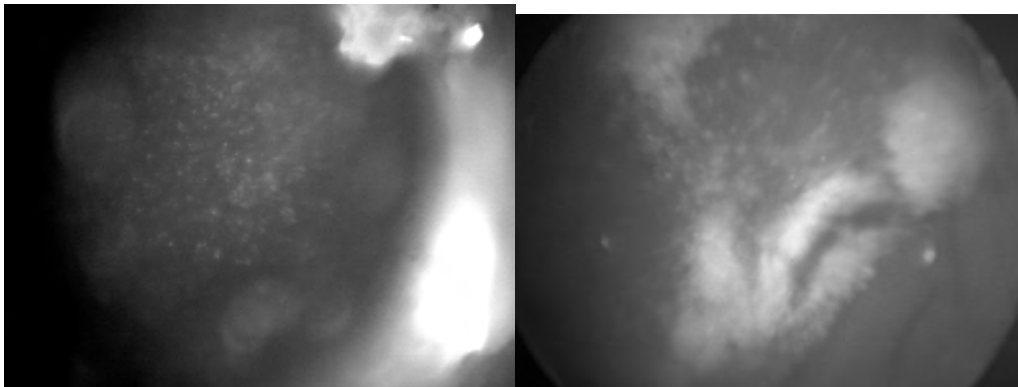


Figure 138 - Representative images from two animals injected with AAV9.CamkII.GCamp6f.WPRE.SV40 acquired with the Inscopix camera under anaesthesia. The punctate staining indicates successful transfection. Top: Dental cement used to mount the base plate was not darkened. Reflection of the light source from the dental cement appears along the right edge. Bottom: Dental cement used to mount the base plate was darkened. The larger blood vessels are visible in ark contrast.

Figure 139 illustrates an image acquired by the Inscopix camera with this preparation. The GCamp6f positive cells are clearly visible as distinct puncta. We found that white or clear dental cement reflects the incident light and produces background fluorescence. We successfully eliminated this by darkening the cement with ink. This image was acquired under anaesthesia during base plate mounting. While we clearly saw transfected cells we could not see many calcium fluctuations either under anaesthesia or when awake. That we don't see activity under anaesthesia is unsurprising and expected, as it is well known that anaesthesia suppresses the activity of most neurons. However, there are two possible reasons for observing no activity when awake. The first is that the plane of best focus shifts after the dental acrylic hardens. The Inscopix camera lacks the ability to focus as it was designed to be lightweight to be mounted on the head. The plane of best focus is determined during base plate mounting and the base plate is cemented at that height with dental cement. We calculated that as the acrylic hardens it shrinks and lowers the base plate by 100-200 μm . Given that the stratum pyramidale is only 50 μm thick, this shift changes the optimal field of view. We did this by placing milar membranes (used in shock tubes) in increments of 25 or 50 or 100 μm between the camera and the baseplate until the cells focused on during base plate mounting are in focus again. We have redesigned the base plate so that it can move 100-200 μm in the dorso-ventral direction and does not need to be cemented to the skull. The prototypes are printed and we will shortly be testing these. The second is that CA1 pyramidal cells only respond to specific stimuli. To address this, we injected AAV9.hSyn.GCamp6f.WPRE.SV40 to broaden expression to all neurons (Fig 140). Additionally, we centered the cannula at the injection site as opposed to in our previous preparations wherein we implanted it slightly offset from the injection site as per camera manufacturer's protocols. Once again, just as under the CamKII promoter, we saw distinct puncta indicative of cells. However, we also saw increased background fluorescence from the neuropil. Based on our results that head constrained blast animals show deficits in open field exploration we focused on imaging exploration in an open field. We figured, that as the animal explores place cells would fire. However, as the number and distribution of place cells in the population of CA1 pyramidal cells are unknown and appears to be sparse from electrophysiology we constructed a prototype for a linear treadmill. Recent literature indicates that firing rate of CA1 neurons increases when the animal is running on a treadmill and that the place cells have unidirectional fields. We are currently training animals preparatory to imaging and refining the prototype.

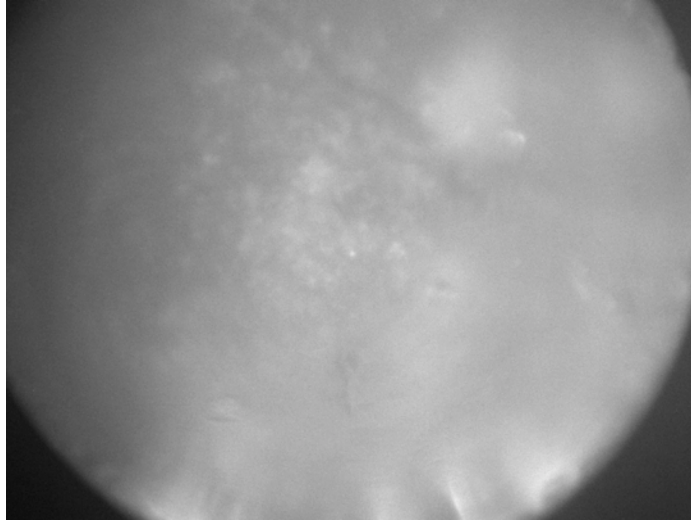


Figure 139 - Representative images from two animals injected with AAV9.Syn.GCamp6f.WPRE.SV40 acquired with the Inscopix camera under anaesthesia. Once again the punctate staining indicates successful transfection. Note the background fluorescence from the neuropil.

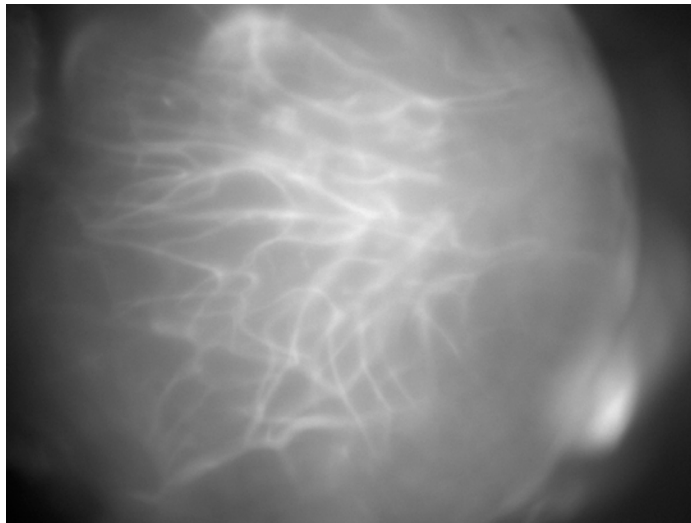


Figure 140 - Fluorescein angiogram image of the vasculature acquired with the Inscopix system. FITC was injected through the tail vein. The animal was under isoflurane anaesthesia.

We injected all the animals prepared for imaging with FITC to image the vasculature (Fig 141). We found that the Inscopix system can be used to study useful questions about blood flow in the brain. In addition, we blasted two implanted animals in the head constrained position. We found that we need to modify the shoulder collar as the current one compresses the preparation resulting in bleeding under and adjacent to the cement. Consequently, the imaging preparation was dislodged a little while after blast.

Future Work

We are presently focused on incorporating the ability to focus in our camera setup. However, we are also working in parallel on a few other aspects. 1. As mentioned above, we are building a treadmill in the required dimensions to stimulate CA1 pyramidal cells. 2. We are also modifying the shoulder collar to constrain the animal's head during blast exposure. The first prototype is ready for testing. 3. We are working on the preparatory surgical procedure for imaging from the deeper brain structures. The difference is in the second or implantation step. Similar to the wide field hippocampal preparation above a craniotomy is performed and the bone and dura are removed. A longer GRIN lens with half the diameter of the one used for wide field is then gently and carefully inserted into the tissue to the desired depth. After insertion the GRIN lens is sealed to the skull with dental cement. The remaining procedures are identical. 4. We are also working on imaging from the cortex. Once again the difference is in the second step. A craniotomy is performed encompassing the injection site and the bone and dura are removed. A glass coverslip is placed over the exposed cortical surface, which is then be fixed to the brain with an adhesive. Dental cement will then be applied to the remaining portion of the exposed skull to create a cap. 5. We are working on imaging changes in blood brain barrier immediately after blast using FITC and on quantifying blood flow with microspheres.

References:

- Effgen, G. B., Hue, C. D., Vogel, E., 3rd, Panzer, M. B., Meaney, D. F., Bass, C. R., & Morrison, B., 3rd. (2012). A Multiscale Approach to Blast Neurotrauma Modeling: Part II: Methodology for Inducing Blast Injury to in vitro Models. *Front Neurol*, 3, 23. doi: 10.3389/fneur.2012.00023
- Geddes, D. M., Cargill, R. S., 2nd, & LaPlaca, M. C. (2003). Mechanical stretch to neurons results in a strain rate and magnitude-dependent increase in plasma membrane permeability. *J Neurotrauma*, 20(10), 1039-1049. doi: 10.1089/089771503770195885
- Panzer, M. B., Matthews, K. A., Yu, A. W., Morrison, B., 3rd, Meaney, D. F., & Bass, C. R. (2012). A Multiscale Approach to Blast Neurotrauma Modeling: Part I - Development of Novel Test Devices for in vivo and in vitro Blast Injury Models. *Front Neurol*, 3, 46. doi: 10.3389/fneur.2012.00046
- Patel, T., Ventre, S., & Meaney, D. (2012). Dynamic Changes in Neural Circuit Topology Following Mild Mechanical Injury In Vitro. *Annals of Biomedical Engineering*, 40(1), 23-36. doi: 10.1007/s10439-011-0390-6
- Patel, T. P., Man, K., Firestein, B. L., & Meaney, D. F. (2015). Automated quantification of neuronal networks and single-cell calcium dynamics using calcium imaging. *Journal of Neuroscience Methods*, 243, 26-38. doi: <http://dx.doi.org/10.1016/j.jneumeth.2015.01.020>
- Patel, T. P., Ventre, S. C., Geddes-Klein, D., Singh, P. K., & Meaney, D. F. (2014). Single-Neuron NMDA Receptor Phenotype Influences Neuronal Rewiring and Reintegration following Traumatic Injury. *The Journal of Neuroscience*, 34(12), 4200-4213. doi: 10.1523/jneurosci.4172-13.2014

Brain derived exosomes as detectors of brain injury state

In the United States, 1.74 million people every year seek medical attention for traumatic brain injury, of which 80% are considered to have a mild Traumatic Brain Injury (mTBI).⁽¹⁾ However, it is estimated that only 25% of those who experience a mTBI ever seek medical evaluation or care, suggesting that the incidence of mTBI can be significantly higher than indicated in previous studies.⁽¹⁾ Most mTBI patients will recover within one year following their incident, but an approximate 10-20% of mild cases result in a long-term disability including seizures and emotional and behavioral issues.⁽²⁾ Currently, because there are few molecular markers to measure an individual's injury and subsequent recovery, diagnostics to prospectively identify patients in need of intervention and to guide them towards personalized, efficacious treatment are limited to monitoring for symptoms that may appear months to years following an injury. Similarly, the conventional use of patient reported symptoms to evaluate therapies is hindered by the lack of accepted criteria to measure and report post injury complications, the inaccuracy endemic to patient self-reporting, and the common comorbidity of mTBI with polytrauma and substance abuse.^(3, 4) In this light, discovering accessible, clearly defined biomarkers would significantly improve the evaluation of TBI therapeutics.

Although there is great interest in developing biomarkers for both the detection and treatment of mTBI, efforts in this area have proven challenging. One fundamental hurdle in the discovery of biomarkers for mTBI is that the Blood-Brain Barrier (BBB) remains largely intact after injury, limiting the number of possible targets that can be detected in accessible body fluids.^(3, 5) Most past biomarker work focuses on protein biomarkers in Cerebral Spinal Fluid (CSF) or blood, including Tau^(6, 7), calcium-binding proteins S100B,⁽⁸⁾ neuron-specific enolase,^(8, 9) ubiquitin carboxy-terminal hydrolase L1 (UCHL1),⁽⁹⁾ myelin basic protein (MBP),⁽¹⁰⁾ and metabolites such as glucose⁽¹¹⁾, and miRNA⁽¹²⁾. However, these efforts face detection sensitivity challenges because of the low concentration (fM-pM) of circulating molecular markers, as well as the proteolytic degradation, clearance by the liver or kidney, and binding of potential biomarkers to carrier proteins.⁽⁵⁾ Moreover, due to the diversity of head injury types and severity and the complex and personalized recovery that each individual experiences, it is difficult for any single biomarker to sufficiently characterize the complex state of the injured and recovering brain.⁽¹³⁾ Imaging techniques, such as Magnetic Resonance Imaging (MRI) and Computerized Tomography (CT), which are used successfully to classify severe head injuries, have difficulty stratifying subtypes of mTBI injuries and have limited accessibility due to their high cost.^(13, 14)

Recently, exosomes derived from brain cells, small (30-200 nm diameter) membrane-bound vesicles that carry proteins, RNA, and DNA from their mother cells have been found to pass through the BBB, offering a new opportunity to evaluate molecular changes in neurons and glia behind the barrier after trauma.⁽¹⁵⁻¹⁷⁾ In previous work, increases in circulating exosomes have been observed in the blood of TBI patients following injury.^(3, 18, 19) Despite their enormous potential, the use of exosome biomarkers to improve patient care faces several challenges. Due to their small sizes (30-200 nm), conventional size-based isolation of exosomes is time consuming (> 6 hr), results in co-purification of cell debris, and cannot selectively isolate specific sub-populations of exosomes or differentiate exosomes from other extracellular vesicles (e.g. microvesicles, oncosomes).^(15, 20) While microfluidics can precisely sort and detect cells from complex media, applying these approaches to nanoscale exosomes is limited by the low throughput and susceptibility to clogging of nanofluidics. We solved this problem by

developing a new approach to nanofluidic sorting of brain-derived exosomes, wherein millions of nanofluidic devices are incorporated onto a microchip platform and operated in parallel, increasing throughput by a million fold and eliminating susceptibility to clogging from unprocessed clinical samples. As this device's nanofluidic geometry matches the size-scale of exosomes, it can precisely balance magnetophoretic and drag forces to selectively enrich for exosomes based on expression of specific surface markers. .

Our approach measures multiple exosomal miRNA biomarkers to capture a more comprehensive view of the injured and recovering brain than is possible with a single biomarker. **(Fig. 1A)** Our goal was threefold: (1) to use these novel miRNA biomarkers to accurately differentiate serum collected from uninjured and injured mice, (2) to determine the key signaling pathways activated in the injured brain, providing information for possible treatment approaches and (3) to use the exosomal biomarkers to predict injury severity and injury history, key clinical variables that will guide therapy. Conventional methods relying on only a single molecular biomarker are often not sufficiently specific and only give a limited view of the recovering brain. (3) Because exosomes package multiple biomarkers from the injured and recovering brain, there is an opportunity to measure a panel of molecular biomarkers to more fully describe the complex state of the recovering brain. To analyze these multiple molecular biomarkers, we use machine learning algorithms to reduce a panel of exosomal miRNA biomarkers into a set of optimized linear discriminators. By choosing relevant states of injury and training the machine learning algorithm to find patterns that optimally classify this set, we can outperform any individual marker. In this study, we isolated brain-derived exosomes based on their expression of the AMPA receptor subunit (GluR2), measured multiple miRNA biomarkers packaged in these exosomes, and then combined these biomarkers using Linear Discriminant Analysis (LDA) to specifically classify the injured and recovering brain. **(Fig. 142A)** We used an established murine model for blast injury, which produces a mild TBI with neurobehavioral impairments 5 days after injury(21), to develop and characterize this method, and demonstrated successful classification of injured mice versus healthy controls, identified key pathways activated in the injured brain, and successfully classified between various injury levels and between different histories of previous injuries. We additionally validated the translatability of this approach to humans by using the biomarkers identified in our mouse study and successfully classified (AUC = 0.9) a cohort of clinical samples ($N = 54$), identifying healthy controls versus those that experienced TBIs with an Abbreviated Injury Score (AIS) 2-5, using < 1 mL of serum.

Results

Surface marker specific nanomagnetic isolation of brain-derived exosomes

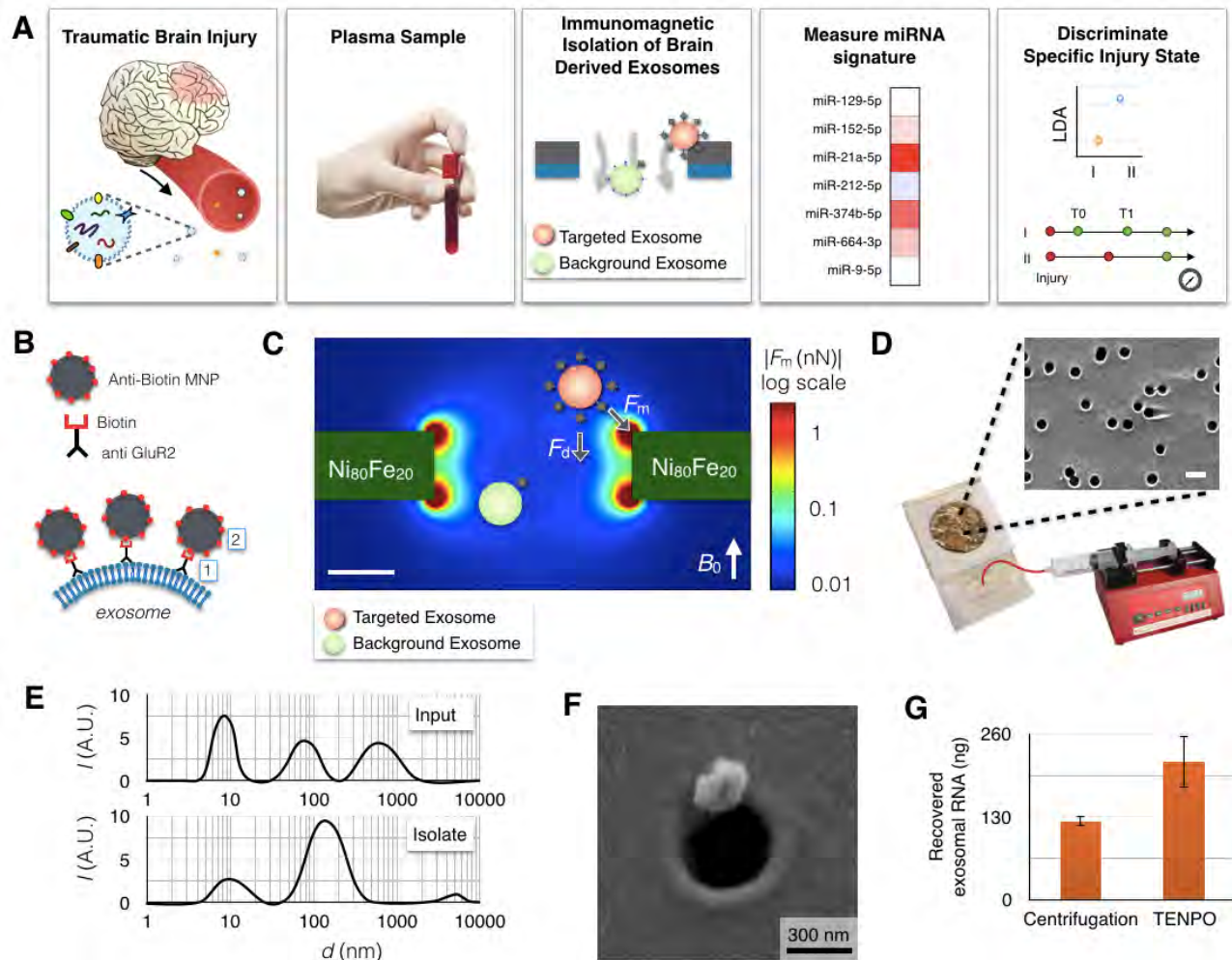
We developed a new nanofluidic architecture to precisely isolate and enrich for specific subpopulations of circulating exosomes directly from unprocessed serum or plasma, based on the targeted exosomes' positive expression of a surface marker. Immunomagnetic sorting has the advantage that biological material is inherently not magnetic, enabling high contrast between targeted exosomes and background material.(22) We labeled exosomes with magnetic nanoparticles ($r = 25$ nm), functionalized with affinity ligands to label GluR2+ surface markers.**(Fig. 142B)** We used an antibody for the AMPA receptor subunit, glutamate receptor 2 (GluR2) because GluR2 is known to be found preferentially in neuronal

exosomes.(19, 23) Our Exosome sorting Track-Etched magnetic NanoPOre (ExoTENPO) chip consists of an ion track-etched polycarbonate membrane with 600 nm diameter pores coated with a soft magnetic film ($\text{Ni}_{80}\text{Fe}_{20}$).(**Fig. 142C**), rotating conventional microfluidic sorting by 90° to form magnetic traps at the edges of pores instead of in channels. Using ExoTENPO, we can isolate exosome sub-populations directly from $V \cong 10$ mL of serum or plasma in less than 30 minutes, using either pan-exosome surface markers or brain specific surface markers. Importantly, this architecture is insensitive to clogging from unprocessed clinical samples because blockage of any individual pore causes the flow to be diverted to neighboring pores, and does not affect overall device behavior. Finite element simulations were used to model the magnetophoretic force, and the strong trapping forces at the edge of the pore motivated us to make the pores as small as possible, without inadvertently trapping objects based on size, to bring targeted exosomes close to the regions of strong forces.(**Fig. 142C**) The capture rate, i.e. the fraction of captured targeted exosome, decreases as a function of flow rate but can be fully recovered by stacking multiple ExoTENPO membranes in series, enabling high capture rate at flow rates as high as $\phi = 10$ mL/hr.

The ExoTENPO uses a track etching process for manufacturing, a process that is widely available and therefore makes ExoTENPO suitable for translation from the laboratory environment to practical clinical settings. In this work, we build off of our previous work in which we used magnetic micropores with a diameter $d = 5 \mu\text{m}$ to isolate bacteria(24) and $d = 30 \mu\text{m}$ to isolate mamalian cells(25). Track etching allows this approach to be scaled to the nanoscale ($d = 600$ nm), to tailor it to the isolation of exosomes, without requiring electron beam lithography.(**Fig. 142D**) The orders of magnitude decrease in cost relative to conventional nanolithography comes at the expense of not controlling the pores' location, not a critical feature for this application. These ExoTENPO membranes are incorporated into a microfluidic device using laser micromachined layers of adhesive-coated polymer sheets.(24) In this paper, we used ExoTENPO with a pore size $d = 600$ nm, a membrane area $A = 15.2 \text{ cm}^2$, a pore density $\rho > 10^7$ pores / cm^2 , and $N = 6$ membranes in series.

To characterize the performance of the ExoTENPO for isolating brain-derived exosomes, we first used an *in vitro* cell culture model of TBI.(26) To validate that the vesicles isolated by our device have a size consistent with exosomes, we measured the size distribution of particles in the media from mixed cortical neuron/astrocyte cultured cells and compared it to ExoTENPO isolated particles from that media. The GluR2+ exosomes in 20 mL of media were magnetically labeled and ran through our device at $\phi = 10$ mL/hr. The isolated vesicles were eluted (System Biosciences) and their size distribution was profiled and compared to that of the input using Dynamic Light Scattering (DLS). We found that our device isolated particles with a size distribution $\langle d \rangle = 140$ nm consistent with that of exosomes.(**Fig. 142E**) Additionally, we fixed the exosomes directly on our device after capture, and imaged them using scanning electron microscopy (SEM) (Electron Microscopy Resource Laboratory, University of Pennsylvania).(**Fig. 142F**) We observed 150-200 nm vesicles, with a morphology consistent with that of exosomes, captured at the edge of the pores, consistent with the trapping mechanism of ExoTENPO. We also integrated the extraction of exosomal RNA for downstream analysis directly on the ExoTENPO. We first lysed the exosomes and then extracted total exosomal RNA. We achieved 1.8x improvement in RNA yield from 20 ml of cortical neuron/astrocyte

cultured media compared to a centrifugal technique (Total Exosome Isolation kit, Life



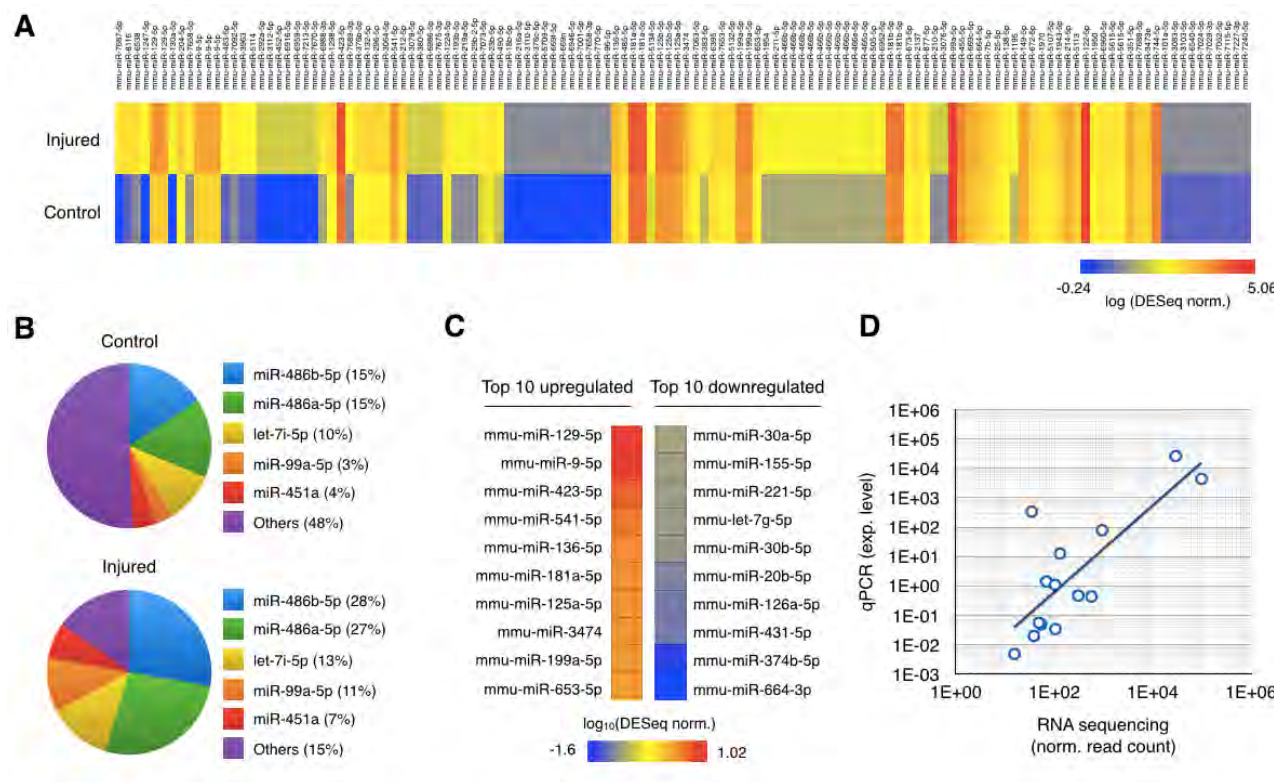
technologies).(26)(**Fig. 142G**)

Figure 141 - Immunomagnetic isolation of brain-derived exosomes using ExoTENPO. **A.** The workflow of our machine learning based TBI diagnostics that uses brain-derived exosomes isolated using EXO TENPO. **B.** Exosomes are immunomagnetic labeled using biotin anti-GluR2 antibody and anti-biotin magnetic nanoparticles (MNP). **C.** Finite element simulation of the magnetic field gradient generated by the ExoTENPO's permalloy-coated nanopores. The highest magnetic field gradient is at the edges of the pores where the labelled exosomes are captured. **D.** The ExoTENPO consists of millions of magnetic nanopores (600 nm diameter), which are incorporated into an acrylic reservoir. Fluid is pulled through the chip from the output using a syringe pump. **E.** Size distribution of exosomes measured with DLS. Input is cortical neuron cultured media and isolate are GluR2+ exosomes eluted from ExoTENPO. The input has a peak in its size distribution at 8.7 nm, 78.8 nm, and 615 nm whereas the isolate has a major peak at 141.8 nm. **F.** Scanning electron microscopy (SEM) image of an exosome captured using EXO TENPO. The exosome has $s \sim 200$ nm with morphology consistent with exosomes. **G.** Total exosomal RNA yield (ng) comparison between centrifugation method (122.7 ng) and EXO TENPO (216.2 ng). Exosomes are isolated from 20ml of cortical neuron cultured media.

RNA sequencing of brain-derived exosomal miRNAs for biomarker identification

To accomplish our first objective and identify miRNA biomarkers to classify injury state in mice, we first sequenced exosomal miRNAs from both mice that were injured using our blast model (415kPa, N=5 pooled) and mice that were uninjured (N=5 pooled).(**Fig. I43A**) GluR2+ exosomes were isolated on the ExoTENPO. For every animal a volume of 400-600 μ L of serum was processed. From each mouse, we attained 15-25 ng of total RNA, and so pooled the samples to maximize the sensitivity of sequencing, at the expense of being able to resolve animal-to-animal variability in the sequencing data. NEBNext Small RNA Library Prep Set for Illumina (BioLabs) was used to make a library, and then sequenced on a NextSeq500.

We analyzed the sequencing data to identify the exosomal miRNA markers to include in our diagnostic. The top 3 most abundant miRNAs were the same in the injured and uninjured samples, miR-486b-5p, miR-486a-5p, and let-7i-5p, but their relative abundance was significantly different.(P < 0.05) (**Fig. I43B**) We identified 7 biomarkers to use in our multiplexed assay,(**Fig. I43C**) based on either a maximally positive or negative differential expression in the injured versus the healthy control samples. Subsequent to the sequencing experiment, we isolated exosomes from N = 10 individual injured mice and N = 10 healthy animals, and measured the 7 candidate markers with qPCR. We found positive correlation between qPCR



and the sequencing. (Pearson Correlation Coefficient R = 0.37)(**Fig. I43D**)

Figure I42 - miRNA sequencing of brain-derived exosomes from injured and control mice. A. Brain-derived exosomal miRNAs were isolated using GluR2+ labeling and ExoTENPO isolation and sequenced from pooled

blast injured (415kPa) and control mice. DESeq normalized expression levels of individual miRNAs were plotted using a heat map. B. The five most abundantly expressed miRNAs from control

KEGG pathway	p-value	#genes	#miRNAs
Axon guidance	0.0000000633	69	39
Long-term potentiation	0.0000589	39	29
Glutamatergic synapse	0.0000589	54	34
Oxytocin signaling pathway	0.0000671	77	39
GABAergic synapse	0.001291407	34	27
Dopaminergic synapse	0.001778928	60	30
Neurotrophin signaling pathway	0.001809901	57	33
Cholinergic synapse	0.03748049	51	31

Table I. KEGG pathway analysis for blast injured (415kPa) mice versus healthy mice. 8 different pathways related to traumatic brain injury were found to be statistically significant ($P < 0.05$) and their relevant genes and regulating miRNAs were analyzed.

and injured groups are plotted. **C.** Top 10 upregulated and downregulated miRNAs after the injury **D.** From this list, 7 miRNAs biomarkers were selected and validated using qPCR. We used RNU6 for normalization. Expression levels from qPCR were compared to RNA sequencing. ($R^2 = 0.62$)

To accomplish our second objective and uncover the complex signaling pathways that were activated after mTBI, we submitted the full set of sequencing data for a bioinformatics analysis. We performed a Kyoto Encyclopedia of Genes and Genomes (KEGG) pathway analysis of the differentially expressed miRNAs and found several intriguing pathways activated in injured samples that included synaptic remodeling, axonal targeting, and inhibitory circuit remodeling pathways. Some of these pathways were supported with previous studies in the literature(27, 28), while others represented entirely new pathways (**Table I**)

Developing machine learning algorithms to classify blast injured mice

To accomplish our last objective and demonstrate the value of combining a panel of measured exosomal miRNA markers to discriminate specific states of injury and recovery, we measured a cohort of mice that experienced a blast injury ($N = 10$) and a cohort of mice that were uninjured ($N = 10$). The expression level was calculated by normalizing to RNU6. Amongst the panel of miRNAs that we measured, several miRNAs were expressed with a statistically significant difference between the groups, e.g. miR-152-5p ($P < 0.05$). However, due to mouse-to-mouse variability within the groups, there was no exosomal biomarker that could accurately classify all of the mice. For example, the best performing biomarker miR-152-5p achieved only an Area Under the Curve (AUC) = 0.86.

To classify the mice, we used LDA, where we can identify linear combinations of the miRNA biomarkers that discriminate injured versus healthy mice better than any single biomarker. **(Fig. I44A)** In LDA, we first measured our panel of exosomal miRNA for a training set of subjects \mathbf{w}_T , where we *a priori* know each subject's true injury state. This training is fed into the LDA algorithm (Matlab) to generate a LDA vector \mathbf{x} . The LDA vector \mathbf{x} is the same length as the number of miRNA measured in the panel. This vector \mathbf{x} is used to calculate a LDA score $\mathbf{w} \cdot \mathbf{x}$ for each mouse that can be used to optimally classify the mice, where every mouse with a LDA score above a defined threshold value Ψ is one group and every mouse below it is the other group. To first validate this approach, we used N-I cross validation. Subsequently, we tested this approach using a set of measurements on subjects \mathbf{w}_B where we are *a priori* blinded to their true injury state. The use of blinded test sets allow us to validate our ability to perform classification and to avoid overfitting.

To first demonstrate the utility of our LDA approach of classifying injury and recovery using exosomal miRNA, we classify mice injured with Blast (415kPa) versus healthy mice. We used a training set consisting of $N = 5$ mice that were injured and $N = 5$ healthy controls. We subsequently tested the performance of our discrimination using $N = 11$ mice, where we were blinded to the injury state of the mice. N-I cross validation on the training set with stepwise regression produced the best combination of markers for the test set. **(Fig. I44B)** Subsequently, we evaluated the blinded test set by using the combination of markers found in the training set where the prediction algorithm generated LDA scores for individual mice. **(Fig. I44C)** Using the LDA scores, the algorithm correctly classified every mouse in the blinded test set. **(Fig. I44D)**

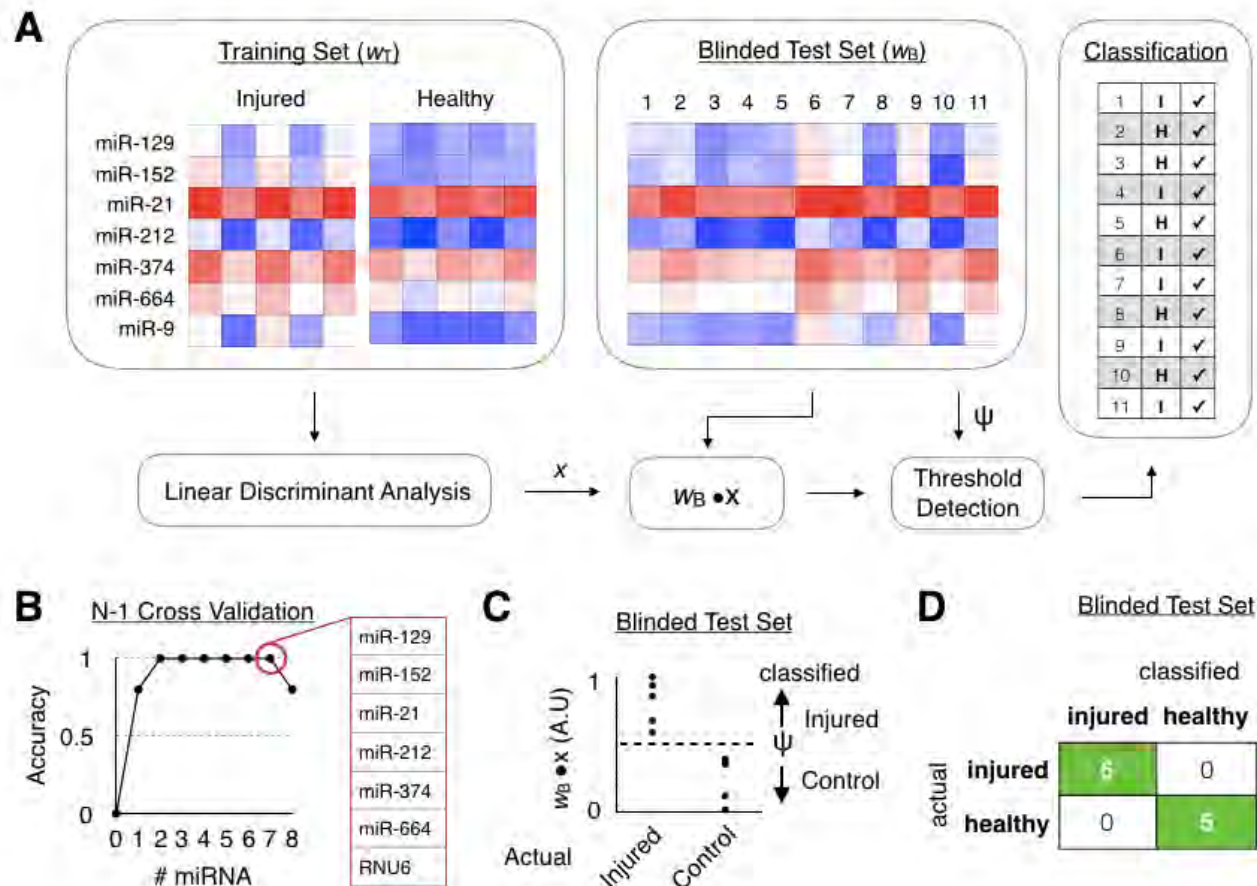


Figure 143 - Machine learning based diagnostics for blast injured mice. A. A **training set of data w_T** , where the true state of the mice is **a priori known**, is fed into an **LDA algorithm** to generate an **LDA vector x** . This **LDA vector** is then evaluated using a **blinded test set ($w_B \cdot x$)**, where the true state of the mice was **not a priori known**, to classify samples into different groups. B. The training set was first tested using **N-1 cross validation**. **Stepwise regression** was performed to find the best combination of markers. C. When the blinded test set is plotted by their **LDA score ($w_B \cdot x$)** the mice can be classified into the **correct group** by choosing a **threshold value ψ** . D. A **confusion matrix** was generated to summarize the results of classifying the blinded test set.

Discriminating injury severity, time, and history from a blood test

One important characteristic for clinical biomarkers is to determine the relative injury severity level and possible injury history, providing a clinical tool for treatment and patient management. To evaluate the potential of our exosome-based technique to predict injury severity, we expanded the approach in the section above to additional cohorts of injured animals including various severities of blast injury, multiple time points after injury, and histories of previous brain injury. We first considered two cohorts of mice, with a low level of blast injury (215kPa) and with a higher level of blast injury (415kPa). We measured a training set of $N = 5$ mice per condition and $N = 5$ healthy controls to generate the LDA scores to separate low blast, from high blast, from healthy controls. We subsequently evaluated a user blinded test set with $N = 6$ high blast, $N = 5$ low blast, and $N = 5$ control, and we were able to classify both high blast from healthy (AUC = 1)($P < 0.005$, Fisher's Exact Test),(**Fig. 145A**) low blast from healthy (AUC =

1)($P < 0.005$, Fisher's Exact Test)(**Fig. I45B**), and low blast from high blast (AUC = 0.97)($P < 0.05$, Fisher's Exact Test)(**Fig. I45C**)

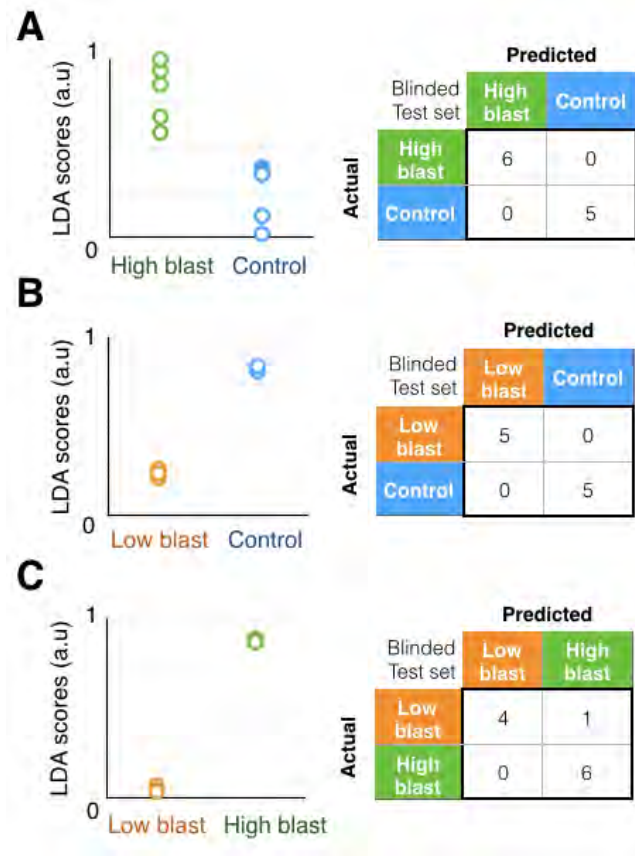


Figure I44 - Classification of severity of injury. **A.** Mice with a high blast injury (415kPa) were classified versus control mice. A training set of data (N=5 injured, N=5 control) is shown on the left and blinded test set (N = 11) is shown on the right. **B.** Classification of mice with a low blast injury (215kPa) was performed versus control mice, using a training set (N=5 injured, N=5 control) and validated with a blinded test set (N = 10). **C.** Classification of high blast injured mice (415kPa) versus low blast injured mice (215kPa) using a training set (N=5 low blast, N=5 high blast) and a validated with a blinded test set (N = 11).

Next we evaluated how long after an injury the exosomal RNA signature persisted. We generated a cohort of mice, each of which received a low level blast injury (215kPa), and blood was collected from cohorts of mice at 1 hour, 1 day, 4 days, and 14 days after the injury. (**Fig. I46A**) For each time point, a set of N = 5 mice was measured and included into a single training set. The training set was tested using N-1 cross validation where we performed stepwise regression to find the best working combination of markers, which were 4 markers including miR-129, miR-21, miR-374, and miR-664. (**Fig. I46A**) Using these markers, an independent, user blinded test set of each of the time points was evaluated where all N=20 mice from these cohorts (N = 5 mice each) were classified correctly versus N = 5 healthy controls (AUC = 1) ($P < 0.005$, Fisher's Exact Test). (**Fig. I46B**) Although all time points were classified correctly, the difference in its LDA score versus the healthy control degraded slowly as time increased. By measuring multiple exosomal miRNAs, we outperformed exosome counting where we measured number of GluR2+ exosomes in our previous study. (**Fig. I46C**) (19)

We next evaluated the effect of a history of prior injuries on the exosomal signature. We evaluated (a) mice that were measured 1 hour after a single blast injury (215kPa) versus (a+b) mice that were measured 1 hour after a single blast injury (215kPa) that had received the same injury 24 hours prior. (**Fig. I46E**) As a control, we also considered mice that had only (b) a single injury 24 hours before being measured and healthy controls. We first generated LDA vectors using a training set of $N = 5$ mice for each condition (a), (a+b), and (b). Then, we created an independent test set where we saw clustered groups along their LDA vectors. (**Fig. I46F**) We successfully classified 14 mice from three groups into the correct category. (**Fig. I46G**)

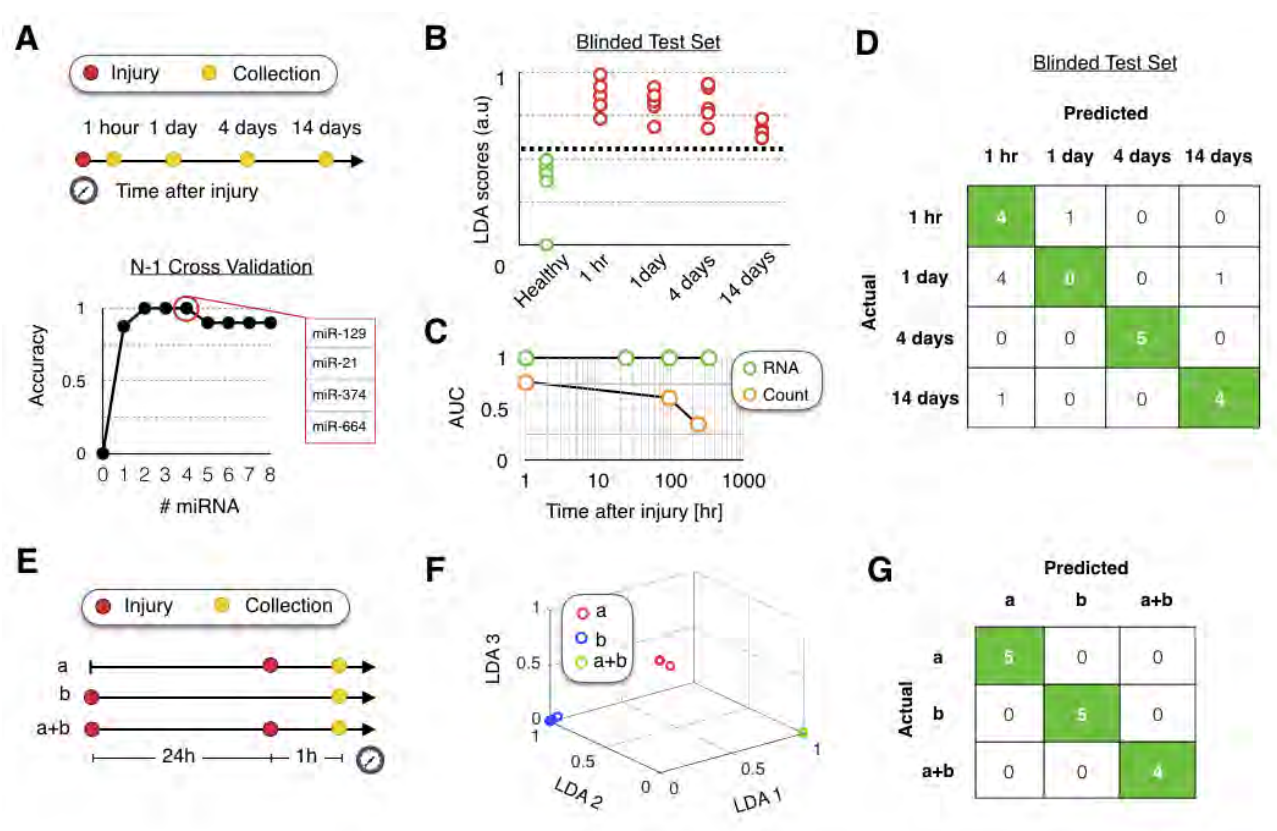


Figure I45 - Classification of injury versus time and history of blast injury. **A.** Mice were **Injured and then classified at various time points after the injury. Using N-1 cross validation we performed a stepwise regression to identify the optimal combination of exosomal RNA to identify injury states over time.** **B.** LDA scores at multiple time points after injury. **C.** The AUC at time points after injury compared to ELISA-based detection of GluR2+ protein level on the surface of the exosomes. **D.** Classification of the time point after the injury state. **E.** Mice were injured with different histories of injury. **F.** Plot of mice with different histories of injury using LDA. **H.** Confusion matrix of classification of three different injured groups.

Detection of exosomal miRNA signatures of injury in clinical samples

To explore the potential of our approach in clinical samples, we conducted a study on a cohort of $N = 52$ patients, which included those with an Abbreviated Injury Score (AIS) of 2-5 ($N=34$)

and healthy controls (N=18). For each sample, we performed GluR2+ exosome isolation on the ExoTENPO using 0.6 mL serum and measured the miRNA biomarker panel that was identified using our mouse model. We first measured the exosomal miRNA profile from a training set of N = 5 injured patients, and N = 5 healthy controls. Amongst the panel of miRNA that we measured, several were differentially expressed between the groups (e.g. miR-129-5p (P<0.0001), but no single miRNA correctly classified individual patients into the correct groups due to the variance in expression amongst patients within groups. Using the training set data, we selected the best possible combination of markers with N-1 cross validation by generating LDA vectors to maximally separate the patients into the correct group. (**Fig. 147A**) Using the selected markers, we ran LDA analysis on a user blinded test set where we obtained LDA scores for individual samples. (**Fig. 147B**) We classified N = 29 patients (including N = 5 AIS 2, N = 6 AIS 3, N = 14 AIS 4, and N = 4 AIS5) patients from (N = 13) healthy controls (AUC = 0.90, P < 0.0005 Fisher's Exact Test). (**Fig. 147C, D**) For this clinical study, we did not control time from injury to sample collection. Rather, we used samples that were collected 0.4-120 hours after injury, a heterogeneity which can be observed in real life.

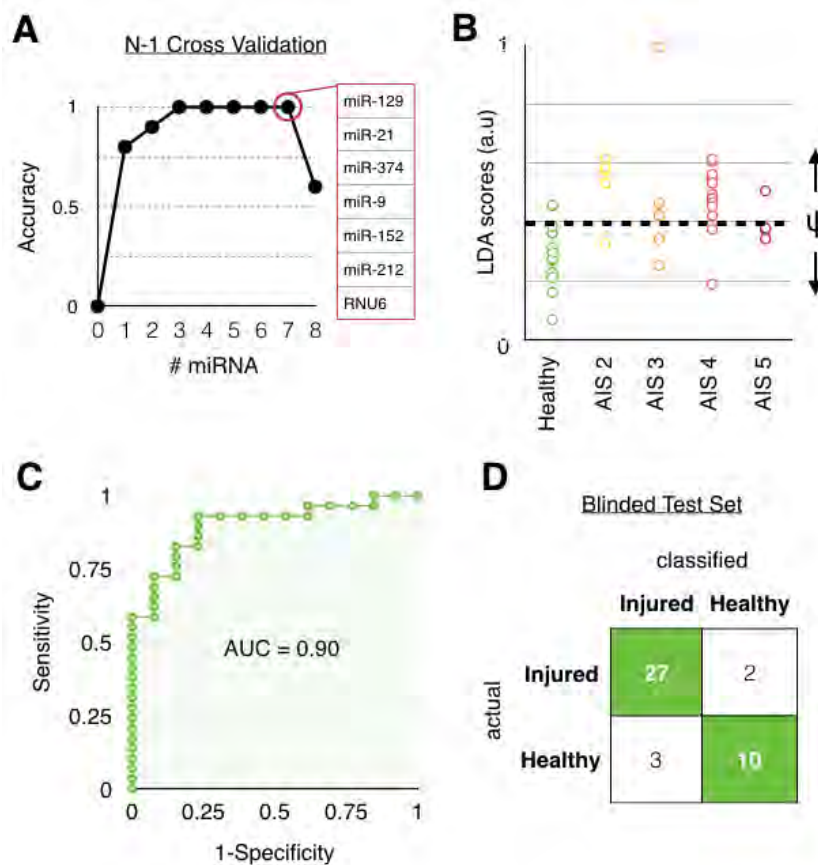


Figure 146 - TBI diagnosis using clinical samples. A. Stepwise regression on the training set using N-1 cross validation. Performance was evaluated as accuracy for different combination of markers. B. LDA score plot that shows distribution of individual samples from different categories (AIS2-5, healthy control). C. ROC curve for LDA analysis of healthy vs. AIS 2-5. AUC=0.90 was achieved for classification. D. Confusion matrix of a blinded test set that shows actual groups and classified groups for injured patients and healthy donors.

Discussion

In this work we demonstrate that brain-derived exosomes contain miRNA signatures that can be used to classify specific states of traumatic brain and recovery and to identify the primary signaling pathways activated in the brain after injury. Moreover, we showed that the precision of nanofluidic immunomagnetic exosome isolation can be applied to the enrichment of brain-derived exosomes directly from serum, and that this method can be successfully applied in both a murine model and clinical samples. Importantly, this work serves as a demonstration of the potential of identifying and using signatures of injury in a panel of biomarkers, rather than searching for a single marker with the specificity and understood biogenesis and mechanism to identify complex states of injury and recovery. We believe that by building on the approach described in this paper, there is enormous potential to guide treatment decisions for individuals with mTBI by monitoring recovery. Moreover, because our ExoTENPO approach miniaturizes exosome isolation into a handheld device and speeds up the isolation from half a day to less than an hour, there is great potential to translate this technology into a point-of-care device by pairing it with a miniaturized miRNA detection.(29, 30) In its most successful form, this technology can be used in the home for monitoring recovery and treatment effectiveness.(1) Additionally, a point-of-care device can be deployed to military and sports settings where rapid evaluation can help better evaluate and guide those with injuries to the help that they need.

In comparison to prior work isolating exosomes, our work has several key advantages: the ability to diagnose specific states of brain injury, the ability to uncover major pathways that are activated following injury, and the demonstration that these changes persist for much longer than simpler, exosome count estimates of injury. In comparison to size-based techniques, ExoTENPO can isolate subsets of exosomes that originate from specific tissue.(15) In this paper, this ability allows us to enrich for brain-derived exosomes from the vast background of other materials including other exosomes, microvesicles, and cell debris, and resolve the signatures of mTBI injury and recovery.(15, 31, 32)} The ExoTENPO differentiates itself from prior published(33, 34) and commercial work (e.g. Dynabeads, ThermoFisher) where surface marker specific isolation of exosomes is used. Chiefly, prior works have isolated exosomes onto bulk functionalized surfaces, where specificity is defined entirely by the capture antibody. In the ExoTENPO, because the feature size matches that of the exosomes, we can emulate what has been done for decades in microfluidics to sort cells(35, 36), and precisely balance the drag force and the magnetic capture force. Thus, analogous to flow cytometry, we can define a threshold number of magnetic nanoparticle labels required for an exosome to be captured on our device, allowing greatly improved specificity. This work builds on the work of others that have identified biomarkers to measure mTBI. We believe that a robust mTBI diagnostics could be developed by combining currently identified mTBI biomarkers to generate a signature using machine learning algorithms, rather than evaluating the performance of each biomarker individually. As shown in our study, even though we designed our study as an open-ended approach for biomarker discovery by performing RNA sequencing, the best miRNA marker was unable to achieve $AUC > 0.9$ whereas the combination of multiple miRNAs could achieve $AUC = 1$. Therefore, we think that there is a great opportunity developing machine learning based diagnostics for accurately predicting and tracking complex states of mTBI.

This study can be further developed by incorporating more than one ExoTENPO module to pull down multiple populations of exosomes - e.g. astrocytes, microglia, excitatory/inhibitory neurons, etc. - to capture an increasingly comprehensive picture of the recovery brain. In this

study, we used miRNA biomarkers identified from a single murine injury to identify miRNA implicated in injury and recovery. Building on this work, we plan to sequence a variety of injury types, severities, and states of recovery in both cohorts of mice and in humans. Our method combines three different components—novel isolation technology for brain-derived exosomes, biomarker discovery via small RNA sequencing, and machine learning based diagnostics—which enabled us to develop potential diagnostics for mTBI. Since exosomes are shed from almost all types of cells, our platform could be further utilized in different brain-related diseases or even in other diseases.

References

1. V. Y. Ma, L. Chan, K. J. Carruthers, Incidence, prevalence, costs, and impact on disability of common conditions requiring rehabilitation in the United States: stroke, spinal cord injury, traumatic brain injury, multiple sclerosis, osteoarthritis, rheumatoid arthritis, limb loss, and back pain, *Archives of physical medicine and rehabilitation* 95, 986–995 (2014).
2. R. A. Stern, D. O. Riley, D. H. Daneshvar, C. J. Nowinski, R. C. Cantu, A. C. McKee, Long-term consequences of repetitive brain trauma: chronic traumatic encephalopathy, *PMJ* 3, S460–S467 (2011).
3. C. B. Jeter, G. W. Hergenroeder, M. J. Hylin, J. B. Redell, A. N. Moore, P. K. Dash, Biomarkers for the diagnosis and prognosis of mild traumatic brain injury/concussion, *Journal of neurotrauma* 30, 657–670 (2013).
4. P. M. Kochanek, R. P. Berger, H. Bayr, A. K. Wagner, L. W. Jenkins, R. S. B. Clark, Biomarkers of primary and evolving damage in traumatic and ischemic brain injury: diagnosis, prognosis, probing mechanisms, and therapeutic decision making, *Current opinion in critical care* 14, 135–141 (2008).
5. H. Zetterberg, D. H. Smith, K. Blennow, Biomarkers of mild traumatic brain injury in cerebrospinal fluid and blood, *Nature Reviews Neurology* 9, 201–210 (2013).
6. A. C. McKee, R. C. Cantu, C. J. Nowinski, E. T. Hedley-Whyte, B. E. Gavett, A. E. Budson, V. E. Santini, H.-S. Lee, C. A. Kubilus, R. A. Stern, Chronic traumatic encephalopathy in athletes: progressive tauopathy after repetitive head injury, *Journal of Neuropathology & Experimental Neurology* 68, 709–735 (2009).
7. M. Bulut, O. Koksall, S. Dogan, N. Bolca, H. Ozguc, E. Korfali, Y. O. Ilcol, M. Parlak, Tau protein as a serum marker of brain damage in mild traumatic brain injury: preliminary results, *Advances in therapy* 23, 12–22 (2006).
8. K. De, JR, P. Leffers, P. P. C. A. Menheere, S. Meerhoff, A. Twijnstra, S-100B and neuron-specific enolase in serum of mild traumatic brain injury patients A comparison with healthy controls, *Acta neurologica scandinavica* 103, 175–179 (2001).
9. R. Diaz-Arrastia, K. K. W. Wang, L. Papa, M. D. Sorani, J. K. Yue, A. M. Puccio, P. J. McMahon, T. Inoue, E. L. Yuh, H. F. Lingsma, others, Acute biomarkers of traumatic brain injury: relationship between plasma levels of ubiquitin C-terminal hydrolase-L1 and glial fibrillary acidic protein, *Journal of neurotrauma* 31, 19–25 (2014).
10. R. P. Berger, P. D. Adelson, M. C. Pierce, T. Dulani, L. D. Cassidy, P. M. Kochanek, Serum neuron-specific enolase, S100B, and myelin basic protein concentrations after inflicted and noninflicted traumatic brain injury in children, *Journal of Neurosurgery: Pediatrics* 103, 61–68 (2005).
11. A. K. Wagner, H. Bayir, D. Ren, A. Puccio, R. D. Zafonte, P. M. Kochanek, Relationships between cerebrospinal fluid markers of excitotoxicity, ischemia, and oxidative damage after severe TBI: the impact of gender, age, and hypothermia, *Journal of neurotrauma* 21, 125–136 (2004).
12. J. B. Redell, A. N. Moore, I. I. I. Ward, Norman H, G. W. Hergenroeder, P. K. Dash, Human traumatic brain injury alters plasma microRNA levels, *Journal of neurotrauma* 27, 2147–2156 (2010).

13. J. A. Pineda, K. K. W. Wang, R. L. Hayes, Biomarkers of proteolytic damage following traumatic brain injury, *Brain Pathology* 14, 202–209 (2004).
14. N. B. Topal, B. Hakyemez, C. Erdogan, M. Bulut, O. Koksai, S. Akkose, S. Dogan, M. Parlak, H. Ozguc, E. Korfali, MR imaging in the detection of diffuse axonal injury with mild traumatic brain injury, *Neurological research* 30, 974–978 (2008).
15. J. Ko, E. Carpenter, D. Issadore, Detection and isolation of circulating exosomes and microvesicles for cancer monitoring and diagnostics using micro-/nano-based devices, *Analyst* (2015).
16. H. Shao, J. Chung, L. Balaj, A. Charest, D. D. Bigner, B. S. Carter, F. H. Hochberg, X. O. Breakefield, R. Weissleder, H. Lee, Protein typing of circulating microvesicles allows real-time monitoring of glioblastoma therapy, *Nature medicine* 18, 1835–1840 (2012).
17. J. Nilsson, J. Skog, A. Nordstrand, V. Baranov, L. Mincheva-Nilsson, X. O. Breakefield, A. Widmark, Prostate cancer-derived urine exosomes: a novel approach to biomarkers for prostate cancer, *British journal of cancer* 100, 1603–1607 (2009).
18. D. D. Taylor, C. Gercel-Taylor, Exosome platform for diagnosis and monitoring of traumatic brain injury, *Phil. Trans. R. Soc. B* 369, 20130503 (2014).
19. J. Ko, M. A. Hemphill, D. Gabrieli, L. Wu, V. Yelleswarapu, G. Lawrence, W. Pennycooke, A. Singh, D. F. Meaney, D. Issadore, Smartphone-enabled optofluidic exosome diagnostic for concussion recovery, *Scientific Reports* 6, (2016).
20. K.-A. Hyun, J. Kim, H. Gwak, H.-I. Jung, Isolation and enrichment of circulating biomarkers for cancer screening, detection, and diagnostics, *Analyst* 141, 382–392 (2016).
21. M. Beamer, S. R. Tummalala, D. Gullotti, C. Kopil, S. Gorka, T. Abel, R. Cameron, B. Morrison, A. S. Cohen, D. F. Meaney, others, Primary blast injury causes cognitive impairments and hippocampal circuit alterations, *Experimental neurology* 283, 16–28 (2016).
22. M. Muluneh, D. Issadore, Microchip-based detection of magnetically labeled cancer biomarkers, *Advanced drug delivery reviews* 66, 101–109 (2014).
23. J. Faure, G. Lachenal, M. Court, J. Hirrlinger, C. Chatellard-Causse, B. Blot, J. Grange, G. Schoehn, Y. Goldberg, V. Boyer, others, Exosomes are released by cultured cortical neurones, *Molecular and Cellular Neuroscience* 31, 642–648 (2006).
24. M. Muluneh, W. Shang, D. Issadore, Track-Etched Magnetic Micropores for Immunomagnetic Isolation of Pathogens, *Advanced healthcare materials* 3, 1078–1085 (2014).
25. J. Ko, V. Yelleswarapu, A. Singh, N. Shah, D. Issadore, Magnetic Nickel iron Electroformed Trap (MagNET): a master/replica fabrication strategy for ultra-high throughput (> 100 mL h⁻¹) immunomagnetic sorting, *Lab on a Chip* 16, 3049–3057 (2016).
26. T. A. Lusardi, J. A. Wolf, M. E. Putt, D. H. Smith, D. F. Meaney, Effect of acute calcium influx after mechanical stretch injury in vitro on the viability of hippocampal neurons, *Journal of neurotrauma* 21, 61–72 (2004).
27. N. Balakathiresan, M. Bhomia, R. Chandran, M. Chavko, R. M. McCarron, R. K. Maheshwari, MicroRNA let-7i is a promising serum biomarker for blast-induced traumatic brain injury, *Journal of neurotrauma* 29, 1379–1387 (2012).
28. A. Sharma, R. Chandran, E. S. Barry, M. Bhomia, M. A. Hutchison, N. S. Balakathiresan, N. E. Grunberg, R. K. Maheshwari, Identification of serum microRNA signatures for diagnosis of mild traumatic brain injury in a closed head injury model, *PloS one* 9, e112019 (2014).
29. A. Niemz, T. M. Ferguson, D. S. Boyle, Point-of-care nucleic acid testing for infectious diseases, *Trends in biotechnology* 29, 240–250 (2011).
30. J. Ping, R. Vishnubhotla, A. Vrudhula, A. T. C. Johnson, Scalable Production of High-Sensitivity, Label-Free DNA Biosensors Based on Back-Gated Graphene Field Effect Transistors, *ACS nano* 10, 8700–8704 (2016).

31. H. Im, H. Shao, Y. I. Park, V. M. Peterson, C. M. Castro, R. Weissleder, H. Lee, Label-free detection and molecular profiling of exosomes with a nano-plasmonic sensor, *Nature biotechnology* 32, 490–495 (2014).
32. G. Raposo, W. Stoorvogel, Extracellular vesicles: exosomes, microvesicles, and friends, *J Cell Biol* 200, 373–383 (2013).
33. S. S. Kanwar, C. J. Dunlay, D. M. Simeone, S. Negrath, Microfluidic device (ExoChip) for on-chip isolation, quantification and characterization of circulating exosomes, *Lab on a Chip* 14, 1891–1900 (2014).
34. M. He, J. Crow, M. Roth, Y. Zeng, A. K. Godwin, Integrated immunoisolation and protein analysis of circulating exosomes using microfluidic technology, *Lab on a Chip* 14, 3773–3780 (2014).
35. J. D. Adams, U. Kim, H. T. Soh, Multitarget magnetic activated cell sorter, *Proceedings of the National Academy of Sciences* 105, 18165–18170 (2008).
36. N. Xia, T. P. Hunt, B. T. Mayers, E. Alsberg, G. M. Whitesides, R. M. Westervelt, D. E. Ingber, Combined microfluidic-micromagnetic separation of living cells in continuous flow, *Biomedical Microdevices* 8, 299–308 (2006).